symmetry

Symmetry in Engineering Sciences II

Edited by
Raúl Baños and Francisco G. Montoya

Printed Edition of the Special Issue Published in *Symmetry*

MDPI

Symmetry in Engineering Sciences II

Symmetry in Engineering Sciences II

Editors

Raúl Baños
Francisco G. Montoya

Editors
Raúl Baños
University of Almeria
Spain

Francisco G. Montoya
University of Almeria
Spain

This is a reprint of articles from the Special Issue published online in the open access journal *Symmetry* (ISSN 2073-8994) (available at: https://www.mdpi.com/journal/symmetry/special_issues/Symmetry_Engineering_Sciences_II).

For citation purposes, cite each article independently as indicated on the article page online and as indicated below:

LastName, A.A.; LastName, B.B.; LastName, C.C. Article Title. *Journal Name* **Year**, *Article Number*, Page Range.

Contents

About the Editors

Raúl Baños is an associate professor with the Department of Engineering, University of Almeria (Spain). He received his first Bachelor's degree in Computer Science at the University of Almeria and his second Bachelor's degree in Economics by the National University of Distance Education (UNED). He wrote his Ph.D. dissertation on computational methods applied to optimization of energy distribution in power networks and water distribution networks. His research activities include computational optimization, engineering optimization, power systems, renewable energy systems, and energy economics. His research is being conducted at Napier University (Edinburgh, U.K.) and at the Universidade do Algarve (Portugal). As a result of his research, he has published more than 150 papers in peer-reviewed journals, books, and conference proceedings.

Francisco G. Montoya is a professor with the Engineering Department and the Electrical Engineering Section in the University of Almeria (Spain), received his M.S. from the University of Malaga and his Ph.D. from the University of Granada (Spain). He has published about 75 papers in JCR journals and is the author or co-author of books published by MDPI, RA-MA, and others. His main interests are power quality, smart metering, smart grids and evolutionary optimization applied to power systems, and renewable energy. Recently, he has become passionately interested in geometric algebra as applied to power theory.

Preface to "Symmetry in Engineering Sciences II"

Symmetry can be understood from two different perspectives: as a property or as a principle. The symmetry that can be observed in nature is a result of the symmetries of physical laws. The principles of symmetry have been used to solve mechanical problems since antiquity. Today, these principles are still being researched, for example, the property of crystal lattices in their spatial symmetry in chemical engineering or oscillators where the temporal symmetry can be observed in its periodic processes in electrical engineering. Due to the high complexity of engineering applications, the inherent symmetry is not easily recognizable; although, in certain cases, certain symmetry properties can be detected, these may be partial, whereas others may not be perceived. Some systems have imperfect symmetry characteristics that can be measured in terms of similarity, whereas non-symmetry is a measure of difference.

Therefore, many open research areas remain in engineering that need further research efforts to determine symmetrical and asymmetrical properties. This book includes recent theoretical or practical advances in symmetry in multidisciplinary engineering applications (electrical, mechanical, civil, etc.) so that readers can familiarize themselves with the new problems and methods directly explained by experts in the field.

Raúl Baños, Francisco G. Montoya
Editors

Editorial

Symmetry in Engineering Sciences II

Francisco G. Montoya *, Raúl Baños, Alfredo Alcayde and Francisco Manzano-Agugliaro

Department of Engineering, University of Almeria, ceiA3, 04120 Almeria, Spain; rbanos@ual.es (R.B.); aalcayde@ual.es (A.A.); fmanzano@ual.es (F.M.-A.)
* Correspondence: pagilm@ual.es; Tel.: +34-950-015791; Fax: +34-950-015491

Abstract: Symmetry can be understood in two different ways: as a property or as a principle. As Plato said, the symmetry that can be seen in nature is not random in itself, because it is a result of the symmetries of the physical laws. Thus, the principles of symmetry have been used to solve mechanical problems since antiquity. Today, these principles are still being researched; for example, in chemical engineering, the spatial symmetry properties of crystal lattices are being studied, or in electrical engineering, the temporal symmetry of the periodic processes of oscillators can be observed. This Special Issue is dedicated to symmetry in engineering sciences (electrical, mechanical, civil, and others) and aims to cover both engineering solutions related to symmetry and the search for patterns to understand the phenomena observed.

1. Introduction

Symmetry is a common standard that is extensively studied in various areas of research. In particular, complex systems with symmetric and asymmetric properties have emerged in the engineering sciences. For example, the study of asymmetric and symmetric failures in power systems is a fundamental issue in electrical engineering. Symmetrical and synchronized systems are often used to meet the stability criteria of rotating structures in mechanical engineering. On the other hand, in telecommunications engineering, since the speed or the amount of data is the same in both directions, many systems are symmetrical. In civil engineering, the stability of objects depends on symmetry, and there have been studies of the equilibrium statics of structures. Moreover, as a final example, symmetric network structures and symmetric algorithms are usually studied in computer engineering. In this Special Issue, researchers are invited to submit innovative scientific papers and review contributions related to all engineering fields in which symmetry is considered in theory or practice. The topics of interest include symmetry in:

- Electrical engineering: power, electronics, electromechanics, computer, control, microwaves, telecommunications, etc.
- Mechanical engineering: acoustical, aerospace, automotive, marine, railway, thermal, etc.
- Civil engineering: architectural, construction, earthquakes, environmental, hydraulics, mining, structural, transportation, etc.
- Chemical engineering: biochemical, molecular, processes, thermodynamics, etc.
- Other interdisciplinary engineering disciplines: agricultural, biomedical, graphical modeling, industrial, information, materials, metallurgy, military, nanotechnology, control, automation, robotics, etc.
- Topology of complex networks in engineering.

2. Publication Statistics

Details of the call for papers for this Special Issue regarding the articles that were published or rejected are follows: number of articles submitted (26), rejected (10; 38.5%), and published (16; 61.5%).

The regional distribution of authors by countries for the published articles is presented in Table 1, in which it is possible to observe that 74 authors were included, from seven countries. Note that it is usual for an item to be signed by more than one author and for authors to be collaborating with others from different affiliations. The mean number of authors per published manuscript was between four and five.

Table 1. Regional distribution of authors by country.

Country	Number of Authors
China	47
Spain	15
Pakistan	8
Australia	1
USA	1
Germany	1
Taiwan	1
Total	74

3. Authors' Affiliations

This Special Issue's authors and their first affiliations are reflected in Table 2.

Table 2. Authors' affiliations.

Author	First Affiliation	Reference
Gómez–Déniz, E.	University of Las Palmas de Gran Canaria	[1]
Gómez, L.	University of Las Palmas de Gran Canaria	[1]
Zhang, F.	Shanghai University	[2]
Chen, S.	Chinese Academy of Sciences	[2]
He, Y.	Shanghai University	[2]
Ye, G.	Ningbo Ruyi Joint Stock Co	[2]
Zhang, C.	Chinese Academy of Sciences	[2]
Yang, G.	Chinese Academy of Sciences	[2]
Shang, X.	University of Mining and Technology	[3]
Zhang, Z.	University of Mining and Technology	[3]
Su, J.	Beijing Jiaotong University	[4]
Jie, Y.	Beijing Jiaotong University	[4]
Niu, X.	Beijing Municipal Engineering Research Institute	[4]
Liu, C.	Beijing Jiaotong University	[4]
Liu, X.	Beijing Jiaotong University	[4]
Velázquez, J.S.	Technical University of Cartagena	[5]
Cavas, F.	Technical University of Cartagena	[5]
Bolarín, J.M.	Miguel Hernández University	[5]
Alió, J.L.	Miguel Hernández University	[5]
Zhang, S.	Zaozhuang University	[6]
Sun, Z.	Zaozhuang University	[6]
Lu, J.	Zaozhuang University	[6]
Li, L.	Zaozhuang University	[6]
Yu, C.	Zaozhuang University	[6]
Cao, D.	Hebei University of Technology	[6]
García–Vallejo, D.	Universidad de Sevilla	[7]
Alcayde, A.	Universidad de Almeria	[7]

Table 2. *Cont.*

Author	First Affiliation	Reference
López-Martínez, J.	Universidad de Almeria	[7]
Montoya, F.G.	Universidad de Almeria	[7]
Wang, S.	Nanjing University of Aeronautics and Astronautics	[8]
Wang, X.	Nanjing University of Aeronautics and Astronautics	[8]
Wang, Y.	Beihang University	[8]
Ye, H.	Beihang University	[8]
Qin, H.	Beihang University	[9]
Wu, Z.	Beihang University	[9]
Li, Y.	China University of Mining and Technology	[10]
Dai, S.	Stevens Institute of Technology	[10]
Zhao, L.	China University of Mining and Technology	[10]
Yan, X.	China University of Mining and Technology	[10]
Shi, Y.	Stevens Institute of Technology	[10]
Alcayde, A.	Universidad de Almeria	[11]
Velilla, C.	Universidad Politécnica de Madrid	[11]
San Antonio–Gómez, C.	Universidad Politécnica de Madrid	[11]
Peña–Fernández, A.	Universidad de Almeria	[11]
Pérez–Romero, A.	Universidad de Sevilla	[11]
Manzano–Agugliaro, F.	Universidad de Almeria	[11]
Niu, K.	Beijing Jiaotong University	[12]
Liu, J.	Beijing Jiaotong University	[12]
Wang, Y.	Beijing Jiaotong University	[12]
Hanif, M.H.	Pakistan Institute of Engineering & Technology	[13]
Adnan, M.	Pakistan Institute of Engineering & Technology	[13]
Shah, S.A.R.	Pakistan Institute of Engineering & Technology	[13]
Khan, N.M.	Pakistan Engineering Council	[13]
Nadeem, M.	Pakistan Institute of Engineering & Technology	[13]
Javed, J.	Pakistan Institute of Engineering & Technology	[13]
Akbar, M.W.	Pakistan Institute of Engineering & Technology	[13]
Farooq, A.	Pakistan Institute of Engineering & Technology	[13]
Waseem, M.	University of Bayreuth	[13]
Yang, K.	Chinese Academy of Sciences	[14]
Yang, G.	Chinese Academy of Sciences	[14]
Chen, S.L.	Chinese Academy of Sciences	[14]
Wang, Y.	Chinese Academy of Sciences	[14]
Zhang, C.	Chinese Academy of Sciences	[14]
Fang, Z.	Chinese Academy of Sciences	[14]
Zheng, T.	Chinese Academy of Sciences	[14]
Wang, C.	Chinese Academy of Sciences	[14]
Zhang, L.	Beijing Jiaotong University	[15]
Feng, X.	Guangxi Traffic Technician College	[15]
Yang, Y.	Beijing Jiaotong University	[15]
Ding, C.	Beijing Jiaotong University	[15]
Su, G.D.	Fuqing Branch of Fujian Normal University	[16]
Chang, C.C.	Feng Chia University	[16]
Lin, C.C.	Providence University	[16]

4. Topics

Table 3 summarizes the research carried out by identifying the topics to which the manuscripts belong, according to the proposed topics in the Special Issue. It was noted that the topic of symmetry within two particular fields has come to dominate the rest: electrical engineering and civil engineering.

Table 3. Symmetry topics.

Symmetry in	Number of Manuscripts
Electrical Engineering	2
Mechanical Engineering	6
Civil Engineering	4
Chemical Engineering	0
Other Interdisciplinary Engineering Disciplines	2
Topology of Complex Networks in Engineering	2
Total	

References

1. Gómez-Déniz, E.; Gómez, L. The rayleigh birnbaum saunders distribution: A general fading model. *Symmetry* **2020**, *12*, 389. [CrossRef]
2. Zhang, F.; Chen, S.-L.; He, Y.; Ye, G.; Zhang, C.; Yang, G. A Kinematic Calibration Method of a 3T1R 4-Degree-of-Freedom Symmetrical Parallel Manipulator. *Symmetry* **2020**, *12*, 357. [CrossRef]
3. Shang, X.; Zhang, Z. Elastic-plastic-damaged zones around a deep circular wellbore under non-uniform loading. *Symmetry* **2020**, *12*, 323. [CrossRef]
4. Su, J.; Jie, Y.; Niu, X.; Liu, C.; Liu, X. Mechanical behavior of tunnel lining with cracks at different positions. *Symmetry* **2020**, *12*, 194. [CrossRef]
5. Velázquez, J.; Cavas, F.; Bolarín, J.M.; Alió, J. 3D Printed personalized corneal models as a tool for improving patient's knowledge of an asymmetric disease. *Symmetry* **2020**, *12*, 151. [CrossRef]
6. Zhang, S.; Sun, Z.; Lu, J.; Li, L.; Yu, C.; Cao, D. Spring effects on workspace and stiffness of a symmetrical cable-driven hybrid joint. *Symmetry* **2020**, *12*, 101. [CrossRef]
7. García-Vallejo, D.; Alcayde, A.; Lopez, J.; Montoya, F.G. Detection of communities within the multibody system dynamics network and analysis of their relations. *Symmetry* **2019**, *11*, 1525. [CrossRef]
8. Wang, S.; Wang, X.; Wang, Y.; Ye, H. An equivalent damping numerical prediction method for the ring damper used in gears under axial vibration. *Symmetry* **2019**, *11*, 1469. [CrossRef]
9. Qin, H.; Wu, Z. Angle Tracking observer with improved accuracy for resolver-to-digital conversion. *Symmetry* **2019**, *11*, 1347. [CrossRef]
10. Li, Y.; Dai, S.; Zhao, L.; Yan, X.; Shi, Y. Topological design methods for mecanum wheel configurations of an omnidirectional mobile robot. *Symmetry* **2019**, *11*, 1268. [CrossRef]
11. Alcayde, A.; Velilla, C.; San-Antonio-Gómez, C.; Peña, A.; Pérez-Romero, A.; Manzano-Agugliaro, F. Basket-handle arch and its optimum symmetry generation as a structural element and keeping the aesthetic point of view. *Symmetry* **2019**, *11*, 1243. [CrossRef]
12. Niu, K.; Liu, J.; Wang, Y. Research methodology: Application of railway luggage and package transportation scheme formulation based on a dynamic time–space service network. *Symmetry* **2019**, *11*, 1226. [CrossRef]
13. Hanif, M.H.; Adnan, M.; Shah, S.A.R.; Khan, N.M.; Nadeem, M.; Javed, J.; Akbar, M.W.; Farooq, A.; Waseem, M. Rainfall runoff analysis and sustainable soil bed optimization engineering process: Application of an advanced decision-making technique. *Symmetry* **2019**, *11*, 1224. [CrossRef]
14. Yang, K.; Yang, G.; Chen, S.-L.; Wang, Y.; Zhang, C.; Fang, Z.; Zheng, T.; Wang, C. Study on stiffness-oriented cable tension distribution for a symmetrical cable-driven mechanism. *Symmetry* **2019**, *11*, 1158. [CrossRef]

15. Zhang, L.; Feng, X.; Yang, Y.; Ding, C. Ding routing for hazardous materials transportation in urban areas. *Symmetry* **2019**, *11*, 1091. [CrossRef]
16. Su, G.-D.; Chang, C.-C.; Lin, C.-C. High-precision authentication scheme based on matrix encoding for AMBTC-compressed images. *Symmetry* **2019**, *11*, 996. [CrossRef]

Article

The Rayleigh Birnbaum Saunders Distribution: A General Fading Model

Emilio Gómez–Déniz [1],* and Luis Gómez [2]

[1]   Department of Quantitative Methods and Institute of Tourism and Sustainable Economic Development (TIDES), University of Las Palmas de Gran Canaria, 35017 Las Palmas, Spain
[2]   Electronic Engineering and Automatic Department, University of Las Palmas de Gran Canaria, 35017 Las Palmas, Spain; luis.gomez@ulpgc.es
*   Correspondence: emilio.gomez-deniz@ulpgc.es

Abstract: A new compound non-symmetric distribution for modeling arbitrary fading-shadowing wireless channels is introduced and studied here. This distribution has some advantages in front of other well-known non-symmetric fading distributions such as the Rayleigh–lognormal distribution and the K distribution especially in the tails. We give closed-form expressions for the average BER of DPSK and MSK when the new distribution is used. Applications to compare how the new distribution works in comparisons with the Rayleigh–lognormal, K distributions and others recently proposed in the literature of fading channel are also provided.

Keywords: bit error rate; birnbaum saunders distribution; fading channels, average channel capacity

1. Introduction

Systems of mobile communications rising to the challenge of the 5G framework demand high data rates at a low latency [1,2]. This new communication paradigm includes device-to-device, vehicular communications, machine-to-machine as well as *traditional* communications provided by ground base stations. Such mobile systems face several challenges that degrade signal strength. Among them, fading is the more relevant and it has been widely researched in past decades. Generally speaking, fading refers to the interference of multiple scattered radio paths (*radio waves*) between the base station (ground base station or another emitter) and the vicinity of the mobile receptor. As mentioned above, this definition is now enhanced to account for the new device-to-device communication systems, although in this case, new constraints hold (because the channels are symmetric from left-to-right and right-to-left, they become indistinguisable). Due to signal fading, the received signal at the device exhibits fast signal level fluctuations which are normally Rayleigh distributed. The direct consequence of fading is the complete loss of signal (or a large decrease of the received power).

In a simplified manner, although the emitter emits a unique wave (a ray), the received radio signal is composed of the superposition of the set of many waves (randomly distributed) that come from the multiple dispersion experimented by the original wave. Each of these scattered waves may have a different amplitude and phase. Therefore, what was originally a single path channel is now transformed into a multichannel one. This complex channel can be modeled as a truly physical communication channel characterized by its bandwidth and gain (see the seminal work by Beckmann [3] for a complete description of modeling of multi-path channels). For the common case of a mobile radio channel characterized by a constant gain and a linear phase response across the bandwidth greater than the bandwidth of the

transmitted signal (common real situation), the signal at the terminal will show what is known as *flat fading*, which is the most common and consequently the most researched [4]. Due to fading, the strength of the received signal will show oscillations (even very fast oscillations) in time caused by the multi-path effects.

Figure 1 shows a simplified fading model for a stationary source (emitter at ground base station) and a mobile receptor (*vehicle*) where several signal components are involved (see a complete description of fading modeling in [4–7]). A similar figure can be used to account for device-to-device 5G mobile terminals. First, for the case of clear line of sight between stationary source (emitter) and moving receptor, no scattering mechanism would be involved, although Doppler effects would be taken into account. Moreover, the multi-path component, also known as the diffuse component (phase-incoherent wave) is caused by the several (*random*) reflections (*scattering processes*) of the signal with scattered elements such as buildings and mountains or other elements (vehicles, people...). This component exhibits little directivity and its magnitude is usually assumed to be Rayleigh distributed, while its phase is distributed uniformly. The other component shown in this figure is the specular component: a phase-coherent ground-reflected wave caused by close points to where the receptor (moving vehicle in this case) is dynamically located [8]. It is responsible for deep fades (probable critical loss of signal power), with its amplitude comparable to the one for the direct component, although its phase is opposite [9].
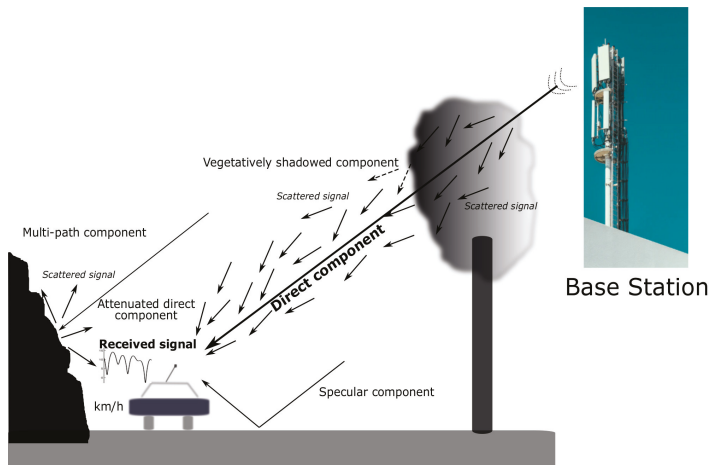
Figure 1. Illustration of fading components.

In the same figure, the case of blocked line of sight between the stationary source (*emitter*) and the mobile receptor is also shown. In this case, the diffuse component shows a similar behavior than before (and it can be also modeled by a Rayleigh distribution based on the assumption of a sufficiently large number of received waves at mobile terminal), but a new component appears: the shadowed direct component. This component is due to the scattering of the signal by branches, leaves, and limbs of nearby trees and surrounded vegetation in general. This scattering mechanism is indeed very complex to model. As a consequence of that, the signal is attenuated. The amount of signal attenuation depends on the length of the path of the signal through the scattered element (tree, bushes, etc.). The fading related to this process is known as fading-shadowing and it may be suitably modeled by the Rayleigh–lognormal distribution (RLN in advance) [10] which has a difficult integral form. It can be better modeled by the well-known K

distribution [11]. The K distribution is indeed a Rayleigh distribution with a gamma distribution, and it has a simpler form than the RLN.

In this paper, we focus on the fast fading-shadowing mechanisms. Furthermore, as our work also includes the Rayleigh as a general case, it also may be applied to dealing with the diffuse component.

From above, it is clear that a precise characterization of the received radio signal is not possible and, as the nature of the wireless channel is random, statistical characterization through suitable probability density distributions is required [12]. For a given probability distribution aiming to efficiently model fading effects, it is desirable for it to be expressed by means of simple mathematical formulas and it shall embed the Rayleigh distribution as a particular case. This latter condition comes from the fact that Rayleigh modeling of scattered signal resembles as the natural approach for multi-path fading modeling and it provides a direct physical explanation for parameters involved (signal phase and signal power). For such fading distributions, the estimation of parameters is easy, and metrics commonly used to characterize fading effects (LCR, level crossing-rate, AFD, average fade duration, BER, average bit error rate, DPSK, differential phase-shift keying or MSK, minimum shift keying) are also easily obtained (see [13–15]), for a thorough explanation of these well-known quality indices for measuring channel capacity and reliability).

Since the work provided by Beckmann [3] to describe the statistical fading envelope (summation of all scattered waves) of the received signal, a plethora of distributions in this setting has been proposed. As seen from the revision of related works, such statistical models span from classical distributions such as the Rayleigh (see a review of fading channels modeled by using the Rayleigh distribution in [16]) to new ones, such as the Nakagami distribution [17,18], also including joint distributions such as the Rayleigh–lognormal [19] or other distributions [20,21].

In [22], a new two-parameter fading distribution, the SR (Slashed Rayleigh), was proposed. This distribution naturally includes the Rayleigh distribution as a particular case when one of its two parameters is reasonably large, thus facilitating the physical modeling of multi-path signal propagation by suitable phasors (complex signal representation). The SR fading distribution is competitive with the Rayleigh–lognormal distribution and the K distribution.

In this work, we present the two-parameter compound distribution RBS (Rayleigh Birnbaum Saunders) for multi-path fading modeling. This distribution has some advantages in front of the Rayleigh–lognormal distribution and the K distribution, especially in the tails. We give closed-form expressions for the average BER of DPSK and MSK when the new distribution is used. We complete the description of the RBS distribution by explaining how to simulate it by means of Monte Carlo analysis, and what is mandatory for a fading distribution, by simulating it as a summation of phasors also including Doppler effects (that is, a physical description) by suitable embedding of the RBS distribution into the well-known Clarke's model [4] for flat fading.

We remark that although fading effects are more noticeable for mobile communications (i.e., people in urban areas quiet or moving), fading is more remarkable for land mobile vehicles because, as they are travelling faster, most received signal is due to multi-path components instead of the direct component. However, for a stationary receiver (for instance, working with a tablet), if the surrounding objects are moving faster than the mobile terminal, Doppler shift on multi-path components may significantly influence the transmitted signal quality. Therefore, the models discussed in this work are also valid for both situations: stationary receptor and moving receptor.

The outline of this paper is as follows. A catalog of the distribution functions usually used in this setting is provided in Section 2. This Section also includes the Birnbaum Saunders distribution and its more important properties. The proposed new fading model is provided in Section 3. Section 4 is concerned with most important measures of interest in the setting of a fading channel, such as the channel capacity, the AF and the BER for DPSK and MSK when the distribution introduced here is used for fading channel

modeling. Comparisons with other distributions usually used in the setting of fading channel are given in Section 5. Simulation results are provided in Section 6, and conclusions are in the last Section.

2. Background

Rayleigh fading is a reasonable model when there are many objects in the environment that scatter the radio signal before it arrives at the receiver. The central limit theorem holds that if there is sufficient scatter, the channel impulse response will be well modeled as a Gaussian process irrespective of the distribution of the individual components. If there is no dominant component to the scatter, then such a process will have zero mean and phase uniformly distributed between 0 and 2π radians. The envelope of the channel response will therefore be Rayleigh distributed, with probability density function (pdf)

$$g_R(r;\theta) = \frac{r}{\theta}\exp\left\{-\frac{r^2}{2\theta}\right\}, \quad r \geq 0, \tag{1}$$

where $E(R^2) = 2\theta$ is the expected value of R^2 being $\theta \in \Theta = (0,\infty)$. In this case we will write $R \sim R(\theta)$.

As Tse ([23] p. 49) has pointed out, [sic] *the model based on the Rayleigh fading, is quite reasonable for scattering mechanisms where there are many small reflectors, but is adopted primarily for its simplicity in typical cellular situations with a relatively small number of reflectors.* Due to the fact that several alternatives to Rayleigh fading have been proposed in the literature, some of them will be shown next. The Rayleigh–lognormal distribution (RLN) with pdf is given by [10,24]

$$f_X(x) = \int_0^\infty \frac{x}{\sigma}\frac{\exp\left(-x^2/(2\sigma)\right)}{\sigma\sqrt{2\pi\lambda^2}}\exp\left[-\frac{(\log\sigma - \mu)^2}{2\lambda^2}\right]d\sigma, \quad \lambda > 0, \mu \in \mathbb{R}.$$

The Rayleigh-Gamma distribution (K distribution) [11] obtained by compounding a Rayleigh distribution with a gamma distribution is similar to the RLN distribution but it has a simpler form and its pdf admits a closed form but, due to the Bessel function, the estimates of the parameters are not direct. Its pdf is given by,

$$f_X(x) = \frac{2}{a\,\Gamma(b+1)}\left(\frac{x}{2a}\right)^{b+1}K_b\left(\frac{x}{a}\right), \quad x \geq 0, a > 0, b > -1,$$

with $\Gamma(\cdot)$ being the usual gamma function and

$$K_\nu(z) = \left(\frac{z}{2}\right)^\nu\frac{\sqrt{\pi}}{\Gamma(\nu + \frac{1}{2})}\int_1^\infty(\tau^2 - 1)^{\nu-1/2}\exp(-z\tau)\,d\tau$$

denoting the modified Bessel function of the second kind of order ν and argument z.

The Rayleigh-inverse Gaussian (RIG) distribution has pdf given by

$$f_X(x) = \sqrt{\frac{2\kappa}{\pi}}x\exp(\kappa/\delta)\left[\frac{(x^2+\kappa)\delta^2}{\kappa}\right]^{-3/4}K_{-\frac{3}{2}}\left(\frac{1}{\delta}\sqrt{\kappa(x^2+\kappa)}\right), \quad x > 0,$$

with $\kappa > 0$ and $\delta > 0$.

The generalized Rayleigh distribution (GR in advance), built as a mixture of the Rayleigh distribution with a geometric one, proposed in [25], has pdf given by

$$f_X(x) = \frac{(1+\vartheta)x}{\omega}\frac{\exp(x^2/(2\omega))}{[(1+\vartheta)\exp(x^2/(2\omega)) - \vartheta]^2}, \quad x > 0,$$

with $\vartheta > 0$ and $\omega > 0$.

Finally, we consider the Slash-Rayleigh distribution (SR), recently proposed by [22] which has the pdf given by

$$f_X(x) = \frac{qx \exp(-r^2/(2\sigma))}{\sigma(q+2)} {}_1F_1\left(1; \frac{q}{2}+2; \frac{x^2}{2\sigma}\right), \ x > 0,$$

where $q > 0$, $\sigma > 0$ and ${}_1F_1$ represents the Kummer confluent hypergeometric function.

It is interesting to note that this special function appears in most of the statistical packages available the market, such as R, MATLAB and Mathematica, which has been widely used in this work (see [26]). Other alternatives based on the lognormal distribution apart of the RLN distribution, which will not be used here, are the Rayleigh-inverse Gaussian distribution (RIG) [27] with the same restriction as the above distribution and the generalization of the Rayleigh distribution proposed recently by [25], which overcomes many of the disadvantages of the mentioned distributions.

The Birnbaum Saunders Distribution

From the pioneering work about the Birnbaum Saunders distribution proposed by [28,29] a lot of works about this distribution have been proposed in the statistical and applied statistical literature. For a comprehensive reading of this distribution see [30]. The distribution was introduced in the context of fatigue life problems although today it is applied in very different contexts. A continuous random variable X follows a Birnbaum Saunders distribution with parameters $\alpha > 0$ and $\beta > 0$ if its pdf is given by

$$\pi_X(x; \alpha, \beta) = \frac{1 + x\beta}{2\alpha\sqrt{x^3\beta}} \phi\left(\frac{x\beta - 1}{\alpha\sqrt{x\beta}}\right), \quad x > 0, \tag{2}$$

where $\phi(z) = (1/\sqrt{2\pi}) \exp(-z^2/2)$ represents the pdf of the standard normal distribution. The raw k-moment of the distribution is given by

$$E(X^k; \alpha, \beta) = \frac{\exp(\alpha^{-2})}{2\alpha\beta^k\sqrt{2\pi}} \left[K_{k-\frac{1}{2}}(\alpha^{-2}) + K_{k+\frac{1}{2}}(\alpha^{-2})\right], \tag{3}$$

from which we get the mean and variance of (2) given by

$$E(X) = \frac{2 + \alpha^2}{2\beta},$$
$$var(X) = \frac{\alpha^2(4 + 5\alpha^2)}{4\beta^2},$$

respectively, while the cumulative distribution function, $\Pi(x) = \Pr(X \leq x)$, is given by

$$\Pi(x) = \Phi\left(\frac{1 - x\beta}{\alpha\sqrt{x\beta}}\right),$$

where $\Phi(\cdot)$ is the survival function of the standard normal distribution. The moment generating function is given by

$$M_X(t) = \frac{1}{2}\left(1 + \frac{1}{\mathcal{T}_{t,\alpha,\beta}}\right) \exp\left[\frac{1 - \mathcal{T}_{t,\alpha,\beta}}{\alpha^2}\right], \tag{4}$$

where $\mathcal{T}_{t,\alpha,\beta} = \sqrt{1 - 2t\alpha^2/\beta}$.

3. The Proposed Fading Channel Model

The compound distribution proposed here is obtained by compounding the Rayleigh distribution given in (1) with the Birnbaum Saunders distribution provided in (2) and has pdf (see details in the Appendix A) given by

$$f_R(r;\alpha,\beta) = \frac{r\beta\left[\varphi_{\alpha,\beta}(r)(1 + \varphi_{\alpha,\beta}(r)) + \alpha^2\right]}{2\left[\varphi_{\alpha,\beta}(r)\right]^3}\exp\left[\frac{1 - \varphi_{\alpha,\beta}(r)}{\alpha^2}\right], \tag{5}$$

where $\varphi_{\alpha,\beta}(r) = \sqrt{1 + \beta(r\alpha)^2}$. In what follows, when a random variable R follows this distribution it will be written as $R \sim RBS(\alpha,\beta)$ to denote that the distribution is obtained by compounding the classical Rayleigh distribution with the Birnbaum Saunders distribution.

The new distribution is unimodal with a modal value being the solution of the equation

$$\frac{1}{r} + \frac{r\alpha^2\beta}{\varphi_{\alpha,\beta}(r)}\left[\frac{1 + 2\varphi_{\alpha,\beta}(r)}{\varphi_{\alpha,\beta}(r)(1 + \varphi_{\alpha,\beta}(r)) + \alpha^2} - \frac{1}{\alpha^2} - \frac{3}{\varphi_{\alpha,\beta}(r)}\right] = 0$$

Some graphics of the pdf of the $RBS(\alpha,\beta)$ distribution are shown in Figure 2 where the dependency of the scale parameter α and the shape parameters β (the fading) can be appreciated.
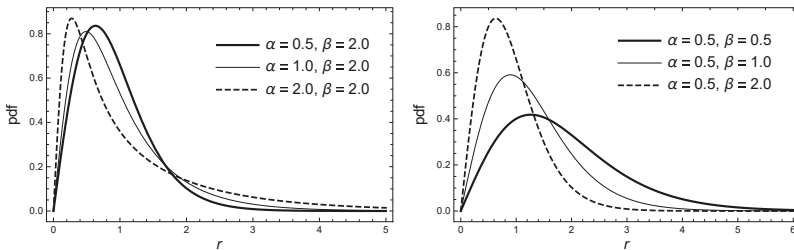
Figure 2. Probability density function of the $RBS(\alpha,\beta)$ distribution for different parameter values.

Additional Features

The survival function (the probability that the envelope of the received signal does not exceed a specified value of r), $\bar{F}_R(r) = \Pr(R > r)$ of $R \sim RBS(\alpha,\beta)$ is given by (see the Appendix A)

$$\bar{F}_R(r;\alpha,\beta) = \frac{1 + \varphi_{\alpha,\beta}(r)}{2\varphi_{\alpha,\beta}(r)}\exp\left[\frac{1 - \varphi_{\alpha,\beta}(r))}{\alpha^2}\right],$$

which can be used to get the hazard function of the random variable $R \sim RBS(\alpha,\beta)$, given by

$$h_R(r;\alpha,\beta) = \frac{r\beta}{\varphi_{\alpha,\beta}(r)}\left[1 + \frac{\alpha^2}{\varphi_{\alpha,\beta}(r)\left(1 + \varphi_{\alpha,\beta}(r)\right)}\right]. \tag{6}$$

Some plots of the hazard rate function in (6) are displayed in Figure 3 for special cases of parameters.

Let $R \sim RBS(\alpha, \beta)$. Then, for $k = 1, 2, \ldots$ and $q > k$, it follows that k-th moment of the proposed distribution is given by

$$E(R^k; \alpha, \beta) = \Gamma\left(1 + \frac{k}{2}\right)\left(\frac{2}{\beta}\right)^{k/2}\left[K_{\frac{1+k}{2}}(\alpha^{-2}) + K_{\frac{1-k}{2}}(\alpha^{-2})\right]\exp(\alpha^{-2}), \tag{7}$$

which can be obtained by compounding taking into account that the kth moment of the Rayleigh distribution are given by

$$E(R^k; \theta) = (2\theta)^{k/2}\Gamma\left(1 + \frac{k}{2}\right), \quad k = 1, 2, \ldots$$
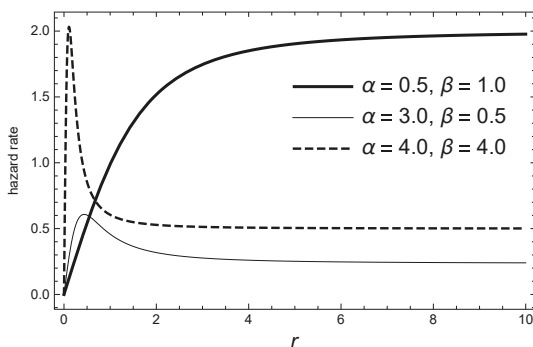
Figure 3. Illustration of the hazard rate function of $RBS(\alpha, \beta)$ distribution for a set of different parameter values.

Therefore, by using (7) we get the mean and the second raw moment of the distribution, which are given by

$$E_R(R; \alpha, \beta) = \frac{\exp(\alpha^{-2})}{2\alpha\sqrt{\beta}}\left[K_0(\alpha^{-2}) + K_1(\alpha^{-2})\right], \tag{8}$$

$$E_R(R^2; \alpha, \beta) = \frac{2 + \alpha^2}{\beta}, \tag{9}$$

respectively. Now, the variance can be obtained directly from (8) and (9). Maximum likelihood estimation can be obtained by maximizing the log-likelihood function, which is proportional to

$$\begin{aligned}\ell(\alpha, \beta; \bar{r}) \quad \propto \quad & n\log\beta + \sum_{i=1}^{n}\log\left[\varphi_{\alpha,\beta}(r_i)(1 + \varphi_{\alpha,\beta}(r_i)) + \alpha^2\right] \\ & -3\sum_{i=1}^{n}\log\varphi_{\alpha,\beta}(r_i) + \sum_{i=1}^{n}\frac{1 - \varphi_{\alpha,\beta}(r_i)}{\alpha^2}\end{aligned} \tag{10}$$

where n is the size of the sample $\tilde{r} = (r_1, \ldots, r_n)$. Thus, the estimators of the parameters can be obtained by solving the equations,

$$
\begin{aligned}
\frac{\partial \ell(\alpha, \beta; \tilde{r})}{\partial \alpha} &= \sum_{i=1}^{n} \frac{\varphi_{\alpha,\beta}^{\alpha}(r_i)(1 + 2\varphi_{\alpha,\beta}(r_i)) + 2\alpha}{\varphi_{\alpha,\beta}(r_i)(1 + \varphi_{\alpha,\beta}(r_i)) + \alpha^2} - 3\sum_{i=1}^{n} \frac{\varphi_{\alpha,\beta}^{\alpha}(r_i)}{\varphi_{\alpha,\beta}(r_i)} \\
&\quad - \frac{1}{\alpha^3}\sum_{i=1}^{n}\left[\alpha \varphi_{\alpha,\beta}^{\alpha}(r_i) + 2(1 - \varphi_{\alpha,\beta}(r_i))\right] = 0,
\end{aligned}
$$

$$
\begin{aligned}
\frac{\partial \ell(\alpha, \beta; \tilde{r})}{\partial \beta} &= \frac{n}{\beta} + \sum_{i=1}^{n} \frac{\varphi_{\alpha,\beta}^{\beta}(r_i)(1 + 2\varphi_{\alpha,\beta}(r_i)) + 2\alpha}{\varphi_{\alpha,\beta}(r_i)(1 + \varphi_{\alpha,\beta}(r_i)) + \alpha^2} - 3\sum_{i=1}^{n} \frac{\varphi_{\alpha,\beta}^{\beta}(r_i)}{\varphi_{\alpha,\beta}(r_i)} \\
&\quad - \frac{1}{\alpha^2}\sum_{i=1}^{n} \varphi_{\alpha,\beta}^{\beta}(r_i) = 0,
\end{aligned}
$$

where

$$
\varphi_{\alpha,\beta}^{\alpha}(r_i) = \frac{2\beta \alpha r_i^2}{\varphi_{\alpha,\beta}(r_i)}, \qquad \varphi_{\alpha,\beta}^{\beta}(r_i) = \frac{2\alpha^2 r_i^2}{\varphi_{\alpha,\beta}(r_i)}
$$

are the partial derivatives of $\varphi_{\alpha,\beta}(r_i)$ with respect to α and β, respectively.

Furthermore, since the RBS distribution can be represented as a mixture (compound) of the Rayleigh distribution and the Birnbaum Saunders distribution, this representation of the distribution also facilitates parameter estimation via the Expectation Maximization (EM) algorithm.

4. The RBS Channel Phasor

In this section, we demonstrate that the RBS distribution can be obtained as an exact sum of mutually independent Gaussian stochastic processes, as is required for the simulation of the fading channel, i.e., to estimate the signal envelope.

Rayleigh fading envelopes can be generated from the zero-mean complex Gaussian random variables. Other fading distributions (see for instance [31] for the Nakagami-m case) and the generalized Rayleigh distribution in [25] can also be obtained in a similar manner after some mathematical considerations. Following those works, it is necessary to prove that the phase of a given propagating signal is uniformly distributed in the interval $[0, 2\pi]$ and that the amplitude follows a RBS distribution.

Following (Beckmann [3] p. 118),

$$
S = Re^{i\theta} = \sum_{i=1}^{n} A_j e^{i\Psi_j} = (X, Y) = (R\cos\theta, R\sin\theta),
$$

where $i = \sqrt{-1}$, the terms X (the in-phase phasor) and Y (quadrature phasor) are independent uniformly distributed phasors (UDP) and the A_j are all distributed identically. When n is large and we assume that A_j is not correlated with the Ψ_j, both X and Y will be distributed normally with mean 0 and variance $\frac{1}{2}n = \sum_{j=1}^{n} A_j^2$. [32], see page 69, has pointed out that under some conditions this is also true for small n. Let now $\frac{1}{2}n = \sum_{j=1}^{n} A_j^2 = \theta$. Then, the joint distribution of X and Y is

$$
\pi(x, y) = \frac{1}{2\pi\theta} \exp\left\{-\frac{x^2 + y^2}{2\theta}\right\}. \tag{11}
$$

Then, expressing (11) in polar coordinates results

$$\pi(r,\theta) = \frac{r}{2\pi\theta} \exp\left\{-\frac{r^2}{2\theta}\right\}, \quad 0 \le \theta \le 2\pi, \ r \ge 0. \tag{12}$$

Thus, it is simple to see that the phase distribution is uniform, i.e., $\pi(\theta) = \frac{1}{2\pi}$, $0 \le \theta \le 2\pi$. On the other hand, the (unconditional) amplitude distribution is given by (5).

Some Measures of Interest in the Setting of Fading Channel

Since the RBS distribution studied here can be obtained easily as a mixture of the Rayleigh distribution and the Birnbaum Saunders distribution this strongly facilitates the calculus of relevant measures of interest (*quality indices*) within the framework of fading channel: the amount of fading (this is known in the literature also as strength of intensity fluctuations), AF and the BER for DPSK and MSK when the distribution introduced here are applied to modeling a mobile communication channel.

For a SISO (single-input-single-output) system, the amount of fading, a unified measure for the severity of fading (see for instance [33]), is based on the moments of the fading distribution and is given by $AF = var(R^2)/E^2(R^2)$. For the $RBS(\alpha, \beta)$ distribution studied here is given by

$$AF = \frac{4 + \alpha^2(12 + 11\alpha^2)}{(2 + \alpha^2)^2},$$

which does not depend on β and is larger than 1, the value of AF for the Rayleigh, $R(\theta)$, distribution. Observe that when $\alpha \to 0$ we have $AF \to 1$.

From [11], it is known that for the standard Rayleigh distribution, $R(\theta)$, the BER for DPSK and MSK are given by

$$P_{b,DPSK}(\theta) = \frac{1}{2(1 + 2\gamma\theta)},$$

$$P_{b,MSK}(\theta) = \frac{1}{2}\left[1 - \sqrt{\frac{2\gamma\theta}{1 + 2\gamma\theta}}\right],$$

respectively.

Now, we can obtain, by compounding, and for the special case in which $|2\gamma\theta| < 1$ the corresponding average BER of DPSK and MSK for the RBS distribution. They are given in the following result.

Proposition 1. *Suppose that $|2\gamma\theta| < 1$, then the average BER of DPSK and MSK for the RBS distribution are given by*

$$\bar{P}_{b,DPSK} = \frac{\exp(\alpha^{-2})}{2\alpha\sqrt{2\pi}} \sum_{j=0}^{\infty} (-1)^j \left(\frac{2\gamma}{\beta}\right)^j \left[K_{j-\frac{1}{2}}(\alpha^{-2}) + K_{j+\frac{1}{2}}(\alpha^{-2})\right],$$

$$\bar{P}_{b,MSK} = \frac{1}{2}\left\{1 - \frac{\exp(\alpha^{-2})}{\alpha} \sum_{j=0}^{\infty} \left(\frac{2\gamma}{\beta}\right)^j \left[K_{j+1}(\alpha^{-2}) + K_j(\alpha^{-2})\right]\right\},$$

respectively. Here $\gamma = E_b/N_0$, where E_b is the transmitted energy per bit and N_0 is the noise power spectral density.

Proof. Using the negative binomial series

$$(z+a)^{-m} = \sum_{j=0}^{\infty} (-1)^j \binom{m+j-1}{j} z^j a^{-m-j}, \quad |z| < a, \tag{13}$$

and using the composite rule we get

$$\begin{aligned}
\bar{P}_{b,DPSK} &= \int_0^{\infty} P_{b,DPSK}(\theta) \pi_{\Theta}(\theta; \alpha, \beta)\, d\theta \\
&= \frac{1}{2} \sum_{j=0}^{\infty} (-1)^j (2\gamma)^j \int_0^{\infty} \theta^j \pi(\theta; \alpha, \beta)\, d\theta,
\end{aligned}$$

from which $\bar{P}_{b,DPSK}$ is obtained now by using (3). $\bar{P}_{b,MSK}$ is calculated in a similar manner. $\square$

The average channel capacity for fading channel is a good metric as it gives an estimation of the information rate that the channel can support with small probability of error. Channel capacity, C, (see for instance [34,35], among others) is defined as

$$C_R(\theta) = B \int_0^{\infty} \log_2(1+r) g_R(r; \theta)\, dr,$$

where B is the received signal bandwidth. Following [34] it is known that the Shannon capacity of the Rayleigh fading channel is given by

$$C_R(d, \theta) = B \exp\left(\frac{1}{2d\theta}\right) E_1\left(\frac{1}{2d\theta}\right), \tag{14}$$

where $E_n(x) = \int_1^{\infty} \exp(-xt)/t\, dt$, $d = S/(N_0 B)$, S the average transmit power receiving bandwidth B and the mean channel gain $\sqrt{\theta \pi/2}$. Thus, the unconditional channel capacity can be obtained numerically by computing the following integral

$$C_{RBS}(d, \alpha, \beta) = B \int_0^{\infty} \exp\left(\frac{1}{2d\theta}\right) E_1\left(\frac{1}{2d\theta}\right) \pi_{\Theta}(\theta; \alpha, \beta)\, d\theta.$$

Another way of computing the latter integral is to use the series representation of the exponential integral function (see [36,37]) which establishes that

$$E_1(z) = -\gamma^* - \log z + \sum_{j=1}^{\infty} (-1)^j \frac{z^j}{jj!},$$

where $\gamma^* \approx 0.577216$ is the Euler's constant.

5. Some Measures for Comparing

In Figure 4, the average BERs are plotted for DPSK and MSK for RLN, K and SR distributions for the three sets of parameter values given in Table 1. The BER for RLN and K distributions were numerically obtained for DPSK and MSK using the same values of parameters for the K distribution taken by [33] in three settings. Setting A is for $b = 0.35$ value, Setting B is for $b = -0.37$ value and Setting C is for $b = -0.65$ value. For all the cases $a = 1$, as indicated in the same table. The corresponding values of the parameters for the RLN and RBS distributions were obtained by equating the population moments to the moments of the K distribution obtained from the above a and b values. Recall that the population

moments of the K and RLN distributions are given by $E(R^k) = (2a)^k \Gamma(1 + k/2)\Gamma(1 + b + k/2)/\Gamma(b+1)$ and $E(R^k) = 2^{k/2}\Gamma(1 + k/2)\exp[\mu k/2 + (\lambda k)^2/8]$, $k = 1, 2, \ldots$, respectively. Moments of the RIG, GR and SR distributions can be found in [22,25,27], respectively. First and second moments of the RBS distribution were taken from (3). The estimated parameter values of the RLN distribution, λ and μ, obtained here are different from the ones obtained by [33] since they used the approximation provided in [11].
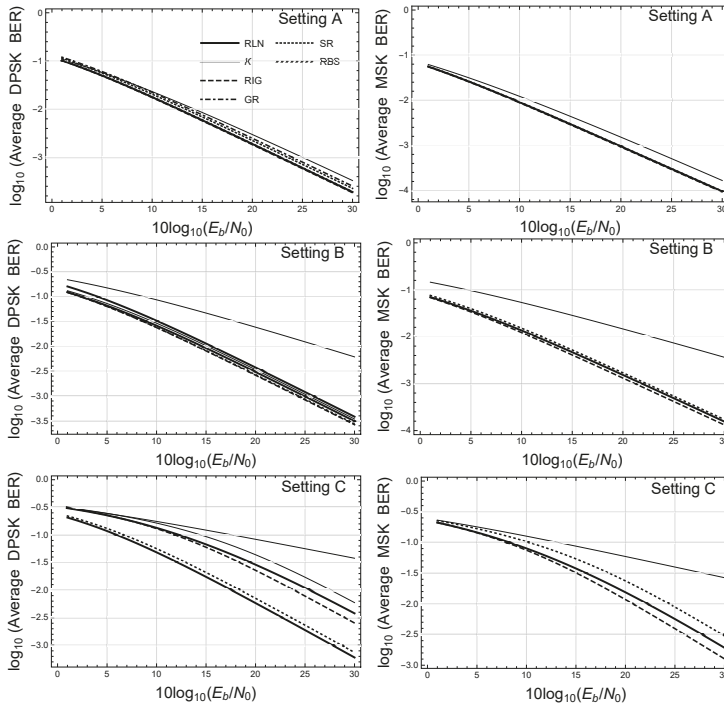
Figure 4. Average BERs of DPSK and MSK for RLN, K, RIG, SR and RBS distributions assuming values for the parameters given in different settings provided in Table 1.

In view of the graphs, the utility of the RBS distribution for the prediction of BER in multi-path dispersion fades can be inferred. We must also influence the good fit, compared to the distribution K, between the proposed distribution and the RLN distribution. The third scenario is conclusive in this case. Recall that the RLN distribution is commonly used in all DPSK and MSK modulation schemes. It is also worth noting that for the RLN distribution, there is no closed-form expression for the average BER, which must be calculated by means of numerical integration methods (generally, the Gauss–Hermite method). An exact but complicated formula for estimating the BER in the DPSK case when the RLN distribution is used is reported in [38].

On the other hand, comparing the analytical expressions of the proposed distribution and the K distribution, both include special functions in their formulation—the incomplete gamma function and the modified Bessel function, respectively. Then, from this point of view both are similar and therefore an alternative to it, which has been used as a substitute for the RLN distribution.

From the above, it is clear that the proposed distribution can be applied to deal with the bleached shading aspects of the wireless channels.

Table 1. Values of the parameters for RLN, K and RBS distributions.

		Setting		
Model	**Parameters**	**A**	**B**	**C**
RLN	μ	0.63	0.51	−1.57
	λ	0.85	1.21	1.56
K	a	1.00	1.00	1.00
	b	0.35	−0.37	−0.65
RIG	κ	2.71	1.29	0.11
	δ	2.69	3.47	0.70
GR	ϑ	4.76	24.07	155.48
	ω	7.33	25.86	21.61
SR	q	3.45	2.80	2.48
	σ	1.14	0.36	0.14
RBS	α	0.94	1.54	2.52
	β	0.53	0.63	5.96

Figure 5 shows the pdf of the different distributions used for parameters given in Settings A and B. It seems that all distributions provide similar tails.
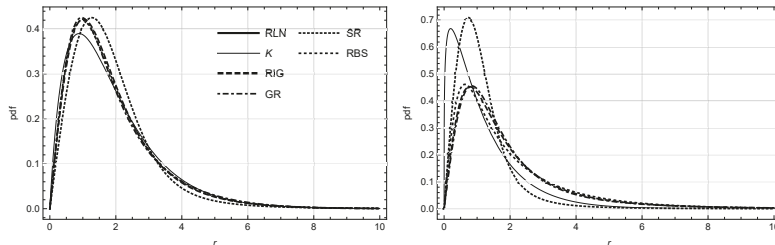
Figure 5. Graphics of the pdf of the different distributions for parameters given in Settings A (**left**) and B (**right**).

Comparison with the RL, K and RIG Distributions

It is well known that we can study the distance or relative information between two probability distributions by using the Kullback–Leibler divergence measure (see [39], among others) which is defined as follows: Let f and g be probability densities on such that f is absolutely continuous with respect to g (that is, $g(x) = 0$ implies $f(x) = 0$), then the relative information or Kullback–Leibler divergence, $D_{KL}(f||g)$ of f with respect to g is

$$D_{KL}(f||g) = \int_0^\infty f(x) \log \left[\frac{f(x)}{g(x)} \right] dx, \tag{15}$$

with the convention that $0/0 = 1$. When f is not absolutely continuous with respect to g we define $D_{KL}(f||g) = \infty$. One of the disadvantages of (15) is that the Kullback–Leibler divergence is not symmetric

and therefore is not a genuine distance metric. To surpass that, the Jensen–Shanon divergence (see for instance, [40]) given by

$$D_{JSD}(f||g) = \frac{1}{2}\left(D_{KL}(f||m) + D_{KL}(g||m)\right),\tag{16}$$

where $m = (f + g)/2$, and the integrated squared error, ISE, [41] given by

$$D_{ISE}(f||g) = \int_0^{\infty} (f(x) - g(x))^2 \, dx,\tag{17}$$

will be used.

Table 2 includes the Jensen–Shannon divergence for all the distributions considered here. We can see that the RBS distribution provides a distance similar to the ones provided with the rest of the distribution. Here the RL distribution was taken as the reference distribution.

Table 2. JSD and ISE measures for K and SR distributions (compared to the RLN distribution).

Measure	Model	Setting		
		A	**B**	**C**
JSD	K	0.001	0.049	0.032
	RIG	3.0×10^{-5}	2.9×10^{-4}	0.001
	GR	5.5×10^{-4}	9.6×10^{-4}	0.005
	SR	0.188	0.050	0.025
	RBS	8.5×10^{-5}	1.0×10^{-3}	0.007
ISE	K	0.002	0.090	0.328
	RIG	3.9×10^{-5}	5.1×10^{-4}	0.007
	GR	3.5×10^{-4}	1.5×10^{-3}	0.030
	SR	5.2×10^{-3}	0.068	0.122
	RBS	8.1×10^{-5}	1.7×10^{-3}	0.047

6. Simulating the Proposed Distribution

To model a fading process, simulation of a random variable is required following the distribution. Additionally, this task must be done at low computational cost (because not a single variable, but thousands of them, are needed). In the literature, there are many methods to do that. In this work, we follow the same method used in [25], applying the standard inverse transform method because this method is simple and easy to implement. In Algorithm **??** a simplified version of the inverse transform method is summarized. The cdf (cumulative density function) corresponds to $h_R(r; \alpha, \beta)$, i.e., expression (8). Indeed to $1 - h_R(r; \alpha, \beta)$, which is obtained at low computational cost and can be even pre-calculated for a set of α and β parameters to speed up the simulation.

The simulation of the variable was coded in MATLAB and executed on an i7-7700HQ CPU @ 2.80 GHz (16 GB RAM), taking around 0.048824 seconds to generate $N = 1,000,000$ (one million) random variates. The program is efficiently coded in a matrixial way (it does not use loops). The computational cost is indeed low, hence, well suited to fading channel modeling.

By Monte Carlo simulations, two large datasets were obtained (1,000,000 samples) and compared with the analytical RBS pdfs. In Figure 6, the analytical pdf for the RBS distribution and the ones from simulated data, which clearly show a good fit for both datasets, can be seen. As expected, the error for the variance is larger than for the case of the mean but certainly low for both measures for the two cases shown. See also the analyticle and simulated values for the mean and variance in Table 3.

However, to properly simulate the fading effects for a communication channel, the simulation must be done in terms of phasors (see Section 4) and coupled to physical variables (signal carrier frequency, signal sampling, speed of receiver and Doppler effects) related to the channel. These issues are discussed in the next section.
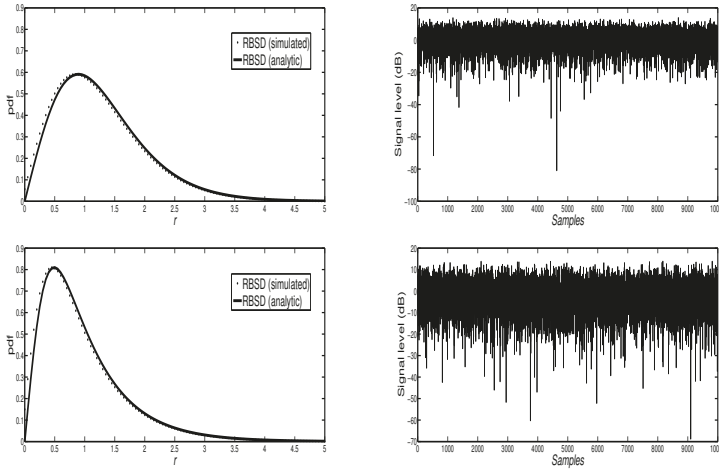
Figure 6. Comparison of the analytic RBS($\alpha = 0.5$, $\beta = 1$) magnitude pdf and the Monte Carlo simulated dataset (**top**). Comparison of the analytic RBS ($\alpha = 1$, $\beta = 2$) magnitude pdf and the Monte Carlo simulated dataset (**bottom**). Simulated samples (1,000,000) for both cases are also represented (**right** column).

Table 3. Mean and variance values for the analytic RBS distribution and those estimated from the simulated samples for two sets of parameters.

	RBS ($\alpha = 0.5$, $\beta = 1$)	RBS ($\alpha = 1$, $\beta = 2$)
Mean (Analytic)	**1.2909**	**0.9831**
Mean (simulated data)	1.2772	0.9685
Relative error	1.05%	1.48%
Variance (analytic)	0.5836	0.5335
Variance (simulated data)	0.5698	0.5078
Relative error	2.37%	4.82%

The RBS Distribution for Modeling Fading Effects

In this section, we proceed as in [22]—which is also based on the classical well-known Clarke's model [4], but we present the model for the sake of completeness of this work. First, we reformulate the phasors obtained in Section 4 as follows:

$$S = Re^{i\theta} = \sum_{i=1}^{n} A_j e^{i\Phi_j} = (X, Y) = (R\cos\theta, R\sin\theta),$$

as explained, for instance, by [4] as follows,

$$(X_i(t), Y_i(t)) \quad = \quad \left(\sum_{j=1}^{N} A_{ij} \cos(w_{ij}t - \varphi_{ij}), \sum_{j=1}^{N} A_{ij} \sin(w_{ij}t - \varphi_{ij}) \right),$$

where A_{ij} is the amplitude of the transmitted signal ($< \sum_{j=1}^{N} A_{ij}^2) >= 1$). The phase θ is replaced by the term $\theta = w_{ij}t - \varphi_{ij}$. The phase φ_{ij} is the random phase (uniformly distributed in the interval $[-\pi, \pi]$), $w_{ij} = \beta v \cos(\psi_{ij})$ accounts for the Doppler shift, where v is the receptor velocity, $\beta = 2\pi/\lambda$ represents the wave number, λ is the wavelength and βv is the maximum Doppler shift (in units of radians per second). The angle of arrival of the transmitted wave is ψ_{ij}, also distributed in $[-\pi, \pi]$, and N is the number of harmonic waves, which, if large enough (as expected in the real case), ensures that both $X_i(t)$ and $Y_i(t)$ are Gaussian processes. From that, the RBS signal envelope is given by $r^2 = X_i^2 + Y_i^2$, and $i = 1, 2, \ldots$ The amplitude of the envelope is then suitably fitted to the RBS (α, β) amplitude of the transmitted signal to assure that $r \sim \text{RBS}(\alpha, \beta)$.

By using this model, a Monte Carlo simulation (using 15 scattered random phasors and 20,000 samples) was performed to obtain the dataset (random samples) and from that, the pdf is ensembled to compare it with the analytic RBS pdf. This comparison is plotted in Figure 7 (left column) for two sets of RBS distributions ($\alpha = 0.5, \beta = 3$ and, $\alpha = 1, \beta = 2$). As can be seen, a reasonably good fit between the analytic and the physical models is obtained. On the right column of the same figure, a set of simulated samples for both cases is shown. As expected, these samples are mostly near the mean value provided by the parameter setting. Deep fading effects (≈ 60 dB) are present. Hence, the RBS distribution naturally accounts for the presence of large fading values related to minimal power received at the terminal).
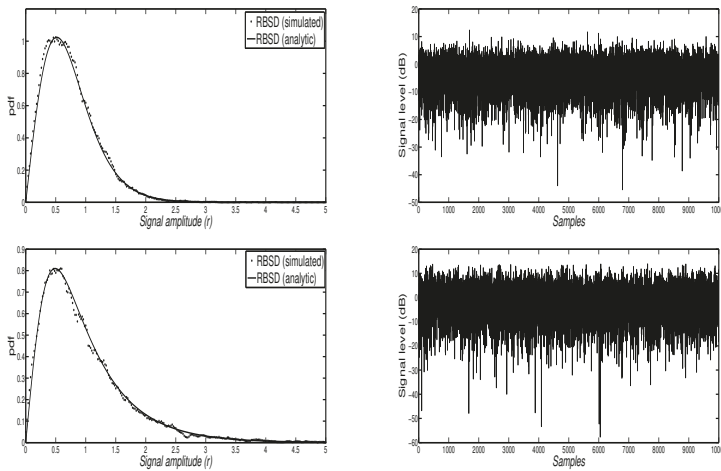
Figure 7. Samples simulated by using phasors of the RBS distribution ($\alpha = 0.5, \beta = 3$) (**top**, **left**) and a set of simulated samples (**top**, **right**). Samples simulated by using phasors of the RBS distribution ($\alpha = 1, \beta = 2$) (**bottom**, **left**) and a set of simulated samples (**bottom**, **right**). For both cases, the analytic RBS distribution is also shown, for the sake of comparison.

Table 4 contains the analytical means and variances compared with those estimated from the Monte Carlo data. The relative errors (percentual values) for both measures and for both datasets are acceptable (less than 5% and lower that 1% for the variance for the set $\alpha = 0.5$ and $\beta = 3$), but noticeably larger than when the data were generated directly from the respective cdfs. This is due to the complexity of this simulation, which accounts for physical effects (wave scattering).

Table 4. Means and variances for the analytic RBS (α, β) distribution and, the values estimated using phasors for two-parameter sets.

	RBS(0.5, 3)	RBS(1, 2)
Mean (Analytic)	**0.7453**	**0.9831**
Mean (simulated data)	0.7213	0.9533
Relative error	3.21%	3.03%
Variance (analytic)	0.1945	0.5335
Variance (simulated data)	0.1937	0.5080
Relative error	0.42%	4.78%

Figure 8 illustrates SR, the RLN, and the proposed RBS distribution. The parameters used in all cases are those providing similar mean (emitted power) and standard deviation values, and are plotted spaced 0.1 wavelength apart for the 0 dB mean value. As can be seen, the RBS distribution shows a behavior similar to the Rayleigh and to the SR distributions but capturing deep fading effects. Additionally, the RBS distribution seems more suited to modern communication systems, and more robust to fading effects.
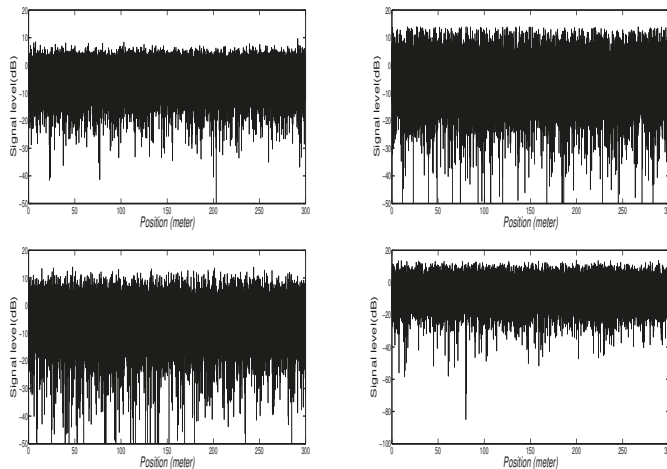
Figure 8. Simulated samples (using phasors) of the Rayleigh fading distribution (**top left**), the SR fading distribution (**top right**), the RLN fading distribution (**bottom left**) and, the proposed RBS fading distribution. The parameters used in all cases are those providing similar mean and standard deviation values, and are represented spaced 0.1 wavelength apart for the 0 dB mean value.

Finally, a simulation of the physical channel is performed to illustrate that the proposed RBS distribution efficiently models fading effects. In what follows, we also proceed as in [22].

Algorithm 1 details the pseudo-code used for the channel simulation (Clarke's model). To generate a realistic fading spectrum (that is, to generate time-correlated fading waveforms), a common baseband Doppler filter was also included in the simulations.

Figure 9 shows the simulated fading signal for the RBS($\alpha = 0.6625$, $\beta = 1.7419$) distribution, corresponding to a signal with a power mean value of 1. Fifteen Rayleigh processes (*rays*) and 20,000 samples were simulated to obtain the envelope. In this case, the envelope includes deep fading levels (relative to the low power used) due to fast fading in long-distance HF (High frequency) propagation ([31]). The results discussed above were for two vehicles at velocities 50 km/h and 120 km/h, respectively. As expected, the Doppler effect is more noticeable as the vehicle velocity increases.

The physical meaning of the parameters of the RBS distribution has not been discussed in this paper. However, from expression (8), and also from Algorithm 1, it seems clear that they depend on the average signal power strength of the emitter. However, a deeper analysis must be done.

To get all data shown in this paper, a fading channel program has been developed (coded in MATLAB and using a friendly graphic interface). The prototype implements the Clarke's model, and it also includes standard signal processing routines (filters) and all the metrics to characterize the channel as well as the other standard fading distributions (i.e., Rayleigh, SR and RLN).
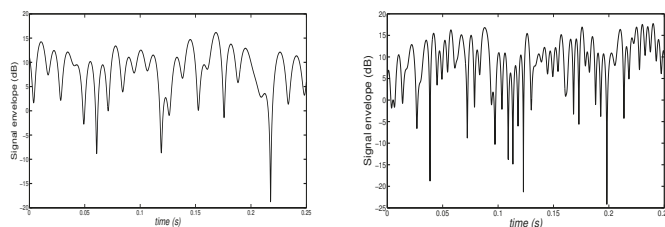
Figure 9. Fading signal for the RBS distribution ($\alpha = 0.66$, $\beta = 1.74$); carrier frequency = 1 GHz and speed = 50 Km/h (**left**) and speed = 120 km/h (**right**).

7. Final Comments

In this work, we proposed a new distribution, the two-parameter Rayleigh Birnbaum Saunders Distribution, which shows some benefits in comparison with the Rayleigh–lognormal distribution, the SR distribution and, the K distribution. The Rayleigh distribution is included as a particular case when one of its parameters is large enough. The estimation of the parameters of the proposed distribution has been also taken into account. The new distribution we propose shows clear advantages when compared to the Rayleigh–lognormal distribution within the framework of fading signal modeling. Signal envelope has been obtained through two different methods: from the analytic pdf and from physical simulation of the communication channel by means of phasors using Clarke's model. The common metrics for estimating the quality of the received signal (the bit error rate (BER) for DPSK and MSK modulations) have also been derived in closed form for the new fading distribution. Future work will focus on providing a physical meaning for the parameters of the RBS distribution, α and β, although some preliminary clues were already given above.

Data Availability

Reproducibility of data used to support the findings of this work can be done through the mathematical formulas and algorithm explanations included within the article. Additionally, codes

---

Algorithm 1: Fading simulation.

   Input:
        Alpha: α parameter ($\alpha \in \mathbb{R}$)
        Beta: β parameter ($\beta \in \mathbb{R}$)
        Rays: number of emitted signals (Rays $\in \mathbb{N}$)
        Ref: number of reflections (Ref $\in \mathbb{N}$)
        Speed: average speed of vehicle (Speed $\in \mathbb{R}$)
        Freq: carrier frequency (Freq $\in \mathbb{R}$)
        TimeF: simulation time (TimeF $\in \mathbb{R}$)
        TimeS: sampling time (TimeS $\in \mathbb{R}$)
   Output:
        r: signal envelope
   Begin:
   A $\leftarrow$ getPower(Alpha, Beta)   ▷*Get average signal strength and variance*
   Phi $\leftarrow$ rand(Rays, Ref) $\cdot 2 \cdot \pi$ ▷*Uniformly distributed phase*
   Psi $\leftarrow$ rand(Rays, Ref)$\cdot 2 \cdot \pi$ ▷*Uniformly distributed arriving signal*
   D $\leftarrow 2 \cdot \pi \cdot$ Freq$\cdot$ 3.3e-03   ▷*Maximum Doppler frequency shift*
   w $\leftarrow D \cdot Speed \cdot cos(Psi)$ ▷*Consider Doppler effects*
   t $\leftarrow$ 0: TimeS : TimeF   ▷*Time span*
   X $\leftarrow$ 0
   Y $\leftarrow$ 0
        Df $\leftarrow w \cdot t - Phi$ ▷*Obtain Doppler phase shift*
        $X \leftarrow X + A \cdot \cos(Df)$ ▷*In-phase component*
        $Y \leftarrow Y + A \cdot \sin(Df)$ ▷*Quadrature component*
   end for
   end for
   $r \leftarrow \sqrt{X^2 + Y^2}$ ▷*Calculate the signal envelope*
   End

---

used are available from the corresponding author upon request. These data include Mathematica and MATLAB codes, therefore users should have their corresponding software licenses.

Appendix A. Proof of the cdf and pdf of the RBS Distribution

We start by getting the unconditional survival function of the standard Rayleigh distribution. That is,

$$
\begin{aligned}
\bar{F}(r) &= \int_0^\infty \bar{F}(r;\theta)\, d\theta = \int_0^\infty \exp\left\{-\frac{r^2}{2\theta}\right\} \pi(\theta;\alpha,\beta)\, d\theta \\
&= \int_0^\infty \frac{1+\theta\beta}{2\alpha\sqrt{2\pi\beta\theta^3}} \exp\left\{-\frac{1+\beta^2\theta^2-2\beta\theta+\beta\alpha^2 r^2}{2\beta\alpha^2\theta}\right\} d\theta \\
&= \int_0^\infty \frac{1+\theta\beta}{2\alpha\sqrt{2\pi\beta\theta^3}} \exp\left\{-\frac{(\beta\theta-\varphi_{\alpha,\beta}(r))^2 - 2\beta\theta(1-\varphi_{\alpha,\beta}(r))}{2\beta\alpha^2\theta}\right\} d\theta,
\end{aligned}
$$

where $\varphi_{\alpha,\beta}(r) = \sqrt{1+\beta(r\alpha)^2}$. Thus,

$$
\bar{F}(r) = \exp\left\{\frac{1-\varphi_{\alpha,\beta}(r)}{\alpha^2}\right\} \int_0^\infty \frac{1+\theta\beta}{2\alpha\sqrt{2\pi\beta\theta^3}} \exp\left\{-\frac{\beta^2(\theta-\varphi_{\alpha,\beta}(r)/\beta)^2}{2\alpha^2}\right\} d\theta.
$$

Let now,

$$
\begin{aligned}
\Lambda_{\alpha,\beta}(r) &= \frac{\varphi_{\alpha,\beta}(r)}{\alpha\sqrt{\beta}}, \\
\Omega_{\alpha,\beta,r}(\theta) &= \exp\left\{-\frac{\Lambda_{\alpha,\beta}(r)^2(\theta-\varphi_{\alpha,\beta}(r)/\beta)^2}{2(\varphi_{\alpha,\beta}(r)/\beta)^2\theta}\right\}.
\end{aligned}
$$

Then, we have that

$$
\begin{aligned}
\bar{F}(r) &= \exp\left\{\frac{1-\varphi_{\alpha,\beta}(r)}{\alpha^2}\right\} \int_0^\infty \frac{(1+\theta\beta)\Lambda_{\alpha,\beta}(r)}{2\varphi_{\alpha,\beta}(r)\sqrt{2\pi\theta^3}} \Omega_{\alpha,\beta,r}(\theta)\, d\theta \\
&= \frac{1+\varphi_{\alpha,\beta}(r)}{2\varphi_{\alpha,\beta}(r)} \exp\left\{\frac{1-\varphi_{\alpha,\beta}(r)}{\alpha^2}\right\},
\end{aligned} \tag{A1}
$$

where we have identified, after arranged parameters, the last integral with the pdf of the inverse Gaussian distribution (see for instance [42]) given by

$$
f(x) = \sqrt{\frac{\lambda}{2\pi x^3}} \exp\left\{-\frac{\lambda(x-\mu)^2}{2\mu^2 x}\right\}, \quad x > 0,
$$

with $\lambda > 0$ and mean $\mu > 0$.

Finally, (5) is obtained after computing the derivative of (A1) with respect to r.

Proposition A1. *The average Shannon capacity of the Rayleigh Birnbaum Saunders fading channel is given by*

$$C_{RBS}(d,\alpha,\beta) = B\left(-\frac{\gamma^*}{2}\mathcal{H}^1_{d,\alpha,\beta} + 2\mathcal{H}^2_{d,\alpha,\beta} + \mathcal{H}^3_{d,\alpha,\beta}\right)\exp(\alpha^{-2}),$$

where

$$
\begin{aligned}
\mathcal{H}^1_{d,\alpha,\beta} &= \left(1 + \mathcal{D}_{d,\alpha,\beta}\right)\mathcal{A}_{\alpha,\beta,d}, \\
\mathcal{H}^2_{d,\alpha,\beta} &= (1 + \mathcal{D}_{d,\alpha,\beta})\alpha\,\mathcal{A}_{d,\alpha,\beta}\sqrt{\frac{\pi\beta}{2}}\log\left(\frac{\beta\mathcal{D}_{d,\alpha,\beta}}{2d}\right) \\
&\quad + \sqrt{\beta\mathcal{D}}\left[\left(1 - \frac{\alpha^2\beta}{d}\right)\mathcal{D}_{d,\alpha,\beta}K'_{-\frac{1}{2}}\left(\frac{1}{\alpha^2\mathcal{D}_{d,\alpha,\beta}}\right) + K'_{\frac{1}{2}}\left(\frac{1}{\alpha^2\mathcal{D}_{d,\alpha,\beta}}\right)\right], \\
\mathcal{H}^3_{d,\alpha,\beta} &= \sum_{j=1}^{\infty}\frac{(-1)^j}{jj!}\left(\frac{\beta}{2d}\right)^j\frac{\mathcal{D}^{j-1/2}_{d,\alpha,\beta}}{\alpha\sqrt{2\pi}}\left[\mathcal{D}_{d,\alpha,\beta}K_{j+\frac{1}{2}}\left(\frac{1}{\alpha^2\mathcal{D}_{d,\alpha,\beta}}\right)\right. \\
&\quad \left. + K_{j-\frac{1}{2}}\left(\frac{1}{\alpha^2\mathcal{D}_{d,\alpha,\beta}}\right)\right],
\end{aligned}
$$

where

$$
\begin{aligned}
\mathcal{A}_{d,\alpha,\beta} &= \exp\left[\left(\frac{\beta}{d} - \frac{1}{\alpha^2}\right)\mathcal{D}_{d,\alpha,\beta}\right], \\
\mathcal{D}_{\alpha,\beta,d} &= \sqrt{\frac{d}{d - \alpha^2\beta}}
\end{aligned}
$$

and $\gamma^* \approx 0.577216$ is the well-known Euler's constant.

Proof. Again, by using the composite rule, using (14), we get

$$C_{RBS}(d,\alpha,\beta) = B\int_0^\infty \exp\left(\frac{1}{2d\theta}\right)E_1\left(\frac{1}{2d\theta}\right)\pi_\Theta(\theta;\alpha,\beta)\,d\theta.$$

It is known (see [36,37]) that

$$E_1(z) = -\gamma^* - \log z + \sum_{j=1}^{\infty}(-1)^j\frac{z^j}{jj!}.$$

Thus, we have

$$
\begin{aligned}
C_{RBS}(d,\alpha,\beta) &= -B\int_0^\infty \exp\left(\frac{1}{2d\theta}\right)\left[\gamma^* + \log\left(\frac{1}{2d\theta}\right)\right. \\
&\quad \left. - \sum_{j=1}^{\infty}\frac{(-1)^j}{jj!}\left(\frac{1}{2d\theta}\right)^j\right]\pi_\Theta(\theta;\alpha,\beta)\,d\theta,
\end{aligned}
$$

from which we get the result after using (4), the results provided in the Appendix A and some algebraic manipulation. □

References

1. Zikria, Y.B.E.A. 5G mobile services and scenatios: Challenges and solutions. *Sustainability* **2018**, *10*, 3626. [CrossRef]

2. Liu, G.; Jiangl, D. 5G: Vision and Requirements for Mobile Communication System towards Year 2020. *Chin. J. Eng.* **2016**, *2016*, 5974586. [CrossRef]

3. Beckmann, P. *Probability in Communication Engineering*; Harcourt, Brace & World: New York, NY, USA, 1967.

4. Rappaport, T.S. *Wireless Communications: Principles and Practice, 2nd ed.*; Prentice Hall Communications Engineering and Emerging Technologies Series: Upper Saddle River, NJ, USA, 2001.

5. Barts, R.M.; Stutzman, W.L. Modeling and simulation of mobile satellite propagation. *IEEE Trans. Antennas Propag.* **1992**, *40*, 375–382. [CrossRef]

6. Borhani, A.; Stüber, G.L.; Pätzold, M. A random trajectory approach for the development of nonstationary channel models capturing different scales of fading. *IEEE Trans. Veh. Technol.* **2017**, *66*, 2–14.

7. Lopez-Fernandez, J.; Paris, J.F.; Martos-Naya, E. Bivariate Rician shadowed fading model. *IEEE Trans. Veh. Technol.* **2018**, *67*, 378–384. [CrossRef]

8. Romero-Jerez, J.M.; López-Martínez, F.J.; Peña-Martin, J.P.; Abdi, A. Stochastic Fading Channel Models with Multiple Dominant Specular Components for 5G and Beyond. *arXiv* **2019**, arXiv:1905.03567.

9. Suh, S. *A Propagation Simulator for Land Mobile Satellite*. 1998. Available online: https://vtechworks.lib.vt.edu/handle/10919/36632 (accessed on 30 December 2019).

10. Hansen, F.; Meno, F. Mobile Fading-Rayleigh and Lognormal Superimposed. *IEEE Trans. Vehic. Technol* **1977**, *26*, 332–335. [CrossRef]

11. Abdi, A.; Kaveh, M. K distribution: An appropriate substitute for Rayleigh-lognormal distribution in fading-shadowing wireless channels. *IEEE Electron. Lett.* **1998**, *9*, 851–852. [CrossRef]

12. Sharme, S.; Mishra, R. A simulation model for Nakagami-m fading channel with $m > 1$. *Int. J. Adv. Comput. Sci. Appl.* **2015**, *6*, 298–305.

13. Proackis, J.; Salehi, M. *Digital Communications*; McGraw-Hill Education: New York, NY, USA, 2007.

14. Adachi, F.; Feeney, M.T.; Parsons, J.D. Level crossing rate and average fade duration for time diversity reception in Rayleigh fading conditions. *IEE Proc. F - Commun. Radar Signal Process.* **1988**, *135*, 501–506. [CrossRef]

15. Subbarayan, P. Minimum shift keying: A spectrally efficient modulation. *IEEE Commun. Mag.* **1979**, *17*, 14–22.

16. Sklar, B. Rayleigh fading channels in mobile digital communication systems .I. Characterization. *IEEE Commun. Mag.* **1997**, *35*, 90–100. [CrossRef]

17. Nakagami, M. *The m-Distribution—A General Formula of Intensity Distribution of Rapid Fading*; Statistical Methods in Radio Wave Propagation; Hoffman, W., Ed.; Pergamon: Oxford, UK, 1960.

18. Yacoub, M.; Silva, C.R.C.M.; Vargas, B.J.E.J. Second-order statistics for diversity-combining techniques in Nakagami-fading channels. *IEEE Trans. Veh. Technol.* **2001**, *50*, 1464–1470. [CrossRef]

19. Kao, C.Y.; Mar, J. Performance simulations of a mobile radio network using contention-based WIMA protocol under Rayleigh- and log-normal-fading environments. *IEEE Trans. Veh. Technol.* **2002**, *51*, 1247–1252.

20. Dias, U.S.; Yacoub, M.D. The $\kappa - \mu$ phase-envelope joint distribution. *IEEE Trans. Commun.* **2010**, *58*, 40–45. [CrossRef]

21. Ermolova, N.Y.; Tirkkonen, O. Bivariate $\eta - \mu$ Fading Distribution with Application to Analysis of Diversity Systems. *IEEE Trans. Wirel. Commun.* **2011**, *10*, 3158–3162. [CrossRef]

22. Gómez-Déniz, E.; Gómez, L.; Gómez, W.H. The Slashed-Rayleigh Fading Channel Distribution. *Math. Probl. Eng.* **2019**, *2019*, 1–14. [CrossRef]

23. Tse, D. *Fundamentals of Wireless Communication*; Cambridge University Press: Cambridge, UK, 2005.

24. Stuber, G. *Principles of Mobile Communication*; Kluwer: Boston, MA, USA, 1996.

25. Gómez-Déniz, E.; Gómez, L. A generalisation of the Rayleigh distribution with applications in wireless fading channels. *Wirel. Commun. Mob. Comput.* **2013**, *13*, 85–94. [CrossRef]

26. Ruskeepaa, H. *Mathematica Navigator. Mathematics, Statistics, and Graphics, 3rd ed.*; Academic Press: Burlington, NC, USA, 2009.

27. Karmeshu, R. On efficacy of Rayleigh-inverse Gaussian distribution over K-distribution for wireless fading channels. *Wirel. Commun. Mob. Comput.* **2007**, *7*, 1–7. [CrossRef]
28. Birnbaum, Z.; Saunders, S. A new family of life distributions. *J. Appl. Probab.* **1969**, *6*, 319–327. [CrossRef]
29. Birnbaum, Z.; Saunders, S. Estimation for a family of life distributions with applications to fatigue. *J. Appl. Probab.* **1969**, *6*, 328–347. [CrossRef]
30. Leiva, V. *The Birnbaum-Saunders Distribution*; ELSEVIER: Amsterdam, The Netherlands, 2016.
31. Yacoub, M.; Bautista, J.; Guedes, L. On higher order statistics of the Nakagami-m distribution. *IEEE Trans. Veh. Technol.* **1999**, *48*, 790–794. [CrossRef]
32. Goldsmith, A. *Wireless Communications*; Cambridge University Press: Cambridge, England, 2005.
33. Abdi, A.; Kaveh, M. Comparisons of DPSK and MSK bit error rates for K and Rayleigh-lognormal fading distributions. *IEEE Commun. Lett.* **2000**, *4*, 122–124. [CrossRef]
34. Li, J.; Bose, A.; Zhao, Y. Rayleigh Flat Fading Channels' Capacity. In Proceedings of the 3rd Annual Communication Networks and Services Research Conference (CNSR'05), Halifax, NS, Canada, 16–18 May 2005; pp. 1–8.
35. Singh, R.; Rawat, M. Closed-form Distribution and Analysis of a Combined Nakagami-lognormal Shadowing and Unshadowing Fading Channel. *J. Telecommun. Inf. Technol.* **2015**, *4*, 81–87.
36. Gautschi, W.; Harris, F.; Temme, N. Expansions of the exponential integral in incomplete Gamma functions. *Appl. Math. Lett.* **2003**, *16*, 1095–1099. [CrossRef]
37. Lin, S.D.; Chao, Y.S.; Srivastava, H. Some expansions of the exponential integral in series of the incomplete Gamma function. *Appl. Math. Lett.* **2005**, *18*, 513–520. [CrossRef]
38. Cygan, D. Analytical evaluation of average bit error rate for the land mobile satellite channel. *Int. J. Sat. Commun.* **1989**, *7*, 99–102. [CrossRef]
39. Hall, P. On Kullback-Leibler loss and Density estimation. *Ann. Stat.* **1987**, *15*, 1491–1519. [CrossRef]
40. Lin, J. Divergence measures based on the Shannon entropy. *IEEE Trans. Inf. Theory* **1991**, *37*, 145–151. [CrossRef]
41. Bowman, A. An alternative method of cross-validation for the smoothing of density estimates. *Biometrika* **1984**, *71*, 351–360. [CrossRef]
42. Seshadri, V. *The Inverse Gaussian Distribution: Statistical Theory and Applications*; Springer: New York, NY, USA, 1999.

A Kinematic Calibration Method of a 3T1R 4-Degree-of-Freedom Symmetrical Parallel Manipulator

Fengxuan Zhang [1,2], Silu Chen [2,*], Yongyi He [1], Guoyun Ye [3], Chi Zhang [2] and Guilin Yang [2]

[1]   School of Mechatronic Engineering and Automation, Shanghai University, Shanghai 200444, China;
      zhangfengxuan@nimte.ac.cn (F.Z.); heyongyishu@163.com (Y.H.)
[2]   Zhejiang Key Laboratory of Robotics and Intelligent Manufacturing Equipment Technology,
      Ningbo Institute of Materials Technology and Engineering, Chinese Academy of Sciences,
      Ningbo 315201, China; zhangchi@nimte.ac.cn (C.Z.); glyang@nimte.ac.cn (G.Y.)
[3]   Ningbo Ruyi Joint Stock Co., Ltd., Ningbo 315600, China; zgs2132@163.com
*   Correspondence: chensilu@nimte.ac.cn; Tel.: +86-574-8668-6981

Abstract: This paper proposes a method for kinematic calibration of a 3T1R, 4-degree-of-freedom symmetrical parallel manipulator driven by two pairs of linear actuators. The kinematic model of the individual branched chain is established by using the local product of exponentials formula. Based on this model, the model of the end effector's pose error is established from a pair of symmetrical branched chains, and a recursive least square method is applied for the parameter identification. By installing built-in sensors at the passive joints, a calibration method for a serial manipulator is eventually extended to this parallel manipulator. Specifically, the sensor installed at the second revolute joint of each branched chain is saved, replaced by numerical calculation according to kinematic constraints. The simulation results validate the effectiveness of the proposed kinematic error modeling and identification methods. The procedure for pre-processing compensation on this 3T1R parallel manipulator is eventually given to improve its absolute positioning accuracy, using the inverse of the calibrated kinematic model.

1. Introduction

Compared with serial manipulators, parallel manipulators have the advantages of high rigidity and high loading capacity [1], but also have the disadvantages of complex structure and relatively small workspace. Recently, a 3T1R symmetrical parallel manipulator with a simple structure and a large working space has received widespread attention in academia and industrial applications [2]. This symmetrical parallel manipulator uses four open branched chains to connect the fixed platform with the moving platform. It can achieve three-degree-of-freedom translation along the X, Y, and Z axes and one-degree-of-freedom rotation around the Z axis (3T1R), for a total of four degrees of freedom. Its advantages such as large workspace and high speed make it be widely applicable to industrial automation scenarios such as pick-and-place and sorting, if its absolute positioning accuracy meets the particular requirements of these applications. Therefore, it is necessary to develop an effective calibration method to improve the absolute positioning accuracy of this symmetrical parallel manipulator [3,4].

The kinematic error of the manipulator is defined as the end effector's error between the actual pose and the nominal one, which is mainly caused by geometric tolerances, such as assembly and

manufacturing error. Kinematic calibration is the most effective and economical method to improve accuracy [5]. This method is generally divided into four steps. First is to establish a kinematic error model that consists of parameters to be identified and the measurable variables. Second is to acquire measurements from built-in or external sensors. Third is to perform the identification of parameters in the error model. Fourth is to carry out simulation verification of the calibrated kinematic model and to perform relevant calibration experiments [6,7].

Establishing a proper kinematic error model is the basis for parallel manipulator calibration. The essence of this process is the mapping between the pose error of the moving platform and the error source [8]. Although many modeling methods involving parallel manipulators have been proposed, the modeling method of kinematic error for such a 3T1R complex symmetrical parallel manipulator has not been mentioned yet. Compared with traditional manipulators' calibration methods such as the Denavit–Hartenberg (D-H) model based method [9] and the zero-position reference model method [10], the error model based on the local product of exponentials (POE) formula has some advantages [11,12]. First, the parameters of the kinematic model on the POE formula change smoothly with the change of the joint axis. This ensures that the singularity will not occur in the kinematic error model [11,13]. Secondly, according to Chase's theorem, any rigid body motion can be regarded as a screw motion, so the calibration model established by the POE formula is also complete [14]. Last but not least, on the POE formula, all joint axes are described based on Lie geometry, so they are represented uniformly for the translation and rotation joints of the robot [14].

Since Okamura and Park first introduced the POE formula to robotic kinematics calibration in 1996 [13], the establishment of a kinematic error model using the POE formula has received widespread attention. Two ways have been proposed till now, using the global POE formula [14,15] or the local POE formula [11,16]. The main difference between them is on the choice of reference frames to describe the relative motion of the robot joints. In the global POE formula, the relative motion of the robot joints is described in the base coordinate system. In the local POE formula, each link of the robot is assigned a local coordinate system, and all joint motions are expressed in the corresponding local coordinate system. The main advantage of building the kinematic error model using the local POE formula is that the pose error of the end effector is considered to be solely caused by the accumulation of the pose error of each link.

The accuracy of measurement has a great impact on the calibration. Various devices have been used to perform the calibration experiments on parallel manipulators, such as the ball and stick system [17], the magnetic processing ball [18], vision [19], the laser tracker [20], etc. Since there are multiple passive joints in the 3T1R parallel manipulator, installation of sensors on every passive joint for calibration purposes will be costly. The identification of the kinematic error model parameters is performed by minimizing the deviation between the theoretical and measured values of kinematic error, such as nonlinear least squares optimization [21], but the optimization efficiency may be low due to the nonlinear nature of the model. The error pre-processing compensation will be performed after obtaining the kinematic error model. This step is to use the identified parameters to modify the active joint variables, so that the absolute positioning accuracy of the parallel manipulator is enhanced [22].

The 3T1R parallel manipulator has a "two-layer, binary-tree"-like symmetrical mechanism, while symmetry issues have received widespread attention in academia [23–25]. In this paper, the development of its kinematic calibration method is studied. Its symmetrical structure leads to the establishment of the kinematic model and the associated error model from two branched chains symmetrically. In detail, the local POE formula method is used for modeling its kinematic error firstly. This approach attributes the errors to the initial pose of each joint, resulting in a simpler kinematic error model. In addition, this work uses the pose of the end effector from two branched chains to evaluate the kinematic error. Compared with the kinematic error modeling methods using the metric of the distance of two points on the end effector [26,27], setting up the equality of pose errors from two branched chains improves the error model fitness. In the measurement stage, a method of combining a built-in sensor with an external measurement device is adopted. Although this 3T1R parallel manipulator

has multiple passive joints, all of them can be treated as active ones as in the series robot, if sensors are attached to them during calibration. In this way, the calibration method by the local POE formula used for serial robots can be directly applied to parallel manipulators with passive joints. Specifically, to save the number of sensors used in the revolute joints, the angle of the second revolute joint of each branched chain is computed numerically according to the kinematic constraints of the mechanism. Eventually, a linear-in-parameter error model is synthesized, which greatly improves the efficiency in the coming least squares estimation of parameters. Due to the symmetry of this mechanism, the idle pair of branched chains can be used for cross-validation of the kinematic and error models, thereby ensuring the model accuracy. A simulation study of the calibration algorithm is performed to verify the effectiveness of the algorithm. Last but not least, the pre-processing compensation procedure of the command pose is suggested for this 3T1R parallel manipulator.

2. Kinematics of a Symmetrical 3T1R Parallel Manipulator

In order to establish a kinematic model for the symmetrical 3T1R parallel manipulator, the basic structure of this parallel manipulator is firstly introduced. Subsequently, its forward kinematics based on the local POE formula is derived. It lays the foundation for the subsequent establishment of the kinematic error model for this parallel manipulator.

2.1. Structure of the 3T1R Parallel Manipulator

As shown in Figure 1, it has two identical branched chains, yielding symmetrical structures. Each branched chains has two identical sub-branches, so the whole mechanism can be treated as a "binary-tree" structure. This parallel manipulator is driven by four linear actuators installed on the base, and two linear actuators on one side share one stator. The entire manipulator mechanism looks like the shape of the letter "M", and it can move along the X, Y, and Z axes and rotate about the Z axis.
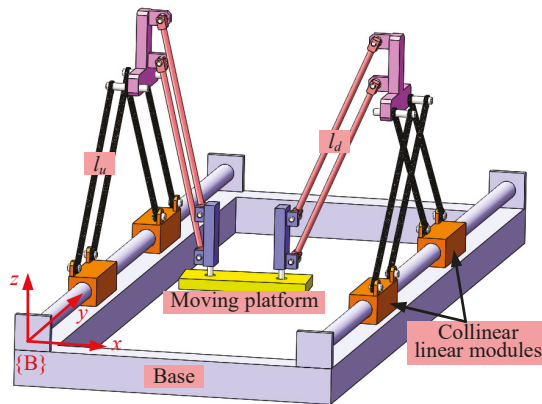
Figure 1. Basic structure figure of this 3T1R parallel manipulator.

2.2. Dyad kinematics Based on local POE formula

The *Dyad* branched chain is shown in Figure 2. Based on the traditional local POE formula method of building in Figure 2a, the *Dyad* kinematics can be obtained as (1):

$$T_{j-1,j} = T_{j-1}(0) \cdot e^{\hat{s}_j q_j},\tag{1}$$

where $T_{j-1,j} \in SE(3)$, represents the pose of $\{O_j\}$ relative to $\{O_{j-1}\}$ and uses the representation method of the local coordinate system. $\hat{s}_j$ is the corresponding element for $T_{j-1,j}$ in $se(3)$.
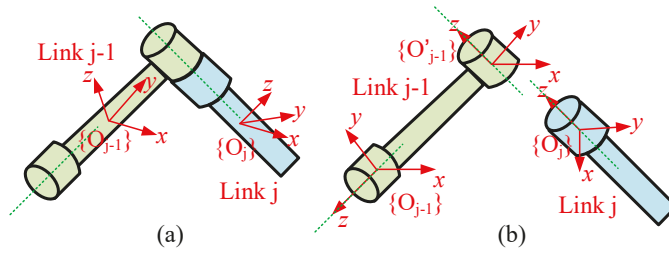
Figure 2. *Dyad* kinematics based on different methods of establishing coordinate systems for the local POE formula. (**a**) to establish a coordinate system arbitrarily, (**b**) to establish a coordinate system which leads to reduced number of kinematic parameters.

According to the characteristics of the local POE formula, it is known that the local coordinate system of the POE formula can be assigned arbitrarily, that is the pose of $\{O_j\}$ is arbitrary, so it requires 13 parameters to completely define $T_{j-1,j}$. Among them, the 13 parameters include: 6 parameters within initial pose $T_{j-1}(0) \in SE(3)$, 6 parameters within joint twist $\hat{s}_j \in se(3)$, and 1 parameter within joint variable $q_j \in R^{1X1}$. Compared with the D-H method, which only needs four parameters to define the kinematics, this method of establishing the kinematic model requires too many parameters.

In order to reduce the number of parameters in the kinematic model, a new method of assigning the local coordinate systems is proposed, as shown in Figure 2b. In this method, the origin of the coordinate system $\{O_{j-1}\}$ is at the center of the joint, and the direction of the z axis is along the joint line. Furthermore, an additional local coordinate system $\{O'_{j-1}\}$ is on the same link at the joint j. Now, (1) is written as:

$$T_{j-1,j} = T_{j-1,j}(0) \cdot e^{\hat{s}_j q_j}, \tag{2}$$

where $T_{j-1,j}(0)$ represents the pose transformation of $\{O'_{j-1}\}$ relative to $\{O_{j-1}\}$. $e^{\hat{s}_j q_j}$ represents the pose transformation of $\{O_j\}$ relative to $\{O'_{j-1}\}$.

According to the transformation between Lie groups and Lie algebras, $T_{j-1,j}(0) \in SE(3)$, at least one $\hat{t}_j \in se(3)$ exists, making $T_{j-1,j}(0) \in SE(3)$. Therefore, $T_{j-1,j}(0) = e^{\hat{t}_j}$, and (2) is written as:

$$T_{j-1,j} = e^{\hat{t}_j} \cdot e^{\hat{s}_j q_j}, \tag{3}$$

2.3. Branched Chain Kinematics Based on the Local POE Formula

Based on (2), consider a single branched chain of the parallel manipulator with $(n+1)$ links, numbered sequentially in the order 0, 1, 2···, n from base coordinate system $\{0\}$ to tool coordinate system $\{n\}$; the forward kinematics is expressed as:

$$g_{0,n}(q_1, q_2, \ldots, q_n) = T_{0,1}(q_1) T_{1,2}(q_2) \ldots T_{(n-1),n}(q_n) = \prod_{i=1}^{n} (T_{(i-1),i}(0) e^{\hat{s}_i q_i}). \tag{4}$$

2.4. Kinematics of the Parallel Manipulator Branched Chain i Based on the Local POE Formula

The schematic of the 3T1R parallel manipulator is shown in Figure 3a. It has a symmetrical structure, dividing it into two identical parts, I and II. This parallel manipulator contains four linear actuators B_1, B_2, B_3, and B_4. Each linear actuator to the midpoint of the end effector p is regarded as a branched chain. On side I, the branched chains formed by B_1 and B_2 to the end p point are recorded as i and $\underline{i}$, respectively, where $i = 1$; on side II, the branched chains formed by B_3 and B_4 to the end p point are recorded as i and $\underline{i}$, respectively, where $i = 2$. Any one of the branched chains from B_1 and B_2 and any one from B_3 and B_4 are chosen to build the entire parallel manipulator kinematics, so there are

four possible combinations. In this article, B_1 and B_3 are chosen for kinematic calibration and recorded as the ith branched chain, $i = 1, 2$, which is the structure indicated by the dark solid line in Figure 1. Surely, because this parallel manipulator structure is symmetrical, the remaining two branch chains can be used to carry out the calibration as well for cross-validation. This also helps to enhance the accuracy of the kinematic model.

There are four joint modules within each branched chain i ($i = 1, 2$), which are one active translation joint and three passive rotation joints. The coordinate systems are established as shown in Figure 1, and the way of naming is referenced in Nomenclature. The joint ij is an active joint for $i = 1, 2$ and $j = 1$, and the joint ij is a passive joint for $i = 1, 2$ and $j = 2, 3, 4$. The pose of the end effector coordinate system $\{P\}$ relative to the parallel manipulator base coordinate system $\{B\}$ is defined as the forward kinematics.
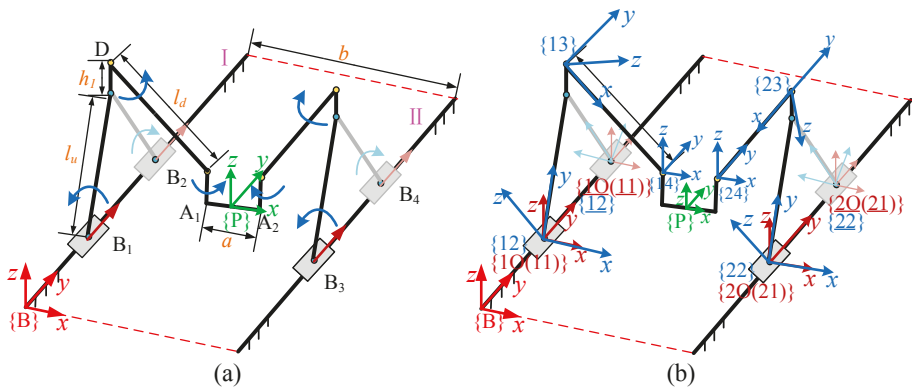
Figure 3. Mechanism schematic of this 3T1R parallel manipulator. (**a**) the schematic of the 3T1R parallel manipulator; (**b**) the establishment of the coordinate system.

The kinematic equation of the mechanism is given as:

$$g_i = T_{B,i0} \cdot T_{i0,i1}(0) \cdot e^{\hat{s}_{i1}q_{i1}} \cdot T_{i1,i2}(0) \cdot e^{\hat{s}_{i2}q_{i2}} \cdot T_{i2,i3}(0) \cdot e^{\hat{s}_{i3}q_{i3}} \cdot T_{i3,i4}(0) \cdot e^{\hat{s}_{i4}q_{i4}} \cdot T_{i4,P}(0). \quad (5)$$

3. Establishing the Kinematic Error Model for this 3T1R Parallel Manipulator

Since this parallel manipulator is a closed-chain mechanism, the kinematic error at the end effector of the parallel manipulator should be the same if they are calculated from individual branched chains.

3.1. Establishment of the Kinematic Error Model from a Single Branched Chain

An error model of the 3T1R parallel manipulator, considering the kinematic errors of the single branched chain, is established. Due to the part manufacturing and assembly error, the actual pose of the end effector is different from its nominal value. Since:

$$T_{B,i1}(0) = T_{B,i0} \cdot T_{i0,11}(0),$$

$T_{B,i1}(0)$ is the kinematic transformation from coordinate system $\{i1\}$ to coordinate system $\{B\}$. The kinematic Equation (5) of a single branched chain is simplified as:

$$g_i = T_{B,i1}(0) \cdot e^{\hat{s}_{i1}q_{i1}} \cdot T_{i1,i2}(0) \cdot e^{\hat{s}_{i2}q_{i2}} \cdot T_{i2,i3}(0) \cdot e^{\hat{s}_{i3}q_{i3}} \cdot T_{i3,i4}(0) \cdot e^{\hat{s}_{i4}q_{i4}} \cdot T_{i4,P}(0), \quad (6)$$

If $\hat{t} \in se(3)$ for a given $T(0) \in SE(3)$, then $e^{\hat{t}} = T$ holds. Therefore, for the initial pose $T_{i(j-1),ij}(0)$, $e^{\hat{t}_{ij}} = T_{i(j-1),ij}(0)$ holds, and $\hat{t}_{ij} \in se(3)$ $(i = 1, 2; j = 1, 2, 3, 4)$, so (6) is simplified to:

$$g_i = e^{\hat{t}_{i1}} e^{\hat{s}_{i1}q_{i1}} \cdot e^{\hat{t}_{i2}} e^{\hat{s}_{i2}q_{i2}} \cdot e^{\hat{t}_{i3}} e^{\hat{s}_{i3}q_{i3}} \cdot e^{\hat{t}_{i4}} e^{\hat{s}_{i4}q_{i4}} \cdot e^{\hat{t}_P}. \tag{7}$$

From (6), it is known that the modeling method using the local POE formula, whose forward kinematics g_i is a function of the initial pose $T(0) = [T_{B,i1}(0), T_{i1,i2}(0), T_{i2,i3}(0), T_{i3,i4}(0), T_{i4,P}(0)]^T$, the joint twist $s = [s_{i1}, s_{i2}, s_{i3}, s_{i4}]^T$, and the joint variable $q = [q_{i1}, q_{i2}, q_{i3}, q_{i4}]^T$, that is,

$$g_i = f(T(0), s, q). \tag{8}$$

Differentiate the kinematic parameters of (8) to obtain the calibration model, yielding:

$$\delta g_i \cdot g_i^{-1} = \left(\frac{\partial f}{\partial T(0)} \delta T(0) + \frac{\partial f}{\partial s} \delta s + \frac{\partial f}{\partial q} \delta q \right) g_i^{-1}, \tag{9}$$

where $\delta T \cdot T^{-1}$ represents the end effector's pose error of this parallel manipulator base coordinate system $\{B\}$ through the branched chain i, and the motion parameter error is $\delta T(0), \delta s, \delta q$. The purpose of the kinematic calibration algorithm is to find the appropriate $\delta T(0), \delta s, \delta q$, achieving the least squares fitting between two sides of (9), which is:

$$\min \left(\sum \left\| \delta g_i \cdot g_i^{-1} - \left(\frac{\partial f}{\partial T(0)} \delta T(0) + \frac{\partial f}{\partial s} \delta s + \frac{\partial f}{\partial q} \delta q \right) g_i^{-1} \right\| \right). \tag{10}$$

From earlier analysis, the kinematic error model consists of 13 parameters from the initial poses, joint twists, and joint variables. In order to simplify the calibration model, we assign the coordinate systems in the way shown in Figure 2b. Since the initial pose coordinate system in the local POE formula can be established at any point on the link, the initial pose $T(0)$ is floating. Therefore, the kinematic error is regarded as only due to the deviation of the initial poses $T(0)$, while the joint twists and joint variables are regarded as being accurate [12]. Therefore, (9) and (10) are simplified to:

$$\delta g_i \cdot g_i^{-1} = \frac{\partial f}{\partial T(0)} \delta T(0) g_i^{-1}, \tag{11}$$

$$\min \left(\sum \left\| \delta g_i \cdot g_i^{-1} - \frac{\partial f}{\partial T(0)} \delta T(0) g_i^{-1} \right\| \right). \tag{12}$$

By using two branched chains for kinematic calibration, the goal of optimization is revised as:

$$\min \sum_{i=1}^{2} \left(\left\| \delta g_i \cdot g_i^{-1} - \frac{\partial f}{\partial T(0)} \delta T(0) g_i^{-1} \right\| \right). \tag{13}$$

From (7), δg_i used in (11) and (13) is obtained as:

$$
\begin{aligned}
\delta g_i = {} & \delta(e^{\hat{t}_{i1}}) e^{\hat{s}_{i1}q_{i1}} \cdot e^{\hat{t}_{i2}} e^{\hat{s}_{i2}q_{i2}} \cdot e^{\hat{t}_{i3}} e^{\hat{s}_{i3}q_{i3}} \cdot e^{\hat{t}_{i4}} e^{\hat{s}_{i4}q_{i4}} \cdot e^{\hat{t}_P} + e^{\hat{t}_{i1}} e^{\hat{s}_{i1}q_{i1}} \cdot \delta(e^{\hat{t}_{i2}}) e^{\hat{s}_{i2}q_{i2}} \cdot e^{\hat{t}_{i3}} e^{\hat{s}_{i3}q_{i3}} \cdot e^{\hat{t}_{i4}} e^{\hat{s}_{i4}q_{i4}} \cdot e^{\hat{t}_P} \\
& + e^{\hat{t}_{i1}} e^{\hat{s}_{i1}q_{i1}} \cdot e^{\hat{t}_{i2}} e^{\hat{s}_{i2}q_{i2}} \cdot \delta(e^{\hat{t}_{i3}}) e^{\hat{s}_{i3}q_{i3}} \cdot e^{\hat{t}_{i4}} e^{\hat{s}_{i4}q_{i4}} \cdot e^{\hat{t}_P} + e^{\hat{t}_{i1}} e^{\hat{s}_{i1}q_{i1}} \cdot e^{\hat{t}_{i2}} e^{\hat{s}_{i2}q_{i2}} \cdot e^{\hat{t}_{i3}} e^{\hat{s}_{i3}q_{i3}} \cdot \delta(e^{\hat{t}_{i4}}) e^{\hat{s}_{i4}q_{i4}} \cdot e^{\hat{t}_P} \\
& + e^{\hat{t}_{i1}} e^{\hat{s}_{i1}q_{i1}} \cdot e^{\hat{t}_{i2}} e^{\hat{s}_{i2}q_{i2}} \cdot e^{\hat{t}_{i3}} e^{\hat{s}_{i3}q_{i3}} \cdot e^{\hat{t}_{i4}} e^{\hat{s}_{i4}q_{i4}} \cdot \delta(e^{\hat{t}_P}).
\end{aligned}
\tag{14}
$$

If the parameter error is relative to its local coordinate system, $\delta(e^{\hat{t}_{ij}}) = e^{\hat{t}_{ij}} \delta \hat{t}_{ij}$, so (14) is further expressed as:

$$
\begin{aligned}
\delta g_i = {} & e^{\hat{t}_{i1}} \delta \hat{t}_{i1} e^{\hat{s}_{i1}q_{i1}} \cdot e^{\hat{t}_{i2}} e^{\hat{s}_{i2}q_{i2}} \cdot e^{\hat{t}_{i3}} e^{\hat{s}_{i3}q_{i3}} \cdot e^{\hat{t}_{i4}} e^{\hat{s}_{i4}q_{i4}} \cdot e^{\hat{t}_P} + e^{\hat{t}_{i1}} e^{\hat{s}_{i1}q_{i1}} \cdot e^{\hat{t}_{i2}} \delta \hat{t}_{i2} e^{\hat{s}_{i2}q_{i2}} \cdot e^{\hat{t}_{i3}} e^{\hat{s}_{i3}q_{i3}} \cdot e^{\hat{t}_{i4}} e^{\hat{s}_{i4}q_{i4}} \cdot e^{\hat{t}_P} \\
& + e^{\hat{t}_{i1}} e^{\hat{s}_{i1}q_{i1}} \cdot e^{\hat{t}_{i2}} e^{\hat{s}_{i2}q_{i2}} \cdot e^{\hat{t}_{i3}} \delta \hat{t}_{i3} e^{\hat{s}_{i3}q_{i3}} \cdot e^{\hat{t}_{i4}} e^{\hat{s}_{i4}q_{i4}} \cdot e^{\hat{t}_P} + e^{\hat{t}_{i1}} e^{\hat{s}_{i1}q_{i1}} \cdot e^{\hat{t}_{i2}} e^{\hat{s}_{i2}q_{i2}} \cdot e^{\hat{t}_{i3}} e^{\hat{s}_{i3}q_{i3}} \cdot e^{\hat{t}_{i4}} \delta \hat{t}_{i4} e^{\hat{s}_{i4}q_{i4}} \cdot e^{\hat{t}_P} \\
& + e^{\hat{t}_{i1}} e^{\hat{s}_{i1}q_{i1}} \cdot e^{\hat{t}_{i2}} e^{\hat{s}_{i2}q_{i2}} \cdot e^{\hat{t}_{i3}} e^{\hat{s}_{i3}q_{i3}} \cdot e^{\hat{t}_{i4}} e^{\hat{s}_{i4}q_{i4}} \cdot e^{\hat{t}_P} \delta \hat{t}_P.
\end{aligned}
\tag{15}
$$

By multiplying (15) with g_i^{-1} on both its left and right sides, where $g_i^{-1} = e^{-\hat{t}_P} \cdot e^{-\hat{s}_{i4}q_{i4}}e^{-\hat{t}_{i4}} \cdot e^{-\hat{s}_{i3}q_{i3}}e^{-\hat{t}_{i3}} \cdot e^{-\hat{s}_{i2}q_{i2}}e^{-\hat{t}_{i2}} \cdot e^{-\hat{s}_{i1}q_{i1}}e^{-\hat{t}_{i1}}$, this yields:

$$
\begin{aligned}
\delta g_i \cdot g_i^{-1} =\ & e^{\hat{t}_{i1}} \cdot \delta \hat{t}_{i1} \cdot e^{-\hat{t}_{i1}} + e^{\hat{t}_{i1}} e^{\hat{s}_{i1}q_{i1}} e^{\hat{t}_{i2}} \cdot \delta \hat{t}_{i2} \cdot e^{-\hat{t}_{i2}} e^{-\hat{s}_1 q_1} e^{-\hat{t}_1} \\
& + e^{\hat{t}_{i1}} e^{\hat{s}_{i1}q_{i1}} e^{\hat{t}_{i2}} e^{\hat{s}_{i2}q_{i2}} e^{\hat{t}_{i3}} \cdot \delta \hat{t}_{i3} \cdot e^{-\hat{t}_{i3}} e^{-\hat{s}_{i2}q_{i2}} e^{-\hat{t}_{i2}} e^{-\hat{s}_{i1}q_{i1}} e^{-\hat{t}_{i1}} r \\
& + e^{\hat{t}_{i1}} e^{\hat{s}_{i1}q_{i1}} e^{\hat{t}_{i2}} e^{\hat{s}_{i2}q_{i2}} e^{\hat{t}_{i3}} e^{\hat{s}_{i3}q_{i3}} e^{\hat{t}_{i4}} \cdot \delta \hat{t}_{i4} \cdot e^{-\hat{t}_{i4}} e^{-\hat{s}_{i3}q_{i3}} e^{-\hat{t}_{i3}} e^{-\hat{s}_{i2}q_{i2}} e^{-\hat{t}_{i2}} e^{-\hat{s}_{i1}q_{i1}} e^{-\hat{t}_{i1}} \\
& + e^{\hat{t}_{i1}} e^{\hat{s}_{i1}q_{i1}} e^{\hat{t}_{i2}} e^{\hat{s}_{i2}q_{i2}} e^{\hat{t}_{i3}} e^{\hat{s}_{i3}q_{i3}} e^{\hat{t}_{i4}} e^{\hat{s}_{i4}q_{i4}} e^{\hat{t}_P} \cdot \delta \hat{t}_P r \\
& \cdot e^{-\hat{t}_P} e^{-\hat{s}_{i4}q_{i4}} e^{-\hat{t}_{i4}} e^{-\hat{s}_{i3}q_{i3}} e^{-\hat{t}_{i3}} e^{-\hat{s}_{i2}q_{i2}} e^{-\hat{t}_{i2}} e^{-\hat{s}_{i1}q_{i1}} e^{-\hat{t}_{i1}}.
\end{aligned}
\tag{16}
$$

From the adjoint transformation $\mathrm{Ad}_X y = XyX^{-1}$, (16) is simplified to:

$$
\begin{aligned}
\delta g_i \cdot g_i^{-1} =\ & \mathrm{Ad}_{T_{B,i1}(0)} \delta \hat{t}_{i1} + \mathrm{Ad}_{g_{0,1} \cdot T_{i1,i2}(0)} \delta \hat{t}_{i2} \\
& + \mathrm{Ad}_{g_{0,2} \cdot T_{i2,i3}(0)} \delta \hat{t}_{i3} + \mathrm{Ad}_{g_{0,3} \cdot T_{i3,i4}(0)} \delta \hat{t}_{i4} + \mathrm{Ad}_{g_{0,4} \cdot T_{i4,P}(0)} \delta \hat{t}_P,
\end{aligned}
\tag{17}
$$

where:

$$
g_{0,k} = e^{\hat{t}_{i1}} e^{\hat{s}_{i1}q_{i1}} \cdot e^{\hat{t}_{i2}} e^{\hat{s}_{i2}q_{i2}} \cdots e^{\hat{t}_{ik}} e^{\hat{s}_{ik}q_{ik}}.
$$

For (17), the left term $\delta g_i \cdot g_i^{-1} \in se(3)$ represents the end effector's pose error in the base coordinate system $\{B\}$, according to the definition of the logarithm of the matrix on $SE(3)$:

$$
\left(\delta g_i \cdot g_i^{-1} \right)^\vee = \log \left(g_i^a \cdot g_i^{-1} \right),
\tag{18}
$$

where g_i^a is the pose measured at the end of the branched chain i and g_i^{-1} is the inverse of nominal pose matrix at the end of the branched chain i. From (17) and (18), we get:

$$
\log \left(g_i^a \cdot g_i^{-1} \right) = \left[\mathrm{Ad}_{T_{B,i1}(0)}, \mathrm{Ad}_{g_{0,1} \cdot T_{i1,i2}(0)}, \mathrm{Ad}_{g_{0,2} \cdot T_{i2,i3}(0)}, \mathrm{Ad}_{g_{0,3} \cdot T_{i3,i4}(0)}, \mathrm{Ad}_{g_{0,4} \cdot T_{i4,P}(0)} \right]
\begin{bmatrix} \delta t_{i1} \\ \delta t_{i2} \\ \delta t_{i3} \\ \delta t_{i4} \\ \delta t_P \end{bmatrix}.
\tag{19}
$$

(19) is written as a linear-in-parameter form:

$$
y_i = J_i x_i,
\tag{20}
$$

where y_i is the pose error of the end effector from the branched chain i, J_i is the error Jacobian matrix of the branched chain i, and x_i is the kinematic parameter error of the branched chain i, given as:

$$
\begin{aligned}
y_i &= \log \left(g_i^a \cdot g_i^{-1} \right) \in R^{6 \times 1}, \\
J_i &= \left[\mathrm{Ad}_{T_{B,i1}(0)}, \mathrm{Ad}_{g_{0,2} \cdot T_{i1,i2}(0)}, \mathrm{Ad}_{g_{0,2} \cdot T_{i2,i3}(0)}, \mathrm{Ad}_{g_{0,3} \cdot T_{i3,i4}(0)}, \mathrm{Ad}_{g_{0,4} \cdot T_{i4,P}(0)} \right] \in R^{6 \times 30}, \\
x_i &= [\delta t_{i1}, \delta t_{i2}, \delta t_{i3}, \delta t_{i4}, \delta t_P]^T \in R^{30 \times 1}.
\end{aligned}
$$

3.2. Establishment of the Overall Kinematic Error Model

The kinematic error of the end effector calculated from the kinematic error models of different branched chains should be identical. This yields:

$$
Y = AX,
\tag{21}
$$

where:

$$
\begin{aligned}
Y &= y_1 = y_2 \in R^{6\times1}, \\
A &= [J_1, J_2] \in R^{6\times60}, \\
X &= \left[x_1^T, x_2^T\right]^T \in R^{60\times1}.
\end{aligned}
$$

In the above error model, it has a total of 60 error parameters to describe the kinematic error. Through the discernibility analysis of the error model deduced from the POE formula, the maximum number of independent motion parameters of a universal non-over-constrained parallel manipulator after eliminating redundant error components is $4r + 2p + 6$, where r and p represent equivalent rotation joints and translation joints, respectively [12]. In the 3T1R parallel manipulator, there are six equivalent rotation joints and two translation joints. Therefore, the maximum number of identifiable parameters after eliminating redundant error components is 34. According to (21), the number of errors obtained using the method described in this article is 60, so the error model does have redundancy in terms of the number of parameters.

4. Method to Reduce the Number of Sensors Used in Passive Joints

In general, since the parallel manipulator contains many passive joints, a sensor will be installed on each passive joint to measure the corresponding joint angle throughout the calibration process. The required measurements for calibration are accomplished by both built-in sensors and external measurement device. The built-in sensors are used for measuring rotation of the passive joints, and a laser tracker is used for measuring the end effector's pose. As the 3T1R parallel manipulator has many passive joints and such a measurement scheme is costly, a recursive method is proposed to estimate one of the joint angles in each branched chain, so that the number of sensors being used is reduced.

This recursive method is based on the coordinates of the end point A_i and uses the local POE formula method to establish the branched chain kinematics of the end point A_i, such as (22):

$$
\begin{bmatrix} p_i \\ 1 \end{bmatrix} = T_{B,i1}(0) \cdot e^{\hat{s}_{i1}q_{i1}} \cdot T_{i1,i2}(0) \cdot e^{\hat{s}_{i2}q_{i2}} \cdot T_{i2,i3}(0) \cdot e^{\hat{s}_{i3}q_{i3}} \cdot \begin{bmatrix} p_i' \\ 1 \end{bmatrix}, \tag{22}
$$

where p_i represents the coordinates of point A_i on the branched chain i relative to the base coordinate system $\{B\}$ and p_i' represents the coordinates of the point A_i on the branched chain i relative to the coordinate system $\{i3\}$.

By setting:

$$
\begin{bmatrix} p_i \\ 1 \end{bmatrix} = P_i, \quad \begin{bmatrix} p_i' \\ 1 \end{bmatrix} = P_i', \tag{23}
$$

(22) is re-written as:

$$
P_i = T_i \cdot e^{\hat{s}_{i3}q_{i3}} P_i', \tag{24}
$$

The difference between the nominal and actual distance of two revolute joints at the end effector is given by:

$$
d_{12} - \left\| \overrightarrow{A_1 A_2} \right\| = d \left\| \overrightarrow{A_1 A_2} \right\| \equiv dd, \tag{25}
$$

where $\left\| \overrightarrow{A_1 A_2} \right\|$ represents the nominal distance of between A_1 and A_2 and d_{12} represents the actual distance between A_1 and A_2. Here,

$$
\left\| \overrightarrow{A_1 A_2} \right\|^2 = (P_2 - P_1)^T (P_2 - P_1). \tag{26}
$$

Differentiating (26), we get:

$$\mathrm{d}d = \frac{(P_2 - P_1)^T}{\|A_1 A_2\|} (\mathrm{d}P_2 - \mathrm{d}P_1),$$ (27)

$$\mathrm{d}P_i = T_i \cdot e^{\hat{s}_{i3} \cdot q_{i3}} \cdot \hat{S}_3 \cdot P_i' \cdot \mathrm{d}q_3,$$ (28)

With (25), (26), (27), and (28), it yields:

$$\mathrm{d}q = J^{-1} \cdot \mathrm{d}d,$$ (29)

where:

$$\mathrm{d}q = \begin{pmatrix} \mathrm{d}q_{13} \\ \mathrm{d}q_{23} \end{pmatrix}, J = \begin{pmatrix} \dfrac{-(P_2 - P_1)^T}{\|A_1 A_2\|} \cdot \dot{P}_1 & \dfrac{(P_2 - P_1)^T}{\|A_1 A_2\|} \cdot \dot{P}_2 \end{pmatrix},$$

$$\dot{P}_i = T_i \cdot e^{\hat{s}_{i3} \cdot q_{i3}} \cdot \hat{s}_3 \cdot P_i'.$$

(29) is written in a recursive form as:

$$q^{(k+1)} = q^{(k)} + \left(J^{-1} \cdot \mathrm{d}d \right)^{(k)},$$ (30)

where k is the number of iterations.

This means, by utilizing the geometric constraints of the mechanism, the proposed recursive method is able to estimate the rotation angle of the second revolute joint of each branched chain. This saves one rotation sensor for each branched chain during calibration.

5. A Recursive Least Squares Method to Identify the Parameters in the Kinematic Error Model

In order to improve the efficiency, a recursive least squares method is used in the parameter identification process for the kinematic error model. Suppose that when measuring positions of m points, there will be m position error vectors, and the Jacobian matrix will be expanded to m terms, so the kinematic error vector X will remain unchanged. Hence, (31) is obtained as:

$$\tilde{Y} = \tilde{A}X,$$ (31)

where:

$$\begin{aligned} \tilde{Y} &= \begin{bmatrix} Y_1 & Y_2 & \dots & Y_m \end{bmatrix}^T \in R^{6m \times 1}, \\ \tilde{A} &= \text{column} \left[A_1, A_2, \dots, A_m \right] \in R^{6m \times 60}, \\ X &= \begin{bmatrix} x_1^T, x_2^T \end{bmatrix}^T \in R^{60 \times 1}. \end{aligned}$$

The solution in the least squares sense for X is given as:

$$X = \left(\tilde{A}^T \tilde{A} \right)^{-1} \tilde{A}^T \tilde{Y}.$$ (32)

(32) can be further simplified by recursion. Once the kinematic error parameter X is determined, the initial pose $T_{i(j-1),ij}(0)$ will be updated by substituting X into the following equation:

$$T_{i(j-1),ij}^c(0) = e^{\hat{t}_{ij}} e^{\delta \hat{t}_{ij}} = T_{i(j-1),ij}(0) e^{\delta \hat{t}_{ij}},$$ (33)

until the norm $\|X\|$ of X approaches zero. Therefore, the pose computed from the calibrated kinematic model approaches the actual pose.

6. Simulation Results

The kinematic modeling schematic diagram and the establishment of the coordinate system are shown in Figure 3, where $l_u = 0.7$, $l_d = 0.7$, $a = 0.3$, $b = 1.0$ (units: m). According to the modeling method using the local POE formula given in Nomenclature, the values of the initial pose and joint twist of adjacent links of two branched chains are given as:

$$T_{B,11}(0) = \begin{bmatrix} 1 & 0 & 0 & 0 \\ 0 & 1 & 0 & 0.03 \\ 0 & 0 & 1 & 0 \\ 0 & 0 & 0 & 1 \end{bmatrix}, T_{11,12}(0) = \begin{bmatrix} 1 & 0 & 0 & 0 \\ 0 & 1 & 0 & 0 \\ 0 & 0 & 1 & 0 \\ 0 & 0 & 0 & 1 \end{bmatrix},$$

$$T_{12,13}(0) = \begin{bmatrix} 1 & 0 & 0 & 0 \\ 0 & \cos(-\alpha) & -\sin(-\alpha) & l_u \\ 0 & \sin(-\alpha) & \cos(-\alpha) & 0 \\ 0 & 0 & 0 & 1 \end{bmatrix}, T_{13,14}(0) = \begin{bmatrix} \cos(-\beta) & 0 & \sin(-\beta) & l_d \\ 0 & 1 & 0 & 0 \\ -\sin(-\beta) & 0 & \cos(-\beta) & 0 \\ 0 & 0 & 0 & 1 \end{bmatrix},$$

$$T_{14,P}(0) = \begin{bmatrix} 1 & 0 & 0 & a/2 \\ 0 & 1 & 0 & 0 \\ 0 & 0 & 1 & 0 \\ 0 & 0 & 0 & 1 \end{bmatrix}, T_{B,21}(0) = \begin{bmatrix} 1 & 0 & 0 & b \\ 0 & 1 & 0 & 0.03 \\ 0 & 0 & 1 & 0 \\ 0 & 0 & 0 & 1 \end{bmatrix}, T_{21,22}(0) = \begin{bmatrix} 1 & 0 & 0 & 0 \\ 0 & 1 & 0 & 0 \\ 0 & 0 & 1 & 0 \\ 0 & 0 & 0 & 1 \end{bmatrix},$$

$$T_{22,23}(0) = \begin{bmatrix} 1 & 0 & 0 & 0 \\ 0 & \cos(-\alpha) & -\sin(-\alpha) & l_u \\ 0 & \sin(-\alpha) & \cos(-\alpha) & 0 \\ 0 & 0 & 0 & 1 \end{bmatrix}, T_{23,24}(0) = \begin{bmatrix} -\cos(\beta) & 0 & -\sin(\beta) & l_d \\ 0 & 1 & 0 & 0 \\ \sin(\beta) & 0 & -\cos(\beta) & 0 \\ 0 & 0 & 0 & 1 \end{bmatrix},$$

$$T_{24,P}(0) = \begin{bmatrix} 1 & 0 & 0 & -a/2 \\ 0 & 1 & 0 & 0 \\ 0 & 0 & 1 & 0 \\ 0 & 0 & 0 & 1 \end{bmatrix},$$

$$s_{11} = \begin{bmatrix} 0 & 1 & 0 & 0 & 0 & 0 \end{bmatrix}^T, s_{12} = \begin{bmatrix} 0 & 0 & 0 & 1 & 0 & 0 \end{bmatrix}^T,$$

$$s_{13} = \begin{bmatrix} 0 & 0 & 0 & 0 & 1 & 0 \end{bmatrix}^T, s_{14} = \begin{bmatrix} 0 & 0 & 0 & 0 & 0 & 1 \end{bmatrix}^T,$$

$$s_{21} = \begin{bmatrix} 0 & 1 & 0 & 0 & 0 & 0 \end{bmatrix}^T, s_{22} = \begin{bmatrix} 0 & 0 & 0 & 1 & 0 & 0 \end{bmatrix}^T,$$

$$s_{23} = \begin{bmatrix} 0 & 0 & 0 & 0 & 1 & 0 \end{bmatrix}^T, s_{24} = \begin{bmatrix} 0 & 0 & 0 & 0 & 0 & 1 \end{bmatrix}^T.$$

In order to simulate the deviation of kinematic parameters from the nominal ones, the errors δt, δs, and δq are applied to the initial poses, joint twists, and joint variables in the theoretical model. Noise is introduced in the measurement of joint variables to test the robustness of the parameter identification method. In this way, an actual model is obtained, where the actual initial pose is:

$$T^a_{i(j-1),ij}(0) = e^{\hat{t}_{ij}} e^{\delta \hat{t}_{ij}} = T_{i(j-1),ij}(0) e^{\delta \hat{t}_{ij}}, \tag{34}$$

the actual joint twist is:

$$s^a_{ij} = s_{ij} + \delta s_{ij}, \tag{35}$$

the actual joint variable is:

$$q^a_{ij} = q_{ij} + \delta q_{ij}. \tag{36}$$

Hence, the kinematic model of the actual branched chain i is:

$$g_i = T^a_{B,i1}(0)e^{\hat{s}^a_{i1}q^a_{i1}} \cdot T^a_{i1,i2}(0)e^{\hat{s}^a_{i2}q^a_{i2}} \cdot T^a_{i2,i3}(0)e^{\hat{s}^a_{i3}q^a_{i3}} \cdot T^a_{i3,i4}(0)e^{\hat{s}^a_{i4}q^a_{i4}} \cdot T^a_{i4,P}(0). \tag{37}$$

Add deviations δt, δs, and δq to the nominal values to get the actual value of the parallel manipulator simulation, as shown in Table 1. Each joint, regardless of being active or passive, is considered as a joint with one degree of freedom, so the error vector of the spin volume should be orthonormal, that is $\|w_i + \delta w\| = 1$, $(w_i + \delta w)^T (v_i + \delta v) = 0$.

Table 1. Preset error of each link (all units are in SI).

Dyad	δt	δs	δq
B-11	$\begin{bmatrix} 0.002 & 0.002 & 0.002 & 0.001 & 0.001 & 0.001 \end{bmatrix}^T$	$\begin{bmatrix} 0 & 0 & 0 & 0 & 0 & 0 \end{bmatrix}^T$	0.02
11-12	$\begin{bmatrix} 0.002 & 0.002 & 0.002 & 0.001 & 0.001 & 0.001 \end{bmatrix}^T$	$\begin{bmatrix} 0 & 0 & 0 & -1 + \cos 0.02 & \sin 0.02 & 0 \end{bmatrix}^T$	0.02
12-13	$\begin{bmatrix} 0.002 & 0.002 & 0.002 & 0.001 & 0.001 & 0.001 \end{bmatrix}^T$	$\begin{bmatrix} 0 & 0 & 0 & 0 & -1 + \cos 0.02 & \sin 0.02 \end{bmatrix}^T$	0.02
13-14	$\begin{bmatrix} 0.002 & 0.002 & 0.002 & 0.001 & 0.001 & 0.001 \end{bmatrix}^T$	$\begin{bmatrix} 0 & 0 & 0 & 0 & \sin 0.02 & -1 + \cos 0.02 \end{bmatrix}^T$	0.02
14-P	$\begin{bmatrix} 0.002 & 0.002 & 0.002 & 0.001 & 0.001 & 0.001 \end{bmatrix}^T$	⌒	⌒
B-21	$\begin{bmatrix} 0.002 & 0.002 & 0.002 & 0.001 & 0.001 & 0.001 \end{bmatrix}^T$	$\begin{bmatrix} 0 & 0 & 0 & 0 & 0 & 0 \end{bmatrix}^T$	0.02
21-22	$\begin{bmatrix} 0.002 & 0.002 & 0.002 & 0.001 & 0.001 & 0.001 \end{bmatrix}^T$	$\begin{bmatrix} 0 & 0 & 0 & 1 - \cos 0.02 & \sin 0.02 & 0 \end{bmatrix}^T$	0.02
22-23	$\begin{bmatrix} 0.002 & 0.002 & 0.002 & 0.001 & 0.001 & 0.001 \end{bmatrix}^T$	$\begin{bmatrix} 0 & 0 & 0 & 0 & -1 + \cos 0.02 & \sin 0.02 \end{bmatrix}^T$	0.02
23-24	$\begin{bmatrix} 0.002 & 0.002 & 0.002 & 0.001 & 0.001 & 0.001 \end{bmatrix}^T$	$\begin{bmatrix} 0 & 0 & 0 & 0 & \sin 0.02 & -1 + \cos 0.02 \end{bmatrix}^T$	0.02
24-P	$\begin{bmatrix} 0.002 & 0.002 & 0.002 & 0.001 & 0.001 & 0.001 \end{bmatrix}^T$	⌒	⌒

Now, the simulation process of the kinematic error modeling and parameter identification is summarized as follows:

1. Use the numerical forward kinematics algorithm to obtain the joint displacements and joint angles of 20 different parallel manipulator poses;
2. Assign errors to kinematic parameters, such as δt, δs, and δq, as shown in Table 1.
3. Simulate the actual initial pose using $T^a_{i(j-1),ij}(0) = T_{i(j-1),ij}(0)e^{\delta \hat{t}_{ij}}$;
4. The actual joint twist is computed as $s^a_{ij} = s_{ij} + \delta s_{ij}$;
5. The actual joint variable is computed as $q^a_{ij} = q_{ij} + \delta q_{ij}$;
6. The recursive calibration algorithm is used to identify the kinematic errors of the parallel manipulator.

The initial pose after calibration is recorded as $T^c_{i(j-1),ij}(0)$, as shown in Table 2. When $\text{trace}(R) \neq -1$, $1 + 2\cos\phi = \text{trace}(R)$, and $\|\omega\| < \pi$, we get $\log(T) = t$. That is,

$$\log \begin{bmatrix} R & p \\ 0 & 1 \end{bmatrix} = \begin{bmatrix} \hat{\omega} & A^* p \\ 0 & 0 \end{bmatrix} \in se(3), \tag{38}$$

where,

$$\hat{\omega} = \log R = \frac{\phi}{2\sin\phi}(R - R^T),$$

$$A^* = I - \frac{1}{2}\hat{\omega} + \frac{2\sin\|\omega\| - \|\omega\|(1 + \cos\|\omega\|)}{2\|\omega\|^2 \sin\|\omega\|}\hat{\omega}^2,$$

If ϕ is small, $\hat{\omega} \approx (R - R^T)/2$. When $\text{trace}(R) = -1$, $\log R = (2k + 1)\pi\hat{v}$. In this case, k is any integer, and v is a unit eigenvector of $\log R$ with an eigenvalue of one.

Table 2. Kinematic error of each link versus its calibration pose (all units are in SI).

Dyad	**Kinematic Errors**	$T^c_{i(j-1),ij}(0)$
$B-11$	$(1.824, 2.272, 1.183, 0.02000, 0.00128, 0.00100)^T$	$\begin{bmatrix} 1.00000 & -0.00099 & 0.00129 & 1.794 \\ 0.00102 & 0.99980 & -0.02000 & 32.255 \\ -0.00127 & 0.02000 & 0.99980 & 1.805 \\ 0 & 0 & 0 & 1 \end{bmatrix}$
$11-12$	$(1.794, 2.272, 1.783, 0.02000, 0.00128, 0.00165)^T$	$\begin{bmatrix} 1.00000 & -0.00164 & 0.00128 & 1.793 \\ 0.00165 & 0.99999 & -0.00201 & 2.272 \\ -0.00128 & 0.00201 & 1.00000 & 1.784 \\ 0 & 0 & 0 & 1 \end{bmatrix}$
$12-13$	$(2.855, 2.868, -1.922, 0.00225, 0.00207, 0.00152)^T$	$\begin{bmatrix} 1.00000 & -0.00253 & 0.00039 & 1.791 \\ 0.00152 & 0.70869 & 0.70551 & 702.869 \\ -0.00207 & -0.70551 & 0.70870 & 0.344 \\ 0 & 0 & 0 & 1 \end{bmatrix}$
$13-14$	$(-0.647, 1.134, 3.916, -0.00107, 0.00210, 0.00163)^T$	$\begin{bmatrix} 0.50182 & -0.00163 & -0.86497 & 699.353 \\ 0.00174 & 1.00000 & -0.00087 & 2.273 \\ 0.86497 & -0.00107 & 0.50182 & 2.445 \\ 0 & 0 & 0 & 1 \end{bmatrix}$
$14-P$	$(1.794, 2.063, 2.139, 0.000874, 0.00237, 0.00140)^T$	$\begin{bmatrix} 1.00000 & -0.00140 & 0.00237 & 151.795 \\ 0.00140 & 1.00000 & -0.00087 & 2.273 \\ -0.00237 & 0.00088 & 1.00000 & 1.782 \\ 0 & 0 & 0 & 1 \end{bmatrix}$
$B-21$	$(1.790, 2.153, 2.123, 0.02000, 0.00175, 0.00100)^T$	$\begin{bmatrix} 0.99999 & -0.00099 & 0.00176 & 1001.760 \\ 0.00102 & 0.99980 & -0.02000 & 33.147 \\ -0.00174 & 0.02000 & 0.99980 & 1.007 \\ 0 & 0 & 0 & 1 \end{bmatrix}$
$21-22$	$(1.761, 3.155, 0.977, 0.00165, 0.00175, 0.00050)^T$	$\begin{bmatrix} 1.00000 & -0.00050 & 0.00175 & 1.761 \\ 0.00051 & 1.00000 & -0.00165 & 3.155 \\ -0.00174 & 0.00165 & 1.00000 & 0.978 \\ 0 & 0 & 0 & 1 \end{bmatrix}$
$22-23$	$(2.009, 2.922, -0.003, 0.00273, 0.00159, 0.00035)^T$	$\begin{bmatrix} 1.00000 & -0.00137 & 0.00088 & 1.759 \\ 0.00036 & 0.70903 & 0.70518 & 702.924 \\ -0.00159 & -0.70517 & 0.70903 & -0.00154 \\ 0 & 0 & 0 & 1 \end{bmatrix}$
$23-24$	$(-1.726, 3.529, 2.156, -0.00256, 0.00160, -0.00053)^T$	$\begin{bmatrix} -0.49861 & 0.00053 & -0.86682 & 698.275 \\ 0.00248 & 1.00000 & -0.00081 & 3.157 \\ 0.86682 & -0.00256 & -0.49861 & 1.034 \\ 0 & 0 & 0 & 1 \end{bmatrix}$
$24-P$	$(1.761, 3.598, 0.759, 0.00082, 0.00145, 0.00295)^T$	$\begin{bmatrix} 1.00000 & -0.00295 & 0.00145 & -148.243 \\ 0.00295 & 1.00000 & -0.00081 & 3.157 \\ -0.00145 & 0.00082 & 1.00000 & 0.977 \\ 0 & 0 & 0 & 1 \end{bmatrix}$

The kinematic error between the calibrated value T^c and the actual value T^a is obtained through the above method, as shown in Table 2, including the orientation and position error at the end effector. The orientation error is the angular difference between the actual value of the end effector and the calibrated one. Position error is the norm of the coordinate difference between the actual value of the midpoint of the moving platform and the calibration one. Note that the derivation of kinematic parameters was arbitrarily assumed in this simulation example, and it may not truly reflect the actual situation in the parameter space due to manufacturing and assembly error. However, through the end effector's pose error simulation result as in Figure 4, it is seen that both the orientation and position errors converged, and they were reduced by at least 10 times, thereby verifying the effectiveness of the calibration algorithm. Compared with other methods based on the deviation of the distance between points on the end-effector of parallel manipulators [26,27], our method gave better fitness of the pose error at the central point of the end effector. Since the model was linear-in-parameter, the pose fit with higher matching and better fitting conversion effects. Therefore, in the case of a linear error model, the pose error was used for fitting so that the error reduction only needed one iteration.
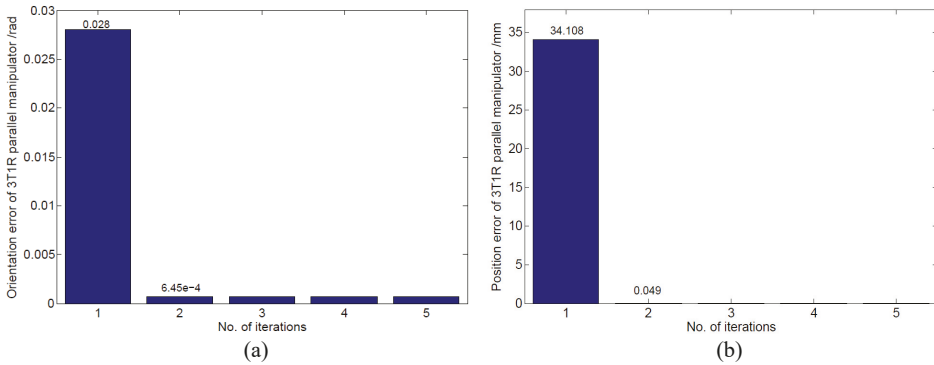
Figure 4. The end effector's pose error simulation result. (**a**) Orientation error; (**b**) position error.

To guide the future calibration experiments, the flowchart of the calibration process is given in Figure 5. The meanings of various symbols in the flowchart can be referenced in Nomenclature.
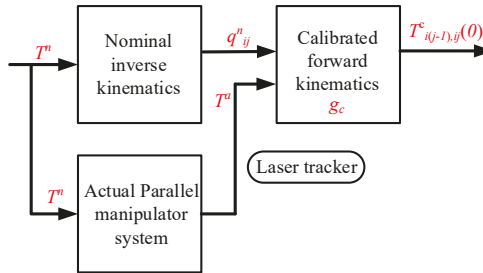
Figure 5. Flowchart of the calibration.

7. Pre-Processing Compensation

Since some robot controllers cannot directly utilize the calibrated active and passive joint angles to drive the robot, the joint variables were preprocessed to obtain the pose of the end effector that could be directly utilized by the robot.

First, the initial pose $T^c_{i(j-1),ij}(0)$ after calibration of each link was obtained through the calibration process described above, as shown in Table 2. Combined with the commanded end pose T_{co}, the calibrated joint angle q^c_{ij} was calculated using the inverse kinematics after calibration. Since the manipulator could not directly use q^c_{ij}, the following conversion was required. By bringing q^c_{ij} into the positive kinematics solution based on the nominal kinematics parameters, the compensated end effector pose T_{cp} could be obtained. At this time, T_{cp} could be directly used for offline programming. The flowchart of this process is shown in Figure 6. The meaning of various symbols is listed in Nomenclature.
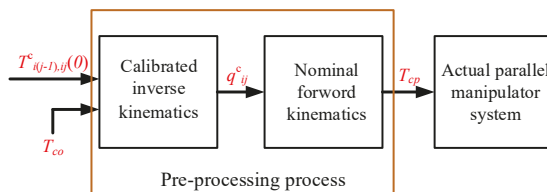
Figure 6. Flowchart of pre-processing compensation.

8. Conclusions

In this paper, a kinematic model of a symmetrical 3T1R parallel manipulator was proposed based on the local POE formula. By using local POE formula for kinematic error modeling, the joint twists and joint variables could maintain their nominal values, and the errors were set to be concentrated in the matrices of initial poses. As the end effector's pose errors of the parallel manipulator established through different branched chains were identical, the entire pose error of the parallel manipulator's end effector was formed by equaling the pose error of the end effector calculated in individual branched chains.In addition, the joint angle of the second revolute joint was calculated by a recursive algorithm according to the inherent kinematic constraints. This saved the rotary sensors installed at the second revolute joint of each branched chain. Through simulation, it was shown that the deviation between the actual and calibrated end effector's pose could be reduced by at least 10 times with the proposed kinematic error modeling and parameter identification methods. The procedures to use this error model for profile pre-compensation in the actual testbed were also proposed.

Conflicts of Interest: The authors declare no conflict of interest.

Abbreviations

The following abbreviations are used in this manuscript:

3T1R parallel manipulator	The parallel manipulator can achieve three degrees of freedom of translation along the X, Y, and Z axes and one degree of freedom of rotation around the Z axis
POE formula	The product of exponentials formula
D-H convention	The Denavit-Hartenberg convention

Nomenclature

For the ease of reference, the definition of the symbols used in this article are listed as follows:

n	The number of passive joints
i	Represents the parallel manipulator B_1, B_3 branched chains ($i = 1$, 2)
$\underline{i}$	Represents the parallel manipulator B_2, B_4 branched chains ($i = 1$, 2)
j	The number of joints on each branched chain ($j = 1$, 2, 3, 4)
g_i	Forward kinematics of these parallel manipulator branched chains i
$T_{i(j-1),ij}(0)$	The initial pose of the coordinate system $\{ij\}$ relative to the coordinate system $\{i(j-1)\}$
$T^c_{i(j-1),ij}(0)$	After calibration, the initial pose of the coordinate system $\{ij\}$ relative to the coordinate system $\{i(j-1)\}$
$T^a_{i(j-1),ij}(0)$	The actual initial pose of the coordinate system $\{ij\}$ relative to the coordinate system $\{i(j-1)\}$
q_{ij}	Standard representation of joint variable; it represent the joint angle or joint displacement
q^n_{ij}	Standard representation of the nominal joint variable
q^c_{ij}	Standard representation of the joint variable after calibration
$\{B\}$	Base coordinate system of the parallel manipulator
$\{i0\}$, $\{\underline{i0}\}$	Base coordinate system of these parallel manipulator branched chains i and $\underline{i}$
$\{i1\}$, $\{\underline{i1}\}$	The translational motion coordinate system of these parallel manipulator branched chains i and $\underline{i}$
$\{i2\}$, $\{\underline{i2}\}$	The rotational motion coordinate system where it is connected to the modules of these parallel manipulator branched chains i and $\underline{i}$
$\{i3\}$	The coordinate system of l_d link rotates around the D point of these parallel manipulator branched chains i and $\underline{i}$
$\{i4\}$	The parallel manipulator moving platform rotational motion coordinate system around the A_i point
$\{P\}$	Midpoint coordinate system of the end effector
g_c	Forward kinematics after calibration of the parallel manipulator
T^n	The nominal pose of the end effector
T^a	The actual pose of the end effector
T_{co}	The command pose of the end effector during error compensation
T_{cp}	The end pose after compensation
Ad_{g_i}	The adjoint transformation of g_i, also written as $\text{Ad}_{(g_i)}$, $g_i \in SE(3)$
$\delta g_i \cdot g_i^{-1}$	The representation of the end error on these parallel manipulator branched chains i in the base coordinate system $\{B\}$
$\delta \hat{t}_{ij}$	The error of t in coordinate system $\{ij\}$
J_i	Error Jacobian matrix of these parallel manipulator branched chains i
J	Error Jacobian matrix of the entire parallel manipulator

References

1. Stewart, D. A platform with six degrees of freedom. *Proc. Inst. Mech. Eng.* **1965**, *180*, 371–386. [CrossRef]
2. Wu, C.; Yang, G.; Chen, C.; Liu, S.; Zheng, T. Kinematic design of a novel 4-dof parallel manipulator. In Proceedings of the 2017 IEEE International Conference on Robotics and Automation (ICRA), Singapore, 29 May–3 June 2017; pp. 6099–6104.
3. Wu, J.-F.; Zhang, R.; Wang, R.-H.; Yao, Y.-X. A systematic optimization approach for the calibration of parallel kinematics machine tools by a laser tracker. *Int. J. Mach. Tools Manuf.* **2014**, *86*, 1–11. [CrossRef]
4. Chanal, H.; Duc, E.; Ray, P.; Hascoet, J.Y. A new approach for the geometrical calibration of parallel kinematics machines tools based on the machining of a dedicated part. *Int. J. Mach. Tools Manuf.* **2007**, *47*, 1151–1163. [CrossRef]
5. Fu, J.; Gao, F.; Chen, W.; Pan, Y.; Lin, R. Kinematic accuracy research of a novel six-degree-of-freedom parallel robot with three legs. *Mech. Mach. Theory* **2016**, *102*, 86–102. [CrossRef]
6. Song, Y.; Zhang, J.; Lian, B.; Sun, T. Kinematic calibration of a 5-dof parallel kinematic machine. *Precis. Eng.* **2016**, *45*, 242–261. [CrossRef]
7. Sun, T.; Zhai, Y.; Song, Y.; Zhang, J. Kinematic calibration of a 3-dof rotational parallel manipulator using laser tracker. *Robot. -Comput.-Integr. Manuf.* **2016**, *41*, 78–91. [CrossRef]
8. Liu, H.; Gong, M.; O, M.Z.H.A. Error analysis and calibration of a 4-dof parallel mechanism. *Robot* **2005**, *27*, 6–9.

9. Hartenberg, R.S.; Denavit, J. A kinematic notation for lower pair mechanisms based on matrices. *J. Appl. Mech.* **1955**, *77*, 215–221.

10. Mooring, B.W. An improved method for identifying the kinematic parameters in a six axes robots. In *Computers in Engineering, Proceedings of the International Computers in Engineering Conference and Exhibit*; American Soc of Mechanical Engineers (ASME): New York, NY, USA, 1984; Volume 1, pp. 79–84.

11. Yang, G.; Chen, I.-M.; Lee, W.K.; Yeo, S.H. Self-calibration of three-legged modular reconfigurable parallel robots based on leg-end distance errors. *Robotica* **2001**, *19*, 187–198. [CrossRef]

12. Chen, G.; Kong, L.; Li, Q.; Wang, H.; Lin, Z. Complete, minimal and continuous error models for the kinematic calibration of parallel manipulators based on poe formula. *Mech. Mach. Theory* **2018**, *121*, 844–856. [CrossRef]

13. Okamura, K.; Park, F.C. Kinematic calibration using the product of exponentials formula. *Robotica* **1996**, *14*, 415–421. [CrossRef]

14. He, R.; Zhao, Y.; Yang, S.; Yang, S. Kinematic-parameter identification for serial-robot calibration based on poe formula. *IEEE Trans. Robot.* **2010**, *26*, 411–423.

15. Wang, H.; Shen, S.; Lu, X. A screw axis identification method for serial robot calibration based on the poe model. *Ind. Robot. Int. J.* **2012**, *39*, 146–153. [CrossRef]

16. Chen, I.-M.; Yang, G.; Tan, C.T.; Yeo, S.H. Local poe model for robot kinematic calibration. *Mech. Mach. Theory* **2001**, *36*, 1215–1239. [CrossRef]

17. Nubiola, A.; Bonev, I.A. Absolute robot calibration with a single telescoping ballbar. *PRecision Eng.* **2014**, *38*, 472–480. [CrossRef]

18. Joubair, A.; Slamani, M.; Bonev, I.A. Kinematic calibration of a five-bar planar parallel robot using all working modes. *Robot. -Comput.-Integr. Manuf.* **2013**, *29*, 15–25. [CrossRef]

19. Du, G.; Zhang, P. Online robot calibration based on vision measurement. *Robot. Comput.-Integr. Manuf.* **2013**, *29*, 484–492. [CrossRef]

20. HuangFu, Y.; Hang, L.; Cheng, W.; Yu, L.; Shen, C.; Wang, J.; Qin, W.; Wang, Y. Research on robot calibration based on laser tracker. In *Mechanism and Machine Science*; Springer: Berlin/Heidelberg, Germany, 2016; pp. 1475–1488.

21. Elatta, A.Y.; Gen, L.P.; Zhi, F.L.; Daoyuan, Y.; Fei, L. An overview of robot calibration. *Inf. Technol. J.* **2004**, *3*, 74–78.

22. Wu, L.; Yang, X.; Chen, K.; Ren, H. A minimal poe-based model for robotic kinematic calibration with only position measurements. *IEEE Trans. Autom. Sci. Eng.* **2014**, *12*, 758–763. [CrossRef]

23. Sareh, P. The least symmetric crystallographic derivative of the developable double corrugation surface: Computational design using underlying conic and cubic curves. *Mater. Des.* **2019**, *183*, 108128. [CrossRef]

24. Chen, J.; San, H.; Wu, X.; Chen, M.; He, W. Structural design and characteristic analysis for a 4-degree-of-freedom parallel manipulator. *Adv. Mech. Eng.* **2019**, *11*, 1687814019850995. [CrossRef]

25. Yang, L.; Tian, X.; Li, Z.; Chai, F.; Dong, D. Numerical simulation of calibration algorithm based on inverse kinematics of the parallel mechanism. *Optik* **2019**, *182*, 555–564. [CrossRef]

26. Huang, K.; Liu, R.G.; Wu, J.S.; Lao, X.R.; Mo, J.H. Parameter calibration method based on screw theory for articulated coordinate measuring arm. In *Advanced Materials Research*; Trans Tech Publ: Zurich, Switzerland, 2011; Volume 189, pp. 4049–4052.

27. Gu, L.; Yang, G.; Fang, Z.; Shen, W.; Zheng, T.; Chen, C.; Zhang, C. A two-step self-calibration method with portable measurement devices for industrial robots based on poe formula. In *International Conference on Intelligent Robotics and Applications*; Springer: Berlin/Heidelberg, Germany, 2019; pp. 715–727.

Elastic-Plastic-Damaged Zones around a Deep Circular Wellbore under Non-Uniform Loading

Xiaoji Shang [1] and Zhizhen Zhang [1,2,*]

[1] State Key Laboratory of Geomechanics and Deep Underground Engineering, School of Mechanics and Civil Engineering, China University of Mining and Technology, Xuzhou 221116, China; Shangxj2016@cumt.edu.cn

[2] Department of Civil Engineering, Monash University, Melbourne VIC 3800, Australia

* Correspondence: zzzhang@cumt.edu.cn

Abstract: Wellbores are largely constructed during coal mining, shale gas production, and geothermal exploration. Studying the shape and size of the disturbed zone in surrounding rock is of great significance for wellbore stability control. In this paper, a theoretical model for elastic-plastic-damage analysis around a deep circular wellbore under non-uniform compression is proposed. Based on the elastoplastic softening constitutive model and Mohr-Coulomb strength criterion, the analytical expressions of stresses in the elastic, plastic and damaged zones around a circle wellbore are derived. Further, the boundary line equations among the three zones are obtained according to the conditions of stress continuity. Then, the influence rules of non-uniform in-situ stress and mechanical parameters on the stress distribution and plastic zone size in surrounding rock mass are analyzed. The plastic and the damaged zones are both approximately elliptical in shape. When the lateral stress coefficient of the in-situ stress field takes the value 1, the model degenerates into the Yuan Wenbo's Solution. If the brittleness coefficient of the surrounding rock is 0, the model degenerates into the Kastner's Equation. Finally, the results are compared with those under two special cases (in the elastoplastic softening rock under a uniform stress field, in the ideal elastoplastic rock under a non-uniform stress field) and a common approximation method (the perturbation method).

Keywords: wellbore; non-uniform loading; plastic zone; damaged zone; elastoplastic softening model; analytical solution; Mohr-Coulomb

1. Introduction

In recent years, with the rapid development of the economy and society, unconventional oil and gas production, geothermal exploitation, and deep underground space development become major national strategic demands of China [1,2]. In these projects, drilling is one of the most basic and extensive operations. Under the influence of deep in-situ stress, the surrounding rock of the wellbore would be deformed and fractured, and three different zones (a damaged zone, a plastic zone, and an elastic zone) would be formed, which have a significant impact on the borehole wall stability [3,4]. On the other hand, in-situ stress and geomechanical properties of the surrounding rock mass can also be determined based on the information on rock deformation and failure at a borehole [5,6]. In addition, support stress also plays an important role in actual practice [7,8]. Therefore, the elastic-plastic-damage analysis of the surrounding rock has important engineering significance.

The elastoplastic analysis of the surrounding rock around a wellbore is a classic fundamental mechanics problem. There are a large number of theoretical, experimental and engineering investigations. In terms of theoretical analysis, in general, it is divided into two major areas:

(1) Considering that the in-situ stress field is a uniform stress field, Fenner simplified the underground circular wellbore into an isotropic plane strain model under uniform force in 1938 and analyzed the stress, strain, and displacement of the ideal elastoplastic rock mass around the

wellbore. Based on this model and the rock mass volume constant assumption, Kastner obtained the distribution of the elastic and plastic zones in the surrounding rock, namely the famous Kastner's Equation [9], which was followed by many scholars [10–17]. The improvement is mainly considering the strain-softening and volume expansion effect of the rock mass. Yuan et al. [10] considered the softening effect of rock and obtained the distribution of elastic zone, plastic zone and damaged zone in surrounding rock based on Mohr-Coulomb strength criterion. Jiang et al. [11] simplified the constitutive relationship of the rock in the plastic zone and damaged zone into two horizontal straight lines and obtained the stress and strain of rock mass by non-associative elastoplastic analysis. Sharan [12–14] and Park et al [15] used the elastic-brittle-plastic constitutive model to carry out the elastic-brittle-plastic analysis of circular tunnels based on Hoek-Brown criterion and Mohr-Coulomb criterion, respectively. Zhang et al. [16] proposed a multi-step brittle-plastic constitutive model to describe the parameter change behavior of the post-peak stage, which was used to carry out the round-hole elastoplastic analysis. Lv et al. [17] used the elastic-softening-plastic constitutive model of borehole surrounding rock to analyze the stress-strain response around the borehole. The above are all studying the phenomenon of borehole compression, and Li et al. [18] carried out the elastoplastic calculation of borehole expansion for the hydraulic fracturing problem based on these previous research.

(2) When the circular wellbore is subjected to non-uniform in-situ stress, that is, there is a certain proportional relationship between the vertical and horizontal stresses. In this case, the elastoplastic problem is very difficult to solve, and just approximate solutions were found. In 1946, Galin [19] first obtained the plastic zone boundary equation and elastoplastic solution of circular holes under non-uniform loads, assuming that the plastic zone near the edge of the hole completely surrounds the hole. The Galin's solution is widely recognized and used, but the results are only applicable to frictionless Tresca materials. Detournay et al. [20–22] then extended the Galin's solution to the material that accords with cohesive-frictional yield strength and solved the equation of the elastoplastic boundary line by using the complex variable function. The results show that the elastoplastic boundary equation is a Gaussian hypergeometric equation. Ostrosablin [23] suggested a new method for finding coefficients of the transformation function and gave an example for an accurate solution of determining the plastic zone based on Galin's solution. Tokar [24] presented a correction to Galin's error of omitting the explicit condition for the general balance of forces in bending by means of a modified analytical approach, applying Coulomb's yield criterion in the plastic zone and assuming continuous or discontinuous stress distributions at the elastoplastic interface. Leitman et al. [25] presupposed the elastic-plastic boundary is an ellipse and solved a case that Galin's method cannot solve, in which the plastic domain does not completely surround the hole. Ochensberger et al. [26] corrected a minor reshaping mistake at the Galin's solution and provided an amendment to the analytical solution, which was verified by the finite element simulation. Lu et al. [27,28] employed the conformal transformation method of complex variable function to map the non-circular elastic regions in the physical plane to the outer regions of the unit circle in the image plane and presented analytical solutions for determination of the plastic zone in the vicinity of a circular tunnel based on the Mohr-Coulomb [28] or Hoek-Brown failure criterion [27]. Zhuang and Yu [29,30] used the complex variable theory in the elastic analysis to obtain two-dimensional solutions for elastoplastic stress analysis around a cylindrical cavity during both loading and unloading.

In addition, some scholars used approximation methods to solve the elastoplastic problem of circular holes under the non-uniform stress field [31–35]. Wei [31] used the perturbation method to solve the stress in the elastic region, and obtained the elastoplastic zone stress and elastoplastic boundary line equation of the surrounding rock based on Mohr-Coulomb criterion. The results show that the shape of the boundary line of the elastoplastic zone is similar to the ellipse. Hou et al [32] also used the perturbation method to conduct a similar study on the Drucker-Prager criterion. Chen et al. [33] substituted the stress analytical solution (Kirsh's Solution) in the elastic area into the plastic yield condition to obtain the expression and geometry of the elastic-plastic boundary line. Sun et al. [34] used the stress function obtained by the trial method to solve the elastic stress, and obtained the approximate

solution of the plastic zone boundary based on the modified elastic solution. The analytical solutions are valid when the plastic zone is comparatively large and the lateral pressure coefficients $1 \leq \lambda < 3$. Ma et al. [35] adopted the stress concentration solution of the circular hole in the elastic plate and the deviatoric stress method in plastic mechanics to solve the problem.

However, as shown in Figure 1, most of the current research is based on the ideal elastoplastic constitutive model or the elastic-brittle-plastic model, while most of the rocks in engineering practice actually exhibit the strain-softening effect, which is not fully considered in the elastoplastic analysis. In addition, the in-situ stress field is often oversimplified to be uniform. In this paper, the theoretical model describing the elastic-plastic-damaged behavior of strain-softening rock mass around a circular wellbore under the non-uniform in-situ stress field is presented, and the analytical solutions of stress distribution and regional boundary line among elastic zone, plastic zone, and damaged zone are obtained. Then, the influence rules of non-uniform in-situ stress and mechanical parameters on the stress distribution and plastic zone size in surrounding rock mass are analyzed. Finally, comparative analyses are carried out with other solutions.
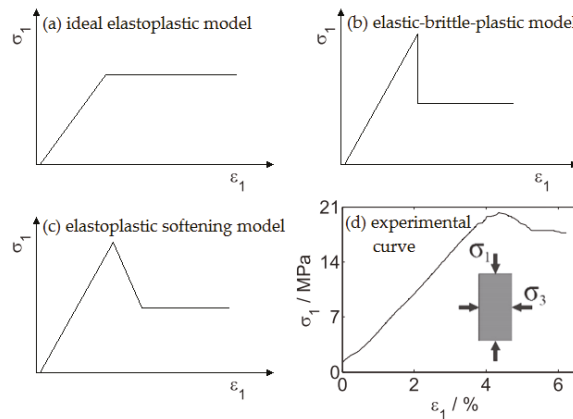
Figure 1. Rock mass behavior models (modified from Reference [18]).

2. Problem Description and Fundamental Theory

2.1. The Stress State around a Wellbore

In deep underground engineering activities, drilling is usually carried out in deep rock formations below the ground surface. When the buried depth is greater than or equal to 20 times the wellbore radius (or its width or height), there is

$$Z \geq 20R_0 \tag{1}$$

where Z is the buried depth and R_0 is the radius of the wellbore. Studies have shown that the weight of the rock mass within the influence range of the wellbore can be neglected, and the error from the original problem does not exceed 5%. Therefore, the horizontal in-situ stress can be simplified to be uniform, so that the original problem becomes the plane strain problem of a circular hole, in which the vertical in-situ stress is P, the horizontal in-situ stress is λP (λ is the lateral stress coefficient), shown in Figure 2.
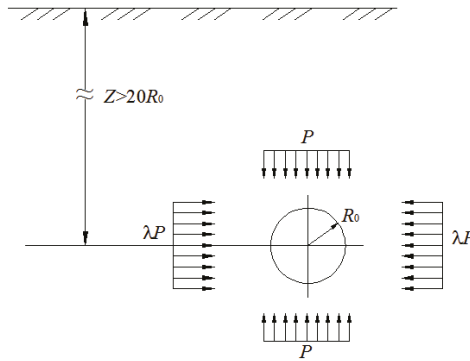
Figure 2. Deep buried wellbore.

2.2. Basic Assumptions and Constitutive Model

(1) The rock mass is approximately considered to be anisotropic, homogeneous continuous medium.

(2) The deep-buried circular wellbore is in a far-field non-uniform in-situ stress where the vertical stress is P and the horizontal stress is λP, and the inner boundary of the wellbore is subjected to the uniform support stress of P_1, which is constant along the lengthwise direction of the well.

(3) The compressive stress of the rock mass is positive, and the displacement in the direction of the wellbore center is positive.

(4) The surrounding rock is an elastoplastic softening medium. The simplified stress-strain curve is shown in Figure 3a. It is a three-section line. The first straight line corresponds to the elastic deformation stage, and the second straight line corresponds to the plastic softening stage. The horizontal straight line corresponds to the plastic flow stage.

(a) simplified stress-strain curve   (b) three zones around a wellbore
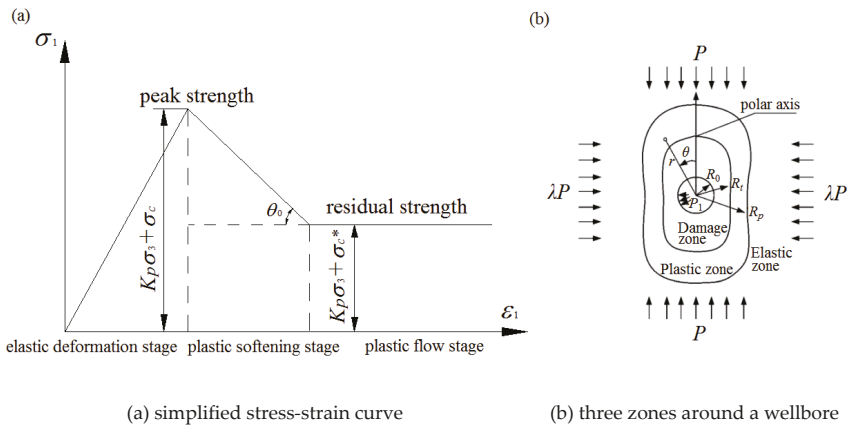
Figure 3. The elastoplastic softening model and the three different zones around a circle wellbore.

The softening degree of the rock mass is expressed by the angle θ_0. When the angle is 0°, the model becomes the ideal elastoplastic model, and when it is 90°, it becomes the elastic-brittle-plastic model. For the surrounding rock of the well, it can be approximated that the angle does not change within the drilling range, and according to the existing research results [10], the brittleness coefficient of the rock mass can be defined as

$$\beta = \frac{M_0}{E_0},$$

(2)

where E_0 is the elastic modulus of the rock mass, M_0 is the softening modulus of the rock mass, $M_0 = \tan \theta_0$.

2.3. Fundamental Equations

It can be seen from Figure 3a that the stress-strain curve of the surrounding rock is divided into three stages, and the surrounding rock regions corresponding to the three stages are respectively called the elastic zone, the plastic zone, and the damaged zone, as shown in Figure 3b. Assuming the radius of the circular well is R_0, the radius of the elastic-plastic boundary is R_p, and the radius at the junction of the plastic zone and the damaged zone is R_t, each stage and area must meet certain basic equations:

(1) Elastic deformation stage

The rock mass obeys Hooke's law in the elastic phase and satisfies the Mohr-Coulomb strength criterion when yielding.

$$\tau = \sigma_n \tan \varphi + c, \tag{3}$$

or

$$\sigma_1 = K_p \sigma_3 + \sigma_c, \tag{4}$$

where τ and σ_n are the shear stress and normal stress on the shear plane respectively, c is the cohesion of the rock mass, φ is the internal friction angle, σ_1 and σ_3 are the maximum and minimum principal stress, $K_p = \frac{1+\sin \varphi}{1-\sin \varphi}$ is the confining stress coefficient of rock strength, $\sigma_c = \frac{2c \cdot \cos \varphi}{1-\sin \varphi}$ is the uniaxial compressive strength.

In the elastic zone, the displacement of the rock mass due to drilling excavation is [10]

$$u = \frac{B_0}{E_0} \frac{R_p^2}{r}, \tag{5}$$

where B_0 is the coefficient, $B_0 = \frac{(1+\mu)\left[(K_p-1)P+\sigma_c\right]}{(K_p+1)} = (1+\mu)(c\cos\varphi + P\sin\varphi)$, μ is the Poisson's ratio, r is the distance to the wellbore center.

(2) Plastic softening stage

In the plastic softening stage, the attenuation law of compressive strength can be expressed as $\sigma_1 = f(\sigma_3, \varepsilon_1^p)$. According to the results obtained by a large number of rock shear and anti-friction tests, the above formula can be simplified to [10,18]

$$\sigma_1 = K_p \sigma_3 + \bar{\sigma}_c(\varepsilon_1^p), \tag{6}$$

where ε_1^p is a plastic strain component.

For the elastoplastic softening model as shown in Figure 3, there is

$$d\bar{\sigma}_c = -M_0 d(\varepsilon_1^p). \tag{7}$$

Integrating the Equation (7) and applying the boundary condition that $\bar{\sigma}_c = \sigma_c$ at $r = R_p$, we can get

$$\bar{\sigma}_c = \sigma_c - M_0(\varepsilon_1 - \varepsilon_1^e), \tag{8}$$

where ε_1^e is an elastic strain component, so according to Equation (5), there is

$$\bar{\sigma}_c = \sigma_c - \beta B_0 \left[\left(\frac{R_p}{r} \right)^2 - 1 \right]. \tag{9}$$

(3) Plastic flow stage

During the plastic flow stage, the compressive strength of the rock mass is reduced to a stable residual value, that is

$$\sigma_1 = K_p\sigma_3 + \sigma_c^*, \tag{10}$$

where σ_c^* is the residual strength of the rock mass under uniaxial compression.

3. Analytical Solution of Stress and Boundary Line Equation

3.1. Elastic Zone

The non-uniform in-situ stress field can be decomposed into a uniform compressive stress field and a two-sided compressive and two-sided tensile stress field, as shown in Figure 4, so the general form of the stress component of the rock mass in the non-uniform stress field is also the superposition of the two cases.
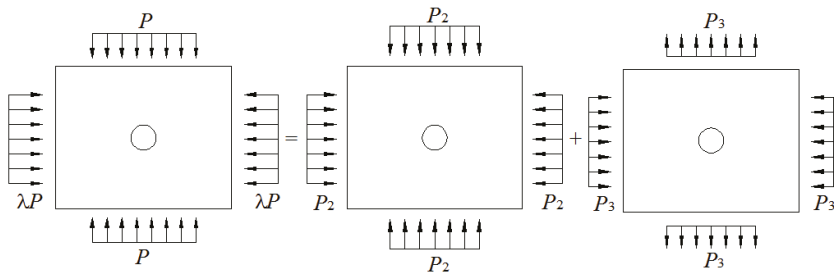
Figure 4. Schematic diagram of stress field decomposition: (**a**) the in-situ stress field, (**b**) the uniform compressive stress field, (**c**) the two-sided compressive and two-sided tensile stress field.

Figure 4a shows the in-situ stress field, Figure 4b shows the uniform compressive stress field, and Figure 4c shows the two-sided compressive and two-sided tensile stress field, and there are $P_2 = \frac{(1+\lambda)}{2}P$ and $P_3 = \frac{(\lambda-1)}{2}P$.

The general form of the stress in the elastic zone under the uniform compressive stress field is [10,36]

$$\sigma_r = A + B/r^2, \sigma_\theta = A - B/r^2, \tag{11}$$

where σ_r and σ_θ are the radial stress and the hoop stress respectively, A and B are two constants to be determined.

The general form of the stress in the elastic zone under the two-sided compressive and two-sided tensile stress field is [36]

$$\left.\begin{array}{l} \sigma_r = -(2D + 4E/r^2 + 6F/r^4)\cos 2\theta \\ \sigma_\theta = (12Cr^2 + 2D + 6F/r^4)\cos 2\theta \\ \tau_{r\theta} = (6Cr^2 + 2D - 2E/r^2 - 6F/r^4)\sin 2\theta \end{array}\right\}, \tag{12}$$

where $\tau_{r\theta}$ is the shear stress, C, D, E and F are pending constants.

By superposing Equation (11) and Equation (12), the general form of the stress component in the elastic zone under the non-uniform in-situ stress field is obtained as

$$\left.\begin{array}{l} \sigma_r = A + B/r^2 - (2D + 4E/r^2 + 6F/r^4)\cos 2\theta \\ \sigma_\theta = A - B/r^2 + (12Cr^2 + 2D + 6F/r^4)\cos 2\theta \\ \tau_{r\theta} = (6Cr^2 + 2D - 2E/r^2 - 6F/r^4)\sin 2\theta \end{array}\right\}. \tag{13}$$

Boundary conditions are

$$\left.\begin{aligned}
\sigma_r|_{r\to\infty} &= P/2[1+\lambda+(\lambda-1)\cos 2\theta] \\
\sigma_\theta|_{r\to\infty} &= P/2[1+\lambda-(\lambda-1)\cos 2\theta] \\
\tau_{r\theta}|_{r\to\infty} &= P/2[(1-\lambda)\sin 2\theta]
\end{aligned}\right\}, \tag{14}$$

Substituting Equation (14) into Equation (13) and simplifying it, we can get

$$\left.\begin{aligned}
\sigma_r &= P(1+\lambda)/2 + B/r^2 - \left[P(1-\lambda)/2 + 4E/r^2 + 6F/r^4\right]\cos 2\theta \\
\sigma_\theta &= P(1+\lambda)/2 - B/r^2 + \left[P(1-\lambda)/2 + 6F/r^4\right]\cos 2\theta \\
\tau_{r\theta} &= \left[P(1-\lambda)/2 - 2E/r^2 - 6F/r^4\right]\cos 2\theta
\end{aligned}\right\}. \tag{15}$$

Applying the boundary condition

$$r = R_p, \sigma_\theta = K_p \sigma_r + \sigma_c, \tau_{r\theta} = 0, \tag{16}$$

Solutions can be obtained that

$$\left.\begin{aligned}
B &= \frac{\sigma_c + P/2(K_p-1)(1+\lambda)}{-K_p-1}R_p^2 \\
E &= \frac{P(K_p+1)(1-\lambda)}{2(1-K_p)}R_p^2 \\
F &= \frac{P(3K_p+1)(\lambda-1)}{12(1-K_p)}R_p^4
\end{aligned}\right\}. \tag{17}$$

Substituting Equation (17) into Equation (15), the stress in the elastic zone is obtained as

$$\left.\begin{aligned}
\sigma_r &= \frac{P(1+\lambda)}{2} - \frac{\sigma_c + p/2(K_p-1)(1+\lambda)}{K_p+1}\left(\frac{R_p}{r}\right)^2 - \left[\frac{P(1-\lambda)}{2} + \frac{2P(K_p+1)(1-\lambda)}{1-K_p}\left(\frac{R_p}{r}\right)^4\right. \\
&\quad \left. + \frac{P(3K_p+1)(\lambda-1)}{2(1-K_p)}\left(\frac{R_p}{r}\right)^4\right]\cos 2\theta \\
\sigma_\theta &= \frac{P(1+\lambda)}{2} + \frac{\sigma_c + P/2(K_p-1)(1+\lambda)}{K_p+1}\left(\frac{R_p}{r}\right)^2 + \left[\frac{P(1-\lambda)}{2} + \frac{P(3K_p+1)(\lambda-1)}{2(1-K_p)}\right]\cos 2\theta \\
\tau_{r\theta} &= \left[\frac{P(1-\lambda)}{2} - \frac{P(K_p+1)(1-\lambda)}{1-K_p}\left(\frac{R_p}{r}\right)^2 - \frac{P(3K_p+1)(\lambda-1)}{2(1-K_p)}\right]\sin 2\theta
\end{aligned}\right\}, \tag{18}$$

so at the junction of the elastic and plastic zone, there are

$$\left.\begin{aligned}
\sigma_r|_{r=R_p} &= \frac{P(1+\lambda)-\sigma_c}{K_p+1} + \frac{2P(1-\lambda)}{K_p-1}\cos 2\theta \\
\sigma_\theta|_{r=R_p} &= \frac{P(1+\lambda)K_p+\sigma_c}{K_p+1} + \frac{2P(1-\lambda)K_p}{K_p-1}\cos 2\theta \\
\tau_{r\theta}|_{r=R_p} &= 0
\end{aligned}\right\}. \tag{19}$$

3.2. Plastic Zone

In the plastic softening stage, the Equation (9) is substituted into the equilibrium differential equation for integration and used the boundary condition of stress continuity, that is Equation (19), the stress distribution can be solved.

The equilibrium differential equation in the plastic zone is

$$\frac{\partial \sigma_r}{\partial r} + \frac{1-K_p}{r}\sigma_r = \frac{\sigma_c - \beta B_0\left[\left(\frac{R_p}{r}\right)^2 - 1\right]}{r}, \tag{20}$$

Integrate the Equation (20), we can get

$$\sigma_r = \frac{\sigma_c}{1-K_p} + \frac{\beta B_0}{K_p+1}\left(\frac{R_p}{r}\right)^2 + \frac{\beta B_0}{1-K_p} + [c_0(\theta)+c_1]r^{K_p-1}, \tag{21}$$

where $c_0(\theta)$ is a function of θ, c_1 is a constant.

Therefore, the hoop stress can be obtained as

$$\sigma_\theta = \frac{\sigma_c}{1-K_p} + \frac{-\beta B_0}{K_p+1}\left(\frac{R_p}{r}\right)^2 + \frac{\beta B_0}{1-K_p} + K_p[c_0(\theta)+c_1]r^{K_p-1}, \tag{22}$$

Substituting $r = R_p$ into Equation (21) and Equation (22), there are

$$\left.\begin{array}{l} \sigma_r|_{r=R_p} = \frac{\sigma_c+\beta B_0}{1-K_p} + \frac{\beta B_0}{K_p+1} + [c_0(\theta)+c_1]R_p^{K_p-1} \\[2mm] \sigma_\theta|_{r=R_p} = \frac{\sigma_c+\beta B_0}{1-K_p} - \frac{\beta B_0}{K_p+1} + K_p[c_0(\theta)+c_1]R_p^{K_p-1} \end{array}\right\}, \tag{23}$$

And using the boundary condition, expressed by Equation (19), the radial and hoop stresses in the plastic zone can be solved, which are

$$\left.\begin{array}{l} \sigma_r = \frac{\sigma_c+\beta B_0}{1-K_p} + \frac{\beta B_0}{K_p+1}\left(\frac{R_p}{r}\right)^2 + \left[\frac{P(1+\lambda)-\sigma_c-\beta B_0}{K_p+1} + \frac{\sigma_c+\beta B_0}{K_p-1}\right]\left(\frac{R_p}{r}\right)^{1-K_p} \\[3mm] + \frac{2P(1-\lambda)}{K_p-1}\left(\frac{R_p}{r}\right)^{1-K_p}\cos 2\theta \\[3mm] \sigma_\theta = \frac{\sigma_c+\beta B_0}{1-K_p} - \frac{\beta B_0}{K_p+1}\left(\frac{R_p}{r}\right)^2 + K_p\left[\frac{P(1+\lambda)-\sigma_c-\beta B_0}{K_p+1} + \frac{\sigma_c+\beta B_0}{K_p-1}\right]\left(\frac{R_p}{r}\right)^{1-K_p} \\[3mm] + \frac{2PK_p(1-\lambda)}{K_p-1}\left(\frac{R_p}{r}\right)^{1-K_p}\cos 2\theta \end{array}\right\}. \tag{24}$$

3.3. Damaged Zone

The stress component in the damaged zone satisfies the Equation (10), so the equilibrium differential equation in the damaged zone is

$$\frac{\partial \sigma_r}{\partial r} + \frac{1-K_p}{r}\sigma_r = \frac{\sigma_c^*}{r}. \tag{25}$$

There is a certain proportional relationship between the radius of the damaged zone and the plastic zone, which is denoted as t (t is not necessarily constant). Substituted this relationship into Equation (9) and used the boundary condition, that is $\overline{\sigma}_c = \sigma_c^*$ when $r = R_t = tR_p$, we can get

$$t = \sqrt{\frac{\beta B_0}{\sigma_c - \sigma_c^* + \beta B_0}}. \tag{26}$$

Integrate Equation (25) and simplify, there are

$$\left.\begin{array}{l} \sigma_r = \frac{\sigma_c^*}{1-K_p} + [c_2(\theta)+c_3]r^{K_p-1} \\[2mm] \sigma_\theta = \frac{\sigma_c^*}{1-K_p} + K_p[c_2(\theta)+c_3]r^{K_p-1} \end{array}\right\}, \tag{27}$$

where $c_2(\theta)$ is the function of θ, c_3 is a constant.

Using the boundary condition, $\overline{\sigma}_c = \sigma_c^*$ when $r = R_t = tR_p$, the stress in the damaged zone is

$$
\left.
\begin{aligned}
\sigma_r &= \left\{ \frac{2}{K_p+1}\left[\frac{P(1+\lambda)}{2} + \frac{\sigma_c+\beta B_0}{K_p-1}\right]t^{K_p-1} - \frac{2(\sigma_c-\sigma_c^*+\beta B_0)}{K_p^2-1}\right\}\left(\frac{r}{tR_p}\right)^{K_p-1} \\
&\quad + \frac{2P(1-\lambda)}{K_p-1}\left(\frac{r}{R_p}\right)^{K_p-1}\cos 2\theta + \frac{\sigma_c^*}{1-K_p} \\
\sigma_\theta &= K_p\sigma_r + \sigma_c^*
\end{aligned}
\right\}.
\tag{28}
$$

3.4. Boundary Line Equation

There are two boundary lines, the boundary line between the elastic zone and the plastic zone, and the boundary line of the plastic zone and the damaged zone.

It is assumed that the plastic zone of the surrounding rock is completely formed, but the damaged zone is still not produced, which is a critical state. The radius of the plastic zone in this critical state is denoted by R_c. From Equation (24) and the inner boundary conditions, $\overline{\sigma}_c = \sigma_c^*$ and $\sigma_r = P_1$ when $r = R_0$, we can get

$$
R_c = R_0\left[\frac{\frac{P(1+\lambda)-\sigma_c-\beta B_0}{K_p+1} + \frac{\sigma_c+\beta B_0+2P(1-\lambda)\cos 2\theta}{K_p-1}}{P_1 + \frac{2(\sigma_c+\beta B_0)}{K_p^2-1} + \frac{\sigma_c^*}{K_p+1}}\right]^{\frac{1}{K_p-1}}.
\tag{29}
$$

In the non-uniform in-situ stress field, the shape of the damaged zone is no longer circular, so it is necessary to classify the above formula to determine whether there is a damaged zone in the surrounding rock. There are four special locations in the damaged zone, that is, the points when $\theta = 0, \pi/2, \pi, 3\pi/2$ on the inner boundary of the wellbore in the polar coordinates, and the plastic zone ranges in several different cases are discussed below for these four locations.

$$
R_{c1} = R_0\left[\frac{\frac{P(1+\lambda)-\sigma_c-\beta B_0}{K_p+1} + \frac{\sigma_c+\beta B_0-2P(1-\lambda)}{K_p-1}}{P_1 + \frac{2(\sigma_c+\beta B_0)}{K_p^2-1} + \frac{\sigma_c^*}{K_p+1}}\right]^{\frac{1}{K_p-1}} \quad (\theta = \pi/2, 3\pi/2),
\tag{30}
$$

$$
R_{c2} = R_0\left[\frac{\frac{P(1+\lambda)-\sigma_c-\beta B_0}{K_p+1} + \frac{\sigma_c+\beta B_0+2P(1-\lambda)}{K_p-1}}{P_1 + \frac{2(\sigma_c+\beta B_0)}{K_p^2-1} + \frac{\sigma_c^*}{K_p+1}}\right]^{\frac{1}{K_p-1}} \quad (\theta = 0, \pi).
\tag{31}
$$

(a) If $R_0/t = R_{c1}$, it shows that the surrounding rock is in a critical state that the damaged zone does not appear, there is $R_p = R_c$,

(b) If $R_0/t > R_{c1}$, it is indicated that there is no damaged zone in the surrounding rock, and according to the Equation (9) and Equation (24), as well as the boundary condition, $\sigma_r = P_1$ when $r = R_0$, we can get

$$
\begin{aligned}
&\frac{\sigma_c+\beta B_0}{1-K_p} + \frac{\beta B_0}{K_p+1}\left(\frac{R_p}{R_0}\right)^2 + \left[\frac{P(1+\lambda)-\sigma_c-\beta B_0}{K_p+1} + \frac{\sigma_c+\beta B_0}{K_p-1}\right]\left(\frac{R_p}{R_0}\right)^{1-K_p} \\
&\quad + \frac{2P(1-\lambda)}{K_p-1}\left(\frac{R_p}{R_0}\right)^{1-K_p}\cos 2\theta - P_1 = 0
\end{aligned}
\tag{32}
$$

Solve the Equation (32) to get the expression of the radius of the plastic zone R_p,

(c) If $R_{c2} < R_0/t < R_{c1}$, it shows that a local damaged zone is generated in the surrounding rock, that is, the fracture appears on the upper and lower sides of the wellbore, while the left and right sides have not yet broken, and the situation is the most complicated,

(d) If $R_0/t \leq R_{c2}$, it shows that a complete damaged zone is generated in the surrounding rock, that is, the damaged zone completely surrounds the wellbore. Using Equation (28) and the boundary condition, $\sigma_r = P_1$ when $r = R_0$, the radius of the plastic zone can be solved as

$$R_p = \left[\dfrac{\left\{ \dfrac{2}{K_p+1} \left[\dfrac{P(1+\lambda)}{2} + \dfrac{\sigma_c + \beta B_0}{K_p-1} \right] t^{K_p-1} - \dfrac{2(\sigma_c - \sigma_c^* + \beta B_0)}{K_p^2-1} \right\} \left(\dfrac{R_0}{t} \right)^{K_p-1} + \dfrac{2P(1-\lambda)}{K_p-1} R_0^{K_p-1} \cos 2\theta}{P_1 + \dfrac{\sigma_c^*}{K_p-1}} \right]^{\frac{1}{K_p-1}}. \quad (33)$$

The corresponding radius of the damaged zone is $R_t = tR_p$. This situation is the most common for deep-buried drilling.

4. Parameter Analysis

Based on the above analytical solutions, we know that the mechanical parameters of the surrounding rock, such as the internal friction angle, cohesion, brittleness coefficient, etc., the lateral stress coefficient, the support force, and other parameters affect the stress distribution and plastic zone size in the surrounding rock. These influence laws are then further analyzed.

4.1. Stress Distribution in Surrounding Rock Mass

Equation (18), Equation (24) and Equation (28) show that the common parameters affecting the stress distribution in the three zones are the internal friction angle, the cohesion, and the lateral stress coefficient. In order to make the results more intuitive, the stress at the line $\theta = 60°$ is representatively selected as the research object.

4.1.1. Effect of the Internal Friction Angle

The mechanical parameters of surrounding rock at Nantun mine in Shandong Province in Table 1 are utilized, and the internal friction angles are taken as $20°$, $25°$, $30°$, and $35°$, respectively. Substituting these data into the Equation (18), Equation (24) and Equation (28), and the radial and hoop stresses in the surrounding rock mass can be calculated, shown in Figure 5.

Table 1. Mechanic parameters of surrounding rock.

P/MPa	$\varphi/°$	μ	R_0/m	c/MPa	σ_c^*/MPa	β	λ	P_1/MPa
6.527	30	0.22	1.25	1.2	1.3	1	1.2	0

It can be seen from Figure 5 that the hoop stress is always larger than the radial stress. The maximum hoop stress appears at the interface between the elastic and plastic zones, and the stress concentration factor is about 2. In the plastic and the damaged zones, the hoop stress gradually increases with increasing distance to the wellbore, while in the elastic zone, it decreases to approximately the in-situ stress with the distance trending to infinity. In sharp contrast, the radial stress keeps increasing smoothly with distance to the wellbore, which means that it is continuous in the surrounding rock mass, even passing through the interface between the different zones [18]. As the internal friction angle increases, the maximum hoop stress increases slightly, and the location is closer to the wellbore. In addition, in the plastic and the damaged zones, both the hoop and radial stresses and their gradients become larger.
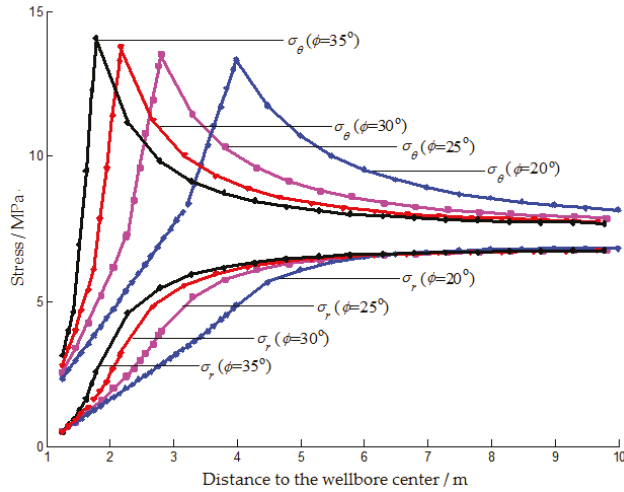
Figure 5. The radial and hoop stress in the surrounding rock mass with different internal friction angles.

4.1.2. Effect of the Cohesion

The data in Table 1 are also utilized, and the cohesion is taken as 0.5 MPa, 1 MPa, 1.5 MPa, and 2 MPa, respectively. Based on Equation (18), Equation (24) and Equation (28), the radial and hoop stresses can be also calculated, as seen in Figure 6.
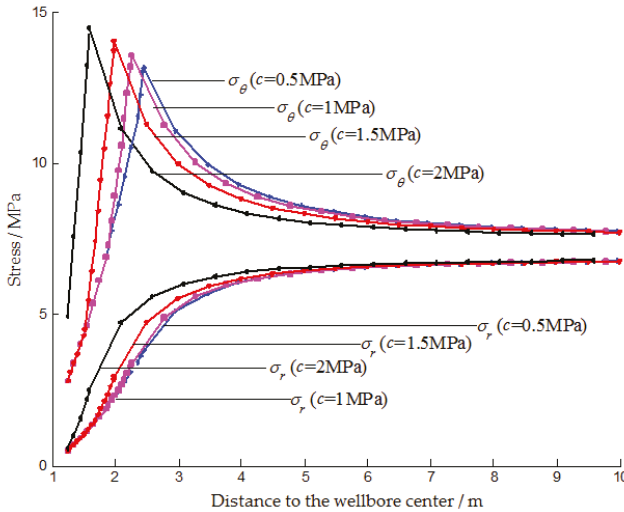
Figure 6. The radial and hoop stress in the surrounding rock mass with different cohesion.

Figure 6 shows that when the cohesion is larger, the maximum hoop stress is larger and the distance between its location and the wellbore is smaller. The radial stress is always in the increasing trend. These laws are similar to those in Figure 5, but the difference in stress values under different cohesion is not so large, which means the stress distribution is less sensitive to cohesion than the internal friction angle. At a distance greater than 5 m from the wellbore, the effect of cohesion on stress is very weak.

4.1.3. Effect of the Lateral Stress Coefficient

Similarly, the lateral stress coefficient is taken as 1, 1.2, 1.4, and 1.6, respectively. The calculation results can show the effect of the lateral pressure coefficient on the stress distribution in the surrounding rock mass, seen in Figure 7.
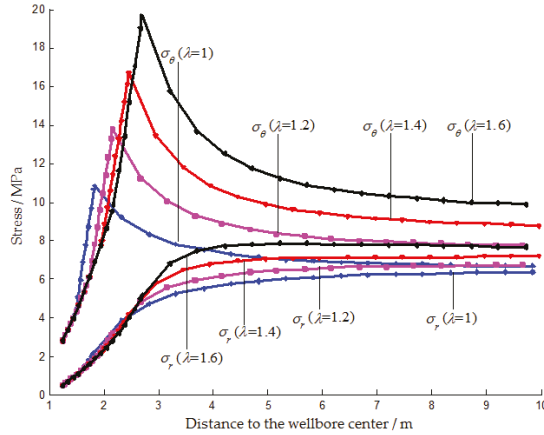
Figure 7. The radial and hoop stress in the surrounding rock mass under different lateral stress coefficients.

The lateral pressure coefficient has a significant effect on the stress distribution in the three regions, as shown in Figure 7. As it increases, the stress concentration becomes stronger, the maximum hoop stress and radial stress both increases significantly, and the boundary between the plastic and elastic zones moves farther away from the wellbore. It is also interesting to observe that the stress curves in the same area are close to parallel under different lateral stress coefficients, which seems to mean that the lateral stress coefficient only affects the stress value without affecting the stress gradient.

4.2. Size of the Plastic Zone

Determining the size of the plastic zone in the surrounding rock mass plays an important role in controlling the stability of the wellbore. According to Equation (33), we can know that multiple parameters collectively affect the size of the plastic zone, including internal friction angle, cohesion, residual strength, in-situ stress, support force, lateral stress coefficient, brittleness coefficient, well radius, etc. Here, we mainly analyze four factors as follows.

Taking the data listed in Table 1 as reference parameters, when discussing the influence of a certain factor on the radius of the plastic zone, only change the value of this parameter, while other parameters are kept unchanged. Since the boundary of the plastic zone is symmetrical in all four quadrants, only a quarter of the curve is drawn from 0° to 90°, and the radius of the plastic zone at other angles can be obtained through the symmetry relationship.

4.2.1. Effect of the Internal Friction Angle

Taking the internal friction angles as 20°, 25°, 30°, and 35°, and substituting them into the expression of the radius of the plastic zone shown in Equation (33), a series of values of the radius of the plastic zone changing with the angle θ are obtained, which can be shown by the curves in Figure 8.
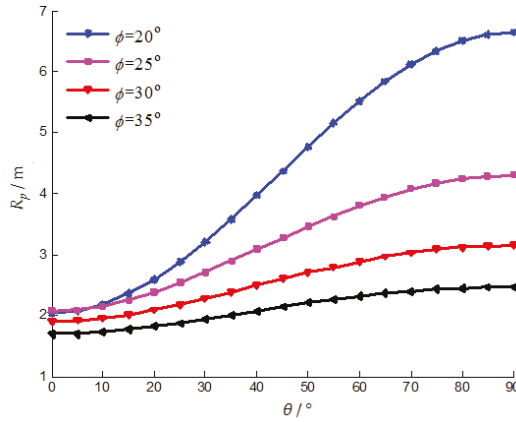
Figure 8. The effect of the internal friction angle on the radius of the plastic zone.

As can be seen from Figure 8, the effect of the internal friction angle on the radius of the plastic zone is quite significant. As the internal friction angle increases, the radius of the plastic zone decreases at all locations, but the magnitude of the reduction is different. The radius of the plastic zone decreases the least at $\theta = 0°$, and decreases most at $\theta = 90°$. The difference in the radius of the plastic zone at each location is gradually decreasing with the increasing internal friction angle, that is, the shape of the plastic zone is getting closer to a circle.

4.2.2. Effect of the Cohesion

Take the cohesion as 0.5 MPa, 1 MPa, 1.3 MPa, and 1.6 MPa respectively, and draw the calculated plastic zone radius value, then the curves of the radius of the plastic zone as a function of the cohesion can be obtained, shown in Figure 9. Similar to the influence of the internal friction angle in Figure 8, the radius of the plastic zone decreases with increasing cohesion. However the difference is that the amplitude of the reduction at the position of $\theta = 0°$ is greater than that at $\theta = 90°$, which means that the plastic zone is becoming flattened.
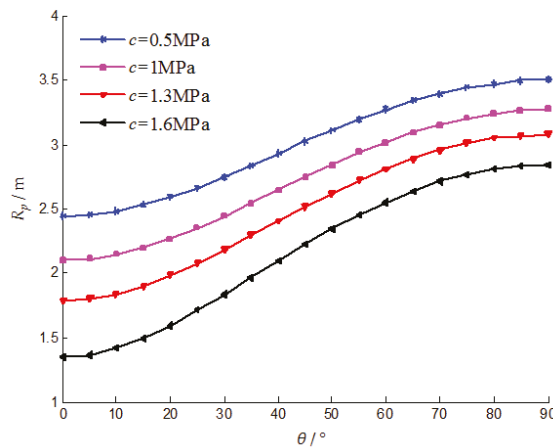
Figure 9. The effect of cohesion on the radius of the plastic zone.

4.2.3. Effect of the Brittleness Coefficient

The brittleness coefficient characterizes the degree of strain-softening of the rock mass and can be expressed by Equation (2). Take the brittleness coefficient as 0.3, 0.5, 0.8, 1.2, 5, 10, 15, 30 in order, and draw the curves of the plastic zone radius with the brittleness coefficient, as shown in Figure 10.
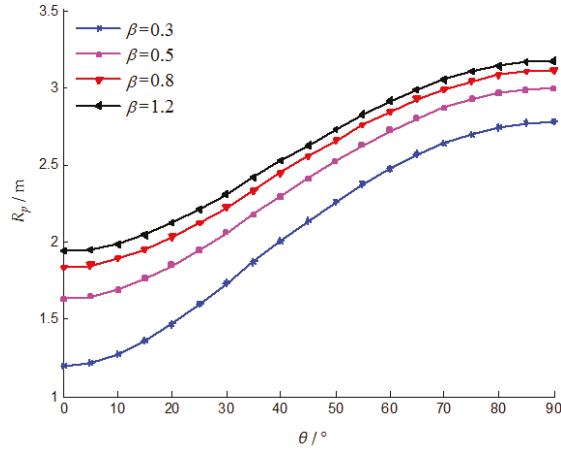
(a) $\beta < 5$
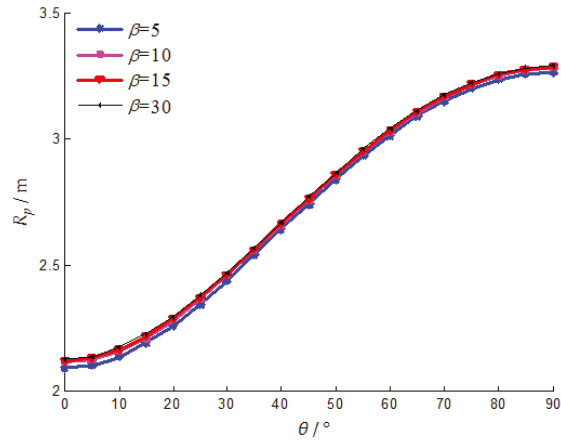
(b) $\beta > 5$

Figure 10. The effect of the brittleness coefficient on the radius of the plastic zone.

The radius of the plastic zone increases with the increase of the brittleness coefficient, and the difference of the increased amplitude at each location is small, which means that the plastic zone is enlarged approximately in proportion. A very significant feature is that when the brittleness coefficient is small ($\beta < 5$), as shown in Figure 10a, as the brittleness coefficient increases, the gradient of the increase in the radius of the plastic zone becomes smaller and smaller. When it is large ($\beta > 5$), the radius of the plastic zone hardly increases, and the plastic zones almost coincide, as shown in Figure 10b.

4.2.4. Effect of the Lateral Stress Coefficient

Take the lateral pressure coefficient as 0.8, 1.1, 1.2, and 1.3 in order, and draw the curves of the plastic zone radius with the lateral pressure coefficient, as shown in Figure 11.
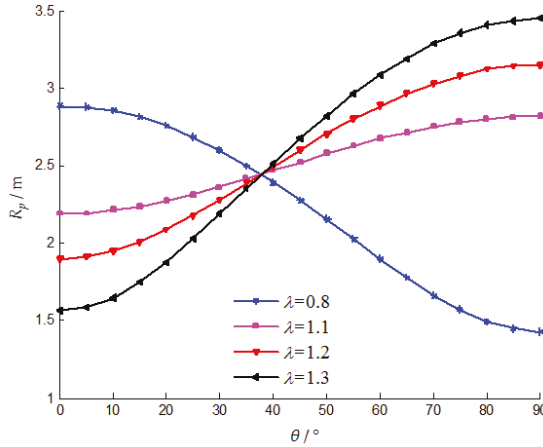
Figure 11. The effect of the lateral stress coefficient on the radius of the plastic zone.

The influence of the lateral pressure coefficient on the radius of the plastic zone is very significant. When $\lambda < 1$, that is, the vertical stress is higher than the horizontal stress, the radius of the plastic zone decreases with increasing angle, which means that the plastic zone is long in the horizontal direction and short in the vertical direction. The situation is reversed when $\lambda > 1$. There is a clear demarcation point, which is around $\theta = 37°$. With the increase of the lateral stress coefficient, the changing trend is opposite on both sides of this demarcation point, the radius of the plastic zone becomes larger in the region of $\theta > 37°$, but smaller in $\theta < 37°$ section. The difference between the radius of the plastic zone at $\theta = 0°$ and $\theta = 90°$ is getting bigger, which means that the plastic zone is getting flatter.

5. Comparison of Results

The deformation and fracture behavior of the rock mass around the borehole is mainly affected by the in-situ stress and the mechanical properties of the surrounding rock. The present model solves the stress and plastic zone distribution in the elastoplastic softening rock mass under the non-uniform in-situ stress, and it can degenerate into solutions under simple conditions after modifying some parameters. When $\lambda = 1$, it becomes the case under uniform in-situ stress, and the obtained result is completely consistent with Yuan Wenbo's Solution [10], if $\beta = 0$, the model becomes the Kastner's Equation further [9]. Next, the present model is compared with two special cases (using the elastoplastic softening model under a uniform stress field, using the ideal elastoplastic model under a non-uniform stress field) and an approximation method with high precision (the perturbation method) to highlight its characteristics.

5.1. Comparison with the Results Using the Elastoplastic Softening Model under Uniform Stress Field

It can be known from Equation (33) that if the mechanical parameters of the surrounding rock are determined, the radius of the plastic zone is only a function of the angle θ, so the shape of the boundary line between the elastic zone and plastic zone is no longer a circle. Furthermore, the radius of the plastic zone is a function of $\cos2\theta$, and it is related to the lateral stress coefficient λ.

According to the in-situ stress and mechanical parameters of the surrounding rock at Nantun mine in Shandong Province (seen in Table 1), substituting them into the Equation (26) and Equation (33),

the area and the shape of the plastic zone and the damaged zone around the wellbore under the non-uniform stress field and the uniform stress field can be calculated, shown in Figure 12.
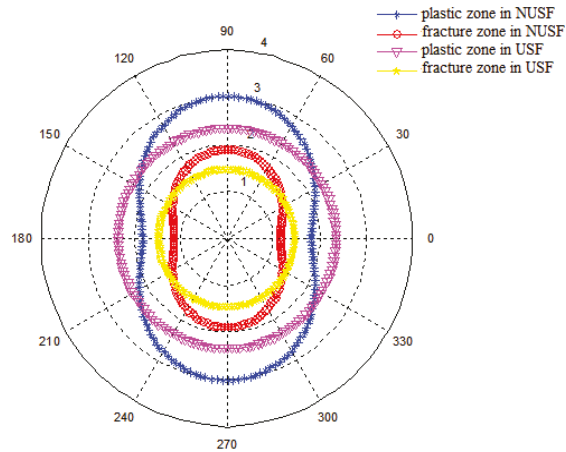
Figure 12. Comparison of the plastic zone and the damaged zone in surrounding rock under the non-uniform stress field (NUSF) and uniform stress field (USF).

It can be seen from Figure 12 that when the lateral stress coefficient $\lambda > 1$, that is, the horizontal stress is greater than the vertical stress, the plastic zone and the damaged zone are both approximately elliptical, short in the horizontal direction and long in the vertical direction, and have concaves on the left and right sides. Compared with the case of uniform stress field ($\lambda = 1$) [10,11,16–18], the plastic and fracture area on the left and right sides of the wellbore become significantly smaller, while that on the upper and lower sides increase. It can be predicted that, when $\lambda < 1$, that is, the horizontal stress is less than the vertical stress, the plastic area on the left and right sides of the well is larger than that on the upper and lower sides, and the damaged zone is also the same.

5.2. Comparison with the Results Using the Ideal Elastoplastic Model under Non-Uniform Stress Field

The selection of the constitutive model of the surrounding rock has a great influence on the results. In this part, the elastoplastic softening model and the ideal elastoplastic model are compared. Considering the Mohr-Coulomb criterion is adopted for the yield of the surrounding rock, so the comparison is performed under different values of internal friction angle and cohesion.

5.2.1. Effect of the Internal Friction Angle

Similarly, the surrounding rock parameters in Table 1 are used, and the internal friction angles are taken as 20°, 25°, 30°, and 35°, respectively, and the different two models are substituted to solve the shape of the plastic zone, as shown in Figure 13.

It can be seen from Figure 13 that the plastic zone under the elastoplastic softening model is concave on the left and right sides, while it is approximately elliptical under the ideal elastoplastic model. The plastic zone size difference between the two models is significant. On the left and right sides of the well (the angle is 0° or 180°), the radiuses of the plastic zones calculated by the two models are close, and the gap increases with the angle. It is getting bigger and bigger until the upper and lower sides reach the maximum. In addition, with the increase of the internal friction angle, the radius of the plastic zone under the two models decrease to different extents, and the difference between them becomes smaller and smaller.

Figure 13. Comparison of plastic zone shape between elastoplastic softening model and ideal elastoplastic model with different internal friction angles.

The reason is that the stress in the plastic deformation stage of the ideal elastoplastic model remains constant and is greater than the stress in the elastic stage. The rock mass in the plastic zone can still maintain a stable state under the in-situ stress so that the boundary of the plastic zone would not change suddenly, and thus the shape of the plastic zone is relatively regular [26–28]. However, in the elastoplastic softening model, when the stress exceeds the compressive strength of the rock mass, the strain-softening effect will reduce the strength. The strength of the rock mass at different positions is different, and thus the deformation is different. Therefore, the boundary shape of the plastic zone is irregular. Specifically, the plastic zone on the left and right sides of the wellbore is concave, and this tendency tends to increase as the lateral stress coefficient increases.

5.2.2. Effect of the Cohesion

The surrounding rock parameters in Table 1 are still used, and the cohesive is taken as 0.5 MPa, 1 MPa, 1.3 MPa, and 1.6 MPa, respectively, and the different two models are substituted to solve the shape of the plastic zone, as shown in Figure 14.

It can be seen from Figure 14 that as the cohesion increases, the radius of the plastic zone under the two models decreases, and the difference between them increases. The plastic zone shape under the ideal elastoplastic model is always approximately elliptical, under the elastoplastic softening model it changes from approximately elliptical to concave on the left and right sides. In general, the area of the plastic zone calculated by the elastoplastic softening model is larger than that by the ideal elastoplasticity model.
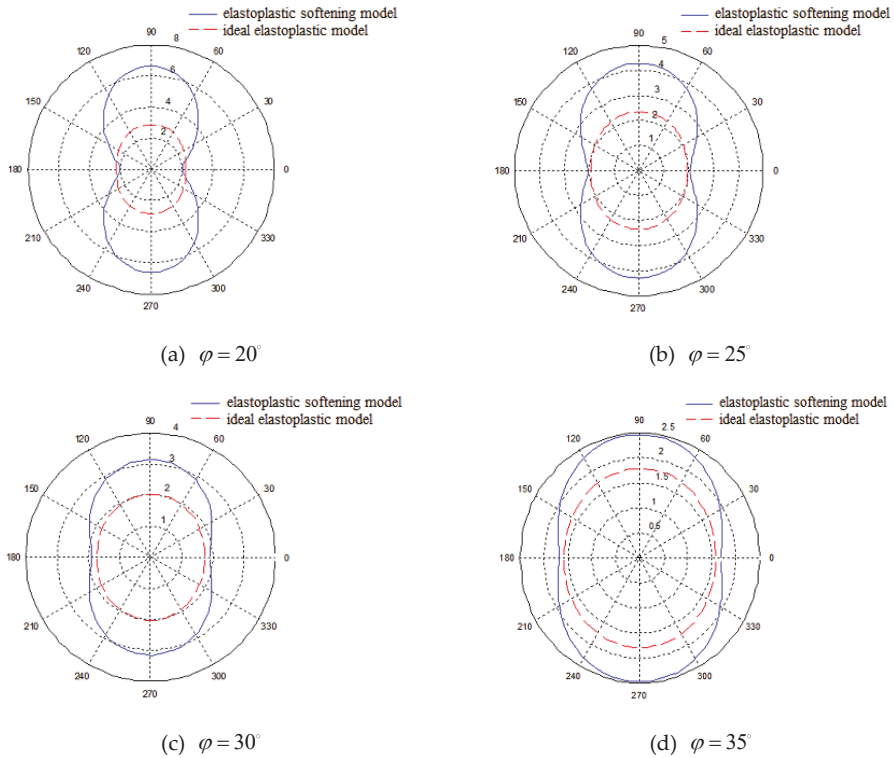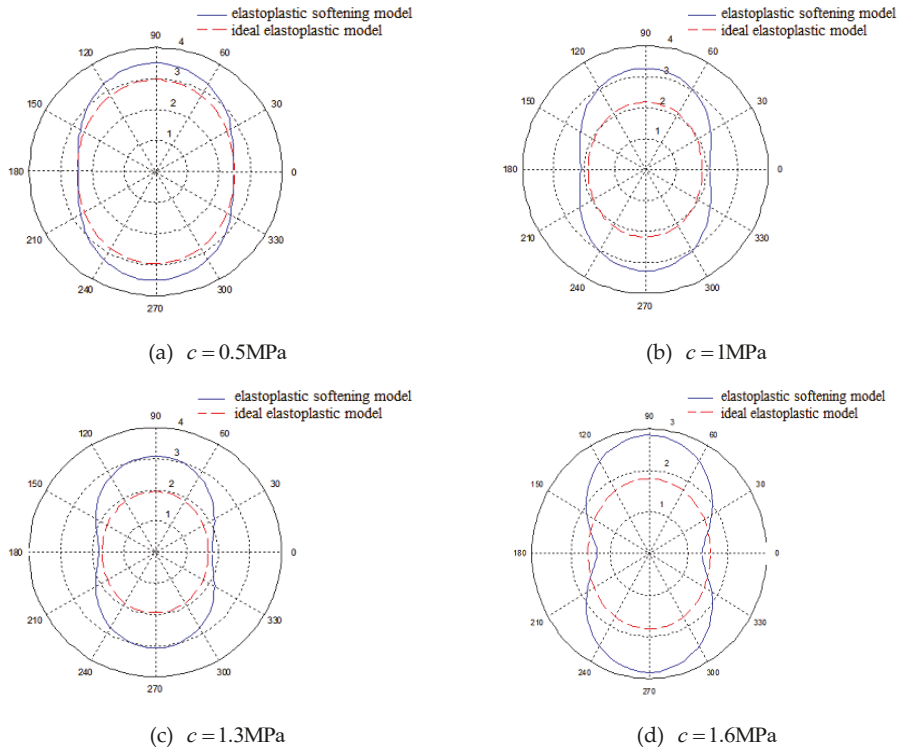
Figure 14. Comparison of plastic zone shape between elastoplastic softening model and ideal elastoplastic model with different cohesion.

As can be seen from Figures 13 and 14, the internal friction angle and the cohesion significantly affect the difference between the calculation results of the two models. The internal friction angle of the rock mass characterizes the frictional effect, including the sliding friction caused by the surface roughness of the mineral particles when they mutually slip, and the occlusal friction caused by the movement of the mineral particles in the state of embedding, interlocking and detachment. The larger internal friction angle leads to the more significant friction effect of the rock mass, and the concave phenomenon in the plastic zone will be weakened. Cohesion is the mutual attraction between adjacent parts of a substance, which is the expression of molecular forces. In the case of effective stress, the cohesion is obtained by subtracting the total shear strength from the friction strength. Therefore, as the cohesion increases, the concave phenomenon in the plastic zone will be enhanced. In general, the increasing internal friction angle and cohesion will enhance the shear strength of the surrounding rock, so the plastic zone area around the wellbore will gradually decrease.

5.3. Comparison with the Results of the Perturbation Method

The perturbation method, also known as the small parameter expansion method, is a method for solving the mathematical physics problem with high precision [31,32]. Since the solution using the perturbation method in the existing literature is based on the ideal elastoplastic model of the rock mass, in order to facilitate the comparison, some parameters in the present model need to be changed to transform into a special one under the ideal elastoplastic model. Make the corresponding change to

the Equation (33), that is, substituting $\sigma_c^* = \sigma_c$ and $\beta = 0$ into the equation, the radius of the plastic zone becomes

$$R_p = \left[\frac{\frac{2}{K_p+1}\left[\frac{P(1+\lambda)}{2} + \frac{\sigma_c}{K_p-1} \right] R_0^{K_p-1} + \frac{2P(1-\lambda)}{K_p-1} R_0^{K_p-1} \cos 2\theta}{P_1 + \frac{\sigma_c}{K_p-1}} \right]^{\frac{1}{K_p-1}}. \tag{34}$$

The radius of the plastic zone obtained by the perturbation method is [31]

$$R_p = R_0 \left[\frac{(P+c\cot\varphi)(1-\sin\varphi)}{P_1+c\cot\varphi} \right]^{\frac{1}{K_p-1}} \left\{ 1 + (\lambda-1)\frac{P(1-\sin\varphi)(1-2\cos 2\theta)}{4(P\sin\varphi+c\cos\varphi)} \right.$$
$$\left. + (\lambda-1)^2 \frac{P^2(1-\sin\varphi)}{32(P\sin\varphi+c\cos\varphi)^2} [5 + \sin\varphi + 4(1-3\sin\varphi)\cos 2\theta - 2(3-5\sin\varphi)\cos 4\theta] \right\} \tag{35}$$

According to the form of the above two equations, Equation (34) and Equation (35), it is difficult to visually see the difference in the shape of the resulting curves. Therefore, the specific parameters in Table 1 are still used for calculation. Considering the influence of the mechanical properties of the surrounding rock, they are compared under different internal friction angles and cohesion, as shown in Figure 15.

(a) $\varphi = 25°$, $c = 1.2$MPa

(b) $\varphi = 35°$, $c = 1.2$MPa

(c) $\varphi = 30°$, $c = 0.5$MPa

(d) $\varphi = 30°$, $c = 1.6$MPa
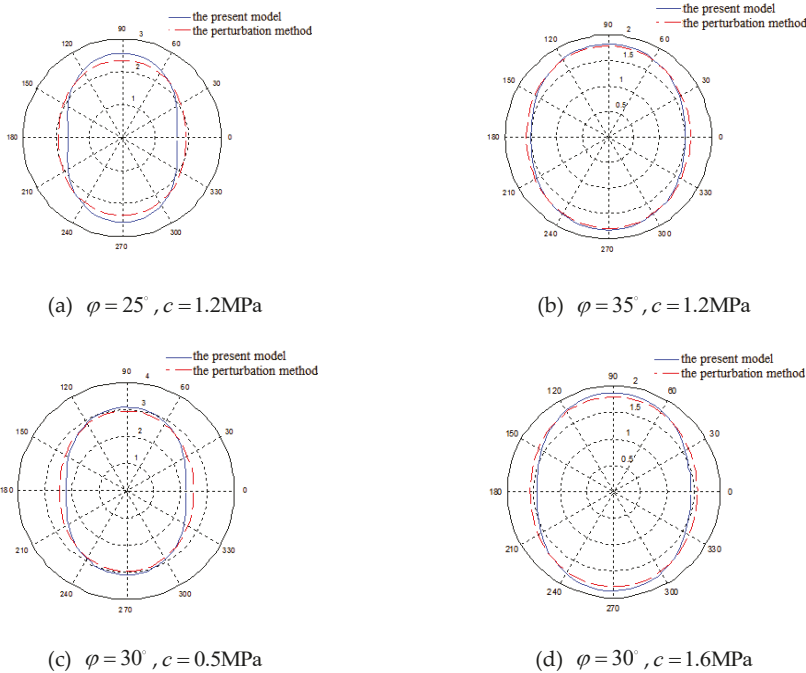
Figure 15. Comparison between the proposed method and the perturbation method.

It can be seen from Figure 15 that the area of the plastic zone obtained by the two methods is basically the same, and the relative error is within 5%. In terms of the shape of the plastic zone, the curve calculated by the perturbation method is more elliptical, while it is slightly slender by the proposed method, that is, the plastic zone size on the left and right sides of the wellbore is smaller than that obtained by the perturbation method, and it is bigger on the upper and lower sides.

From the principle of the perturbation method and the expression of the radius of the plastic zone, it is basically a correction to the Kastner's equation [9]. When $\lambda = 1$ is taken in Equation (35),

the Kastner's equation can be obtained [32]. Therefore, the shape of the plastic zone obtained by the perturbation method is theoretically approximately elliptical and will become closer to a circle when certain conditions are met. However, the proposed model is based on the premise of the non-uniform in-situ stress field, and the elastoplastic softening model is adopted, so it has certain advantages since the perturbation method cannot solve such problems.

It is worth noting that there is another approach to solve the stresses and the displacements around a borehole, that is, by assuming that Young's modulus varies around a circular opening according to a given function, which arises from strain-induced damage or from confining stress effects in a material with stress-dependent stiffness, a radius-dependent modulus (RDM) model was proposed to quantify the concept of a variably damaged zone around an opening [37]. Compared with the present model, the RDM model is mathematically simpler and easier to calculate, but the chosen Young's modulus function would bring more uncertainty to the calculation result, and a closed-form solution cannot be obtained. In addition, the RDM model cannot distinguish between the plastic zone and the damaged area. From the calculation results of stress distribution, as shown in Figures 5–7, the two models are similar that the hoop stress reduces at the borehole wall and reaches a maximum at some distance from the wall, while the radial stress increases monotonically with distance to the borehole. More detailed comparative studies will be conducted in the future.

6. Conclusions

In this study, based on the elastoplastic softening model of rock and the Mohr-Coulomb strength criterion, the stress distribution of elastic zone, plastic zone and damaged zone in the surrounding rock of a circular wellbore is obtained by the in-situ stress field decomposition method, and the boundary line equations of the plastic and damaged zone are further obtained. Then, the influence rules of lateral stress coefficient and mechanical parameters on the stress distribution and plastic zone size in surrounding rock mass are analyzed. Finally, the proposed model is compared with the cases of the uniform in-situ stress field, the ideal elastoplastic model and the perturbation method. The main conclusions are as follows:

(1) The proposed model solves the stress and the plastic-damaged zone distribution in the elastoplastic softening rock mass in the non-uniform in-situ stress field. After modifying the model parameters, it can be degraded into solutions under simple conditions. When $\lambda = 1$, it becomes the case of a uniform in-situ stress field, and the obtained result is completely consistent with Yuan Wenbo's Solution. If $\beta = 0$, then the model is transformed into Kastner's Equation.

(2) The effect of the non-uniform in-situ stress field: As the lateral stress coefficient increases, the stress concentration becomes stronger, the maximum hoop stress and radial stress both increase significantly. The shape of the plastic zone and the damaged zone under the uniform in-situ stress is circular, but under the non-uniform in-situ stress, it becomes an approximately elliptical shape and getting flatter with increasing lateral stress coefficient.

(3) The effect of the mechanical properties of the surrounding rock: As the internal friction angle and the cohesion increase, both the hoop and radial stresses and their gradients become larger, and the area of the plastic zone is significantly reduced. The plastic zone increases approximately proportionally with the increasing brittleness coefficient, and finally reaches a stable value. When the brittleness coefficient is greater than 5, it almost never increases.

(4) Comparison with the perturbation method: The plastic zones obtained by the present method and the perturbation method are basically the same when the ideal elastoplastic model is adopted. However, the perturbation method cannot solve the problem in the elastoplastic softening rock mass under the non-uniform in-situ stress field.

References

1. Xie, H.P.; Wang, J.A.; Ju, Y.; Liu, J.Z. *Coal Industry Reform: Strategies and Directions*; Science Press: Beijing, China, 2018; pp. 1–10.
2. Wang, Z.; Luo, Y.Y.; Li, P.C.; Cai, X.Q. Problem orientated analysis on China's shale gas policy. *Energies* **2018**, *11*, 2962. [CrossRef]
3. Zhang, Z.Z.; Gao, F. *Energy Evolution Mechanism during Rock Deformation and Failure*; China University of Mining Science and Technology Press: Xuzhou, China, 2014; pp. 2–20.
4. Deangeli, C.; Omwanghe, O.O. Prediction of mud pressures for the stability of wellbores drilled in transversely isotropic rocks. *Energies* **2018**, *11*, 1944. [CrossRef]
5. Han, H.X.; Yin, S.D. Determination of in situ stress and geomechanical properties from borehole deformation. *Energies* **2018**, *11*, 131. [CrossRef]
6. Zhang, H.; Yin, S.D.; Aadnoy, B.S. Finite-element modeling of borehole breakouts for in situ stress determination. *Int. J. Geomech.* **2018**, *18*, 04018174. [CrossRef]
7. Han, W.; Wang, G.; Liu, C.; Luan, H.; Wang, K. Time-Dependent Behavior of a Circular Symmetrical Tunnel Supported with Rockbolts. *Symmetry* **2018**, *10*, 381. [CrossRef]
8. Gao, H.; He, P.; Chen, Z.; Li, X. Study on a Surrounding Rock Pressure Calculation Method for Super-Large Section Highway Tunnels. *Symmetry* **2019**, *11*, 1133. [CrossRef]
9. Kastner, H. *Statik des Tunnel-und Stollenbaues*; Springer: Berlin, Germany, 1962.
10. Yuan, W.B.; Chen, J. Analysis of plastic zone and loose zone around opening in softening rock mass. *J. China Coal Soc.* **1986**, *11*, 77–86.
11. Jiang, B.S.; Zhang, Q.; He, Y.N.; Han, L.J. Elastoplastic analysis of cracked surrounding rocks in deep circular openings. *Chin. J. Rock Mech. Eng.* **2007**, *26*, 982–986.
12. Sharan, S.K. Elastic-brittle-plastic analysis of circular openings in Hoek-Brown media. *Int. J. Rock Mech. Min. Sci.* **2003**, *40*, 817–824. [CrossRef]
13. Sharan, S.K. Analytical solutions for stresses and displacements around a circular opening in a generalized Hoek-Brown rock. *Int. J. Rock Mech. Min. Sci.* **2008**, *45*, 78–85. [CrossRef]
14. Sharan, S.K. Exact and approximate solutions to displacements around circular openings in an elastic-brittle-plastic hoek-brown rock. *Int. J. Rock Mech. Min. Sci.* **2005**, *42*, 529–542. [CrossRef]
15. Park, K.H.; Kim, Y.J. Analytical solution for a circular opening in an elastic–brittle–plastic rock. *Int. J. Rock Mech. Min. Sci.* **2006**, *43*, 616–622. [CrossRef]
16. Zhang, Q.; Jiang, B.S.; Wang, S.L.; Ge, X.R.; Zhang, H.Q. Elasto-plastic analysis of a circular opening in strain-softening rock mass. *Int. J. Rock Mech. Min. Sci.* **2012**, *50*, 38–46. [CrossRef]
17. Lv, A.; Masoumi, H.; Walsh, S.D.C.; Roshan, H. Elastic-Softening-Plasticity around a borehole: An analytical and experimental study. *Rock Mech. Rock Eng.* **2019**, *52*, 1149–1164. [CrossRef]
18. Li, Y.; Cao, S.G.; Fantuzzi, N.; Liu, Y.B. Elasto-plastic analysis of a circular borehole in elastic-strain softening coal seams. *Int. J. Rock Mech. Min. Sci.* **2015**, *80*, 316–324. [CrossRef]
19. Galin, L.A. Plane elastic-plastic problem: Plastic regions around circular holes in plates and beam. *Prik. Mat. Mekh.* **1946**, *10*, 365–386.
20. Detournay, E. An approximate statical solution of the elastoplastic interface for the problem of Galin with a cohesive-frictional material. *Int. J. Solids Struct.* **1986**, *22*, 1435–1454. [CrossRef]
21. Detournay, E.; Fairhurst, C. Two-dimensional elastoplastic analysis of a long, cylindrical cavity under non-hydrostatic loading. *Int. J. Rock Mech. Min. Sci.* **1987**, *24*, 197–211. [CrossRef]
22. Detournay, E.; John, C.M.S. Design charts for a deep circular tunnel under non-uniform loading. *Rock Mech. Rock Eng.* **1988**, *21*, 119–137. [CrossRef]
23. Ostrosablin, N.P. Plastic zone around a round hole in a plane with a nonuniform basic stressed state. *J. Appl. Mech. Tech. Phys.* **1990**, *31*, 783–792. [CrossRef]
24. Tokar, G. Generalization of Galin's problem to frictional materials and discontinuous stress field. *Int. J. Solids Struct.* **1990**, *26*, 129–147. [CrossRef]

25. Leitman, M.J.; Villaggio, P. Plastic zone around circular holes. *J. Eng. Mech.* **2009**, 135. [CrossRef]
26. Ochensberger, W.; Celigoj, C.C.; Ulz, M.H. Amendment to the Galin plane elastoplastic solution. *J. Eng. Mech.* **2013**, 139. [CrossRef]
27. Lu, A.Z.; Wang, S.J.; Zhang, X.L.; Zhang, N. Solution of the elasto-plastic interface of circular tunnels in Hoek–Brown media subjected to non-hydrostatic stress. *Int. J. Rock Mech. Min. Sci.* **2018**, *106*, 124–132. [CrossRef]
28. Lu, A.Z.; Zhang, X.L.; Wang, S.J. Analytic method for elasto-plastic analysis of circular tunnels under non-axisymmetric stresses. *Chin. J. Rock Mech. Eng.* **2018**, *37*, 14–22.
29. Zhuang, P.Z.; Yu, H.S. A unified analytical solution for elastic–plastic stress analysis of a cylindrical cavity in Mohr–Coulomb materials under biaxial in situ stresses. *Géotechnique*, 2019; 69, 369–376.
30. Zhuang, P.Z.; Yu, H.S. Two-dimensional elastoplastic analysis of cylindrical cavity problems in Tresca materials. *Int. J. Numer. Anal. Methods Geomech.* **2019**, *43*, 1612–1633. [CrossRef]
31. Wei, Y.G. Perturbation solutions for elasto-plastic analysis of circular tunnels under unequal compression in two directions. *Chin. J. Geotech. Eng.* **1990**, *12*, 11–20.
32. Hou, G.Y.; Li, J.J.; Zhao, W.W.; Liu, Y.; Chen, Z.C.; Tian, L. Perturbation solutions for elasto-plastic problems of circular tunnel under unequal compression. *Chin. J. Rock Mech. Eng.* **2014**, *33*, 3639–3647.
33. Chen, L.W.; Peng, J.B.; Fan, W.; Sun, P. Analysis of surrounding rock mass plastic zone of round tunnel under non-uniform stress field based on the unified strength theory. *J. China Coal Soc.* **2007**, *32*, 20–23.
34. Sun, J.S.; Lu, W.B. Analytical elastoplastic solutions to supporting rock mass of circular tunnels under asymmetric load. *Rock Soil Mech.* **2007**, *28*, 327–332.
35. Ma, N.J.; Li, J.; Zhao, Z.Q. Distribution of the deviatoric stress field and plastic zone in circular roadway surrounding rock. *J. China U. Min. Techno.* **2015**, *44*, 206–213.
36. Xu, Z.L. *Elasticity*, 5th ed.; Higher Education Press: Beijing, China, 2016.
37. Nawrocki, P.A.; Dusseault, M.B. Modelling of damaged zones around openings using radius-dependent Young's modulus. *Rock Mech. Rock Eng.* **1995**, *28*, 227–239. [CrossRef]

Mechanical Behavior of Tunnel Lining with Cracks at Different Positions

Jie Su [1,*], Yinming Jie [1], Xiaokai Niu [2], Chang Liu [1] and Xuan Liu [1]

[1]   Key Laboratory of Urban Underground Engineering of Ministry of Education, Beijing Jiaotong University, Beijing 100044, China; 16121041@bjtu.edu.cn (Y.J.); 19115030@bjtu.edu.cn (C.L.); 10231082@bjtu.edu.cn (X.L.)
[2]   Beijing Municipal Engineering Research Institute, Beijing 100037, China.; metronxk@126.com
*   Correspondence: sujie@bjtu.edu.cn; Tel.: +86-136-8360-1318

Abstract: Cracks in the lining significantly reduce the safety of a tunnel during operation. It is urgent to figure out the influence of cracks on tunnel carrying capacity. In this paper, three-dimensional model tests were conducted to investigate deformation, internal force, and deterioration laws of the lining with prefabricated cracks at different positions. The main conclusions were obtained as follows: (1) The carrying capacity of the lining structure with prefabricated cracks was reduced, and the deformation of the lining structure increased. The penetration of the vault crown crack accelerated the damage of the lining structure, and structural failure occurred when the crack went through at the left arch spring. (2) The internal force of the lining was greatly affected by the positions of prefabricated cracks. The internal forces of the lining structure decreased with the existence of prefabricated cracks. Whether or not there were prefabricated cracks, tension cracks appeared in the inside fiber of the vault and inverted arch. (3) The deformation of the lining structure with the existence of prefabricated cracks increased. When the prefabricated crack was located at the vault, the deformation was the largest, followed by the arch spring, side wall, and arch shoulder. (4) The analysis shows that prefabricated cracks at the vault are the most damaging under stress and deformation of the lining structure, so longitudinal cracks at the vault should be strengthened.

Keywords: prefabricated crack of tunnel lining; 3D-model test; mechanical behavior; deformation behavior; carrying capacity of tunnel lining

---

1. Introduction

In recent years, the safety of tunnel construction, especially the stability of the tunnel face [1–4] and the deformation of the ground and neighboring structures [5,6], has been a research hotspot in the field of tunnel engineering. With the large-scale expansion of the Chinese Railway Network, the problems of tunnel structure damage continue to arise. The hidden danger of tunnel operation caused by defects of the metro structure is a problem that cannot be ignored. It is necessary to evaluate and classify the safety status of the metro structure. It is widely accepted that the carrying capacity of the lining structure is reduced due to existing cracks, and the service life of tunnels is greatly shortened [7]. Therefore, research on lining cracks is of great significance. Much research has been carried out to study the damage of tunnels; the cause is summarized and analyzed by on-site investigation of the number, length, inclination, and width of lining cracks and the depth of typical cracks [8,9]. Studies on the failure of concrete structures have been carried out based on numerical analysis [10,11]. Based on model tests and numerical calculations, the influence of tunnel excavation on existing cracks in the surrounding rock was studied, and the crack propagation law and structural damage mode of surrounding rock were obtained [12]. The mechanism of cracking and the process of failure of the secondary lining of a highway tunnel were studied by a field investigation and model test [13]. A detailed investigation was carried out on the cracking and leakage of a tunnel in Japan after an

earthquake, and suggestions were given from the perspective of the design layer on the construction of tunnels in an earthquake zone [14]. The mechanical properties of the lining structure with cracks were studied by means of field investigation, numerical analysis, and model tests. Based on this, a calculation method for analyzing the mechanical properties of multifractured lining structures was proposed [15]. Li et al. [16] considered the width and length of cracks, the spalling of lining concrete, the deterioration of materials, and the leakage of water, and determined classification criteria for structural damage of tunnels constructed by the mining method. Feng [17] took the crack width of a tunnel as an evaluation index and classified the condition of lining cracks into four grades (A, B, C, and D) according to the condition of railway and highway tunnels in Japan and China. Zhang [18] first put forward the concept of the degree of health of the tunnel structure, and established a quantitative method to evaluate the safety status of the tunnel structure based on data of an engineering inspection. He [19] designed a 1:25 model test of the Bijiashan tunnel and studied the influence of backfilling and grouting, inner surface reinforcement of the lining, combined reinforcement, and the stress field on the carrying capacity of tunnel structures with cracks. Liu et al. [20] developed a 1:10 full-circumferential closed tunnel model loading device, studied the influence of crack depth and position on the carrying capacity of the tunnel structure, and established a relationship between crack depth and carrying capacity. It can be seen that research on tunnel damage has achieved some success, but from the existing research results, the model tests on lining cracks are mostly based on the plane strain model. Based on the background, in order to investigate the influence of longitudinal cracks on the carrying capacity of the lining structure, the mechanical and deformation behavior of lining with cracks at different positions are carried out, relying on a self-developed 3D test bench with a geometric ratio of 1:10. Then the internal force, deformation, and progressive failure law of the lining are analyzed to reveal the impact of lining cracks on the carrying capacity of the lining to provide a reference for the treatment of lining cracks in similar subway projects.

2. Laboratory Model Test

2.1. Engineering Overview

Based on Line 14 of the Beijing Metro, this paper selected Shi-Lihe Station to Nan-Balizhuang Station as the research section. The overall length of the tunnel (stake number: K25+723.000–K26+704.950) is 981.95 m and the buried depth of the tunnel is 7.5–17 m. The mining method was adopted for construction, with a tunneling footage of 1.2 m. The thickness of both the primary support and the secondary lining is 30 cm. The design parameters of a typical cross-section are shown in Figure 1.
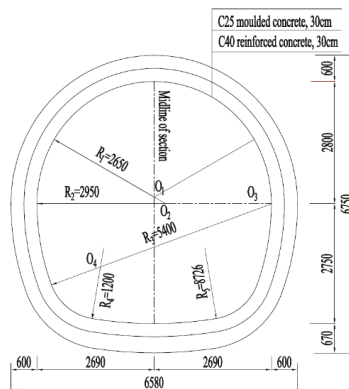
Figure 1. Design parameters of a typical cross-section (unit: mm).

According to the drilling data and indoor geotechnical test results, the soil layers within the exploration range of the project site were divided into four large layers: artificial fill (*Qml*), Quaternary neosediment, Quaternary Late Pleistocene alluvial–diluvial (*Q4al+pl*), and Tertiary Chang Xin Dian Formation clastic rocks. There are clastic rocks in the Late Pleistocene alluvial deposit (*Q3al+pl*) and the Lower Tertiary Chang Xin Dian Formation (*E2c*). The formation in this area is mainly composed of silty clay and fine sand, and their lateral pressure coefficients are 0.45 and 0.40, respectively.

According to the statistical results of the lining cracks of 15 subway lines in Beijing, many cracks are less than 10 m in length. Therefore, we basically regarded the length of all cracks as less than 10 m. On this basis, taking into account the geometric dimensions of the model, test repeatability, test operability, and reliability, we determined that the geometric similarity ratio of the test model would be 1:10, and the hydraulic loading device was used to simulate the effect of stratum on the lining structure. The research object of this paper is the 12 m lining structure (equivalent to 10 construction footings).

2.2. Test Platform

The test platform uses a three-dimensional full-cycle loading device. The test platform is mainly composed of five parts: bench, reaction frame, wheel-rail device, loading system, and measurement system. The dimensions of the bench are 120 cm × 120 cm (width × height). The overall layout of the loading system is shown in Figure 2. In order to simulate the stress of the tunnel, jacks on the top are used as vertical loading groups to simulate vertical earth pressure, and the other jacks are used as horizontal loading groups to simulate lateral earth pressure. The whole test is completed under symmetrical loading mode.
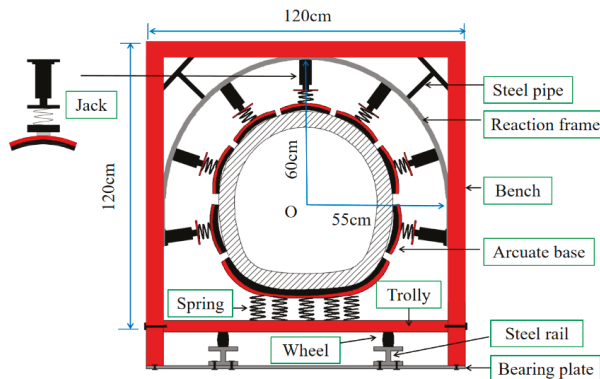
Figure 2. Overall layout of loading system.

The model test included a pre-preparation, experimental loading, and data acquisition and analysis phase. In order to keep the loading process stable, the experimental loading should be kept slow, and the jacks of the symmetric points should be simultaneously raised to ensure that the lateral pressure coefficient is around 0.4 (the lateral pressure coefficient is determined by the actual engineering). After the graded load, the oil pressure was kept constant and the load of each stage was stable for more than 5 min. The crack development and the whole gypsum model change were observed throughout the stationary stage of loading. The trend of crack propagation and the change of geometry were observed over time. The model experiment ended with main through-cracks appearing and the lining structure deforming sharply. The measurement system includes a pressure sensor, displacement sensor, strain gauge, and data acquisition system. The overall layout of the test platform can be seen in Figure 3. Concrete strain gauges were arranged on the inner and outer surfaces of the middle part of the model. As shown in Figure 4, 16 strain gauges were arranged on the lining, O1–O8 on the outside of the lining and I1–I8 on the inside.
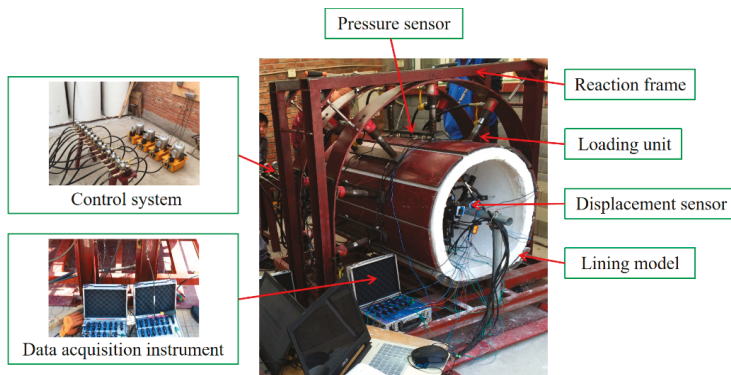
Figure 3. Test platform.
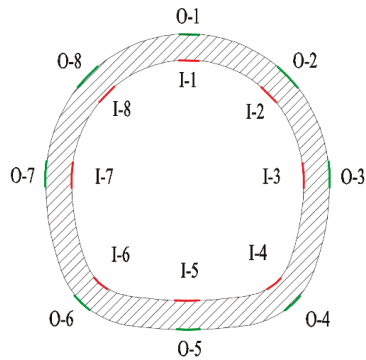
Figure 4. Layout of strain gauges for lining model.

2.3. Similar Relations and Materials

In this part, the similarity ratio of geometry (C_L) is determined as 10. According to the similarity theorem, the similarity ratio of Poisson's ratio (C_γ) and strain (C_ε) is 1, and the similarity ratio of strength (C_R), stress (C_σ), and elastic modulus (C_E) is 10. This realistic prototype scale model has been simplified to define the reduced-scale model. The mechanical property of gypsum is similar to that of concrete. Both are brittle materials with a Poisson's ratio of about 0.2, and their compressive strength is much larger than their tensile strength. In this similar model test of similarities, the mix proportion of the lining material is water: gypsum: cementing material = 0.65:1:0.01.

The primary lining prototype was cast in situ with C25 shotcrete, and the secondary lining prototype is a reinforced concrete structure with C40 concrete. In this test, the primary and secondary lining were poured with C30 concrete simultaneously. The mechanical parameters of the lining are based on actual engineering. The elastic modulus and compressive strength of the lining are 30 GP and 30 MPa, respectively. The parameters of the materials are shown in Table 1. The cross-section of the lining shows a two-lane and five-center-circle section; the thickness is 0.6 m (including primary and secondary lining), the span length is 6.58 m, the height is 6.75 m, and the axial length is 12 m. The dimensions of the model are 120 cm × 65.8 cm × 67.5 cm (length × width × height) and the thickness of the lining is 6 cm. The dimensions of the model are shown in Figure 5.

Table 1. Physical and mechanical parameters of lining.

	Elastic Modulus (GPa)	Compressive Strength (GPa)	Poisson's Ratio
Prototype lining	30	30	0.2
Model lining	2.9	3.1	0.2
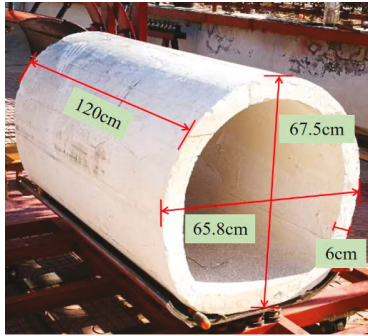
Figure 5. Dimensions of lining model.

2.4. Experimental Scheme

The failure behavior of the lining with longitudinal prefabricated cracks at different positions was investigated by five model tests. Test 1 was a baseline case with no prefabricated crack. Tests 2–5 had a lining structure with a prefabricated longitudinal crack at the tunnel vault, the arch shoulder, the sidewall, and the arch spring, respectively. The schemes of the model tests are listed in Table 2, and the model tests of prefabricated cracks at different positions are schematically described in Figure 6. According to the inspection results of Line 14 of the Beijing Metro, the length, width, and depth of the prefabricated cracks were 60 cm, 0.2 mm, and 1 cm, respectively.

Table 2. Schemes of model tests.

Scheme	Position of Crack
Test 1	None (baseline case)
Test 2	Vault
Test 3	Shoulder
Test 4	Sidewall
Test 5	Arch spring
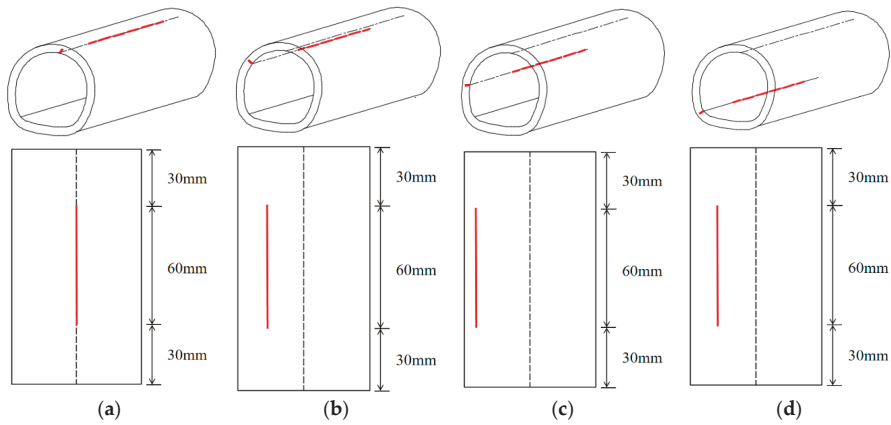
Figure 6. Diagram of prefabricated cracks at different positions: (**a**) test 2; (**b**) test 3; (**c**) test 4; (**d**) test 5.

3. Test Results Analysis

3.1. Results Analysis of Lining with No Prefabricated Crack

3.1.1. Mechanical behavior of the lining

The internal force of the lining at the vault, arch spring, and inverted arch were analyzed. Figure 7 shows the curves of internal force with the external load at the vault. In the early loading stage, the axial force of monitoring points 1, 2, and 8 linearly increased with load. As the loading continued, the increased magnitude of axial force at monitoring point 8 was greater than that at monitoring point 2. When the load reached 70 kPa, tension crack 1 appeared in the intrados of the vault. When the load increased to 135 kPa, tension crack 2 appeared in the extrados of the left arch waist. In the next loading period, there were several cracks in the arch waist and the left arch spring, but they had little impact on the internal force of the lining at the vault. The bending moment of the arch lining increased with increased external load, in which monitoring point 1 was a positive bending moment and monitoring points 2 and 8 were negative, which implies that the outer part of the vault was under compression and the inner side was under tension.
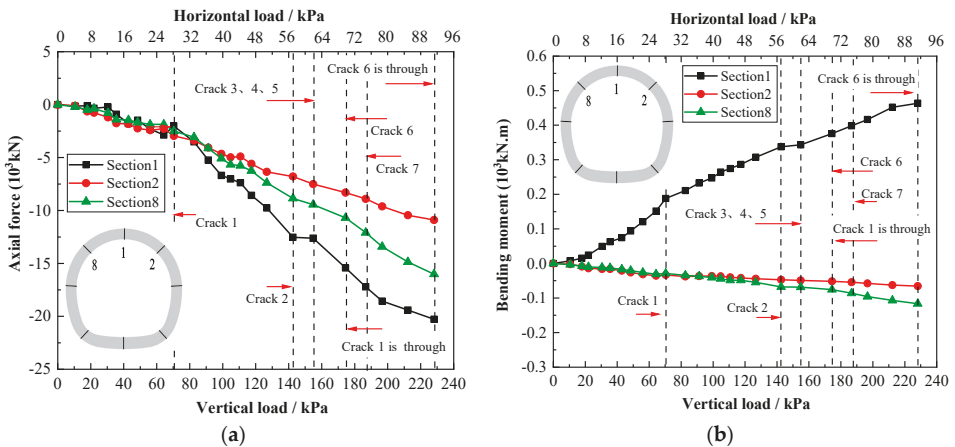
Figure 7. Internal forces curves of lining at vault: (**a**) axial force; (**b**) bending moment.

Internal force curves of the lining on the sidewall are shown in Figure 8. The axial force and bending moment of monitoring points 3 and 7 were similar. When the load was in the range of 0 to 70 kPa, axial force and bending moment increased slowly. After crack 1 appeared, the increased ratio of axial force and bending moment of monitoring point 7 was greater than that of monitoring point 3, until a tension crack appeared on the outside of the lining near monitoring point 7. As the external load continued to increase, tension cracks 4 and 5 appeared near monitoring point 3.
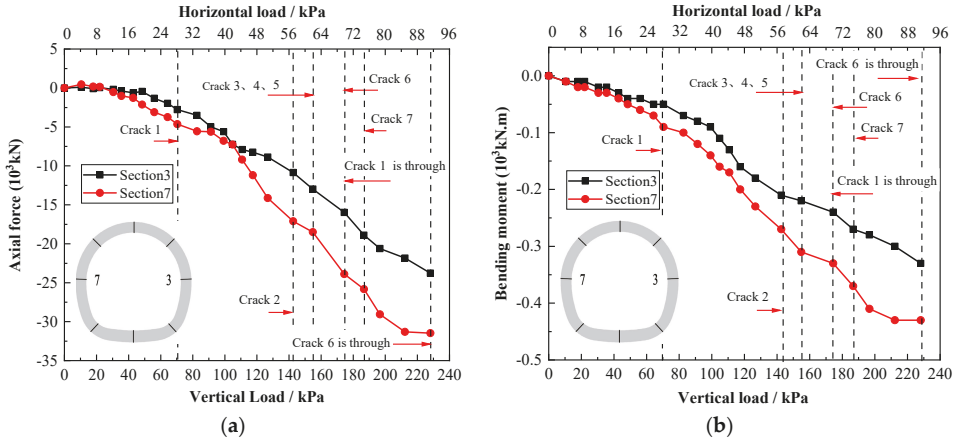
Figure 8. Internal force curves of lining at sidewall: (**a**) axial force; (**b**) bending moment.

Figure 9 shows the internal force curves of the lining at the sidewall. It can be seen that the axial force at measuring point 5 of the inverted arch was significantly less than that at the arch spring, and the internal side of the lining of the inverted arch was subjected to a positive bending moment, which increased gradually with the increased load. When the load was less than 70 kPa, the change law of axial force at all positions was similar. When tensile crack 1 appeared at the vault, the structural integrity was destroyed, resulting in reduced axial force at the inverted arch, while the increased axial force at the arch spring presented an obvious stress concentration phenomenon. When the load reached 174 kPa, tension crack 6 appeared in the left arch spring. As the load increased, the cracks in the left arch spring penetrated, and the lining structure lost its carrying capacity.
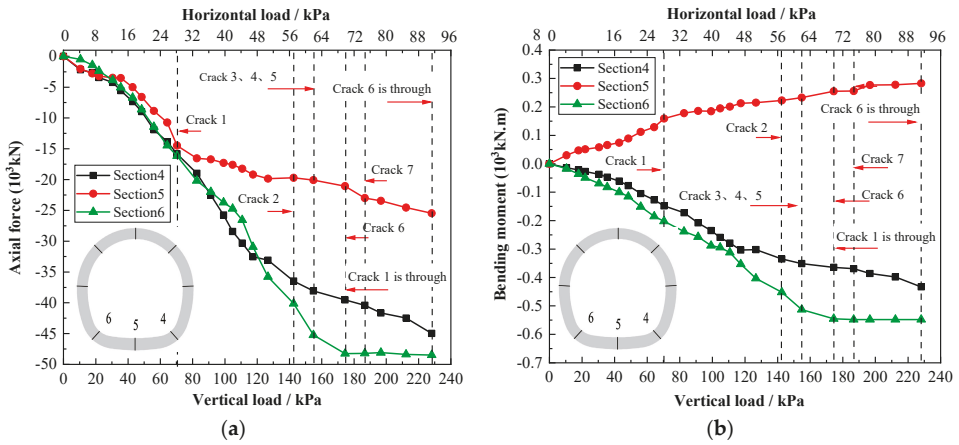
Figure 9. Internal force curves of lining at arch spring and inverted arch: (**a**) axial force; (**b**) bending moment.

An internal force diagram of lining failure is shown in Figure 10. The positive bending moments appeared at the inverted arch and crown, indicating that the inner side of the lining was under tension. It shows that the axial force of the substructure of the lining was larger than that of the superstructure, and stress concentration occurred at both arch springs. Due to the uneven distribution of structural materials and other factors in the process of model making, the internal force on the left side of the lining was a little bit larger than that on the right side. Finally, the crack at the left arch spring penetrated, and the lining structure lost its carrying capacity. In terms of the bending moment, the internal lining of the vault and inverted arch was subjected to tension, and a tension crack first appear at the vault crown, while the bending moment of the left side wall and the arch spring was greater than that of the right side. The distribution of cracks of the lining is depicted in Figure 11.
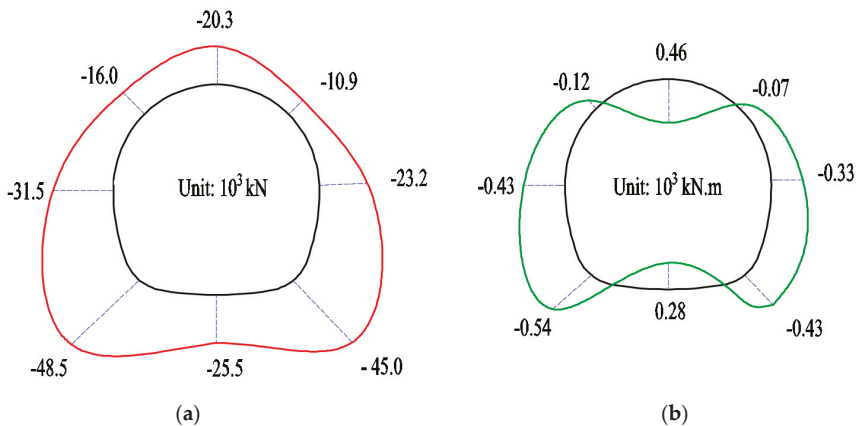
Figure 10. Distribution of lining internal force in the ultimate state: (**a**) axial force; (**b**) bending moment. (The green line represents axial force, and the red line represents bending moment.)
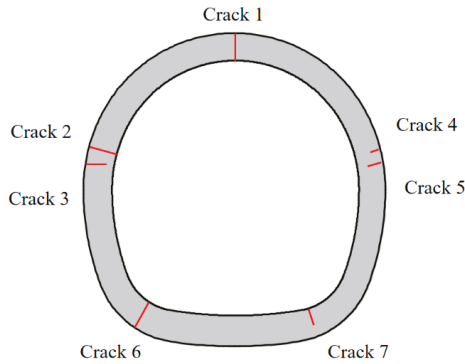
Figure 11. Distribution of cracks in the lining.

3.1.2. Deformation behavior of lining

To investigate the deformation law of the lining during the test, vertical and horizontal convergence of the lining are analyzed in this part. Figure 12 shows the relation curve between deformation and load. When the external load was between 0 and 70 kPa, vertical convergence increased slowly, and horizontal displacement increased linearly with the increased load. When crack 1 appeared, the vertical convergence ratio increased, and when the load reached 174 kPa (through-crack 1), vertical deformation increased sharply. The appearance of through-crack 1 indicates that the vault of the lining was damaged, decreasing the load transferring from the arch to the sidewall. At this time, horizontal displacement tended to be gentle, however, vertical deformation increased sharply until structural failure occurred. It can be concluded that vertical displacement was greatly affected by the crack at the vault, while the appearance of cracks in other parts of the lining had little influence on vertical deformation.
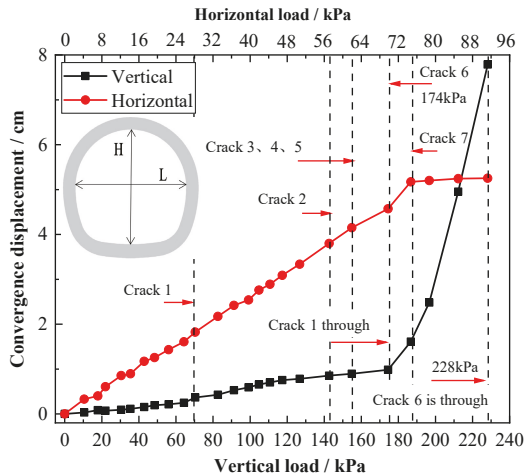
Figure 12. Relation curve between load, deformation, and cracks.

3.2. Analysis of Prefabricated Cracks at Different Positions

3.2.1. Mechanical Behavior Analysis

The distribution of lining internal force in the ultimate state under different tests are depicted in Figure 13. The internal force of the lining was greatly affected by the positions of the prefabricated cracks. The internal forces of the lining structure decreased by different degrees with the existence of prefabricated cracks. Vertical displacement was greatly affected by crack 1 at the vault, while the appearance of cracks in other parts had little effect on vertical deformation. When prefabricated cracks were located at the arch shoulder, sidewall, and arch spring, the lining axial force and bending moment were asymmetrically distributed. In tests 3 and 5, with increased positive bending moment at the inverted arch, tension cracks appeared on the inside of the inverted arch.

(**a**)

(**b**)

Figure 13. *Cont.*

(c)

(d)
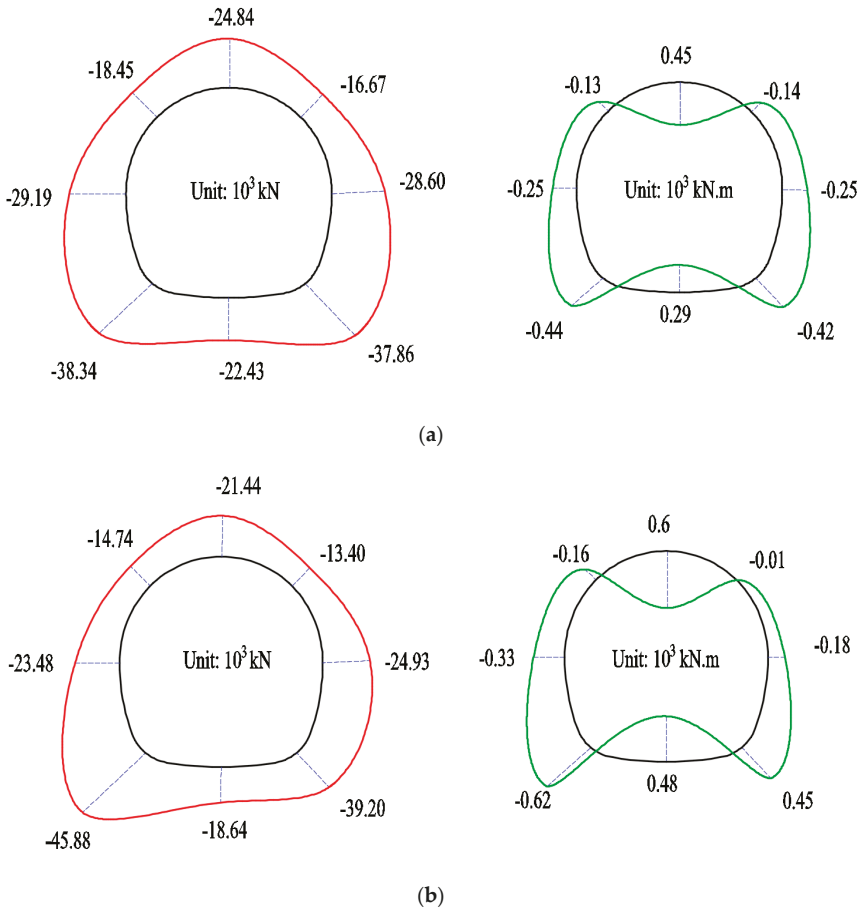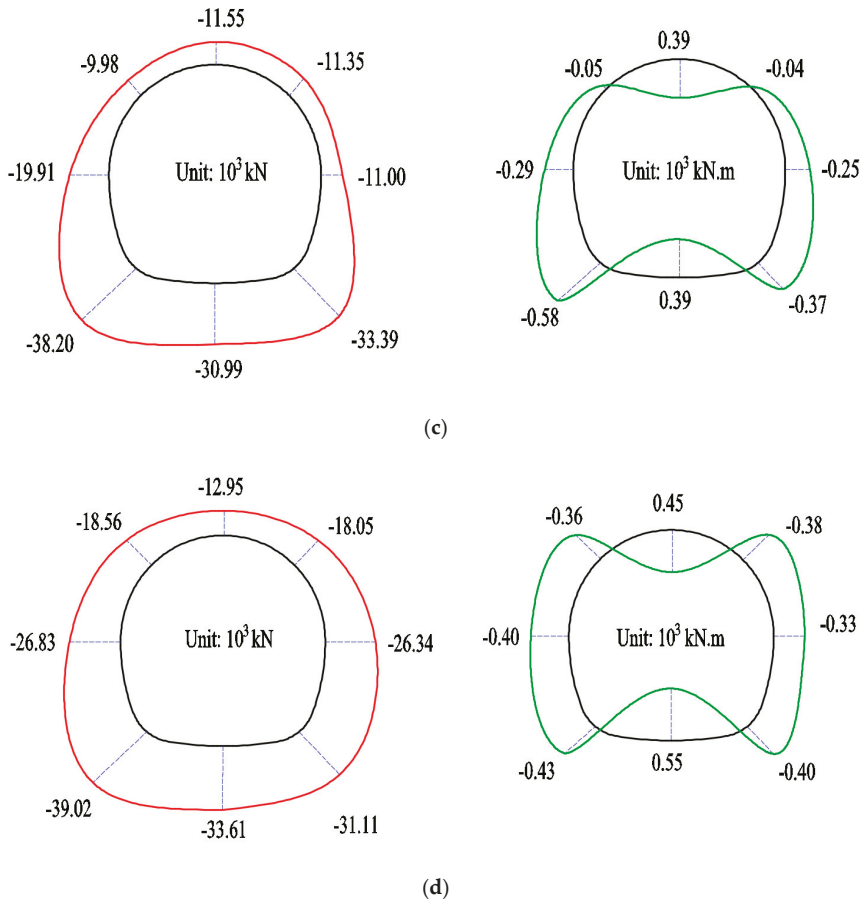
Figure 13. Distribution of lining internal force in the ultimate state: (**a**) test 2; (**b**) test 3; (**c**) test 4; (**d**) test 5. (The green line represents axial force, and the red line represents bending moment.)

3.2.2. Deformation Behavior Analysis

The distribution of lining internal force in the ultimate state is shown in Figure 14. It can be seen that the overall variation in vertical and horizontal convergence curves of the tests is similar. When the external load was between 0 and 70 kPa, the speed of horizontal deformation was significantly higher than that of vertical convergence. The vertical and horizontal convergence ratio increased after crack 1 appeared. When crack 1 became a through-crack, vertical convergence increased sharply until the crack at the left arch spring was through, then the model lost its carrying capacity. However, the horizontal convergence curve became gradually stable at this stage.

As for test 2, when the external load reached 60 kPa, the prefabricated crack at the vault began to expand, and the external load was greatly reduced compared with test 1 (no prefabricated crack) when the crack at the vault penetrated. The ultimate load of the structure was 215 kPa, which is lower than that of test 1 (228 kPa).

As for tests 2 and 4, the prefabricated cracks were located at the vault and sidewall, respectively. The cracks appeared in the same sequence during the loading of the two tests, but the prefabricated cracks did not expand. Cracks in the vault and side wall appeared first at the inner fiber of the tunnel vault, second at the outer fiber of the lining at the left arch waist, third at the outer fiber of the lining

at the right arch waist, and then at the inner fiber of the lining at the left arch spring. As for tests 3 and 5, prefabricated cracks were located at the arch shoulder and arch spring, respectively. The cracks appeared in the same sequence during the loading of the two tests. The cracks first appeared at the vault, then, as the load reached the tensile limit of the inner fiber of the lining, tensile crack 2 appeared at the inverted arch, then cracks 3 and 4 appeared on the outside of the left and right arch waist, respectively. Finally, the crack at the left arch spring went through, and the structure lost its carrying capacity.
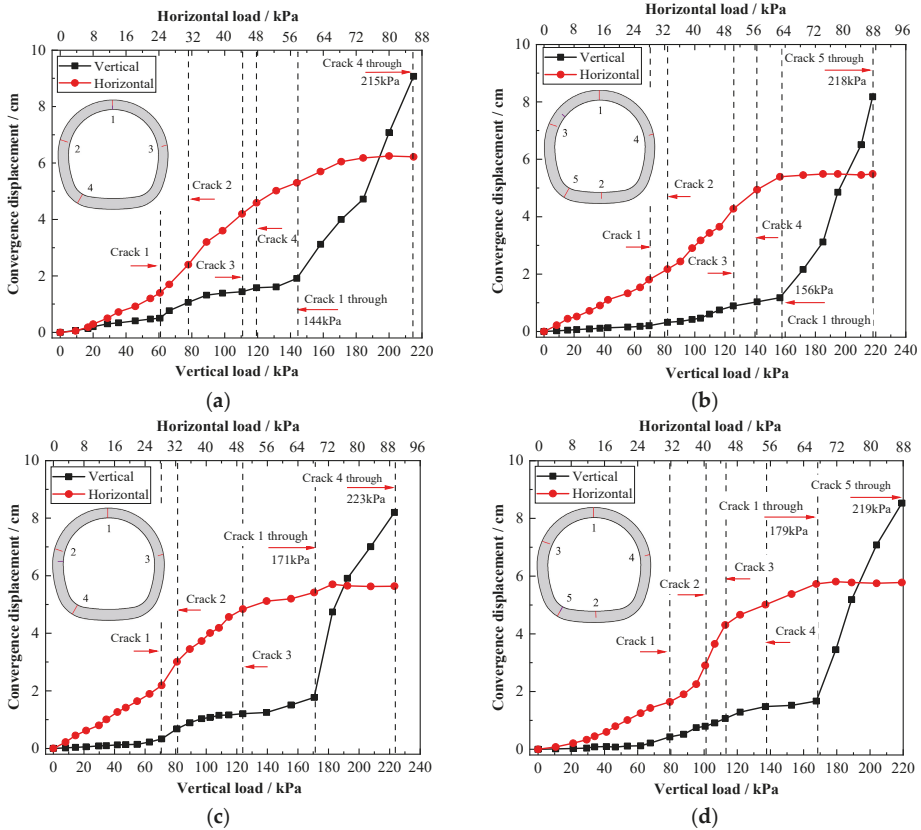
Figure 14. Relation curves between load, deformations, and cracks: (**a**) test 2; (**b**) test 3; (**c**) test 4; (**d**) test 5.

Figure 15 shows a comparison diagram of vertical and horizontal convergence curves of lining under different tests. The deformation of the lining structure increased when there was a prefabricated crack. The final vertical and horizontal convergence of the four models in descending order was as follows: the prefabricated crack was located at the vault, then at the arch spring, side wall, and arch shoulder. It can be seen that the influence on deformation due to prefabricated cracks at the vault and arch spring was greater than at the sidewall and arch shoulder.
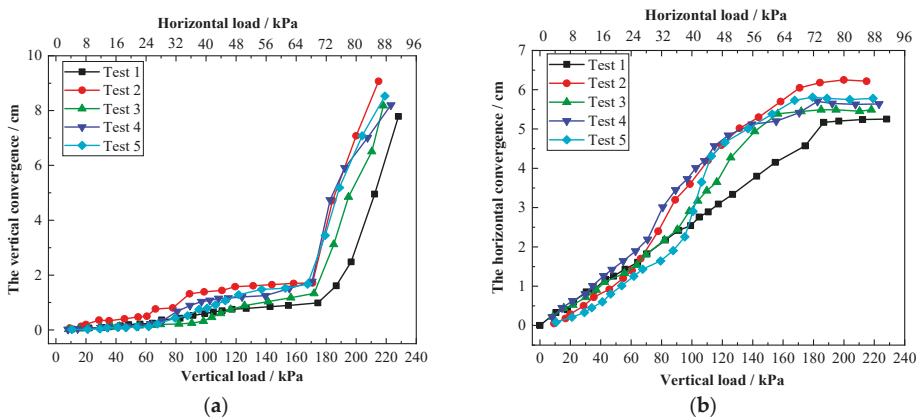
Figure 15. Relation curves between load and deformation of all tests: (**a**) vertical; (**b**) horizontal.

4. Analysis of Carrying Capacity of Lining

It can be seen from the above analysis that the penetration of cracks at the vault accelerated the damage of the lining structure. It is considered that the carrying capacity is the load beyond which the lining fails. Table 3 shows the load when the crack at the vault went through and the ultimate load of all tests. The carrying capacity of the lining structure was reduced when there were prefabricated cracks. In test 2 (prefabricated crack at the vault), the load was 144 kPa when crack 1 became a through-crack. When the prefabricated cracks were located at the arch shoulder, sidewall, and arch spring, the load increased gradually.

When the prefabricated crack was located at the vault, the ultimate load of the structure decreased by 6% compared with test 1, and when the prefabricated cracks were located at the arch shoulder and sidewall, the ultimate load decreased slightly. During the test process, the structure failed when the arch spring cracked through, while the prefabricated crack at the arch spring accelerated the penetration of the crack, and the ultimate load decreased by 4% (219 kPa) compared with test 1. It can be concluded that the presence of a prefabricated crack at the vault accelerated the crack's propagation, and as the prefabricated cracks were far from the vault, the load at the vault crack increased. The ultimate load of the lining structure was reduced by the presence of prefabricated cracks, and the reduction was greater when the cracks were located at the vault and the arch than at the side wall and arched shoulder.

Table 3. Load when crack is through at the vault and failure load.

Scheme	Load When Crack at Vault is Through (kPa)	Failure Load (kPa)	Carrying Capacity Reduction Ratio
Test 1	174	228	–
Test 2	144	215	5.7%
Test 3	156	218	4.4%
Test 4	171	223	2.2%
Test 5	179	219	3.9%

5. Conclusions

Based on the horseshoe cross-section tunnel structure of the Beijing subway, mechanical and deformation characteristics of the lining structure with prefabricated cracks at different positions were studied by 3D-model tests. The main conclusions are as follows:

(1) The carrying capacity of the lining with prefabricated cracks was reduced, and the deformation of the lining structure increased. Cracks located at the vault fully extended along longitudinal

direction accelerated the speed of lining damage. When the crack located at the left arch spring extended along longitudinal direction, the tunnel lining failed.

(2) The internal force of the lining was greatly affected by the positions of prefabricated cracks. The internal forces of the lining structure decreased with the existence of prefabricated cracks. Whether or not a prefabricated crack existed, the outer fiber of the vault and inverted arch were under compression and the inner fiber was under tension, so a tension crack appeared at the inside fiber of the vault and inverted arch, while compressive stress concentration appeared at both sides of the arch springs.

(3) The deformation of the lining structure with the existence of prefabricated cracks increased. When the prefabricated crack was located at the vault, the deformation was the largest, followed by the arch spring, side wall, and arch shoulder. Vertical deformation was greatly affected by the crack at the vault; however, the appearance of cracks in other parts had little influence on vertical deformation. The through-crack at the tunnel vault indicated failure of the vault of the lining. At this time, the load transferring from the arch to the sidewall decreased in order to reduce horizontal deformation, while vertical deformation increased greatly until the structure was damaged.

(4) The ultimate carrying capacity of the lining was reduced due to the existence of prefabricated cracks, and the carrying capacity of the lining structure was greatly reduced when the prefabricated crack was located at the vault. It can be concluded that the crack at the vault was the most damaging under the stress and deformation of the lining structure, so treatment of longitudinal cracks at the vault should be strengthened and receive more attention during projects.

References

1. Zhang, C.P.; Han, K.H.; Zhang, D.L. Face stability analysis of shallow circular tunnels in cohesive-frictional soils. *Tunn. Undergr. Space Technol.* **2015**, *50*, 345–357. [CrossRef]

2. Zhang, C.P.; Li, W.; Zhu, W.J.; Tan, Z.B. Face stability analysis of a shallow horseshoe-shaped shield tunnel in clay with a linearly increasing shear strength with depth. *Tunn. Undergr. Space Technol.* **2020**, *97*, 103291. [CrossRef]

3. Han, K.H.; Zhang, C.P.; Zhang, D.L. Upper-bound solutions for the face stability of a shield tunnel in multilayered cohesive–frictional soils. *Comput. Geotech.* **2016**, *79*, 1–9. [CrossRef]

4. Li, W.; Zhang, C.P. Face Stability Analysis for a Shield Tunnel in Anisotropic Sands. *Int. J. Geomech.* **2020**. [CrossRef]

5. Zhang, C.P.; Zhang, X.; Fang, Q. Behaviors of existing twin subway tunnels due to new subway station excavation below in close vicinity. *Tunn. Undergr. Space Technol.* **2018**, *81*, 121–128. [CrossRef]

6. Zhang, X.; Zhang, C.P.; Wang, J.C. Effect of closely spaced twin tunnel construction beneath an existing subway station: A case study. *J. Test. Eval.* **2018**, *46*, 1559–1573. [CrossRef]

7. Briffaut, M.; Benboudjema, F.; D'Aloia, L. Effect of fibres on early age cracking of concrete tunnel lining. Part I: Laboratory ring test. *Tunn. Undergr. Space Technol.* **2016**, *59*, 215–220. [CrossRef]

8. Ansell, A. Investigation of shrinkage cracking in shotcrete on tunnel drains. *Tunn. Undergr. Space Technol.* **2010**, *25*, 607–613. [CrossRef]

9. Kamel, T.; Limam, A.; Silvani, C. Residual strength of underground structures in service. *Can. Geotech. J.* **2016**, *53*, 988–999. [CrossRef]

10. Carvalho, J.P.; Lehmann, H.; Bartelt, H.; Magalhães, F.; Amezcua-Correa, R.; Santos, J.L.; Knight, J.C. Structural diagnosis of a concrete dam with cracking and high nonrecoverable displacements. *J. Perform. Construct. Facil.* **2016**, *30*, 04016021.

11. Kong, C.; Gao, X.Q.; Cao, L.; Liu, K. Analysis of the failure of primary support of a deep-buried railway tunnel in silty clay. *Eng. Fail. Anal.* **2016**, *66*, 259–273. [CrossRef]

12. Zhou, L.; Zhu, Z.; Dong, Y.; Ying, P.; Wang, M. Study of the fracture behavior of mode I and mixed mode I/II cracks in tunnel under impact loads. *Tunn. Undergr. Space Technol.* **2019**, *84*, 11–21. [CrossRef]

13. Song, W.; Lai, H.; Liu, Y.; Yang, W.; Zhu, Z. Field and laboratory study of cracking and safety of secondary lining for an existing highway tunnel in loess ground. *Tunn. Undergr. Space Technol.* **2019**, *88*, 35–46. [CrossRef]

14. Zhang, X.P.; Jiang, Y.J.; Sugimoto, S. Seismic damage assessment of mountain tunnel: A case study on the Tawarayama tunnel due to the 2016 Kumamoto Earthquake. *Tunn. Undergr. Space Technol.* **2018**, *71*, 138–148. [CrossRef]

15. Xu, G.; He, C.; Lu, D.; Wang, S. The influence of longitudinal crack on mechanical behavior of shield tunnel lining in soft-hard composite strata. *Thin-Walled Struct.* **2019**, *144*, 106282. [CrossRef]

16. Li, Y.J.; Wang, M.S.; Xu, H.J.; Zhang, Y. Study on the Damage Classification Criterion and Reinforcement Strategies of Mine Construction Subway. *Urban Rapid Rail Transit.* **2014**, *27*, 86–89. (In Chinese)

17. Feng, X.Y. Study on Tunnel Damage Classification and Lining Crack Control Technology. Master's Thesis, Beijing Jiaotong University, Beijing, China, 2012. (In Chinese).

18. Zhang, S.L. Study on Health Diagnosis and Evaluation of Tunnel Lining Structure. Ph.D. Thesis, Beijing Jiaotong University, Beijing, China, 2012. (In Chinese).

19. He, C.; Tang, Z.C.; Wang, B.; She, J. Research on effect of inner surface reinforcing on structure bearing capacity by model test in defective tunnel. *Rock Soil Mech.* **2009**, *30*, 406–412. (In Chinese)

20. Li, X.Z.; Li, W.Y.; Song, Y.L.; Gu, Y.C. Experiment on the influence of cracking characteristics under unsymmetrical load on stresses or forces in tunnel lining. *China Civ. Eng. J.* **2015**, *48*, 119–128. (In Chinese)

symmetry

MDPI

3D Printed Personalized Corneal Models as a Tool for Improving Patient's Knowledge of an Asymmetric Disease

Jose S. Velázquez [1], Francisco Cavas [1,*], José M. Bolarín [2] and Jorge L. Alió [3,4,5]

[1]   Department of Structures, Construction and Graphical Expression, Technical University of Cartagena, 30202 Cartagena, Spain; jose.velazquez@upct.es

[2]   Technology Centre for IT and Communications (CENTIC), Scientific Park of Murcia, 30100 Murcia, Spain; bolarin5@hotmail.com

[3]   Division of Ophthalmology, Miguel Hernández University, 03550 Alicante, Spain; jlalio@vissum.com

[4]   Keratoconus Unit of Vissum Corporation, 03016 Alicante, Spain

[5]   Department of Refractive Surgery, Vissum Corporation, 03016 Alicante, Spain

*   Correspondence: francisco.cavas@upct.es; Tel.: +34-968-328856

Abstract: Additive manufacturing is a vanguard technology that is currently being used in several fields in medicine. This study aims to evaluate the viability in clinical practice of a patient-specific 3D model that helps to improve the strategies of the doctor-patient assistance. Data obtained from a corneal topographer were used to make a virtual 3D model by using CAD software, to later print this model by FDM and get an exact replica of each patient's cornea in consultation. Used CAD and printing software were open-source, and the printing material was biodegradable and its cost was low. Clinic users gave their feedback by means of a survey about their feelings when perceiving with their senses their own printed cornea. There was 82 surveyed, 73.8% (9.74; SD: 0.45) of them considered that the model had helped them a lot to understand their disease, expressing 100% of them their intention of taking home the printed model. The majority highlighted that this new concept improves both quality and clinical service in consultation. Custom-made individualized printed models allow a new patient-oriented perspective that may improve the communication strategy from the ophthalmologist to the patient, easing patient's understanding of their asymmetric disease and its later treatment.

1. Introduction

Keratoconus (KC) is an asymmetric condition in which the cornea, at a local level, becomes thinner and develops a cone-like bulge. Prevalence of this corneal degeneration is variable: many studies suggest a value ranging from 50 to 230 cases per 10,000, due to variability of diagnostic criteria. Keratometry, slit-lamp biomicroscopy, corneal topography and retinoscopy are the most common exams used for KC diagnosis [1,2].

Currently, there is an increasing need from patients to be better informed about clinical practice [3], however, improving patient information in ophthalmology consultations remains a clinical challenge [4], as ophthalmologists develop their doctor-patient assistance strategies using conventional techniques based in bi-dimensional (2D) images [5]. Many of the patients that attend consultations suffer from severely diminished visual acuity, something that is particularly frequent in advanced cases of KC, impeding the explanation of their pathology to them by means of drawn pictures or 3D renders on a screen. Consequently, as patients cannot take advantage from the benefits of three-dimensional

(3D) images to spatially conceptualize the real extent of their pathology, new approaches need to be explored in the patient–doctor's communication process.

The fundamental pillar for a successful clinical consultation is the ability that the ophthalmologist shows to manage patient expectations, as frequently patients do not understand the true nature of their medical condition in KC disease, which leads to a scenario of frustration and poor outcomes [6]. In clinical practice, several authors have demonstrated that the use of physical 3D models of biological structures improves the understanding of the disease by the patients [7–9], which suggests that the use of senses over a three-dimensional physical model makes patient's learning easier, providing a better understanding of the pathology and its later treatment. Thus, it would be of great interest, in the field of ophthalmology, to develop a new concept of information and education of patients that promoted success in ophthalmological consultations (Figure 1).
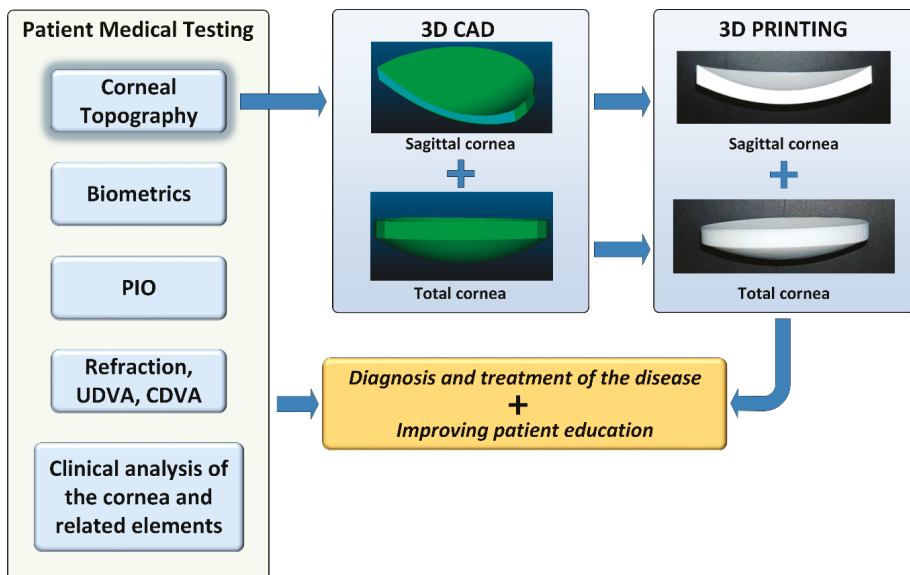
Figure 1. New concept of information and education in clinical practice.

Additive manufacturing (AM) is a disruptive and sustainable innovation [10] that allows the fabrication of three-dimensional (3D) objects. This term comprises many subcategories, such as rapid prototyping, direct digital manufacturing (DDM) and 3D printing (3DP), among others [11], all of them increasingly useful in automotive [12,13] and aerospace/defense [14,15] industries. When combined with reverse engineering and CAD modeling techniques, AM technologies can end up the design process in engineering, allowing more freedom when designing, higher customization, less waste production and manufacturing complex structures in a faster way [16,17].

In the field of medicine, AM technology is used for the manufacture of highly customized vanguard devices, as well as printing tissues and soft organs [6]. In addition, the advent of new technologies has propelled AM to become an accessible and cost-effective technology for medical community [18], being it also used in different fields for the fabrication of personalized models used in surgical planning, residents teaching or patients education [19–29]. Furthermore, these designs are frequently available in the Internet in open access for the medical community, promoting the development of collaborative networks between doctors and researchers, which turns them into a fundamental tool in translational research [30,31].

Our research group has validated a virtual 3D model of the cornea for each specific patient by using proprietary software [32]. These models have been used for the diagnosis of KC in virtual environments [33,34], but can also be used for 3D printing, so the printed physical model will reflect the abnormal irregularities and asymmetry that characterizes the cornea as KC disease progresses, in a way that patients would be capable of conceiving the geometrical variability of their cornea comparing it with a healthy one. This way, patients will be able to conceptualize the physical cause that inducts their loss of visual acuity, and consequently, their quality of life. Furthermore, and in the framework of promotion of the collaborative research networks, in this research work we propose the use of open-source software for the generation of the files of the virtual 3D models of the patients, so they can be used for any member of the international scientific community.

Thus, in this research work, it is proposed a new concept of patient information that uses 3D printed models of the cornea in the clinical practice of a hospital, using for its creation open-source software, both for the generation of the CAD models and the 3D printing files. The main objective pursued is improving the communication strategy of the ophthalmologist with the patient, easing the patient's process of understanding their disease and its later treatment, and avoiding a situation in which patients do not realize the real dimension of their disease, that could lead them to a scenario of frustration and poor outcomes.

2. Material and Methods

2.1. Patients

This article presents an observational comparative study that included 30 corneas of healthy patients (13 men and 17 women, average age 28.01 ± 14.19) and 52 of patients with keratoconus (22 men and 30 women, average age 26.71 ± 13.41). Keratoconus patients were also divided in several sub-groups, depending on the disease severity in the Amsler-Krumeich grading system [2,35]: 20 grade I, 14 grade II, 12 grade III and 6 grade IV.

The tenets of the Declaration of Helsinki (7th rev., Oct-2013, Fortaleza, Brazil) were followed for the development of the research, and it was backed up by the Committee of Ethics of the hospital participating in this study, signing all patients their consent to participate. The subjects whose data were used in this study were diagnosed in Vissum Corporation Alicante (a centre in affiliation with Miguel Hernández University of Elche, Spain), and their data is stored in the "Iberia" database of KC eyes that has been developed for the National Network for Clinical Research In Ophthalmology RETICS-OFATARED.

The procedure to discriminate between normal and KC patients was made according to validated up-to-date topographical and clinical verifications [2,5]. The exclusion criteria were the subsequent: contact lenses use in the thirty days that preceded their initial visit, ocular surface irritation, any previous ocular surgical procedure, mild or acute dry eye or presence of any other ocular comorbidity. Healthy eyes selected were all those that did not coincide with any of the exclusion criteria, while the diagnosis of keratoconus according to standard guidelines was the criterion to be included in the KC group.

2.2. Methods

Corneal tomographers based on Scheimpflug technology allow us to obtain a file in comma-separated values (CSV format), which can be used for different studies [36–39]. This file is composed of a spatial cloud of points in matrix form that represent corneal surfaces [32].

In this research work, Sirius tomographer (CSO, Italy) has been used. It is equipment that has proved its validity in clinical practice [5]. For the selection of data, just the topographies showing the highest acquisition quality were included in the study.

The custom-made individualized printed model reconstruction procedure consists of the following successive stages (Figure 2): I) surface and 3D model generation, II) 3D printable model preparation and III) 3D model printing in clinical practice.
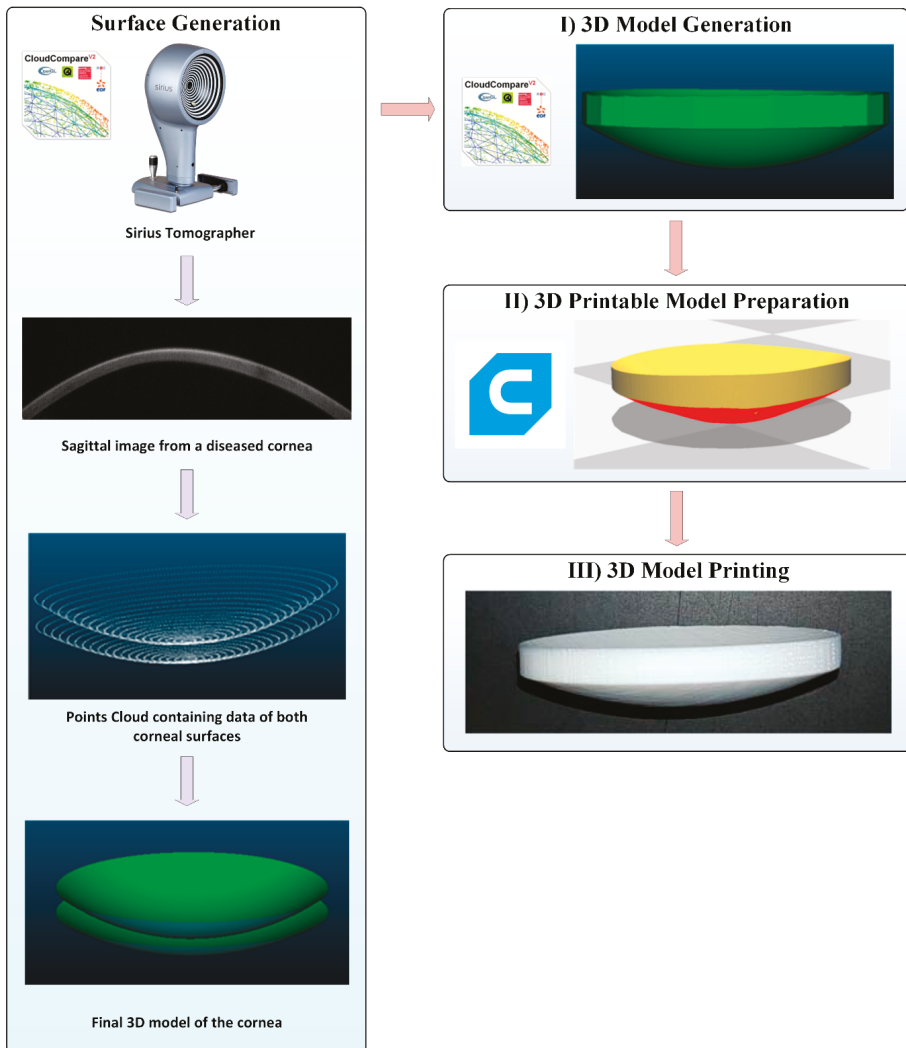
Figure 2. Proposed methodology for custom-made individualized model printing.

I. Surface and 3D model generation. At this point, a volumetric dataset was calculated from the available CSV file. This task can be performed by several software applications. In this study, CloudCompare 2.9.1 open-source software was the one used to generate the 3D model, using its "Delaunay 2.5D (best fitting plane)" option to generate a mesh from the point cloud of each surface. Then, the perimeter surface was created and, using Boolean operations, it was merged with the anterior and posterior corneal surfaces to create the final volume, which was then cut by a sagittal plane that passed through the optical axis and the minimum thickness points (anterior/posterior) of the corneal surfaces. CloudCompare entities are saved as BIN files, a format that is highly compatible with most open source 3D graphics software, so they can be easily used by any collaborative research network.

II. 3D Printable Model Preparation. 3D Printing process needs to define the surfaces of the solid model as a polygonal triangle mesh. However, even doing so, the virtual 3D model is still unfinished and its rough borders have to be refined. Other surface improvements can also be done, such as

inspecting and modifying any overlying surfaces, and simplifying the image file to increase printing efficiency. For this purpose, Cura 2.5 free software (Ultimaker, Netherlands) was used. To do so, files generated in CloudCompare were exported into STL (Stereolithography, Standard Triangle Language or Standard Tessellation Language) format [40], which is a very versatile and greatly compatible format with all 3D printers. Then, printing parameters were set in Cura, and a file containing all printing information (points, trajectories, speed, filling, etc.) was then generated as a GCODE file, which was lately uploaded to the 3D printer controller using a USB pendrive. 3D model files (.stl) and printing information files (.gcode) for both a healthy and an advanced KC cornea, complete and by a sagittal cut, have been attached as Supplementary Materials.

III. 3D Printing. The printer selected for this project was a FDM (fused deposition modeling) model designed by the UPCT-Makers organization, named "3D Printer ETSII –UPCT" [41]. This 3D printer is part of the RepRap project [42], so its drawings and technical data are open-source and available in the Internet, allowing its construction by any user. It was endowed with an Arduino MEGA controller, RAMPS 1.4 and drivers V. 88.25, and was programmed with Marlin software. It can be considered a low cost printer, as it had an approximate cost of less than 120 €, with an average life expectancy of 2000 duty hours.

The material used for 3D printing was polylactic acid (PLA), it is a rigid biodegradable polymer [43], that is stable to ultra-violet light, has low flammability and its characteristics are similar to PET polymer. Its properties, along with main printing parameters, can be checked in Table 1.

Table 1. 3D printer parameters.

Parameter	Values/Settings
Material	PLA
Quality: layer height	0.2–0.3 mm
Fusing material density	1.25 g/cm^3
Fusing material fusion point	160 °C
Printing temperature	225 °C
Nozzle diameter	1 mm
Flow rate	100%
Print speed	500 mm/s
Travel speed	130 mm/s
Printing area	22 cm × 23 cm × 20 cm

In our study, two physical models of cornea were printed per patient: a complete cornea, which corresponds to its full structure geometry, in which patient can see and perceive with his own senses the possible existence of morphological alterations at surface (anterior/posterior) level and the corneal volume; and another cornea, which corresponds to one half of a full cornea, defined by a sagittal plane that passes through the geometrical axis and the minimum thickness points (anterior/posterior) of the corneal surfaces (Figure 3), in which the patient can perceive with his senses the possible existence of morphological alterations in corneal thickness and the variation of curvature at surface (anterior/posterior) level.

As corneal real diameter is about 12 mm, and at that size corneal alterations were difficult to perceive, the use of a 1:1 scale for the model was discarded. Conversely, using big size models makes perception easier, but also significantly increases printing costs, so finally a 5:1 scale was used, as it was the smallest one that allowed an easy detection of slight changes in thickness and/or curvature.

The average time for all the process (3D modeling and 3D printing) was of 24.8 ± 3.4 min.
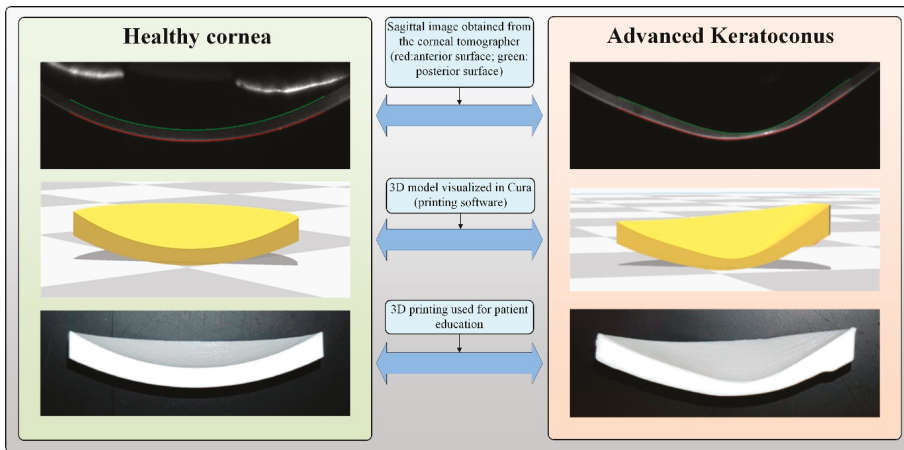
Figure 3. Healthy cornea (male patient of 24 years, Oculus Sinister (OS), Corrected Distance Visual Acuity (CDVA) = 1, astigmatism = 0.45, comma of like = 0.27, spherical-like = 0.23, Q8mm = −0.16 central thickness= 534). Advanced keratoconus (female patient of 20 years, Oculus Dexter (OD), CDVA = 0.44, astigmatism = 1.17, comma of like = 2.27, spherical-like = 2.50, Q8mm = −2.42 central thickness = 402).

2.3. Questionnaire

Finally, in order to assess the usefulness of the 3D model, a questionnaire was passed to each patient (82 in total). If the patient suffered from keratoconus, his custom 3D printed model was compared with a typical healthy cornea model, and their condition was explained to them, filling the questionnaire just after finishing the explanation. Questions made can be seen in Table 2. When selecting the scale for each question, for Q1, Q2 and Q5 we used 10 levels Likert items instead of the most common five level ones, looking for minimizing central tendency bias, while for questions Q3 and Q4, we opted for an absolute scale (yes/no/neutral).

Table 2. Questions made to the patients.

Number	Question Test	Possible Answer
Q1	What usefulness do you attribute to this custom 3D model?	From 1 = not useful at all to 10 = very useful
Q2	How much did the custom 3D model help you to better understand your condition?	From 1 = nothing at all to 10 = a huge lot
Q3	Would you like to take the custom 3D model with you after the consultation?	Yes/No/Neutral
Q4	Would you consider that using this custom 3D model improves the quality of our clinical service?	Yes/No/Neutral
Q5	How much do you consider that patients would benefit from the use of these custom 3D models in consultations?	From 1 = nothing at all to 10 = a huge lot

3. Results

The study lasted from January 2018 to March 2019, in Vissum Hospital in Alicante (Spain). Table 3 reports the collected answers to the five questions proposed to the patients.

Table 3. Questionnaire results.

Number	Possible Answer	Percentage	Average	Standard Deviation (SD)
Q1	From 1 = not useful at all to 10 = very useful	-	9.67	0.53
Q2	From 1 = nothing at all to 10 = a huge lot	-	9.74	0.45
Q3	Yes No Neutral	100.0 0.0 0.0		
Q4	Yes No Neutral	95.2 0.0 4.8		
Q5	From 1 = nothing at all to 10 = a huge lot	-	8.62	0.58

Results of Q1 show that the majority of patients found the 3D custom model "very useful", with more than half of the answers (69%) placed in top of the graduated scale (9.67; SD:0.53).

Similarly, 73.8% of patients considered that the use of the 3D personalized model had helped them "a huge lot" to understand their disease (9.74; SD: 0.45) when they answered question Q2.

In relation with question Q3, 100% of patients expressed their will to take the model home with them.

Results of question Q4 show that the vast majority of (95.2%) consider that the use of the personalized 3D model improves the clinical service rendered, being remarkable that only 4.8% believe that it does not make it better nor worse, and none of them consider that it makes it worse.

Finally, the results of question Q5 suggest that patients have considered that the use of personalized 3D models has improved the clinical service rendered in a high degree (8.62; SD:0.58).

To estimate the cost of realization of the 3D model, we considered the following: cost of data acquisition (0 €, included in consultation costs), proportional part of the cost of buying of the printer (120 € divided by 2000 h of life, 0.06 € per hour), labor of the laboratory technician (6 min at 5.66 €/hour, 0.57 €), software (0 €, as it was all open source) and material (30 g. of PLA at 18 €/kg, 0.47 €). The final estimated cost for each piece was around 1.10 €.

4. Discussion

In medical consultation, it has been demonstrated that a combination of both physical models and conventional 2D techniques of bone structures, gives patients a better comprehension of their disease [44]. Furthermore, in terms of teaching human anatomy, it has been proved that physical 3D models are more efficient to determine the existence of the disease than corpse models [45,46].

Physical 3D modeling has the capability of creating exact models of the human anatomy, thus being a fundamental tool not only for research [47], but also to educate patients [3].

However, using AM for biomedical applications has also its limitations: small anatomical features and structural details are difficult to replicate, and the number of biocompatible materials and resins available is limited, making AM expensive sometimes [48].

In the field of ophthalmology, AM applications are, conceptually speaking, not very different from the ones used in other fields of medicine. In scientific literature, there have been described works related with the printing of the first artificial cornea [49], fetal face modeling [50], intraocular lenses [51–54] or rigid permeable gas contact lenses [55], ocular prosthesis [56–59], intraocular tumor visualization [60], medical staff education [61,62], tissue bio-printing [63–65], printing of surgical instruments [66] or medical devices [67] or goggles for patients with deformations of unusual facial features [68]. However, we have not found proof of the use of the AM as a tool for improving doctor–patient communication strategies in KC disease.

In this research work, we describe our experience using AM techniques in ophthalmological clinical practice to obtain a custom-made individualized printed model, by means of a low-cost material, such as PLA. The objective is that patients acquire, basing on the physical model built, knowledge of the real dimension of the asymmetrical morphological changes that their cornea suffers when the disease progresses, and that affect their optical capacity, and therefore their quality of life.

For the building of the physical model, it is necessary to start from a virtual 3D model. However, in all different collaborative platforms of medical research related with virtual models [30,31,69], we have not found any virtual models of healthy or keratoconus-diagnosed corneas. Thus, virtual models have been generated from the data provided by the Sirius (CSO, Italy) tomographer, by using the open-source software CloudCompare, although these data can be obtained from any tomographer based in Scheimpflug technology [5]. In our study, two virtual models have been generated for each patient, one of a complete cornea, and another of a cornea with a sagittal cut defined from the minimum thickness points. These virtual models can be a fundamental tool in translational research, if shared through the collaborative open-access platforms [69].

From these patient-specific virtual models, and using open-source software, as well as low-cost and freely available manufacture hardware, the physical models used in this study were produced.

For this work, different printing speeds, layer thicknesses and nozzle sizes were tested, and it could be observed that a higher speed generally implied higher layer thicknesses, and therefore, a worse surface finishing in the model, which is in accordance with other authors works [70]. Finally, we opted for the speed, thickness and nozzle size indicated in Table 1 to get an acceptable surface finishing, with printing times below 30 min, that is the mean time that patients wait after the clinical tests to enter the doctor's consultation to be informed of the diagnosis. With these parameters, the printing is a bit cheaper than usual in other cases [71], and gives printed cornea a "stepped" aspect, although with enough precision to show, in an evident way, the differences between a normal cornea and one with its thickness locally diminished.

The fabrication cost of the 3D printed model, due to its simplicity and low cost of PLA, was of only 1.10 € each, which remains wide below the 490 € that can cost a model of more complex organs, such as kidneys, made in photopolymer materials [72].

Regarding the questionnaire answers, results of Q1 confirm the results obtained in other similar studies [73]. Similarly, answers to question Q2 are in line with what have been observed in other previous investigations, which used 3D models to explain patients their condition or the surgery that they will undergo [72]. Furthermore, the results obtained are in line with the ones obtained by Precee et al. [7], who demonstrated that the use of the touch and sight senses, with regard to a physical 3D model, improve the learning curve of the patients in relation with their disease.

In relation with question Q3, results contrast with the results obtained in other studies, in which 39% of the patients expressed that they would not be interested in buying the model [71], and can be explained by the fact that the low fabrication cost of the model allows the clinic to offer this service without any additional charge to the patient, integrating its cost in the cost of the medical consultation itself, making the patient more willing to take it home.

Results of question Q4 are in line with the ones presented by other authors, in which they demonstrated the usefulness of the 3D printing to improve the education in clinical practice [18], more precisely, in this study 95.8% of the surveyed considered useful the 3D models.

Finally, the results of question Q5 are in line with the values obtained for other studies (9.4/10) when patients have been asked about the degree of satisfaction with the medical services after the use of 3D models for their education [72].

Our study has, however, some limitations. First, the cross-sectional nature of the study presents a limited extension of the patient's cohort due to the low prevalence of this corneal degeneration; and second, the use of patients of just one hospital for the study. A longitudinal study with a larger sample size and including patients from different hospitals would be needed to further investigate the clinical

utility and viability, in clinical practice, of a patient-specific 3D model that helped to improve the strategies in doctor–patient assistance.

5. Conclusions

In this paper, the authors evaluated the possible benefits of using custom made 3D printed models of the cornea as a tool for increasing patient's knowledge and understanding of their asymmetric condition, with the aim of improving the level of quality perceived for the services rendered in medical consultations.

The results show that owning a custom 3D printed model of their cornea was considered interesting for the totality of the patients that participated in the study, and that the comparison of their pathologic cornea with the 3D model of a healthy one, helped them "a lot" (9.71/10, SD:0.45) to understand their disease, considering the vast majority (>95%) of the participants that using the 3D printed realistic models increased the quality of services rendered in the clinic.

In addition, the use of open-source and free software, as well as a RepRap 3D printer, whose drawings are available for everyone, make the approach described in this work accessible not only to high-end clinics, but to any clinic, whatever its budget is.

In conclusion, 3D printing has allowed the creation of precise physical models that reflects asymmetric modifications due to keratoconus pathology. The visual and tactile perception of these models allow patients to better understand and manage the perspective of treatment of their disease, making the clinicians job more efficient and therefore increasing the perception of quality of the service they render.

Although the use of 3D printing is increasing currently, the true potential of this technology will be achieved when function and form become fully integrated, as for example happens in the bio printing of tissues or organs, such as the cornea, that even if it has not been fully reached yet, the first steps have started to be successfully taken [49].

References

1. Rabinowitz, Y.S. Keratoconus. *Surv. Ophthalmol.* **1998**, *42*, 297–319. [CrossRef]
2. Cavas-Martinez, F.; De la Cruz Sanchez, E.; Nieto Martinez, J.; Fernandez Canavate, F.J.; Fernandez-Pacheco, D.G. Corneal topography in keratoconus: State of the art. *Eye Vis. (Lond. UK)* **2016**, *3*, 5. [CrossRef] [PubMed]
3. Salisbury, H. Helen Salisbury: The informed patient. *BMJ* **2019**, *364*, l638. [CrossRef] [PubMed]
4. Huang, W.; Zhang, X. 3D Printing: Print the future of ophthalmology. *Investig. Ophthalmol. Vis. Sci.* **2014**, *55*, 5380–5381. [CrossRef]
5. Pinero, D.P. Technologies for anatomical and geometric characterization of the corneal structure and anterior segment: A review. *Semin. Ophthalmol.* **2015**, *30*, 161–170. [CrossRef]
6. Bauermeister, A.J.; Zuriarrain, A.; Newman, M.I. Three-Dimensional Printing in Plastic and Reconstructive Surgery: A Systematic Review. *Ann. Plast. Surg.* **2016**, *77*, 569–576. [CrossRef]
7. Preece, D.; Williams, S.B.; Lam, R.; Weller, R. "Let's get physical": Advantages of a physical model over 3D computer models and textbooks in learning imaging anatomy. *Anat. Sci. Educ.* **2013**, *6*, 216–224. [CrossRef]

8. Watson, R.A. A low-cost surgical application of additive fabrication. *J. Surg. Educ.* **2014**, *71*, 14–17. [CrossRef]

9. Hoang, D.; Perrault, D.; Stevanovic, M.; Ghiassi, A. Surgical applications of three-dimensional printing: A review of the current literature & how to get started. *Ann. Transl. Med.* **2016**, *4*, 456. [CrossRef]

10. Labonnote, N.; Rønnquist, A.; Manum, B.; Rüther, P. Additive construction: State-of-the-art, challenges and opportunities. *Autom. Constr.* **2016**, *72*, 347–366. [CrossRef]

11. Gibson, I.; Rosen, D.; Stucker, B. *Additive Manufacturing Technologies: 3D Printing, Rapid Prototyping, and Direct Digital Manufacturing*, 2nd ed.; Springer: New York, NY, USA, 2015; pp. 1–498. [CrossRef]

12. Böckin, D.; Tillman, A.M. Environmental assessment of additive manufacturing in the automotive industry. *J. Clean. Prod.* **2019**, *226*, 977–987. [CrossRef]

13. Goh, G.D.; Dikshit, V.; Nagalingam, A.P.; Goh, G.L.; Agarwala, S.; Sing, S.L.; Wei, J.; Yeong, W.Y. Characterization of mechanical properties and fracture mode of additively manufactured carbon fiber and glass fiber reinforced thermoplastics. *Mater. Des.* **2018**, *137*, 79–89. [CrossRef]

14. Espalin, D.; Muse, D.W.; MacDonald, E.; Wicker, R.B. 3D Printing multifunctionality: Structures with electronics. *Int. J. Adv. Manuf. Technol.* **2014**, *72*, 963–978. [CrossRef]

15. Mangum, P., Jr.; Fisher, Z.; Cooksey, K.D.; Mavris, D.; Spero, E.; Gerdes, J.W. An automated approach to the design of small aerial systems using rapid manufacturing. In Proceedings of the ASME 2015 International Design Engineering Technical Conferences and Computers and Information in Engineering Conference, Boston, MA, USA, 2–5 August 2015.

16. Ngo, T.D.; Kashani, A.; Imbalzano, G.; Nguyen, K.T.Q.; Hui, D. Additive manufacturing (3D printing): A review of materials, methods, applications and challenges. *Compos. B Eng.* **2018**, *143*, 172–196. [CrossRef]

17. Tucker, C.S.; Saint John, D.B.; Behoora, I.; Marcireau, A. Open source 3D scanning and printing for design capture and realization. In Proceedings of the ASME 2014 International Design Engineering Technical Conferences and Computers and Information in Engineering Conference, Buffalo, NY, USA, 17–20 August 2014.

18. Jones, D.B.; Sung, R.; Weinberg, C.; Korelitz, T.; Andrews, R. Three-Dimensional Modeling May Improve Surgical Education and Clinical Practice. *Surg. Innov.* **2016**, *23*, 189–195. [CrossRef]

19. Abudayyeh, I.; Gordon, B.; Ansari, M.M.; Jutzy, K.; Stoletniy, L.; Hilliard, A. A practical guide to cardiovascular 3D printing in clinical practice: Overview and examples. *J. Interv. Cardiol.* **2018**, *31*, 375–383. [CrossRef]

20. Jastifer, J.R.; Gustafson, P.A. Three-Dimensional Printing and Surgical Simulation for Preoperative Planning of Deformity Correction in Foot and Ankle Surgery. *J. Foot Ankle Surg. Off. Publ. Am. Coll. Foot Ankle Surg.* **2017**, *56*, 191–195. [CrossRef]

21. Pucci, J.U.; Christophe, B.R.; Sisti, J.A.; Connolly, E.S., Jr. Three-dimensional printing: Technologies, applications, and limitations in neurosurgery. *Biotechnol. Adv.* **2017**, *35*, 521–529. [CrossRef]

22. Soon, D.S.; Chae, M.P.; Pilgrim, C.H.; Rozen, W.M.; Spychal, R.T.; Hunter-Smith, D.J. 3D haptic modelling for preoperative planning of hepatic resection: A systematic review. *Ann. Med. Surg.* **2016**, *10*, 1–7. [CrossRef]

23. Zhong, N.; Zhao, X. 3D printing for clinical application in otorhinolaryngology. *Eur. Arch. Otorhinolaryngol.* **2017**, *274*, 4079–4089. [CrossRef]

24. Tanner, J.A.; Jethwa, B.; Jackson, J.; Bartanuszova, M.; King, T.S.; Bhattacharya, A.; Sharma, R. A Three-Dimensional Print Model of the Pterygopalatine Fossa Significantly Enhances the Learning Experience. *Anat. Sci. Educ.* **2020**. [CrossRef] [PubMed]

25. Barabas, J.I.; Ghimessy, A.K.; Renyi-Vamos, F.; Kocsis, A.; Agocs, L.; Meszaros, L.; Pukacsik, D.; Andi, J.; Laki, A.; Voros, F.; et al. Innovation in medicine: Opportunities of 3D modeling and printing for perioperative care of cardio and thoracic surgical patients. Experiences in Hungary. *Orv. Hetil.* **2019**, *160*, 1967–1975. [CrossRef] [PubMed]

26. Panesar, S.S.; Magnetta, M.; Mukherjee, D.; Abhinav, K.; Branstetter, B.F.; Gardner, P.A.; Iv, M.; Fernandez-Miranda, J.C. Patient-specific 3-dimensionally printed models for neurosurgical planning and education. *Neurosurg. Focus* **2019**, *47*, E12. [CrossRef] [PubMed]

27. Kim, P.S.; Choi, C.H.; Han, I.H.; Lee, J.H.; Choi, H.J.; Lee, J.I. Obtaining Informed Consent Using Patient Specific 3D Printing Cerebral Aneurysm Model. *J. Korean Neurosurg. Soc.* **2019**, *62*, 398–404. [CrossRef] [PubMed]

28. Biro, M.; Kim, I.; Huynh, A.; Fu, P.; Mann, M.; Popkin, D.L. The use of 3-dimensionally printed models to optimize patient education and alleviate perioperative anxiety in Mohs micrographic surgery: A randomized controlled trial. *J. Am. Acad. Dermatol.* **2019**, *81*, 1339–1345. [CrossRef]

29. Zhuang, Y.D.; Zhou, M.C.; Liu, S.C.; Wu, J.F.; Wang, R.; Chen, C.M. Effectiveness of personalized 3D printed models for patient education in degenerative lumbar disease. *Patient Educ. Couns.* **2019**, *102*, 1875–1881. [CrossRef]

30. Gross, B.C.; Erkal, J.L.; Lockwood, S.Y.; Chen, C.; Spence, D.M. Evaluation of 3D printing and its potential impact on biotechnology and the chemical sciences. *Anal. Chem.* **2014**, *86*, 3240–3253. [CrossRef]

31. National Institutes of Health. 3D Print Exchange. Available online: http://3dprint.nih.gov (accessed on 13 May 2019).

32. Cavas-Martinez, F.; Fernandez-Pacheco, D.G.; de la Cruz-Sanchez, E.; Nieto Martinez, J.; Canavate, F.J.F.; Alio, J.L. Virtual biomodelling of a biological structure: The human cornea. *Dyna* **2015**, *90*, 647–651.

33. Cavas-Martinez, F.; Bataille, L.; Fernandez-Pacheco, D.G.; Canavate, F.J.F.; Alio, J.L. Keratoconus Detection Based on a New Corneal Volumetric Analysis. *Sci. Rep.* **2017**, *7*, 15837. [CrossRef]

34. Cavas-Martinez, F.; Bataille, L.; Fernandez-Pacheco, D.G.; Canavate, F.J.F.; Alio, J.L. A new approach to keratoconus detection based on corneal morphogeometric analysis. *PLoS ONE* **2017**, *12*, e0184569. [CrossRef]

35. Krumeich, J.H.; Daniel, J.; Knulle, A. Live-epikeratophakia for keratoconus. *J. Cataract. Refract. Surg.* **1998**, *24*, 456–463. [CrossRef]

36. Ariza-Gracia, M.A.; Zurita, J.; Pinero, D.P.; Calvo, B.; Rodriguez-Matas, J.F. Automatized Patient-Specific Methodology for Numerical Determination of Biomechanical Corneal Response. *Ann. Biomed. Eng.* **2016**, *44*, 1753–1772. [CrossRef] [PubMed]

37. Asher, R.; Gefen, A.; Moisseiev, E.; Varssano, D. An analytical approach to corneal mechanics for determining practical, clinically-meaningful patient-specific tissue mechanical properties in the rehabilitation of vision. *Ann. Biomed. Eng.* **2015**, *43*, 274–286. [CrossRef] [PubMed]

38. Lanchares, E.; Del Buey, M.A.; Cristobal, J.A.; Calvo, B. Computational Simulation of Scleral Buckling Surgery for Rhegmatogenous Retinal Detachment: On the Effect of the Band Size on the Myopization. *J. Ophthalmol.* **2016**, *2016*, 3578617. [CrossRef] [PubMed]

39. Simonini, I.; Pandolfi, A. Customized Finite Element Modelling of the Human Cornea. *PLoS ONE* **2015**, *10*, e0130426. [CrossRef] [PubMed]

40. Grimm, T. *User's Guide to Rapid Prototyping*; Society of Manufacturing Engineers: Dearborn, MI, USA, 2004.

41. ETSII UPCT Printer/es. Available online: https://reprap.org/mediawiki/index.php?title=ETSII_UPCT_Printer/es&oldid=156702 (accessed on 3 June 2019).

42. Jones, R.; Haufe, P.; Sells, E.; Iravani, P.; Olliver, V.; Palmer, C.; Bowyer, A. RepRap—The replicating rapid prototyper. *Robotica* **2011**, *29*, 177–191. [CrossRef]

43. Sanchez-Tena, M.A.; Alvarez-Peregrina, C. Application of 3D Printing Technology in Scleral Cover Shell Prosthesis. *J. Med. Syst.* **2019**, *43*, 149. [CrossRef]

44. Hughes, A.J.; DeBuitleir, C.; Soden, P.; O'Donnchadha, B.; Tansey, A.; Abdulkarim, A.; McMahon, C.; Hurson, C.J. 3D Printing Aids Acetabular Reconstruction in Complex Revision Hip Arthroplasty. *Adv. Orthop.* **2017**, *2017*, 8925050. [CrossRef]

45. Banks, J. Adding value in additive manufacturing: Researchers in the United Kingdom and Europe look to 3D printing for customization. *IEEE Pulse* **2013**, *4*, 22–26. [CrossRef]

46. Ventola, C.L. Medical Applications for 3D Printing: Current and Projected Uses. *P T A Peer-Rev. J. Formul. Manag.* **2014**, *39*, 704–711.

47. Clemente, C.; Esposito, L.; Speranza, D.; Bonora, N. Firecracker eye exposure: Experimental study and simulation. *Biomech. Model. Mechanobiol.* **2017**, *16*, 1401–1411. [CrossRef] [PubMed]

48. Estomba, C.; González-Fernández, I.; Iglesias-Otero, M. 3D Printing for Biomedical Applications: Where are we now? *Eur. Med J.* **2017**, *2*, 16–22.

49. Isaacson, A.; Swioklo, S.; Connon, C.J. 3D bioprinting of a corneal stroma equivalent. *Exp. Eye Res.* **2018**, *173*, 188–193. [CrossRef] [PubMed]

50. Speranza, D.; Padula, F.; Motyl, B.; Tornincasa, S.; Marcolin, F.; Vezzetti, E.; Martorelli, M. Parenthood Perception Enhancement Through Interaction with 3D Printed Fetal Face Models. In *Advances on Mechanics, Design Engineering and Manufacturing II*; Springer: Cham, Switzerland, 2019; pp. 527–535.

51. Bassnett, S.; Shi, Y.; Vrensen, G.F. Biological glass: Structural determinants of eye lens transparency. *Philos. Trans. R. Soc. Lond. Ser. B Biol. Sci.* **2011**, *366*, 1250–1264. [CrossRef]

52. Debellemaniere, G.; Flores, M.; Montard, M.; Delbosc, B.; Saleh, M. Three-dimensional Printing of Optical Lenses and Ophthalmic Surgery: Challenges and Perspectives. *J. Refract. Surg. (Thorofare NJ 1995)* **2016**, *32*, 201–204. [CrossRef]

53. Donaldson, P.J.; Grey, A.C.; Maceo Heilman, B.; Lim, J.C.; Vaghefi, E. The physiological optics of the lens. *Prog. Retinal Eye Res.* **2017**, *56*, e1–e24. [CrossRef]

54. Hejtmancik, J.F.; Shiels, A. Overview of the Lens. *Prog. Mol. Biol. Transl. Sci.* **2015**, *134*, 119–127. [CrossRef]

55. Zhao, F.; Zhao, G.; Weijie, F.; Chen, L. Application of 3D printing technology in RGPCL simulation fitting. *Med. Hypotheses* **2018**, *113*, 74–76. [CrossRef]

56. Callahan, A.B.; Campbell, A.A.; Petris, C.; Kazim, M. Low-Cost 3D Printing Orbital Implant Templates in Secondary Orbital Reconstructions. *Ophthalmic Plast. Reconstr. Surg.* **2017**, *33*, 376–380. [CrossRef]

57. Dave, T.V.; Tiple, S.; Vempati, S.; Palo, M.; Ali, M.J.; Kaliki, S.; Naik, M.N. Low-cost three-dimensional printed orbital template-assisted patient-specific implants for the correction of spherical orbital implant migration. *Indian J. Ophthalmol.* **2018**, *66*, 1600–1607. [CrossRef]

58. Fan, B.; Chen, H.; Sun, Y.J.; Wang, B.F.; Che, L.; Liu, S.Y.; Li, G.Y. Clinical effects of 3-D printing-assisted personalized reconstructive surgery for blowout orbital fractures. *Graefe's Arch. Clin. Exp. Ophthalmol.* **2017**, *255*, 2051–2057. [CrossRef] [PubMed]

59. Ruiters, S.; Sun, Y.; de Jong, S.; Politis, C.; Mombaerts, I. Computer-aided design and three-dimensional printing in the manufacturing of an ocular prosthesis. *Br. J. Ophthalmol.* **2016**, *100*, 879–881. [CrossRef] [PubMed]

60. Furdova, A.; Sramka, M.; Thurzo, A.; Furdova, A. Early experiences of planning stereotactic radiosurgery using 3D printed models of eyes with uveal melanomas. *Clin. Ophthalmol. (Auckl. N. Z.)* **2017**, *11*, 267–271. [CrossRef] [PubMed]

61. Adams, J.W.; Paxton, L.; Dawes, K.; Burlak, K.; Quayle, M.; McMenamin, P.G. 3D printed reproductions of orbital dissections: A novel mode of visualising anatomy for trainees in ophthalmology or optometry. *Br. J. Ophthalmol.* **2015**, *99*, 1162–1167. [CrossRef] [PubMed]

62. Scawn, R.L.; Foster, A.; Lee, B.W.; Kikkawa, D.O.; Korn, B.S. Customised 3D Printing: An Innovative Training Tool for the Next Generation of Orbital Surgeons. *Orbit (Amst. Neth.)* **2015**, *34*, 216–219. [CrossRef] [PubMed]

63. Kim, H.; Jang, J.; Park, J.; Lee, K.P.; Lee, S.; Lee, D.M.; Kim, K.H.; Kim, H.K.; Cho, D.W. Shear-induced alignment of collagen fibrils using 3D cell printing for corneal stroma tissue engineering. *Biofabrication* **2019**, *11*, 035017. [CrossRef]

64. Kim, H.; Park, M.N.; Kim, J.; Jang, J.; Kim, H.K.; Cho, D.W. Characterization of cornea-specific bioink: High transparency, improved in vivo safety. *J. Tissue Eng.* **2019**, *10*, 2041731418823382. [CrossRef]

65. Ludwig, P.E.; Huff, T.J.; Zuniga, J.M. The potential role of bioengineering and three-dimensional printing in curing global corneal blindness. *J. Tissue Eng.* **2018**, *9*, 2041731418769863. [CrossRef]

66. Navajas, E.V.; Ten Hove, M. Three-Dimensional Printing of a Transconjunctival Vitrectomy Trocar-Cannula System. *Ophthalmologica* **2017**, *237*, 119–122. [CrossRef]

67. Sommer, A.C.; Blumenthal, E.Z. Implementations of 3D printing in ophthalmology. *Graefe's Arch. Clin. Exp. Ophthalmol.* **2019**. [CrossRef]

68. Ayyildiz, O. Customised spectacles using 3-D printing technology. *Clin. Exp. Optom.* **2018**, *101*, 747–751. [CrossRef]

69. Kamali, P.; Dean, D.; Skoracki, R.; Koolen, P.G.L.; Paul, M.A.; Ibrahim, A.M.S.; Lin, S.J. The Current Role of Three-Dimensional (3D) Printing in Plastic Surgery. *Plast. Reconstr. Surg.* **2016**. [CrossRef] [PubMed]

70. Sukindar, N.A. Optimization of the Parameters for Surface Quality of the Open-source 3D Printing. *J. Mech. Eng.* **2017**, *SI3*, 33–43.

71. Speranza, D.; Citro, D.; Padula, F.; Motyl, B.; Marcolin, F.; Calí, M.; Martorelli, M. Additive Manufacturing Techniques for the Reconstruction of 3D Fetal Faces. *Appl. Bionics Biomech.* **2017**, *2017*, 9701762. [CrossRef] [PubMed]

72. Bernhard, J.C.; Isotani, S.; Matsugasumi, T.; Duddalwar, V.; Hung, A.J.; Suer, E.; Baco, E.; Satkunasivam, R.; Djaladat, H.; Metcalfe, C.; et al. Personalized 3D printed model of kidney and tumor anatomy: A useful tool for patient education. *World J. Urol.* **2016**, *34*, 337–345. [CrossRef] [PubMed]

73. Andolfi, C.; Plana, A.; Kania, P.; Banerjee, P.P.; Small, S. Usefulness of three-dimensional modeling in surgical planning, resident training, and patient education. *J. Laparoendosc. Adv. Surg. Tech.* **2017**, *27*, 512–515. [CrossRef] [PubMed]

Article

Spring Effects on Workspace and Stiffness of a Symmetrical Cable-Driven Hybrid Joint

Shan Zhang [1],*, Zheng Sun [1], Jili Lu [1], Lei Li [1], Chunlei Yu [1] and Dongxing Cao [2],*

[1]   College of Mechanical and Electrical Engineering, Zaozhuang University, Zaozhuang 277160, China;
       cumt_sz@163.com (Z.S.); lujili168@163.com (J.L.); a7082928@126.com (L.L.); yclfinder@163.com (C.Y.)
[2]   School of Mechanical Engineering, Hebei University of Technology, Tianjin 300130, China
*   Correspondence: zhangshantybj@163.com (S.Z.); paperss87@163.com (D.C.)

Abstract: This paper aims to investigate how to determine the basic parameters of the helical compression spring which supports a symmetrical cable-driven hybrid joint (CDHJ) towards the elbow joint of wheelchair-mounted robotic manipulator. The joint design of wheelchair-mounted robotic manipulator needs to consider lightweight but robust, workspace requirements, and variable stiffness elements, so we propose a CDHJ which becomes a variable stiffness joint due the spring under bending and compression provides nonlinear stiffness characteristics. Intuitively, different springs will make the workspace and stiffness of CDHJ different, so we focus on studying the spring effects on workspace and stiffness of CDHJ for its preliminary design. The key to workspace and stiffness analysis of CDHJ is the cable tension, the key to calculate the cable tension is the lateral bending and compression spring model. The spring model is based on Castigliano's theorem to obtain the relationship between spring force and displacement. The simulation results verify the correctness of the proposed spring model, and show that the spring, with properly chosen parameters, can increase the workspace of CDHJ whose stiffness also can be adjusted to meet the specified design requirements. Then, the modelling method can be extended to other cable-driven mechanism with a flexible compression spring.

Keywords: cable-driven hybrid joint; spring; lateral bending and compression; workspace; stiffness

---

1. Introduction

Wheelchair-mounted robotic manipulator is a typical type of the service robot which can help users with motor impairments to perform activities of daily living [1–4], such as feeding, drinking, dressing, and retrieval of daily objects. The research of wheelchair-mounted robotic manipulator has been going on for nearly 55 years [1,4]. In the past, there are nearly a dozen wheelchair-mounted robotic manipulators which have been developed. However, due to its poor usability, low payload, and high cost, it is not widely used in the market [3,4]. Specifically, for example, the manipulator is heavy, the joints are bulky, and the flexible motion is limited [5]. These problems may be solved by the cable-driven mechanism (CDM), owing to its following remarkable characteristics: small inertia, large workspace, high payload, good transportability, fully remote actuation, and ideal reconfigurability [5–9]. Based on these characteristics, CDM is widely applied in engineering [6]. Several applications are listed as follows. Chen et al. [10] proposed a cable-driven parallel waist rehabilitation robot; Liu et al. [11] proposed a spatial serpentine tail which used a cable-driven circular shape joint; Eftychios et al. [12] proposed a reconfigurable articulated structure considered the structural concept for reconfigurable buildings; Qiao et al. [13] presented the self-adaptive grasp process of a finger which has three degrees of freedom and under actuated cable truss.

Meanwhile, a wheelchair-mounted robotic manipulator as a collaborative robot [14] must perform compliant motion in order to realize physical human-robot interaction [15], because in the field of

collaborative robotics to realize physical human-robot interaction, impact mitigation is a core issue [14]. That is to say, in the mechanical structure it needs used variable stiffness elements. So far, a number of variable stiffness elements have been developed. One of them is CDM which is considered to be antagonistic variable stiffness mechanism [16,17] inspired by the musculoskeletal system [18,19]. CDM can generate variable stiffness very effectively with large stiffness variations and it need not modify the equilibrium configuration [16]. Yeo et al. [20] proposed cable-driven manipulators with variable stiffness; Xu et al. [21] proposed a cable-driven soft robot arm in the underwater environment; Liu et al. [22] used the mechanism structure of the human arm for reference, proposed a cable-driven manipulator with a high-payload capacity, assembled physical prototype and tested the payload capacity. Besides, the spring is usually used in most of the variable stiffness designs [23–25]. Seriani et al. [14] investigated the preloaded structures for impact mitigation used the fundamental preloaded element, a spring; However, Wu et al. [26] proposed the linear variable-stiffness mechanisms used the preloaded element, a curved beam. López-Martínez et al. [27] proposed a passive mechanical system which consists in a flexible linkage used a preloaded compression spring. Azadi et al. [16] pointed out that changing the geometry of the system can change the stiffness, such as controlling the active coils number of a coil spring, using regulable pitching stiffness, and changing the gap between two leaf springs. Overall, CDM coupled with stiffness adjustability may address some issues of wheelchair-mounted robotic manipulator joint design with relatively low energy consumption and low cost.

As is known to all, cables must remain in tension while performing tasks. Therefore, the study of the CDM workspace must consider the cable tension. There are some different workspaces which have been identified like static equilibrium workspace, wrench-closure workspace, and wrench-feasible workspace [28,29]. Analysis of these workspace generally starts from static equilibrium equations. Static equilibrium workspace and wrench-closure workspace are essentially the same, which are the set of poses where the end-effector can physically maintain equilibrium and all cables are in tension; nevertheless, wrench-feasible workspace is defined as the set of poses where cables tension remains within a prescribed range, the range is usually from the allowable minimum cable tension value to the maximum cable tension value [28–31]. In addition, many applications require the end-effector to bear certain force/moment combinations in the workspace. Accordingly, the wrench-feasible workspace is considered as the most appropriate workspace [31], which is able to connect with the physical world, and is the most practical workspace for CDM [29]. In this paper, the mentioned workspace is wrench-feasible workspace.

CDM stiffness analysis can be divided into static stiffness analysis and dynamic stiffness analysis [32,33]. Yuan et al. [32] and Nguyen et al. [34] pointed out that analysis and improvement of the static positioning accuracy is the purpose of static stiffness analysis of CDM, especially in the pick-and-place application. In this paper, the mentioned stiffness is static stiffness. However, the vibration analysis is the purpose of dynamic stiffness analysis of CDM in those applications [32,33], requiring high performances [35], especially dynamic performances [36]. Most researchers took cables as massless springs which just considered axial stiffness of cables when CDM is with the light-weighted [34], low speed [33], and small size [37,38], and used the Jacobian-based stiffness analysis method [32,39–42] to make static stiffness analysis to describe the Cartesian stiffness matrix which is the function of the manipulator's configuration and mechanism stiffness values. However, it needs to consider transversal stiffness when the cable profile is a sagging curve, the Jacobian-based stiffness analysis method is not applicable [32]. Amare et al. [33] made dynamic stiffness analysis of the CDM in three-dimensional inclined plane with external forces exerted by hydraulic cylinder on the system. Yuan et al. [43] solved the vibration problems of structures used dynamic stiffness matrix method which is used to identify the system natural frequencies.

Spring, as a common component, has been applied in various fields. Although the helical compression spring is commonly used to increase the performance of CDM, only a few studies attempted to systematically analyze springs effects on the workspace and stiffness of CDM. Duan

et al. just analyzed the effects on the workspace of CDM with springs which are parallel to the cable, and had no detailed analysis of the effects of spring basic parameters [44]. Similarly, in [45,46], they also took spring as spring cable. Mustafa and Agrawal studied spring placement effects on altering the cable tension required and increasing the feasible workspace [45]. Taghavi et al. [46] investigated adding springs in between the links to improve the wrench-feasible workspace of a two-link CDM. Essentially Duan et al. [44], Mustafa and Agrawal [45], and Taghavi et al. [46] treat springs as passive cables in a straight line shape. During the whole CDM movement, the spring stiffness did not change. In [5,36,47,48], they proposed a CDM with a linear compression spring spine which presents the nonlinear stiffness characteristics under bending and compression, but they did not analyze the impact of adding springs on the workspace and stiffness of CDM in detail. Gao et al. [47], Zhang et al. [5], and Zhang et al. [36] treated the helical spring as a spatially curved bar. This concept of an equivalent column of helical spring is in most engineering applications in [49]. Yigit et al. analyzed helical spring using Castigliano's Theorem [48]. The same idea is used for helical spring analysis as in [50].

This paper focuses on the spring effects on workspace and stiffness of a symmetrical cable-driven hybrid joint (CDHJ) towards the elbow joint of wheelchair-mounted robotic manipulator for its preliminary design in detail. That is to say, though the spring effects analysis, the basic parameters of the helical compression spring of CDHJ can be determined, which makes preparations for the next assembly prototype. Using Castigliano's Theorem, which is proposed in [48,50], the helical spring is analyzed to obtain the relationship between spring force and spring displacement. On the basis the statics, the Cartesian stiffness matrix is derived by the Jacobian-based stiffness analysis method [32,39–42] to deduce static stiffness analysis index of CDHJ. Intuitively, a spring, with properly chosen parameters, can help in keeping cables taut resulting in larger workspace and adjusting CDHJ stiffness to satisfy the specified design requirements.

This paper aims to investigate how to determine the basic parameters of the helical compression spring. Used Castigliano's theorem the relationship between spring force and displacement is obtained, which is determined by the spring configuration, the geometry, and material properties. The spring parameters are determined by the spring effects on workspace and stiffness of CDHJ. This study is a first step in the CDHJ design. Hence, this research method can guide the design of other CDM with a flexible compression spring with workspace and stiffness requirements. With relatively large workspace, smooth motion, and light structure, the proposed CDHJ might have potential use for wheelchair-mounted robotic manipulator elbow joint.

This paper is organized as follows. The concept of CDHJ and the kinematic modeling is presented in Section 2; next, the modeling of spring lateral bending and compression is given in Section 3; the workspace and stiffness index of CDHJ is given in Section 4; the springs effects on the workspace and stiffness of CDHJ are studied in Section 5; and finally, discussions obtained from the results are presented in the last section.

2. CDHJ Description and Kinematic Analysis

2.1. CDHJ Description

The muscles which control the movement of the human elbow joint are the triceps and the biceps. The elbow joint movement are the antagonistic movement. Flexion occurs when the biceps contracts and the triceps relaxes, while extension occurs when the biceps relaxes and the triceps contracts. Hence, the musculoskeletal mechanism of the human elbow joint reflects symmetry. Based on the mechanism, in order to realize the symmetry of motion, an elbow joint driven by 2 cables and supported by a compression spring in the central position has been designed for the elbow joint of the wheelchair-mounted robotic manipulator. As shown in Figure 1a, cable 1 and cable 2 drive the upper platform (moving platform), and imitate biceps brachii and triceps brachii, respectively. The two platforms are supported by a compression spring, which is the parallel part; two rigid shafts with a rotating pair are in the center of the spring, and rigid shaft 1 passes through the moving

platform, forming the series part. Overall, this elbow joint is a symmetrical cable-driven hybrid joint. This symmetry is reflected not only in structure but also in motion, in other words, the upper platform motion of the spring clockwise bend as Figure 1b is the same as the spring counter clockwise bend, so in the next analysis, only the clockwise motion shown in Figure 1b will be analyzed.
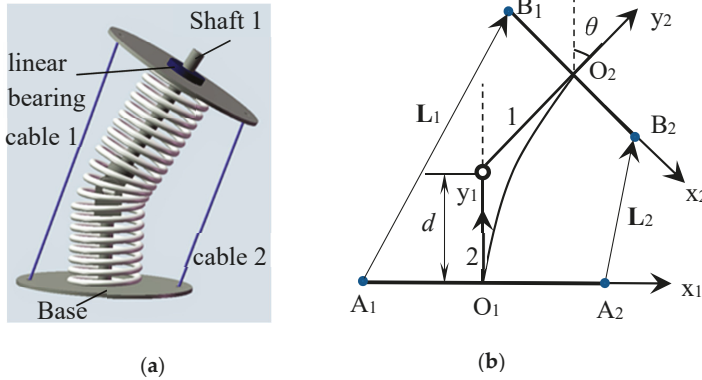
Figure 1. Diagram of the cable-driven hybrid joint (CDHJ). (**a**) 3-D joint mechanism. (**b**) 2-D joint diagram.

Due under bending and compression linear helical compression spring provides nonlinear stiffness characteristics, the CDHJ is a variable stiffness joint. Rigid shaft 1 passes through the upper platform, therefore the CDHJ stiffness can be adjusted by translational motion of the upper platform. Due to the limitation of the intermediate rigid shaft, the CDHJ has a total of two degrees of freedom. Therefore, CDHJ is the simplification of variable stiffness mechanism. That is to say, the CDHJ with stiffness adjustability towards wheelchair-mounted robotic manipulator elbow joint may ameliorate some safety issues in the physical human-robot interaction due to its relatively low energy consumption and low cost.

2.2. Kinematic Analysis

The cables whose profile is a straight line are assumed to have negligible mass. The diagram of the CDHJ is illustrated in Figure 1b. $\{O_{1 \times 1}y_1\}$ is the global coordinate system, $\{O_2x_2y_2\}$ is a local coordinate frame, all the coordinate origins are at the center of the platform. The upper and lower platforms are thin round plates, their radii are b and a, respectively. Denote A_1, B_1, A_2, and B_2 as the connecting points of cables 1 and 2, respectively; and the distance from O_1 to the rotating pair center as d. The spring is simplified and drawn as an arc.

As mentioned in the previous section, the CDHJ has a total of 2 degrees of freedom: the rotation around the z-axis, and the translational motion on the x-y plane. According to the right hand rule, when the bend direction is clockwise as shown in Figure 1b, θ is negative. Under the rigid restraint of the rotating pair in the center of the spring, the relationship between translational component along the x-axis and that along the y-axis in the global coordinate system can be expressed as:

$$x = -(y - d)\tan\theta \qquad (1)$$

Denote $\mathbf{L}_m$ as the vector defining the mth cable, (m = 1,2), in the global coordinate system; $\mathbf{L}_{O_1O_2}$ is $\overrightarrow{O_1O_2}$, $\mathbf{L}_{O_1A_m}$ is $\overrightarrow{O_1A}_m$, in the global coordinate system; $\mathbf{L}_{O_2B_m}^{O_2}$ is $\overrightarrow{O_2B_m}$, in the local coordinate system.

The input of CDHJ is (l_1, l_2), the output is (y, θ). The kinematic relationship between the input and output can be obtained used the closed loop vector method:

$$\mathbf{L_M} = \mathbf{L}_{O_1O_2} + {}^{O_1}_{O_2}\mathbf{RL}^{O_2}_{O_2B_m} - \mathbf{L}_{O_1A_m} \tag{2}$$

where ${}^{O_1}_{O_2}\mathbf{R} = \begin{bmatrix} \cos\theta & -\sin\theta & 0 \\ \sin\theta & \cos\theta & 0 \\ 0 & 0 & 1 \end{bmatrix}$.

Since $m = 1, 2$, Equation (2) can be expanded as $\mathbf{L}_1 = \begin{bmatrix} x - b\cos\theta + a \\ y - b\sin\theta \\ 0 \end{bmatrix}$ and

$\mathbf{L}_2 = \begin{bmatrix} x + b\cos\theta - a \\ y + b\sin\theta \\ 0 \end{bmatrix}$. Hence, the cable lengths is $\mathbf{l} = \begin{bmatrix} l_1 \\ l_2 \end{bmatrix}$, $l_1 = \|\mathbf{L}_1\|$, and $l_2 = \|\mathbf{L}_2\|$.

Equation (1) differentiates time, and we obtain:

$$\dot{x} = -\dot{y}\tan(\theta) - (y - d)\sec^2\theta\,\dot{\theta} \tag{3}$$

The dot product of $\mathbf{L}_m$ is as follows.

$$l_m{}^2 = \left(\mathbf{L}_{O_1O_2} + {}^{O_1}_{O_2}\mathbf{RL}^{O_2}_{O_2B_m} - \mathbf{L}_{O_1A_m}\right)^T\left(\mathbf{L}_{O_1O_2} + {}^{O_1}_{O_2}\mathbf{RL}^{O_2}_{O_2B_m} - \mathbf{L}_{O_1A_m}\right) \tag{4}$$

Equation (4) differentiates time, using $\mathbf{a}\cdot(\mathbf{b} \times \mathbf{c}) = \mathbf{b}\cdot(\mathbf{c} \times \mathbf{a}) = (\mathbf{c} \times \mathbf{a})\cdot\mathbf{b}$, and substitute Equation (3) into it and simplify it, and we obtain:

$$\mathbf{B\dot{q}} = \mathbf{A\dot{X}} \tag{5}$$

where $\mathbf{B}_{2\times2} = \begin{bmatrix} l_1 & 0 \\ 0 & l_2 \end{bmatrix}$; $\dot{\mathbf{q}}_{2\times1} = \begin{bmatrix} \dot{l}_1 \\ \dot{l}_2 \end{bmatrix}$; $\mathbf{A}_{2\times2} = \begin{bmatrix} -L_{1x}\tan\theta + L_{1y} & -L_{1x}(y - d)\sec^2\theta - b\cos\theta L_{1y} + b\sin\theta L_{1x} \\ -L_{2x}\tan\theta + L_{2y} & -L_{2x}(y - d)\sec^2\theta + b\cos\theta L_{2y} - b\sin\theta L_{2x} \end{bmatrix}$;

$\dot{\mathbf{X}}_{2\times1} = \begin{bmatrix} \dot{y}_1 \\ \dot{\theta}_2 \end{bmatrix}$.

Hence,

$$\dot{\mathbf{X}} = \mathbf{J\dot{q}} \tag{6}$$

where $\mathbf{J} = \mathbf{A}^{-1}\mathbf{B}$. Thus, the velocity Jacobian matrix $\mathbf{J}$ is obtained. It is the nonlinear mapping between the position change of the upper platform and the length change of the cable, and it is necessary for the analysis of CDHJ stiffness.

3. Modeling of Spring Lateral Bending and Compression

The spring in this CDHJ is subjected to bending and compression effects. The key to cable tension analysis and CDHJ stiffness is spring lateral bending and compression model. In most engineering applications, the coil spring under lateral buckling could be treated as an elastic beam [5,36,47,49,51]. Based this concept of an equivalent beam of helical spring, although wrenches of the spring exerted on the moving platform can be calculated, the influence of different springs on the performance of the mechanism cannot be analyzed by using this model. Therefore, in this paper, spring lateral bending and compression analysis uses the idea in [48,50] to study the effects of different spring parameters on the joint workspace and stiffness in detail. The essence of this modelling idea is to obtain the relationship between spring force and spring displacement based on Castigliano's theorem. This modeling is developed based each coil of the spring analyzed separately, but the concept of an equivalent beam of helical spring is to simply crumple all the coils into one beam. Hence, according to this idea, the helical spring lateral bending and compression model diagram is shown in Figure 2.

Figure 2a is the spring force analysis of the CDHJ. Cable forces $\mathbf{T}_1$ and $\mathbf{T}_2$ acting on the upper plate are equivalent to generalized forces $\mathbf{F}_{1e}$, $\mathbf{F}_{2e}$, and $\mathbf{M}_e$. The frame $\{O_k x_k y_k z_k\}$ is attached to the center of the helix section corresponding to the helix end point of each coil. The variable k is the index number of the active coils. Two Cartesian coordinate systems $\{O_0 x_0 y_0 z_0\}$ and $\{Oxyz\}$ are fixed to the lower and upper platforms, respectively, with $\{O_0 x_0 y_0 z_0\}$ being the global coordinate system coincident on the center of helix section corresponding to helix initiation point of the first coil. The number of spring active coils is n. Each coil frame is rotated around its z-axes in equally, finally y_n-axis and y-axis are tangent. In order to use Castigliano's theorem, Figure 2b shows the infinitesimal elements defined in the helical spring as. The infinitesimal element angular position on k-th coil is defined as α on x_k-z_k plane. Two forces exert on each spring coil infinitesimal element. One is on tangential direction coincident on ϵ_z, the other is on normal direction coincident on ϵ_x.
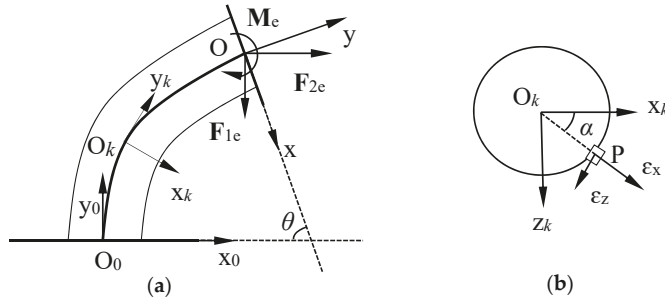
Figure 2. Helical spring lateral bending and compression model diagram. (**a**) Spring force analysis diagram on x-y plane. (**b**) Infinitesimal element on x-z plane from top view.

The position vector $\mathbf{OP}^k$ is with respect to the local frame $\{O_k x_k y_k z_k\}$. Obviously, $\mathbf{OP}^k = \mathbf{OO}_k{}^k + \mathbf{O}_k \mathbf{P}^k$. $\mathbf{O}_k \mathbf{P}^k$ is denoted as the position of the infinitesimal element in the particular coil frame $\{O_k x_k y_k z_k\}$. In the deformed configurations of the spring bend, it is desired that it is the shape of a circular arc. Meanwhile, due the platform motion is symmetric, the analysis only discusses the clockwise bend as shown in Figure 1b. Hence, θ is negative. $\mathbf{O}_k \mathbf{P}^k = [R\cos\alpha, -R_c\theta\alpha/2n\pi, R\sin\alpha]^T$, where $R_c = -y/\sin\theta$, R is radius of the helical spring, and n is the active coils number.

The position vector $\mathbf{OO}_k$ is with respect to the global coordinate system. And $\mathbf{OO}_k =$. $[R_c(1 - \cos k\theta/n) - x, -R_c\sin k\theta/n - y, 0]^T$, so $\mathbf{OO}_k{}^k = \mathbf{Rot}_z(-k\theta/n)\mathbf{OO}_k$

The generalized forces vectors $\mathbf{F}_{1e}$, $\mathbf{F}_{2e}$, and $\mathbf{M}_e$ are with respect to the global coordinate system. So, $\mathbf{F}_{1e} = [0, -F_{1e}, 0]^T$, $\mathbf{F}_{2e} = [F_{2e}, 0, 0]^T$, and $\mathbf{M}_e = [0, 0, -M_e]^T$. Then, $\mathbf{F}_{1e}{}^k = \mathbf{Rot}_z(-k\theta/n)\mathbf{F}_{1e}$, $\mathbf{F}_{2e}{}^k = \mathbf{Rot}_z(-k\theta/n)\mathbf{F}_{2e}$, and $\mathbf{M}_e{}^k = \mathbf{Rot}_z(-k\theta/n)\mathbf{M}_e$. So far, $\mathbf{M}^k$ can be obtained as follows, which is the total moment acting on the infinitesimal element.

$$\mathbf{M}^k = \mathbf{M}_{1e}{}^k + \mathbf{M}_{2e}{}^k + \mathbf{M}_e{}^k \tag{7}$$

where, $\mathbf{M}_{1e}{}^k = \mathbf{OP}^k \times \mathbf{F}_{1e}{}^k$, which is the moment acting on the element resulting from the equivalent force vector $\mathbf{F}_{1e}$. Similarly, $\mathbf{M}_{2e}{}^k = \mathbf{OP}^k \times \mathbf{F}_{2e}{}^k$.

According to the Castigliano's theorem, it should be defined in the element specific frame $\{\varepsilon_x \varepsilon_y \varepsilon_z\}$. The moment vector $\mathbf{M}^\varepsilon = \mathbf{Rot}_y(\alpha)\mathbf{M}^k$.

The strain energy in k-th coil, due to each element of moment vector $\mathbf{M}^\varepsilon$ is given by

$$U_{b1,k} = \int_0^{2\pi} \frac{(M_x^\varepsilon)^2}{2EI} R d\alpha \tag{8a}$$

$$U_{b2,k} = \int_0^{2\pi} \frac{\left(M_y^\varepsilon\right)^2}{2EI} R d\alpha \tag{8b}$$

$$U_{t,k} = \int_0^{2\pi} \frac{\left(M_z^\varepsilon\right)^2}{2GJ} R d\alpha \tag{8c}$$

where the modulus of elasticity is E, the shear modulus is G, the moment inertia is I, the polar moment inertia is J. So, strain energy in the k-th coil is the summation of three strain energies.

$$U_k = U_{b1,k} + U_{b2,k} + U_{t,k} \tag{9}$$

The spring total strain energy is the summation of all the coil strain energies.

$$U = \Sigma_1^k U_k \tag{10}$$

Castigliano's theorem is now invoked to determine the relationship between spring force and spring displacement.

$$\Delta x = \frac{\partial U}{\partial F_{2e}} \tag{11a}$$

$$\Delta y = \frac{\partial U}{\partial F_{1e}} \tag{11b}$$

$$\theta = \frac{\partial U}{\partial M_e} \tag{11c}$$

Equations (11a), (11b), and (11c) can be written in given form in Equation (12).

$$\begin{bmatrix} \Delta x \\ \Delta y \\ \theta \end{bmatrix} = \mathbf{D} \begin{bmatrix} F_{2e} \\ F_{1e} \\ M_e \end{bmatrix} \tag{12}$$

where $\mathbf{D}$ is a 3×3 matrix. Let $\mathbf{K_p}$ be $\mathbf{D}^{-1}$, then the important relationship becomes:

$$\begin{bmatrix} F_{1e} \\ F_{2e} \\ M_e \end{bmatrix} = \mathbf{K_p} \begin{bmatrix} \Delta y \\ \Delta x \\ \theta \end{bmatrix} \tag{13}$$

where $\mathbf{K_p} = \begin{bmatrix} K_{11} & K_{12} & K_{13} \\ K_{21} & K_{22} & K_{23} \\ K_{31} & K_{32} & K_{33} \end{bmatrix}$. From Equation (1), $\Delta x = -(y - d)\sec^2\theta\Delta\theta - \tan\theta\Delta y$, substitute it into $\mathbf{K_p}$ and simplify, Equation (13) can become:

$$\begin{bmatrix} F_{1e} \\ F_{2e} \\ M_e \end{bmatrix} = \mathbf{K} \begin{bmatrix} \Delta y \\ \theta \end{bmatrix} \tag{14}$$

where $\mathbf{K} = \begin{bmatrix} K_{11} - K_{12}\tan\theta & -K_{12}(y - d)\sec^2\theta + K_{13} \\ K_{21} - K_{22}\tan\theta & -K_{22}(y - d)\sec^2\theta + K_{23} \\ K_{31} - K_{32}\tan\theta & -K_{32}(y - d)\sec^2\theta + K_{33} \end{bmatrix}$.

Equation (14) reveals the nonlinear force-deformation relation or stiffness equation of the spring. Wrenches of the spring exerted on the moving platform can be calculated by Equation (14), and then through the static analysis of the moving platform, the cable tension can be obtained. Matrix $\mathbf{K}$ is a more complex form of proportionality factor, which is determined by the spring configuration,

the geometry and material properties and is not a constant. That is to say, the linear helical compression spring became a nonlinear stiffness spring under the bending and compression effects. So, CDHJ is a variable stiffness joint. Through translational motion, the stiffness of the spring is adjusted which determines the joint system stiffness.

4. Workspace and Stiffness Index of CDHJ

4.1. Workspace Index

The workspace for CDHJ shows the set of poses for which the joint can be satisfied with positive cable tension within the specified actuation cable limits. This workspace is generated by the following conditions.

Wrench-feasible condition:

$$0 < T_{min} \leq T_i \leq T_{max}, \ i = 1, 2 \tag{15}$$

The cable length should meet the following condition.

$$0 < l_{min} \leq l_i, \ i = 1, 2 \tag{16}$$

The translational should be restricted. From Equation (1), the translation component along the x-axis is limited by (y, θ). Meanwhile, the translation motion is restricted by structural size of CDHJ. Hence,

$$x_{min} \leq x \leq x_{max} \tag{17}$$

The constant orientation workspace when θ is fixed, is defined as:

$$W^c = \left\{ \begin{array}{c} y \in \mathrm{R}: \ \mathbf{f}\left(\theta^{fix}, y, \mathbf{1}\right) = \mathbf{0}; T_{min} \leq T_i \leq T_{max}, l_{min} \leq l_i, \ i = 1, 2, \\ x_{min} \leq x \leq x_{max} \text{ and } y_{min} \leq y \leq y_{max} \end{array} \right\} \tag{18}$$

The total workspace should be the intersection of all constant orientation workspaces in the range between θ_{min} and θ_{max} [52], is defined as:

$$W = \left\{ \begin{array}{c} y \in \mathrm{R}: \ \mathbf{f}(y, \theta, \mathbf{1}) = \mathbf{0}; T_{min} \leq T_i \leq T_{max}, l_{min} \leq l_i, \ i = 1, 2, \\ \theta_{min} \leq \theta \leq \theta_{max}, x_{min} \leq x \leq x_{max} \text{ and } y_{min} \leq y \leq y_{max} \end{array} \right\} \tag{19}$$

In order to evaluate and compare the different spring effects on the CDHJ workspace, the authors need to develop workspace index A_w, which is the area of joint workspace and is used to assess the size of the workspace. The boundary values in arbitrary units, corresponding to that showed in Equations (15)–(17) for the following numerical examples, are given in Table 1.

Table 1. Boundary values of variables.

Parameters	Value
T_{min} (N)	1
T_{max} (N)	300
l_{min} (m)	0.01
x_{min} (m)	0
x_{max} (m)	0.08
θ_{min} (rad)	−1.48
θ_{max} (rad)	0
y_{min} (m)	0.035
y_{max} (m)	0.095

4.2. CDHJ Stiffness Index

This section focuses on analyzing static stiffness analysis of CDHJ. For a massless cable whose profile is a straight line, static stiffness analysis generally uses the Jacobian-based stiffness analysis method [32,39–42] to describe the Cartesian stiffness matrix which is the function of the manipulator's configuration and mechanism stiffness values. For CDHJ, the Cartesian stiffness matrix $\mathbf{K_J}$, the relationship between the incremental displacement $\delta \mathbf{X}$ i, and the incremental wrench $\delta \mathbf{W}$ [39,42] are as follows:

$$\delta \mathbf{W} = \mathbf{K_J} \delta \mathbf{X} \tag{20}$$

$$\mathbf{K_J} = - \left[\begin{array}{cc} \frac{\partial \mathbf{S}}{\partial y} \mathbf{T} & \frac{\partial \mathbf{S}}{\partial \theta} \mathbf{T} \end{array} \right] - \mathbf{S K_l J^{-1}} \tag{21}$$

where $\mathbf{K_l} = \left[\begin{array}{cc} k_1 & 0 \\ 0 & k_2 \end{array} \right]$, k_1 and k_2 are rigidity of cable 1 and cable 2, respectively; $\mathbf{S_{3\times2}} = - \left[\begin{array}{cc} \hat{l}_{1x} & \hat{l}_{2x} \\ \hat{l}_{1y} & \hat{l}_{2y} \\ r_{1z} & r_{2z} \end{array} \right]$, $\hat{\mathbf{l}}_m = \frac{\mathbf{l}_m}{l_m}$, $m = 1, 2$; $^{O_1}_{O_2}\mathbf{RL}^{O_2}_{O_2B_m} \times \hat{\mathbf{l}}_1$ as $\mathbf{r}_1$, and $^{O_1}_{O_2}\mathbf{RL}^{O_2}_{O_2B_m} \times \hat{\mathbf{l}}_2$ as $\mathbf{r}_2$; $\mathbf{T_{2\times1}} = \left[\begin{array}{c} T_1 \\ T_2 \end{array} \right]$, T_1 and T_2 are the tension of cable1 and cable 2, respectively.

In order to evaluate and compare the different spring effect on the CDHJ stiffness, the stiffness indices based on the stiffness matrix should be developed. Due the previous Cartesian stiffness matrix namely Equation (21) is inhomogeneous.

$$\left[\begin{array}{c} F_x(\mathrm{N}) \\ F_y(\mathrm{N}) \\ M_z(\mathrm{N \cdot m}) \end{array} \right]_{3\times1} = \left[\begin{array}{cc} \left[K_{J11}(\mathrm{N/m}) \right]_{2\times1} & \left[K_{J12}(\mathrm{N}) \right]_{2\times1} \\ \left[K_{J21}(\mathrm{N}) \right]_{1\times1} & \left[K_{J22}(\mathrm{N \cdot m}) \right]_{1\times1} \end{array} \right]_{3\times2} \left[\begin{array}{c} y(\mathrm{m}) \\ \theta(\mathrm{rad}) \end{array} \right]_{2\times1} \tag{22}$$

The Cartesian stiffness matrix needs to be homogenized first. This paper adopts the method introduced in [40,42], which divides the unit-inconsistent matrix into unit-consistent translational and rotational components.

Denote λ_{Jt1} and λ_{Jt2} as the eigenvalues of $\mathbf{G_{JF}G_{JF}^T}$, and λ_{Jr} is $\mathbf{G_{JM}G_{JM}^T}$, where $\mathbf{G_{JF}} = \left[\begin{array}{cc} \mathbf{K_{J11}} & \mathbf{K_{J12}} \end{array} \right]_{2\times2}$ is a dimensionally homogeneous matrix in N; $\mathbf{G_{JM}} = \left[\begin{array}{cc} \mathbf{K_{J21}} & \mathbf{K_{J22}} \end{array} \right]_{1\times2}$ is a dimensionally homogeneous matrix in N·m. The directions of maximum and minimum translational stiffness are the eigenvectors of $\mathbf{G_{JF}G_{JF}^T}$, and the stiffness magnitudes in these directions are the corresponding eigenvalues λ_{Jt1} and λ_{Jt2}. $\mathbf{G_{JM}G_{JM}^T}$ represents the rotational part of the stiffness, which is reduced to a scalar value. Therefore, denote $k_{Jt} = \min(\sqrt{\lambda_{Jt1}}, \sqrt{\lambda_{Jt2}})$ as the translational stiffness index. Similarly, denote the rotational stiffness index as, $k_{Jr} = \sqrt{\lambda_{Jr}}$. The two performance indices k_{Jt} and k_{Jr} indicate the joint stiffness behaviors, and a higher index means higher rigidity [40,42]. In order to evaluate the CDHJ stiffness, the index f_J is defined as:

$$f_J = k_{Jt}k_{Jr} \tag{23}$$

In order to evaluate and compare the different spring effects on the spring stiffness, spring stiffness matrix $\mathbf{K}$ also uses the above method to be homogenized. Thus, denote the translational stiffness index as k_t. Similarly, denote the rotational stiffness index as k_r. The index f is used to evaluate the helical spring stiffness, and $f = k_t k_r$.

5. Numerical Simulation

5.1. Cable Parameters

In this paper, we recommend that this cable-driven hybrid joint will be applied to the elbow joint of wheelchair-mounted robotic manipulator. The manipulator's service object is the special group of the elderly and the disabled, so the speed and acceleration need low; the working objects are daily necessities such as water cups, toothbrushes, books, etc., so the manipulator is lightweight robot;

the manipulator is mounted on wheelchair, and its working environment is home or office, so it has small size. According to the application characteristics (light-weighted, small size, low speed, pick-and-place application) of wheelchair-mounted robotic manipulator, cables are modeled as a massless spring. Spring cable model is suitable for the robots with the light-weighted [34], low speed [33], and small size [37,38], whose profile is a straight line. For the cable actuators, 6×7 wire rope is considered. d_c is diameter of steel wire, 2 mm. According to the method utilized in [42], the stiffness of the ith cable is formulated as:

$$k_i = \frac{E_C A_C}{l_i + l_{cw}} \tag{24}$$

where E_C denotes the modulus of elasticity of the cable, 68 Gpa; A_C denotes the cross-sectional area of the cable, 5.28 mm^2; l_{cw} denotes the length of the actuating winch, which is assumed to be constant, 30 mm.

5.2. Numerical Analysis of Spring Effects on CDHJ Workspace and Stiffness

Helical compression spring basic parameters are the radius of the spring R, the radius of the spring wire r, the modulus of elasticity of the spring material E, the shear modulus of that material G, and the active coils number n. Different parameters determine different helical compression springs. In order to use Castigliano's theorem to derive the nonlinear force-deformation relation of the spring, the total strain energy of the spring should be calculated using the above values, and then calculate the cable tension. This section analyses these spring parameters effects on CDHJ workspace and stiffness. Furthermore, the basic parameters of the compression spring of CDHJ can be determined. Structural parameters a, b, and d are 0.08 m, 0.0623 m, and 0.025 m, respectively.

5.2.1. Spring Parameters (n, E/G) on CDHJ Workspace and Stiffness

Spring as a common part, its parameters are discrete. In this section, spring materials are selected as carbon spring steel wire, oil quenched-tempered spring steel wire, alloy spring steel wire, stainless steel wire for spring, copper and copper alloy wire, beryllium bronze wire, spring steel. The modulus of elasticity and the shear modulus, namely E/G of these materials are in Table 2. Due to structural size restriction, compression spring free height is 105 mm, active coils numbers are 5, 8, 10, 13, 16, 20, and 25. In order to make a clear explanation of spring parameters (n, E/G) effects, the other parameters of spring are selected primarily, namely $R = 0.02$ m, $r = 0.0015$ m. Figure 3 shows spring parameters on CDHJ workspace. The horizontal coordinate is spring material marked as shown in Table 2. Figure 4 shows spring parameters on CDHJ stiffness. Every pose point of the joint stiffness calculation is all in the workspace. The longitudinal coordinate is the minimum value of joint stiffness under this configuration.

Table 2. *E/G* of spring materials.

Spring Materials	Mark	*E* (Gpa)	*G* (Gpa)
carbon spring steel wire, oil quenched-tempered spring steel wire, alloy spring steel wire, spring steel	1	206	78.5
stainless steel wire for spring (A)	2	185	70
stainless steel wire for spring (B), (C)	3	195	73
copper and copper alloy wire	4	93.1	40.2
beryllium bronze wire	5	129.4	42.1
spring-tempered steel	6	195	81.5
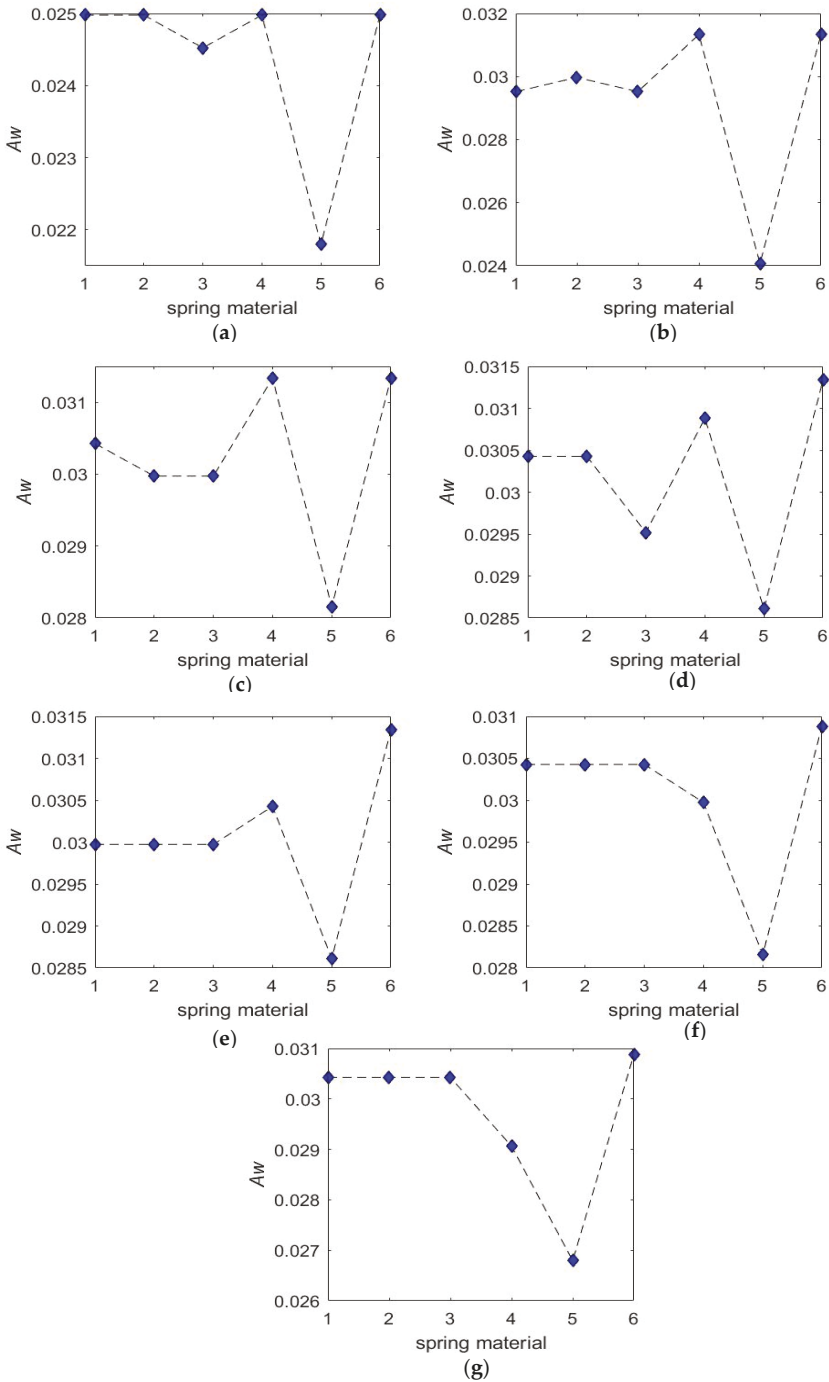
Figure 3. Spring parameters (n, E/G) on CDHJ workspace. (**a**) A_w at $n = 5$; (**b**) A_w at $n = 8$; (**c**) A_w at $n = 10$; (**d**) A_w at $n = 13$; (**e**) A_w at $n = 16$; (**f**) A_w at $n = 20$; (**g**) A_w at $n = 25$.
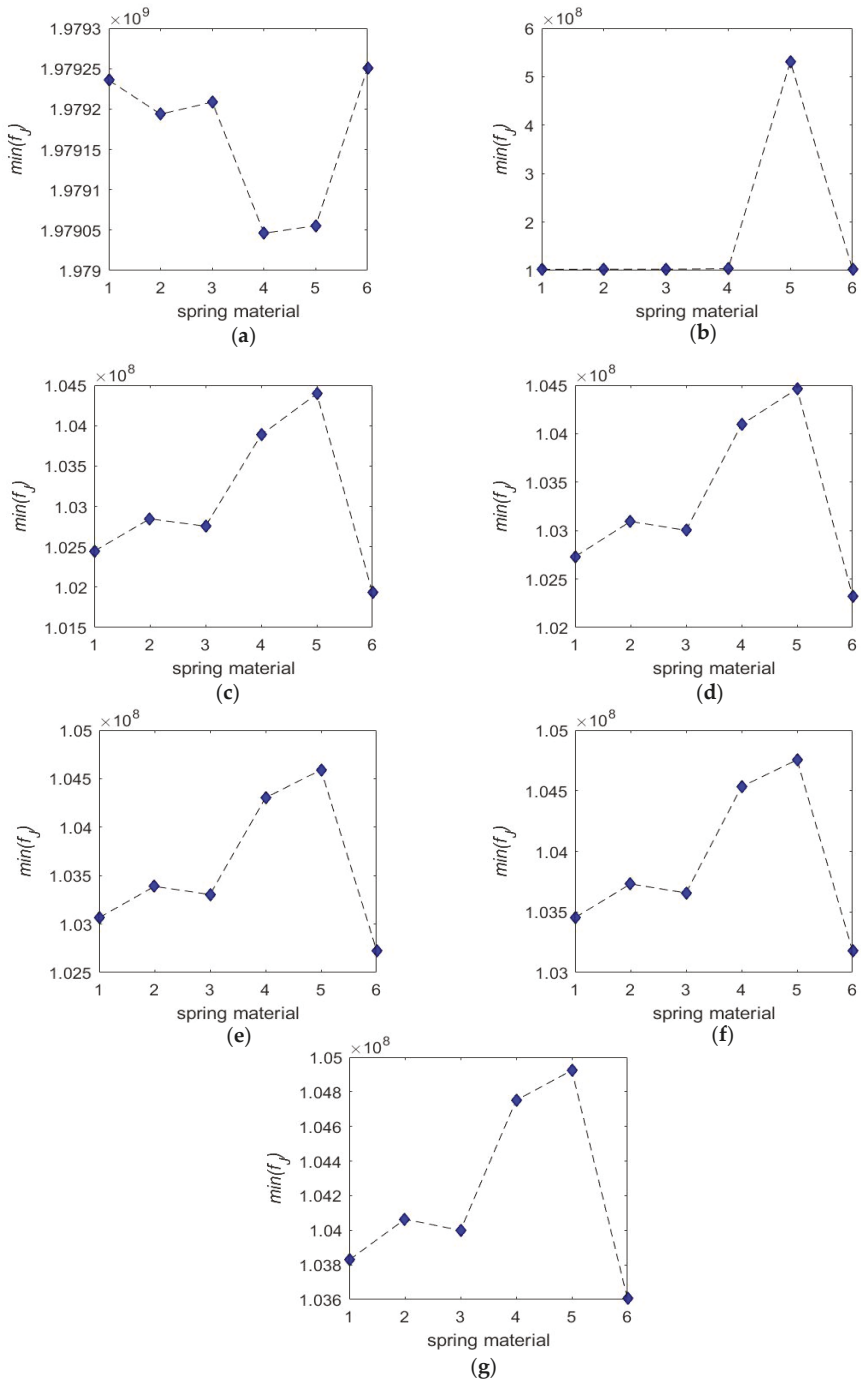
Figure 4. Spring parameters (n, E/G) on CDHJ stiffness. (**a**) min(f_J) at $n = 5$; (**b**) min(f_J) at $n = 8$; (**c**) min(f_J) at $n = 10$; (**d**) min(f_J) at $n = 13$; (**e**) min(f_J) at $n = 16$; (**f**) min(f_J) at $n = 20$; (**g**) min(f_J) at $n = 25$.

As shown in Figure 3, the minimum of CDHJ workspace area A_w is all at No. 5 material, the maximum of A_w is all the same at $n = 8$ for No. 4 material and No. 6 material, $n = 10$ for No. 4 material and No. 6 material, $n = 13$ for No. 6 material, and $n = 16$ for No. 6 material. When CDHJ is the same material, A_w is all the minimum at $n = 5$. Contrarily, when CDHJ is the same material, the minimum value of joint stiffness $\min(f_J)$ is the maximum at $n = 5$ as shown in Figure 4. If $n = 5$ is removed, $\min(f_J)$ under No. 1, No. 2, No. 3, No. 4, and No. 6 material increases with the increase of n.

In conclusion, if the larger CDHJ workspace is firstly considered, and the larger joint stiffness is secondly considered, then the selection of n and E/G is 10 and 93.1/40.2 Gpa (No. 4 material). So, the next analysis is based on this.

5.2.2. Variable Stiffness Spring Effects on the CDHJ Stiffness

Linear helical compression spring became a nonlinear stiffness spring under combined bending and compression effects as shown in Figure 5. Spring stiffness f increases with the increase of θ, and decreases with the increase of compression Δy as shown in Figure 6a,c. Therefore, CDHJ is the simplification of nonlinear stiffness mechanism, and CDHJ stiffness adjustment is achieved by the additional translation motion as shown in Figure 6a,c. From Figure 5, when θ is zero, the change of spring stiffness is not affected by the translational motion. Thus, it can be called as a singular position for stiffness [48]. In fact, at $\theta = 0°$, the compression spring is a linear spring, which meets Hooke's law. That is to say, no matter how y is adjusted, the spring stiffness remains unchanged. From Figure 6a,c, obviously, spring stiffness f is smaller at $n = 10$ for No. 4 material than at $n = 5$ for No. 1 material.

From Figure 6b,d, intuitively, the tension of one cable increases, the tension of other cable decreases, and the antagonistic characteristics of two cables are in line with the antagonistic characteristics of CDM, which verifies the correctness of the spring lateral bending and compression model. Meanwhile, comparing Figure 6a,b with Figure 6c,d, when the spring stiffness f is large, the corresponding cable tension is also large, which also verifies the correctness of the spring lateral bending and compression model.

In summary, the spring stiffness under lateral bending and compression is changing, which makes CDHJ stiffness variable, and when CDHJ is at work, its stiffness can be adjusted by the additional translation motion. In addition, when spring stiffness is large, the cable tension is also required to be large, which agrees with the rule of thumb.
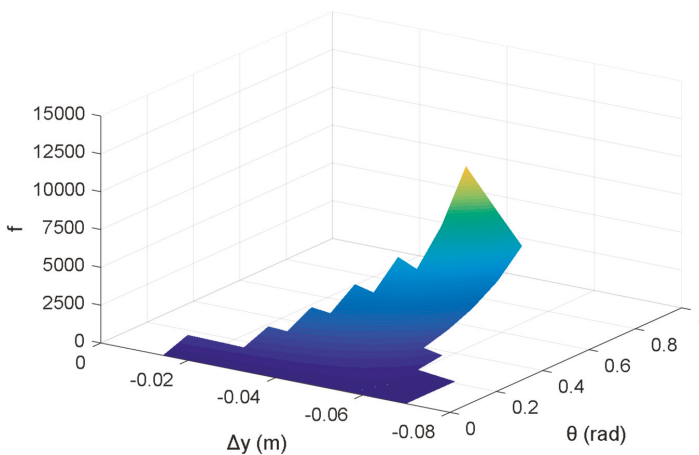
Figure 5. Spring stiffness f at $n = 5$ for No. 1 material.
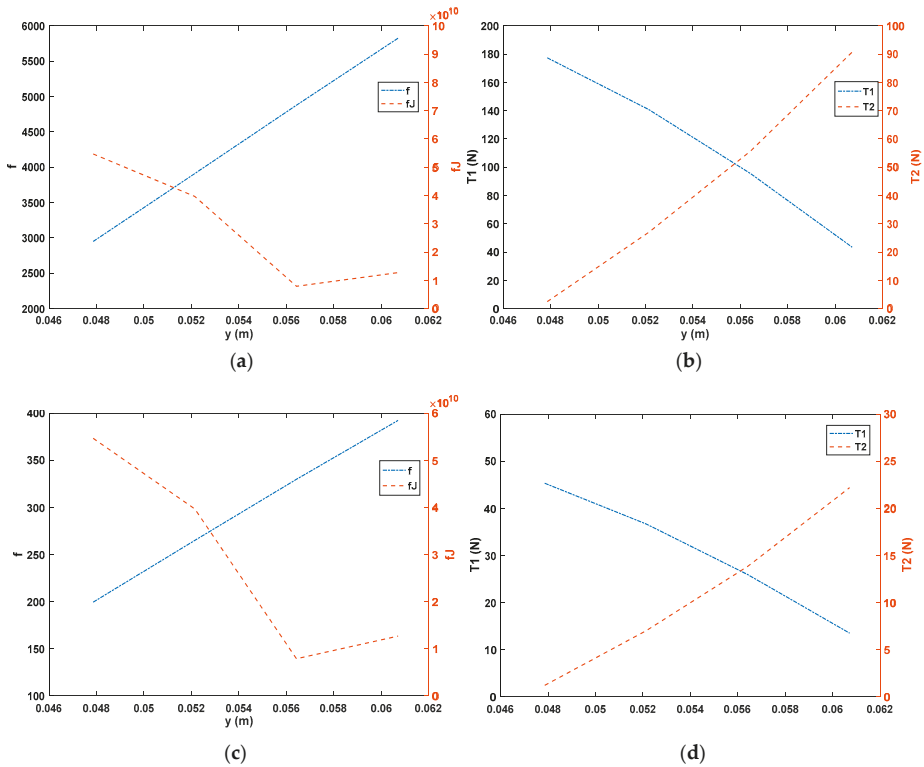
Figure 6. Spring stiffness on CDHJ stiffness and cable tension at $\theta = -36°$. (**a**) f_J and f at $n = 5$ for No. 1 material; (**b**) T_1 and T_2 at $n = 5$ for No. 1 material; (**c**) f_J and f at $n = 10$ for No. 4 material; (**d**) T_1 and T_2 at $n = 10$ for No. 4 material.

5.2.3. Spring Parameters (R, r) on CDHJ Workspace and Stiffness

Alike the idea of the last section, the spring radius R is 0.015 m, 0.0175 m, 0.02 m, 0.0225 m, 0.025 m, 0.0275 m, and 0.0325 m. The spring wire radius r is 0.00075 m, 0.001 m, 0.00125 m, 0.0015 m, 0.00175 m, and 0.002 m. Figure 7 shows spring parameters (R, r) on CDHJ workspace. The horizontal coordinate is spring radius R. Figure 8 shows spring parameters (R, r) on CDHJ stiffness f_J. The longitudinal coordinate is the minimum value of joint stiffness under this configuration.

As shown in Figure 7, except $r = 0.002$ m, CDHJ workspace area A_w decreases with the increase of R. Except $R = 0.015$ m, CDHJ workspace area A_w increases with the increase of r. Whether how much r is, the maximum of A_w is at $R = 0.015$ m. The A_w maximum is at $r = 0.0015$ m, and 0.00175 m. A_w approaches 0 at $r = 0.00075$ m, $R = 0.0225$ m, and $r = 0.001$ m, $R = 0.0325$ m. The minimum of A_w is 0 at $r = 0.00075$ m, $R = 0.025$ m, 0.0275 m, and 0.0325 m.

As shown in Figure 8, CDHJ stiffness $\min(f_J)$ increases with the increase of R. CDHJ stiffness $\min(f_J)$ decreases with the increase of r. Contrarily with the effects on joint workspace, the maximum of $\min(f_J)$ is at $r = 0.00075$ m, $R = 0.025$ m, 0.0275 m, and 0.0325 m. When A_w approaches 0 at $r = 0.00075$ m, $R = 0.0225$ m, and $r = 0.001$ m, $R = 0.0325$ m, $\min(f_J)$ is relatively large. The difference is too large, therefore the value of $\min(f_J)$ approaches 0 at Figure 8a,b. In fact, they are 1.054×10^8 and 1.0432×10^8 and are relatively large compared with other cases.

Comprehensive comparison of Figures 7 and 8, it can be inferred that when the workspace is large, stiffness is relatively small. Obviously this is in accord with common sense. We always hope that

the workspace is larger, and there is a certain degree of stiffness. So the selection of R and r is 0.015 m and 0.0015 m.
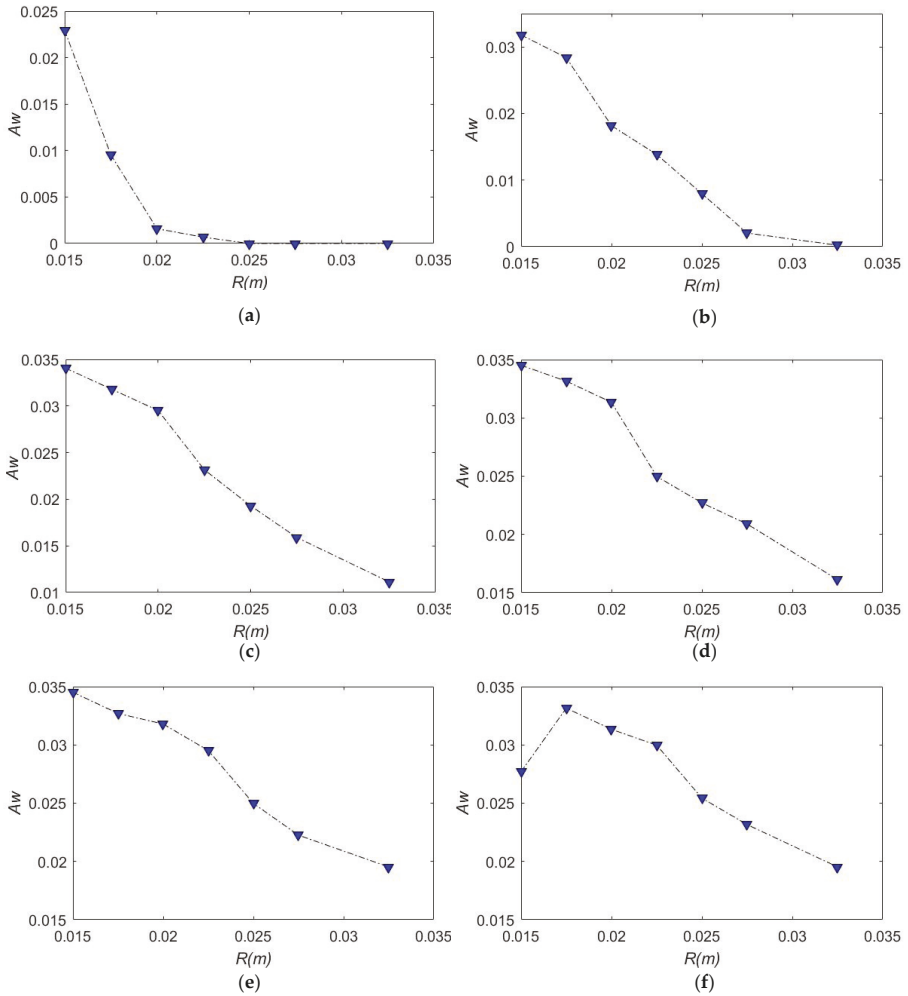
Figure 7. Spring parameters (R, r) on CDHJ workspace. (**a**) A_w at $r = 0.00075$ m; (**b**) A_w at $r = 0.001$ m; (**c**) A_w at $r = 0.00125$ m; (**d**) A_w at $r = 0.0015$ m; (**e**) A_w at $r = 0.00175$ m; (**f**) A_w at $r = 0.002$ m.
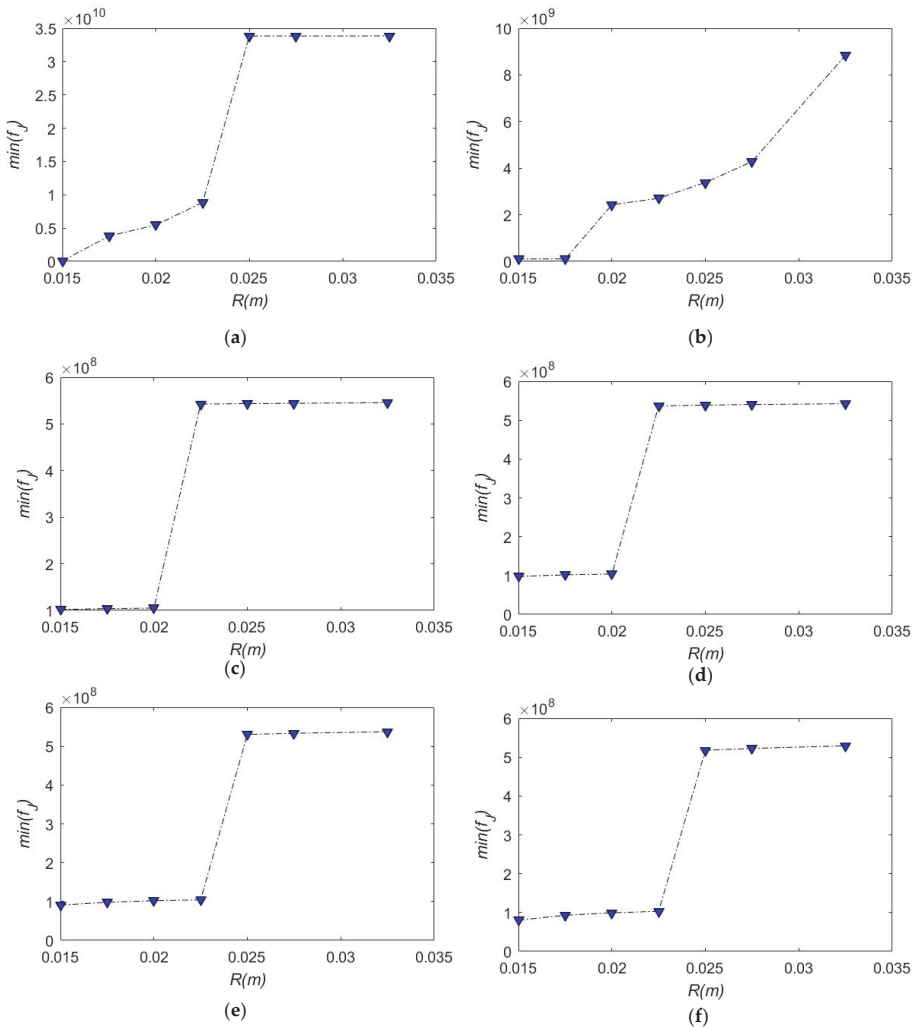
Figure 8. Spring parameters (R, r) on CDHJ stiffness. (**a**) min(f_J) at $r = 0.00075$ m; (**b**) min(f_J) at $r = 0.001$ m; (**c**) min(f_J) at $r = 0.00125$ m; (**d**) min(f_J) at $r = 0.0015$ m; (**e**) min(f_J) at $r = 0.00175$ m; (**f**) min(f_J) at $r = 0.002$ m

6. Discussion

In order to determine the spring basic parameters, this paper puts forward spring effects on CDHJ. After introducing the symmetry design, the kinematic analysis of the joint is carried out to calculate the velocity Jacobian matrix. Then, in order to calculate the cable tension, it analyzes lateral bending and compression modeling of the spring based on Castigliano's theorem. This method may be applied to other CDM with spring spines. Finally, it analyzes spring effects on CDHJ workspace and stiffness with Matlab. This is actually similar to the stiffness feasible workspace mentioned in [53], which can provide ideas for the optimal design of other CDM. First, because the linear helical compression spring became a nonlinear stiffness spring under the bending and compression effects as shown in Figure 5, the CDHJ is a variable stiffness mechanism, whose stiffness adjustment can be realized by the translational motion of the upper platform as shown in Figure 6a,c. From Figure 6, when spring stiffness is relatively large,

the cable tension is also required to be large, this can verify the correctness of the spring lateral bending and compression model. Second, when the spring is different, workspace and stiffness of CDHJ is different. Comparing Figure 3 with Figure 4, and Figure 7 with Figure 8, when the CDHJ workspace is relatively large, the stiffness is relatively small. This agrees with the rule of thumb, and indirectly verifies the correctness of the spring lateral bending and compression model. Due spring as a common part, its parameters are discrete. After analyzing the spring basic parameters (n, E/G, R, r) selected in the paper, it can be inferred that joint workspace is larger, and there is a certain degree of stiffness at $n = 10$, $E/G = 93.1/40.2$ Gpa, $R = 0.015$ m, $r = 0.0015$ m, whose workspace is as shown in Figure 9. Due the upper platform motion being symmetric, Figure 9 only shows the workspace of the spring clockwise bend as shown in Figure 1b. From Figure 9, the larger the rotation angle, the smaller the translation range, this shows that the larger the rotation angle, the smaller the adjustable range of CDHJ stiffness. In addition, due to the restriction of the intermediate spring, the CDHJ rotation angle will not exceed 70°, but the CDHJ will be an elbow joint for wheelchair-mounted robotic manipulator to perform activities of daily living which is needed elbow range of motion of 110° [54], so the proposed CDHJ may be of the potential use for wheelchair-mounted robotic manipulator elbow joint featured with stiffness adjustability, large workspace, smooth motion, and light structure. Therefore, the next work is to assemble the CDHJ prototype based on the spring basic parameters determined by the simulation results. The future research will study the shoulder and wrist joints (3 or 4 cables driven) and assemble them into a wheelchair-mounted robotic manipulator.
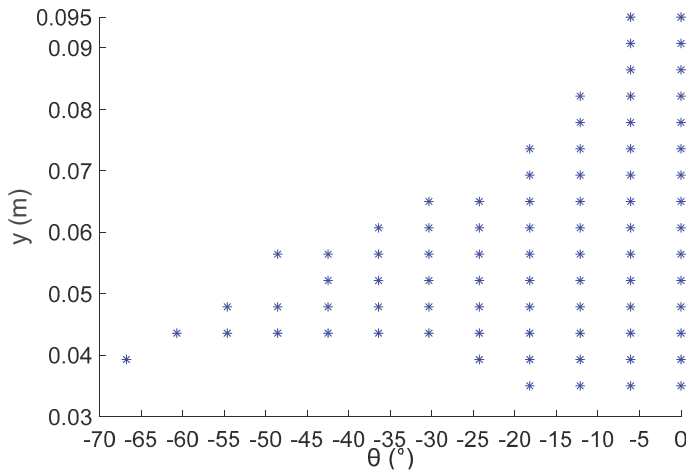
Figure 9. CDHJ workspace at $n = 10$ for No. 4 material, $R = 0.015$ m, $r = 0.0015$ m.

Author Contributions: Conceptualization, Z.S.; methodology, Z.S. and S.Z.; software, Z.S., S.Z., and C.Y.; validation, L.L., J.L., and D.C.; formal analysis, L.L.; investigation, Z.S. and D.C.; resources, D.C.; data curation, S.Z. and J.L.; writing—original draft preparation, Z.S. and S.Z.; writing—review and editing, Z.S.; visualization, J.L.; supervision, Z.S. and D.C.; project administration, Z.S. and D.C.; funding acquisition, Z.S. and D.C. All authors have read and agreed to the published version of the manuscript.

Conflicts of Interest: The authors declare no conflict of interest.

References

1. Chung, C.S.; Wang, H.; Cooper, R.A. Functional assessment and performance evaluation for assistive robotic manipulators: Literature review. *J. Spinal. Cord. Med.* **2013**, *36*, 273–289. [CrossRef] [PubMed]
2. Hersh, M. Overcoming Barriers and Increasing Independence–Service Robots for Elderly and Disabled People. *Int. J. Adv. Robot. Syst.* **2015**, *12*, 1–33. [CrossRef]
3. Jiang, H.R.; Zhang, T.; Wachs, J.P.; Duerstock, B.S. Enhanced control of a wheelchair-mounted robotic manipulator using 3-D vision and multimodal interaction. *Comput. Vis. Image Und.* **2016**, *149*, 21–31. [CrossRef]
4. Bilyea, A.; Seth, N.; Nesathurai, S.; Abdullah, H.A. Robotic assistants in personal care: A scoping review. *Med. Eng. Phys.* **2017**, *49*, 1–6. [CrossRef] [PubMed]
5. Zhang, S.; Cao, D.X.; Li, S.; Min, H.; Fan, F. Inverse kinematic tension analysis and optimal design of a cable-driven parallel-series hybrid joint towards wheelchair-mounted robotic manipulator. *J. Eur. Syst. Autom.* **2018**, *51*, 59–74.
6. Yang, K.S.; Yang, G.L.; Chen, S.L.; Wang, Y.; Zhang, C.; Fang, Z.J.; Zheng, T.J.; Wang, C.C. Study on stiffness-oriented cable tension distribution for a symmetrical cable-driven mechanism. *Symmetry* **2019**, *11*, 1158. [CrossRef]
7. Gagliardini, L.; Caro, S.; Gouttefarde, M.; Girin, A. Discrete reconfiguration planning for cable-driven parallel robots. *Mech. Mach. Theory* **2016**, *100*, 313–337. [CrossRef]
8. Zi, B.; Lin, J.; Qian, S. Localization, obstacle avoidance planning and control of a cooperative cable parallel robot for multiple mobile cranes. *Robot. Comput. Int. Manuf.* **2015**, *34*, 105–123. [CrossRef]
9. Kaluarachchi, M.M.; Ho, J.H.; Yahya, S. Design of a single motor, tendon driven redundant manipulator with reduced driving joint torques. *Mech. Based Des. Struct. Mach.* **2018**, *46*, 591–614. [CrossRef]
10. Chen, Q.; Zi, B.; Sun, Z.; Li, Y.; Xu, Q.S. Design and development of a new cable-driven parallel robot for waist rehabilitation. *IEEE/ASME Trans. Mechatron.* **2019**, *24*, 1497–1507. [CrossRef]
11. Liu, Y.J.; Wang, J.M.; Ben-Tzv, P. A cable length invariant robotic tail using a circular shape universal joint mechanism. *J. Mech. Robot.* **2019**, *11*, 051005. [CrossRef]
12. Christoforoua, E.G.; Phocasb, M.C.; Matheoub, M.; Müller, A. Experimental implementation of the 'effective 4-bar method' on a reconfigurable articulated structure. *Structures* **2019**, *20*, 157–165. [CrossRef]
13. Qiao, S.L.; Guo, H.W.; Liu, R.Q.; Deng, Z.Q. Self-adaptive grasp process and equilibrium configuration analysis of a 3-DOF UACT robotic finger. *Mech. Mach. Theory* **2019**, *133*, 250–266. [CrossRef]
14. Seriani, S.; Gallina, P.; Scalera, L.; Lughi, V. Development of n-DoF preloaded structures for impact mitigation in cobots. *J. Mech. Robot.* **2018**, *10*, 051009. [CrossRef]
15. Beckerle, P.; Salvietti, G.; Ünal, R.; Prattichizzo, D.; Rossi, S. A Human-robot interaction Perspective on Assistive and rehabilitation robotics. *Front. Neurorobot.* **2017**, *11*, 1–6. [CrossRef]
16. Azadi, M.; Behzadipour, S.; Faulkner, G. Antagonistic variable stiffness elements. *Mech. Mach. Theory* **2009**, *44*, 1746–1758. [CrossRef]
17. Boehler, Q.; Vedrines, M.; Abdelaziz, S.; Poignet, P.; Renaud, P. Synthesis method for the design of variable stiffness components using prestressed singular elastic systems. *Mech. Mach. Theory* **2018**, *121*, 598–612. [CrossRef]
18. Nam, K.H.; Kim, B.S.; Song, J.B. Compliant actuation of parallel-type variable stiffness actuator based on antagonistic actuation. *J. Mech. Sci. Technol.* **2010**, *24*, 2315–2321. [CrossRef]
19. Petit, F.; Friedl, W.; Hoppner, H.; Grebenstein, M. Analysis and synthesis of the bidirectional antagonistic variable stiffness mechanism. *IEEE/ASME Trans. Mechatron.* **2015**, *20*, 684–695. [CrossRef]
20. Yeo, S.H.; Yang, G.L.; Lim, W.B. Design and analysis of cable-driven manipulators with variable stiffness. *Mech. Mach. Theory* **2013**, *69*, 230–244. [CrossRef]
21. Xu, F.; Wang, H.; Au, K.W.S.; Chen, W.; Miao, Y. Underwater dynamic modeling for a cable-driven soft robot arm. *IEEE/ASME Trans. Mechatron.* **2018**, *23*, 2726–2738. [CrossRef]
22. Liu, F.; Xu, W.F.; Huang, H.L.; Ning, Y.H. Design and analysis of a high payload manipulator based on a cable-driven serial-parallel mechanism. *J. Mech. Robot.* **2019**, *11*, 051006. [CrossRef]
23. Scalera, L.; Palomba, I.; Wehrle, E.; Gasparetto, A.; Vidoni, R. Natural motion for energy saving in robotic and mechatronic systemsand. *Appl. Sci.* **2019**, *9*, 3516. [CrossRef]

24. Ham, R.V.; Sugar, T.G.; Vanderborght, B.; Hollander, K.W.; Lefeber, D. Compliant actuator designs. *IEEE Robot. Autom. Mag.* **2009**, *16*, 81–94. [CrossRef]

25. Vanderborght, B.; Albu-Schaeffer, A.; Bicchi, A.; Burdet, E.; Caldwell, D.G.; Carloni, R.; Catalano, M.; Eiberger, O.; Friedl, W.; Ganesh, G.; et al. Variable impedance actuators: A review. *Robot. Auton. Syst.* **2013**, *61*, 1601–1614. [CrossRef]

26. Wu, Y.S.; Lan, C.C. Linear variable-stiffness mechanisms based on preloaded curved beams. *J. Mech. Des.* **2014**, *136*, 122302. [CrossRef]

27. López-Martínez, J.; Blanco-Claraco, J.L.; García-Vallejo, D.; Giménez-Fernández, A. Design and analysis of a flexible linkage for robot safe operation in collaborative scenarios. *Mech. Mach. Theory* **2015**, *92*, 1–16. [CrossRef]

28. Lau, D.; Oetomo, D.; Halgamuge, S. Wrench-Closure Workspace Generation for Cable Driven Parallel Manipulators using a Hybrid Analytical-Numerical Approach. *ASME J. Mech. Des.* **2011**, *133*, 071004. [CrossRef]

29. Duan, Q.J.; Duan, X.C. Workspace Classification and Quantification Calculations of Cable-Driven Parallel Robots. *Adv. Mech. Eng.* **2014**, *6*, 358727. [CrossRef]

30. Phama, C.B.; Yeo, H.S.; Yang, G.L.; Chen, M. Workspace analysis of fully restrained cable-driven manipulators. *Robot. Auton. Syst.* **2009**, *57*, 901–912. [CrossRef]

31. Bosscher, P.; Riechel, A.; Ebert-Uphoff, I. Wrench-feasible workspace generation for cable-driven robots. *IEEE Trans. Robot.* **2006**, *22*, 890–902. [CrossRef]

32. Yuan, H.; Courteille, E.; Deblaise, D. Static and dynamic stiffness analyses of cable-driven parallel robots with non-negligible cable mass and elasticity. *Mech. Mach. Theory* **2015**, *85*, 64–81. [CrossRef]

33. Amare, Z.; Zi, B.; Qian, S.; Du, J.L.; Ge, Q.J. Three-dimensional static and dynamic stiffness analyses of the cable driven parallel robot with non-negligible cable mass and elasticity. *Mech. Based Des. Struct.* **2017**, *46*, 455–482. [CrossRef]

34. Nguyen, D.Q.; Gouttefarde, M.; Company, O.; Pierrot, F. On the Simplifications of Cable Model in Static Analysis of Large-Dimension Cable-Driven Parallel Robots. In Proceedings of the IEEE/RSJ International Conference on Intelligent Robots and Systems (IROS), Tokyo, Japan, 3–7 November 2013; pp. 928–934.

35. Rogier, D.R.; Mitchell, R.; Amir, K. Out-of-plane vibration control of a planar cable-driven parallel robot using a multi-axis reaction system. *IEEE/ASME Trans. Mech.* **2018**, *23*, 1684–1692.

36. Zhang, S.; Cao, D.X.; Hou, B.; Li, S.; Min, H.; Zhang, X.L. Analysis on variable stiffness of a cable-driven parallel-series hybrid joint toward wheelchair-mounted robotic manipulator. *Adv. Mech. Eng.* **2019**, *11*, 1–12. [CrossRef]

37. Nguyen, D.Q.; Gouttefarde, M. Stiffness Matrix of 6-DOF Cable-Driven Driven Parallel Robots and Its Homogenization Advances in Robot Kinematics. In *Advances in Robot Kinematics*; Springer: Cham, Switzerland, 2014; pp. 181–191.

38. Khalilpour, S.A.; Taghirad, H.D.; Habibi, H. Wave-Based Control of Suspended Cable Driven Parallel Manipulators. In Proceedings of the 2017 5th International Conference on Control Instrumentation and Automation, Shiraz, Iran, 21–23 November 2017; pp. 173–178.

39. Behzadipour, S.; Khajepour, A. Stiffness of cable-based parallel manipulators with application to stability analysis. *ASME J. Mech. Des.* **2006**, *128*, 303–310. [CrossRef]

40. Wu, G. Stiffness analysis and optimization of a co-axial spherical parallel manipulator. *Model. Ident. Control* **2014**, *35*, 21–30. [CrossRef]

41. Hoevenaars, A.G.L.; Lambert, P.; Herder, J.L. Jacobian-based stiffness analysis method for parallel manipulators with non-redundant legs. *J. Mech. Eng.* **2016**, *230*, 341–352. [CrossRef]

42. Anson, M.; Alamdari, A.; Krovi, V. Orientation workspace and stiffness optimization of cable-driven parallel manipulators with base mobility. *J. Mech. Robot.* **2017**, *9*, 031011. [CrossRef]

43. Yuan, H.; Courteille, E.; Gouttefarde, M.; Hervé, P. Vibration analysis of cable-driven parallel robots based on the dynamic stiffness matrix method. *J. Sound. Vib.* **2017**, *394*, 527–544. [CrossRef]

44. Duan, Q.J.; Vashista, V.; Agrawal, S.K. Effect on wrench-feasible workspace of cable-driven parallel robots by adding springs. *Mech. Mach. Theory* **2015**, *86*, 201–210. [CrossRef]

45. Mustafa, S.K.; Agrawal, S.K. Force-Closure of Spring-Loaded Cable-Driven Open Chains: Minimum Number of Cables Required & Influence of Spring Placements. In Proceedings of the 2012 IEEE International Conference on Robotics and Automation, Saint Paul, MN, USA, 14–18 May 2012; pp. 1482–1487.

46. Taghavi, A.; Behzadipour, S.; Khalilinasab, N.; Zohoor, H. Workspace Improvement of Two-Link Cable-Driven Mechanisms with Spring Cable. In *Cable-Driven Parallel Robots*; Springer: Berlin, Germany, 2013; pp. 201–213.

47. Gao, B.T.; Song, H.G.; Zhao, J.G.; Guo, S.X.; Sun, L.X.; Tang, Y. Inverse kinematics and workspace analysis of a cable-driven parallel robot with a spring spine. *Mech. Mach. Theory* **2014**, *76*, 56–69. [CrossRef]

48. Yigit, C.B.; Boyraz, P. Design and modeling of a cable-driven parallel-series hybrid variable stiffness joint mechanism for robotics. *Mech. Sci.* **2017**, *8*, 65–77. [CrossRef]

49. Krużelecki, J.; Życzkowski, M. On the concept of an equivalent column in the stability problem of compressed helical springs. *Arch. Appl. Mech.* **1990**, *60*, 367–377. [CrossRef]

50. Leech, A.R. A Study of the Deformation of Helical Springs under Eccentric Loading. Ph.D. Thesis, Naval Postgraduate School, Monterey, CA, USA, 1994.

51. Timoshenko, S.; Gere, J. *Theory of Elastic Stability*; McGraw-Hill: New York, NY, USA, 1961; p. 142.

52. Hay, A.M.; Snyman, J.A. Optimization of a planar tendon-driven parallel manipulator for a maximal dextrous workspace. *Eng. Optimiz.* **2005**, *37*, 1–20. [CrossRef]

53. Bolboli, J.; Khosravi, M.A.; Abdollahi, F. Stiffness feasible workspace of cable-driven parallel robots with application to optimal design of a planar cable robot. *Mech. Mach. Theory* **2019**, *114*, 19–28. [CrossRef]

54. Raiss, P.; Rettig, O.; Wolf, S.; Loew, M.; Kasten, P. Range of Motion of Shoulder and Elbow in Activities of Daily Life in 3D Motion Analysis. *Z. Orthop. Unfall.* **2007**, *145*, 493–498. [CrossRef]

Detection of Communities within the Multibody System Dynamics Network and Analysis of Their Relations

Daniel García-Vallejo [1,*,†]**, Alfredo Alcayde** [2,†]**, Javier López-Martínez** [2,†] **and Francisco G. Montoya** [2,†]

1   Department of Mechanical Engineering and Manufacturing, Universidad de Sevilla, 41092 Seville, Spain
2   Department of Engineering, Universidad de Almeria, 04120 Almería, Spain; aalcayde@ual.es (A.A.); javier.lopez@ual.es (J.L.-M.); pagilm@ual.es (F.G.M.)
*   Correspondence: dgvallejo@us.es; Tel.: +34-954-481354
†   These authors contributed equally to this work.

Abstract: Multibody system dynamics is already a well developed branch of theoretical, computational and applied mechanics. Thousands of documents can be found in any of the well-known scientific databases. In this work it is demonstrated that multibody system dynamics is built of many thematic communities. Using the Elsevier's abstract and citation database SCOPUS, a massive amount of data is collected and analyzed with the use of the open source visualization tool Gephi. The information is represented as a large set of nodes with connections to study their graphical distribution and explore geometry and symmetries. A randomized radial symmetry is found in the graphical representation of the collected information. Furthermore, the concept of modularity is used to demonstrate that community structures are present in the field of multibody system dynamics. In particular, twenty-four different thematic communities have been identified. The scientific production of each community is analyzed, which allows to predict its growing rate in the next years. The journals and conference proceedings mainly used by the authors belonging to the community as well as the cooperation between them by country are also analyzed.

Keywords: multibody; cooperation; community; modularity

1. Introduction

Since the amazing designs of Leonardo da Vinci to our days, the complexity of the mechanisms that man has used has only increased. Lighter materials, more economical designs, harder operating conditions, etc., are some of the objectives that the mechanical engineers of our days face. Fortunately, the level of difficulty that we face today is a reflection of the degree of development that has been achieved in mechanical engineering.

A mechanism can be understood as a set of solids interconnected with the purpose of transferring movements and/or forces from a source to an output [1]. The study of mechanisms has traditionally been dealt with by the theory of machines and mechanisms. However, the complexity in the design of mechanisms seems to be unlimited and, therefore, the interest in this branch of mechanics has been growing over time. In a multibody system, the subject of study of multibody system dynamics, in general, one can find rigid and flexible solids interconnected by ideal or non-ideal kinematic joints and subjected to the action of external forces and/or movement restrictions.

The first textbook entirely dedicated to the dynamics of multibody systems appeared in 1977 and was written by Wittenburg [2]. The computational approach seems to be a common characteristic

of the works that fall within multibody system dynamics (MBS) and one that confers a character not always present in the whole field of the theory of machines and mechanisms.

In 1977, supported by the IUTAM (international union of theoretical and applied mechanics), the first international symposium on multibody system dynamics (MBS) was held in Munich. It might be said that another important milestone was the big international conference around the MBS that took place in Iowa City in 1983, organized by the NATO advanced study institute. In our days there are many institutions that concentrate their interest on the MBS and in almost all conferences on mechanical engineering a session on MBS is included. The interest continues to grow in such a way that nowadays the already consolidated techniques of the MBS are exported to many fields of technology, such as the dynamics of railway vehicles [3], satellites [4], or nano and micro-mechanical systems [3,5]. In 1997, the international journal *Multibody System Dynamics* was born including in its first number two review articles signed by A. Shabana [6] and W. Schielen [3] where a journey through the history of the MBS is made and some of the applications that were most beginning to arouse interest were pointed out. In 2007, Werner Schiehlen [7] retrospectively looked at the first ten years of life of the journal *Multibody System Dynamics*, identifying a multibody system dynamics community and pointing out the research trends during that decade. Today, there are two international journals, *Multibody System Dynamics* and *Proceedings of the Institution of Mechanical Engineers, Part K: Journal of Multi-body Dynamics*, fully dedicated to MBS and many others that accept contributions from this field. The present paper proposes a step forward in the characterization of the MBS network. By using an automated paper metadata extraction tool, together with visualization and programming tools, a massive amount of documents will be analyzed to look for thematic communities that have grown inside the MBS network around certain topics. This will allow to understand which are the topics in which the research activity is more intense and to find communities that might be unknown for many members of the MBS network. In addition, once the communities are defined this paper aims at studying the activity trends along time.

The tools developed by MBS are supported by the most elementary laws of physics. In fact, already d'Alembert in 1743 [8] raised the equations of a system of rigid bodies subject to certain constraints, where the concept of reaction forces was already included. However, the first systematic analysis of a system of interconnected bodies was made by Lagrange in 1788 [8] laying the bases of what is today known as analytical mechanics. The equations of the first and second kind presented by Lagrange [8] constituted the DAE systems (differential algebraic equations) and ODE (ordinary differential equations) that describe the motion of a multibody system. Unfortunately, at that time there were no numerical techniques nor computers that would allow to obtain the solution of any system. Today, the complexity of the equations of motion has motivated the search for procedures that allow them to be obtained with the least possible effort. A wide review of these procedures can be found in the work of H. Bremer [9].

The development of computer science and numerical techniques has been, therefore, of central importance for the consolidation of the MBS. Several general-purpose programs for the analysis and simulation of multibody systems such as ADAMS, RECURDYN or DADS have been released to the market. In addition, there are open source simulation codes that might be used in MBS applications. Multibody system dynamics follows a continuous development and simultaneously offers tools in an excellent state of maturity.

In a multibody system, the absolute motion of a solid with respect to a reference, which is defined by a set of absolute coordinates, can be considered as the superposition of large rotations and deformations. This motion with respect to the inertial reference is mathematically defined by the time evolution of a set of variables. If a body is rigid, there is a minimum of six variables that completely define its spatial motion. In addition, the motion of a rigid body can be described by a larger set of variables that satisfies certain relationships. Such relationships translate into mathematical constraint equations that are solved together with the system differential equations of motion. Nevertheless, if the bodies are flexible the number of degrees of freedom is in principle infinite. The concept of symmetry

has been used many times to find simplified and computationally efficient multibody models, either rigid or flexible, in vehicle dynamics, biomechanics and other fields of application.

The dynamics of the rigid bodies included in a certain multibody system can be described by different sets of coordinates. In some cases it is possible to use the Lagrange equations of the second kind, that is, using a minimum set of coordinates equal to the number of degrees of freedom [8]. In such a case, one talks about 'independent coordinates'. However, the use of this type of coordinate is not systematic and, therefore, the programming of the equations of motion is reduced to some particular cases.

Using a larger set of variables to obtain the equations of motion usually leads to less cumbersome mathematical equations [10]. The dynamic problem can be formulated according to Lagrange's equations of the first kind, which constitutes a system of differential algebraic equations, and the set of coordinates are called 'dependent'.

Within dependent coordinates, 'relative', 'reference point coordinates' or 'Cartesian' coordinates are used. Relative coordinates refer to position or orientation of any body with respect to another one to which it is connected [11]. On the other hand, the reference point or Cartesian coordinates refer the position and orientation of each body to a global frame [12]. In general, reference point coordinates contain the components of a vector of position and a set of angles or angular parameters that define the orientation of a body reference frame in the global frame.

During the 1980s, a new methodology for a rigid multibody system based on fully Cartesian coordinates appeared. Such coordinates were known as 'natural coordinates' [13,14]. Unlike reference point coordinates, which include angles or angular parameters [15], the natural coordinates are composed of vectors of position of material points or vectors that define trajectories in solids [13], that is, exclusively Cartesian coordinates. The method of natural coordinates allows sharing coordinates between different solids since, in general, such coordinates belong to points or vectors that define the kinematic joints that connect solids to each other. This feature results in a significant reduction in the total number of coordinates required to model a mechanism. Unda et al. [16] performed a comparative study between the use of natural coordinates and the point of reference, concluding that the number of natural coordinates is always lower than that of the reference point coordinates.

The dynamics of flexible multibody systems (FMBS) has been a subject of major interest over time. In 2003, Wasfy and Noor [5] published an exhaustive bibliographic review (including 877 references) of the work carried out in the field of flexible MBS. In that reference, the different formulations for FMBS are classified into three groups according to the type of reference frames used to define the system variables. These three groups are the methods that use a floating frame of reference, those that use co-rotational reference frames and those that use the inertial frame only. The description of the deformation that a flexible body undergoes during general motion usually requires the use of a large number of coordinates. There are many approaches that have been successfully used in MBS, each one characterized by a certain choice of coordinates, measurement of deformations, etc.

The floating frame of reference formulation (FFR) appeared in the 1960s as a result of the research carried out in the field of machine dynamics, aerospace applications and the finite element method [6]. As a logical extension of the formulations based on reference point coordinates, the FFR uses the description of the motion of a moving reference frame linked to the flexible body to represent large rotations. The motion of such a reference frame can be described using any of the coordinate sets used for rigid solids. The most used set of coordinates has been the reference point coordinates [17]. Moreover, the natural coordinates are successfully employed to describe the motion of the floating frame of reference [18]. In the FFR, deformation has been described by different techniques such as the modal expansion [18] or the finite element method [17]. The FFR is mainly appropriate for applications where deformations are small, although non-linear effects such as geometric stiffening could also be addressed in this formulation [19]. In addition, the FFR allows the use of component mode synthesis [17] to reduce the number of system coordinates.

Co-rotational formulations use a frame of reference, called the co-rotational frame, which follows approximately the rigid body motion of each finite element. In this sense, this formulation differs from the FFR, which uses a single reference system for all the elements of the same body. This procedure was initially used by Belitschko and Hsieh [20] to triangular plate elements and two-dimensional beam elements. One can follow different criteria to define the co-rotational frame in which its motion does not need to coincide with the motion of any point of the finite element. This formulation made possible the use of non-isoparametric elements by incremental procedures, given that these elements can only describe small rotations. When using this approach, the use of integration methods that conserve energy and momentum is important, especially when the number of time increments used in the integration is large [20]. In co-rotational approaches, geometrically non-linear effects are incorporated automatically. However, component mode synthesis is not easily applicable.

Methods based on inertial coordinates use a single reference frame to describe the general motion of the flexible body. All variables are defined in the global inertial frame. The first applications of this kind of method in MBS are the works of Simo [21] and Simo and Vu-Quoc [22,23]. In the formulation of Simo [22], the position of an arbitrary point in an element is obtained by interpolation of the position vectors of the nodes and the rotations of the extreme sections. It is possible to use a similar description in which, instead of interpolating rotations that define the orientation of the cross section reference frame, one interpolates the vectors of the element frame itself [14,24]. This description must include non-linear constraints that ensure orthogonality and normality of the frame vectors. Both formulations, that of Simo [21,22] and Avello [24], fit within the so-called 'large rotation vector formulations'.

The formulation in absolute nodal coordinates, the absolute nodal coordinate formulation (ANCF) [17,25,26], also uses a set of coordinates defined in an inertial reference frame. This formulation was originally developed using a local reference frame to measure the deformations of the finite elements [17,27], so it could be considered as a co-rotational method. However, subsequent works on this formulation focused on the use of the inertial reference frame as the unique frame to measure deformations in the finite elements [28–31]. For this reason, non-linear deformation measures such as Green–Lagrange stress tensor where introduced. From these works on, the ANCF can be considered a fully inertial method. The identifying characteristic of the ANCF is the use of partial derivatives of the nodal position vector with respect to the geometrical parameters of the elements, also called slopes, as nodal variables, instead of small or large rotations [17]. The element mass matrix is constant in most of the developed elements and no terms appear due to centrifugal or Coriolis inertial forces in the equations of motion. The ANCF lacks some of the problems associated with incremental formulations related to the description of rigid body inertia [32]. From the work of Omar and Shabana [29], finite isoparametric elements are parametrized as surfaces, in two-dimensional models, or volumes [30,31,33]. In beam or plate elements, shear and cross-section deformations are inherently included. The use of a non-linear deformation measure as the tensor of Green–Lagrange together with the volumetric description of the kinematics of beam elements gave rise to an inaccurate displacement field due to several numerical locking effects [34,35]. With time, many of these numerical shortcomings were overcome. Over the years, many researchers have contributed to the development of the ANCF, see, for instance, references [36–38], and many applications have been dealt with by this formulation. An extensive review on the use and application of the ANCF can be found in Gerstmayr et al. [39].

After briefly introducing some important issues of the multibody system dynamics, the work described in this document is outlined as follows. In order to analyze the presence of thematic communities within the field of multibody system dynamics, a massive amount of data has been collected from Scopus, the well acknowledged abstract and citation database owned by Elsevier. This information is gathered with the help of a bot as explained in the next section. This information is processed in a visualization software called Gephi [40], which is specially designed to explore large networks. The information is represented as a large set of nodes with connections to study their graphical distribution and explore geometry and symmetries. A randomized radial symmetry is found in the graphical representation of the collected information. The main results of the analysis are the

detection of a main community and a number of thematic communities, twenty-four of which are identified. A summary and conclusions drawn from the analysis are included in the last section.

2. Methodology

This section explains the methodology followed in this work to obtain and analyze the information on scientific publications in the field of multibody system dynamics. The methodology consists of two main steps. In the first step, specific software is used to gather the information from the literature, in particular the relevant information from the publications indexed in Scopus. In the second step, all the data obtained is processed to determine the relationship between the different elements and graphically identify the different scientific collaboration networks.

2.1. Automatically Gathering Information

The information was obtained from the Scopus database. Elsevier's Scopus was chosen because of its extensive coverage of peer-reviewed journals, being slightly higher in number than that of Web of Science [41]. To get the information, the research network bot (ResNetBot) [42] was used. ResNetBot is a software for the automatic extraction of information from Scopus and has previously been used in bibliometric studies in different scientific fields [43,44]. ResNetBot makes use of the API interface of Scopus to obtain information from articles, authors and institutions. The way this bot works is shown in the flowchart of Figure 1, which is divided into three phases:

(1) Get publication data. In the first phase ResNetBot obtains information from all publications (journal papers, conference proceedings and books) that contain the words 'multibody' or 'multi-body' in the title, abstract or keywords and are stored in the bot database.
(2) Get author data. For each unique author identification number (Author ID) extracted in the previous phase, ResNetBot obtains and stores the information available in Scopus about the author: Affiliations, publications and dates, number of citations and h-index.
(3) Collect collaboration networks. For each Author ID, the bot gets the Author IDs from the co-authors it has collaborated with, along with their affiliation, city and country.

Analyzing the papers that include the words 'multibody' or 'multi-body' in the abstract, keywords or title does not lead to the complete set of documents that could be included in the field of multibody system dynamics. In fact, a significant number of papers published in the journal *Multibody System Dynamics* do not meet this criterion. This research does not claim to be an analysis of the complete literature on multibody system dynamics. Instead, this research aims at collecting a sufficiently large amount of documents so that the different communities detected would be represented. According to the large number of documents that are analyzed (see following sections) the objective seems to have been fulfilled.

The data collected by ResNetBot is structured according to its corresponding field and is stored as a set of plain-text files using the JavaScript Object Notation (JSON) format [45]. Because the Scopus database contains a large amount of information from different sources, it is common to find inconsistencies in the data [46,47]. Thus, for example, when checking the keywords obtained from publications, one can find different expressions such as 'multi-body system dynamics', 'multibody system dynamics' or 'dynamics of multibody systems' with the same meaning. To resolve this inconsistency some of the refining algorithms of the OpenRefine software [48] have been applied, including the nearest neighbor and key collision methods [49–51]. Finally, all collected and refined information is organized in spreadsheets and stored in a local database.
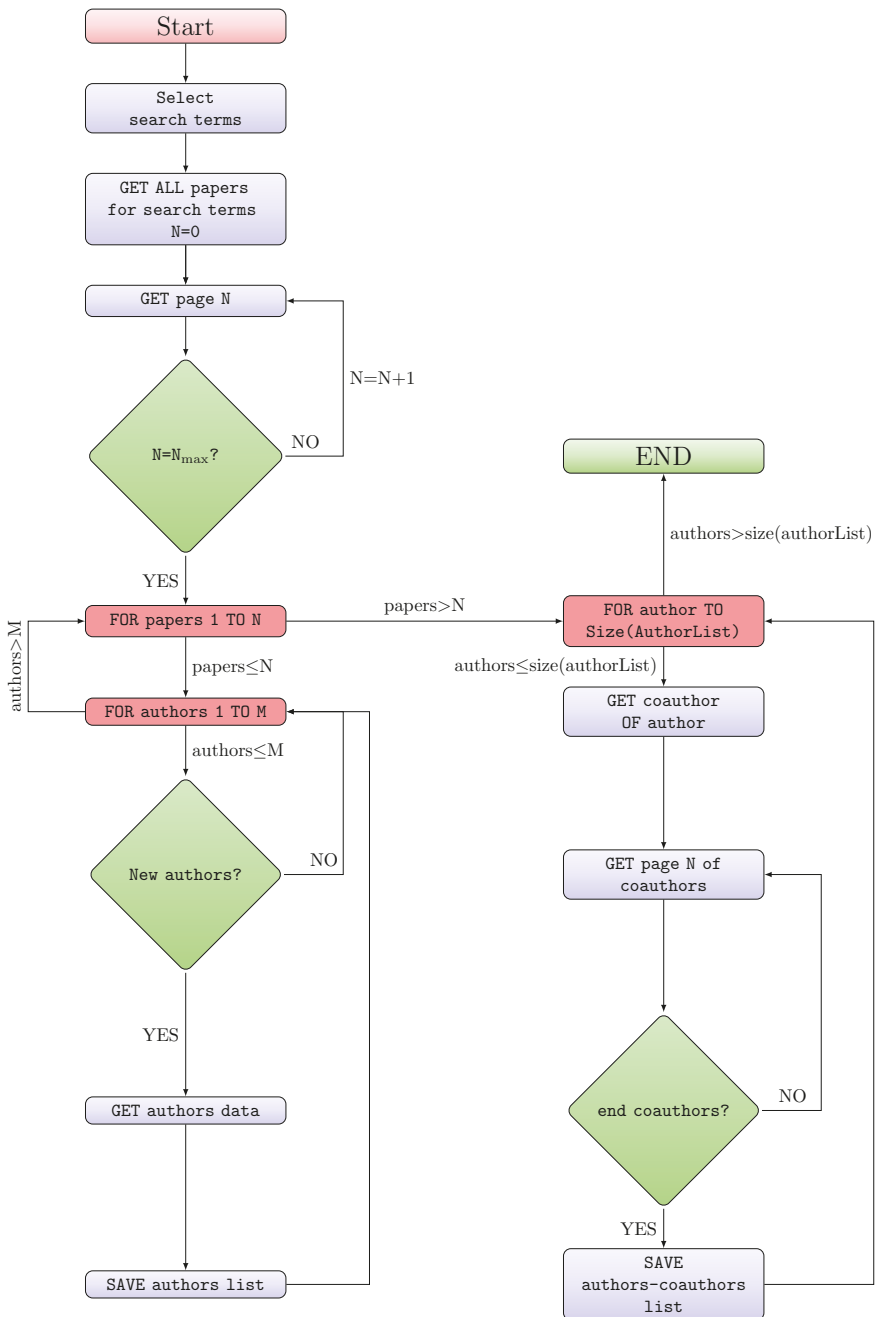
Figure 1. Flowchart of the implementation of ResNetBot.

2.2. Graphical Detection of Communities

Within a set of data (nodes) with common characteristics, a community consists of a group of nodes that are more interconnected with each other than with the rest of nodes in the network.

The problem of community detection therefore seeks to identify those nodes that, for a given special relationship, are connected in a denser way [52,53]. In bibliometric analysis the nodes may be the publications, and the connections the citations between them. Thus, a community could be determined as those groups of publications that are most cited in between them. In a different analysis the nodes may be the authors and the connections between them indicate that they have collaborated in some publication (they are co-authors). In this case a community will be identified as that group of authors who carry out more research together.

Given the large amount of data collected by ResNetBot, to help identify the presence of communities it is necessary to process the information using statistical analysis and graph-based visualization tools. The graphical representation will make it possible to visually identify the relationship between the nodes in the network. A node is represented as a point or vertex and the relationships between two nodes are shown with a line or edge joining both nodes. Graph-based visualization software includes several powerful visualization tools that allow detailed analysis and interpretation of graphical results. In this work, the open-source graph visualization tool Gephi [40] has been used.

Among others features, Gephi allows to modify the size of the nodes and the thickness of the edges according to some characteristics defined by the user, to group in the space the nodes that are more interconnected and to use different colors to identify in a fast way the relation between them and the presence of communities. For the detection of communities within the data network, Gephi uses modularity. Modularity [54] applies objective functions for the detection of communities and provides numerical values that represent the accuracy of the community structure. Together with the graphical visualization of the results, Gephi also offers a comprehensive statistical analysis of the data.

3. Analysis of Scientific Production and Community Detection

In order to find a sufficiently large amount of data that could be representative of the scientific work and authors related to multibody system dynamics, Scopus was used. An advanced query was launched, giving as a result a list of 20,050 papers including the words 'multibody' or 'multi-body' either in the title or in the abstract or in the keywords. The query was formulated as follows

```
(AUTHKEY(multibod*) OR AUTHKEY(multi-bod*) OR
ABS(multibod*) OR ABS(multi-bod*) OR
TITLE(multibod*) OR TITLE(multi-bod*)).
```

This query was launched at the end of July 2019 and included documents from 1953 to 2020. As explained in the previous section, all the information was downloaded with the help of the ResNetBot.

In order to process all the information in the visualization software Gephi, a list of nodes was generated, a node being a published document which is visible in SCOPUS. It must be recalled that SCOPUS includes journal papers, conference proceedings and books. A list of connections or edges between the nodes is generated by using the reference of the papers. Therefore, a document appears in the graph connected to all the documents it cites as well as to those documents that cite it. Loading the nodes and the relations, one can extract a lot of information from this massive amount of data.

3.1. Detection of a Main MBS Community

The first important result that can be visualized in Gephi is that not all the documents should be included in the MBS community. To explain this issue, Figure 2 is used. Figure 2a is the result of visualizing the 20,050 nodes with their relations. The layout tool ForceAtlas2 was used to distribute the documents using the concept of gravity to generate attraction between the nodes. Once this is done, Figure 2a appears showing that there is a large amount of papers, distributed in a ring shaped area that are not connected to the central community. This may be because these papers do not use the words 'multibody' or 'multi-body' in the same sense as the members of the community, and, in fact, they do not cite papers that belong to the main community. Therefore, a main community called the multibody

system community or MBS community is detected and shown for the first time in Figure 2b, where the unconnected documents (those in the ring) have been filtered.

According to the previous procedure, after filtering, the MBS community detected has a total of 11,511 documents.

(**a**) (**b**)
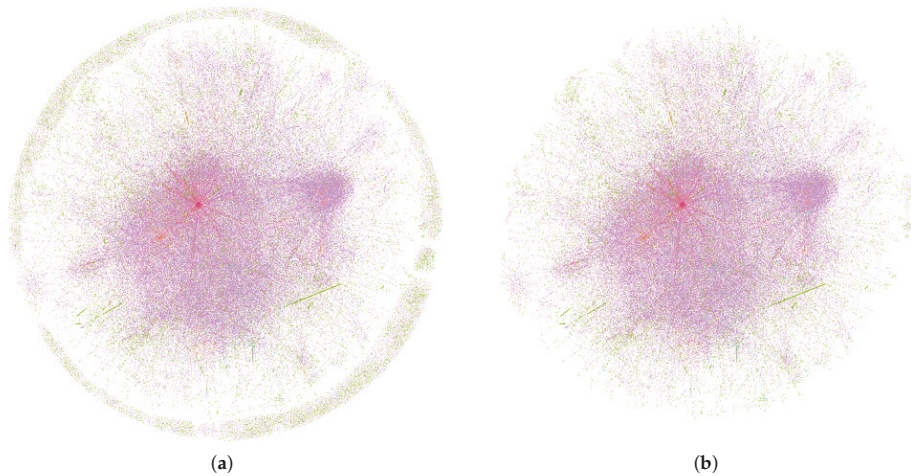
Figure 2. (**a**) Graph of all papers including either 'multibody' or 'multi-body' in the title, abstract or keywords; (**b**) graph of all the papers in the left picture showing connection (citations) between them.

In order to understand the most important topics that describe the community, the keywords of all the documents were collected. Using a Python subroutine, they were all translated to the lower case and the singular forms. A total of 36,774 keywords were collected. Then, the function 'Counter' from the module 'Collections' was used to count the number of appearances of all keywords. Table 1 shows the most utilized keywords in the document analyzed. From a view to the list of keywords, one may conclude that:

1. The most used keyword is *multibody dynamics*.
2. Multibody systems documents are mainly concerned with dynamics.
3. Simulation is a key issue in the community.
4. Flexibility appears as a top issue in the community.
5. It is interesting that one of the well known approaches for flexible multibody systems, the absolute nodal coordinate formulation, has achieved a high position in the rank, showing the large development that this formulation achieved in the last years.
6. 'Vehicle dynamics', 'optimization' and 'friction' are highly important issues according to their position in the rank of used keywords.

3.2. Detection of Thematic Communities

Within the main MBS community, one can find some thematic communities by analyzing the modularity class of all the papers included in it. The modularity tool in Gephi, which relays the algorithm from Blondel et al. [55], also known as the Louvain method, has been run with a resolution parameter value of 1.0, finding 32 communities with different sizes. Modularity is a scale value that measures the density of relations (citations) inside communities to relations outside communities. All these communities are shown in Figure 3 in different colors. The 32 detected communities have different sizes (number of papers included) ranging from 1103 for the biggest one to 4 for the smallest one. Since such small sizes do not seem to realistically define a community, only the first 24 detected communities have been analyzed in this work. The smallest of these 24 communities includes 152

papers, which allow one to understand the goal of such a community. In what follows, the 24 analyzed communities have been numbered from the largest (comm-1) to the smallest (comm-24).

Table 1. List of most commonly used keywords.

Keyword	# of Appearances	% of Appearance
multibody dynamics	1254	3.41
multibody system	751	2.04
simulation	302	0.82
dynamics	275	0.75
multibody	252	0.69
flexible multibody dynamics	226	0.61
multibody system dynamics	199	0.54
flexible multibody system	194	0.53
multibody simulation	166	0.45
finite element method	162	0.44
absolute nodal coordinate formulation	142	0.39
vehicle dynamics	140	0.38
optimization	125	0.34
friction	120	0.33
multibody model	114	0.31
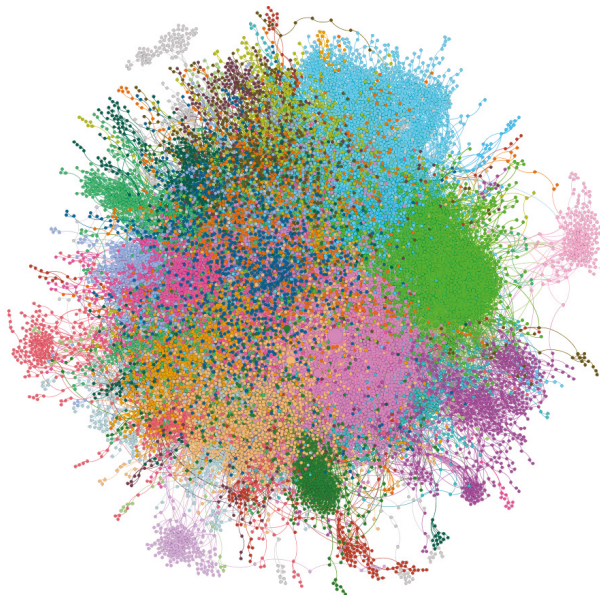
Figure 3. Graph of the detected communities inside the main multibody system dynamics (MBS) community.

Figure 3 shows a representation of the main MBS community and the 32 thematic communities. The community layout, that is, the distribution of individuals, was obtained by using the ForceAtlas2 algorithm included in Gephi. This algorithm uses the concept of gravity to calculate the attraction of the individuals. In the figure, all papers that cite one another are connected by an edge. The shape of the thematic communities is also meaningful. For a shape, size and distribution analysis of the communities, the selected 24 communities were plotted separately using the same reference frame in Appendix A. It may be noted that the shapes of the different communities are quite different. For example, there are some communities that are well concentrated in areas of the main MBS

community, while others are spread and overlap with each other. This behavior might be a consequence of the main topics of the community being either too specific or too general. The ones dealing with general topics are connected to documents of other (maybe many) communities and therefore are most likely to appear spread.

Once the communities are automatically identified by the modularity class tool, a careful review of the documents included in each community allows the identification of the main goals. It is interesting that every community usually has a number of highly cited documents, which is represented with a larger circle in Figure 3. The size is proportional to the number of relations (citations). In view of these goals, a representative name is given to each thematic community. The twenty-four identified communities are presented as follows.

comm-1 Flexible multibody systems in general. This is the largest community in terms of published documents, with a total of 1103. The documents in it cover many aspects related with the flexibility in the presence of large rotations and deformations. Significant attention has been paid in this community to the pioneering work of Kane et al. [56] about centrifugal stiffening in rotating beams. A very complete review of the work in this community was carried out by Noor and Wasfy [5].

comm-2 Railway. This community, with 1027 documents, deals with the dynamics of railway systems in general. There are many documents that focus on the problem of wheel/rail contact. As a highly cited reference, the work of Shabana et al. [57] presents an elastic contact method which seems to be highly efficient for simulation purposes.

comm-3 Absolute nodal coordinate formulation. Interestingly, a well structured community devoted to the development and application of the absolute nodal coordinate formulation is found with 963 documents. According to the shape and location of this community, see Appendix A, the documents are clearly attracted by the documents of this community but also by some of the flexible multibody systems in general. A particular book by Shabana [17] is a highly cited document . There is an extensive review of the work done by this community by Gerstmyer et al. [39].

comm-4 Contact and non-ideal joints. A community dedicated to contact problems with 890 references is found. This community is easily identified by the modularity class tool and appears well concentrated, see green community in Appendix A. Many documents have paid attention to elastic or continuous contact models with the work of Lankarani and Nikravesh [58] and Machado et al. [59] as highly visible references. Clearance in joints is also a highly investigated topic within this community.

comm-5 Computational aspects of differential algebraic equations (DAE). The particular numerical problems presented in differential algebraic equations (DAE) have attracted many researchers over time. Problems such as the numerical fulfillment of constraint equations, the numerical stability of integrators, etc., are present in this community with 841 documents. The review work of Bauchau and Laulusa [60] and the one about projection methods by Bayo and Ledesma [61] are highly cited within this community.

comm-6 Optimization and sensitivity. Optimization and sensitivity analysis in multibody systems deserves the interest of many researchers because of their benefits for design. The work of D. Bestle [62] has been a pioneer in this community and counts 592 references in our analysis.

comm-7 Two-wheelers. The dynamics of motorcycles and bicycles have been a specific topic of research for many authors of the multibody system network. The work of Cossalter and Lot [63] about a motorcycle multibody model is a remarkable reference that identifies the goals of this community well. An already old review by W. Kortüm [64] has received many citations from documents from a community that includes 525 works.

comm-8 Biomechanics. The use of multibody dynamics techniques in biomechanics has experienced a huge development in recent years, with even the release of proprietary (AnyBody) as well as open software (OpenSim) highly extended in the community which, counts 517 documents.

Multibody models for biomechanics usually include the dynamics of the biological actuators and are redundantly actuated, requiring the use of optimization methods. A highly cited work is the one by Damsgaard et al. [65] where the software AnyBody is presented to the community. Some of the results of the authors of this community have served as a basis for other applied and fundamental investigations, see, for example references [66,67].

comm-9 Accurate and efficient integrators. This community of 459 documents is mainly devoted to the development of efficient and accurate numerical integrators. The documents belonging to this community are well connected to those in the flexible multibody systems in general and the absolute nodal coordinate formulation communities. The topic of energy and momentum conserving numerical methods is one that is more present among the documents of this community. The work of Bauchau [68] and Betsch [69] have received many citations from the community.

comm-10 Robots as multibody systems. This community with 429 documents is concerned mainly with the applications of multibody systems techniques to robotics, including robots with flexible linkages, trajectory planning through optimization or the use of recursive formulations. There appears a highly cited book by A. Jain [70] that exemplifies the goals of this community.

comm-11 The vibration and transfer matrix method. Multibody systems containing elastic or restoring forces are susceptible of vibration. Linear and non-linear equations of motion are many times obtained with the methods of multibody systems. The transfer matrix method, which is connected to vibrating systems and extended by Rui et al. [71] to general multibody systems has a high impact in the works belonging to this community, which counts 421 documents.

comm-12 Aeronautic applications. The methods of multibody systems have encountered a large development and application in aeronautics as reflects this community with 406 documents. Problems of aeroelasticity, modeling of specific parts as rotors, landing gears, etc., or the stability of flight are presented in the documents of this community. The work of Masarati et al. [72] has been highly cited within the community.

comm-13 Marine applications. A total of 401 documents are encountered in this community, where hydrodynamic interaction, floatation and drift issues are of interest and are analyzed together with multibody models. There is a recent review of applications of MBS to ships and offshore structures by Lee and Roh [73].

comm-14 Powertrain elements. This community counts 399 documents that are mainly devoted to important aspects of powertrain dynamics as explained by Novotny and Pistek [74]. The high angular speeds in powertrain systems together with the flexibility of some components were the causes for the application of MBS techniques in this field, giving birth to a specific community. The dynamics of crankshafts is a topic of high interest in this community.

comm-15 Road vehicle dynamics. Multibody system dynamics has encountered a large application in vehicle system dynamics. The existence of this community with 321 documents probes this fact. The generation of a full vehicle multibody model with detailed suspension systems or the analysis of ride comfort or handling are hot topics in this community. The book by Blundell and Harty [75] is a highly cited reference in the community.

comm-16 Wind turbines. The analysis and simulation of wind turbines is the subject of many papers from this community of 308 documents. Within it, the modeling and simulation of gear box dynamics is a hot topic as reported by Helsen et al. [76]. In addition, modal analysis and aeroelasticity issues are also accounted for in many documents.

comm-17 Complex terrain and tracked vehicles. A community with 301 documents dedicated to the modeling and simulation of tracked vehicles has also been found. Among others, the work of Rubinstein and Hitron [77] has received many citations. Due to the special nature of this kind of vehicle, this community pays great attention to the modeling of complex terrains.

comm-18 Non-smooth contact. This community of 258 documents in our analysis focuses also on contact, but with a slightly different hint related to the discretization of the contact surfaces. Non matching discretizations are studied with the help of the concept of dual Lagrange

multiplier space, see reference [78]. In general, the works found in this community are strongly related with the finite element method in multibody contact situations, see Laursen and Simo [79], with geometric problems arising from the different discretizations of the contact surfaces. Friction and frictionless situations are considered with a focus on the formulation of equations and constraints more than on the frictional phenomenon.

comm-19 Space applications. There appeared a community with 227 documents that applies the methods of multibody system dynamics to space problems as attitude control of satellites or assembly of space structures by robotic manipulators. Control issues both for linear and nonlinear multibody systems are important in this kind of application, and is most of the time realized by autonomous systems. As an example, the work of Umetani and Yoshida [80] has a significant impact in the community.

comm-20 Friction. A community with a size of 196 documents around friction is found. Since friction requires contact, this community is related with both the contact and non-ideal joints (comm-4) and the non-smooth contact (comm-18) communities. It might make sense to group together the three mentioned communities into a large one (1295 documents). However, the particular hint of this community seems to be the friction phenomenon itself and for this reason the entity of the community has been respected. Complementary problems have been useful for the modeling of friction forces as, for example, reported by Anitescu and Potra [81].

comm-21 Flapping wings. A community with a size of 182 documents mainly focused on the analysis and modeling of flapping wings has been detected. Within this community one may find documents dealing with insect flight, micro aerial vehicles or different kinds of ornithopters, see reference [82]. Flapping wings are modeled as flexible structures for which the methods of flexible multibody systems encountered a challenging application.

comm-22 Accident reconstruction. Multibody system dynamics has been successfully applied to the reconstruction of accidents. Among other studies the kind of accident due to impacts of vehicle/pedestrian or falls are the most common. The dynamic simulation has been used to evaluate potential injuries as well as safety conditions. For example, in the highly cited document by Crocetta et al. [83] the influence of the vehicle front-end design on pedestrian ground impact is investigated. This community counts 169 documents in this analysis.

comm-23 Fatigue and life assessment. A community of 162 documents with the fatigue of materials as a main issue has been detected. Flexible multibody dynamics methods have proven to be useful for the evaluation of alternating stresses that can be used together with fatigue failure criteria for life assessment of components. As an example, the work of Dietz et al. [84] in the context of railway dynamics has received many citations.

comm-24 Computer numerical control (CNC) machining. This is the smallest community analyzed in this paper, with a size of 152 documents. Machining by computer numerical control (CNC) units is also fertile soil for application of multibody system dynamics. In this community, the evaluation of geometrical errors in the trajectory of the tool and their compensation are of major importance. CNC machines have different designs, with many axes and large mobility, that are successfully modeled with multibody system dynamics techniques. As a highly representative reference, one may take the work of Zhu et al. [85].

As a consequence of the common aspects of the documents of each community, by examining a list of the most used keywords one may also understand the goals of each community. Tables 2–5 show the most used fifteen keywords in each community. In order to find a more meaningful list of keywords for each community, the keywords 'multibody', 'multibody dynamics', 'multibody system' and 'multibody system dynamics' were excluded.

Table 2. List of most commonly used keywords in communities 1 to 6. The number of appearances of the keyword is included in parenthesis.

Most Commonly Used Keywords in the Following Communities: *Flexible Multibody Systems in General* (**comm-1**), *Railway* (**comm-2**), *Absolute Nodal Coordinate Formulation* (**comm-3**), *Contact and Non-ideal Joints* (**comm-4**), *Computational Aspects of DAE* (**comm-5**) and *Optimization and Sensitivity* (**comm-6**).

comm-1	comm-2	comm-3	comm-4	comm-5	comm-6
flexible multibody system (90)	wheel-rail contact (77)	absolute nodal coordinate formulation (178)	clearance joint (52)	differential-algebraic Equations (35)	flexible multibody system (41)
dynamics (33)	multibody simulation (37)	flexible multibody system (133)	friction (51)	dynamics (21)	sensitivity analysis (39)
elastic multibody system (24)	railway vehicle (36)	large deformation (38)	contact force (43)	vehicle dynamics (19)	optimization (24)
finite element method (23)	railway dynamics (33)	dynamics (29)	impact (42)	simulation (19)	crashworthiness (23)
model reduction (23)	wear (32)	finite element method (27)	contact (35)	real-time simulation (17)	topology optimization (17)
model order reduction (20)	vehicle dynamics (32)	simulation (25)	clearance (26)	redundant constraints (14)	vehicle dynamics (16)
simulation (18)	derailment (27)	absolute nodal coordinate (24)	dynamics (26)	constrained multibody system (14)	simulation (16)
modal analysis (15)	finite element method (25)	finite element (18)	contact dynamics (25)	numerical integration (12)	parameter identification (15)
rigid-flexible coupling (14)	vehicle-track interaction (25)	modeling (15)	joint clearance (25)	subsystem synthesis method (11)	dynamics (12)
dynamic stiffening (13)	simulation (21)	large displacements (14)	revolute clearance joint (24)	flexible multibody system (10)	elastic multibody system (11)
modeling (11)	high-speed train (20)	floating frame of reference (13)	contact model (17)	dae (10)	suspension (10)
floating frame of reference (10)	rolling contact fatigue (19)	flexible multibody system dynamics (12)	contact mechanics (17)	equations of motion (10)	optimal control (9)
stability (10)	locomotive (19)	model reduction (11)	simulation (17)	computer aided analysis (8)	adjoint variable method (8)
bifurcation (10)	co-simulation (19)	floating frame of reference formulation (11)	flexible multibody system (16)	impact (8)	vibrations (8)
component mode synthesis (10)	multibody model (18)	sliding joint (11)	unilateral constraints (15)	multibody simulation (8)	structural optimization (7)

Table 3. List of most commonly used keywords in communities 7 to 12. The number of appearances of the keyword is included in parenthesis.

Most Commonly Used Keywords in the Following Communities: *Two-wheelers* **(comm-7),** *Biomechanics* **(comm-8),** *Accurate and Efficient Integrators* **(comm-9),** *Robots as Multibody Systems* **(comm-10),** *Vibration and Transfer Matrix Method* **(comm-11)** *and Aeronautic Applications* **(comm-12).**

comm-7	comm-8	comm-9	comm-10	comm-11	comm-12
vehicle dynamics (27)	biomechanics (55)	flexible multibody dynamics (27)	dynamics (19)	transfer matrix method (80)	co-simulation (22)
motorcycle (26)	finite element analysis (34)	optimal control (24)	spatial operator algebra (11)	dynamics (21)	multibody simulation (18)
simulation (25)	multibody model (30)	lie groups (20)	high-speed train (11)	simulation (19)	stability (14)
modeling (22)	inverse dynamics (24)	differential-algebraic Equations (14)	simulation (10)	multiple launch rocket system (16)	aeroelasticity (12)
motorcycle dynamics (21)	simulation (21)	aeroelasticity (12)	polynomial chaos (9)	launch dynamics (16)	dynamics (8)
stability (20)	optimization (17)	time integration (12)	optimization (9)	vibration (10)	rotor (7)
dynamics (15)	gait (16)	constrained mechanical system (11)	uncertainty quantification (9)	discrete time transfer matrix method (9)	landing gear (7)
graph theory (12)	kinematics (15)	dynamics (9)	aerodynamics (8)	transfer matrix (8)	solver coupling (7)
bicycle dynamics (11)	multibody simulation (14)	natural coordinate (9)	inverse dynamics (8)	control (8)	turbocharger (6)
bond graph (11)	validation (14)	wind turbine (8)	uncertainty (8)	multibody simulation (8)	tiltrotor (6)
weave (10)	multibody dynamics analysis (12)	conserving time integration (7)	parallel computing (7)	natural frequency (8)	multibody model (5)
control (8)	musculoskeletal model (11)	finite rotations (7)	recursive algorithm (7)	rigid-flexible coupling (8)	helicopter (5)
flexible multibody system (8)	contact mechanics (11)	simulation (7)	flexible multibody system (6)	virtual prototype (7)	rotor dynamics (5)
wobble (8)	whiplash (10)	multibody model (6)	vehicle dynamics (6)	flexible multibody system (7)	vibration control (5)
optimal control (8)	knee (10)	nonlinear dynamics (6)	forward dynamics (6)	vibration control (7)	flight dynamics (5)

Table 4. List of most commonly used keywords in communities 13 to 18. The number of appearances of the keyword is included in parenthesis.

Most Commonly Used Keywords in the Following Communities: *Marine Applications* **(comm-13)**, *Powertrain Elements* **(comm-14)**, *Road Vehicle Dynamics* **(comm-15)**, *Wind Turbines* **(comm-16)**, *Complex Terrain and Tracked Vehicles* **(comm-17)** and *Non-smooth Contact* **(comm-18)**.

comm-13	comm-14	comm-15	comm-16	comm-17	comm-18
simulation (15)	vibration (23)	simulation (35)	wind turbine (49)	tracked vehicle (42)	finite element (14)
floating crane (14)	finite element method (19)	modelling (19)	gearbox (15)	dynamic simulation (14)	friction (11)
numerical simulation (14)	noise (18)	suspension (17)	drivetrain (12)	simulation (11)	multibody contact (11)
computational fluid dynamics (12)	diesel engine (17)	adams (15)	modal analysis (11)	terramechanics (9)	domain decomposition (9)
wave energy converter (10)	dynamics (14)	vehicle dynamics (14)	wind turbine gearbox (9)	virtual prototype (7)	frictional contact (8)
hydrodynamic interaction (9)	crankshaft (14)	dynamics (12)	drive train (9)	recurdyn (6)	finite element method (7)
dynamic response (8)	torsional vibration (12)	multibody model (10)	gear dynamics (8)	cvt (6)	dual lagrange multipliers (7)
virtual prototype (8)	simulation (12)	ride comfort (10)	dynamic response (8)	dynamics (5)	durability (7)
flexible multibody system dynamics (8)	flexible multibody dynamics (9)	vehicle handling (7)	simulation (8)	collaborative simulation (5)	linear elasticity (7)
dynamics (7)	crank train (8)	optimization (7)	flexible multibody (7)	rough terrain (5)	primal-dual active set strategy (6)
finite element method (7)	fatigue life (6)	leaf spring (7)	aeroelasticity (7)	deep ocean mining system (5)	fatigue life (6)
bond graph (6)	virtual prototype (6)	vibration (6)	flexible blade (7)	multibody dynamic model (5)	mortar finite element method (6)
drift force (6)	mixed lubrication (6)	virtual prototyping (6)	reliability (7)	suspension system (4)	scalability (6)
fpso (6)	harshness (6)	dynamic simulation (6)	dynamics (6)	electric vehicle (4)	contact problems (5)
hydrodynamics (6)	ic engine (6)	tyre model (5)	superelement (6)	track link (4)	multibody contact problem (5)

Table 5. List of most commonly used keywords in communities 19 to 24. The number of appearances of the keyword is included in parenthesis.

Most Commonly Used Keywords in the Following Communities: *Space Applications* **(comm-19)**, *Friction* **(comm-20)**, *Flapping Wings* **(comm-21)**, *Accident Reconstruction* **(comm-22)**, *Fatigue and Life Assessment* **(comm-23)** and *CNC Machining* **(comm-24)**.

comm-19	comm-20	comm-21	comm-22	comm-23	comm-24
optimal control (10)	coulomb friction (10)	co-simulation (12)	accident reconstruction (37)	fatigue life (12)	geometric error (29)
space robot (7)	contact (10)	vehicle (8)	head injury (21)	finite element method (10)	multibody system theory (26)
object manipulation (7)	friction (9)	semi-active suspension (8)	pedestrian (19)	fatigue life prediction (9)	error modeling (21)
attitude control (7)	parallel computing (7)	simulation (7)	multibody simulation (16)	fatigue analysis (6)	error compensation (20)
on-orbit servicing (7)	rigid bodies (6)	machine tool (6)	numerical simulation (11)	high-speed train (6)	machine tool (14)
motion planning (6)	collision detection (6)	dynamics (6)	madymo (10)	vibration (6)	sensitivity analysis (14)
numerical simulation (6)	contact dynamics (5)	flapping flight (6)	pedestrian safety (9)	simulation (6)	error identification (8)
flexibility (5)	rigid body dynamics (5)	insect flight (5)	impact biomechanics (7)	rigid-flexible coupling (6)	machining accuracy (8)
space manipulator system (5)	simulation (5)	modeling (5)	accident analysis (6)	fem (6)	five-axis machine tool (5)
underactuated system (5)	frictional contact (4)	ride comfort (5)	falls (6)	fatigue (5)	force ellipsoid (5)
space robots (5)	optimization (4)	vehicle engineering (4)	biomechanics (6)	virtual prototype (5)	multibody kinematics (5)
dynamics modelling (5)	complementarity (4)	control (4)	optimization (6)	dynamic stress analysis (5)	error measurement (4)
robotics (5)	modified state space (3)	aerial refueling (4)	vehicle-pedestrian collision (6)	carbody structure (5)	stiffness field (4)
rigid-flexible multibody system (5)	femdem (3)	butterfly (4)	crash simulation (6)	recurdyn (5)	ultra-precision machine (4)
nonlinear control (4)		optimization (4)	multibody model (5)	lunar lander (5)	homogeneous coordinate transformation (4)

3.3. Activity of the Communities along the Time

Once the communities have been introduced, it is easy to analyze the activity of each community. In this work, the activity is measured by the number of documents published per year in the community. This was done again by using the Counter subroutine of Python Collections library. The period analyzed comprises the years from 1970 to 2018. While some information is available for 2019 and 2020, these years were excluded from the analysis because the information is not complete. To reduce the noise in the trend lines of each community, a moving average using the numbers of two consecutive years was used. Figure 4 shows the trend lines obtained for the twenty-four communities.
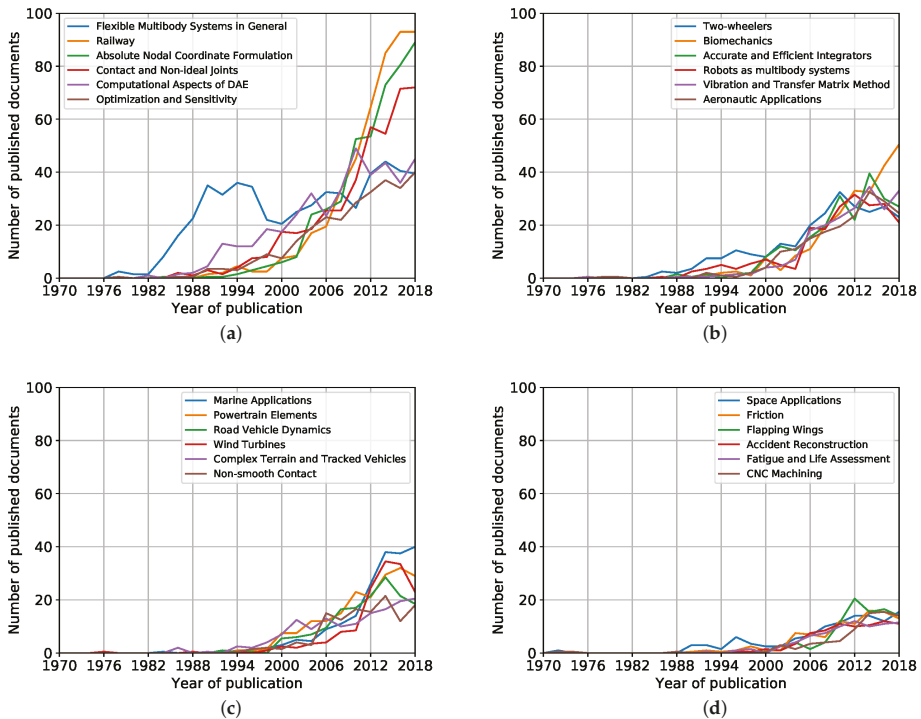
Figure 4. Activity of the communities measured as the number of journal papers per year: (**a**) comm-1 to comm-6; (**b**) comm-7 to comm-12; (**c**) comm-13 to comm-18; and (**d**) comm-19 to comm-24.

In general, Figure 4 shows a continuous increase in the number of published documents in all communities. From a look at Figure 4a, one may see that Flexible Multibody Systems in General was the first community to grow with a great interest in the eighties and early nineties. While it continues with moderate activities, other communities as *Railways*, *Absolute Nodal Coordinate Formulation* and *Contact and Non-ideal Joints* show a large activity and growing trend for the coming years. From Figure 4b, it is interesting how *Two-wheelers* was an early developed community that nowadays follows a moderate activity. The growing activity of the *Biomechanics* community predicts an increasing interests for the near future. From Figure 4c,d, the increasing activities of *Marine Applications* and *Space Applications* are remarkable.

3.4. Most Used Journals by MBS Community Members

Gephi allows an easy analysis of which journals prefer to use the authors of the MBS network. The analysis was done as follows. The total of 11,511 documents were filtered by type, selecting only journal publications. In this way, a total of 7579 journal publications were considered. Table 6 shows the percentages of the 7579 journal publications that were published in the fifteen most used journals. From a view to the table, it remains clear that the main journal is *Multibody System Dynamics*, which since 1997 has consolidated as a highly reputable journal. The position in the rank of two journals from the context of vehicle dynamics (*SAE Technical Papers* and *Vehicle System Dynamics*) is remarkable. With percentages close to 2.5%, a third group of journals is composed of *Nonlinear Dynamics*, *Journal of Computational and Nonlinear Dynamics* and *Proceedings of the Institution of Mechanical Engineers, Part K: Journal of Multi-body Dynamics*.

Table 6. List of the fifteen journals that have published more papers belonging to the MBS community.

Journal Name	% of Papers Published in the Journal
Multibody System Dynamics	7.76
SAE Technical Papers	4.22
Vehicle System Dynamics	4.20
Nonlinear Dynamics	2.61
Journal of Computational and Nonlinear Dynamics	2.57
Proceedings of the Institution of Mechanical Engineers, Part K: Journal of Multi-body Dynamics	2.44
Mechanism and Machine Theory	1.91
International Journal for Numerical Methods in Engineering	1.37
Journal of Sound and Vibration	1.35
Journal of Mechanical Science and Technology	1.28
Zhendong yu Chongji/Journal of Vibration and Shock	1.27
Computer Methods in Applied Mechanics and Engineering	1.25
Journal of Guidance, Control, and Dynamics	1.21
Computers and Structures	1.19
Civil-Comp Proceedings	1.07

3.5. Most Used Conference Proceedings by MBS Community Members

In a similar manner, the most used conference proceedings were analyzed. The total of 11,511 documents were filtered by type, selecting only conference proceeding publications. In this way, a total of 3236 conference proceeding publications was considered. Table 7 shows the percentages of the 3236 documents that were published in the fifteen most used conference proceedings.

From Table 7 it can be concluded that the *Proceedings of the ASME Design Engineering Technical Conference* together with the very successful *Proceedings of the ECCOMAS Thematic Conference on Multibody Dynamics* are the leading options in terms of number of published documents. However, it must be clarified that ASME publishes within the *Proceedings of the ASME Design Engineering Technical Conference* articles from conferences organized from 2001 to today. The presence in the rank of the *Proceedings of the International Offshore and Polar Engineering Conference* or *Proceedings of the International Astronautical Congress* are understood from the existence of thematic communities that have an affinity with the topic of these conferences. For the sake of comparison, the percentage of papers published in the proceedings of some serial conferences were analyzed next. To do that, all editions of the *ASME Design Engineering Technical Conferences* were grouped together. The same thing was done for all editions of the *Proceedings of the ECCOMAS Thematic Conference on Multibody Dynamics* and the *Proceedings of the International Astronautical Congress, IAC* and the results are shown together in Table 8. The percentage shown is calculated from the total number of conference proceeding papers.

Table 7. List of the fifteen conference proceedings that have published more papers belonging to the MBS community.

Conference Name	% of Papers Published in the Proceedings
Proceedings of the ASME Design Engineering Technical Conference	12.7
Proceedings of the ECCOMAS Thematic Conference on Multibody Dynamics 2013	2.19
ASME International Mechanical Engineering Congress and Exposition, Proceedings (IMECE)	2.16
Proceedings of the ASME International Design Engineering Technical Conferences and Computers and Information in Engineering Conference—DETC2005	2.13
Proceedings of the ECCOMAS Thematic Conference on Multibody Dynamics 2015, Multibody Dynamics 2015	2.04
Proceedings of the International Offshore and Polar Engineering Conference	1.95
2007 Proceedings of the ASME International Design Engineering Technical Conferences and Computers and Information in Engineering Conference, DETC2007	1.82
Proceedings of the International Conference on Offshore Mechanics and Arctic Engineering—OMAE	1.70
Annual Forum Proceedings—AHS International	1.67
Collection of Technical Papers—AIAA/ASME/ASCE/AHS/ASC Structures, Structural Dynamics and Materials Conference	1.45
Proceedings of the International Astronautical Congress, IAC	1.42
Proceedings of the 8th ECCOMAS Thematic Conference on MULTIBODY DYNAMICS 2017, MBD 2017	1.36
Proceedings - IEEE International Conference on Robotics and Automation	1.36
Advances in the Astronautical Sciences	1.36
5th Asian Conference on Multibody Dynamics 2010, ACMD 2010	1.30

Table 8. Conference proceedings grouped by series that have published a significant amount of papers of MBS community.

Conference Name	% of Papers Published in the Proceedings
Proceedings of the ASME Design Engineering Technical Conference	17.4
Proceedings of the ECCOMAS Thematic Conference on Multibody Dynamics	5.51
Proceedings of the International Astronautical Congress, IAC	2.08

3.6. Analysis of Collaborations of Authors by Country

As explained in Section 2, all the authors that have published a document including the words 'multibody' or 'multi-body' in the title, abstract or keywords were considered. The information of a total of 30,502 authors was gathered and analyzed. This massive amount of information is represented in Figure 5a where the layout algorithm ForceAtlas2 has been used to find a meaningful representation. As mentioned before, the ForceAtlas2 layout is based on the concept of gravity, which is used to generate attraction between connected nodes. On the contrary, non-connected nodes generate repulsion between each other. As may be seen in the figure, there is a group of authors represented in green near the center of the graph that show no connection with surrounding authors. The same situation is shown for a group represented in gray near the mid-south part of the graph. Both groups of authors are strongly attracted between them but unconnected to the rest of the nodes. In addition, there are small clusters of authors allocated at the outermost part of the graph. Again, the giant component filter of Gephi has been used to separate the large network of authors contributing to the MBS communities. The MBS network is represented independently in Figure 5b. Once the main network of authors, which counts 9148 authors, is obtained, it will be redistributed with the ForceAtlas2 layout. The result is shown in Figure 6 where each color represents a different country. It must be emphasized that the affiliation considered for each author is the current (or last) one. The analysis presented does not take into account that an author might have had a different affiliation in the past. Therefore, the results shown in this section may be considered as a current picture of the community.
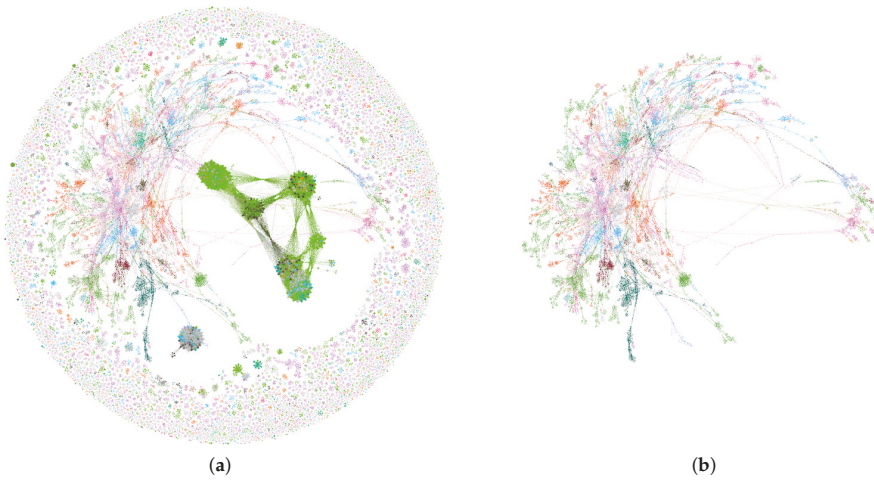
Figure 5. (**a**) Graph of all authors who have published a paper including the word 'multibody' in the title, abstract or keywords; (**b**) graph of all authors in the left picture that are included to the MBS network.
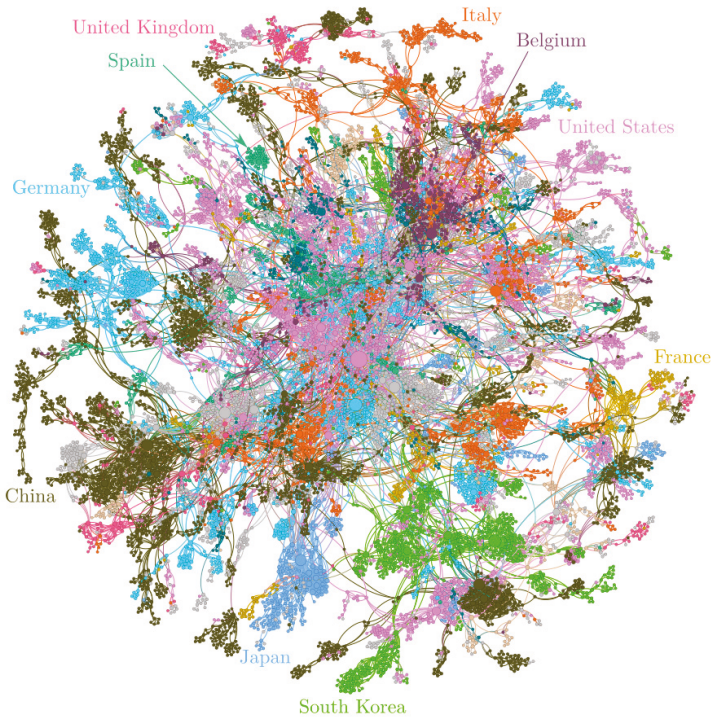
Figure 6. Graph of authors network by country of affiliation after redistribution.

The shape and location of the different countries in Figure 6 is interesting. Note that when a color is too concentrated in a small area, it means that the authors of that country are mainly working within them, that is without international cooperation. This is approximately the case of South Korea and Japan, which at the same time show large percentages of authors in Table 9. This table shows the

percentage of authors that belong to the twenty countries with the largest number of researchers in the network. The top ten countries have been colored in Figure 6. On the other hand, the authors of United States (purple color) are spread all along the graph, which means this country has a large international cooperation. In Figure 6, there are some nodes that have a comparatively large size. The size in the graph is proportional to the number of connections of the node. In this way, the largest node in the graph is in purple color and corresponds to Prof. A. Shabana. It must be mentioned that there is a certain amount of nodes in gray. They all belong to the rest of the countries not included in the top ten.

Table 9. Table of the twenty most active countries in MBS according to the total number of researches that have published at least one document.

Country	Percentage of Authors by Country
China	22.05
United States	16.33
Germany	11.43
Italy	8.38
South Korea	6.34
Japan	3.66
United Kingdom	3.21
Spain	2.83
Belgium	2.69
France	2.68
Canada	2.51
Netherlands	2.36
Austria	1.88
Sweden	1.08
Finland	1.04
Portugal	1.04
Denmark	0.80
Australia	0.71
Switzerland	0.67
Czech Republic	0.59

4. Summary and Conclusions

This work contains an analysis of a massive amount of information about publications and authors in the multibody system dynamics community. The information was gathered automatically by a dedicated bot that connects to the SCOPUS database. The amount of authors and documents considered are 30,502 and 20,050, respectively. The query to SCOPUS was launched in July 2019. This massive amount of data is treated with the software Gephi, which allows for filtering and detecting communities. The modularity class was used to detect a high number of communities within the multibody system dynamics network. Each community was commented on and a representative reference was given for each one. Once the communities were detected, the scientific production of each community was studied chronologically. The most used journals and conference proceedings were obtained. Finally, the cooperation of authors was studied by country. The main conclusions of this work are enumerated as follows:

1. ResNetBot was highly efficient at collecting a huge amount of data from the abstract and citation database, SCOPUS. Such an amount of data could be analyzed by using the software Gephi.
2. There appear to be 32 communities from the analysis of the modularity. In this paper, only the 24 largest communities were studied. The community detection carried out showed a reasonable result since the documents conforming to a community have meaningful similarities and common objectives.
3. The five largest communities are flexible multibody systems in general, railway, absolute nodal coordinate formulation, contact and non-ideal joints, computational aspects of DAE.

4. The recent activity analyzed by communities predicts an increasing interest in railway, absolute nodal coordinate formulation, contact and non-ideal joints and biomechanics.
5. The fifteen journals most used for publishing by researchers were obtained, with the journal *Multibody System Dynamics* being the one that has published the largest number of papers from the analyzed network.
6. The fifteen conference proceedings most used for publishing by researchers were obtained. The list included conferences from fields like astronautical sciences or offshore engineering.
7. Authors from many countries are contributing to the multibody system dynamics communities. The most active countries in the network have been found. Their cooperation was analyzed, obtaining interesting patterns of collaborations in the graph.

As could be checked, the multibody system community continues to grow and attract researchers. Its formalisms and techniques have been applied in many fields from railway to the simulation of the flight of ornithopters or the reconstruction of accidents.

Author Contributions: D.G.-V. performed the literature review and article writing. D.G.-V., A.A., J.L.-M. and F.G.M. analyzed the data using community detection methods. D.G.-V., A.A., J.L.-M. and F.G.M.: Research idea, article writing, and formatting; they jointly contributed to the structure and aims of the manuscript, paper drafting, editing, and review. All authors have read and approved the final manuscript.

Conflicts of Interest: The authors declare no conflict of interest.

Appendix A. Fingerprint Images of all Detected Communities

This section shows a picture of each one of the twenty-four analysed communities, where the shape, distribution and size of each one can be appreciated (Figures A1 and A2).

comm-1   comm-2   comm-3

comm-4   comm-5   comm-6
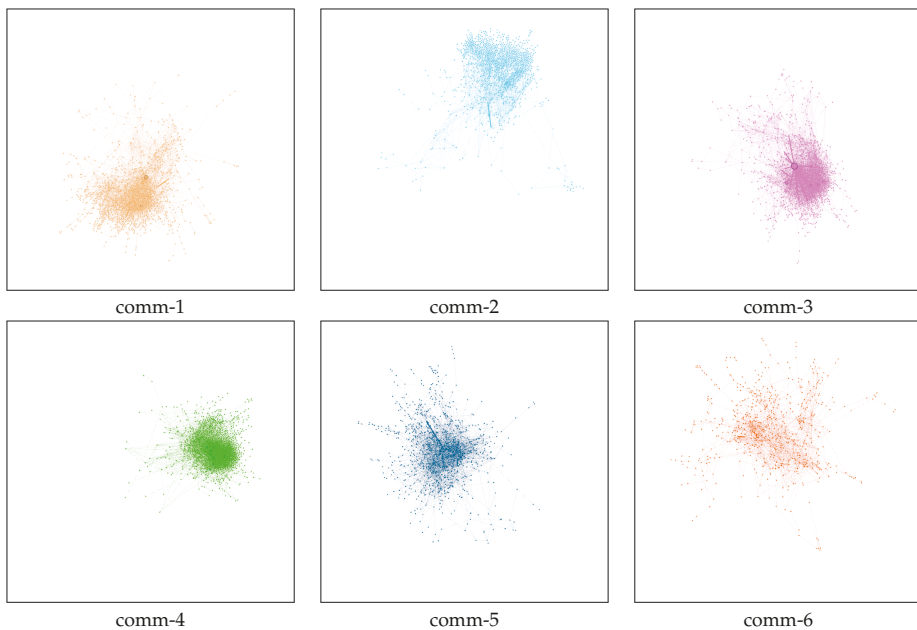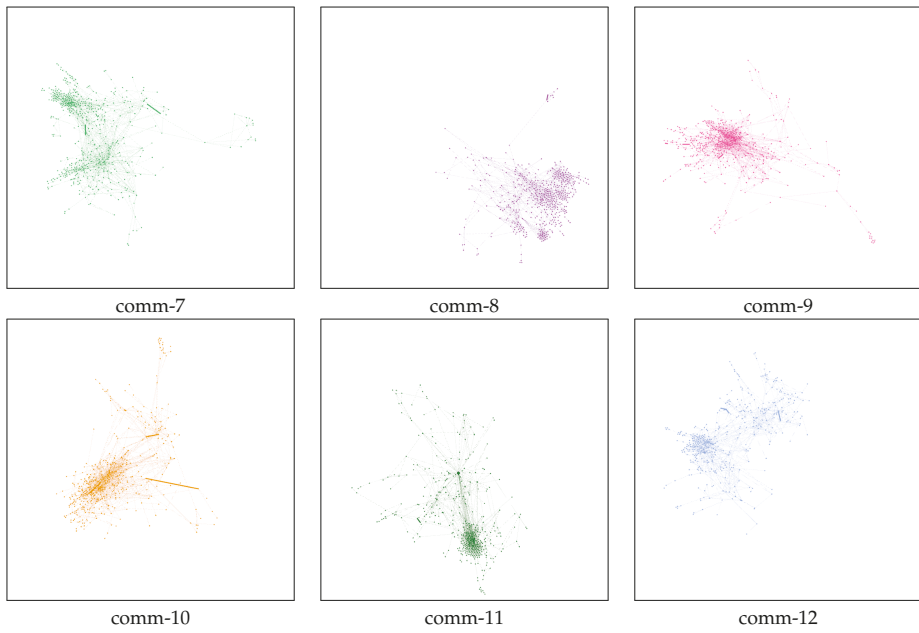
Figure A1. *Cont.*

Figure A1. Graph of the first group of the twelve most crowded communities (in order from left to right and top to bottom).
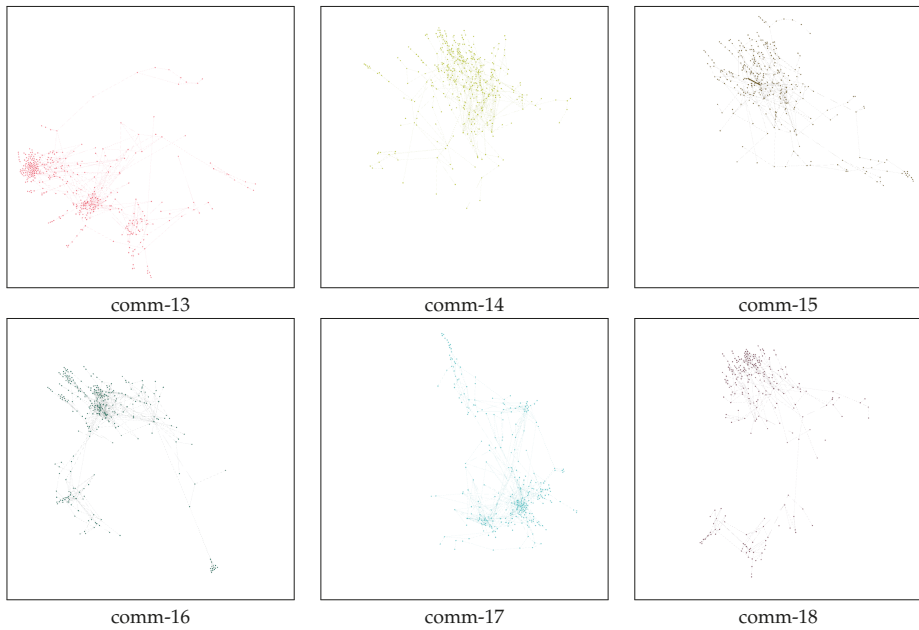
Figure A2. *Cont.*
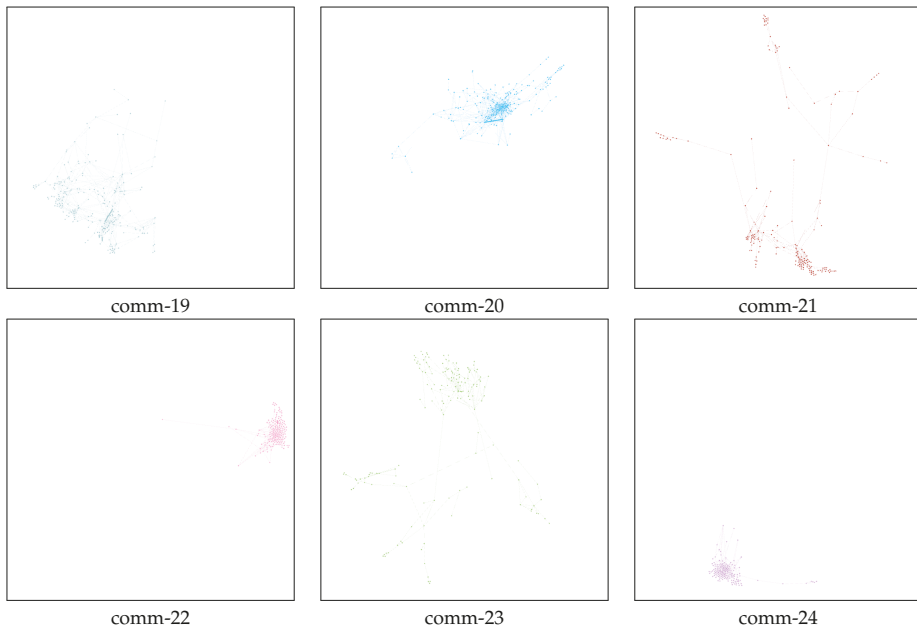
Figure A2. Graph of the second group of the twelve most crowded communities (in order from left to right and top to bottom).

References

1. Erdman, A.G.; Sandor, G.N. *Diseño de Mecanismos, Análisis y Síntesis*, tercera ed.; Prentice Hall: México city, Mexico, 1998.
2. Wittenburg, J. *Dynamics of Systems of Rigid Bodies*; Teubner: Stuttgart, Germany, 1977.
3. Schiehlen, W. Multibody system dynamics: Roots and perspectives. *Multibody Syst. Dyn.* **1997**, *1*, 149–188. [CrossRef]
4. Valverde, J.; Escalona, J.; Mayo, J.; Domínguez, J. Dynamic analysis of a light structure in outer space: Short Electrodynamic Tether. *Multibody Syst. Dyn.* **2003**, *10*, 125–146. [CrossRef]
5. Wasfy, T.M.; Noor, A.K. Computational strategies for flexible multibody systems. *Appl. Mech. Rev.* **2003**, *56*, 553–613. [CrossRef]
6. Shabana, A.A. Flexible multibody dynamics: review of past and recent developments. *Multibody Syst. Dyn.* **1997**, *1*, 189–222. [CrossRef]
7. Schiehlen, W. Research trends in multibody system dynamics. *Multibody Syst. Dyn.* **2007**, *18*, 3–13. [CrossRef]
8. Gantmájer, F. *Mecánica Analítica*; MIR: Moscú, Russia, 1996.
9. Bremer, H. On the dynamics of elastic multibody systems. *Appl. Mech. Rev.* **1999**, *52*, 275–303. [CrossRef]
10. Nikravesh, P.E. *Computer-Aided Analysis of Mechanical Systems*; Prentice-Hall International, Inc.: Upper Saddle River, NJ, USA, 1988.
11. Paul, B.; Krajcinovic, K. Computer analysis of machines with planar motion: Part 1—Kinematics; Part 2—Dynamics. *ASME J. Appl. Mech.* **1970**, *37*, 697–712. [CrossRef]
12. Haug, E. Elements and Methods of Computational Dynamics. In *Computer Aided Analysis and Optimization of Mechanical System Dynamics*; Haug, E., Ed.; Springer: Berlin/Heidelberg, Germany, 1984; pp. 3–38.
13. García de Jalón, J.; Unda, J.; Avello, A.; Jiménez, J. Dynamic analysis of three-dimensional mechanisms in natural coordinates. *ASME J. Mech. Transm. Autom. Des.* **1987**, *109*, 460–465. [CrossRef]
14. García de Jalón, J.; Bayo, E. *Kinematic and Dynamic Simulation of Multibody Systems—The Real-Time Challenge*; Springer: New York, NY, USA, 1993.
15. Shabana, A. *Computational Dynamics*, 2nd ed.; Wiley-Interscience: New York, NY, USA, 2001.

16. Unda, J.; de Jalón, J.G.; Losantos, F.; Enparantza, R. A comparative study on some different formulations of the dynamic equations of constrained mechanical systems. *ASME J. Mech. Transm. Autom. Des.* **1987**, *109*, 466–474. [CrossRef]

17. Shabana, A. *Dynamics of Multibody Systems*; Cambriedge University Press: New York, NY, USA, 1998.

18. Vukasovic, N.; Celigüeta, J.; de Jalón, J.G. Flexible multibody dynamics based on a fully cartesian system of support coordinates. *ASME J. Mech. Des.* **1993**, *115*, 294–299. [CrossRef]

19. Mayo, J. Análisis Geométricamente No Lineal en Dinámica de Mecanismos Flexibles. Ph.D. Thesis, Escuela Técnica Superior de Ingenieros Industriales, Universidad de Sevilla, Sevilla, Spain, 1993.

20. Belytschko, T.; Hsieh, B. Non-linear transient finite element analysis with convected co-ordinates. *Int. J. Numer. Methods Eng.* **1973**, *7*, 255–271. [CrossRef]

21. Simo, J. A finite strain beam formulation. The three-dimensional dynamic problem. Part I. *Comput. Methods Appl. Mech. Eng.* **1985**, *49*, 55–70. [CrossRef]

22. Simo, J.; Vu-Quoc, L. A three-dimensional finite-strain rod model. Part II: Computational aspects. *Comput. Methods Appl. Mech. Eng.* **1986**, *58*, 79–116. [CrossRef]

23. Simo, J.; Vu-Quoc, L. On the dynamics of flexible beams under large overall motions-The plane case: Part I and Part II. *ASME J. Appl. Mech.* **1986**, *53*, 849–863. [CrossRef]

24. Avello, A. Dinámica de Mecanismos Flexibles con Coordenadas Cartesianas y Teoría de Grandes Deformaciones. Ph.D. Thesis, Universidad de Navarra, San Sebastian, Spain, 1990.

25. Shabana, A.A.; Hussien, H.; Escalona, J.L. Application of the absolute nodal coordinate formulation to large rotation and large deformation problems. *ASME J. Mech. Des.* **1998**, *120*, 188–195. [CrossRef]

26. Shabana, A. Computer implementation of the absolute nodal coordinate formulation for flexible multibody dynamics. *Nonlinear Dyn.* **1998**, *16*, 293–306. [CrossRef]

27. Berzeri, M.; Campanelli, M.; Shabana, A. Definition of the elastic forces in the finite-element absolute nodal coordinate formulation and the floating frame of reference formulation. *Multibody Syst. Dyn.* **2001**, *5*, 21–54. [CrossRef]

28. Berzeri, M.; Shabana, A.A. Development of simple models for the elastic forces in the absolute nodal co-ordinate formulation. *J. Sound Vib.* **2000**, *235*, 539–565. [CrossRef]

29. Omar, M.; Shabana, A. A two-dimensional shear deformable beam for large rotation and deformation problems. *J. Sound Vib.* **2001**, *243*, 565–573. [CrossRef]

30. Yakoub, R.; Shabana, A. Three dimensional absolute nodal coordinate formulation for beam elements: Implementation and Applications. *ASME J. Mech. Des.* **2001**, *123*, 614–621. [CrossRef]

31. Shabana, A.; Yakoub, R. Three-dimensional absolute nodal coordinate formulation for beam elements: Theory. *ASME J. Mech. Des.* **2001**, *123*, 606–613. [CrossRef]

32. Shabana, A.A. Finite element incremental approach and exact rigid body inertia. *ASME J. Mech. Des.* **1996**, *118*, 171–178. [CrossRef]

33. Mikkola, A.; Shabana, A. A non-incremental finite element procedure for the analysis of large deformation of plates and shells in mechanical system applications. *Multibody Syst. Dyn.* **2003**, *9*, 283–309. [CrossRef]

34. Sopanen, J.; Mikkola, A. Description of elastic forces in absolute nodal coordinate formulation. *Nonlinear Dyn.* **2003**, *34*, 53–74. [CrossRef]

35. Sopanen, J.; Mikkola, A. Studies on the Stiffness Properties of the Absolute Nodal Coordinate Formulation for Three-dimensional Beams. In *Proceedings of the ASME DETC and CIE Conference*; American Society of Mechanical Engineers Digital Collection: Little Falls, NJ, USA, 2003.

36. Kerkkanen, K.S.; Sopanen, J.T.; Mikkola, A. A geometrically nonlinear beam element for multibody applications. *J. Mech. Des. Trans. ASME* **2005**, *127*, 621–630.

37. Dufva, K.; Sopanen, J.; Mikkola, A. A two-dimensional shear deformable beam element based on the absolute nodal coordinate formulation. *J. Sound Vib.* **2005**, *280*, 719–738. [CrossRef]

38. Dufva, K.; Sopanen, J.; Mikkola, A. Three-dimensional beam element based on a cross-sectional coordinate system approach. *Nonlinear Dyn.* **2005**, in press. [CrossRef]

39. Gerstmayr, J.; Sugiyama, H.; Mikkola, A. Review on the absolute nodal coordinate formulation for large deformation analysis of multibody systems. *J. Comput. Nonlinear Dyn.* **2013**, *8*. [CrossRef]

40. Bastian, M.; Heymann, S.; Jacomy, M. Gephi: An Open Source Software for Exploring and Manipulating Networks. In Proceedings of the Third International AAAI Conference on Weblogs and Social Media, San Jose, CA, USA, 17–20 May 2009.

41. de la Cruz-Lovera, C.; Perea-Moreno, A.J.; de la Cruz-Fernández, J.L.; Alvarez-Bermejo, J.; Manzano-Agugliaro, F. Worldwide research on energy efficiency and sustainability in public buildings. *Sustainability* **2017**, *9*, 1294. [CrossRef]

42. Montoya, F.G.; Alcayde, A.; Baños, R.; Manzano-Agugliaro, F. A fast method for identifying worldwide scientific collaborations using the Scopus database. *Telemat. Inform.* **2018**, *35*, 168–185. [CrossRef]

43. Montoya, F.; Baños, R.; Alcayde, A.; Montoya, M.; Manzano-Agugliaro, F. Power quality: Scientific collaboration networks and research trends. *Energies* **2018**, *11*, 2067. [CrossRef]

44. Alcayde, A.; G Montoya, F.; Baños, R.; Perea-Moreno, A.J.; Manzano-Agugliaro, F. Analysis of Research Topics and Scientific Collaborations in Renewable Energy Using Community Detection. *Sustainability* **2018**, *10*, 4510. [CrossRef]

45. Oracle. Json. Available online: http://www.json.org (accessed on 24 July 2018).

46. Valderrama-Zurián, J.C.; Aguilar-Moya, R.; Melero-Fuentes, D.; Aleixandre-Benavent, R. A systematic analysis of duplicate records in Scopus. *J. Informetr.* **2015**, *9*, 570–576. [CrossRef]

47. Franceschini, F.; Maisano, D.; Mastrogiacomo, L. Empirical analysis and classification of database errors in Scopus and Web of Science. *J. Informetr.* **2016**, *10*, 933–953. [CrossRef]

48. Google. OpenRefine. Available online: http://openrefine.org (accessed on 24 July 2018).

49. Baxter, R.; Christen, P.; Churches, T. A comparison of fast blocking methods for record linkage. In Proceedings of the ACM SIGKDD'03 Workshop on Data Cleaning, Record Linkage, and Object Consolidation, Washington, DC, USA, 27 August 2003; pp. 25–27.

50. Jin, L.; Li, C.; Mehrotra, S. Efficient record linkage in large data sets. In Proceedings of the Eighth International Conference on Database Systems for Advanced Applications (DASFAA 2003), Kyoto, Japan, 26–28 March 2003; pp. 137–146.

51. Cavnar, W.; Trenkle, J. N-gram-based text categorization. In Proceedings of the SDAIR-94, 3rd Annual Symposium on Document Analysis and Information Retrieval, Las Vegas, NV, USA, 11–13 April 1994; pp. 161–175.

52. Abidin, A.F.; Mohamed, A.; Shareef, H. Intelligent detection of unstable power swing for correct distance relay operation using S-transform and neural networks. *Expert Syst. Appl.* **2011**, *38*, 14969–14975. [CrossRef]

53. Montoya, F.G.; Alcayde, A.; Sánchez, P.; Gil, C.; Montoya, M.; Gómez, J. Comparative analysis of power variables in high performance embedded and x86 architectures using GNU/Linux. *Comput. Electr. Eng.* **2011**, *37*, 541–549. [CrossRef]

54. Newman, M.E.; Girvan, M. Finding and evaluating community structure in networks. *Phys. Rev. E* **2004**, *69*, 026113. [CrossRef]

55. Blondel, V.; Guillaume, J.L.; Lambiotte, R.; Lefebvre, E. Fast Unfolding of Communities in Large Networks. *J. Stat. Mech. Theory Exp.* **2008**, *2008*. [CrossRef]

56. Kane, T.; Ryan, R.; Banerjee, A. Dynamics of a cantilever beam attached to a moving base. *J. Guid. Control Dyn.* **1987**, *10*, 139–151. [CrossRef]

57. Shabana, A.; Zaazaa, K.; Escalona, J.; Sany, J. Development of elastic force model for wheel/rail contact problems. *J. Sound Vib.* **2004**, *269*, 295–325. [CrossRef]

58. Lankarani, H.; Nikravesh, P. Contact force model with hysteresis damping for impact analysis of multibody systems. *J. Mech. Transm. Autom. Des.* **1990**, *112*, 369–376. [CrossRef]

59. Machado, M.; Moreira, P.; Flores, P.; Lankarani, H. Compliant contact force models in multibody dynamics: Evolution of the Hertz contact theory. *Mech. Mach. Theory* **2012**, *53*, 99–121. [CrossRef]

60. Bauchau, O.; Laulusa, A. Review of contemporary approaches for constraint enforcement in multibody systems. *J. Comput. Nonlinear Dyn.* **2008**, *3*, 1–8. [CrossRef]

61. Bayo, E.; Ledesma, R. Augmented Lagrangian and mass-orthogonal projection methods for constrained multibody dynamics. *Nonlinear Dyn.* **1996**, *9*, 113–130. [CrossRef]

62. Bestle, D. Analyzing and optimizing multibody systems. *Mech. Struct. Mach.* **1992**, *20*, 67–92. [CrossRef]

63. Cossalter, V.; Lot, R. A motorcycle multi-body model for real time simulations based on the natural coordinates approach. *Veh. Syst. Dyn.* **2002**, *37*, 423–447. [CrossRef]

64. Kortüm, W. Review of Multibody Computer, Codes for Vehicle system Dynamics. *Veh. Syst. Dyn.* **1993**, *22*, 3–31. [CrossRef]

65. Damsgaard, M.; Rasmussen, J.; Christensen, S.; Surma, E.; de Zee, M. Analysis of musculoskeletal systems in the AnyBody Modeling System. *Simul. Model. Pract. Theory* **2006**, *14*, 1100–1111. [CrossRef]

66. Zagrodny, B.; Ludwicki, M.; Wojnicz, W.; Mrozowski, J.; Awrejcewicz, J. Cooperation of mono-and bi-articular muscles: Human lower limb. *J. Musculoskelet. Neuronal Interact.* **2018**, *18*, 176–182.

67. Wojnicz, W.; Zagrodny, B.; Ludwicki, M.; Awrejcewicz, J.; Wittbrodt, E. A two dimensional approach for modelling of pennate muscle behaviour. *Biocybern. Biomed. Eng.* **2017**, *37*, 302–315. [CrossRef]

68. Bauchau, O. Computational Schemes for Flexible, Nonlinear Multi-Body Systems. *Multibody Syst. Dyn.* **1998**, *2*, 169–225. [CrossRef]

69. Betsch, P. The discrete null space method for the energy consistent integration of constrained mechanical systems. Part I: Holonomic constraints. *Comput. Methods Appl. Mech. Eng.* **2005**, *194*, 5159–5190. [CrossRef]

70. Jain, A. *Robot and Multibody Dynamics: Analysis and Algorithms*; Springer: Berlin, Germany, 2011; pp. 1–510. [CrossRef]

71. Rui, X.; Wang, G.; Zhang, J. *Transfer Matrix Method for Multibody Systems: Theory and Applications*; Wiley: Hoboken, NJ, USA, 2017; pp. 1–732. [CrossRef]

72. Masarati, P.; Morandini, M.; Mantegazza, P. An efficient formulation for general-purpose multibody/multiphysics analysis. *J. Comput. Nonlinear Dyn.* **2014**, *9*. [CrossRef]

73. Lee, H.W.; Roh, M.I. Review of the multibody dynamics in the applications of ships and offshore structures. *Ocean Eng.* **2018**, *167*, 65–76. [CrossRef]

74. Novotny, P.; Pistek, V. New efficient methods for powertrain vibration analysis. *Proc. Inst. Mech. Eng. Part D J. Automob. Eng.* **2010**, *224*, 611–629. [CrossRef]

75. Blundell, M.; Harty, D. *The Multibody Systems Approach to Vehicle Dynamics*; Elsevier: Amsterdam, The Netherlands, 2014; pp. 1–741. [CrossRef]

76. Helsen, J.; Vanhollebeke, F.; Marrant, B.; Vandepitte, D.; Desmet, W. Multibody modelling of varying complexity for modal behaviour analysis of wind turbine gearboxes. *Renew. Energy* **2011**, *36*, 3098–3113. [CrossRef]

77. Rubinstein, D.; Hitron, R. A detailed multi-body model for dynamic simulation of off-road tracked vehicles. *J. Terramech.* **2004**, *41*, 163–173. [CrossRef]

78. Wohlmuth, B.; Krause, R. Monotone multigrid methods on nonmatching grids for nonlinear multibody contact problems. *SIAM J. Sci. Comput.* **2003**, *25*, 324–347. [CrossRef]

79. Laursen, T.; Simo, J. A continuum-based finite element formulation for the implicit solution of multibody, large deformation-frictional contact problems. *Int. J. Numer. Methods Eng.* **1993**, *36*, 3451–3485. [CrossRef]

80. Umetani, Y.; Yoshida, K. Resolved Motion Rate Control of Space Manipulators with Generalized Jacobian Matrix. *IEEE Trans. Robot. Autom.* **1989**, *5*, 303–314. [CrossRef]

81. Anitescu, M.; Potra, F. Formulating Dynamic Multi-Rigid-Body Contact Problems with Friction as Solvable Linear Complementarity Problems. *Nonlinear Dyn.* **1997**, *14*, 231–247. [CrossRef]

82. Pfeiffer, A.; Lee, J.S.; Han, J.H.; Baier, H. Ornithopter Flight Simulation Based on Flexible Multi-Body Dynamics. *J. Bionic Eng.* **2010**, *7*, 102–111. [CrossRef]

83. Crocetta, G.; Piantini, S.; Pierini, M.; Simms, C. The influence of vehicle front-end design on pedestrian ground impact. *Accid. Anal. Prev.* **2015**, *79*, 56–69. [CrossRef] [PubMed]

84. Dietz, S.; Netter, H.; Sachau, D. Fatigue life prediction of a railway bogie under dynamic loads through simulation. *Veh. Syst. Dyn.* **1998**, *29*, 385–402. [CrossRef]

85. Zhu, S.; Ding, G.; Qin, S.; Lei, J.; Zhuang, L.; Yan, K. Integrated geometric error modeling, identification and compensation of CNC machine tools. *Int. J. Mach. Tools Manuf.* **2012**, *52*, 24–29. [CrossRef]

Article

An Equivalent Damping Numerical Prediction Method for the Ring Damper Used in Gears under Axial Vibration

Shuai Wang [1,2,*], Xiaolei Wang [1,*], Yanrong Wang [3] and Hang Ye [3]

[1]   National Key Laboratory of Science and Technology on Helicopter Transmission, Nanjing University of Aeronautics and Astronautics, Nanjing 210016, China

[2]   AECC Hunan Aviation Powerplant Research Institute, Zhuzhou 412002, China

[3]   School of Energy and Power Engineering, Beihang University, Beijing 100191, China; yrwang@buaa.edu.cn (Y.W.); yehang@buaa.edu.cn (H.Y.)

[*]   Correspondence: wangshuai608@126.com (S.W.); wxl@nuaa.edu.cn (X.W.)

Abstract: In aircraft gas turbine engines, gears in the transmission system are typically cyclic in structure and inevitably encounter large dynamic loads, such as meshing excitation, resulting in high vibration loads in resonance. To prevent gear resonance failure, a ring damper is employed to reduce the resonance response. As relative motion between the gear and the ring damper occurs, vibration loads can be reduced by friction energy dissipation. Moreover, the gears in the aircraft engine are thin-walled and their axial stiffness is much smaller than radial stiffness; thus, it is easier for axial vibration to cause resonance failure. This paper proposes an equivalent damping numerical prediction method for a ring damper under axial vibration, which greatly shortens the calculation time and prevents the forced response analysis of nonlinear structures. Via this method, the influence of ring damper structural parameters on friction damping in gears under axial vibration is investigated. The results indicate that the friction coefficient and mass of the ring damper have a great influence on damping performance.

Keywords: gear; ring damper; energy dissipation; axial vibration; friction damping

---

1. Introduction

In an aircraft's gas turbine engine, the transmission system transmits power to accessories, such as the oil pump (as shown in Figure 1). In order to reduce the weight of the engine, the transmission gears often have a thin-walled structure. However, these gears also easily cause resonance in the operating speed range, stressing on the need to reduce vibration and avoid resonance failure. Common strategies to prevent this include active and passive damping. Active damping involves redesigning of the gear structure to limit resonance points in the operating range; this is difficult to realize in an aircraft gas turbine engine, where multiple resonance points exist. The passive method utilizes damping devices to increase system damping and subsequently suppress vibration [1]. The ring damper is one such device; its structure is shown in Figure 2.
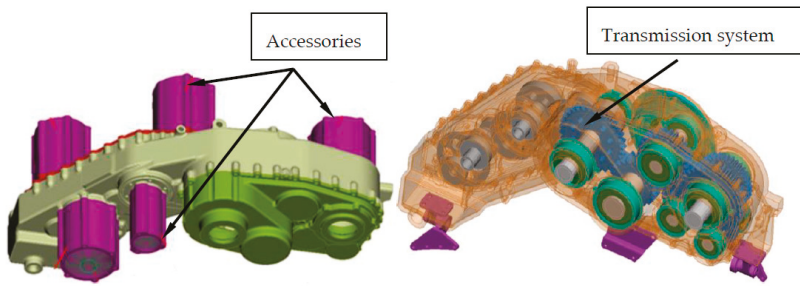
Figure 1. Transmission system and accessories in an aircraft gas turbine engine.

(**a**) Gear model

(**b**) Ring damper model

(**c**) Assembly model of the gear and ring damper
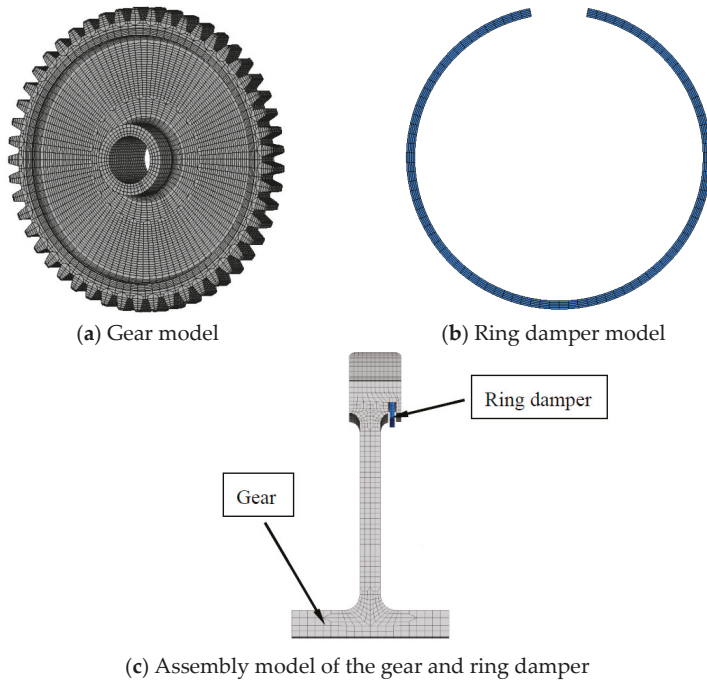
Figure 2. Ring damper shape and a typical gear–ring damper system.

A ring damper is a device used to improve the damping of gears. Via relative motion on the contact interface between the ring damper and the gear, vibration energy is dissipated and vibration amplitude/stress is reduced [2].

Most research is currently focused on analyzing the forced response of the structure with an additional ring damper. Laxalde et al. [3,4] used a dynamic time-frequency conversion method to analyze the forced response of a bladed disk structure with a ring damper; they found that the effect of the ring damper depends on friction energy dissipation on the contact surface between the ring damper and the structure. Zucca et al. [5,6] characterized the frictional force of the contact surface as a function of the tangent and normal stiffness as depending on the amplitude, and calculated the periodic response of the system in the frequency domain via the harmonic balance method. Epureanu et al. [7] expressed nonlinear frictional force as a function of equivalent damping and stiffness to improve the speed of steady-state response iteratively. Tang et al. [8,9] proposed a reduced order model. First, the dynamic substructure method was used to reduce the size of the finite element model. Second,

the time-frequency conversion method was employed to solve the equations of motion in the frequency domain to further reduce the calculation amount of the model [10]. Lopez et al. [11,12] obtained the magnitude of friction energy dissipation under different vibration conditions by deducing the relative motion between the ring damper and the main structure, and concluded that the larger the damping ring mass, the better the vibration reduction, under the condition of small mass rate (mass of the damping ring/mass of the main structure). However, real excitation of the gear is an aircraft engine is complex, and the limitations of these response methods become obvious when the excitation cannot be predicted accurately.

Gear vibration can be divided into two categories: axial and radial. Some vibration modes are mainly in the axial direction, while the others are in a radial direction. In addition, the vibration reduction mechanisms of these two types are different. For radial vibration, since deformation of the ring damper and gear at the same position are different when resonance occurs (yielding a relative motion and friction), vibration energy is dissipated [13]. For axial vibration, inertia induces a relative motion between the ring damper and the gear, in an effort to reduce the vibration [14–16].

The main purpose of this paper is to establish a numerical model to predict the equivalent damping of ring dampers under axial vibration. In this model, friction-induced nonlinear damping (at the interface of the gear and the ring damper) is expressed as equivalent structural damping associated with vibration loads. The macro sliding model is used to calculate the energy dissipation capacity of the ring damper. The influence of ring damper mass and friction coefficient on damping effect is investigated.

2. Vibration Equation of the GEAR-Ring Damper System

The vibration equation of a gear with a ring damper can be expressed as:

$$M\ddot{u} + C\dot{u} + Ku = F_{\text{ext}} - F_{\text{nl}} \tag{1}$$

where u is the vibration displacement; $(\cdot)$ is the differentiation of time; M, C, and K are the mass matrix, damping matrix, and stiffness matrix of the gear system, respectively; F_{ext} is the external exciting force with time; F_{nl} is the nonlinear friction force on the surface of the groove, which can be expressed as the equivalent damping and equivalent stiffness form:

$$F_{\text{nl}} = C_{\text{eq}}\dot{u} + K_{\text{eq}}u \tag{2}$$

Therefore, from the orthogonality of the mode vector, Equation (1) can be expressed as a linear superposition of the orthogonal mode of the undamped gear system.

$$u = \Phi q \tag{3}$$

where Φ is the gear system modal matrix; q is the modal displacement vector.

Taking Equations (2) and (3) into Equation (1) and multiplying Φ^T:

$$I\ddot{q} + Z\dot{q} + \Lambda q + Z_{\text{eq}}\dot{q} + \Lambda_{\text{eq}}q = Q \tag{4}$$

where

$$I = \Phi^T M \Phi, Z = \Phi^T C \Phi, \Lambda = \Phi^T K \Phi, Z_{\text{eq}} = \Phi^T C_{\text{eq}} \Phi, \Lambda_{\text{eq}}q = \Phi^T K_{\text{eq}} \Phi, Q = \Phi^T F_{\text{ext}}$$

I is the unit matrix, and Z, Λ, Z_{eq}, Λ_{eq} are diagonal matrices. When the system vibrates at the jth natural frequency, the jth mode is dominant, and the contribution of other modes is negligible. Therefore, Equation (1) can be expressed as:

$$\ddot{q}_j + 2(\zeta_j + \zeta_{j,\text{eq}})\omega_j \dot{q}_j + (k_j + k_{j,\text{eq}})q_j = Q_j \tag{5}$$

where ζ_j and $\zeta_{j,\text{eq}}$ are the intrinsic modal damping ratio of the jth mode of the gear and the equivalent modal damping ratio provided by the ring damper under the jth mode of the gear, respectively. k_j and $k_{j,\text{eq}}$, respectively, represent the jth modal stiffness of the gear and the equivalent stiffness of the ring damper under the jth mode of the gear, and $k_j = \omega_j^2$. ω_j represents the jth natural frequency (rad/s) of the undamped gear. Both $\zeta_{j,\text{eq}}$ and $k_{j,\text{eq}}$ depend on the gear amplitude, and when the amplitude is 0, $\zeta_{j,\text{eq}} = 0$, $k_{j,\text{eq}} = 0$.

Generally, ring damper mass is much smaller than gear mass, which is a requirement of the dry friction damper. Define damping ring mass rate as:

$$\beta = \frac{m_\text{d}}{m_\text{g}} \tag{6}$$

where m_d represents the mass of the ring damper and m_g represents the mass of the gear.

In this paper, ring damper mass rate β is less than 5%. It should be noted that the mass of the gear and the amplitude of the stiffness matrix are much larger than the magnitude of the nonlinear friction. Therefore, $k_{j,\text{eq}}$ is much smaller than k_j This means that the ring damper hardly affects the stiffness and mode shape of the structure, and only touches the amplitude. Therefore, the effect of the ring damper on resonant frequency of the gear is negligible. Other scholars [4,5,7] have also shown that the effect of the ring damper on resonant frequency of the structure is less than 1%. The ring damper mainly reduces the amplitude and vibration loads of the structure by friction energy dissipation.

It can be seen from Equation (5) that the deformation of the gear under static load is $q_1 = Q_j/k_j$. For a gear system without a ring damper, the response amplitude at the jth order resonance frequency q_re is:

$$q_\text{re} = \frac{q_1}{2\zeta_j} = \frac{Q_j}{2\zeta_j k_j} \tag{7}$$

For a gear with given excitation and damping, the response amplitude q_re in Equation (7) can be obtained by forced response analysis. For a gear system with a damper ring, the response amplitude at the jth order resonant frequency q_re is:

$$q_\text{re,d} = \frac{q_1}{2\left(\zeta_j + \zeta_{j,\text{ed}}\right)} = \frac{Q_j}{2\left(\zeta_j + \zeta_{j,\text{ed}}\right)k_j} \tag{8}$$

where the equivalent modal damping ratio $\zeta_{j,\text{ed}}$ provided by the ring damper is a function of the response amplitude $q_\text{re,d}$.

Equation (8) shows that for a particular structure, the resonance peak is proportional to the magnitude of the excitation force and inversely proportional to the modal damping ratio. Under small vibration amplitude (within the linear elastic range), vibration loads are related to the differential of the vibration displacement. For a given mode shape, the amplitude q_re is linear with the vibration loads σ_re. Therefore, the relationship among the vibration loads σ, the excitation amplitude of the jth order mode of the gear, and the damping ratio can be written as:

$$\sigma = \alpha_j \frac{Q_j}{\zeta_j + \zeta_{j,\text{ed}}} \tag{9}$$

where α_j represents the proportional coefficient under the jth mode, and the proportional coefficient is hardly affected by the damper.

The finite element method is used to analyze the natural vibration characteristics of the gear system. The modal vibration mode and modal stress of the gear are used as reference. The relationship

between allowable vibration loads σ_a, allowable vibration amplitude q_a, reference modal stress σ_{ref}, and reference modal displacement q_{ref} can be obtained:

$$q_a = \frac{\sigma_a}{\sigma_{ref}} q_{ref} \tag{10}$$

Through Equation (10), the amplitude-dependent friction damping can be transformed into a relationship with the vibration loads, which facilitates the analysis of the ring damper design.

3. Theoretical Analysis of Friction Energy Dissipation

3.1. Motion State of the Slider

The ring damper is usually mounted in a damper groove on the gear rim and mounted on the gear by interference preload and centrifugal force. Since the amplitude of the damper groove varies circumferentially, the ring damper is discretized into mass units, each mass unit forming a basic sliding unit.

The basic model of friction energy dissipation is the flat plate-slider system, as shown in Figure 3. The slider (mass unit) placed on the moving plate is subjected to the frictional force, and the relationship between the energy is dissipated by friction and structural parameters, obtained by solving the equation of motion of the slider. The mass of the slider is m_1, the normal force is F_N, and the displacement equation of the plate is:

$$x_0(t) = A \sin (\omega_0 t) \tag{11}$$

where A is the vibration amplitude of the structure (in Section 3, the structure is the plate, and in Section 4, the structure is the gear), and ω_0 is the circular vibration frequency of the plate; the motion state of the plate is not affected by the slider. The displacement of the slider is $x_1(t)$, and the relative motion (trend) between the plate and the slider creates friction. This is called a viscous state when there is no relative displacement between the slider and the plate; it is called a sliding state when there is relative displacement between the slider and the plate.
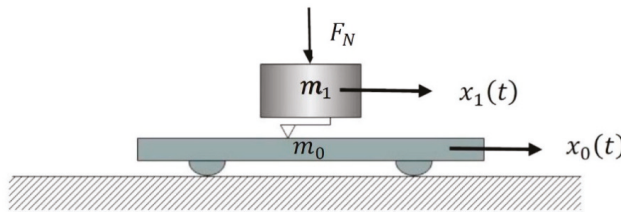
Figure 3. Flat plate-slider system.

The motion of the plate is not affected by the damper, so the velocity and acceleration equations of the plate can be obtained by the plate displacement equation:

$$\left. \begin{array}{l} \dot{x}_0(t) = \omega_0 A \cos (\omega_0 t) \\ \ddot{x}_0(t) = -\omega_0^2 A \sin (\omega_0 t) \end{array} \right\} (t_0 < t < t_0 + \frac{2\pi}{\omega_0}) \tag{12}$$

3.1.1. Equation of Motion of the Slider in the Viscous-Sliding State

When the inertial force of the slider is smaller than the maximum static frictional force of the slider, the movement of the slider and the plate is completely synchronized, which is called a viscous state. The speed and acceleration equations for the slider are:

$$\left. \begin{array}{l} \dot{x}_1(t) = \dot{x}_0(t) = \omega_0 A \cos (\omega_0 t) \\ \ddot{x}_1(t) = \ddot{x}_0(t) = -\omega_0^2 A \sin (\omega_0 t) \end{array} \right\} (t_0 < t < t_1) \tag{13}$$

where t_1 indicates the end of the viscous phase and begins to enter the sliding phase.

When the inertial force of the slider is equal to the maximum static friction force, the acceleration of the slider reaches maximum value. And:

$$\sin(\omega_0 t) = \pm \frac{F_f}{A\omega_0^2 m_1} = \pm \frac{\mu F_N}{A\omega_0^2 m_1} = \pm k \tag{14}$$

where F_f is the frictional force, μ is the coefficient of friction, Equation (14) defines a normalized frictional parameter k, which represents the ratio of the dynamic friction experienced by the slider to the maximum external force required to maintain the synchronous movement of the slider with the plate. It can be seen from Equation (14) that t_1 exists only when $|k| < 1$. Equation (14) also gives the upper limit of the frictional force in the presence of relative displacement, i.e., $F_f = A\omega_0^2 m_1$. When $|k| \geq 1$, the slider and the plate are completely viscous, and displacement, velocity, and acceleration are the same.

When the frictional force of the slider is insufficient to provide synchronous movement of the slider with the plate, i.e., $|k| < 1$, a sliding stage is entered, and the slider is subjected to sliding frictional force. The sliding frictional force is only related to the normal force and the friction coefficient, and is independent of the motion state of the slider itself. Therefore, the speed and acceleration equation of the slider are:

$$\left. \begin{array}{l} \dot{x}_1(t) = \omega_0 A[\mp\omega_0 k(t - t_1) + \cos(\omega_0 t_1)] \\ \ddot{x}_1(t) = \mp k\omega_0^2 A \end{array} \right\} (t_1 < t < t_2) \tag{15}$$

It can be seen from Equations (12) and (15) that the speed of the slider changes linearly with time in the sliding phase, while the velocity of the flat plate changes with time in sine form. Therefore, when the speed of the slider and the speed of the flat plate are equal, the sliding phase ends. And:

$$\dot{x}_1(t_2) = \dot{x}_0(t_2) \tag{16}$$

where t_2 can be obtained by Equations (12), (14) and (15).

$$\omega_0 k(t_2 - t_1) = \mp[\cos(\omega_0 t_2) - \cos(\omega_0 t_1)] \tag{17}$$

t_1, t_2 gives the sliding interval in half cycle, and likewise t_3, t_4 gives the sliding interval in the corresponding other half cycle. Equation (18) can be obtained by Equations (15) and (17):

$$t_3 = t_1 + \frac{\pi}{\omega_0}, \ t_4 = t_2 + \frac{\pi}{\omega_0} \tag{18}$$

When $t_1 < t < t_2$, a slip occurs between the slider and the plate; when $t_2 < t < t_3$, sticking occurs; when $t_3 < t < t_4$, it slides again; when $t_4 < t < t_1 + 2\pi/\omega_0$, it sticks again. This phenomenon is defined in this paper as a viscous-sliding state. Figure 4 shows the acceleration, velocity, and displacement of the slider and the plate in the viscous-sliding state ($k = 0.8$). As can be seen from Figure 4, although the motion of the slider is periodic, it does not change as a sine (or cosine) function.

(**a**) Acceleration

(**b**) Velocity
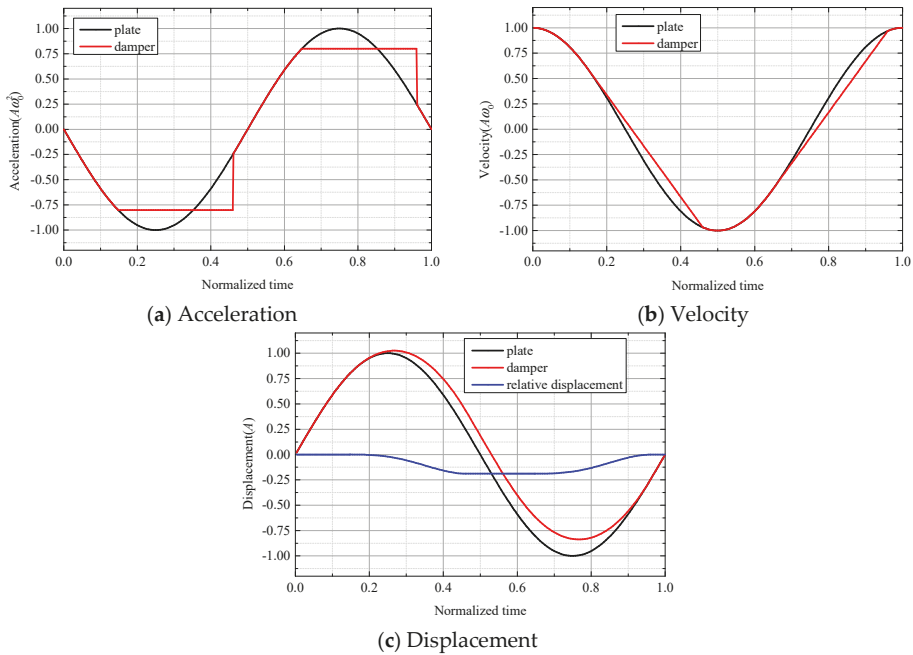
(**c**) Displacement

Figure 4. Velocity and displacement of the slider and plate in a viscous-sliding state (k = 0.8).

3.1.2. The Motion State of the Slider in the Fully Sliding State

As the value of k continues to decrease, the slider may slide continuously during a vibration cycle without viscous. In this case, it can be considered that the end of the viscous phase is the same as the initial moment, such that:

$$t_2 = t_3 = t_1 + \pi/\omega_0, t_4 = t_1 + 2\pi/\omega_0 \tag{19}$$

From Equations (17) and (19) can be obtained:

$$k\pi = 2\cos(\omega_0 t_1) \tag{20}$$

Using Equation (20) in Equations (17) can obtain the critical normalized frictional force:

$$k|_{\text{critical}} = \sqrt{\frac{1}{1 + \pi^2/4}} \approx 0.537 \tag{21}$$

When the normalized frictional force is equal to the critical normalized frictional force, viscous a state begins to appear in the vibration cycle, as shown in Figure 5. When the normalized frictional force is less than this value, there is no viscous state in one cycle, and the slider continuously slides, which is defined as full sliding, as shown in Figure 6. When the normalized frictional force is greater than the critical normalized frictional force and is less than 1, the sliding and viscous phenomena, respectively, appear in different stages in one cycle, that is, the viscous-sliding state described above, as shown in Figure 4.

(**a**) Acceleration

(**b**) Velocity
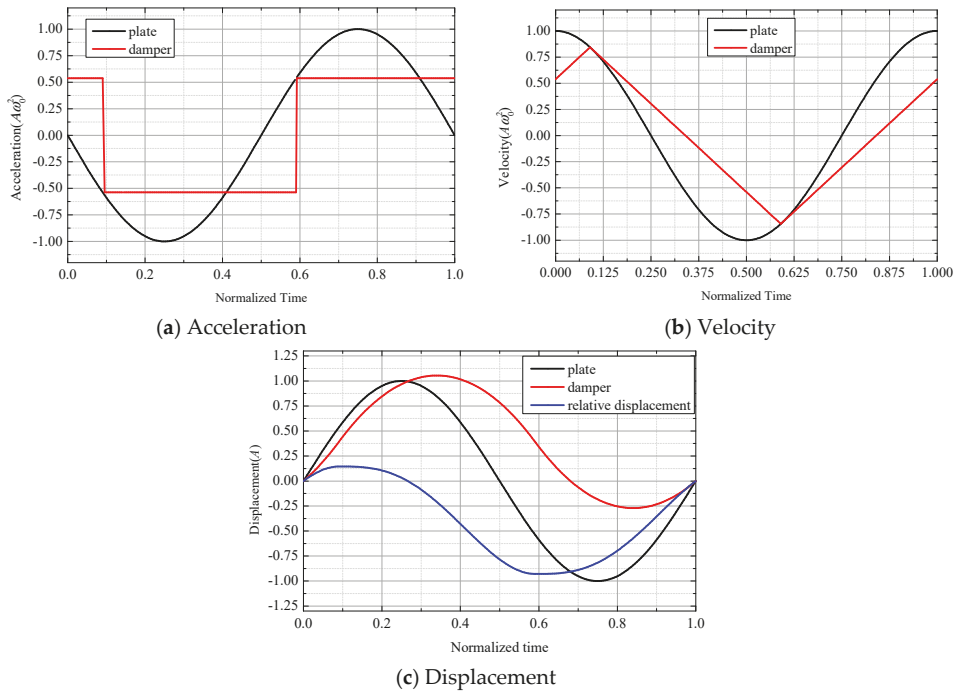
(**c**) Displacement

Figure 5. Acceleration, velocity, and displacement of slider and plate in critical state ($k = 0.537$).

(**a**) Acceleration

(**b**) Velocity
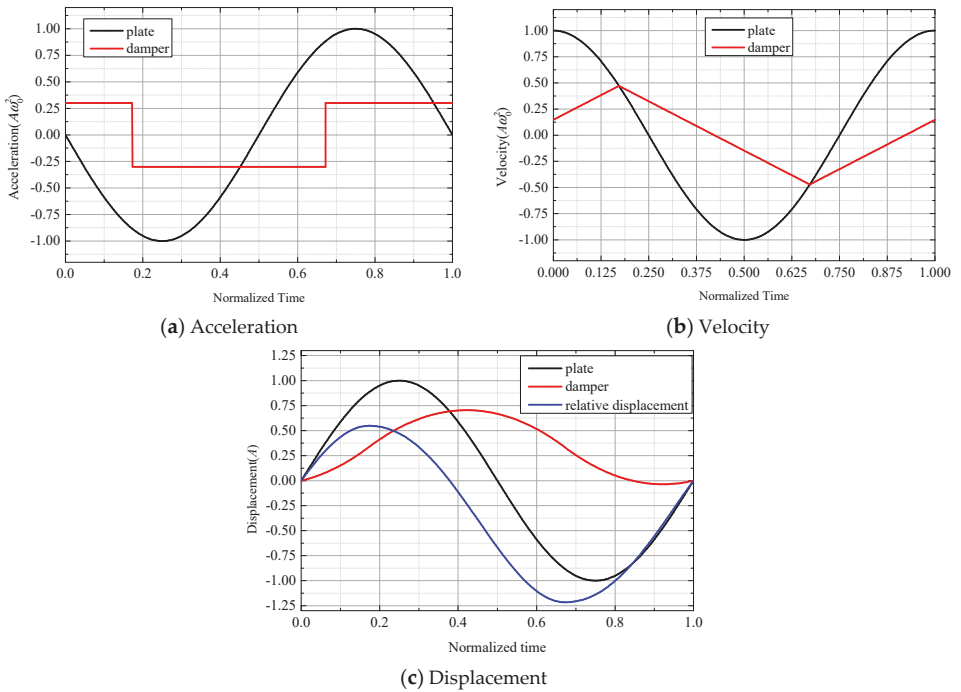
(**c**) Displacement

Figure 6. Velocity and displacement of the slider and the plate in full sliding state ($k = 0.3$).

3.2. Friction Energy Dissipation Model

According to previous analyses, for different friction, there are two sliding regions with the same motion state in one motion cycle. The energy dissipated per cycle can be obtained by integrating the relative speed between the slider and the plate by friction. Relative velocity exists only in the sliding phase, and the energy dissipated in the two sliding phases in the same cycle is equal, so the dissipated energy of any period in the steady state can be expressed as:

$$\Delta W = 2 \int_{t_1}^{t_2} F_f(\dot{x}_1(t) - \dot{x}_0(t)) \mathrm{d}t \tag{22}$$

Substituting Equation (15) into Equation (22), the friction energy dissipation in each cycle can be expressed as:

$$
\begin{aligned}
\Delta W &= 2F_f \int_{t_1}^{t_2} \{\omega_0 A[-\omega_0 k(t - t_1) + \cos(\omega_0 t_1)] - \omega_0 A \cos(\omega_0 t)\} \mathrm{d}t \\
&= 2F_f \omega_0 A\left[\frac{-\omega_0 k(t_2 - t_1)^2}{2} + \cos(\omega_0 t_1) \cdot (t_2 - t_1) - \frac{\sin(\omega_0 t_2) - \sin(\omega_0 t_1)}{\omega_0} \right] \\
&= \omega_0^2 A^2 m_1 \cdot 2k\omega_0\left[\frac{-\omega_0 k(t_2 - t_1)^2}{2} + \cos(\omega_0 t_1) \cdot (t_2 - t_1) - \frac{\sin(\omega_0 t_2) - \sin(\omega_0 t_1)}{\omega_0} \right]
\end{aligned}
\tag{23}
$$

η is defined as the normalized friction energy dissipation, and $\eta = \Delta W/(\omega_0^2 A^2 m_1)$. The physical meaning is the ratio of the energy dissipated by the slider to the maximum kinetic energy of the slider during a vibration period. η can be expressed as:

$$\eta = 2k\omega_0\left[\frac{-\omega_0 k(t_2 - t_1)^2}{2} + \cos(\omega_0 t_1) \cdot (t_2 - t_1) - \frac{\sin(\omega_0 t_2) - \sin(\omega_0 t_1)}{\omega u} \right] \tag{24}$$

Equations (23) and (24) are applicable to both full slip and viscous-slip. By using Equations (19), (20) and (24), the relationship between η and k at full slip can be obtained. The relationship between η and k in viscous-sliding can be obtained by Equations (17), (14) and (24), as shown in Figure 7.
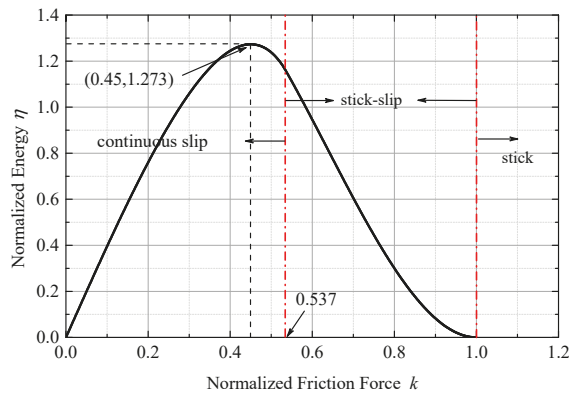
Figure 7. Relationship between normalized frictional force and normalized energy dissipation.

In the full sliding phase, since $t_2 = t_1 + \pi/\omega_0$, Equation (24) can be simplified to:

$$\eta = 4k\sin(\omega_0 t_1) = 4k\sqrt{1 - \frac{\pi^2 k^2}{4}} \tag{25}$$

As can be seen from Figure 6, maximum energy dissipation occurs in the full sliding region. Using Equation (25), the following can be obtained:

$$\eta|_{max} = \frac{4}{\pi} \approx 1.273 \tag{26}$$

The maximum normalized energy dissipation is a constant value. The corresponding optimal normalized frictional force is:

$$k|_{optimum} = \frac{\sqrt{2}}{\pi} \approx 0.45 \tag{27}$$

That is, when $k = 0.45$, the slider dissipates the most energy and the damping effect is optimal. It can be summarized that:

(1) There is optimum friction to maximize friction energy dissipation during a vibration cycle;
(2) The mass of the slider has a positive effect on energy dissipation, i.e., increasing the mass of the damper can increase the friction energy dissipation.

If the friction is constant, the normalized frictional force is changed by varying the amplitude of the plate. When the amplitude is small, the friction can provide acceleration when there is no relative motion between the slider and plate. As the amplitude is further increased, the slider begins to slip. The amplitude of the slider from the fully viscous state to the start of the slip is the critical amplitude, which is:

$$A|_{critical} = \frac{F_f}{\omega_0^2 m_1} \tag{28}$$

Define the normalized amplitude as:

$$\overline{A} = \frac{A}{A|_{critical}} \tag{29}$$

From Equations (14), (17), (19), (20), (24) and (29), the relationship between the normalized amplitude and the normalized energy dissipation can be obtained, as shown in Figure 8. The maximum energy dissipation is consistent with previous analysis. The ideal normalized amplitude is:

$$A|_{optimum} = \frac{\pi}{\sqrt{2}} \approx 2.22 \tag{30}$$
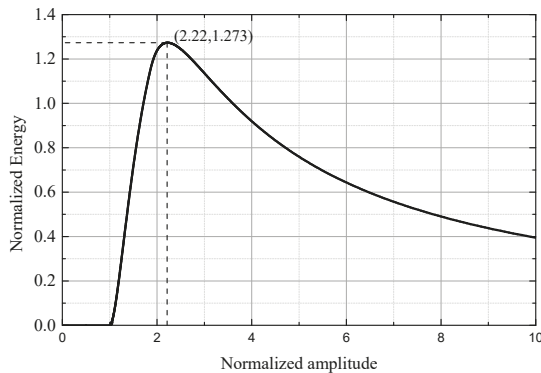
Figure 8. Relationship between normalized energy dissipation and normalized amplitude.

If plate mass is m_0, the equivalent damping ratio due to friction can be expressed as:

$$\zeta = \frac{\Delta W}{4\pi W} = \frac{\eta \omega_0^2 A^2 m_1}{4\pi(\omega_0^2 A^2 m_1 + \omega_0^2 A^2 m_0)} = \frac{\eta m_1}{4\pi(m_1 + m_0)} \tag{31}$$

According to Equation (31), the equivalent damping ratio is related to the mass of the slider and the plate. As the normalized friction energy dissipation remains constant, when the mass of the plate increases, the equivalent damping ratio will decrease, and when the mass of the slider increases, the equivalent damping ratio will increase. When $m_1 \ll m_0$, the energy dissipated by friction in one cycle is approximately linearly related to m_1. The maximum damping ratio due to friction is:

$$\zeta|_{\max} = \frac{\eta|_{\max} \cdot m_1}{4\pi(m_1 + m_0)} = \frac{m_1}{\pi^2(m_1 + m_0)} \tag{32}$$

4. Ring Damper Friction Energy Dissipation Model

The axial displacement equation of the gear damper groove position is:

$$z_0(\theta, t) = A \cdot \cos(N\theta) \cdot \sin(\omega_0 t) \tag{33}$$

where A is the maximum axial amplitude of the damper groove, θ is the circumferential position, $\cos(N\theta)$ represents the amplitude as a cosine distribution in the circumferential direction, and ω_0 represents the vibration circle frequency (rad/s).

The axial displacement equation of the ring damper is $z_1(\theta, t)$, and the motion state of the ring damper is determined by the frictional force. The velocity and acceleration of the ring damper in the viscous state are the same as the velocity and acceleration of the gear damper groove position, which can be obtained by the axial displacement equation of the gear groove:

$$\left. \begin{array}{l} \dot{z}_1(\theta, t) = \dot{z}_0(\theta, t) = \omega_0 \cdot A \cos(N\theta) \cdot \cos(\omega_0 t) \\ \ddot{z}_1(\theta, t) = \ddot{z}_0(\theta, t) = -\omega_0^2 \cdot A \cos(N\theta) \cdot \sin(\omega_0 t) \end{array} \right\} t_0(\theta) < t < t_1(\theta) \tag{34}$$

When the acceleration of the damper ring reaches the maximum acceleration provided by the friction force, the motion state becomes a slip:

$$\sin[\omega_0 t_1(\theta)] = k(\theta) = \frac{\mu \Omega^2 r}{A \omega_0^2 \cos(N\theta)} \tag{35}$$

where Ω is the angular velocity of gear, r is the radius of ring damper. Only when $|k(\theta)| < 1$, Equation (35) has a solution. $|k(\theta)| > 1$ indicates that the maximum frictional force provided by the contact surface is greater than the frictional force required to maintain the synchronous movement of the ring damper and the gear. The ring damper is subjected to static friction and in a viscous state. t_1 is a function of the circumferential position angle θ. Since the normalized frictional force of different circumferential positions of the ring damper is variable, the minimum normalized frictional force occurs at the maximum amplitude, defined as:

$$k(\theta)|_{\min} = \frac{\mu \Omega^2 r}{A \omega_0^2} = k_0 \tag{36}$$

When the damping ring begins to slip, $k_0 = 1$, thereby obtaining the critical amplitude under given conditions.

$$A|_{\text{critical}} = \frac{\mu \Omega^2 r}{\omega_0^2} \tag{37}$$

When a slip occurs, the ring damper is subjected to a sliding frictional force, the acceleration is constant, and the velocity and acceleration equations are:

$$\left. \begin{aligned} \dot{z}_1(\theta,t) &= \omega_0 A \cos(N\theta)\{\mp\omega_0 k(\theta)[t - t_1(\theta)] + \cos[\omega_0 t_1(\theta)]\} \\ \ddot{z}_1(\theta,t) &= \mp k(\theta)\omega_0^2 A \cos(N\theta) \end{aligned} \right\} t_1(\theta) < t < t_2(\theta) \tag{38}$$

When the velocity of the ring damper is equal to the speed of the gear, the motion state will become viscous again, and $\dot{z}_1(\theta, t_2(\theta)) = \dot{z}_0(\theta, t_2(\theta))$.

According to the above equation, the relationship between $t_2(\theta)$ and $t_1(\theta)$ can be obtained:

$$\omega_0 k(\theta)[t_2(\theta) - t_1(\theta)] = \mp[\cos(\omega_0 t_2(\theta)) - \cos(\omega_0 t_1(\theta))] \tag{39}$$

$$\omega_0 k(\theta)[t_2(\theta) - t_1(\theta)] = \mp[\cos(\omega_0 t_2(\theta)) - \cos(\omega_0 t_1(\theta))] \tag{40}$$

When the sliding frictional force is small, there is no viscous state in one vibration cycle, which is called a full sliding state. In this case, $t_3(\theta) = t_2(\theta)$, and:

$$t_1(\theta) = \frac{\arccos\frac{k(\theta)\pi}{2}}{\omega_0}, \quad t_3(\theta) = t_2(\theta) = t_1(\theta) + \frac{\pi}{\omega_0}, \quad t_4(\theta) = t_1(\theta) + \frac{2\pi}{\omega_0} \tag{41}$$

As the sliding frictional force increases, i.e., $k(\theta)$ gradually increases, there is an alternating slip and viscous in a vibration cycle, which is called a viscous-sliding state. In this case, the critical moment of the first slip zone and the viscous zone is obtained by Equation (35):

$$t_1(\theta) = \frac{\arcsin k(\theta)}{\omega_0} \tag{42}$$

$t_2(\theta)$ can be obtained by Equations (39) and (42):

$$\omega_0 k(\theta)\left[t_2(\theta) - \frac{\arcsin k(\theta)}{\omega_0}\right] = -\left[\cos(\omega_0 t_2(\theta)) - \sqrt{1 - k^2(\theta)}\right] \tag{43}$$

It should be noted that $t_2(\theta)$ is a transcendental equation and requires numerical solution.

At the critical value of full sliding and viscous-sliding, the $t_1(\theta)$ obtained by Equations (41) and (42) are equal, and further obtain:

$$k(\theta)\big|_{\text{critical}} = \sqrt{\frac{1}{1 + (\pi/2)^2}} \approx 0.537 \tag{44}$$

The relative displacement of the ring damper to the gear at circumferential position θ can be obtained by integration:

$$\begin{aligned} \Delta s(\theta) &= 2\int_{t_1(\theta)}^{t_2(\theta)} \left[\dot{z}_1(\theta,t) - \dot{z}_0(\theta,t)\right]dt \\ &= 2\omega_0 \cdot A\cos(N\theta)\int_{t_1(\theta)}^{t_2(\theta)} [-\omega_0 k(\theta)(t - t_1(\theta)) + \cos(\omega_0 t_1(\theta)) - \cos(\omega_0 t)]dt \\ &= 2\omega_0 \cdot A\cos(N\theta)\{-\omega_0 k(\theta)[t_2(\theta) - t_1(\theta)]^2 + \cos(\omega_0 t_1(\theta))[t_2(\theta) - t_1(\theta)] \\ &\quad - \frac{1}{\omega_0}[\sin(\omega_0 t_2(\theta)) - \sin(\omega_0 t_1(\theta))]\} \end{aligned} \tag{45}$$

The energy dissipated by the ring damper in one vibration cycle can be calculated by integrating the relative displacement of the circumferential points with the friction product:

$$\Delta W = \int_0^{2\pi} \Delta s(\theta) \cdot \frac{F_f}{2\pi}d\theta = 4N\int_0^{\frac{\pi}{2N}} \Delta s(\theta) \cdot \frac{F_f}{2\pi}d\theta = 4N\int_0^{\frac{\arccos k_{\min}}{N}} \Delta s(\theta) \cdot \frac{F_f}{2\pi}d\theta \tag{46}$$

$\eta = \Delta W / \omega_0^2 A^2 m_r$ is defined as the normalized friction energy dissipation, and m_r is the ring damper mass. The physical meaning of the normalized friction energy dissipation is the ratio of the friction energy dissipation to the maximum kinetic energy of the ring damper. Damping ratio can be expressed as:

$$\zeta = \frac{\Delta W}{4\pi W} = \frac{\Delta W}{4\pi(M_{eq}\omega_0^2 A^2 + m_r \omega_0^2 A^2)} = \frac{\eta m_r}{4\pi(M_{eq} + m_r)} \tag{47}$$

where M_{eq} is the equivalent mass of the gear in a given mode, relating to the vibration form and gear.

$$M_{eq} = \boldsymbol{\Phi M \Phi}^T \tag{48}$$

where $\boldsymbol{M}$ represents the physical mass matrix of the gear and $\boldsymbol{\Phi}$ represents the mode matrix.

Figure 9 shows the relationship between the frictional force and the energy dissipation of the axial-vibration in the flat plate-slider model and ring damper-gear model. The energy dissipation of the flat plate-slider model was found to be greater. This is because the ring damper has a small amplitude near the nodal line under nodal diameter vibration, and its corresponding normalized frictional force is close to 1 or even greater than 1; thus, friction energy dissipation is little. The ring damper-gear model under axial vibration is similar to the flat plate-slider model, and there is a constant optimal normalized frictional force of approximately 0.365, which is smaller than the flat plate-slider model.

Figure 10 shows the relationship between the amplitude and energy dissipation of the axial vibration in the flat plate-slider model and the ring damper-gear model. The definition of normalized amplitude is the same as above. When the amplitude is small, the acceleration provided by the friction can maintain the non-slip motion between the damper and the main structure, so there is no friction energy dissipation. As the amplitude increases, there is a slip in the damper and the main structure. The friction energy dissipation increases rapidly with the increase of the amplitude. After peak energy dissipation, the increase of friction energy dissipation is smaller than the kinetic energy increase of the damper as the amplitude increases, and the normalized energy dissipation begins to decrease. The optimum amplitude of the flat plate-slider model appears at a critical amplitude of 2.22 times. The optimal amplitude of the ring damper under the nodal diameter axial vibration is about 2.74 times the critical amplitude.
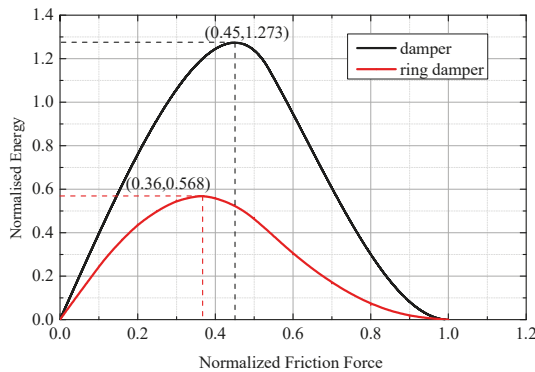
Figure 9. The relationship between the minimum normalized frictional force and the normalized energy dissipation of the slider (black line) and the ring damper (red line).
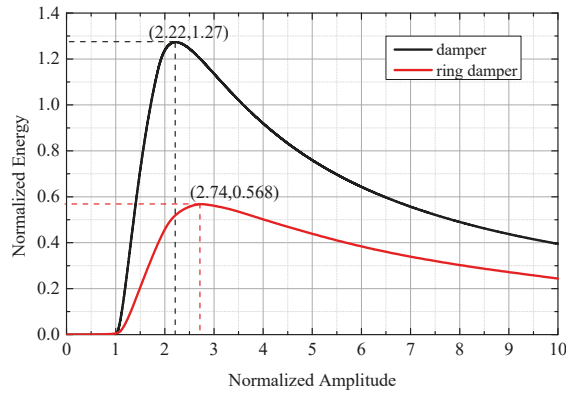
Figure 10. The relationship between the normalized amplitude and the normalized energy dissipation of the slider (black line) and the ring damper (red line).

5. Effect of Ring Damper Parameters

In order to discuss the effect of mass and friction coefficient on equivalent damping, a gear model with the following parameters was used: steel, with a density of 7830 kg/m^3, Poisson's ratio of 0.3 and an elastic modulus of 210 Gpa (room temperature), as shown in Figure 2a. According to the modal calculation, the gear has a 4 nodal diameter resonance at a working speed of 10,590 r/min; a vibration mode diagram is presented in Figure 11. Taking the 4 nodal diameter vibration of the gear as an example, the effect of mass on equivalent damping is shown in Figure 12, and the effect of friction coefficient on equivalent damping is shown in Figure 13.
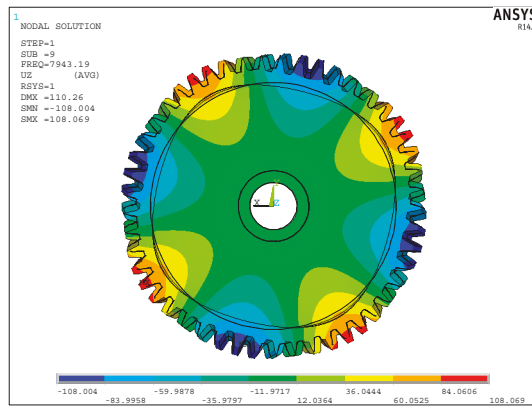
Figure 11. 4 nodal diameter vibration mode.

Figure 12 shows the effect of the ring damper mass on the equivalent damping. Equation (46) shows that the equivalent damping ratio is positively correlated with its mass. When the ring damper mass is much smaller than the gear mass, the equivalent damping ratio of the ring damper under axial vibration is approximately linear. It can be seen from Equation (37) that the critical amplitude is independent of the mass of the ring damper because the frictional force and inertial force of the ring damper are both proportional to its mass, and the critical amplitude is related to the ratio of the frictional force and the inertial force. Therefore, in the computational model of this paper, the ring damper mass is linear with critical amplitude. Increasing the ring damper mass will be beneficial in increasing its equivalent damping.
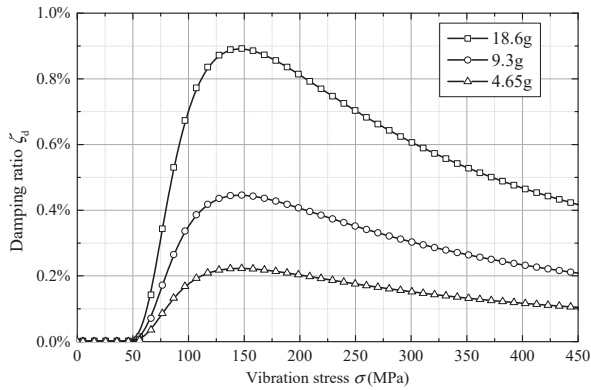
Figure 12. Effect of the ring damper mass on equivalent damping.

Figure 13 shows the effect of friction coefficient on equivalent damping. The friction coefficient is linear with the critical vibration loads, and does not affect the damping ratio peak. In the ring damper design, the critical vibration load must be less than the allowable vibration load, otherwise the ring damper will lose its damping effect; however, when the critical vibration load is too small, it may cause the ring damper to work on the right side of the damping peak. As can be seen from Figure 13, on the right side of the damping peak, the damping ratio decreases as the vibration loads increases. Thus, for a vibration state, there is an optimal friction coefficient provided by the ring damper.
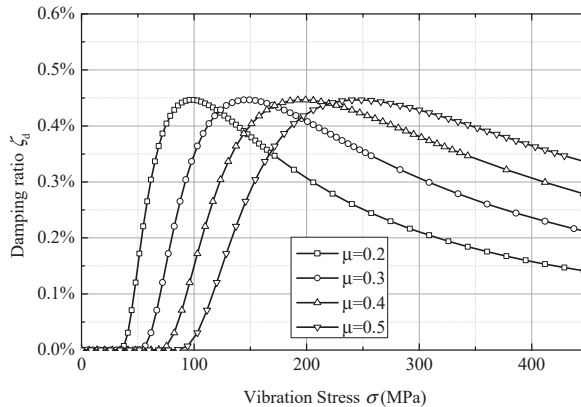
Figure 13. Effect of friction coefficient on equivalent damping.

6. Conclusions

In this paper, an equivalent damping numerical prediction method for a ring damper under axial vibration is proposed. The friction energy dissipation model due to inertia is established by using a flat plate-slider model, and its extension is applied to nodal diameter vibration. This model is used to analyze the influence of ring damper parameters on its equivalent damping. According to the analysis, the following conclusions can be drawn:

(1) Under the axial component of the nodal diameter vibration, friction energy dissipation is caused by the relative motion between the gear and the ring damper.
(2) In the flat plate-slider model, there is a critical amplitude that causes a relative motion between the slider and the plate. When the amplitude is greater than the critical amplitude, the friction

energy dissipation increases with the amplitude. An optimum amplitude maximizes the equivalent damping provided by the slider, and the optimum amplitude is $\pi/\sqrt{2}$ times of the critical amplitude.

(3) For any given model, there is a critical vibration load. When the vibration load does not reach the critical value, the ring damper gets stuck in the gear, and there is no damping effect. When the vibration load is greater than the critical vibration load, the contact surface of the gear and the ring damper slide relative to each other, and the vibration energy is dissipated by the frictional force, thus enabling the ring damper to work. The optimal amplitude is 2.74 times that of the critical amplitude.

(4) When the ring damper mass is much smaller than the gear mass, the equivalent damping provided by the ring damper is proportional to its mass.

(5) When other parameters are constant, the friction coefficient is linear with the critical vibration load, but does not affect the peak damping.

Notation

u	Vibration displacement
C	Damping matrix
F_{ext}	External exciting force
C_{eq}	Equivalent damping
Φ	Gear system modal matrix
ζ	Damping ratio of the gear
β	Damping ring mass rate
m_g	Mass of the gear
α	Proportional coefficient
F_N	Normal force
ω_0	Circular vibration frequency of plate
k	Normalized frictional parameter
η	Normalized friction energy dissipation
θ	Circumferential position
Ω	Angular velocity of gear
r	Radius of ring damper
M	Mass matrix
K	Stiffness matrix of the gear system
F_{nl}	Nonlinear friction force
K_{eq}	Equivalent stiffness
q	Modal displacement vector
ζ_{eq}	Equivalent damping ratio
m_d	Mass of the ring damper
σ	Vibration loads
m_1	Mass of the slider
A	Amplitude of structure
$x(t)$	Displacement of slider
F_f	Maximum static friction force
ΔW	Dissipated energy of any period in the steady state
$z(\theta, t)$	Axial displacement of ring damper
μ	Friction coefficient
$\Delta s(\theta)$	Relative displacement of the ring damper to the gear

References

1. Mclntire, W.L. *How to Reduce Gear Vibration Failures*; AGMA Aerospace Gearing Committee Meeting; American Gear Manufacturers Association: Orlando, FL, USA, 1964.
2. Drago, R.J.; Brown, F.W. The analytical and experimental evaluation of resonant response in high-speed, lightweight, highly loaded gearing. *J. Mech. Des.* **1981**, *103*, 346–356. [CrossRef]
3. Laxalde, D.; Thouverez, F.; Sinou, J.J.; Lombard, J.P. Qualitative analysis of forced response of blisks with friction ring dampers. *Eur. J. Mech. A/Solids* **2007**, *26*, 676–687. [CrossRef]
4. Laxalde, D.; Thouverez, F.; Lombard, J.P. Forced response analysis of integrally bladed disks with friction ring dampers. *J. Vib. Acoust.* **2010**, *132*, 011013. [CrossRef]
5. Zucca, S.; Firrone, C.M.; Facchini, M. A method for the design of ring dampers for gears in aeronautical applications. *J. Mech. Des.* **2012**, *134*, 091003. [CrossRef]
6. Firrone, C.M.; Zucca, S. Passive control of vibration of thin-walled gears: Advanced modelling of ring dampers. *Nonlinear Dyn.* **2014**, *76*, 263–280. [CrossRef]
7. Baek, S.; Epureanu, B. Reduced-order modeling of bladed disks with friction ring dampers. *J. Vib. Acoust.* **2017**, *139*, 061011. [CrossRef]
8. Tang, W.; Baek, S.; Epureanu, B.I. Reduced-order models for blisks with small and large mistuning and friction dampers. *J. Eng. Gas Turbines Power* **2017**, *139*, 012507. [CrossRef]
9. Tang, W.; Epureanu, B.I. Nonlinear dynamics of mistuned bladed disks with ring dampers. *Int. J. Non-Linear Mech.* **2017**, *97*, 30–40. [CrossRef]
10. Tang, W.; Epureanu, B.I. Geometric optimization of dry friction ring dampers. *Int. J. Non-Linear Mech.* **2019**, *109*, 40–49. [CrossRef]
11. Lopez, I.; Busturia, J.M.; Nijmeijer, H. Energy dissipation of a friction damper. *J. Sound Vib.* **2004**, *278*, 539–561. [CrossRef]
12. Lopez, I.; Nijmeijer, H. Prediction and validation of the energy dissipation of a friction damper. *J. Sound Vib.* **2009**, *328*, 396–410. [CrossRef]
13. Ziegert, J.C. Optimal design of split ring dampers for gas turbine engines. *J. Eng. Gas Turbines Power* **1995**, *117*, 569.
14. Lopez, I. Theoretical and Experimental Analysis of Ring-Damped Railway Wheels. Ph.D. Thesis, Universidad de Navarra, Pamplona, Spain, November 1998.
15. Tangpong, X.W.; Wickert, J.A.; Akay, A. Finite element model for hysteretic friction damping of traveling wave vibration in axisymmetric structures. *J. Vib. Acoust.* **2008**, *130*, 011005. [CrossRef]
16. Tangpong, X.W.; Wickert, J.A.; Akay, A. Distributed friction damping of travelling wave vibration in rods. *Philos. Trans. R. Soc. Lond. A Math. Phys. Eng. Sci.* **2008**, *366*, 811–827. [CrossRef] [PubMed]

Angle Tracking Observer with Improved Accuracy for Resolver-to-Digital Conversion

Haoye Qin and Zhong Wu *

School of Instrumentation and Optoelectronic Engineering, Beihang University, Beijing 100191, China; hoyqen@buaa.edu.cn
* Correspondence: wuzhong@buaa.edu.cn; Tel.: +86-10-8233-9703

Abstract: A resolver is an absolute shaft sensor which outputs pair signals with ortho-symmetric amplitudes. Ideally, they are sinusoidal and cosinusoidal functions of the shaft angle. In order to demodulate angular position and velocity from resolver signals, resolver-to-digital conversion (RDC) is necessary. In software-based RDC, most algorithms mainly employ a phase-locked loop (PLL)-based angle tracking observer (ATO) to form a type-II system. PLL can track the detected angle by regulating the phase error from the phase detector which depends on the feature of orthogonal symmetry in the resolver outputs. However, a type-II system will result in either steady-state errors or cumulative errors in the estimation of angular position with constant accelerations. Although type-III ATOs can suppress these errors, they are still vulnerable to high-order acceleration signals. In this paper, an improved PLL-based ATO with a compensation model is proposed. By using dynamic compensation, the proposed ATO becomes a type-IV system and can reduce position estimation errors for high-order acceleration signals. In addition, the parameters of ATO can be tuned according to the bandwidth, noise level and capability of error suppression. Simulation and experimental results demonstrate the effectiveness of the proposed method.

Keywords: shaft angle sensors; resolver-to-digital conversion (RDC); orthogonal symmetry; position measurement; angle tracking observer; phase-locked loop (PLL); error suppression

---

1. Introduction

Accurate estimation of angular position and velocity for motor drives is a desired feature in high-performance automatic control systems. Resolvers, due to their strong robustness, high ruggedness and relatively low cost, have been widely chosen as shaft sensors to provide precise position information. However, the output of a resolver is two modulated analog signals which need to be demodulated by adopting resolver-to-digital conversion (RDC) before the angular position can be obtained.

The solutions to RDC are mainly comprised of hardware-based RDC and software-based RDC [1]. The hardware-based RDC method mainly employs a special integrated circuit (IC) [2,3]. However, since the high-precision demodulation chip is expensive and limited by the bandwidth and temperature drift of the hardware itself (external resistances and capacitances), the use of hardware-based RDC may cause deviations, thereby affecting the measurement accuracy of the angle measuring system.

Software-based RDC can solve the problems that hardware RDC faces. A commonly used software RDC method includes open-loop arctangent method with look-up table [4] and type-II angle tracking observer (ATO)-based on phase-locked loop (PLL) technique. The arctangent method calculates the angle position by inverse arctangent operation using the sine and cosine values with a fast-dynamic response [5] and less hardware resources. However, this method is susceptible to electromagnetic noise and also introduces great nonlinearity in the system [2,5].

Therefore, most commercially available close-loop converters employ PLL technique to overcome noise and achieve tracking the input position signal with high resolution and wide bandwidth. A conventional PLL-based ATO consists of a phase detector, a loop filter (LF) and a voltage-controlled oscillator. The sinusoidal phase detector is used to generate the estimated error, which is proportional to the difference between the input signal and output signal. Then the error signal goes into a low-pass filter to remove high frequency noise. To complete the loop, the voltage-controlled oscillator works as an integrator for the filtered signal. It is important to note that the form of LF is $(k_P + k_I/s)$, which makes the conventional ATO a type-II system.

In order to improve the performance of conventional ATOs, modifications have been made over the past years. Some ATOs aim to reduce impact of disturbances in analog signals from the resolver [6,7], and thus on the estimated angular position. Sivappagari and Konduru proposed an ATO that utilizes synchronous demodulation of the input signals and reference signal to enhance the precision of position determination [8]. As for the application in sensorless drives, ATO is employed for reducing noise and oscillation in rotor position estimation, compared to those obtained from traditional methods [9,10]. Several works [11–15] have focused on solving the amplitude imbalance-induced position error with modified ATO algorithms for error compensation.

Regarding the instability of ATO in high acceleration applications, a hybrid ATO scheme incorporating an LTI observer and a quadrature encoder was proposed [7]. This hybrid method has a low mean square error and can improve robust stability. Low dynamic response has been investigated by Yim et al. [16], where the conventional proportional-integral (PI)-based LF was transformed into a "bang-hang"-type phase comparator for fast tracking capability.

Another limitation of the conventional ATO is that it will cause a steady-state error with a speeding up signal at a constant acceleration. To reduce this error, several PLLs based on the third-order tracking loop have emerged [17–20]. Li and Wu [2] transformed the conventional type-II ATO system into type-III by changing the low-pass PI filter to an improved proportional–integral–derivative (PID) structure, which enhances the ability to filter high-frequency noise components. Also, Wang et al. [5] designed an error compensation module to eliminate this position error by using the estimated speed to generate a signal proportional to the motor acceleration. The advantages of this approach are its simple implementation and time-saving feature since it only requires one module to be added. Ellis and Krah [19] took advantage of the Luenberger observer for angle tracking, which provides estimations of acceleration signals. Their design actually can also be classified as a type-III system in which the LF is represented as $(k_P + k_I/s + k_D/s^2)$ [20]. Caruso et al. [21] focused on the compensation of position error by making the tracking system have a time-dependent error, which would finally be cancelled by the PI controller. Zhang et al. [22] proposed a composite observer for fast-varying speed using the arctangent method to compensate the estimated speed from ATO. Drawing on advantages from both arctangent and ATO methods, this composite observer enhances accuracy in estimating acceleration-related position. Neural networks have also been applied independently [23] and combined with third-order ATO [18] for reducing position errors, but the implementation is complicated and time-consuming.

However, there are still limited researches on reducing estimated position errors when the motor speeds up with a non-constant acceleration. Jerk and high-order acceleration are involved in some servo systems requiring high mobility, for example, CNC machining for irregular shape and positioning radar in tracking artillery, which places a great demand for ATO method in precise position estimation with high-order acceleration signals.

Therefore, in this paper, we focus mainly on suppressing steady-state errors for input signals with a high-order acceleration and enhancing the accuracy of ATO. The proposed ATO scheme utilizes the estimated speed signal and a compensation feedback loop to form a type-IV system. Simulation and experiments have been carried out to verify the effectiveness of our scheme. These results demonstrate that not only can errors from low-order acceleration signal be eliminated, but also tracking accuracy for high-order signal can be improved.

2. Principles of Resolver-to-Digital Conversion

In this section we first introduce the basic principle of the resolver and its subsequent demodulation methods, and then several previous RDC solutions are presented and evaluated for their advantages and drawbacks.

2.1. Principle of Resolver

A resolver is a position sensor comprising of a stator and a rotor, which is connected to the shaft of the motor for detecting its angular position. The stator portion houses three windings, namely one excitation winding and two output windings (sine and cosine windings), of which the voltage output amplitudes are orthogonally symmetric, specifically, sinusoidally and cosinusoidally related to the shaft angle. The excitation winding is responsible for inducing voltage in the rotator windings through electromagnetic induction. With the shaft angle changing, amplitudes of the two-phase voltages from sine and cosine output windings are measured and employed to determine relative position between the stator and rotor.

Figure 1 illustrates the configuration of a resolver and subsequent software-based RDC scheme, which serves as an integrated position estimation system. The excitation windings are usually applied with a sinusoidal reference voltage of constant amplitude and high frequency, expressed as:

$$u_0(t) = A \sin \omega_{ref} t, \tag{1}$$

where A is the amplitude of the reference voltage and ω_{ref} is the angular frequency.
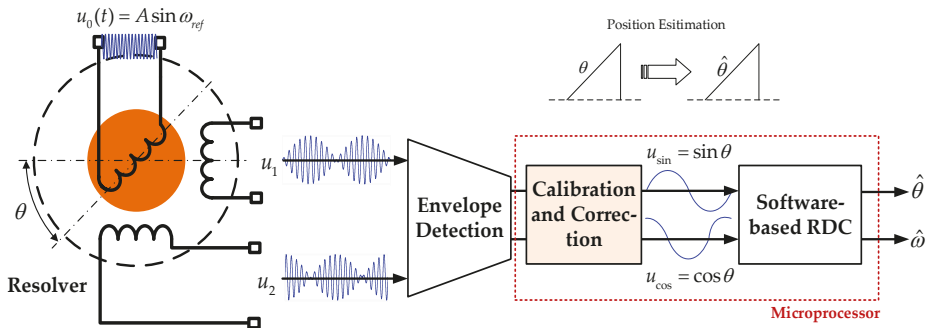
Figure 1. Schematic block diagrams of a resolver and resolver-to-digital conversion (RDC).

When the rotor rotates, the output windings will generate amplitude-modulated pair signals as:

$$\begin{cases} u_1(\theta, t) = A \sin \omega_{ref} t \cdot K \cdot \sin \theta \\ u_2(\theta, t) = A \sin \omega_{ref} t \cdot K \cdot \cos \theta \end{cases}, \tag{2}$$

where K is the effective transformation ratio of the resolver and θ represents the angular position of the rotor with respect to the stator winding. These two modulated signals $u_1(\theta,t)$ and $u_2(\theta,t)$ have the form of sinusoidal and cosinusoidal envelopes. Then, envelope detection is necessary to obtain the needed signal. In practice, there are always disturbances from imperfect characteristics, namely the amplitude imbalances, DC offsets and imperfect quadrature, which arise from eccentric rotor, unequal winding and non-orthogonal symmetry of the windings. Hence, the signal after envelope detection can be expressed in the form:

$$\begin{cases} u_{\sin} = \sin \theta + a_{s0} \\ u_{\cos} = \cos(\theta + \beta) + a_{c0} \end{cases}, \tag{3}$$

where a_{s0} and a_{c0} are the offsets, and β represents the imperfect quadrature. Preprocessing methods (noise reduction, calibration and correction) are carried out to result in:

$$\begin{cases} u_{\sin} = \sin\theta \\ u_{\cos} = \cos\theta \end{cases},$$ (4)

where $u_{\sin}$ and $u_{\cos}$ are two ortho-symmetric signals, whose trigonometric features aid in subsequent demodulation.

Finally, the angular position θ and velocity are calculated through suitable demodulation algorithms (for example, phase-locked loop and arctangent algorithms) to obtain the estimation speed $\hat{\omega}$ and position $\hat{\theta}$.

As is demonstrated in the resolver's principle, the orthogonal symmetry of alignment of two output windings results in the orthogonal symmetry of both envelope signals and post-envelope-detection signals.

2.2. Classical Resolver-to-Digital Conversion

2.2.1. Arctangent Method

A straightforward method is to obtain the angular position θ is through arctangent operation of $u_{\sin}$ and $u_{\cos}$, given by:

$$\theta = \tan^{-1}\left(\frac{u_{\sin}}{u_{\cos}}\right).$$ (5)

As is clearly indicated by Equation (5), the arctangent method suffers from its highly nonlinear arctangent operation and is limited to application on low-speed estimation. Also, with a nonlinear feature, there needs to be a look-up table for the arctangent calculation, which increases the software loads.

2.2.2. Conventional PLL-Based ATO

As shown in Figure 2, the conventional ATO method tracks angular position based on PLL technique. Figure 2a is the actual form of the ATO, where k_I and k_P are the coefficients for the integral and proportional terms, respectively, and Figure 2b shows the linearized structure.
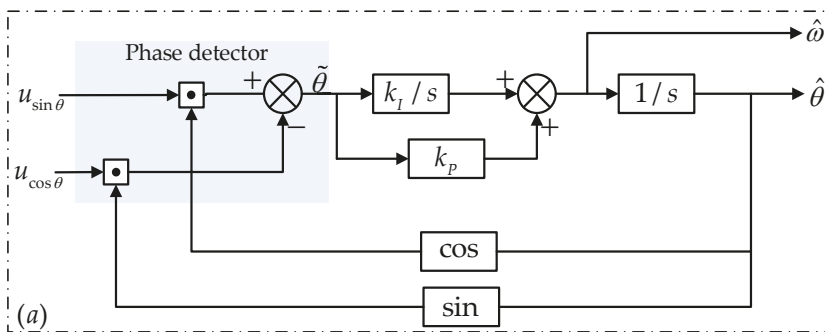
Figure 2. *Cont.*
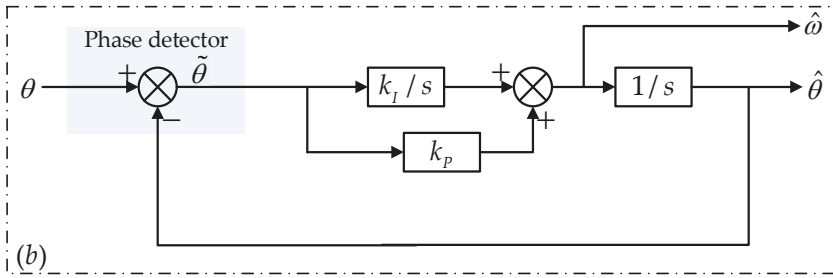
Figure 2. Block diagram of a conventional phase-locked loop (PLL)-based angle tracking observer (ATO): (**a**) actual structure; (**b**) linearized structure.

The estimated angular position is transformed through trigonometric function and multiplied by the demodulated signals. By utilizing the feature of orthogonal symmetry in the resolver signals in Equation (4), the phase error can be derived from the phase detector (PD), expressed as:

$$\varepsilon = \sin\theta\cos\hat{\theta} - \cos\theta\sin\hat{\theta} = \sin(\theta - \hat{\theta}) = \sin\widetilde{\theta}. \tag{6}$$

When the ATO functions properly, the position error is small enough, that is, $\widetilde{\theta} \rightarrow 0$, so the input error signal can be expressed as $\varepsilon = \widetilde{\theta}$. Therefore, linearization of the ATO can be implemented, as shown in Figure 2b, and the closed loop transfer function is derived as:

$$\phi_1(s) = \frac{k_I + k_P s}{s^2 + k_P s + k_I}. \tag{7}$$

The conventional ATO is a representative closed-loop estimation system which overcomes noise and track the input signal with a relatively high precision. The linearized structure of the ATO belongs to a type-II system.

2.2.3. Compensated Type-III ATO

In [5], an acceleration-compensated ATO was proposed by employing the estimated speed to generate a compensation module for the position error, comprising a differentiator and a first-order low-pass filter, which finally makes this ATO a type-III system. The actual scheme of this method is shown in Figure 3 and a linearized structure of this ATO is analogous to Figure 2b. Compared with Figure 2, there is a third parameter T representing the time constant of the low-pass filter.
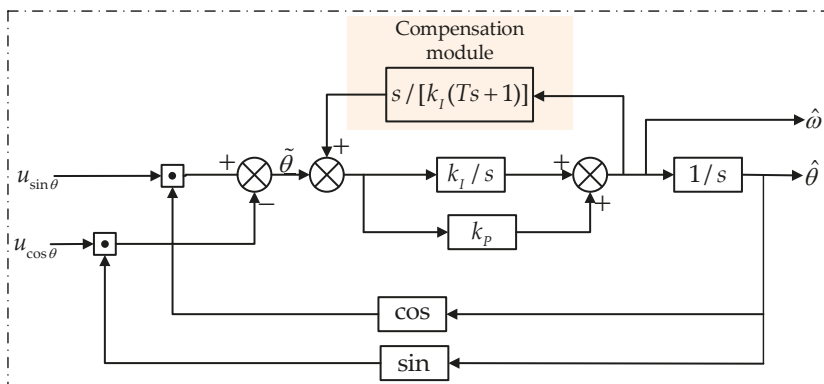
Figure 3. Block diagram of a type-III ATO presented in [5].

The linearized closed-loop transfer function can be denoted as:

$$\phi_2(s) = \frac{Tk_Ps^2 + (Tk_I + k_P)s + k_I}{(T - \frac{k_P}{k_I})s^3 + Tk_Ps^2 + (Tk_I + k_P)s + k_I}. \tag{8}$$

This compensated type-III ATO has the basic structure inherited from the conventional ATO but resolves the steady-error of estimating constant acceleration signal ($\theta = at^2$) with a time-saving and simple technique of adding a compensation module, which achieves a higher precision in tracking the position of an accelerating motor. However, this method fails to eliminate steady-state error resulting from a first- or higher-order acceleration signal.

3. Improved ATO with Dynamic Compensation

Enhanced position estimation accuracy for high-order acceleration signals holds significance and valuable for practical applications in high-precision CNC machines and positioning radar for tracking artillery or other flying targets with high mobility. Although type-III ATO presents a solution to constant acceleration signals, accurately estimating non-constant high-order acceleration signals is still a hard case. To reduce demodulation errors for high-order acceleration signals, a compensated ATO with improved accuracy is proposed in this section. The proposed scheme investigates the error problem and improves the accuracy from the perspective of the internal body of the ATO, which is cost-effective and efficient. Theoretical analysis, simulation and experiments are conducted subsequently to demonstrate the effectiveness of this method.

3.1. Proposed Compensated Scheme of ATO

Figure 4 presents the proposed PLL-based ATO with compensation module that inhibits the steady-state error when applying a first-order acceleration signal ($\theta = at^3$). The estimated speed signal is employed to construct an internal feedback loop. The basic idea of the proposed ATO is to improve the system order of the LF and therefore make the ATO become a type-IV system. By carefully designing the parameters and form of the transfer function, low-order items in the numerator of the system transfer function can be cancelled, leaving only the highest-order item, as is illustrated in the following derivation.
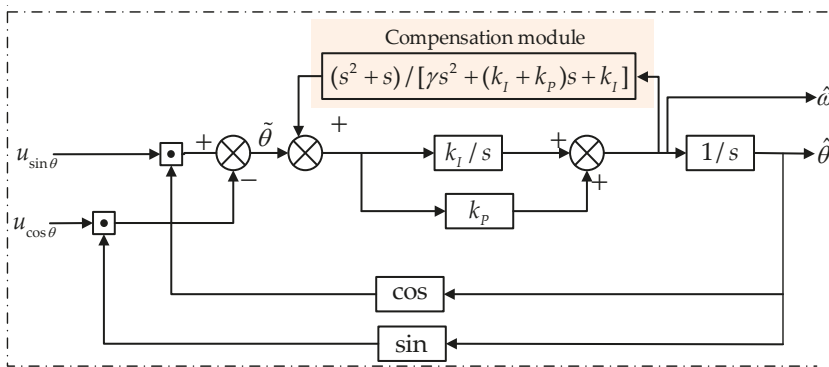
Figure 4. Block diagram of the proposed type-IV ATO.

In contrast with the abovementioned compensated type-III ATO, the proposed structure takes advantage of a second-order compensation module $(s^2 + s)/[\gamma s^2 + (k_I + k_P)s + k_I]$, where γ is a parameter independent from k_I and k_P.

Hence, the closed-loop transfer function $\phi_3(s)$ can be expressed as:

$$\phi_3(s) = \frac{\hat{\theta}(s)}{\theta(s)} = \frac{k_P\gamma s^3 + (k_I\gamma + k_Ik_P + k_P^2)s^2 + (2k_Ik_P + k_I^2)s + k_I^2}{(\gamma - k_P)s^4 + k_P\gamma s^3 + (k_I\gamma + k_Ik_P + k_P^2)s^2 + (2k_Ik_P + k_I^2)s + k_I^2}. \tag{9}$$

According to Equation (9), it is easy to derive the error transfer function of Figure 4 as:

$$\phi_{3e}(s) = \frac{\widetilde{\theta}(s)}{\theta(s)} = 1 - \phi_3(s) = \frac{(\gamma - k_P)s^4}{(\gamma - k_P)s^4 + k_P\gamma s^3 + (k_I\gamma + k_Ik_P + k_P^2)s^2 + (2k_Ik_P + k_I^2)s + k_I^2}. \tag{10}$$

As for a first-order acceleration signal, $\theta = \frac{1}{6}\alpha t^3$, the Laplace transfer is:

$$R(s) = \frac{\alpha}{s^4}. \tag{11}$$

By applying the final value theorem, the steady-state position estimation error can be calculated from Equations (10) and (11) as:

$$e_3(\infty) = \lim_{s \to 0} s \cdot \frac{(\gamma - k_P)s^4}{(\gamma - k_P)s^4 + k_P\gamma s^3 + (k_I\gamma + k_Ik_P + k_P^2)s^2 + (2k_Ik_P + k_I^2)s + k_I^2} \cdot \frac{\alpha}{s^4} = 0. \tag{12}$$

The result from Equation (12) indicates that the proposed RDC scheme can track a signal of no higher than third order regarding time without error, which greatly enhances the precision for measuring the motor's position. While the acceleration order is second, the position steady-state error $e_3(\infty)$ is a constant value with a dependence of Equation (13):

$$e_3(\infty) \propto \frac{\gamma - k_P}{k_I^2}. \tag{13}$$

Although this ATO is still vulnerable to higher-order signal, second-order acceleration and below signals are more common in practical application. Also, according to the Taylor series expansion, even if the signal contains fourth or above components, it is too small to affect the estimation precision.

Theorical analysis shows that the proposed ATO is capable of improving position measurement accuracy by reducing estimation error from high-order acceleration signal, $\theta = \alpha t^n$. To be specific, this ATO can eliminate position errors when n ≤ 3 and reduce error when n ≥ 4.

3.2. Parameter Tuning Guidance

In the proposed ATO structure, there are three free parameters for users to tune, namely k_I and k_P, the coefficients for the integral and proportional terms, respectively, and γ from the compensation module.

3.2.1. Establishing Relationship Between k_I and k_P

Due to the intrinsic structure of the proposed ATO, the existing tuning method for determining k_I and k_P in conventional ATO can be employed [5]. A typical characteristic equation for a second-order system is $s^2 + 2\zeta\omega_n s + \omega_n^2 = 0$, where ζ equals 0.707 when the overshoot and responsiveness reach a satisfying trade-off. In our case where the second-order system in Equation (7) is denoted by $k_I = \omega_n^2$ and $k_P = 2\zeta\omega_n$, the relationship of $k_I = k_P^2/(4 \times 0.707^2)$ can be established.

3.2.2. Determining k_P and γ

The prerequisite for adjusting k_P and γ is to maintain $\gamma > k_P$. Figure 5a shows the relationship between the two parameters and bandwidth. The bandwidth shows a diagonal-tilt increasement, which indicates that a larger k_P and smaller γ will reach a higher bandwidth.
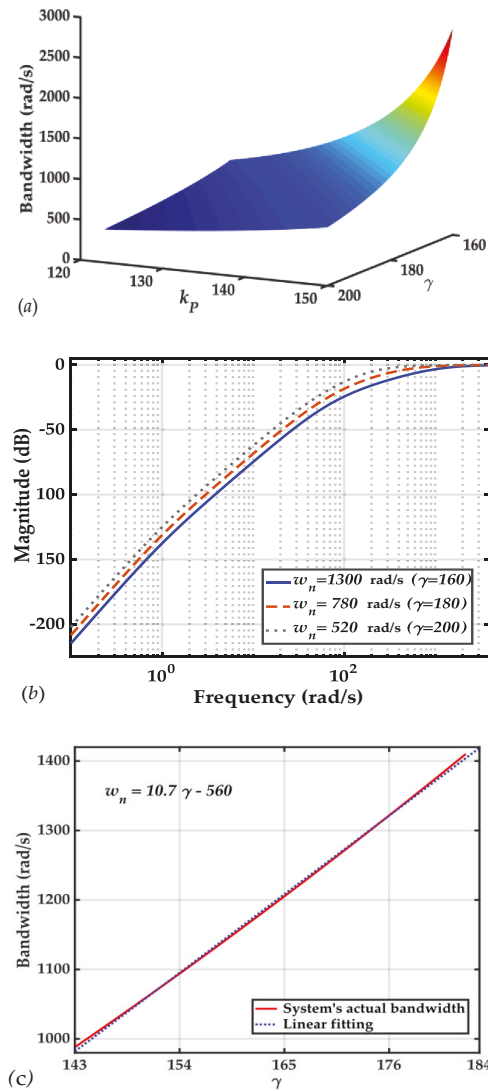
Figure 5. (**a**) Demonstration of relationship between the parameters in the proposed ATO and the system's bandwidth. γ and k_P are variable from 160 to 210 and from 120 to 155, respectively, with k_I determined by $k_I = k_P^2/(4 \times 0.707^2)$. (**b**) Amplitude–frequency response of the proposed ATO's error transfer function with different bandwidths ($\omega_n = 1,300, 780, 520$ rad/s), corresponding to γ equal to 165,185,205 and $k_P = 141.4, k_I = 100^2$. (**c**) Relationship between the ATO's bandwidth and parameter γ, with the other parameters determined by $k_P = \gamma - 23.6$ and $k_I = k_P^2/(4 \times 0.707^2)$. The linearly fitted result corresponds well with this relationship.

Regarding the different bandwidths (denoted as ω_n) of 1300, 780 and 520 rad/s (via varying parameter γ) in Figure 5b, the error transfer function (Equation (10)) of the proposed ATO is investigated under a specific condtion of $k_P = 141.4$ and $k_I = 100^2$. From inspection of these three bandwidths, it

can be concluded that a larger bandwidth (smaller γ) suppresses the position estimation error more effeciently, which corresponds to the analysis of Equations (12) and (13).

It is important to note that an excessive bandwidth will increase the impact of measurement noise, which means γ cannot be too small, or there will be significant oscillations in the estimation results. An experience relation is given as $\gamma \geq k_P + 23.6$; considering a smaller value of γ, the condition results in $\gamma = k_P + 23.6$. Along with $k_P = \gamma - 23.6$ and $k_I = k_P^2/(4 \times 0.707^2)$, Figure 5c evaluates the relationship between γ and the system's bandwidth, which is well-fitted linearly, $\omega_n = 10.7\gamma - 560$. Hence, with a desired bandwidth ω_n, γ can be chosen as $\gamma = 0.0935\omega_n + 53$.

3.2.3. Tuning Guideline

Above all, our tuning guideline is summarized as follows:

(1) Choosing γ according to the desired bandwidth by referring to $\gamma = 0.0935\omega_n + 53$;
(2) Determining k_P via $k_P = \gamma - 23.6$;
(3) Determining k_I via $k_I = k_P^2/(4 \times 0.707^2)$.

4. Simulation and Experimental Results

4.1. Simulation Results

In this section, we implemented a model comprised of conventional ATO, a compensated type-III ATO [5] and the proposed ATO in Simulink to demonstrate their performances. The inputs of the three ATOs are the same ideal sine and cosine signals with different acceleration forms ($\theta = \alpha t^n$) to imitate the demodulated signals coming from RDC.

To compare their accuracy, we tuned the parameters of three ATOs to have the approximate bandwidth of around 1200 rad/s. This bandwidth was chosen for a trade-off between the dynamic performance and measurement noise. Specific parameters for three methods are listed in Table 1.

Table 1. Parameters of the three ATOs.

Method	k_I	k_P	T	γ
Conventional ATO	100^2	141.4	N/A	N/A
Type-III ATO in [5]	100^2	141.4	0.0158	N/A
The proposed ATO	100^2	141.4	N/A	165

Figure 6 shows the position errors with an input signal in the form of $\theta = 4\pi t^2$. Results from the conventional ATO, type-III ATO and the proposed ATO are labelled separately with e_1, e_2 and e_3, respectively.

With a span of 1 second, e_1 demonstrated a steady-state error of 0.145 degree and e_2, e_3 had zero estimation error after 0.2 s. The type-III and proposed ATO experienced an almost similar trend in the observed time span but estimation error from the proposed one had a relatively larger overshoot (8.2×10^{-3} degree) than that of type-III ATO (6.1×10^{-3} degree). However, the settling time was almost the same.

Figure 7 compares the estimation accuracy under the condition of $\theta = 4\pi t^3$. e_1 of conventional ATO shows a large output error range, which presents a theoretically expected linearly increasing trend (at 5 s, $e_1 = 2.18$ degrees). e_2 and e_3 of Figure 7 present that although there is relatively large overshoot and longer settling time, when the systems have enough time to attain steady state, the proposed ATO will present zero position estimation error and type-III ATO will keep a position estimation error of around 7×10^{-4} degree.
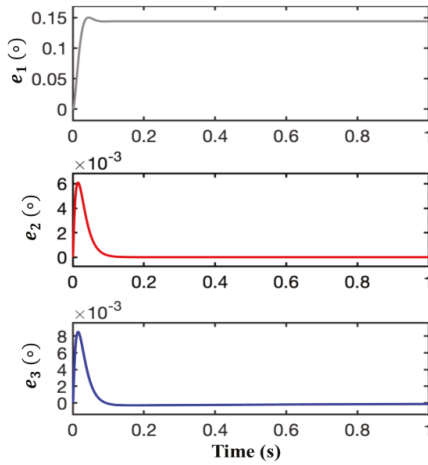
Figure 6. Position errors of different ATOs in the simulation with a constant acceleration input ($\theta = 4\pi t^2$). e_1, e_2 and e_3 are the position estimation errors of conventional ATO, type-III ATO in [5] and the proposed ATO, respectively.
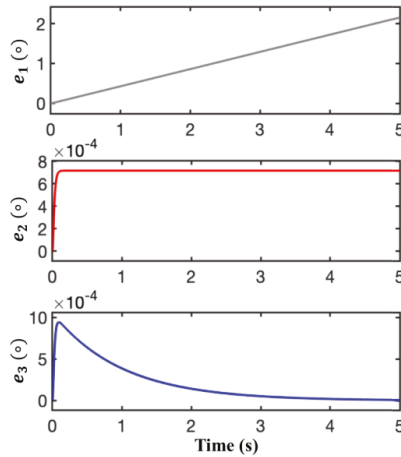
Figure 7. Position errors of different ATOs in the simulation with a first-order acceleration input ($\theta = 4\pi t^3$). e_1, e_2 and e_3 are the position estimation errors of conventional ATO, type-III ATO in [5] and the proposed ATO, respectively.

In order to show the improved accuracy of the ATO even under the condition of higher-order sharp change, we carried out the simulation with the input of $\theta = \pi t^4$. As shown in Figure 8, compared with accumulative errors of 5.3 degrees and 0.0036 degree at 5 s from the conventional and type-III ATO, the proposed one only demonstrates a steady-state error of 7.1×10^{-4} degree.
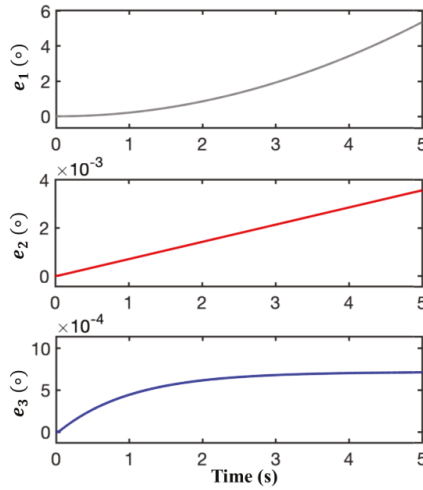
Figure 8. Position errors of different ATOs in the simulation with a second-order acceleration input ($\theta = \pi t^4$). e_1, e_2 and e_3 are the position estimation errors of conventional ATO, type-III ATO in [5] and the proposed ATO, respectively.

Figure 9 demonstrates the estimation errors when the input is set as $\theta = 2\pi + \pi\sin(2\pi t)$. Figure 9a shows the evolution with a time span of 5 seconds and Figure 9b zooms in to omit the large overshoot at the beginning. In the case of sine-wave signal, the proposed ATO is also efficient in error suppression and reduces the error by two orders of magnitude compared to the conventional one.
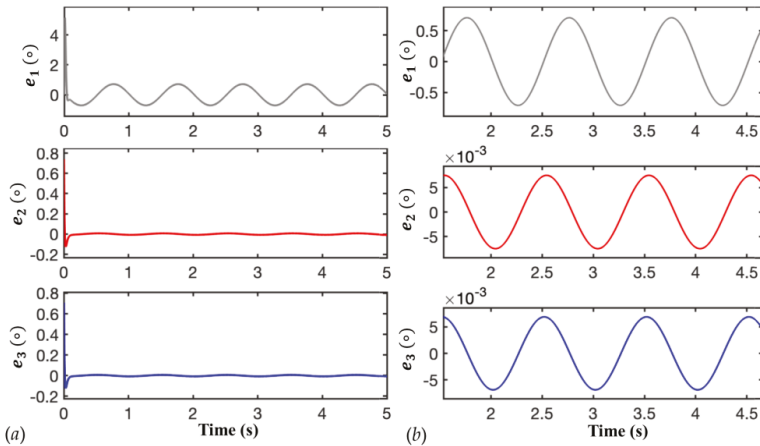
Figure 9. Position errors of different ATOs in the simulation with a sine-wave input, $\theta = 2\pi + \pi\sin(2\pi t)$. e_1, e_2 and e_3 are the position estimation errors of conventional ATO, type-III ATO in [5] and the proposed ATO, respectively. (**a**) Evolution of e_1, e_2 and e_3 with a time span of 5 seconds; (**b**) zoomed-in view of e_1, e_2 and e_3.

From simulation results of different forms of input signal, we can see the proposed ATO eliminates or reduces the position errors on a large scale, which demonstrates its robustness and effectiveness in the estimation of acceleration signal. This provides the potential of the proposed ATO to be

employed in high-precision position estimation for high-order signals and targeted signal with high harmonic components.

4.2. Experimental Results

In order to test the proposed ATO scheme and demonstrate its advantages in an actual situation, an experimental platform based on a hardware-in-loop (HIL) method is set up. This experimental platform mainly comprises a resolver simulator, a signal acquisition/processing board and a master computer (Figure 10).
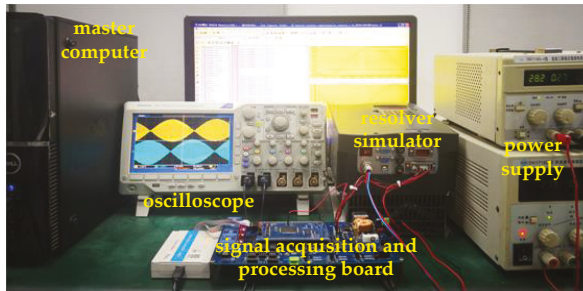
Figure 10. Structure of experimental platform for the hardware-in-loop (HIL) method.

The resolver simulator is in charge of generating two envelope signals based on the programmed rotation acceleration form. Then the envelope signals go through synchronous envelope detection and are converted into two analog output signals ($u_{\sin}$ and $u_{\cos}$). The signal acquisition board works as an analog-to-digital converter (ADC), which can sample the analog output signals and convert them into digital ones. The digital signals will be uploaded to the upper computer and applied with the same three ATO methods used in simulation results. It is noteworthy that, using the HIL method, the actual value of angular position can be known to evaluate error suppression performance of the RDC, whereas a practical resolver fails to provide this information [24].

In the experiments, three conditions, namely first-order acceleration, second-order acceleration and sine-wave signals, were set as inputs for three ATOs to evaluate their performance in position estimation. The sampling frequency was 1 kHz and the rest of the parameter settings were the same as in the simulation.

We first programmed the resolver simulator to make it rotate with a third-order signal regarding time, $\theta = \frac{\pi}{15}t^3$. Figure 11 shows orthogonally symmetric input of the ATO, which is the sampled sine and cosine signals after envelope detection and preprocessing methods.
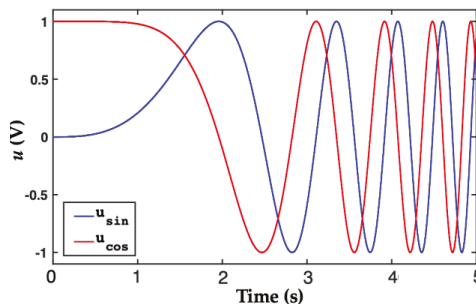
Figure 11. Demonstration of typical sine and cosine signals after envelope detection for $\theta = \frac{\pi}{15}t^3$, recorded from the signal acquisition board.

Figure 12 compares the estimation position errors of the conventional ATO, type-III ATO and the proposed ATO. e_1, e_2 and e_3 are the position errors of the conventional ATO, type-III ATO and the proposed ATO, respectively. With time increasing, the conventional ATO has a linearly growing position error and the type-III ATO has a steady state position error of 4×10^{-5} degree. And the position error of the proposed ATO is fluctuating around 0 degree, which indicates it has the ability to estimate angular position without error.
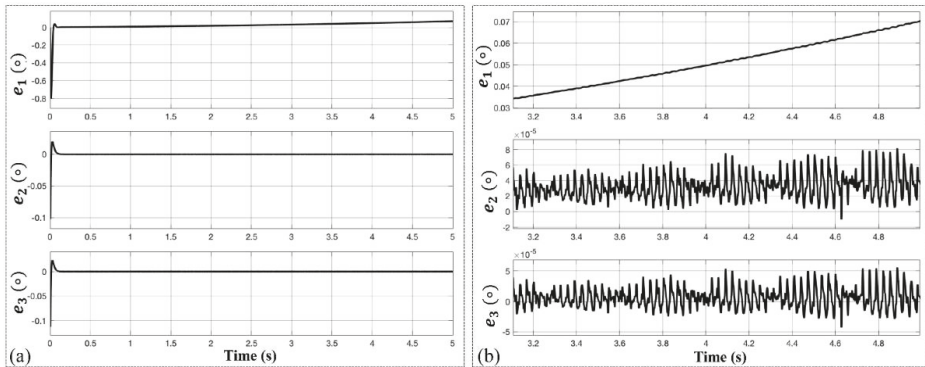
Figure 12. Experimental results of position estimation errors for the three kinds of ATOs at an acceleration signal of $\theta = \frac{\pi}{15} t^3$. e_1, e_2 and e_3 are the estimation errors of the conventional ATO, type-III ATO and the proposed ATO, respectively. (**a**) Errors' evolution with a time span of 5 s. (**b**) Zoomed-in view of e_1, e_2 and e_3.

We also evaluated the performance of the three ATO schemes with a higher factor for the first-order acceleration signal. Figure 13 shows the position error with a factor of π for the acceleration rotation. The results are similar to the former condition with a small acceleration factor, with conventional and type-II ATO having steady-state errors of 0.9 degree and 3×10^{-4} degree to 6×10^{-4} degree, respectively, and nearly zero error for the proposed ATO.
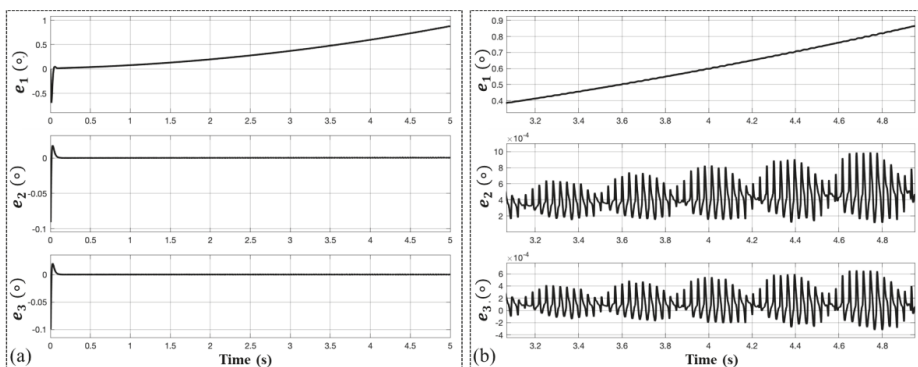
Figure 13. Experimental results of position estimation errors for the three kinds of ATOs at an acceleration signal of $\theta = \pi t^3$. e_1, e_2 and e_3 are the estimation errors of the conventional ATO, type-III ATO and the proposed ATO, respectively. (**a**) Errors evolution with a time span of 5s. (**b**) Zoomed-in view of e_1, e_2 and e_3.

Another feature for the proposed ATO scheme (type-IV) is that it has a constant steady-state position estimation error (shown in Figure 8), compared to the former two ATOs, of which the position errors increase with time. This characteristic is easy to deduct from final-value theorem. Figure 14 verifies this by inputting an acceleration signal with fourth order regarding time. After the output of position estimation comes into steady state, errors of the former two ATO has an inclination of increasing and the proposed ATO has an error of around 1.95×10^{-5} degree. This result is better than conventional one with two orders of magnitude and the error is smaller than the type-III ATO, which ranges from 2.4×10^{-5} degree to 2.8×10^{-5} degree.
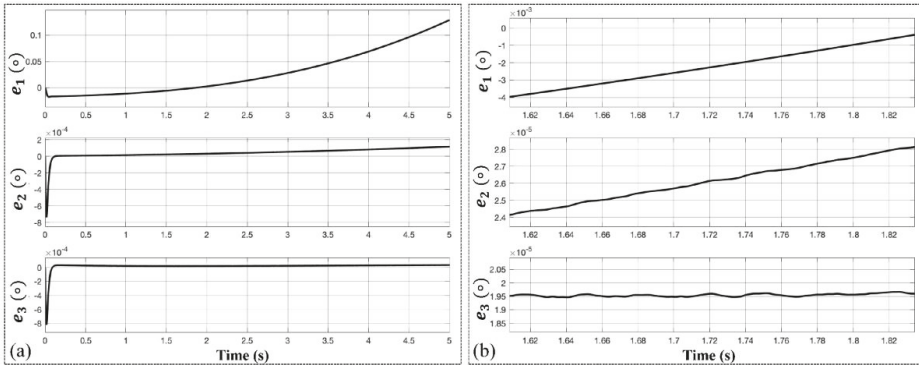
Figure 14. Experimental results of position estimation errors for the three kinds of ATOs at an acceleration signal of $\theta = \frac{\pi}{60} t^4$. e_1, e_2 and e_3 are the estimation errors of the conventional ATO, type-III ATO and the proposed ATO, respectively. (**a**) Errors evolution with a time span of 5s. (**b**) Zoomed-in view of e_1, e_2 and e_3.

In the case of sinusoidal change, Figure 15 shows the angular position estimation error curves of the three ATO schemes when the resolver rotates at a sinusoidal form for its angular position ($\theta = \sin t$). The result demonstrates that the proposed ATO has almost the same capability of error suppression as the type-III ATO, which is an improved accuracy by three orders of magnitude in contrast to the conventional one.
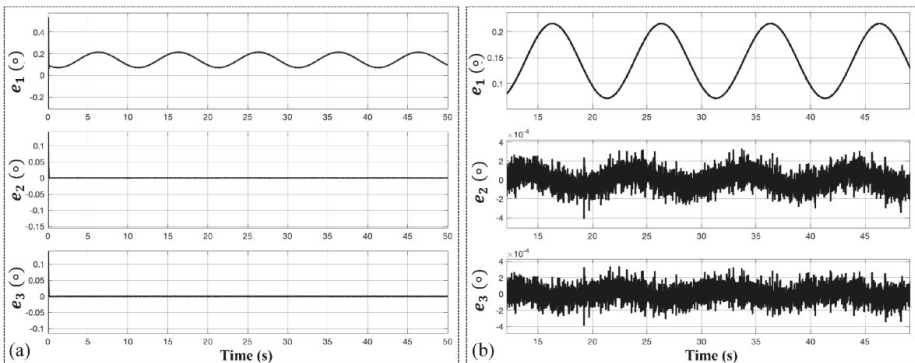
Figure 15. Experimental results of position estimation errors for the three kinds of ATOs at an acceleration signal of $\theta = \sin t$. e_1, e_2 and e_3 are the estimation errors of the conventional ATO, type-III ATO and the proposed ATO, respectively. (**a**) Errors evolution with a time span of 5s. (**b**) Zoomed-in view of e_1, e_2 and e_3.

4.3. Discussion

From the above-mentioned simulation and experimental results, the proposed ATO demonstrates advantages in position estimation accuracy over conventional and type-III ATO.

Hereby, in this section we discuss the novelty and application of the proposed ATO. To our best knowledge, limited research has been conducted to employ a compensation module for improved performance in ATO design, which is relatively simple, time-saving and cost-effective. Also, novelty of this ATO can be demonstrated through that without investigation of non-constant high-order acceleration signals, by simply using this feedback loop of estimated speed the accuracy of position estimation can be improved and error reduction and suppression can be achieved in a wider category of signals, the high-order acceleration signals ($\theta = \alpha t^n$). Hence, we consider the compensation module, parameter design, accuracy improvement and time-saving implementation as points in our novelty.

As for application, this ATO holds great potential for wherever high-accuracy position estimation of a motor is needed, especially for those whose working conditions involve high speed and high acceleration rate. As formerly mentioned, the CNC machine and positioning radar are two special cases.

Since most high-speed CNC machines' fine processing components and parts work within a travel range of only tens to hundreds of millimeters, high acceleration is required to achieve high speed and an instant stop and jerk. When dealing with irregularly shaped components, high-order acceleration signals are applied to the motor of the CNC machine.

Positioning radars need to track highly mobile artillery or other flying targets with high precision. These targets are not subject to a typical moving pattern (constant speed or constant acceleration) and high-order acceleration is usually employed to achieve posture adjustment and avoid being tracked, which places the same requirements on the motor of positioning radar.

Therefore, the proposed ATO scheme solves the urgent demands that motors performing complex accelerating patterns (high-order acceleration) call for in high-precision position estimation.

However, as is observed from the simulation results, the proposed ATO has a larger overshoot and longer settling time in transient response. Compared with two other types of ATO, the dynamic response of this ATO is not as good. Dynamic problems can be resolved by combining with other good-dynamic algorithms. When the error is large, a good-dynamic method is adopted; when the error is less than a set value, one may switch to the proposed method. This can balance both steady-state accuracy and dynamic response. Further research will investigate potential structure revision and refined design to improve its dynamic response.

5. Conclusions

In this paper, an improved compensated type-IV ATO is proposed to suppress position estimation errors with the input of high-order acceleration signal ($\theta = \alpha t^n$). This ATO can eliminate position errors when $n \leq 3$ and is effective at error reduction when $n \geq 4$, which presents a solution for application in precisely estimating high-order acceleration signals. Theoretical analysis, simulation and experiments are carried out to verify and demonstrate the advantages of the proposed ATO over previous ones. We also evaluate the relationship between the parameters and bandwidth, noise level and error suppression of the ATO for succinct tuning guidance. Further research will be focused on improving the dynamic response of the proposed ATO.

Author Contributions: Conceptualization, Z.W.; methodology, H.Q.; validation, H.Q.; writing—original draft preparation, H.Q. and Z.W.

References

1. Khaburi, D.A. Software-based resolver-to-digital converter for DSP-based drives using an improved angle-tracking observer. *IEEE Trans. Instrum. Meas.* **2012**, *61*, 922–929. [CrossRef]
2. Li, Y.L.; Wu, Z. High-accuracy resolver-to-digital conversion via phase locked loop based on PID controller. *IOP Conf. Ser. Mater. Sci. Eng.* **2018**, *339*, 012003. [CrossRef]
3. Attaianese, C.; Tomasso, G. Position measurement in industrial drives by means of low-cost resolver-to-digital converter. *Instrum. Meas. Mag.* **2007**, *56*, 2155–2159. [CrossRef]
4. Sarma, S.; Agrawal, V.K.; Udupa, S. Software-based resolver-to-digital conversion using a DSP. *IEEE Trans. Ind. Electron.* **2008**, *55*, 371–379. [CrossRef]
5. Wang, F.; Shi, T.; Yan, Y.; Wang, Z.; Xia, C. Resolver-to-digital conversion based on acceleration-compensated angle tracking observer. *IEEE Trans. Instrum. Meas.* **2019**, *68*, 3494–3502. [CrossRef]
6. Benammar, M.; Gonzales, A.S. A novel resolver converter based on a modified tracking method. In Proceedings of the 10th IEEE Conference on Networking, Sensing and Control, Paris, France, 10–12 April 2013; pp. 586–590. [CrossRef]
7. Hoseinnezhad, R.; Harding, P. A novel hybrid angle tracking observer for resolver to digital conversion. In Proceedings of the 44th IEEE Conference on Decision and Control, Seville, Spain, 15 December 2005; pp. 7020–7025. [CrossRef]
8. Sivappagari, C.M.R.; Konduru, N.R. Modified ATO algorithm based high accuracy RDC using pulse excitation. In Proceeding of the First International Conference Automation, Control, Energy and Systems, West Bengal, India, 1–2 February 2014; pp. 1–5. [CrossRef]
9. Leszek, J.; Cisek, M.; Opalinski, A. Angle tracking observer for filtering rotor position estimates in sensorless electric drives. *Elektronika ir Elektrotechnika* **2016**, *22*, 38–41. [CrossRef]
10. Zhao, Y.; Qiao, W.; Wu, L. Position extraction from a discrete sliding-mode observer for sensorless control of IPMSMs. In Proceedings of the IEEE International Symposium on Industrial Electronics, Hangzhou, China, 28–31 May 2012; pp. 725–730. [CrossRef]
11. Hwang, S.H.; Kim, H.J.; Kim, J.M.; Liu, L.; Li, H. Compensation of amplitude imbalance and imperfect quadrature in resolver signals for PMSM drives. *IEEE Trans. Ind. Appl.* **2011**, *47*, 134–143. [CrossRef]
12. Bergas, J.J.; Ferrater, S.J.; Gross, G.; Ramírez, P.R.; Galceran, A.S.; Rull, D.J. High-accuracy all-digital resolver-to-digital conversion. *IEEE Trans. Ind. Electron.* **2012**, *59*, 326–333. [CrossRef]
13. Mok, H.S.; Kim, S.H.; Cho, Y.H. Reduction of PMSM torque ripple caused by resolver position error. *Electron Lett.* **2007**, *43*, 646–647. [CrossRef]
14. Kwon, Y.H.; Hwang, S.H.; Kim, J.M.; Ahn, J.W. Compensation of amplitude imbalance of resolver signal for PMSM drives. In Proceedings of the IEEE 6th International Power Electronics and Motion Control Conference, Wuhan, China, 17–20 May 2009; pp. 1827–1831. [CrossRef]
15. Kim, Y.H.; Kim, S. Software resolver-to-digital converter for compensation of amplitude imbalances using d-q transformation. *J. Electr. Eng. Technol.* **2013**, *6*, 1310–1319. [CrossRef]
16. Yim, C.H.; Ha, I.G.; Ko, M.S. A resolver-to-digital conversion method for fast tracking. *IEEE Trans. Ind. Electron.* **1992**, *39*, 369–378. [CrossRef]
17. Liu, H.; Wu, Z. Demodulation of angular position and velocity from resolver signals via chebyshev filter-based type iii phase locked loop. *Electronics* **2018**, *7*, 354. [CrossRef]
18. Nguyen, H.X.; Tran, T.; Park, J.W.; Jeon, J.W. An adaptive linear-neuron-based third-order pll to improve the accuracy of absolute magnetic encoders. *IEEE Trans. Ind. Electron.* **2019**, *66*, 4639–4649. [CrossRef]
19. Ellis, G.; Krah, J.O. Observer-based resolver conversion in industrial servo systems. In Proceedings of the Power Conversion Intelligent Motion Conference, Nuremberg, Germany, 19–21 June 2001; pp. 217–226.
20. Hoseinnezhad, R. Position sensing in brake-by-wire callipers using resolvers. *IEEE Trans. Veh. Technol.* **2006**, *55*, 924–932. [CrossRef]
21. Caruso, M.; Tommaso, A.O.D.; Genduso, F.; Miceli, R.; Galluzzo, G.R. A DSP-based resolver-to-digital converter for high-performance electrical drive applications. *IEEE Trans. Ind. Electron.* **2016**, *63*, 4042–4051. [CrossRef]
22. Zhang, J.; Wu, Z. Composite state observer for resolver-to-digital conversion. *Meas. Sci. Technol.* **2017**, *28*, 065103. [CrossRef]

23. Celikel, R. ANN based angle tracking technique for shaft resolver. *Measurement* **2019**, *148*, 106910. [CrossRef]
24. Wu, Z.; Li, Y. High-accuracy automatic calibration of resolver signals via two-step gradient estimators. *IEEE Sens. J.* **2018**, *18*, 2883–2891. [CrossRef]

Topological Design Methods for Mecanum Wheel Configurations of an Omnidirectional Mobile Robot

Yunwang Li [1,2,*], Sumei Dai [2,3], Lala Zhao [1], Xucong Yan [1] and Yong Shi [2]

[1] School of Mechatronic Engineering, China University of Mining and Technology, Xuzhou 221116, China; lala.zhao@cumt.edu.cn (L.Z.); yxc.cumt@hotmail.com (X.Y.)
[2] Department of Mechanical Engineering, Stevens Institute of Technology, Hoboken, NJ 07030, USA; sumei-dai@hotmail.com (S.D.); yshi2@stevens.edu (Y.S.)
[3] School of Mechanical and Electrical Engineering, Xuzhou University of Technology, Xuzhou 221018, China
* Correspondence: yunwangli@cumt.edu.cn or yunwang.li@stevens.edu

Abstract: A simple and efficient bottom-roller axle intersections approach for judging the omnidirectional mobility of the Mecanum wheel configuration is proposed and proved theoretically. Based on this approach, a sub-configuration judgment method is derived. Using these methods, on the basis of analyzing the possible configurations of three and four Mecanum wheels and existing Mecanum wheel configurations of robots in practical applications, the law determining wheel configuration is elucidated. Then, the topological design methods of the Mecanum wheel configurations are summarized and refined, including the basic configuration array method, multiple wheels replacement method, and combination method. The first two methods can be used to create suitable multiple-Mecanum-wheel configurations for a single mobile robot based on the basic Mecanum wheel configuration. Multiple single robots can be arranged by combination methods including end-to-end connection, side-by-side connection, symmetrical rectangular connection, and distributed combination, and then, the abundant combination configurations of robots can be obtained. Examples of Mecanum wheel configurations design based on a symmetrical four-Mecanum-wheel configuration and three centripetal configurations using these topological design methods are presented. This work can provide methods and a reference for Mecanum wheel configurations design.

1. Introduction

Each Mecanum wheel has three degrees of freedom of motion in a plane [1,2], so a mobile robot system consisting of three or more than three Mecanum wheels can achieve omnidirectional motion in a plane only through the coordination of direction and rotation speed of wheels without the assistance of an auxiliary steering mechanism. Because of the simple structure and good motion flexibility, omnidirectional mobile robots with Mecanum wheels are widely used in various fields. According to application needs in different fields, a variety of Mecanum wheel configurations can be designed to develop various omnidirectional mobile robots. Some service robots usually adopt three or four-Mecanum-wheel configurations [3,4]. In the industrial field, an AGV (automated guided vehicle) with four Mecanum wheels, a kind of omnidirectional mobile robot, is also widely used [5–8]. For transporting large-scale equipment or components, a robot platform with multiple Mecanum wheels [9–11] or multiple-Mecanum-wheeled robot platforms are used cooperatively [12,13]. In order to design an omnidirectional mobile robot, it is necessary to select a reasonable Mecanum wheel configuration for the robot. However, not all combinations of Macanum wheels can implement

omnidirectional motion, and the arrangement of Mecanum wheels also influences the mobility performance of the robot [14]. Therefore, designing a reasonable configuration of Mecanum wheels constitutes the most basic and important technology problem in the design of omnidirectional mobile robots. Firstly, these configurations must satisfy the conditions of realizing omnidirectional movement. Secondly, motion performance, controllability, and structural rationality of these configurations must be evaluated in order to select the optimal Macanum wheel configuration.

Some researchers have paid attention to the study of Mecanum wheel configurations. The kinematics and dynamics of a Mecanum-wheeled mobile robot form the basic premise to judge the robot to achieve omnidirectional movement in theory. Muir et al. [15,16] introduced a methodology for the kinematic modeling of wheeled mobile robots, studied an omnidirectional wheeled mobile robot with four Mecanum wheels, and derived the kinematic model of roller angle dead reckoning robot position wheel slip. Angeles [17] deduced a general kinematics model of the Mecanum-wheeled omnidirectional mobile system by vector method, and gave kinematics and dynamics equations of three-wheel and four-wheel robots, respectively. Campion [18] used a matrix transformation method to study the mobility characteristics of the robot under constraints, gave a unified description of modeling of a wheeled mobile robot, and deduced the kinematics equation of the three-wheeled robot. Gracia and Tornero [19,20] described the singular and heterogeneous types of mobile robots based on Mecanum wheels and Castor wheels using a descriptive geometry method, established the kinematics model of omnidirectional mobile robots under sliding conditions, and further established the Lagrange dynamics model. Zhang and Wang [21,22] analyzed the steering motion of a Mecanum-wheeled omnidirectional mobile platform, and established a control system model and dynamic model in MATLAB and RecurDyn software, respectively. Using joint simulation, the anisotropic motion characteristics of a mobile platform with different slip rates were obtained. Wang and Chang [23,24] analyzed the condition of omnidirectional motion of a Mecanum-wheeled mobile system and found that the Jacobian matrix of inverse kinematics velocity is a column full rank, discussed the possible singularities and solutions in motion, and showed six types of Mecanum wheels layouts and determined the four best Mecanum wheel layouts. Mishra et al. [25] proposed 10 possible configurations of the omnidirectional mobile robot with four Mecanum wheels. Gao et al. [26] studied a type of three-Mecanum-wheel omnidirectional mobile robot with symmetrical and concentric layout structure, and the motion simulation of the three-Mecanum-wheeled platform is compared with that of the symmetrical four-Mecanum-wheeled mobile robot platform. Zhang et al. [27] studied the three- and four-Mecanum-wheeled concentric layouts and analyzed the influence of the angles between wheel axes for a centered layout. He et al. [14] studied the two most used arrangement modes of Mecanum wheels, Type-X and Type-O, and used the inverse velocity Jacobian matrix of the arrangement to judge whether a vehicle can fulfill omnidirectional movement. The main contributions of these studies on wheel configuration include: (1) the method of establishing a kinematics equation of an omnidirectional mobile robot is proposed; (2) the method of judging omnidirectional mobility by rank of the Jacobian matrix of inverse kinematics is obtained; (3) the possible configuration of three or four Mecanum wheels is summarized and analyzed and compared. However, when using an inverse kinematics Jacobian matrix to analyze a multiple-Mecanum-wheeled mobile robot system, the calculation process is complex. Previous studies have not systematically summarized multiple-Mecanum-wheel (more than four wheels) configurations, and have not explicitly proposed a method to obtain the wheel configurations for omnidirectional mobile robots with more than four Mecanum wheels. This study explores a simple and efficient method to judge whether the wheel configurations possess omnidirectional mobility. On this basis, the common wheel configurations are judged and analyzed, the law of wheel configurations is explored, and the topological design methods of wheel configurations for an omnidirectional mobile robot are summarized and refined.

This paper is organized as follows: In Section 2, on the basis of studying the kinematic constraints of a single Mecanum wheel in a mobile system, the kinematics model of an *n*-Mecanum-wheeled mobile robot is further deduced. In Section 3, the relationship between the intersections of bottom-rollers

axles of any three Mecanum wheels and the column rank of the Jacobian matrix of inverse kinematics of the mobile robot is established, and a bottom-rollers axles intersections approach for judging the omnidirectional mobility of Mecanum wheel configurations is proposed and proved theoretically, which is a simple and efficient geometric method. In Section 4, the four-Mecanum-wheel configurations are judged by using a bottom-rollers axles intersections approach, and the optimal four-Mecanum-wheel configuration is selected through comprehensive analysis and theoretical verification. In Section 5: firstly, the above method is used to judge the omnidirectional motion of a combined configuration consisting of two four-Mecanum-wheel configurations, and then the sub-configuration judgment method, which can be extended to N sub-configuration combinations is obtained. Secondly, this judgment method is used to analyze the Mecanum wheel configurations and combination configurations for common omnidirectional mobile robots, and clarify the law determining wheel configuration. Finally, the topological design methods of the Mecanum wheel configurations are summarized and refined, including the basic configuration array method, multiple wheel replacement method and combination method. Furthermore, based on the symmetrical four-Mecanum-wheel configuration, the Mecanum wheel configurations are generated by using the topological design methods.

2. Kinematics Model of an Omnidirectional Mobile Robot with n Mecanum Wheels

2.1. Mecanum Wheel Configurations of the Single Omnidirectional Mobile Robot

For an independent Mecanum-wheeled mobile robot, the wheel configurations can be mainly divided into two categories: centripetal configuration and symmetrical rectangular configuration [24], as shown in Figure 1. In Figure 1, the Mecanum wheel is represented by a rectangle with an oblique line in the middle, in which the oblique line represents the bottom roller that contacts with the ground. In the former configuration, the axles of all wheels intersect at the same intersection point, as shown in Figure 1a. In Figure 1a, the centerline OO_i of the mobile robot coordinate system XOY and wheel local coordinate system $X_iO_iY_i$ is collinear with coordinate axis X_i. In order to balance the load of each wheel, the wheels are evenly distributed in a 360° circumference. This centripetal configuration of an omnidirectional mobile robot usually composes of three [1,26] or four [27] Mecanum wheels. In the symmetrical rectangular configuration in Figure 1b, the Mecanum wheels are symmetrically arranged on both sides of the line going through the center of the robot, and the overall structure is rectangular. Based on the study of the kinematics constraints of a single Mecanum wheel, the kinematics model of an n-Mecanum-wheel mobile robot can be further derived, and then the omnidirectional motion characteristics of the mobile systems can be analyzed.
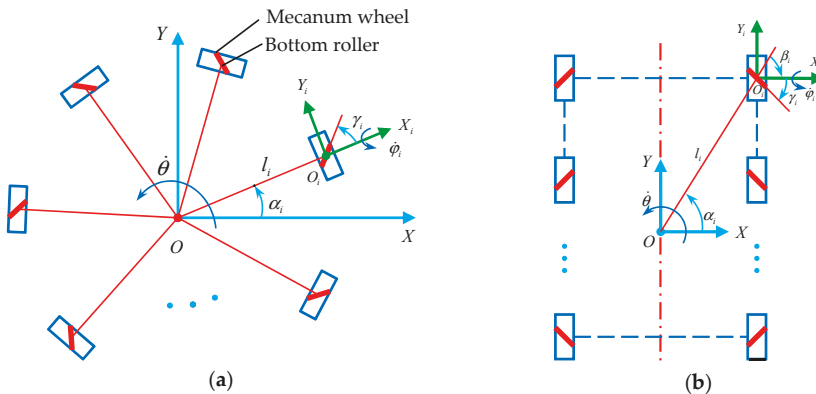
Figure 1. Wheel configurations of the single-Mecanum-wheeled robot: (**a**) centripetal configuration; (**b**) symmetrical rectangular configuration.

2.2. Kinematics Constraint Model of a Single Mecanum Wheel and Kinematics Model of an n-Mecanum-Wheel Robot

The kinematics research of the Mecanum wheel is similar to that of a traditional wheeled mobile system. The kinematics model of the Mecanum-wheel mobile system can also be built by a bottom-up process. Each of the relatively independent Mecanum wheels contributes to the motion of the system and is relatively constrained by the motion of the system. Because the Mecanum wheels are installed on the chassis of a mobile system, the kinematic constraints of each wheel can be combined to describe the kinematic constraints of the whole mobile system.

In this section, the kinematic constraints of a single Mecanum wheel are studied first, and then, the linear mapping relationship between the velocity of the mobile system and the velocity of a single wheel is obtained. Then, the kinematic constraints of each wheel are combined to describe the kinematic constraints of the entire mobile system.

In order to reduce the difficulty of system kinematics modeling, several assumptions are usually introduced to discuss the motion constraint relationship of wheels under ideal conditions. (1) Assuming that the whole mobile robot, especially the wheels, is rigid, it will not undergo mechanical deformation; (2) the entire range of motion is confined to a 2D plane, ignoring the impact of irregular ground; (3) ignoring the factor of rollers slipping, that is, the roller has enough friction with the ground; (4) assuming that the contact point between the roller and the ground is located directly below the wheel center. Based on the above assumptions, the kinematic constraints of a single Mecanum wheel will be derived by a vector method [17] and matrix transformation method [18].

(a)　Vector Method

In order not to lose generality, a mobile robot consisting of n Mecanum wheels is designed, in which the i-th wheel is mounted on the body at a certain angle, as shown in Figure 2. R and r are the radius of the wheel and the radius of the roller, respectively; O_i is the center of the i-th wheel; Z_i represents the direction passing through the wheel center O_i and perpendicular to the ground; P_i is the center of the roller contacting the ground, Q_i is the contact point between the roller and the ground, according to the hypothesis, both of them are under O_i at the same time; z_i represents the direction passing through the roller center P_i and perpendicular to the ground. X_i and h_i represent the rotation axis direction of an active Mecanum wheel and passive roller, respectively. The two angular velocity vectors are $\dot{\varphi}_i$ and $\dot{\phi}_i$, and X_i and Y_i constitute the right-handed Cartesian coordinate system $O_i - X_i Y_i Z_i$, h_i and g_i constitute the right-handed Cartesian coordinate system $P_i - g_i h_i z_i$. (l_i, α_i) is used to describe the relative installation orientation of the origin O of the body coordinate system and the center O_i of the wheel; the angle between the X_i axis and the l_i is β_i, which is defined as the installation attitude angle of the local coordinate system of the wheel; the velocity of the motion center is v_o in the current state, and the angle between the v_o and the X axis is θ_o; $\dot{\theta}$ is the rotation angular velocity of the system when moving in the plane. The angle between the projection of X_i and h_i on the plane is the tilt angle $\gamma_i (0° < |\gamma_i| < 90°)$ of the roller.

According to the above definition, the motion relationship between the active wheel and the passive roller can be expressed by the formula

$$v_{oi} = v_{pi} + v_i. \tag{1}$$

In this formula, v_{oi} is the velocity vector of the center of the i-th wheel; v_{pi} is the velocity vector of the roller in contact with the ground; v_i is the relative velocity vector of point P_i and O_i.
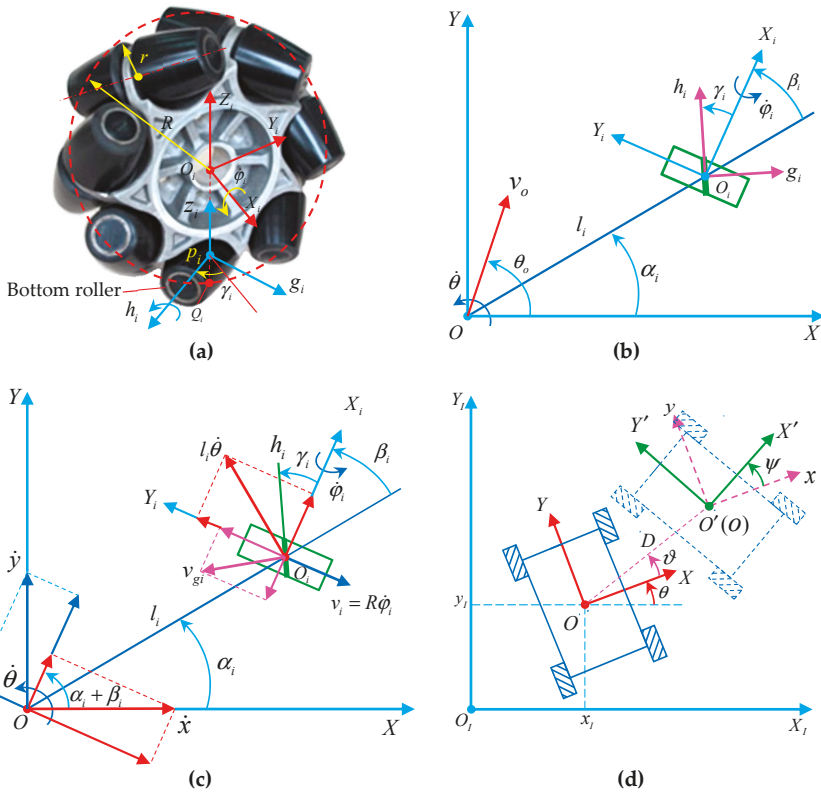
Figure 2. Kinematic constraints of a Mecanum wheel and the coordinate systems of a mobile system: (**a**) structural principle of a Mecanum wheel; (**b**) Kinematic constraints diagram of a Mecanum wheel on the robot using a vector method; (**c**) Kinematic constraint diagram of a Mecanum wheel using a matrix transformation method; (**d**) Location of the mobile robot in the global coordinate system and the relationship regarding position between two local coordinate systems.

$\boldsymbol{\omega}_o$ and $\boldsymbol{\omega}_p$ represent the rotational angular velocity vectors of the active wheel and the passive roller, respectively, as

$$\boldsymbol{\omega}_o = \dot{\theta}\boldsymbol{Z}_i + \dot{\varphi}_i\boldsymbol{X}_i, \ \boldsymbol{\omega}_p = \boldsymbol{\omega}_o + \dot{\phi}_i\boldsymbol{h}_i. \tag{2}$$

then

$$\boldsymbol{v}_{pi} = \boldsymbol{\omega}_p \times \boldsymbol{Q}_i\boldsymbol{P}_i = -r(\dot{\varphi}_i\boldsymbol{Y}_i - \dot{\phi}_i\boldsymbol{g}_i), \ \boldsymbol{v}_i = \boldsymbol{\omega}_o \times \boldsymbol{P}_i\boldsymbol{O}_i = -(R-r)\dot{\varphi}_i\boldsymbol{Y}_i. \tag{3}$$

From Formulas (1) and (3), we obtain

$$\boldsymbol{v}_{oi} = -R\dot{\varphi}_i\boldsymbol{Y}_i + r\dot{\phi}_i\boldsymbol{g}_i. \tag{4}$$

If the known moving system moves in the plane, the relation between the wheel center O_i and the origin O of the body coordinate system can be expressed as

$$\boldsymbol{v}_{oi} = \boldsymbol{v}_o + \dot{\theta}\xi\boldsymbol{l}_i. \tag{5}$$

In this formula,$\xi = \begin{bmatrix} 0 & -1 \\ 1 & 0 \end{bmatrix}$, which means that the vector $\boldsymbol{l}_i$ is rotated 90 degrees counterclockwise.

The following formula can be obtained from Formulas (4) and (5).

$$-R\dot{\varphi}_i Y_i + r\dot{\phi}_i g_i = v_o + \dot{\theta}\xi l_i. \tag{6}$$

According to the definition of vectors, we can obtain

$$h_i \cdot g_i = 0, \ h_i \cdot Y_i = \sin\gamma_i. \tag{7}$$

Since the roller rotates passively, its angular velocity $\dot{\phi}_i$ is an uncontrollable variable. According to the calculation result defined by the vector in Formula (7), multiplying the vector h_i at the same time on both sides of Formula (6), the subformula containing the term $\dot{\phi}_i$ can be eliminated.

$$-R(\sin\gamma_i)\dot{\varphi}_i = h_i^T v_o + h_i^T \dot{\theta}\xi l_i. \tag{8}$$

Then, the inverse kinematics equation of the i-th Mecanum wheel is

$$\dot{\varphi}_i = -\frac{1}{R(\sin\gamma_i)}\begin{bmatrix} h_i^T \xi l_i & h_i^T \end{bmatrix}\begin{bmatrix} \dot{\theta} \\ v_o \end{bmatrix}. \tag{9}$$

Given the kinematic constraint equation of any Mecanum wheel in the plane, the inverse kinematics equation of the omnidirectional motion system composed of n Mecanum wheels whose radii are R can be expressed as

$$\begin{cases} \dot{\varphi} = \begin{bmatrix} \dot{\varphi}_1 & \dot{\varphi}_2 & \cdots & \dot{\varphi}_n \end{bmatrix}^T \\ S = \mathrm{diag}\left(\frac{1}{\sin\gamma_1}, \frac{1}{\sin\gamma_2}, \cdots, \frac{1}{\sin\gamma_n}\right) \\ M = \begin{bmatrix} h_1^T \xi l_1 & h_1^T \\ h_2^T \xi l_2 & h_2^T \\ \vdots & \vdots \\ h_n^T \xi l_n & h_n^T \end{bmatrix} \\ J = -\frac{1}{R}SM \\ t = \begin{bmatrix} \dot{\theta} & v_o \end{bmatrix}^T \\ \dot{\varphi} = Jt \end{cases}. \tag{10}$$

In the formula, $\dot{\varphi}$ is the angular velocity matrix of the wheel; J is the Jacobian matrix of the inverse kinematics velocity of the mobile robot, including the matrix S of tilt angle of rollers and the matrix M of wheel installation orientation; t is the rotation matrix of the mobile system.

In this section, three coordinate transformation matrices—including translation transformation, rotation transformation, and composite transformation—are introduced, which form an important theoretical basis for studying the kinematics constraints of mobile systems. The kinematic constraints of a single Mecanum wheel are derived by the vector method. On this basis, the general kinematic model of the mobile system composed of n Mecanum wheels is obtained.

(b) Matrix Transformation Method

Matrix transformation is another common method for kinematics analysis of a wheeled mobile system, which can be used for kinematics modeling of an omnidirectional wheel. The precondition of using this method to study a single Mecanum wheel still needs to satisfy the above assumptions and start with the study of rolling and sliding constraints of the wheel. The motion constraints of one Mecanum wheel are shown in Figure 2c [23,24].

Based on the above assumptions, the motion between the roller and the ground satisfies the condition of pure rolling, the contact point between the roller and the ground does not slip, and the

instantaneous velocity is 0. According to the constraints of rolling and sliding, the following formulas can be obtained

$$\begin{cases} \dot{x}\sin(\alpha_i+\beta_i) - \dot{y}\cos(\alpha_i+\beta_i) - l_i\dot{\theta}\cos\beta_i = R\dot{\varphi}_i - v_{gi}\cos\gamma_i \\ \dot{x}\cos(\alpha_i+\beta_i) + \dot{y}\sin(\alpha_i+\beta_i) + l_i\dot{\theta}\sin\beta_i = -v_{gi}\sin\gamma_i \end{cases}. \tag{11}$$

In the formula, $\begin{pmatrix} \dot{x} & \dot{y} & \dot{\theta} \end{pmatrix}^T$ is the motion state of the mobile system in its own local coordinate system; v_{gi} is the central velocity of the roller contacting the ground on the i-th Mecanum wheel.

Because the rollers rotate passively, the velocity of motion v_{gi} is an uncontrollable variable, which is usually not taken into account. By eliminating v_{gi} from Formula (11), we obtain

$$\dot{x}\cos(\alpha_i+\beta_i+\gamma_i) + \dot{y}\sin(\alpha_i+\beta_i+\gamma_i) + l_i\dot{\theta}\sin(\beta_i+\gamma_i) = -R\dot{\varphi}_i\sin\gamma_i. \tag{12}$$

The inverse kinematics matrix equation of any Mecanum wheel is

$$\begin{bmatrix} \cos(\alpha_i+\beta_i+\gamma_i) & \sin(\alpha_i+\beta_i+\gamma_i) & l_i\sin(\beta_i+\gamma_i) \end{bmatrix} \begin{bmatrix} \dot{x} \\ \dot{y} \\ \dot{\theta} \end{bmatrix} + R\dot{\varphi}_i\sin\gamma_i = 0. \tag{13}$$

The motion state in a local coordinate system can be mapped to a global coordinate system, as shown in Figure 2d, which is expressed as

$$\begin{bmatrix} \cos(\alpha_i+\beta_i+\gamma_i) & \sin(\alpha_i+\beta_i+\gamma_i) & l_i\sin(\beta_i+\gamma_i) \end{bmatrix} Rot(\theta)\dot{\zeta}_I + R\dot{\varphi}_i\sin\gamma_i = 0. \tag{14}$$

where

$$Rot(\theta) = \begin{bmatrix} \cos\theta & \sin\theta & 0 \\ -\sin\theta & \cos\theta & 0 \\ 0 & 0 & 1 \end{bmatrix}.$$

$$\dot{\zeta}_I = Rot^{-1}(\theta)\dot{\zeta} = Rot^{-1}(\theta)\begin{bmatrix} \dot{x} \\ \dot{y} \\ \dot{\theta} \end{bmatrix}.$$

3. Bottom-Roller Axle Intersections Approach for Judging Robot's Omnidirectional Mobility

3.1. Conditions for Omnidirectional Motion of a Mecanum-Wheeled Mobile Robot System

If the Mecanum wheel configuration of a robot cannot achieve omnidirectional movement, it will lose practical value. Therefore, it is necessary to study the relationship between the wheel configuration and the realization of the omnidirectional movement of the mobile system. The inverse kinematics velocity Jacobian matrix of a mobile system consisting of $n(n \geq 3)$ Mecanum wheels is $J_{n\times3}$. According to the kinematics principle of the robot, if the Jacobian matrix is a column full rank matrix, that is, rank$(J_{n\times3}) = 3$, the mobile robot system will have three degrees of freedom in the plane. The Jacobian matrix $J_{n\times3}$ is written into the form of block matrix, which is expressed as

$$J_{n\times3} = \begin{pmatrix} J_{3\times3} \\ J_{(n-3)\times3} \end{pmatrix}. \tag{15}$$

Assuming that the third-order square matrix $J_{3\times3}$ is an invertible matrix, i.e., rank$(J_{3\times3}) = 3$. According to the elementary transformation theory of a matrix, the simplest matrix of the reversible matrix $J_{3\times3}$ is the unit matrix I_3 of the third order.

$$J_{3\times3} \rightarrow I_3. \tag{16}$$

Extending this conclusion to the whole Jacobian matrix $J_{n\times3}$, then

$$J_{n\times3} \rightarrow \begin{pmatrix} I_3 \\ {}_{(n-3)\times3} \end{pmatrix}. \tag{17}$$

Therefore, in the mobile system composed of n Mecanum wheels, the system can achieve omnidirectional movement, as long as the inverse kinematics velocity Jacobian matrix of any three wheels is a column full rank matrix.

According to the basic theory of coordinate transformation, when the coordinate system changes, the description of the motion state of the mobile system will change accordingly, and the Jacobian matrix of its inverse kinematics velocity will change, which can be expressed by the following formula

$$J'_{n\times3} = J_{n\times3}K_{3\times3}. \tag{18}$$

where, $J'_{n\times3}$ is the inverse kinematics velocity Jacobian matrix in the new coordinate system; $J_{n\times3}$ is the inverse kinematics velocity Jacobian matrix in the original coordinate system; $K_{3\times3}$ is reversible square matrix of the third order, then, $\text{rank}(K_{3\times3}) = 3$.

Let $C = JK$, given K is an invertible matrix, $|K| \neq 0$, the inverse matrix exists, then $CK^{-1} = J$.

According to the properties of matrices—the rank of the product of the matrices is not greater than the rank of each matrix—the following formulas can be derived

$$\begin{cases} \text{rank}(JK) \leq \text{rank}(J) \\ \text{rank}(J) = \text{rank}(CK^{-1}) \leq \text{rank}(C) = \text{rank}(JK) \end{cases}. \tag{19}$$

According to the above formula, the rank of the product of J and K is equal to the rank of J, that is

$$\text{rank}(J') = \text{rank}(JK) = \text{rank}(J). \tag{20}$$

The above deduction shows that the change of the coordinate system will not change the rank of the Jacobian matrix in the mobile system. Under certain circumstances, the appropriate coordinate system can be selected to simplify the calculation of the Jacobian matrix rank.

3.2. Relation Between the Roller Axle Intersection Points Number on Three Mecanum Wheels and the Column Rank of the Jacobian Matrix

The two straight lines in the plane have three positional relations: parallel, intersection, and coincidence, and the corresponding number of intersections is 0, 1, and infinite. In a plane, the number of intersections of three roller axles on three Mecanum wheels is 0, 1, 2, 3, and infinite. Next, we will discuss the relationship between the number of intersections and the rank of the Jacobian matrix. That is, the relationship between Mecanum wheel configurations and omnidirectional motion is studied. In this paper, infinite intersection points are specialized into one intersection point, which is discussed in detail below.

3.2.1. No Intersection of the Three Bottom-Rollers Axles

In Figure 3, the axles of any two bottom-rollers are parallel to each other, and the number of intersections is 0. The mobile system coordinate XOY is established by choosing any point on one of the roller axles as the origin, and then the local wheel coordinate systems $X_iO_iY_i$ ($i = 1, 2, 3$) are established in counterclockwise order. (α_i, β_i, l_i) is used to describe the positional state of each wheel relative to the coordinate system XOY of the mobile robot system. The radius of the Mecanum wheel is R, and the tilt angle of rollers of each Mecanum wheel is γ_i. The relationship of the parameters is shown in Table 1.

Figure 3. Wheel configuration of the mobile robot with three Mecanum wheels whose bottom-roller axles are parallel to each other.

Table 1. Relationship between the parameters of the three Mecanum wheels in Figure 3.

Serial Number	$\|\alpha_i\|\in[0°,360°)$	$\|\beta_i\|\in[0°,180°]$	$\|\gamma_i\|\in(0°,90°)$
1	α_1	β_1	γ_1
2	α_2	β_2	γ_2
3	α_3	β_3	γ_3

The origin O of the coordinate system XOY is located on the bottom-roller axle of wheel O_1, and the axles of any two rollers are parallel to each other, so the following relationship is established as

$$\beta_1 + \gamma_1 = 0, \ \alpha_i + \beta_i + \gamma_i = c_i \ (i = 1, 2, 3). \tag{21}$$

The tilt angles of the axles of the three rollers are the same, so let $c_i = \alpha_1$.

From Formulas (10), (13), and (21), the inverse kinematics velocity Jacobian matrix of the system is obtained as

$$J = -\frac{1}{R} \begin{bmatrix} \frac{\cos\alpha_1}{\sin\gamma_1} & \frac{\sin\alpha_1}{\sin\gamma_1} & \frac{l_1 \sin(\beta_1+\gamma_1)}{\sin\gamma_1} \\ \frac{\cos\alpha_1}{\sin\gamma_2} & \frac{\sin\alpha_1}{\sin\gamma_2} & \frac{l_2 \sin(\beta_2+\gamma_2)}{\sin\gamma_2} \\ \frac{\cos\alpha_1}{\sin\gamma_3} & \frac{\sin\alpha_1}{\sin\gamma_3} & \frac{l_3 \sin(\beta_3+\gamma_3)}{\sin\gamma_3} \end{bmatrix} = -\frac{1}{R}SM. \tag{22}$$

where

$$S = \text{diag}\left(\frac{1}{\sin\gamma_1}, \frac{1}{\sin\gamma_2}, \frac{1}{\sin\gamma_3}\right), \ M = \begin{bmatrix} \cos\alpha_1 & \sin\alpha_1 & l_1 \sin(\beta_1 + \gamma_1) \\ \cos\alpha_1 & \sin\alpha_1 & l_2 \sin(\beta_2 + \gamma_2) \\ \cos\alpha_1 & \sin\alpha_1 & l_3 \sin(\beta_3 + \gamma_3) \end{bmatrix}.$$

The roller tilt angle matrix S is a reversible square matrix of the third order. The rank of inverse kinematics velocity Jacobian matrix J depends on the matrix M that describes the installation orientation information of the Mecanum wheel, that is, $\text{rank}(J) = \text{rank}(SM) = \text{rank}(M)$.

According to Formula (22), the following formula can be obtained.

$$\det(M) = 0, \ \text{rank}(M) \neq 3. \tag{23}$$

According to the multiplication theorem of the determinant, we obtain

$$\det(J) = 0, \ \text{rank}(J) \neq 3. \tag{24}$$

According to the above analysis, in a mobile system composed of three Mecanum wheels, if the axles of rollers are parallel to each other and the number of intersection points is 0, then the mobile

system has singularity. The inverse kinematics velocity Jacobian matrix of the system is not a column full rank matrix, so the mobile system cannot achieve omnidirectional movement.

3.2.2. The Axles of the Three Bottom-Rollers Intersect at One Point

In Figure 4, the axles of the three bottom-rollers intersect at one point, and the coordinate system *XOY* of the mobile robot system is established with the intersection point as the origin, and the local wheel coordinate systems $X_iO_iY_i$ ($i = 1, 2, 3$) are established in a counterclockwise order. The relationship of the parameters is shown in Table 2.
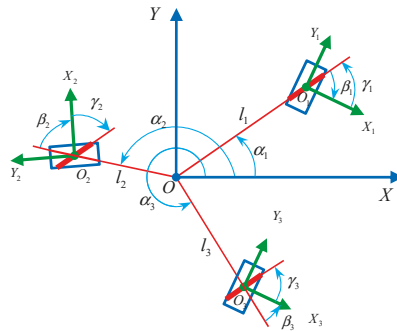

Figure 4. Wheel Configuration of the mobile robot with three Mecanum wheels whose bottom-roller axles intersect at one point.

Table 2. Relationship between the parameters of the three Mecanum wheels in Figure 4.

Serial Number	$|\alpha_i| \in [0°, 360°)$	$|\beta_i| \in [0°, 180°]$	$|\gamma_i| \in (0°, 90°)$
1	α_1	$-\gamma_1$	γ_1
2	α_2	$-180° - \gamma_2$	γ_2
3	α_3	$-\gamma_3$	γ_3

According to the parameters in Table 2, we can obtain

$$\beta_i + \gamma_i = c_i \ (c_i = 0° \text{ or } \pm 180°, \ i = 1, 2, 3) \tag{25}$$

then,

$$\sin(\beta_i + \gamma_i) = 0. \tag{26}$$

The matrix *M* of wheel installation orientation is

$$M = \begin{bmatrix} \cos(\alpha_1 + c_1) & \sin(\alpha_1 + c_1) & l_1 \sin(c_1) \\ \cos(\alpha_2 + c_2) & \sin(\alpha_2 + c_2) & l_2 \sin(c_2) \\ \cos(\alpha_3 + c_3) & \sin(\alpha_3 + c_3) & l_3 \sin(c_3) \end{bmatrix} = \begin{bmatrix} \cos(\alpha_1 + c_1) & \sin(\alpha_1 + c_1) & 0 \\ \cos(\alpha_2 + c_2) & \sin(\alpha_2 + c_2) & 0 \\ \cos(\alpha_3 + c_3) & \sin(\alpha_3 + c_3) & 0 \end{bmatrix}.$$

The values of the third column of matrix *M* are all 0, then,

$$\det(M) = 0, \ \text{rank}(M) \neq 3. \tag{27}$$

then,

$$\det(J) = 0, \ \text{rank}(J) \neq 3. \tag{28}$$

In the mobile system composed of three Mecanum wheels, if the axles of the three bottom-rollers intersect at one point, the mobile system has singularity, and the inverse kinematics velocity Jacobian

matrix does not satisfy the condition of a column full rank matrix; therefore, the mobile system cannot achieve omnidirectional motion.

If the axles of any two bottom-rollers coincide with each other or the axles of three bottom-rollers coincide with each other, it can be concluded that the axles of two bottom-rollers intersect at one point, which also satisfies the inference that the axles of three bottom-rollers intersect at one point. There are four configurations of three Mecanum wheels whose axles intersect at one point, three of which have collinear roller axles.

3.2.3. The Axles of the Three Bottom-Rollers Intersect at Two Points

According to the hypothesis, when two roller axles intersect at one point, the other roller axe must be parallel to one of the roller axles. As shown in Figure 5, if any two roller axles coincide, the result will inevitably be transformed into the case of axles intersecting at one point. The coordinate system *XOY* is established by arbitrarily choosing one of the intersections as the origin *O*, and the local wheel coordinate system $X_iO_iY_i$ ($i = 1, 2, 3$) is also established in counterclockwise order. The relationship of the parameters is shown in Table 3.

Figure 5. Wheel configuration of the mobile robot with three Mecanum wheels whose roller axles intersect at two points.

Table 3. Relationship between the parameters of the three Mecanum wheels in Figure 5.

Serial Number	$|\alpha_i|\in[0°, 360°)$	$|\beta_i|\in[0°, 180°]$	$|\gamma_i|\in(0°, 90°)$
1	α_1	$-\gamma_1$	γ_1
2	α_2	$-180°-\gamma_2$	γ_2
3	α_3	β_3	γ_3

The system coordinate system *XOY* is established at the intersection of the roller axles of wheel O_1 and wheel O_2, then we can obtain

$$\beta_i + \gamma_i = c_i \ (c_i = 0° \text{ or} \pm 180°, \ i = 1, 2), \ \sin(\beta_i + \gamma_i) = 0. \tag{29}$$

The roller axles of wheels O_1 and O_3 are parallel to each other, and the following relations are established

$$\alpha_i + \beta_i + \gamma_i = \alpha_1 \ (i = 1, 3). \tag{30}$$

Thus, the matrix M can be obtained ad

$$M = \begin{bmatrix} \cos(\alpha_1) & \sin(\alpha_1) & l_1 \sin(c_1) \\ \cos(\alpha_2 + c_2) & \sin(\alpha_2 + c_2) & l_2 \sin(c_2) \\ \cos(\alpha_1) & \sin(\alpha_1) & l_3 \sin(\beta_3 + \gamma_3) \end{bmatrix}$$

$$= \begin{bmatrix} \cos(\alpha_1) & \sin(\alpha_1) & 0 \\ \cos(\alpha_2 + c_2) & \sin(\alpha_2 + c_2) & 0 \\ \cos(\alpha_1) & \sin(\alpha_1) & l_3 \sin(\beta_3 + \gamma_3) \end{bmatrix}.$$

The determinant of matrix M is

$$\begin{aligned} |M| &= l_3 \sin(\beta_3 + \gamma_3) [\cos(\alpha_1) \sin(\alpha_2 + c_2) - \sin(\alpha_1) \cos(\alpha_2 + c_2)] \\ &= l_3 \sin(\beta_3 + \gamma_3) \sin(\alpha_2 + c_2 - \alpha_1) \end{aligned} \tag{31}$$

Combining with the discussion in Section 3.2.2, the roller axle of wheel O_3 does not coincide with the straight line l_3, so $\beta_3 + \gamma_3 \neq 0$ or $\pm 180°$, then, $\sin(\beta_3 + \gamma_3) \neq 0$.

Because the roller axles of wheels O_1 and O_2 intersect at one point, $\alpha_2 + \alpha_1 \neq 0$ or $\pm 180°$ and $\sin(\alpha_2 + c_2 - \alpha_1) \neq 0$, then, the following is established

$$\det(M) \neq 0, \ \text{rank}(M) = 3. \tag{32}$$

then,

$$\det(J) \neq 0, \ \text{rank}(J) = 3. \tag{33}$$

In the mobile system consisting of three Mecanum wheels, if the axles of the three bottom-rollers intersect at two points, there is no singularity in the system, and the Jacobian matrix of the inverse kinematics velocity is a column full rank matrix. The mobile system can realize omnidirectional movement in the plane.

3.2.4. The Axles of the Three Bottom-Rollers Intersect at Three Points

When the axles of the three bottom-rollers intersect at three points, no two axles of the bottom-rollers can be parallel or coincide with each other, as shown in Figure 6. The coordinate system XOY is established by arbitrarily selecting one of the intersections as the origin. The relationship of the parameters is shown in Table 4.

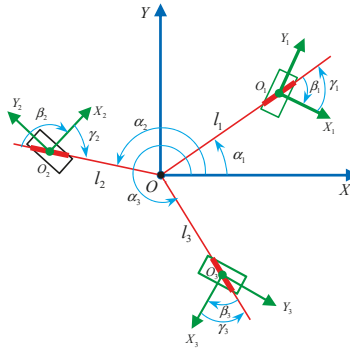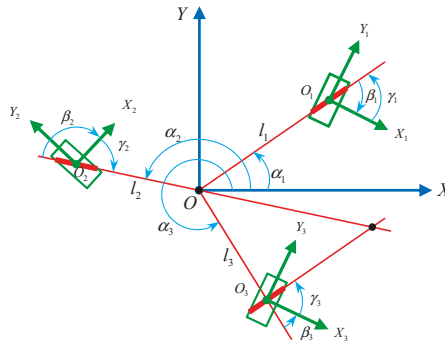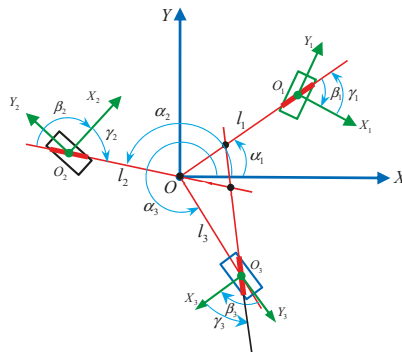**Figure 6.** Configuration of mobile robot with three Mecanum wheels whose roller axles intersect at three points.

Table 4. Relationship between the parameters of the three Mecanum wheels in Figure 6.

Serial Number	$|\alpha_i|\in[0°, 360°)$	$|\beta_i|\in[0°, 180°]$	$|\gamma_i|\in(0°, 90°)$
1	α_1	$-\gamma_1$	γ_1
'2	α_2	$-180°-\gamma_2$	γ_2
3	α_3	β_3	γ_3

The coordinate system XOY is established at the intersection point of roller axles of wheel O_1 and wheel O_2. The following formula can be obtained

$$\beta_i + \gamma_i = c_i \ (c_i = 0 \ \text{or} \ \pm 180°, i = 1, 2), \ \sin(\beta_i + \gamma_i) = 0. \tag{34}$$

The matrix M can be obtained

$$M = \begin{bmatrix} \cos(\alpha_1 + c_1) & \sin(\alpha_1 + c_1) & 0 \\ \cos(\alpha_2 + c_2) & \sin(\alpha_2 + c_2) & 0 \\ \cos(\alpha_3 + \beta_3 + \gamma_3) & \sin(\alpha_3 + \beta_3 + \gamma_3) & l_3 \sin(\beta_3 + \gamma_3) \end{bmatrix}.$$

The determinant of matrix M is

$$\begin{aligned} |M| &= l_3 \sin(\beta_3 + \gamma_3) [\cos(\alpha_1 + c_1) \sin(\alpha_2 + c_2) - \sin(\alpha_1 + c_1) \cos(\alpha_2 + c_2)] \\ &= l_3 \sin(\beta_3 + \gamma_3) \sin(\alpha_2 + c_2 - \alpha_1 - c_1) \end{aligned} \tag{35}$$

According to the discussion results in Sections 3.2.2 and 3.2.3, we can obtain

$$\sin(\beta_3 + \gamma_3) \neq 0.$$

Roller axles of wheel O_1 and wheel O_2 intersect at one point, $\alpha_1 - \alpha_2 \neq 180° \cdot m \ (m = 0, \pm 1, \pm 2, \pm 3)$; therefore, $\sin(\alpha_2 + c_2 - \alpha_1 - c_1) \neq 0$. The value is substituted into Formula (35), we can obtain

$$\det(M) \neq 0, \ \text{rank}(M) = 3. \tag{36}$$

then,

$$\det(J) \neq 0, \ \text{rank}(J) = 3. \tag{37}$$

In a mobile system consisting of three Mecanum wheels, if the axles of the three bottom-rollers intersect at three points, there is no singularity in the system, and the Jacobian matrix of the inverse kinematics velocity satisfies the column full-rank condition, and the mobile system can achieve omnidirectional motion in the plane.

According to the deduction of Formula (17) and the analysis results of the number of intersection points mentioned above, the condition for the omnidirectional motion of the mobile system composed of multiple Mecanum wheels (three wheels or more) is that any three axles of bottom-rollers in contact with the ground in three Mecanum wheels intersect at two or three points, which can be called a 'bottom-roller axle intersections approach. Table 5 illustrates the three-Mecanum-wheel configurations of the omnidirectional mobile robot and shows the relationship between the number of intersection points and the column full rank. Based on these illustrations, we can quickly judge whether the mobile system can achieve omnidirectional movement using only wheel configurations.

Table 5. Three-Mecanum-wheel configurations of the omnidirectional mobile robot.

Number of Intersection Points	Typical Configurations	Column Full Rank
0		No
1		No
2		Yes
3		Yes

3.3. Three-Mecanum-Wheel Configurations of the Mobile Robot

In order to balance the load, the three-wheel configuration usually adopts a circular array arrangement. The common three-Mecanum-wheel configurations include a centripetal circular array configuration [26], a non-centripetal circular array configuration [1], and a star-type circular array configuration, as shown in Figure 7a–c, respectively. Mecanum wheels in three-wheel configurations usually have the same structure, whose rollers have the same inclination. Judging by the bottom-roller axle intersections approach, these configurations all have omnidirectional mobility performance. The wheels in the three-wheel configuration are, typically, special Mecanum wheels whose rollers' axles are orthogonal to the hub axle. These are known as omniwheels, transwheels, or multidirectional wheels, as shown in Figure 7f. In this article, we use an orthogonal Mecanum wheel to name this kind of wheel. The two typical orthogonal Mecanum wheel configurations are the centripetal circular array configuration [18,28,29] and T-configuration, as shown in Figure 7d,e, respectively. The configuration in Figure 7d is a rotational symmetry configuration, and this configuration is often used for indoor mobile service robots and light-duty handling robots. In this article, the orthogonal Mecanum wheel configurations are not studied in depth.
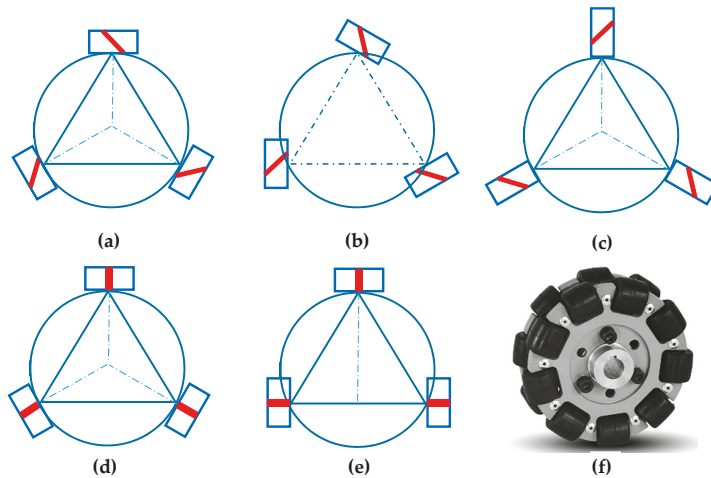
Figure 7. Three-Mecanum-wheel configurations: (**a**) centripetal circular array configuration; (**b**) Non-centripetal circular array configuration; (**c**) star-type circular array configuration; (**d**) centripetal circular array configuration of orthogonal Mecanum wheels; (**e**) T-configuration of the orthogonal Mecanum wheels; (**f**) an orthogonal Mecanum wheel.

4. Symmetrical Wheel Configurations of the Four-Mecanum-Wheel Mobile Robot

4.1. Judging the Four-Mecanum-Wheel Configurations by a Bottom-Roller Axle Intersections Approach

At present, the mobile robot with four Mecanum wheels is the most popular configuration in both scientific research and industrial application. There are many possible wheel configurations for the four-Mecanum-wheel robot [23,25,30], some of them are illustrated in Figure 8. In Figure 8, the inclined line on the wheel in the figure represents the inclined direction of roller in contact with the ground. Figure 8a–j show 10 rectangular configurations of four wheels that are arranged at the corner and whose axles are parallel to the centerline of robot. Figure 8k–n show four possible centripetal configurations of four wheels. Figure 8o shows a centripetal circular array configuration of four omniwheels. In the configurations (a), (f), and (k), any three roller axles are parallel to each other or coincide with each other. The number of intersection points of the three roller axles is 0 or 1 (the overlapping axles are considered to intersect at one point). The column ranks of the Jacobian matrix of these configurations are 2. These configurations obviously cannot achieve omnidirectional movement. In the wheel configurations (b)–(e), (g)–(j), and (l)–(n), the axles of the bottom-rollers of three wheels intersect at two points, so the Jacobian matrices of these wheel configurations are column full-rank matrices. In theory, these configurations can achieve omnidirectional movement in the plane.

In practical applications, besides satisfying the conditions of the column full rank of the Jacobian matrix, the configuration also needs good operability and driving performance. Wheel configurations (b), (c), (d), (g), (h), (i), (l), and (m) can satisfy the conditions of omnidirectional motion, but the symmetry and the driving performance of the mobile system is poor. Considering the influence of dynamic factors, such as friction and moment of inertia, in actual operation, there will be a large deviation in the motion. Therefore, these configurations are generally not used. In addition, if the centers of four wheels in the configuration (j) form a square, the axles of the three bottom-rollers intersect at the one point, the column rank of Jacobian matrix in these configurations will change from 3 to 2, and it is no longer an omnidirectional mobile system. Configuration (n) has omnidirectional mobility, but the motion friction component of the configuration cannot offset itself in the course of movement, and there is a tendency to rotate in situ. Configuration (o) is the configuration (n) using orthogonal Mecanum wheels, mostly for small robotic mobile platforms. The symmetry of wheels configurations

(e) and (j) is the best among these wheel configurations that can achieve omnidirectional motion. However, when rotating on the spot, the mobile robot system with the configuration (j) has a small driving torque and a weak driving effect. Therefore, the configuration (e) is the optimal configuration of a four-Mecanum-wheel system. The characteristics of the Mecanum wheel configurations in Figure 8 are summarized in Table 6.
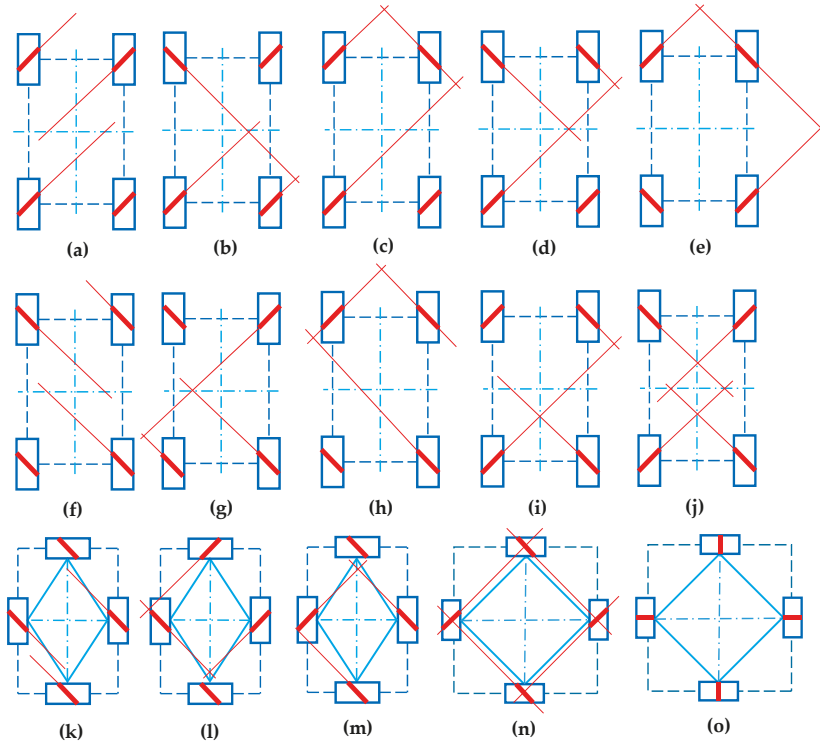
Figure 8. Four-Mecanum-wheel configurations: (**a**)–(**j**) rectangular configurations of four wheels that are arranged at the corner and whose axles are parallel to the centerline of the robot; (**k**)–(**n**) centripetal configurations of four Mecanum wheels; (**o**) centripetal circular array configurations of four orthogonal Mecanum wheels.

Table 6. Characteristics of the Mecanum wheel configurations in Figure 8.

Configurations in Figure 8	a	b	c	d	e	f	g	h	i	J	k	l	m	n
Intersections	0	2	2	2	2	0	2	2	2	2	0	2	2	2
Column rank	2	3	3	3	3	2	3	3	3	3	2	3	3	3
Column full Rank	N	Y	Y	Y	Y	N	Y	Y	Y	Y/N	N	Y	Y	Y
Omnidirectional motion capacity	n	B	B	B	G	n	B	B	B	G/n	N	B	B	G

Note: Y = the Jacobian matrix is a column full-rank matrix, N = not; n = the mobile robot system does not have omnidirectional mobility capacity; B = the omnidirectional motion capacity is not good; G = good motion capacity.

4.2. Theoretical Verification for the Symmetrical Rectangular Configurations with Four Mecanum Wheels

The two symmetrical rectangular configurations of the four-Mecanum-wheel mobile robot are shown in Figure 9. Choosing the geometric symmetry center as the origin O, the rectangular coordinate system *XOY* fixed with the mobile robot is established. The structural parameters of each Mecanum wheel are the same; therefore, $\gamma_1 = -\gamma_2 = \gamma_3 = -\gamma_4 = -\gamma$ (γ is positive) and $|\gamma_i| = 45°$ ($i = 1, 2, 3, 4$).
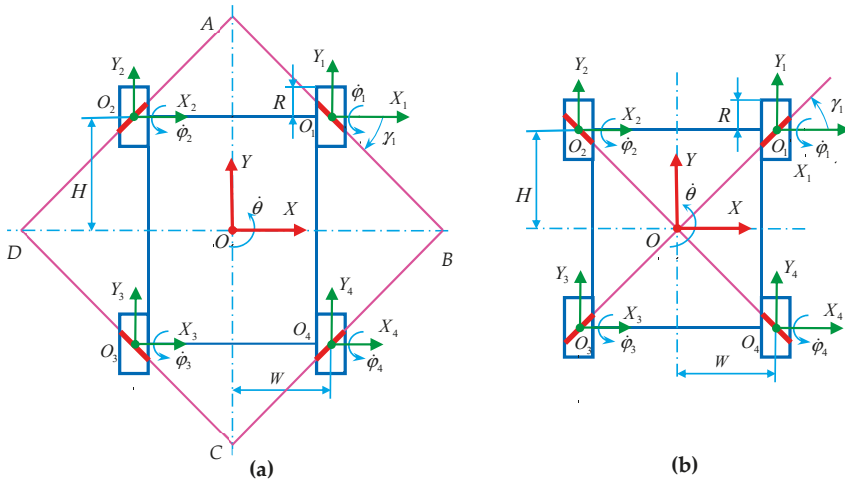
Figure 9. Coordinate system assignments for the four-Mecanum-wheel robot with a symmetrical structure: (**a**) wheel configuration in Figure 7e; (**b**) wheel configuration in Figure 7j.

In Figure 9a, the bottom-rollers' axles of the four Mecanum wheels intersect at points A, B, C, and D. According to the kinematics analysis of a single Mecanum wheel in Section 2.2, the relationship between angle α_1 and angle β_1 corresponding to wheel O_1 can be determined as

$$\alpha_1 + \beta_1 = 0. \tag{38}$$

By substituting the conditions of Formula (38) into Formula (13), we can obtain

$$\begin{bmatrix} \cos\gamma_1 & \sin\gamma_1 & l\sin(\beta_1 + \gamma_1) \end{bmatrix} \begin{bmatrix} \dot{x} \\ \dot{y} \\ \dot{\theta} \end{bmatrix} + R\dot{\varphi}_1 \sin\gamma_1 = 0. \tag{39}$$

Formula (39) can be written as

$$\dot{\varphi}_1 = -\frac{1}{R} \begin{bmatrix} \frac{1}{\tan\gamma_1} & 1 & W - \frac{H}{\tan\gamma_1} \end{bmatrix} \begin{bmatrix} \dot{x} \\ \dot{y} \\ \dot{\theta} \end{bmatrix}. \tag{40}$$

Similarly, the inverse kinematics equations of the other three wheels are expressed as

$$\dot{\varphi}_2 = -\frac{1}{R} \begin{bmatrix} \frac{1}{\tan\gamma_2} & 1 & -W - \frac{H}{\tan\gamma_2} \end{bmatrix} \begin{bmatrix} \dot{x} \\ \dot{y} \\ \dot{\theta} \end{bmatrix}. \tag{41}$$

$$\dot{\varphi}_3 = -\frac{1}{R} \begin{bmatrix} \frac{1}{\tan\gamma_3} & 1 & -W + \frac{H}{\tan\gamma_3} \end{bmatrix} \begin{bmatrix} \dot{x} \\ \dot{y} \\ \dot{\theta} \end{bmatrix}. \tag{42}$$

$$\dot{\varphi}_4 = -\frac{1}{R} \begin{bmatrix} \frac{1}{\tan\gamma_4} & 1 & W + \frac{H}{\tan\gamma_4} \end{bmatrix} \begin{bmatrix} \dot{x} \\ \dot{y} \\ \dot{\theta} \end{bmatrix}. \tag{43}$$

Because $\gamma_1 = -\gamma_2 = \gamma_3 = -\gamma_4 = -\gamma = -45°$, the inverse kinematics equation of the four-Mecanum-wheel mobile robot is [31]

$$
\begin{bmatrix} \dot{\varphi}_1 \\ \dot{\varphi}_2 \\ \dot{\varphi}_3 \\ \dot{\varphi}_4 \end{bmatrix} = -\frac{1}{R} \begin{bmatrix} -\cot\gamma & 1 & W+H\cot\gamma \\ \cot\gamma & 1 & -W-H\cot\gamma \\ -\cot\gamma & 1 & -W-H\cot\gamma \\ \cot\gamma & 1 & W+H\cot\gamma \end{bmatrix} \begin{bmatrix} \dot{x} \\ \dot{y} \\ \dot{\theta} \end{bmatrix} = -\frac{1}{R} \begin{bmatrix} -1 & 1 & W+H \\ 1 & 1 & -(W+H) \\ -1 & 1 & -(W+H) \\ 1 & 1 & W+H \end{bmatrix} \begin{bmatrix} \dot{x} \\ \dot{y} \\ \dot{\theta} \end{bmatrix}. \tag{44}
$$

The inverse kinematics velocity Jacobian matrix is expressed as

$$
J = -\frac{1}{R} \begin{bmatrix} -1 & 1 & W+H \\ 1 & 1 & -(W+H) \\ -1 & 1 & -(W+H) \\ 1 & 1 & W+H \end{bmatrix}.
$$

According to Formula (44), the symmetrical rectangular configuration of the four-Mecanum-wheel robot shown in Figure 9a satisfies the column full rank of the inverse kinematics velocity Jacobian matrix; therefore, it can achieve omnidirectional motion.

In the wheel configuration shown in Figure 9b, the bottom-rollers' axles of the four Mecanum wheels intersect at point O, therefore, $W - H \cot\gamma = 0$. According to Formula (45) and the structural parameters of the configuration shown in Figure 8b, the inverse kinematics equation of the mobile robot is

$$
\begin{bmatrix} \dot{\varphi}_1 \\ \dot{\varphi}_2 \\ \dot{\varphi}_3 \\ \dot{\varphi}_4 \end{bmatrix} = -\frac{1}{R} \begin{bmatrix} \cot\gamma & 1 & W-H\cot\gamma \\ -\cot\gamma & 1 & -(W-H\cot\gamma) \\ \cot\gamma & 1 & -(W-H\cot\gamma) \\ -\cot\gamma & 1 & W-H\cot\gamma \end{bmatrix} \begin{bmatrix} \dot{x} \\ \dot{y} \\ \dot{\theta} \end{bmatrix} = -\frac{1}{R} \begin{bmatrix} 1 & 1 & 0 \\ -1 & 1 & 0 \\ 1 & 1 & 0 \\ -1 & 1 & 0 \end{bmatrix} \begin{bmatrix} \dot{x} \\ \dot{y} \\ \dot{\theta} \end{bmatrix}. \tag{45}
$$

In Formula (45), the third column of the Jacobian matrix is all 0, which limits the central rotation of the mobile robot. The Jacobian matrix of the inverse kinematics velocity is not a column full rank, and the mobile system cannot achieve omnidirectional motion.

The above theoretical derivation verifies the correctness of the roller axle intersection approach. It can be judged whether the wheel configuration has omnidirectional movement performance according to the number of axle intersection points of the bottom-rollers in contact with the ground. The position of the intersection points can also be used to judge whether the wheel configuration has good or bad omnidirectional mobility performance. If the intersection position is symmetrical, the wheel configuration has good omnidirectional mobility. As shown in Figure 9a, the axles of the bottom-rollers of the four wheels of the symmetrical rectangular configuration intersect at four points—A, B, C, and D—and the intersection points are located far from the geometric center and are symmetrical. Therefore, this configuration has good omnidirectional mobility characteristics and is the most widely used four-Mecanum-wheel configuration.

5. Design Method of Mecanum Wheel Configurations for the Omnidirectional Mobile Robot

5.1. Sub-Configuration Judgment Method for Judging the Omnidirectional Motion Capacity of the Wheel Combination Configurations

In some applications, especially for moving large-scale components, it is necessary to combine multiple robots to transport objects cooperatively. Figure 10 is a tandem configuration composed of two four-Mecanum-wheel sub-configurations in Figure 9b. By using a roller axle intersection approach, the omnidirectional movement performance of this configuration can be judged. If the bottom-rollers axles intersect at one point of any four-Mecanum-wheel configuration, the Mecanum configuration cannot achieve omni-directional motion. However, the four-Mecanum-wheel sub-configuration of 3, 4, 5, and 6 wheels does achieve omnidirectional movement, which is the same configuration as that

shown in Figure 9a, and the configuration of 1, 2, 7, and 8 also achieves omnidirectional movement ability. The tandem configuration shown in Figure 10 can move omnidirectionally. Therefore, if a multiple-wheel configuration has any sub-configuration which has omnidirectional motion capacity, it can also achieve omnidirectional motion. This judgment method is evolved from the approach of bottom-roller axle intersection, which can be a called sub-configuration judgment method. As shown below, the conclusion is validated by the Jacobian matrix of the inverse kinematics velocity of the robot mobile system.
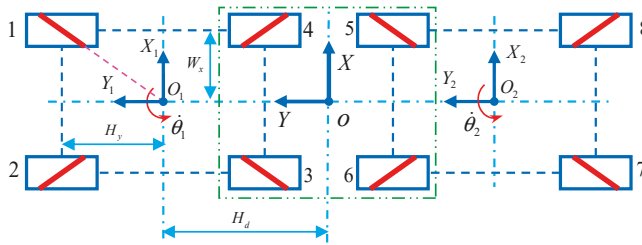
Figure 10. A tandem configuration composed of two symmetrical four-Mecanum-wheel sub-configurations.

In Figure 10, the coordinate system *XOY* located in the symmetric center of the tandem configuration is established. Its offset relative to the two local coordinate systems $X_1 O_1 Y_1$ and $X_2 O_2 Y_2$ is H_d. Let $\left(\begin{array}{ccc} \dot{x} & \dot{y} & \dot{\theta} \end{array} \right)^T$ be the generalized velocity of the system and the angular velocity of the *i*-th Mecanum wheel be $\dot{\varphi}_i$ $(i = 1, 2, \cdots, 8)$. The inverse kinematics equations of the two four-Mecanum-wheel configurations are derived when the original coordinate system is moved to the designated coordinate system *XOY*.

$$\begin{bmatrix} \dot{\varphi}_1 \\ \dot{\varphi}_2 \\ \dot{\varphi}_3 \\ \dot{\varphi}_4 \end{bmatrix} = J_1 K_1^{-1}(H_d, -90°, 0) \begin{bmatrix} \dot{x} \\ \dot{y} \\ \dot{\theta} \end{bmatrix} = -\frac{1}{R} \begin{bmatrix} \cot\gamma & 1 & -H_d\cot\gamma \\ -\cot\gamma & 1 & H_d\cot\gamma \\ \cot\gamma & 1 & -H_d\cot\gamma \\ -\cot\gamma & 1 & H_d\cot\gamma \end{bmatrix} \begin{bmatrix} \dot{x} \\ \dot{y} \\ \dot{\theta} \end{bmatrix}. \tag{46}$$

$$\begin{bmatrix} \dot{\varphi}_5 \\ \dot{\varphi}_6 \\ \dot{\varphi}_7 \\ \dot{\varphi}_8 \end{bmatrix} = J_2 K_2^{-1}(H_d, 90°, 0) \begin{bmatrix} \dot{x} \\ \dot{y} \\ \dot{\theta} \end{bmatrix} = -\frac{1}{R} \begin{bmatrix} \cot\gamma & 1 & H_d\cot\gamma \\ -\cot\gamma & 1 & -H_d\cot\gamma \\ \cot\gamma & 1 & H_d\cot\gamma \\ -\cot\gamma & 1 & -H_d\cot\gamma \end{bmatrix} \begin{bmatrix} \dot{x} \\ \dot{y} \\ \dot{\theta} \end{bmatrix}. \tag{47}$$

where,

$$J_1 = J_2 = -\frac{1}{R} \begin{bmatrix} \cot\gamma & 1 & 0 \\ -\cot\gamma & 1 & 0 \\ \cot\gamma & 1 & 0 \\ -\cot\gamma & 1 & 0 \end{bmatrix}$$

$$K_1^{-1}(H_d, -90°, 0) = \begin{bmatrix} 1 & 0 & -H_d \\ 0 & 1 & 0 \\ 0 & 0 & 1 \end{bmatrix}$$

$$K_1^{-1}(H_d, 90°, 0) = \begin{bmatrix} 1 & 0 & H_d \\ 0 & 1 & 0 \\ 0 & 0 & 1 \end{bmatrix}$$

In the above two formulas, the column rank of the Jacobian matrix of the inverse kinematics velocity of a mobile robot is still 2, which verifies that the change of coordinate system will not change the rank,

and the two mobile robots still cannot achieve omnidirectional motion alone. If the motion of two mobile robots is considered as a whole, the inverse kinematics equation of the eight-Mecanum-wheel configuration is

$$
\begin{bmatrix} \dot\varphi_1 \\ \dot\varphi_2 \\ \dot\varphi_3 \\ \dot\varphi_4 \\ \dot\varphi_5 \\ \dot\varphi_6 \\ \dot\varphi_7 \\ \dot\varphi_8 \end{bmatrix} = \begin{bmatrix} J_1 K_1^{-1}(H_d, -90^\circ, 0) \\ J_2 K_2^{-1}(H_d, 90^\circ, 0) \end{bmatrix} \begin{bmatrix} \dot x \\ \dot y \\ \dot\theta \end{bmatrix} = -\frac{1}{R} \begin{bmatrix} \cot\gamma & 1 & -H_d\cot\gamma \\ -\cot\gamma & 1 & H_d\cot\gamma \\ \cot\gamma & 1 & -H_d\cot\gamma \\ -\cot\gamma & 1 & H_d\cot\gamma \\ \cot\gamma & 1 & H_d\cot\gamma \\ -\cot\gamma & 1 & -H_d\cot\gamma \\ \cot\gamma & 1 & H_d\cot\gamma \\ -\cot\gamma & 1 & -H_d\cot\gamma \end{bmatrix} \begin{bmatrix} \dot x \\ \dot y \\ \dot\theta \end{bmatrix}
$$

$$
= -\frac{1}{R} \begin{bmatrix} 1 & 1 & -H_d \\ -1 & 1 & H_d \\ 1 & 1 & -H_d \\ -1 & 1 & H_d \\ 1 & 1 & H_d \\ -1 & 1 & -H_d \\ 1 & 1 & H_d \\ -1 & 1 & -H_d \end{bmatrix} \begin{bmatrix} \dot x \\ \dot y \\ \dot\theta \end{bmatrix} \tag{48}
$$

According to Formula (48), the inverse kinematics velocity Jacobian matrix of the eight-wheel configuration is a column full rank matrix. The above deduction verifies the correctness of the bottom-roller axle intersection approach and the sub-configuration judgment method. The coordinated motion of the tandem configuration can be realized by controlling the rotational velocities of each wheel of the configuration. This roller axle intersection approach can also be extended to the combination configurations of *N* four-Mecanum-wheel mobile robots.

5.2. Analysis of Mecanum Wheel Configurations and Combination Configurations for Common Omnidirectional Mobile Robots

Figure 11 shows the Mecanum wheel configurations and their application examples in practical production. Based on the analysis of these configurations, the deduction method of multi-wheel configurations can be synthesized. In Section 4, the optimal configuration of the four-Mecanum-wheel robot has been obtained, which is a symmetrical rectangular configuration, and is denoted as configuration W4. The front-right and rear-left wheels are right-handed wheels, and the four Mecanum wheels are mirror-symmetrical in both the front and rear, and are mirror-symmetrical for the left and right. The KUKA omniMove set with four Mecanum wheels, as shown in Figure 11a, adopts this configuration W4.

In order to transport large objects, a single mobile robot system needs to use more wheels to improve its carrying and transportation capacity. Figure 11b is a 12-Mecanum-wheel configuration adopted by KUKA's omniMove platform. This 12-Mecanum-wheel configuration consists of three four-Mecanum-wheel configurations W4, as shown in Figuration 11a, which are connected end and end to form a robot platform. In order to transport objects with larger volume and weight, the 12-Mecanum-wheel configuration robot shown in Figure 11b can be combined to form a 36-Mecanum-wheel combination mobile robot platform. The combined AGVs of the KUKA Omnimove AGV using configuration W36 can carry 63 tons of weight [10]. From Figure 11a–c, we can consider that the configuration W4 shown in Figure 11a is a sub-configuration of the configuration W12 shown in Figure 11b, while the configuration W12 is a sub-configuration of the configuration W36 shown in Figure 11c. Using the sub-configuration judgment method proposed above, both configuration W12 and configuration W36 achieve omnidirectional mobility.

	Schematic Diagram of Wheel Configurations	**Application Examples**
(a)	1 4 2 3 Configuration W4	
(b)	3 W4 Configuration W12	
(c)	3 W12 Configuration W36	
(d)	Same wheels combination 6 W4 Configuration W24	
(e)	Same wheels combination 3-2 1-1 3-1 3-2 3-2 2-1 4-1 3-2 2 W4 Configuration W8	
(f)	2 W8 Configuration W16	
(g)	2 W4 **(g1)** **(g2)**	
(h)	4 W6 2 W12 Configuration W24	

Figure 11. Common symmetrical rectangular wheel configurations and application examples: (**a**) the typical four-Mecanum-wheel configuration W4; (**b**) a 12-Mecanum-wheel configuration W12; (**c**) a combination configuration W36 with three W12; (**d**) a 24-Mecanum-wheel configuration W24; (**e**) an eight-Mecanum-wheel configuration W8, the example: MC-Drive TP 200 of CLAAS; (**f**) the combination configuration W16 with two W8, the example: the combination of two MC-Drive TP 200 [12]; (**g**) an eight-Mecanum-wheel configuration W8, which can combine into a 16-Mecanum-wheel configuration [32]; (**h**) a rectangular combination configuration consisting of four W6 [13]. The examples in (**a–d,h**) are KUKA omniMove AGVs.

The 24-Mecanum-wheel configuration W24 in Figure 11d is adopted by KUKA, and the eight-Mecanum-wheel configuration W8 shown in Figure 11e is adopted by AGV of CLAAS. Configurations W24 and W8 have the same structural characteristics. The middle four-Mecanum-wheel combination in W8 and W24 can be considered as configuration W4, as shown in Figure 11a. The four wheels on both sides of the middle-four wheels constitute the W4 configuration. The configuration is extended outward from the intermediate configuration W4. Configuration W16 in Figure 11f is a combination of the two configurations of W8 in Figure 11e. The middle configuration W4 and the outer layer configuration W4 are also considered as sub-configurations of the entire Mecanum wheels configuration. The configuration W8 in Figure 11e is a sub-configuration of configuration W16 in Figure 11f. The configurations in Figure 11d and 11e can be considered to be obtained by replacing the Mecanum wheels of the basic configuration W4 with the wheel combination including a row of wheels of the same specification. Mecanum wheels 1, 2, 3, and 4 of configuration W4 in Figure 11a are replaced by wheels 1-1 and 1-2, 2-1 and 2-2, 3-1 and 3-2, 4-1 and 4-2, respectively. Thus, the wheel configuration shown in Figure 11e is evolved. In this way, the configuration W4 is evolved into the wheel configuration W8, which is shown in Figure 11e. In the same way, the configuration W24 in Figure 11d can also be analyzed with the method. The configuration shown in Figure 11g1 can also be obtained by replacing the wheel with the coaxial tandem wheel combination. The combination configuration shown in Figure 11g2 is an end-to-end connection combination of the two configurations in Figure 11g1.

Figure 11h shows a 24-Mecanum-wheel omnidirectional mobile system consisting of four six-Mecanum-wheel configurations W6. The four KUKA omniMove platforms using this configuration W24 are applied to move a railcar body at the Siemens plant. These four mobile robot platforms with configuration W6 are not connected to each other, but each robot platform is connected to the railcar body, thus achieving a fixed connection of the four robot platforms. Two six-Mecanum-wheel configurations W6 are vertically connected to form the 12-Mecanum-wheel subsystem. Two 12-Mecanum-wheel subsystems are connected horizontally to form the 24-Mecanum-wheel configuration W24. The six-Mecanum-wheel configuration W6 consists of a W4 sub-configuration with omnidirectional mobility and a wheelset. Although the configuration W6 is not symmetrical in the longitudinal direction, the configuration W6 is used for combination. The 12-Mecanum-wheel configuration W12 and configuration W24 have symmetrical structures and omnidirectional motion capacity.

5.3. Topological Design Methods of Multi-Mecanum Wheel Configuration for Omnidirectional Mobile Robot

The bottom-roller intersection approach can be used to judge whether the wheel configuration of a single mobile robot system has omnidirectional mobility. The omnidirectional mobility of a multiple-wheel configuration can be judged by the sub-configuration judgment method. Through comprehensive analysis and evaluation, the symmetrical wheel configurations are more conducive to design, manufacture, and motion control. The symmetrical rectangular four-Mecanum-wheel configuration is the optimal wheel configuration in the four-wheel configurations. Based on this basic configuration, the multiple-Mecanum-wheel configuration of an omnidirectional mobile robot can be deduced. In this paper, the topological design methods of the Mecanum-wheel configurations are summarized and refined, including the basic configuration array method, multiple wheel replacement method, and combination method. The first two methods can be used to create suitable multiple-Mecanum-wheel configurations for a single mobile robot based on the basic Mecanum wheel configuration.

Next, the topology methods are introduced in conjunction with Figure 12. The basic configuration array method is obtained based on the sub-configuration judgment method, and it includes a linear array method and a circular array method. The former can be used for new wheel configuration designs base on the symmetrical rectangular wheel configuration, which includes end-to-end connection method and side-by-side connection method. The latter can be used for the design of new wheel configurations based on the centripetal wheel configuration. Using the basic configuration array

method, the four-Mecanum-wheel basic configuration is linearly arrayed in two directions; then, the configurations with end-to-end connection and side-by-side connection are obtained, as shown in Figure 12a,b.

Using the multiple wheels replacement method, based on the basic four-Mecanum-wheel configuration, each wheel of the four-Mecanum-wheel configuration is replaced with multiple identical wheels. The wheel can be replaced by two types of wheel combinations: a series of longitudinally arranged wheels and a series of coaxial wheels, and the new configurations can be obtained, as shown in Figure 12c–e. If the number of longitudinally arranged wheels in the front- and rear-array wheels is the same, a symmetrical Mecanum-wheel configuration can be obtained, which is symmetrical in both left and right and in front and back, as shown in Figure 12c. If not, the Mecanum wheel configuration is only symmetrical in left and right, and not in front and back, as shown in Figure 12d. Among these configurations, configurations in Figure 12a,c are more commonly used. Using the above two methods, the suitable wheel configurations for the single mobile robot can be obtained. Multiple single robots can be arranged by combination methods, including end-to-end connection, side-by-side connection, symmetrical rectangular connection, and distributed combination methods; and then, the abundant combination configurations of robots can be obtained, including end-to-end combination configuration (Figure 12f), side-by-side combination configuration (Figure 12h), rectangular combination configuration (Figure 12g), and distributed combination configuration (Figure 12i). The distributed combination configuration means that there is no physical connection among the independent mobile robots. This belongs to the research field of multi-robot cooperative motion. In this article, a detailed analysis of the distributed combination configuration is not carried out.

Using the topological design method for Mecanum wheel configurations proposed in this article, abundant wheel configurations can also be deduced based on other basic Mecanum wheel configurations. Using the circular array method, the centripetal three-Mecanum-wheel configuration shown in Figure 7a can be arrayed as a centripetal six-Mecanum-wheel configuration, as shown in Figure 13a1. Using multiple coaxial wheels replacement method, the wheel configuration in Figure 13a2 can be obtained based on configuration in Figure 7a. Using the multiple wheels replacement method, the configurations in Figure 13b1,b2 are obtained from the basic configurations in Figure 8n and the configurations in Figure 13c1 is obtained from the basic configuration in Figure 8o. Using end-to-end combination method, a combination configuration shown in Figure 13c2 can be obtained based on the configuration in Figure 13c1.
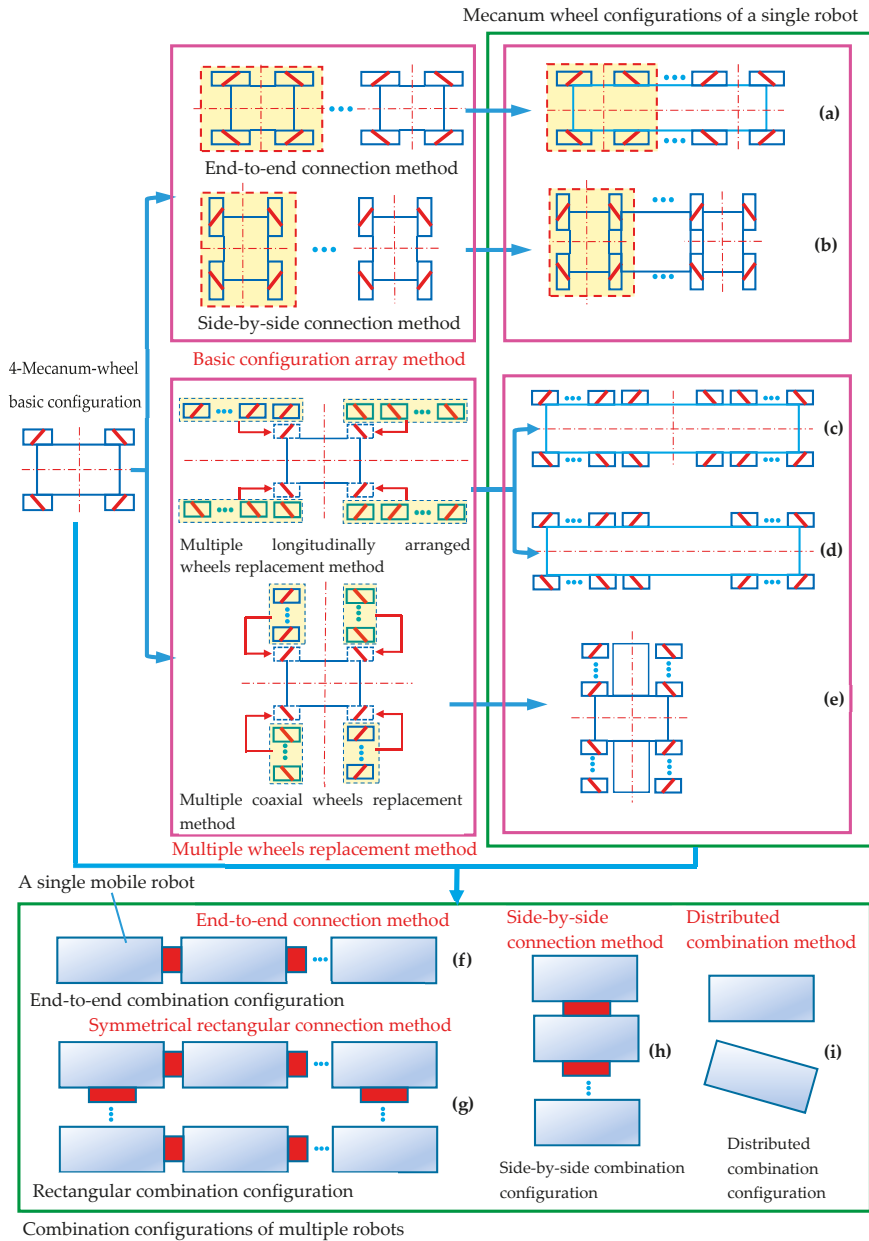
Figure 12. Topological design methods for wheel configurations based on a symmetrical four-Mecanum-wheel configuration: (**a**) end-to-end connection configuration; (**b**) side-by-side connection configuration; (**c**) a front-back symmetric configuration; (**d**) a front-back asymmetric configuration; (**e**) a symmetric configuration with four coaxial wheels series; (**f**) end-to-end combination configuration; (**g**) rectangular combination configuration; (**h**) side-by-side combination configuration; (**i**) distributed combination configuration.
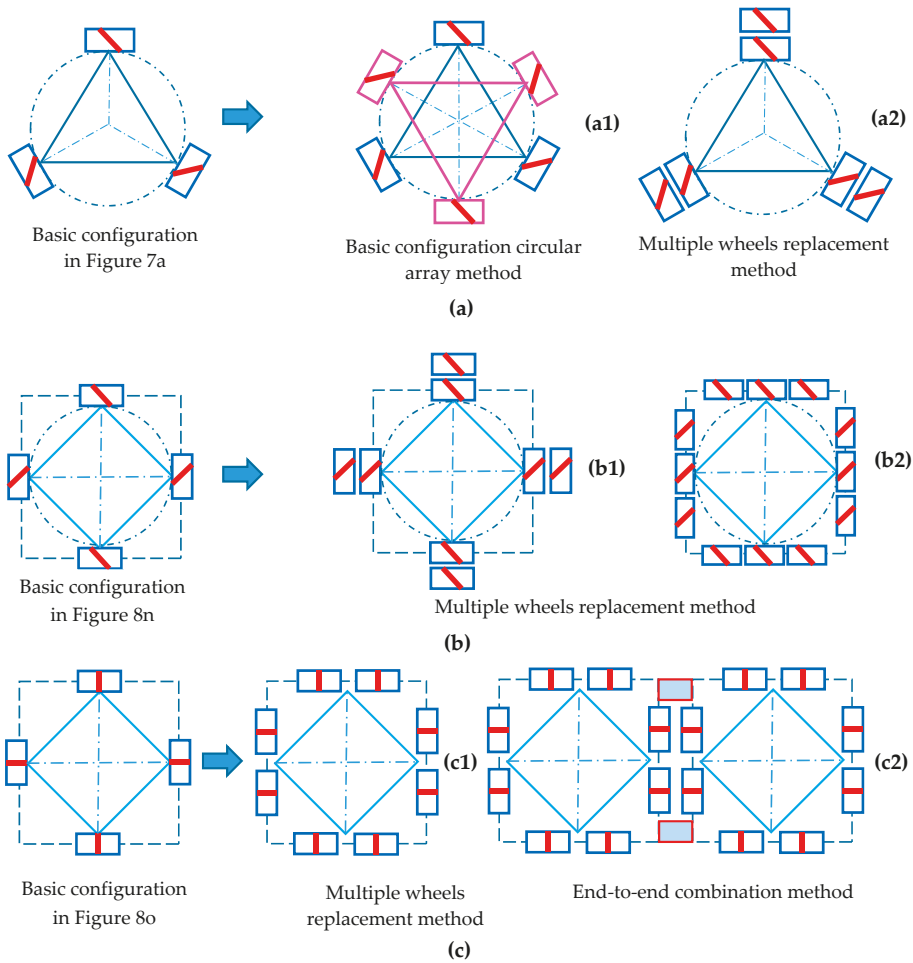
Figure 13. The examples of deducing new wheel configurations based on three basic Mecanum wheel configurations by using the topological method: (**a**) new configurations deduced from a centripetal circular array configuration of three Mecanum wheels in Figure 7a; (**b**) new configurations deduced from centripetal circular array configuration of four Mecanum wheels in Figure 8n; (**c**) new configurations deduced from centripetal circular array configurations of four orthogonal Mecanum wheels in Figure 8o.

6. Conclusions

The condition that the Mecanum wheeled robot can achieve omnidirectional movement is that the inverse kinematics Jacobian matrix of any three Mecanum wheels on the robot is a column full-rank matrix. In this paper, the relationship between the intersections of bottom-rollers axles of any three Mecanum wheels on the robot and the column rank of the Jacobian matrix is established. A bottom-rollers axles intersections approach for judging the omnidirectional mobility of Mecanum wheel configurations is proposed and proved theoretically, which is a simple and efficient geometric method. If the number of axles intersections is 2 or 3, the column rank is full and the robot can achieve omnidirectional motion in a plane; if the number of axles intersections is 0 or 1, this is not the case.

A sub-configuration judgment method for judging whether a Mecanum wheel configuration has omnidirectional mobility is evolved based on the bottom-roller axle intersections approach. According

to this method, if the multiple-Mecanum-wheel configuration has any individual sub-configuration with omnidirectional motion capacity, it can also achieve omnidirectional motion.

The topological design methods of the Mecanum wheel configurations are summarized and refined, including basic configuration array method, multiple wheel replacement method, and combination method. The first two methods can be used to create suitable multiple-Mecanum-wheel configurations for a single mobile robot based on the basic Mecanum wheel configuration. Multiple single robots can be arranged by combination methods including end-to-end connection, side-by-side connection, symmetrical rectangular connection and distributed combination, and then, the abundant combination configurations of robots can be obtained.

Author Contributions: Methodology, Y.L. and S.D.; Validation, L.Z. and Y.S.; Formal analysis, Y.L. and S.D.; Investigation, Y.L. and X.Y.; Writing—original draft preparation, Y.L., S.D., and X.Y.; Writing—review and editing, Y.S. and L.Z.; Project administration, Y.L.

Conflicts of Interest: The authors declare no conflict of interest.

References

1. Gfrerrer, A. Geometry and kinematics of the Mecanum wheel. *Comput. Aided Geom. Des.* **2008**, *25*, 784–791. [CrossRef]

2. Doroftei, I.; Grosu, V.; Spinu, V. Omnidirectional mobile robot-design and implementation. In *Bioinspiration and Robotics: Walking and Climbing Robots*; Habib, M.K., Ed.; I-Tech Education and Publishing: Rijeka, Croatia, 2007; pp. 511–528.

3. Alvito, P.; Marques, C.; Carriço, P.; Freire, J. A Robotic Platform for the Social Robot Project. In Proceedings of the 23rd IEEE International Symposium on Robot and Human Interactive Communication (ROMAN 2014) Workshop on Interactive Robots for Aging and/or Impaired People, Edinburgh, UK, 25–29 August 2014.

4. Sanbot Max. Available online: http://en.sanbot.com/product/sanbot-max/specification (accessed on 20 May 2019).

5. Qian, J.; Zi, B.; Wang, D.; Ma, Y.; Zhang, D. The design and development of an omni-directional mobile robot oriented to an intelligent manufacturing system. *Sensors* **2017**, *17*, 2073. [CrossRef] [PubMed]

6. Sun, S.; Hu, J.; Li, J.; Liu, R.; Shu, M.; Yang, Y. An INS-UWB based collision avoidance system for AGV. *Algorithms* **2019**, *12*, 40. [CrossRef]

7. Adăscăliţei, F.; Doroftei, I. Practical applications for mobile robots based on mecanum wheels-a systematic survey. In Proceedings of the 3rd International Conference on Innovations, Recent Trends and Challenges in Mechatronics, Mechanical Engineering and New High-Tech Products Development(MECAHITECH'11), Bucharest, Romania, 22–23 September 2011; pp. 112–123.

8. Heß, D.; Künemund, F.; Röhrig, C. Linux based control framework for Mecanum based omnidirectional automated guided vehicles. In Proceedings of the World Congress on Engineering and Computer Science 2013, San Francisco, CA, USA, 23–25 October 2013.

9. MC Drive Parade. Available online: https://www.youtube.com/watch?v=yf8x2egJRZ4 (accessed on 20 August 2010).

10. KUKA omniMove. Available online: https://www.kuka.com/en-us/products/mobility/mobile-platforms/kuka-omnimove (accessed on 20 May 2019).

11. Hryniewicz, P.; Gwiazda, A.; Banaś, W.; Sękala, A.; Foit, K. Modelling of a mecanum wheel taking into account the geometry of road rollers. In Proceedings of the IOP Conference Series: Materials Science and Engineering, Sibiu, Romania, 14–17 June 2017; p. 012060.

12. Airbus Rolls Out Its Second A350 XWB Composite Fuselage Demonstrator. Available online: https://www.airbus.com/newsroom/news/en/2009/08/airbus-rolls-out-its-second-a350-xwb-composite-fuselage-demonstrator.html (accessed on 7 August 2009).

13. Automation, K.-R. KUKA omniMove at Siemens Plant Krefeld. Available online: https://www.youtube.com/watch?v=EvOrFgSmQoc (accessed on 2 October 2014).

14. He, C.; Wu, D.; Chen, K.; Liu, F.; Fan, N. Analysis of the Mecanum wheel arrangement of an omnidirectional vehicle. *Proc. Inst. Mech. Eng. Part C J. Mech. Eng. Sci.* **2019**, *233*, 5329–5340. [CrossRef]

15. Muir, P.F.; Neuman, C.P. Kinematic modeling of wheeled mobile robots. *J. Robot. Syst.* **1987**, *4*, 281–340. [CrossRef]

16. Muir, P.F. *Modeling and Control of Wheeled Mobile Robots*; Carnegie Mellon University: Pittsburgh, PA, USA, 1988.

17. Angeles, J. *Fundamentals of Robotic Mechanical Systems: Theory, Methods, and Algorithms*, 4th ed.; Springer: Cham, Switzerland, 2002. [CrossRef]

18. Campion, G.; Bastin, G.; D'Andrea-Novel, B. Structural properties and classification of kinematic and dynamic models of wheeled mobile robots. In Proceedings of the 1993 IEEE International Conference on Robotics and Automation, Atlanta, GA, USA, 2–6 May 1993; pp. 462–469.

19. Gracia, L.; Tornero, J. A new geometric approach to characterize the singularity of wheeled mobile robots. *Robotica* **2007**, *25*, 627–638. [CrossRef]

20. Gracia, L.; Tornero, J. Kinematic modeling of wheeled mobile robots with slip. *Adv. Robot.* **2007**, *21*, 1253–1279. [CrossRef]

21. Zhang, Y.; Wang, S.; Zhang, J.; Su, Q.; Gao, J. Research on motion characteristic of omnidirectional robot based on mecanum wheel. In Proceedings of the 2010 International Conference on Digital Manufacturing & Automation, Washington, DC, USA, 18–20 December 2010; pp. 237–241.

22. Wang, S.; Zhang, Y.; Nie, B.; Xia, Y. Research on steering motion of omnidirectional platform based on Mecanum wheel. In Proceedings of the 2011 Second International Conference on Mechanic Automation and Control Engineering, Inner Mongolia, China, 15–17 July 2011; pp. 5177–5180.

23. Wang, Y.; Chang, D. Motion Performance Analysis and Layout Selection for Motion System with Four Mecanum Wheels. *J. Mech. Eng.* **2009**, *45*, 307–310, 316. [CrossRef]

24. Wang, Y.; Chang, D. Motion restricted condition and singular configuration for mecanum wheeled omni-directional motion system. *J. Shanghai Univ. (Natl. Sci.)* **2009**, *15*, 181–185.

25. Mishra, S.; Sharma, M.; Mohan, S. Behavioural Fault tolerant control of an Omni directional Mobile Robot with Four mecanum Wheels. *Def. Sci. J.* **2019**, *69*, 353–360. [CrossRef]

26. Gao, P.; Peng, J.; Yu, W.; Li, S.; Qin, X. Design and Motion Analysis of a Mecanum Three-Round Omni-Directional Mobile Platform. *J. Northwest. Polytech. Univ.* **2017**, *35*, 857–862.

27. Zhang, Y.N.; Wang, S.S.; Zhang, J.; Song, J. Research on motion characteristic of omnidirectional device based on Mecanum wheel. In Proceedings of the 2011 International Conference on Electric Information and Control Engineering, Wuhan, China, 15–17 April 2011; pp. 6094–6097.

28. Indiveri, G. Swedish wheeled omnidirectional mobile robots: Kinematics analysis and control. *IEEE Trans. Robot.* **2009**, *25*, 164–171. [CrossRef]

29. Wang, C.; Liu, X.; Yang, X.; Hu, F.; Jiang, A.; Yang, C. Trajectory tracking of an omni-directional wheeled mobile robot using a model predictive control strategy. *Appl. Sci.* **2018**, *8*, 231. [CrossRef]

30. Li, J.; Zhang, L. The Teleoperation System of Service Robot Based on Cloud Services. *J. Comput.* **2017**, *28*, 231–245.

31. Li, Y.W.; Dai, S.M.; Shi, Y.; Zhao, L.L.; Ding, M.H. Navigation simulation of a Mecanum wheel mobile robot based on an improved A* algorithm in Unity3D. *Sensors* **2019**, *19*, 2976. [CrossRef] [PubMed]

32. 44 MC DRIVE TP200 700 TDE. Available online: https://www.youtube.com/watch?v=iir0CINszQo (accessed on 24 October 2010).

Basket-Handle Arch and Its Optimum Symmetry Generation as a Structural Element and Keeping the Aesthetic Point of View

Alfredo Alcayde [1], Cristina Velilla [2], Carlos San-Antonio-Gómez [2], Araceli Peña-Fernández [1,3], Antonio Pérez-Romero [4] and Francisco Manzano-Agugliaro [1,3,*]

[1] Department of Engineering, University of Almeria, ceiA3, 04120 Almeria, Spain; aalcayde@ual.es (A.A.); apfernan@ual.es (A.P.-F.)
[2] Department of Ingenieria Agroforestal, Universidad Politécnica de Madrid, Av. De Puerta de Hierro, 28040 Madrid, Spain; cristina.velilla@upm.es (C.V.); c.sanantonio@upm.es (C.S.-A.-G.)
[3] Research Centre CIAIMBITAL, University of Almeria, ceiA3, 04120 Almeria, Spain
[4] Graphic Engineering Department, University of Sevilla, Utrera Road, km 1, 41013 Sevilla, Spain; tao@us.es
* Correspondence: fmanzano@ual.es; Tel.: +34-950-015396; Fax: +34-950-015491

Abstract: The arches were a great advance in construction with respect to the rigid Greek linteled architecture. Its development came from the hand of the great Roman constructions, especially with the semicircular arch. In successive historical periods, different types of arches have been emerging, which in addition to their structural function was taking aesthetic characteristics that are used today to define the architectural style. When, in the construction of a bow, the rise is less than half the springing line, the semicircular arch is no longer used and the segmental arch is used, and then on to another more efficient and aesthetic arch, the basket-handle arch. This study examines the classic geometry of the basket-handle arch also called the three-centered arch. A solution is proposed from a constructive and aesthetic point of view, and this is approached both geometrically and analytically, where the relationship between the radius of the central arch and the radius of the lateral arch is minimized. The solution achieved allows the maximum springing line or clear span to be saved with the minimum rise that preserves the aesthetic point of view, since the horizontal thrust of a bow is greater than the relationship between the springing line of the arch and the rise. This solution has been programmed and the resulting software has made it possible to analyse existing arches in historic buildings or constructions to check if their solutions were close or not from both points of view. Thus, it has been possible to verify that in most of the existing arches analyzed, the proposed solution is reached.

Keywords: aesthetic; basket-handle arch; geometry; optimum; three-centered arch

1. Introduction

The arch is a constructive and structural element whose origin must be sought in the Chaldean architecture of the third millennium BC [1]. Its fundamental development was in the architecture of the great Roman constructions, which surpassed the rigid Greek lintel architecture and allowed them to build immense structures such as thermal baths, bridges and aqueducts [2]. In Rome, the usual arch was the semicircular one, that is to say the arch formed by a semicircle in which its center is at the height of the imposts, the reason why its rise is equal to the half of its clear span or springing line [3]. The variants of the semicircular arch, also used by the Romans, are the stilted arch, whose rise is greater than the half of the clear span; and the segmental arch, which differs from the semicircular arch in that the centre of the circumference is below the line of imposts, so that the circumference is no longer tangent to the walls or pillars where the arch starts.

The semicircular arch with its respective types, see Figure 1A, such as the stilted arch, Figure 1B, the segmental arch, Figure 1C, or the arch which is attached to the barrel vault of a nave to reinforce it and divides it into sections, were also characteristic of Romanesque architecture [4]. However, it lost importance in the Gothic, which gave way to the three-pointed arch, Figure 1E, with its different variants, as an acute arch, Figure 1G, or the depressed arch, Figure 1H [5].
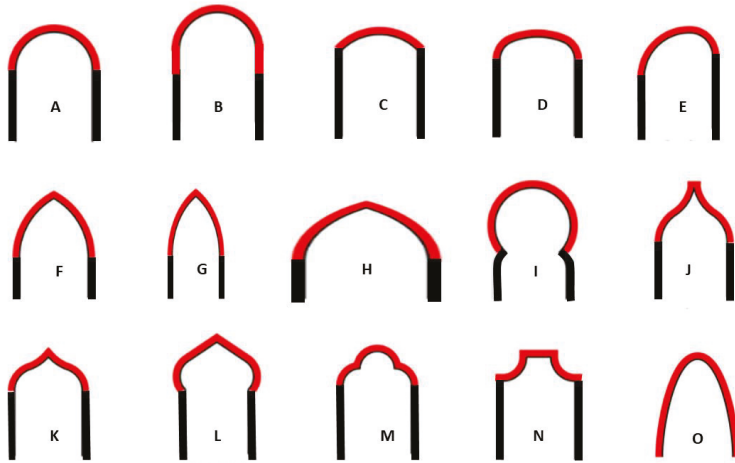
Figure 1. The main arch types used in architecture. (**A**) Semicircular. (**B**) Stilted. (**C**) Segmental. (**D**) Basket-handle or three-centered. (**E**) Rampant. (**F**) Three pointed or Gothic. (**G**) Acute. (**H**) Depressed. (**I**) Keyhole. (**J**) Ogee three-centered. (**K**) Ogee four-centered. (**L**) Oriental. (**M**) Round Trefoil. (**N**) Draped. (**O**) Parabolic.

At the end of the Gothic, a new arch spread with force until well into the Renaissance and even in the Baroque: The basket-handle arch [6], Figure 1D. The basket-handle arch is a symmetrical arch composed of a succession of circumferential arches tangent to each other and with the supports, see Figure 2A.
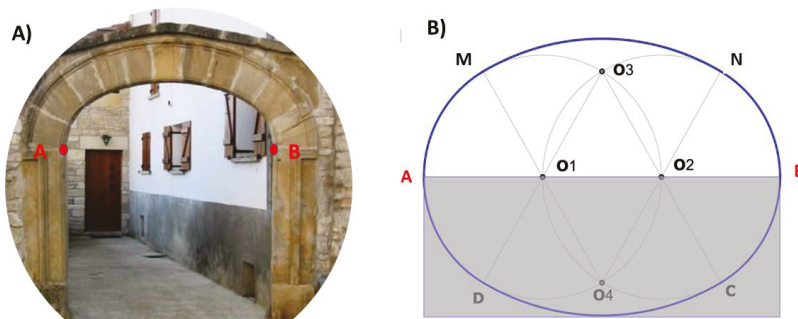
Figure 2. (**A**) Basket-handle arch. (**B**) Basket-handle arch resulting from half an oval.

It is important to emphasize that there are aesthetic conditions that have sometimes made the rules and procedures inspired by nature, e.g., trunks, and branches that simulate arches or vaults [7]. Other examples of arches should be cited, such as the Sicilian-Catalan arch (closely related to the main topic of the research), or the Ottoman arch, Figure 1K, fundamental in the history of such a technical element. Examples of these arches can be found in the literature, especially for bridges, e.g., Malabadi

Bridge [8]. It should be noted that the arches have generally been made with stone masonry, but there are examples made of wood, as the decorative elements in churches, especially the Catholic one, e.g., Borgund church (Norway) [9,10].

The most standard the basket-handle arch is made up of three circumferential arches, although arches of five, seven and nine centers can also be formed. The number of arches is as many as the smaller the rise in relation to the clear span, in any case, the number of arches of circumference is always odd. The basket-handle arch is precisely the upper half of an oval (Figure 2B).

The basket-handle arch was widely used in Spain at the end of the Gothic style and in the *Plateresque* style, where there are interesting examples both in gates of emblematic buildings and in the anonymous architecture of towns and villages [11]. In the facades of the great *Plateresque* buildings, there are important examples such as in the universities of Alcala and Salamanca, see Figure 3. In the American Spanish territories, the *Plateresque* style spread and therefore, there are examples of this architectural style.

Figure 3. Basket-handle arches in Spain. (**A**) University of Alcala. (**B**) University of Salamanca.

In France, great examples can be found in the four rooms that form a cross on the famous open staircase of the Château de Chambord, the largest of the Loire castles (Figure 3), or inside the cathedral of de Rodez (Figure 4A). Another example is the gateway to Chenonceau (Figure 4B), another of the Loire castles.

The basket-handle arch is sometimes combined with the ogee or inflected arch, widely used in 14th and 15th century architecture [12], which is a pointed arch made up of four circumferential arches, two interior arches with a concave shape and two upper convex arches. Among the many examples, there is the gate of the Monastery of San Antonio el Real, by the architect Juan Guas, located in Segovia, Figure 5A. It is also the case to integrate in the same façade the basket-handle, the ogee and the gothic arches as, for example, in the Monastery of Santa Clara located in Palencia (Spain), Figure 5B.

The basket-handle arch was also used in Baroque architecture on both sides of the Atlantic. For example, the sumptuous arches of Blenheim Palace, a monumental country residence located at Woodstock in Oxfordshire County, England, which is the residence of the Dukes of Marlborough, built between 1705 and 1722, see Figure 6A. In Spanish America, there are many examples from both the *Plateresque* and *Baroque* periods where the arches of the Primate Cathedral of Mexico City can be cited, see Figure 6B.
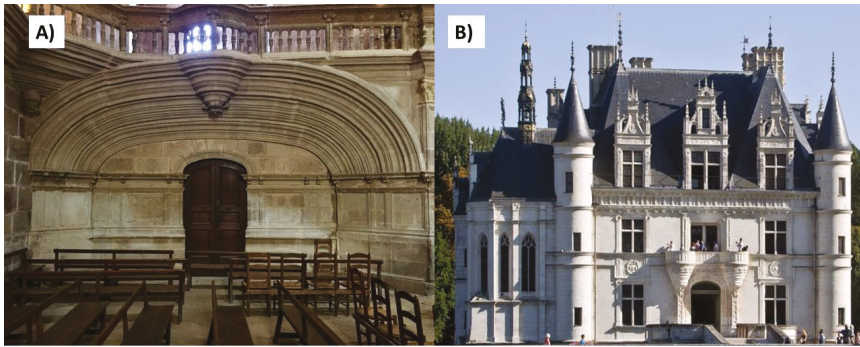
Figure 4. Basket-handle arches in France. (**A**) Rodez Cathedral. (**B**) Gateway to the Château de Chenonceau.
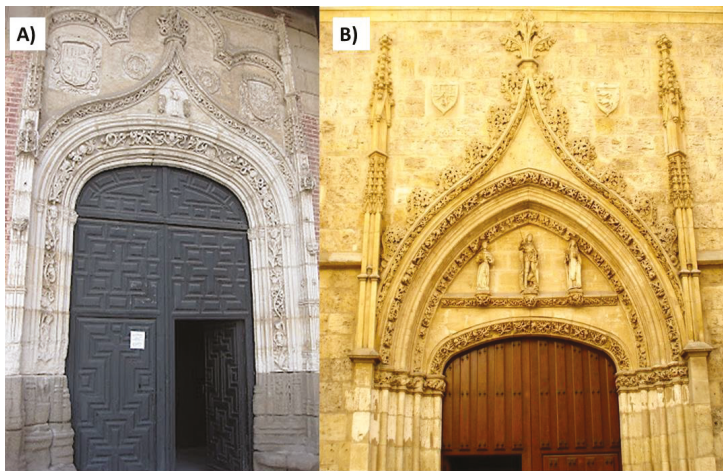
Figure 5. Basket-handle arch integrated with the ogee or inflected arch of the gate of Monasteries in Spain. (**A**) Monastery of San Antonio el Real in Segovia. (**B**) Monastery of Santa Clara in Palencia.

Figure 6. (**A**) Basket-handle arch of one of the galleries of the Blenheim Palace (UK). (**B**) Basket-handle arch of the central nave of the Metropolitan Cathedral of Mexico City.

With the recovery of the historical styles of the late nineteenth and early twentieth centuries, again the basket-handle arches are found as, in the Plaza de España in Seville (Spain), where they appear on marble columns with Corinthian capitals in the outer archery and on brick cores in the porches of those arches (Figure 7). Likewise, in Modernism, in its formal search for a new architecture, it recovers the arc of the basket-handle arch as opposed to the semicircular arch used, almost exclusively, in the neoclassical period that precedes it (Figure 8). Therefore, not only monumental examples are given because, in reality, the element arch is a widely used constructive technology, even in the ordinary architecture.
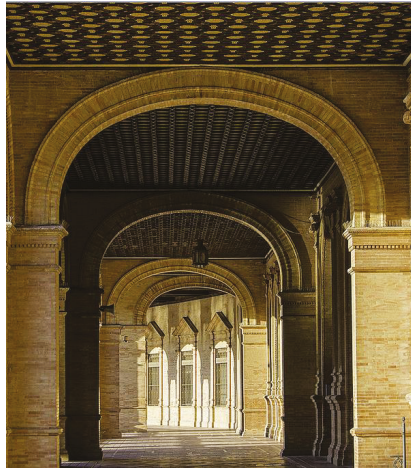
Figure 7. Basket-handle arches on brick cores of the arcades of the Plaza de España in Seville (Spain).
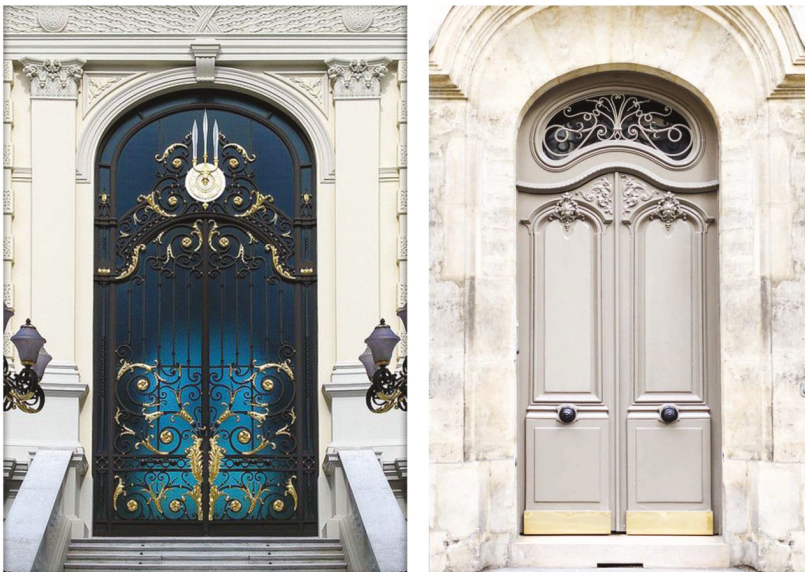
Figure 8. Examples of modernist basket-handle arches.

The design of a basket-handle arch does not present any difficulty as is seen below. However, there is no consensus on which is the optimal basket-handle arch. The objective of this work is to review the state of the art in the execution of the basket-handle of three arches, define which is the

optimal arch geometry as a structural element in the construction, calculate the numerical solution and program it for its calculation and verification of existing arches.

2. Basket-Handle Arch in Architecture

The geometric approach to the design and construction of safe factory buildings has been used since ancient times by master builders in buildings, such as the Pantheon in Rome or Gothic cathedrals [13,14]. The Theory of Structures aims at the project of safe constructions. Considering only equilibrium solutions that respect the essential characteristic of the material, in that it only resists compressions, it has proven to be the most suitable for the analysis and design of masonry structures [15]. Heyman's modern theory, based on equilibrium, is the most effective for understanding masonry constructions or structures where equilibrium states depend on geometry [15].

In the case of the analysis of masonry arches, it is necessary to assume three main conditions [14]: Masonry has no tensile strength; it can withstand infinite compression; and there will be no slippage between the pieces that make up the arch, due to the high friction coefficient between the stones. Several studies provide additional background on limit analysis for masonry arches [16].

The basic element of a masonry structure is the arch. Analyzing the equilibrium, a geometric place is found where the centers of thrust form a line, line of thrusts, whose shape depends on the geometry of the arch, the loads and the joints between the pieces. The solution for a stable arch is not unique, since there are infinite lines of thrust that can be contained within all the pieces that make it up. Thus, the equilibrium of the arch can be shown by the line of thrust, which is a theoretical line representing the path of the resulting compressive forces. The concept was first formulated in the 19th century by Moseley in 1833 [13–17] and redefined at the beginning of the 20th century by Milankovich in 1907 [14–18].

The analysis of limit states, using thrust lines, can establish the relative stability of the structures, as well as the possible collapse mechanisms. The development of interactive tools based on the analysis of thrust lines for masonry structures, using graphical computation, allows establishing the relationship between the structural behaviour of an arch and its geometry [18].

The inclined thrust existing in each element of the arch translates into one vertical (due to weight) and one horizontal (thrust of the arch). There is a maximum thrust corresponding to the most stretched line (Figure 9). The thrust is maximum when the line is tangent to the intrados in correspondence with the section of the keystone of the arch, and is inserted into the abutments or imposts [19], see Figure 9 in red. The minimum line of thrust corresponds to the one that is tangent to the back of the arch, see Figure 9 in blue.

In an arch it is considered that there are no moments in the junctions between stones, being supported on each other, nor in the extreme supports. The only force to be of concern is the horizontal thrust of the arch, since the horizontal thrust of a bow is greater, the greater the relationship between the springing line of the arch and the rise. The stilted arches can give horizontal thrusts smaller than segmental arches.

In ancient architecture, the thrust forms a polygon in whose vertices are applied on the weights of each voussoir (see Figure 9, pieces of stone that make up the arch), can be considered as a system of articulated bars. In the case of a symmetrical arch, the horizontal thrust of its centre corresponds to the reaction in the support, being null in the centre when balancing the two halves of the arch (two unstable semi-arches are transformed into a stable arch) [12–16]. The problem is to know the thrust of the arch in position, magnitude and direction, and then verify by static, the stability of the arch springer. In the case of monolithic stone springer, the result of the reaction is the composition between the horizontal thrust and its weight. In order to avoid slipping and to avoid that the resultant one is in the line of the angle, the stones that compose the abutment were inclined to a certain angle in a coincident way with the angle of friction of the material. This solution was used in very stretched arches.

The normal way was to have staggered abutments, or formed by pieces of the increasing section towards the base of the same one, to obtain that the resulting one remained inside when the push was excessive (low arches) or to load the abutments with weights in order to avoid the turn.
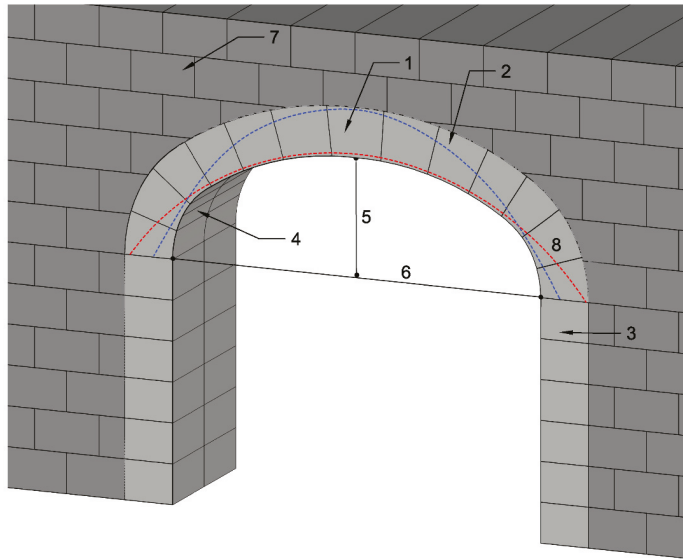
Figure 9. Basket-handle arch elements: (**1**) Keystone, (**2**) Voussoir, (**3**) Impost, (**4**) Intrados, (**5**) Rise or sagita, (**6**) Clear span or springing line. (**7**) Abutment, (**8**) Springer. Red dashed line- Lower thrust line. Blue dashed line- Upper thrust line.

When friction is high ($\mu > 0.7$), as is the case with limestone including marble, the stones that make up the arch (voussoir) do not slide between them, and the supports receive high compressive loads that can induce plastic deformations [20]. Basket-handle arches are lowered arches, which would collapse due to the sinking of the keystone (central part of the arch, see Figure 8), and the tilting of the lower sides towards the outside of the arch, a problem that can be solved by filling or solidifying this area. It should be noted that of the infinite possible directions of the arch's fracture, the vertical is the most crucial as it results in the greatest minimum thickness value of an elliptical arch needed to support its own weight. In addition, in the case of mortars joining the elements that make up the arch perpendicular to the line of intrados, the fracture pattern is the greater value of the minimum thickness allowed [21]. According to this, for a semi arch of clear span or width 2d, height h and thickness t, exposed to its own weight, the minimum thickness obtained to maintain the equilibrium corresponds to the lowest ratio h/2d. That is, the lowered arches, among which is the basket-handle arch, and the greatest thickness would be obtained for the stilted arches. For the arch as a structural element, higher safety factor values are obtained in the lowered arches [22].

From the equilibrium analysis of an arch under external loads, it can be deduced that of the probable thrust lines that satisfy these conditions, the one closest to the geometric axis corresponds to the one that generates the lowest values of the bending moment and shear force in the transversal sections., Thus, it generates a better and uniform distribution of the compressive efforts transmitted through the section itself. It is possible to calculate the safety of the arches, establishing a factor of the degree of safety of the structure, based on the line of thrust contained inside the arch. Heyman suggested reducing the thickness of the arch by changing the extrados and intrados profiles in a homothetic way until they touch the line of thrust. The result is an ideal arch, of reduced thickness, contained within the real arch. The relationship between the thickness of the actual arch and the thickness of the ideal arch that defined it as the safety geometric factor (hreal/hideal) of the structure. This factor gives an idea of the safety of the arches. To calculate the exact value of the geometric safety factor can be arduous, but it is possible to obtain a lower limit easily, for example for a factor of 2, it is expected to be enough to be able to draw a line of thrusts inside the central half of the arch.

The inverse approach to that proposed by Heyman, is based on obtaining the ideal arch in which the line of thrust moves up and down, until it becomes tangent to the curve intrados and extrados of the real arch at least one point, while remaining within its profile [22]. The result is a region that represents the domain of all probable thrust lines, parallel to those provided by the analysis, wholly contained within the thickness of the arch. By doing so, the safety geometric factor, calculated as the ratio between the actual arch thickness and the ideal arch, measured in the vertical direction, can be denoted as the "full safety range factor". Heyman's geometrical factor is a number that increases as the thickness of the arch decreases and is between 1 and infinite, this value being the maximum safety value because the line of thrust coincides exactly with the geometrical axis of the arch in this case. While the full range factor ranges from 0 (maximum risk, unstable arch) to 1 (maximum stability arch). This maximum safety condition means that the shape of such an arch (i.e., its geometric axis) matches exactly the load funicular, i.e., the shape of an inverted catenary. The arch safety evaluation methodology, based on a purely geometric formulation, makes it possible to determine that the thrust line of an arch of constant thickness, subject to its own weight, coincides with its geometric axis, only if the shape of the axis corresponds exactly to an inverted catenary corresponding to the load funicular. In this case, the loads are evenly distributed within the structure and each cross section is requested only by the axial compressive force. With this in mind, the ideal arch within the real one is the domain that contains exactly all states of equilibrium, i.e., all thrust lines parallel to those provided by the analysis.

For an arch to collapse, the structure must allow a mechanism to form. For some types of arches, such as lintels and flying buttresses (as rampant arches), it is not possible to find any disposition of articulations leading to the formation of a mechanism, which makes them safe arches from this point of view [23]. Sometimes, the problem is to support a certain load. In this case, the arch should not collapse when it is possible to draw two straight lines that join the supports with the point of application of the load. This is the case of very thick lowered arches as the segmental arches or also, the flying buttresses performed as rampant arches.

It is also interesting to note that the minimum actual arch thickness is calculated considering the minimum vertical thickness between all thicknesses measured in correspondence with the lines of action of the loads passing through the centroids of the elements. In doing so, the verification procedure can be applied to arcs of any geometry, even those comprising of variable thicknesses. In nearly complete or complete arches, it is concluded that the greater the thickness of an arch, the greater its safety factor. This is due to the line of thrust that best fits within the profile of an arch if its thickness is greater. However, for arcs with small circular segment values, which are considered very safe arcs because their safety factor is close to 1, the increase in thickness does not correlate to an effective increase in the safety factor.

Most studies on the equilibrium limit analysis of the masonry arch adopt a geometric formulation, based on the determination of the line of thrust, and only a few use energy methods. More recently, there has been the problem of determining the minimum thickness that an arch must have to support its own weight. For a semicircular arch of inner radius R and thickness t, the ratio providing the minimum thickness was given by Pierre Couplet in 1730 [21], where $t/R = 0.101$. It was later demonstrated that when a radial rupture occurs in a masonry arch, it is the line of thrust that is tangent to the hinge, not the force of the thrust [24]. Coulomb in 1773 concluded that the failure mechanism in a masonry arch is the generation of hinges in its interior and not the sliding, and seeks to determine the point at which it occurs, determining the maximum and minimum limits of the thrust force at the coronation of the arch necessary to maintain equilibrium [25]. At the beginning of the 19th century, Joaquín Monasterio determined the value of the minimum thickness of the arches based on Coulomb's static theory and concluded that the minimum thickness of a semicircular arch should satisfy the ratio $0.1053 < t/R < 0.1176$, improving the conservative result of Coulomb mentioned above [21].

The thrust line, or resistance line, is defined as the geometric location of the points of application of the resulting thrust force that develops in any cross section of the arch. The minimum line of thrust is the one applied to the extrados of the crown and the base of the arch. A distinction is made between the thrust line and the funicular of forces generated from the lines of action of the thrust forces acting

on the joints between the blocks of masonry. The study of the minimum necessary thickness of an arc, analyzing its limit equilibrium using variational formulation and the principles of potential energy, showed that s vertical rupture in a semi-cylindrical arc, subjected to its own weight and horizontal acceleration due to earthquake, was easier to produce than a radial rupture [26]. Recent research at MIT on interactive analysis of structural forces provides new graphical tools for understanding the behavior of arches. The key mathematical principle is the use of graphical analysis to determine possible equilibrium states [18]. Graphical methods can be complex, however provide good but conservative results [27].

In summary, the methods of analysis of masonry arches mainly consider three types of equations for structural analysis, i.e., those referring to: Equilibrium (static), geometry (compatibility) and materials (stresses). In the case of historical arches, only the first two are necessary since the sections are considered to be subject to stresses lower than the maximum that the materials can withstand (the stones that compose the masonry blocks).

3. Basket-Handle Arch of Three Arches or Three Centered Oval Arches

In the basket-handle arch, the key to adequate transition between arches belonging to different circumferences is that the lateral and central circumferences are tangent to each other at the link point. Since, in a circumference, the tangent direction at any point thereof is perpendicular to the radius passing through that point, it is inferred that the centres of the central arc ($O1$) and of the lateral circumferences (O_2, O_3) and the point of link or tangency (M, N), are aligned. Thus, the points are on the same straight line: (O_1, O_2, N) and (O_1, O_3, M), see Figure 10. Thus, the geometrical construction has been the norm for the execution of the basket-handle arch, see Figure 10, where two different cases are identified depending on which are known parameters.
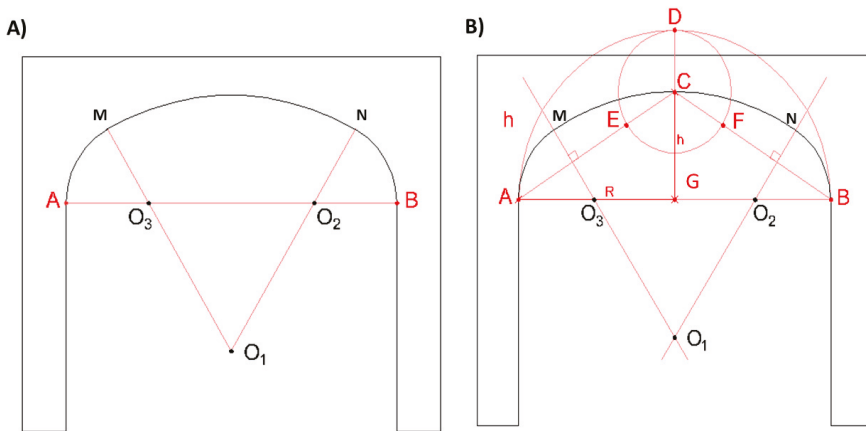
Figure 10. Basket-handle arch of three arches graphically constructed. (**A**) Known A and B (method 1). (**B**) Known A, B and C (method 2).

In the literature, it is possible to find the analytical study of the relationship between the lateral and central circumferences, according to [28]:

for different angles, fixed the clear span and the radius of the lateral circumference.
for different angles, fixed the sagita or rise and the radius of the central circumference.

The determination is of the centers, radius and tangent points of a three-centered oval arch knowing a related proportion between the position of the centers. These solutions explore lateral angle arches equal to: $2l/5$; $3l/5$; $4l/5$; $k \cdot l$ where $k > (l - h)/l$; being l the clear span and h the rise.

3.1. Basket-Handle Arch 1: Known A and B

1. The distance AB is divided into four parts
2. The equilateral triangle is built from the side AB/2
3. The vertices of the triangle (O_1, O_2 and O_3) shall be the centres of the arches. See Figure 10A.

3.2. Basket-Handle Arch 2: Known A, B and C

1. The distance AB is divided into two parts, obtaining the half, point G, see Figure 10B.
2. By point G, the circumference of radius R = GA and the perpendicular line to AB that originate at point D are traced.
3. GA and the perpendicular line to AB that originate at point D are traced.
4. At point M, take the height h and C is obtained. At C, the circumference of the CD radius is drawn.
5. The CA and CB lines are drawn, which in their intersection with said circumference are determined E and F.
6. The mediatrices of AE and BF, define the points O_1, O_2 and O_3 centers of the three arcs that form the basket-handle arch.

4. The Basket-Handle Arch Proposed

Thus, of all the possible basket-handle arches (see Figure 11), there is a relationship between the arches that could be the one that defines the optimal arch. Thus, if the central arch has a radius of R and the lateral has a radius of r, two extreme cases may arise at the outset. If r = 0 it would be known as the segmental arch, which could be understood as a degenerate basket-handle arch where the lateral circumference is a point. In the other extreme case, r = h, it would be another degenerate basket-handle arch that could be understood as a semicircular arch whose highest point is replaced by a rectilinear segment.
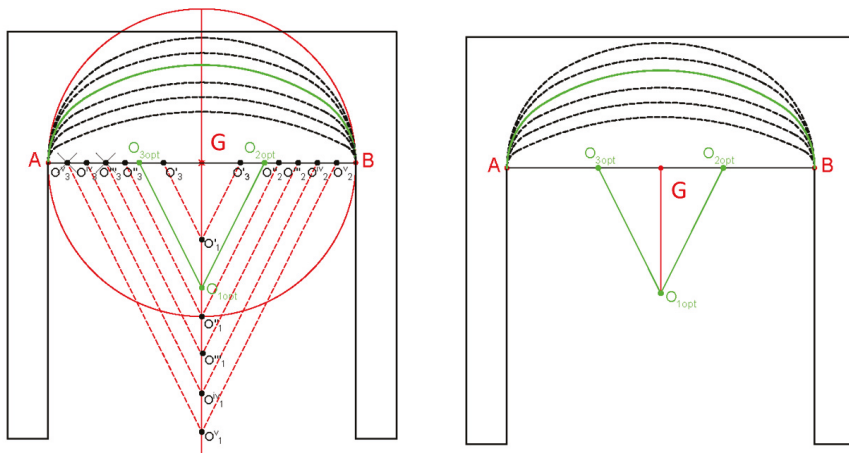
Figure 11. Example of several basket-handle arches for a specific clear span (A-B), and the arch proposed.

Although there are authors who understand that the optimal basket-handle arch is that composed of circumferences with similar curvatures, it is understood that this is only from an aesthetic point of view [29]. Due to the problem of stress transmission seen above, it is understood that the optimum is an arch as low as possible and that it maintains the aesthetic characteristics. That is to say, that of all the possible basket-handle arches, it is the one in which the ratio between the radii (R/r) is the smallest. In Figure 11, possible basket-handle arches have been represented for a specific clear span (A-B), and in green colour, the one that would be the optimal one according to the established criteria.

4.1. Graphical Geometric Construction

This section describes the graphical geometric construction of an optimum basket-handle arch. See Figure 12. Being 2d, the clear span or springing line (distance between walls AB) and h the rise or height of the arch, tracing by the incenter I of AFC the perpendicular to AC, an arc basket-handle of centers O_1, O_2 and O_3 and radii O_1C, O_2B and O_3A is obtained, which is the one with the lowest R/r of all possible basket-handle arches.
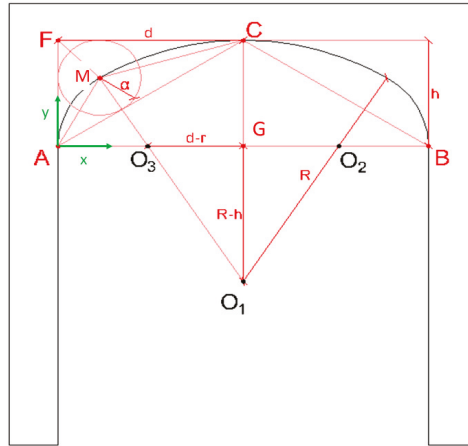
Figure 12. Graphical geometric construction of the basket-handle arch proposed.

4.2. Analytical Calculation

For the analytical calculation, see Figure 12. R and r can be calculated as a function of the semi-distance d (semi-distance between walls AB or the half of the clear span or springing line) and the height or rise h.

Be $\propto$ the radius of the circle (M) inscribed in AFC. Taking as axes MA and MC, there is a straight-line Equation (1):

$$AC \equiv \frac{x}{d} + \frac{y}{h} = 1 <> hx + dy - dh = 0 \tag{1}$$

It is expressed that the distance to here from

$$M(d- \propto, h- \propto) \text{ is } \propto$$

$$\frac{h(d- \propto) + d(h- \propto) - dh}{\sqrt{d^2 + h^2}} = \propto$$

where we get

$$\propto = \frac{d + h - \sqrt{d^2 + h^2}}{2}$$

and therefore

$$M \equiv (d- \propto, h- \propto)$$

given

$$M(\frac{d - h + \sqrt{d^2 + h^2}}{2}, \frac{h - d + \sqrt{d^2 + h^2}}{2})$$

The perpendicular by I to AC is:

$$y - \frac{h - d + \sqrt{d^2 + h^2}}{2} = \frac{d}{h}(x - \frac{d - h + \sqrt{d^2 + h^2}}{2})$$

Doing:

$$x = 0 \; R = \frac{d^2 + h^2 + (d - h)\sqrt{d^2 + h^2}}{2h}$$

$$y = 0 \; r = \frac{d^2 + h^2 - (d - h)\sqrt{d^2 + h^2}}{2d}$$

From where, after simplifying:

$$\frac{R}{r} = \frac{d}{h} \frac{\sqrt{d^2 + h^2} + d - h}{\sqrt{d^2 + h^2} - d + h}$$

Calling $\frac{d}{h} = k$ (ratio between semi-distance and height)

$$\frac{R}{r} = k \frac{\sqrt{k^2 + 1} + k - 1}{\sqrt{k^2 + 1} - k + 1} \; \text{or} \; \frac{\left(\sqrt{k^2 + 1} + k - 1\right)^2}{2}$$

4.3. Computer Software

With the above analytical calculations, a software programmed in MATLAB has been generated. Figure 13 shows the programming flowchart, with the calculations described in the previous section and the form of data input in the software. The software can calculate the arches analytically, entering the coordinates of the 3 points, i.e., the extreme points of the walls (A, B) and the high central point (C), or graphically in a scale image. Whereupon the parameters of the semi-distance d (semi-distance between walls A and B or the half of the clear span or springing line) and the height or rise h are calculated. After that, the coordinates of the three centres of the circumferences (O_1, O_2 and O_3) are calculated also. Finally, the results are shown graphically and mathematically.
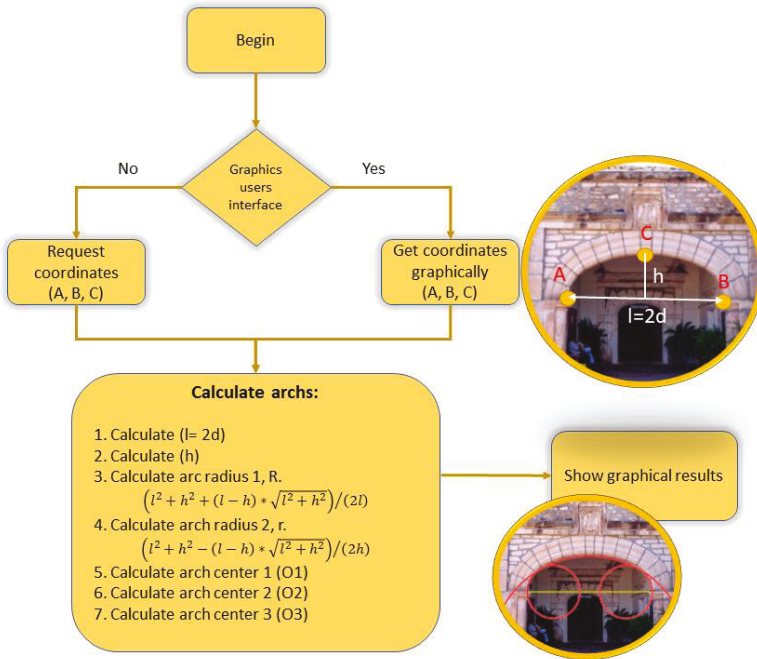
Figure 13. Flow chart of the software for optimal basket-handle arch calculation.

5. Case Studies

In this section, four cases of study of real basket-handle arches calculation have been selected, which are representative cases of outdoor public architecture (Plaza de España de Vitoria), internal structural element (Château de Chambord), and structural and decorative elements at Salamanca Cathedral (Spain) and Moscow subway station. It is essential to clarify that the optimum is to use an image with metric quality, and for this, it is possible to make use of the photogrammetry, as for example the orthophotography, and not just a single front image, since the latter can present distortions due to the perspective of the image [30]. Note that the points chosen for the analysis of the case studies are always the inner points of the arch.

5.1. Château de Chambord (France)

The Castle of Chambord at Loire Valley, in France, a UNESCO World Heritage site since 1981 is located at a distance of approximately 150 km to SW of Paris [31]. Chambord Castle was built in stone between 1519 and 1547 [32]. This castle is one of the most representative castles of the Loire Valley in France [33], and has been the subject of numerous studies, especially on issues related to the degradation of tuffeau, soft siliceous and clayey limestone, widely used in the construction of these castles [34]. One of the most singular elements of the architecture of this castle is its staircase whose layout is as remarkable as its position in the building. A double spiral staircase design is attributed to Leonardo da Vinci and it consists of two staircases that spiral around one another so that two people can pass each other without meeting [35]. There are even several hypotheses that attribute to him the design of this castle as an architect [36]. It was located in the centre of the keep, built with ashlar masonry, where four spacious rooms converge. It is composed of twin helical ramps that twist on top of each other around a hollowed and partially open core. The so-called double helix staircase serves the main floors of the building, up to the crowning terraces, crowned by the castle's tallest tower, the lantern tower. This element has been analyzed, especially the basket-handle arch composition. As can be seen in Figure 14, the basket-handle arch is not optimal from a structural point of view. In the figure, the zone has been marked that does not meet the conditions programmed in the software.
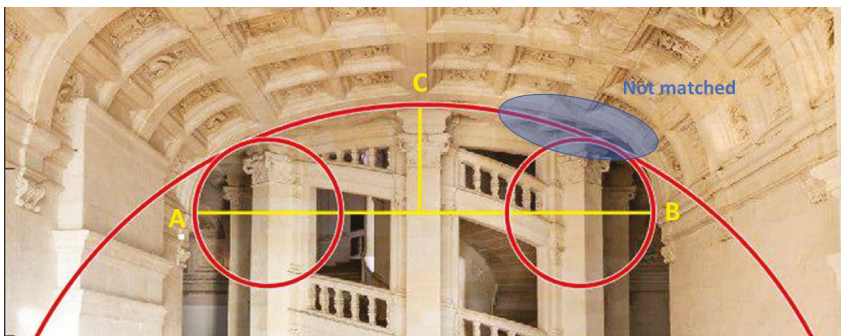
Figure 14. Calculation of the optimal basket-handle arch (in red) over the room giving access to the helicoidal staircase of the Château de Chambord.

5.2. Plaza de España de Vitoria (Spain)

The Plaza de España in Vitoria (Spain) is a neoclassical architectural style construction that forms a perfect square of 61 m. It was built at 1781. This new structure was isolated from the urban context and needed proper accessibility. In addition, to connect the square with the medieval city, the steep slope had to be bridged with the hill, and for its execution, great technical difficulties had to be overcome, as it was necessary to carry out costly and difficult flattening work. The architect solved this problem by constructing a staggered work, consisting of an elevated street under the arcades. In the square construction, ashlar stone, masonry and brick are mixed, although the arches, as can be seen in

Figure 15, are ashlars. The arches have a clear span of 4.5 m. Some literature states that the arches are semicircular, although as can be seen in Figure 15, they are basket-handle arches. Moreover, as can be seen, they are optimal basket-handle arches.
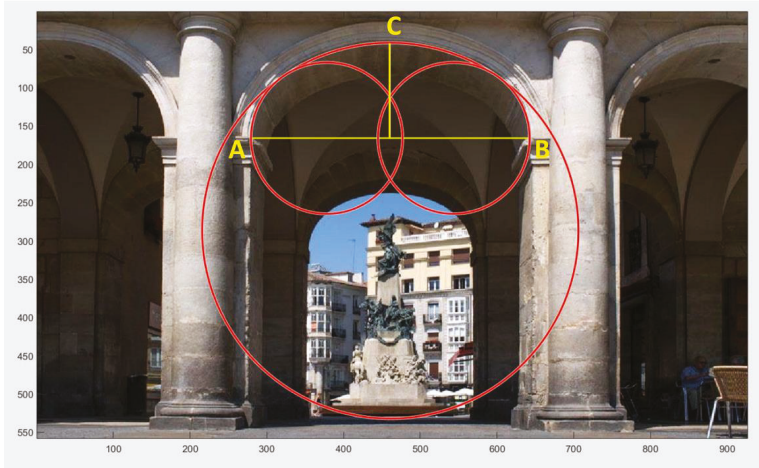
Figure 15. Calculation of the optimal basket-handle arch (in red) over the *Plaza de España* of Vitoria (Spain).

5.3. Salamanca Cathedral (Golden Chapel or Chapel of All Saints)

In Salamanca, there are two cathedrals. The so-called old cathedral and the new cathedral. The Cathedral of the Assumption of the Virgin, is called the New Cathedral. It was built between the sixteenth and eighteenth centuries mixing architectural styles: Late Gothic, Renaissance and Baroque. Of the 24 chapels that the cathedral has, the one that is the object of this study is the Golden Chapel or All Saints' Chapel. It was built in the year 1515. It has several arches that house different sepulchers, and among them the one in Figure 15, where a basket-handle arch appears, with a clear span of 3 m. As was mentioned above, the basket-handle arch is sometimes combined with the ogee or inflected arch, which was widely used in 14th and 15th century architecture. The analyzed arch is an optimal basket-handle arch as can be seen in Figure 16.
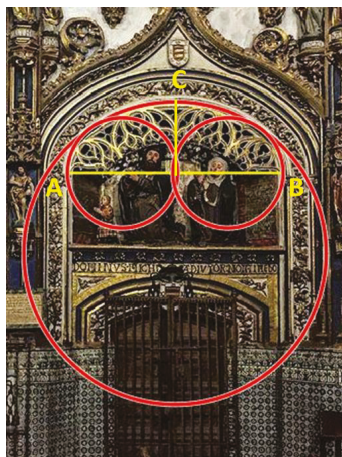
Figure 16. Calculation of the optimal basket-handle arch (in red) over the Chapel of All Saints or Golden Chapel in Salamanca Cathedral (Spain).

5.4. Moscow Subway Station (Mayakovskaya)

On 11 September 1938, Mayakovskaya Metro station was opened to the public. The station is one of the best metro stations of the late 1930s, belonging to the early period of so called Stalinist architecture. It was designed by the Soviet architect, Aleksey Dushkin (1904–1977) [37]. Despite being in the era of Stalin's Empire style, it seems avant-garde enough to be considered an example of Art Deco. As that is one of the deepest underground stations at 52 m, it was used as a bomb shelter during WWII, in particular the German bombing of Moscow in 1941. From an architectural point of view, although the load-bearing structure is made of steel, the succession of arches contributes to emphasise the perspective of the underground construction. Mayakovskaya subway station is a definite inheritor of the Romanesque. It certainly owes much more to Western European Christian architecture, than to the Byzantine tradition [38].

It is a three-vault station with two rows of columns, see Figure 17. Many tourists think that the vault is composed of basket-handle arches, see Figure 17A. This may be by fact that in the vault of the central nave, there are 35 oval ceiling niches surrounded by filament light [39]. However, after an analysis with the performed application, it was observed that the arches of the central vault did not coincide with a basket-handle arch. In any case, it is not of three centers (see the upper part of Figure 17B) but it looks like an elliptical section.

Figure 17. Moscow subway station (Mayakovskaya). (**A**) Original image. (**B**) Analysis of the optimal basket-handle arch (in red).

6. Discussion

In the study of the arches, the problem that is posed is that of supporting a certain load. In this case, the arch will not collapse when it is possible to draw two straight lines that join the supports with the point of application of the load, hence the appearance of the very thick lowered arch and the buttresses. The buttresses were built mainly to support the horizontal thrust of the vaults covering the naves of Gothic churches or cathedrals [23]. Thus, from an inclined beam to a wall as a buttress and then to lighten the structure to the so-called ramp arch [23]. This is a slender two-arch structure characterized by a higher support on one side than the other, see Figure 1E. In elliptical arches in general and in the basket-handle arches in particular, the minimum thickness necessary to support its own weight is slightly greater when it is assumed that the plane of rupture is vertical at the point where the mechanism occurs, and that the structure collapses.

The study of the relationship between the thickness of the arch and its radius is a function of the relationship between the rise (h) and the half of the clear span of the arch (d) (Figure 12). It was concluded that for elliptical arcs (d/h = 0.5), the smallest minimum thickness required was obtained when the rupture was vertical [26]. Thus, if the arch is built with voussoirs, so that the union of the voussoirs follows the line of the intrados of the arch, the plane of rupture begins radially in the intrados and propagates as vertical towards the extrados, while the point where the mechanism is generated does not change [26]. In the structural study of masonry arches, three types of analysis are considered: Equilibrium (static), geometry (compatibility) and materials (tensions). In the case of historical arches,

only the first two are useful, as it is considered that the sections are subjected to stresses lower than the maximum that the materials (rocks) can withstand.

On the other hand, arches in architecture not only fulfil a structural function, but have been traditionally used as an aesthetic element. Therefore, it has been important to maintain the proportions between the clear span and the rise of the arch. Some authors have argued that the relationship between the central arch and the lateral arch should be the maximum [29]. In this study, it has been shown, through the analysis of case studies of historic buildings, that the relationship between the central arch and the lateral arch is the opposite, the minimum.

It is necessary to point out the limitation or drawback of this study. The photographs with metric quality were not available. However, this can be solved, for example, with close range photogrammetry with metric quality obtaining, for example, orthophotographs.

In many of the cases studied, it has been possible to verify first, if they are basket-handle arches of three centers, and second, if the proportion used fulfills the hypothesis raised in this study. It is also necessary to highlight that in those cases in which the solution proposed in this study has not been reached, it has been observed that it is very close. Therefore, it is considered that the study has been valid for arches of this type, basket-handle arches or three centers arches.

7. Conclusions

In this work, the geometry of the basket-handle arch has been reviewed. It has been studied from different approaches. On the one hand, the geometry that is known in classical literature and from the constructive point of view, as a structural element. Since, in a circle, the tangent direction at any point in the circle is perpendicular to the radius passing through that point, it is deduced that the centres of the central arch and of the circles and the point of link or tangency are aligned. The main effort to be considered is the horizontal thrust of the arch, which can be greater, therefore, the greater the relationship between the clear span or the springing line of the arch and the rise. Therefore, raised arches give horizontal thrusts smaller than extended arches. Basket-handle arches are lowered arches that would collapse due to the sinking of the keystone (central piece of the arch) and the overturning of the lower sides towards the outside of the arch. With the increase in the length of the arch span of the basket-handle, the problem of the spatial stability of the arch becomes even more important. Among the infinite solutions, it has been proposed that the optimum solution is an arch as low as possible and that it maintains the aesthetic characteristics. That is to say that of all the possible basket-handle arches, it is the one in which the ratio between the radii (R/r) is the smallest. This study can serve as a basis for the design of basket-handle arches as structural elements maintaining their aesthetic function, which has been used uninterruptedly for centuries.

References

1. Kimball, F.; Edgell, G.H. *A History of Architecture*; Harper & Brothers: New York, NY, USA, 1918.
2. Cowan, H.J. A history of masonry and concrete domes in building construction. *Build. Environ.* **1977**, *12*, 1–24. [CrossRef]
3. DeLaine, J. Structural experimentation: The lintel arch, corbel and tie in western Roman architecture. *World Archaeol.* **1990**, *21*, 407–424. [CrossRef]
4. Joshi, A.M.; Deshmukh, A.M. Quality of space in Romanesque and Gothic Architecture. *Int. J. Eng. Res.* **2018**, *7*, 160–164. [CrossRef]

5. Lengyel, G. Minimum thickness of the gothic arch. *Arch. Appl. Mech.* **2018**, *88*, 769–788. [CrossRef]

6. Calvo-López, J. From Mediaeval Stonecutting to Projective Geometry. *Nexus Netw. J.* **2011**, *13*, 503–533. [CrossRef]

7. Campisi, T.; Saeli, M. Taking inspiration from nature: Rules and procedures for a good building practice. In *ARCHDESIGN'16-III International Architectural Design Conference on Design and Nature*; DAKAM Publishing: Istanbul, Turkey, 2016; pp. 4–17.

8. Ural, A.; Oruç, Ş.; Doğangün, A.; Tuluk, Ö.İ. Turkish historical arch bridges and their deteriorations and failures. *Eng. Fail. Anal.* **2008**, *15*, 43–53. [CrossRef]

9. Campisi, T.; Saeli, M. Structural Uses of Stone and Timber in The European Historical Construction. *J. World Archit.* **2018**, *2*, 1–11.

10. Saeli, M. Mixed Stone-timber Masonry in Traditional Construction: Structural, Architectural and Anti-seismic Features across Europe. *J. Archit. Res. Dev.* **2018**, *2*. [CrossRef]

11. Byne, A.; Byne, M.S. *Spanish Architecture of the Sixteenth Century: General View of the Plateresque and Herrera Styles*; No. 109; GP Putnam's Sons: New York, NY, USA, 1917.

12. Jennings, N. Converso Patronage, Self-Fashioning, and Late-Gothic Art and Architecture in 15th-Century Castile. In *Jews and Muslims Made Visible in Christian Iberia and Beyond, 14th to 18th Centuries*; Brill: Leiden, The Netherlands, 2019; pp. 161–186.

13. Rubiò Bellver, J. *Dificultats per Arribar a la Síntessis Arquitectònica*; Anuario de la Asociación de Arquitectos de Cataluña: Barcelona, Spain, 1913; pp. 63–79.

14. Heyman, J. Beauvais cathedral. *Trans. Newcom. Soc.* **1967**, *40*, 15–35. [CrossRef]

15. Huerta, S. Mecánica de las bóvedas de fábrica: El enfoque del equilibrio. *Inf. Construcción* **2005**, *56*, 73–89. [CrossRef]

16. Huerta Fernández, S. *Arcos, Bóvedas y Cúpulas. Geometría y Equilibrio en el Cálculo Tradicional de Estructuras de fábricaArcos, Bóvedas y Cúpulas. Geometría y Equilibrio en el Cálculo Tradicional de Estructuras de Fábrica*; Instituto Juan de Herrera: Madrid, Spain, 2004.

17. Moseley, H.L. On a new principle in statics, called the Principle of least Pressure. *Lond. Edinb. Dublin Philos. Mag. J. Sci.* **1833**, *3*, 285–288. [CrossRef]

18. Block, P.; DeJong, M.; Ochsendorf, J. As hangs the flexible line: Equilibrium of masonry arches. *Nexus Netw. J.* **2006**, *8*, 13–24. [CrossRef]

19. Ricci, E.; Fraddosio, A.; Piccioni, M.D.; Sacco, E. A new numerical approach for determining optimal thrust curves of masonry arches. *Eur. J. Mech. A/Solids* **2019**, *75*, 426–442. [CrossRef]

20. Alexakis, H.; Makris, N. Limit equilibrium analysis and the minimum thickness of circular masonry arches to withstand lateral inertial loading. *Arch. Appl. Mech.* **2014**, *84*, 757–772. [CrossRef]

21. Alexakis, H.; Makris, N. Limit equilibrium analysis of masonry arches. *Arch. Appl. Mech.* **2015**, *85*, 1363–1381. [CrossRef]

22. Tempesta, G.; Galassi, S. Safety evaluation of masonry arches. A numerical procedure based on the thrust line closest to the geometrical axis. *Int. J. Mech. Sci.* **2019**, *155*, 206–221. [CrossRef]

23. Velilla, C.; Alcayde, A.; San-Antonio-Gómez, C.; Montoya, F.G.; Zavala, I.; Manzano-Agugliaro, F. Rampant Arch and Its Optimum Geometrical Generation. *Symmetry* **2019**, *11*, 627. [CrossRef]

24. Milankovitch, M. Theorie der Druckkurven. *Z. Math. Phys.* **1907**, *55*, 1–27.

25. Heyman, J. The safety of masonry arches. *Int. J. Mech. Sci.* **1969**, *11*, 363–385. [CrossRef]

26. Alexakis, H.; Makris, N. Minimum thickness of elliptical masonry arches. *Acta Mech.* **2013**, *224*, 2977–2991. [CrossRef]

27. Boothby, T.E. Analysis of masonry arches and vaults. *Prog. Struct. Eng. Mater.* **2001**, *3*, 246–256. [CrossRef]

28. Gómez-Collado, M.C.; Roselló, V.C.; Tamborero, E.C. Mathematical modeling of oval arches. A study of the George V and Neuilly Bridges. *J. Cult. Herit.* **2018**, *32*, 144–155. [CrossRef]

29. Casado, E.A.; Sánchez, J.M.D. Geometría del arco carpanel. *Suma Rev. Sobre Enseñanza Aprendiz. Matemáticas* **2015**, *79*, 17–25.

30. San-Antonio-Gómez, C.; Velilla, C.; Manzano-Agugliaro, F. Photogrammetric techniques and surveying applied to historical map analysis. *Surv. Rev.* **2015**, *47*, 115–128. [CrossRef]

31. Al-Omari, A.; Beck, K.; Brunetaud, X.; Török, Á.; Al-Mukhtar, M. Critical degree of saturation: A control factor of freeze–thaw damage of porous limestones at Castle of Chambord, France. *Eng. Geol.* **2015**, *185*, 71–80. [CrossRef]

32. Janvier-Badosa, S.; Beck, K.; Brunetaud, X.; Al-Mukhtar, M. Historical study of Chambord castle: A basis for establishing the health record of the monument. *Int. J. Archit. Herit.* **2013**, *7*, 247–260. [CrossRef]
33. Janvier-Badosa, S.; Beck, K.; Brunetaud, X.; Al-Mukhtar, M. The occurrence of gypsum in the scaling of stones at the Castle of Chambord (France). *Environ. Earth Sci.* **2014**, *71*, 4751–4759. [CrossRef]
34. Al-Omari, A.; Brunetaud, X.; Beck, K.; Al-Mukhtar, M. Effect of thermal stress, condensation and freezing–thawing action on the degradation of stones on the Castle of Chambord, France. *Environ. Earth Sci.* **2014**, *71*, 3977–3989. [CrossRef]
35. Colding, T.H.; Minicozzi, W.P., II. Disks that are double spiral staircases. *Not. AMS* **2003**, *50*, 327–339.
36. Tanaka, H. Leonardo da Vinci, architect of Chambord? *Artibus Hist.* **1992**, *13*, 85–102. [CrossRef]
37. Dushkina, N. Russia: 20th-Century Heritage. Heritage at Risk. 2003, pp. 177–181. Available online: https://journals.ub.uni-heidelberg.de/index.php/heritage/article/download/21204/14973 (accessed on 14 August 2019).
38. Gerin, A. Stories from Mayakovskaya Metro Station: The Production/Consumption of Stalinist Monumental Space, 1938. Ph.D. Thesis, University of Leeds, Leeds, UK, 2000. Available online: http://etheses.whiterose.ac.uk/6749/1/424660.pdf (accessed on 14 August 2019).
39. Shilin, A.A.; Kirilenko, A.M.; Znajchenko, P.A. Complex reconstruction project of Mayakovskaya metro station in the centre of Moscow. In *Structural Analysis of Historical Constructions—Anamnesis, Diagnosis, Therapy, Controls*; Van Balen, K., Verstrynge, E., Eds.; Taylor & Francis Group: London, UK, 2016; pp. 1736–1741. ISBN 978-1-138-02951-4. Available online: http://znayugeo.ru/wp-content/uploads/2016/11/ch234.pdf (accessed on 14 August 2019).

Research Methodology: Application of Railway Luggage and Package Transportation Scheme Formulation Based on a Dynamic Time–Space Service Network

Kaige Niu [1], Jun Liu [2] and Ying Wang [2],*

[1] State Key Laboratory of Rail Traffic Control and Safety, Beijing Jiaotong University, Beijing 100044, China; 17120862@bjtu.edu.cn
[2] School of Traffic and Transportation, Beijing Jiaotong University, Beijing 100044, China; jliu@bjtu.edu.cn
* Correspondence: wangy@bjtu.edu.cn

Abstract: In the current market environment, the formulation of a railway luggage and package transport scheme (RLPTS) is often affected by the specific requirements of the transport organization, the complex composition of the transport service network, and the dynamic changes of transport demands, which make it very difficult. In this paper, a two-stage RLPTS formulation method is proposed that can meet not only transport demands with dynamic changes, but also the requirements of transport timeliness. It is used to solve the problem of current RLPTS formulation. First, a dynamic service network for railway luggage and package transport (RLPT) is constructed based on passenger train schedules, and based on this network, an improved A* algorithm is designed to generate feasible path sets for RLPT demand. Then, based on feasible path sets, a flow distribution model aiming at maximizing the total profit of transportation is established to solve the model in order to enable the flow allocated on the path. Finally, an example calculation shows that the method can implement the RLPTS formulation rapidly.

Keywords: railway luggage and package transport scheme formulation; transport timeliness; time–space service network; K shortest path; A* algorithm

---

1. Introduction

In recent years, with the development of China's e-commerce logistics, the improvement of the railway network, the speeding up of the railway, and the development of freight business, the proportion of express railway in China's capacity structure has increased, and railway capacity has become one of the future directions for express delivery. China Railway Express (CRE) has the largest railway transportation network in the world, but it has relied on enterprise customers, since for a long time there has been a lack of distribution teams at both ends of "door-to-station" and "station-to-door" in the individual consumption layout, which leads to poor timeliness of the whole "door-to-door" business. Timeliness is at the core of competitiveness for express businesses. Most logistics companies refer to timeliness as the core index to divide service levels into different groups of products. For example, S.F. Express has launched several products representing different service levels, such as arrive today, arrive next morning, standard express, and special express. We summarized S.F. Express's levels of express delivery services in 2018, as shown in Table 1 [1]. S.F. Express relies on highways to build medium- and long-distance transportation services. Although its urban distribution service network is considered ideal, its speed is much slower than railway transportation, and it also faces high-cost pressure to maintain air transportation. The two companies recently established CR-SF International Express Co. Ltd (Shenzhen, China) to provide customers with safe, convenient, and efficient pickup

and delivery services. To a certain extent, this amalgamation makes up for the poor timeliness of railway logistics door-to-door business distribution at both ends, but the commitment to creating door-to-door product cooperation still requires seamless connection at both ends of the distribution service. At present, this is a very common mode of transport, but what restricts its development is the formulation of railway luggage and package transport schemes (RLPTSs) from station to station. Therefore, this paper will focus on RLPTS formulation.

Table 1. Levels of service and related indices of S.F. Express in 2018.

Company	Indices		
	Service Levels	**Delivery Time**	**Charges**
S.F. Express	Arrive today	Before 22:00 today	140 yuan **
	Arrive next morning	Before 10:30 next day	25 yuan*, 14 yuan/kg ***
	Standard express	1–2 days after receipt	23 yuan*, 14 yuan/kg ***
	Special express	2–3 days after receipt	18 yuan*, 4 yuan/kg ***

Notes: *, **, *** represent prices for first 1000 g weight, first 500 g weight, and continued weight.

RLPT, taking the baggage cars of passenger trains as carriers, mainly transports small goods at high speed. RLPT organizations are based on RLPTS. After the passenger train operation plan and baggage car hooking plan have been set, RLPTS provides the routes for all luggage and package flow and transfer plans for part of the luggage and package flow. The essence of RLPTS is to match the luggage and package flow with the transport capacity in either the flow volume or direction. However, the theory and method of making RLPTS still have room for improvement.

The issue of implementing RLPTS has been a concern in the research literature for the past few years, and some researchers tried to apply the network flow method to solve the relevant problem [2–4]. One study [2] depicts the RLPT network as a time-varying network and divides the luggage and package routing problem into the shortest path problem of a single origin–destination (OD) without any capacity constraint and multi-commodity flow problem. Another study [3] states that the difficulty of implementing a luggage and package shipping plan is a K-shortest problem, and according to the characteristics of this problem, it needs to establish a complete transfer network, which considers the transfer time, cost, and degree. Thus, an optimized mathematical programming model with the lowest generalized transport cost can be established. A service network dynamic model for this problem is established in Ref. [4], adopting a heuristic approach based on linear programming relaxation, which takes the upper and lower bounds through column generation and rounding to find the best feasible solution.

Though these studies contribute a lot to the problem of making RLPTS, they still cannot solve it perfectly. The routing problem of luggage and packages is discussed in Ref. [2] by ignoring the flow distribution issue with capacity constraint. It is hard to solve using the transfer network completely, as proposed in Ref. [3], which has a problem on large-scale networks. A valuable method to resolve this problem is proposed in Ref. [4], but it does not consider the loading and unloading capacity constraint of stations, which is important to ensure the usability of the results.

Since goods have both time and space information in the whole transportation process, we intend to construct a dynamic time–space service network to study the timeliness of transporting goods. Compared with the traditional static physical network, the advantages of a dynamic time–space network include the ability to represent the transportation state that changes with time, better simulation of the complex time constraints in the station-to-station transportation process, and accurate characterization of the timeliness in the process of transporting goods. The construction method of a dynamic time–space service network is described in detail in Section 3.1.1. Based on the theory and method of service networks, we studied the factors that affect RLPT optimization and established an optimization model with maximum transportation revenue to solve the problem of implementing RLPTS.

The remaining parts of the paper are as follows: Section 2 presents a review of previous studies and analyzes the shortage of studies on this topic. In Section 3, the solution of RLPTS is introduced in two parts. First, a K shortest path search algorithm based on an improved A* algorithm under a dynamic time–space service network is proposed. Then the flow distribution model is constructed on the basis of feasible path sets. Sections 4 and 5 present a numerical example and conclusion, respectively.

2. Literature Review

The essence of the problem of RLPTS formulation is how to choose the right path to meet demand, and its core is how to allocate traffic volume to passenger trains with cargo trailers. Traffic volume distribution refers to the process of reasonably allocating OD flow to the transportation network according to certain objectives. The traffic volume distribution results are the traffic volumes allocated by each road section. The traffic assignment problem based on system optimization is generally a nondeterministic polynomial problem in combinatorial optimization. It cannot calculate or search for the correct results directly in a timely manner. Usually, it needs to simplify the model or use a heuristic algorithm to solve it.

At present, there is little research on the formulation method of RLPTS, and the relevant literature usually only considers the transport time of station-to-station, and the transportation scheme cannot reflect the personal requirements of customers. The current formulation methods of RLPTS can be roughly divided into two types: The first type [5–35] is to build a flow distribution model with capacity constraints on the transport service network and solve the model by designing relevant algorithms. The model established by this method can accurately describe the problem of transportation scheme formulation, but the model is generally difficult to solve, and the optimal solution cannot be obtained in a timely manner when the scale is large. In the second type [36–48], under the conditions of not considering transport timeliness and capacity constraints, all the paths set between package business stations are first calculated, and then the flow distribution model is established based on the feasible path set to solve the problem. The model established by this method is easy to solve, but the description of the problem is not accurate enough, and many unreasonable paths are obtained, which increase the difficulty of flow distribution. At the same time, the transport capacity constraint is not considered sufficiently in the flow distribution, and the result has low accuracy, thus the obtained transport scheme can only be used as a reference.

In addition, with the rapid growth of domestic transportation demand for small-batch, multi-batch, and high-value-added small-piece goods, customers' demands with different characteristics of RLPT will change dynamically. Existing studies on RLPTS formulation methods are mostly because the demand is fixed over a long period of time, and the corresponding transportation scheme is also fixed. When the demand starts to change, it is impossible to formulate a transportation scheme within a short period of time, so customers cannot be promised transport timeliness.

Railway luggage and packages are carried by luggage vehicles, which are mounted behind passenger trains. The passenger train schedule is fixed in a certain period of time. It can be understood that the possible transportation path of the luggage is also fixed in a certain period of time. Based on this, we divide the solution of the problem into two stages and design a two-stage RLPTS formulation method. First, a dynamic time–space service network of RLPT is constructed based on passenger train schedules, station sets, transfer station sets, and demand information. Considering the basic principles of RLPT organization and the relevant constraints, the path search algorithm is designed to calculate OD path sets that conform to station-to-station transportation timeliness. Then, based on the path sets, the flow distribution model is established by taking into full consideration the path transport capacity constraints and the RLPT demands with different aging requirements, aiming to maximize the total transport profit and solve the model to generate the RLPTS.

The innovative points of this paper are as follows:

- Based on passenger schedules and demand information, we include the station-to-station transportation process in the research scope and construct a dynamic time–space service network of RLPT.

- The initial constructed time–space network is processed into a closed time–space network at both ends, and the improved A* algorithm adapted to the network is adopted to generate feasible path sets for all transportation demands. It is suitable for solving large-scale network problems.

- Considering the relevant important constraints, a flow distribution model is constructed. Feasible path search and traffic allocation are part of the important components in the two-stage method. The advantages of the two-stage method include the following: Based on the static timetable of passenger trains in a certain period of time, different timeliness paths can be found. Once the demand changes, only one-time traffic volume can be reallocated through the model to compile the RLPTS in a short period of time. Therefore, the two-stage solution method can not only guarantee the transportation timeliness of demand, but also meet the traffic volume transportation demand and greatly reduce the difficulty when solving the problem and improve the solving efficiency.

Based on the above analysis, we take transportation timeliness as the core and design an effective and feasible path search algorithm based on the dynamic time–space service network of RLPT. Finally, the optimization method of transportation schemes is studied on the basis of the set of feasible paths.

3. Methods

3.1. Feasible Path Search Algorithm Based on Dynamic Time–Space Service Network

3.1.1. Construction of Dynamic Time–Space Service Network

A transportation service network is designed to determine the transportation service set with the minimum cost or maximum profit under existing transportation resources and limited conditions, and at the same time to meet the transportation requirements of customers [20]. For station-to-station RLPT, the transport process between two points can be regarded as a kind of transportation service provided by cars. When we abstract this kind of service into an arc, we can use the dynamic service network to study the optimization of RLPTS. The dynamic time–space service network can flexibly represent the varying transport time and accurately reflect the time–space correlation.

This paper refers to the RLPT service network in the literature [36–49]. As shown in Figure 1, for the vertical axis, S_1 to S_7 are RLPT handling stations. The horizontal axis represents time. The nodes in each row represent the same station at different times, and the nodes in each column represent different stations at the same time. When a car provides RLPT services, a series of arcs will be generated on the network. Figure 1 is a simple RLPT service network with two trains. The solid line is a train running arc (TRA), which represents the operation of passenger trains between RLPT handling stations. There are two types of horizontal dotted lines connected with nodes of the same RLPT handling station. The dotted line connecting the same trains from head to tail is a delayed arc (DA), which means that packages stay at the station waiting to be delivered. The dotted line connecting different trains from head to tail is a transit arc (TA), which means that packages are transferred from one train to another at the station. The main field definitions and data types of time–space nodes and arcs in the whole algorithm are shown in Tables 2 and 3, and their ID indices start from 0. The indices of different time–space arcs are shown in Table 4.

Table 2. Field definitions of time–space network nodes.

Field	Definition	Data Type
node_id	ID index of time–space network node	Int
train_code	Train code on which node is located	String
station	Station corresponding to time–space node	Station class with attributes
time	Time corresponding to time–space node	Double

Table 3. Field definitions of time–space network arcs.

Field	Definition	Data Type
arc_id	ID index of time–space arc	Int
type	Type of time–space arc	Int
train_code	Train code on which time–space arc is located	String
start_node	Head node of time–space arc	Node with attributes
end_node	Tail node of time–space arc	Node with attributes
weight	Time difference between nodes at both ends of arc	Double

Table 4. Type index of different time–space arcs.

Time–space Arc	Type Index
TRA	0
DA	1
TA	2

Unlike the station-to-station transport process, when the two parts of door-to-station and station-to-door are included in the research scope, the constraints of transportation organization time and connection time need to be considered. When goods arrive at the sending or terminal station, the loading and unloading should be organized uniformly for a certain period of time, and the train's stopping time should meet the loading and unloading operation time requirements of the goods. As shown in Figure 1, two trains can reach station S_6 close to destination D, but train 2's departure time is too early, so the goods can only be sent to station S_1 at first, and then transported by train 1. In the process of transportation, the goods can be transferred to train 2 and transported to destination D within time periods T_4 to T_7. Through a combination of a series of service arcs in the network, the process of RLPT is described, which can not only simulate the complex time constraints in the process of RLPT and properly calculate the K shortest path of OD, but also ensure timeliness in the process of transportation.
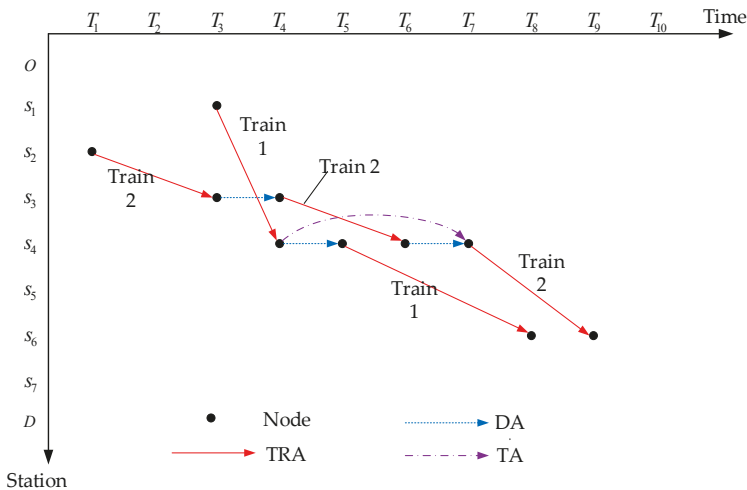

Figure 1. Dynamic time–space service network for RLPT. TRA, train running arc; DA, delayed arc; TA, transit arc.

3.1.2. Principles and Restrictions of Path Search

For an OD pair with a given transport demand, the search for an RLPT path needs to satisfy the following restrictions following the organizational principles of RLPT, such as direct departure, reasonable division of transportation between long and short distances, and regional distribution:

1. Time limit of loading and unloading operations. The loading and unloading of goods must be completed before the departure of the train; otherwise, the goods will not be able to undergo loading and unloading at the station.
2. Minimum transit operating time limit. At the transfer station, the time interval between the arrival of the previous train and the departure of the next train is the transfer connection time. If the transfer connection time does not meet the limit of the shortest transfer operation time, the goods will not be able to undergo transit operation at the station.
3. Limited number of transits. Each transit of goods will be accompanied by a loading and unloading operation, which not only consumes a lot of transportation resources, but also increases the uncertainty and reduces the safety of the transportation process. Therefore, it is stipulated that the maximum number of transits should be two, and any path with more than two transit times will be ignored.
4. Transport timeliness constraint. The transportation time of the searched feasible path should not be too long, and the path should be guaranteed to meet the timeliness requirements of the cargo owner.

3.1.3. Preprocessing of Dynamic Time–Space Service Network before Path Search

In the dynamic service network, there are many feasible paths between the start node and the end node of RLPT demand. The problem of the RLPT path is the problem of searching multiple feasible paths with greater timeliness and satisfying existing restrictions on the dynamic service network, which is essentially the K shortest path problem in the shortest paths. The dynamic time–space service network constructed by the method described in Section 3.1.1 has multiple start and end nodes. However, in graph theory, the path search can only be carried out in a graph with unique start and end nodes. If we search directly on the dynamic service network, we need to consider combinations of different start and end nodes, which will increase the complexity of the search process. A comparison between the initially constructed and processed dynamic time–space networks is shown in Figure 2. Figure 2a contains 11 network nodes, where a_1, a_2, a_3 and b_1, b_2, b_3 represent stations a and b, respectively, at different times. When calculating the path of freight flow from station a to station b, considering the time attributes of stations, there will be three start nodes and three end nodes in the network. The existing path search algorithms are not applicable to this network. As shown in Figure 2b, this problem can be solved by creating a virtual start arc (VSA) and virtual end arc (VEA) at both ends, with a unique virtual start node (VSN) and virtual end node (VEN). The dotted lines are virtual arcs at both ends, so that the whole network is a closed network with unique VSN and VEN. The specific operation methods are as follows: In the initial network, VSN o' and VEN d' with unique attribute identification are created. Since it is impossible to obtain the time when goods are delivered to the sending station, the time attribute of both can be set to 0. The attribute values of VSN and VSN are shown in Table 5. We need to screen the network nodes that correspond to the sending station and consider the TRA that is passing through the particular station. If the train departure time corresponding to the node is later than the arrival time of the goods and the stop time of the train meets the loading operation time of the goods, then the node is connected with VSN o' to form a VSA. Similarly, the VEA connected with VEN d' can be constructed. The properties of virtual arcs at both ends are shown in Table 6. In path search, starting from o' and ending from d', we can search feasible paths for demand in dynamic time–space service networks with only start and end nodes. We set the arc weight of both virtual arcs to 0.
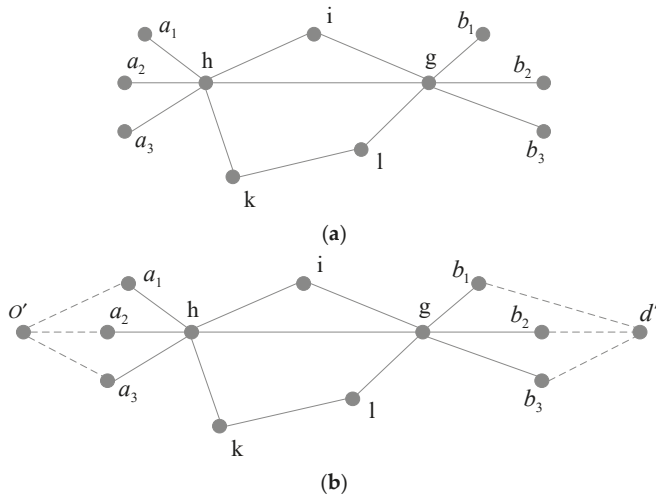
Figure 2. Comparison between (**a**) initially constructed dynamic time–space network and (**b**) dynamic time–space service network with virtual arcs at both ends.

Table 5. Attribute values for virtual start node (VSN) and virtual end node (VEN).

Virtual Node	Node_Id	Train_Code	Station	Time
VSN	N (total number of network nodes) + 1	"0000"	VirtualStartStation	0
VEN	N (total number of network nodes) + 2	"0000"	VirtualEndStation	0

Table 6. Attribute values of virtual start arc (VSA) and virtual end arc (VEA).

Virtual Arc	Arc_Id	Type	Train_Code	Start_Node	End_Node	Weight
VSA	−1	3	"0000"	SN	a_1 or a_2 or a_3	0
VEA	−2	3	"0000"	b_1 or b_2 or b_3	VEN	0

3.1.4. Feasible Path Set Generation Based on Improved A* Algorithm

According to the structure of the dynamic time–space service network and the specific requirements of RLPT organizations, we can solve the K shortest path problem of RLPT by improving the A* algorithm. The existing K shortest path solving methods include double-sweep, A* algorithm, and deviation path algorithm [50,51]. The double-sweep algorithm has advantages in solving the path. However, obtaining path data requires reverse search, which is complex and difficult to understand [52]. In addition, compared with the double-sweep algorithm, the A* algorithm is easier to operate and has higher solution efficiency [53–55]. Therefore, the A* algorithm is used to solve the K shortest path in this study. The evaluation function of the A* algorithm is $f(n) = g(n) + h(n)$, where $g(n)$ is the actual cost from the initial node to the network node n in the state space, and $h(n)$ is the estimated cost of the optimal path from network node n to target node. The values of $g(n)$ and $h(n)$ will change with the change of A* algorithm execution time, but the shortest distance between two nodes is fixed and invariant, reflecting the property of local symmetry. The flowchart of the path search algorithm is shown in Figure 3, and the specific solving steps are as follows:
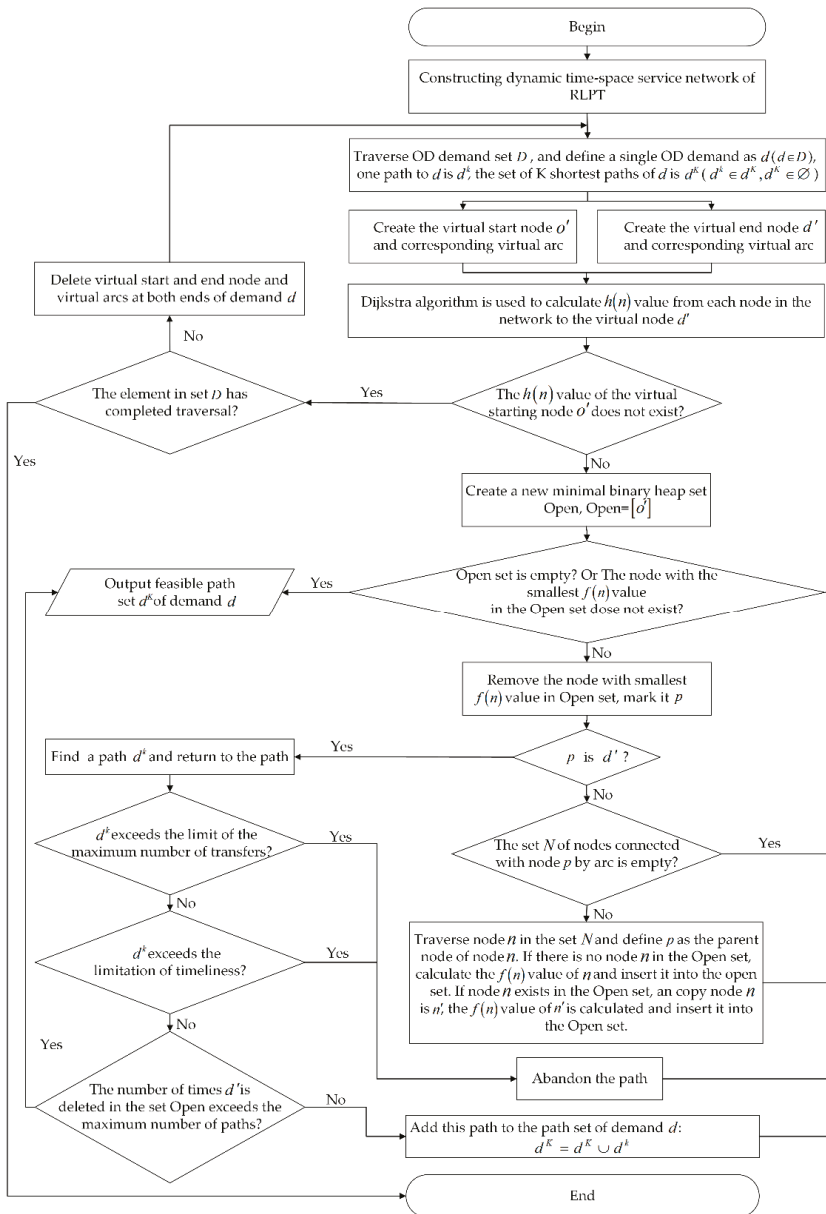
Figure 3. Flowchart of K shortest path search algorithm under dynamic time–space service network based on A* algorithm.

Step 1: Obtain basic dictionaries, such as passenger train schedule, station information, train information, demand set D, etc. Determine the basic parameters, such as minimum loading and unloading operation time and minimum transit operation time of each RLPT handling station, and maximum transit number of paths. According to the basic dictionary and basic parameters, construct the dynamic time–space service network of RLPT.

Step 2: Traverse OD demand set D, and define a single OD demand as $d(d \in D)$; one path to d is d^k, and the set of K shortest paths of d is $d^K (d^k \in d^K, d^K \in \varnothing)$.

Step 3: Determine whether the element in set D has completed traversal. If the set traversal is complete, go to Step 13. Otherwise, according to the origin and destination information of demand d, create VSN o' and VEN d', then construct the virtual arcs at both ends based on the loading and unloading operation time requirements of each station and demand information to complete the network preprocessing of path search of demand d.

Step 4: Reverse arcs in service networks, take d' as the source node, use the Dijkstra algorithm to solve the shortest distance from d' to all nodes, that is, to find the $h(n)$ value of all nodes.

Step 5: Judge whether or not the $h(n)$ value of o' exists. If it does not exist, go to Step 2. Otherwise, go to Step 6.

Step 6: Create new minimum binary heap set Open (nodes in Open set are sorted by $f(n)$ value), insert o' into the Open set. The node in Open is the node through which the shortest path may pass.

Step 7: Determine whether the Open set is empty or the $h(n)$ value of the team head node of the Open set does not exist. If yes, output the feasible path set d^K of demand d, go to Step 2. Otherwise, go to Step 8.

Step 8: Delete the node with the smallest $f(n)$ value in the Open set and mark it p. Determine if p is d'. If yes, find a path d^k of demand d, return to the path, and go to Step 9. Otherwise, judge whether set N of nodes connected with node p by arc is empty. If yes, go to Step 7; otherwise, go to Step 12.

Step 9: Determine if d^k exceeds the limitation of maximum transfer times. If yes, abandon d^k and go to Step 7; otherwise, go to Step 10.

Step 10: Judge whether d^k exceeds the limitation of timeliness. If yes, abandon d^k and go to Step 7; otherwise, go to Step 11.

Step 11: Determine whether the number of d' deleted in the set Open exceeds the maximum number of paths. If yes, output the feasible path set d^K of demand d, and go to Step 2. Otherwise, $d^K = d^K \cup d^k$ and go to Step 7.

Step 12: Traverse node n in set N and define p as the parent node of node n. If there is no node n in the Open set, calculate the $f(n)$ value of n and insert it into the Open set. If node n exists in the Open set and copy node n is n', calculate the $f(n)$ value of n' and insert it into the Open set. Go to Step 7.

Step 13: When the traversal of demand set D is completed, feasible paths of all demands have been found and the algorithm ends.

Through the path search algorithm mentioned above, the path set of all demands can be generated. Our proposed RLPTS formulation model is based on the feasible path set of demand, avoiding the allocation of goods flow on the infeasible path. The model aims to maximize the revenue of transportation enterprises and concentrates on the situation where the transportation demand cannot be satisfied due to the limited path capacity and insufficient luggage vehicle capacity. By solving the model, the flow allocated on each path can be obtained.

3.2. Flow Distribution Model Based on Feasible Path

3.2.1. Assumptions and Parameter Descriptions

Specifically, the decision variables are set up to provide convenience in obtaining the distribution scheme of cargo flows. The decision variables count the transport volume of goods assigned to each path. In this manner, the distribution scheme of cargo flows is obtained.

Without the loss of generality, this study further makes the following assumptions:

1. Theoretically, the loading capacity of the train is limited by its own capacity, volume, and weight of goods. To simplify the solution, only the effect of weight on the train's loading capacity is considered in the model.
2. Without considering the restriction of mixed cargo loading, we studied the formulation of RLPTS from the perspective of system optimization.

3.   Assuming that RLPT handling station has no limitation on capacity, it can meet the requirements of large quantities of stacked goods.

Regardless of the specific composition of each demand, we consider demand as objects that can be split arbitrarily by weight and transported by multiple transportation paths.

The parameter and decision variable definitions of the model are as follows:

Parameter	Description
D	OD set of cargo flows, $d \in D$
A	Set of service arcs, $a \in A$
d^k	kth ($k = 1, 2, \ldots$) path of demand d
d^K	Set of K shortest paths of demand d, $d^k \in d^K$
ω_{d^k}	Cost of demand d transported by path d^k, yuan/kg
x_d	Demand d for volume be transported through path d^k
r_d	Freight of demand d, yuan/t
x_{d^k}	Demand d for volume to be transported through path d^k
τ	Cost per kilogram of cargo loaded and unloaded, yuan/kg
ρ	Penalty charges for unmet demands, yuan/kg
$\gamma_a^{d^k}$	If arc a is selected by path d^k, the value is 1; otherwise, 0
c_a	Transportation capacity of arc a
c_{d^k}	Transportation capacity of path d^k

3.2.2. Objection Function

The model focuses on the objective function of maximum total profit of the transportation enterprise in order to meet customers' demand to the greatest extent. Total profit is the difference between total revenue and total cost. Total revenue comes from completing the transport of goods. Total cost mainly includes transportation and time costs. The time cost of goods describes the timeliness of door-to-door transport. The lower the timeliness, the higher the time cost. Therefore, a model with maximum total profit can ensure priority distribution of goods to the path with high timeliness and ensure the timeliness of door-to-door transportation. The model objective function is as follows:

$$Max\ z\ = \sum_{d \in D} \sum_{d^k \in d^K} \left[x_{d^k} \cdot \left(r_d - \omega_{d^k} - 2\tau \right) \right] - \sum_{d \in D} \left(x_d - \sum_{d^k \in d^K} x_{d^k} \right) \cdot \rho \tag{1}$$

3.2.3. Constraint Conditions

RLPTS is mainly influenced by railway passenger train transport schemes. It is also affected by the total demand of luggage and packages, the loading capacity of luggage vehicles, and the transport capacity of the path. The specific constraints are as follows:

The transport capacity of each path in the RLPT service network is limited, and the demand may require multiple paths to transport. Moreover, due to capacity constraints, some of the demand may not be transported. Therefore, the flow volume of demand to be transported is less than or equal to the total demand:

$$\sum_{d^k \in d^K} x_{d^k} \le x_d \ \ \forall d \in D, d^k \in d^K \tag{2}$$

The maximum loading capacity of a train is the sum of the loading capacity of all luggage and package vehicles on the train. Because the train can be loaded and unloaded at each stop station, it can carry goods in different sections. Therefore, the total demand for goods transported in the same

section should not exceed the maximum loading capacity of the vehicle. That is to say, any TRA in the service network must comply with the following formula:

$$\sum_{d \in D} \sum_{d^k \in d^K} \left(x_{d^k} \cdot \gamma_a^{d^k} \right) \le c_a \quad \forall a \in A \tag{3}$$

The meaning of the decision variable is the traffic volume allocated to each path, with the minimum being 0 and the maximum not exceeding the transport capacity of the path, namely,

$$0 \le x_{d^k} \le c_{d^k} \quad \forall d \in D, d^k \in d^K \tag{4}$$

3.2.4. Evaluation Indices

The result of traffic volume allocation is the traffic volume allocated on each feasible path and can be evaluated by the following indicators:

- Average transit times (ATT)

In this paper, the average transit time of demand is used to describe the transit times of a demand. If demand d is transported by n feasible paths, the completed traffic volume is d_{total} ($d_{total} \le x_d$), the traffic volume on each path is $d_1, d_2, d_3, \ldots, d_n$, and the transit time of each path is $m_1, m_2, m_3, \ldots, m_n$. The ATT $d_{average}$ of demand d is

$$d_{average} = \sum_{i=1}^{n} m_i \frac{d_i}{d_{total}} \tag{5}$$

If the RLPT service network completes the transportation of n demand, the ATT $D_{average}$ of all demands in the transportation is

$$D_{average} = \sum_{i=1}^{n} \frac{d_{average}^n}{n} \tag{6}$$

The closer ATT is to 0, the more the goods tend to be transported by direct mode, which indicates that the flow distribution is better.

- Train capacity utilization ratio (TCUR)

The TCUR reflects the utilization situation of passenger train luggage vehicle capacity. Using statistics of the utilization ratio of train capacity is beneficial to analyze the bottleneck of restricting RLPT. Supposing the train passes through sections $s_1, s_2, s_3, \ldots, s_n$ in sequence, the distance of each section is $l_1, l_2, l_3, \ldots, l_n$, the goods loaded on each section is $k_1, k_2, k_3, \ldots, k_n$, and the carrying capacity of the train is c_{train}, then the formula for calculating the TCUR is as follows:

$$u_{train} = \sum_{j=1}^{n} \frac{l_j \cdot k_j}{c_{train} \cdot \sum\limits_{i=1}^{n} l_i} \tag{7}$$

- Transfer volume of transfer station

The daily transit volume completed by the transit station reflects the daily transit operation of the station. Assume that the paths pass through transfer station T with $\lambda^1, \lambda^2, \lambda^3, \ldots, \lambda^n$, the traffic volume on each path is $\lambda_1, \lambda_2, \lambda_3, \ldots, \lambda_n$. Then the transfer volume T_λ of transfer station T is

$$T_\lambda = \sum_{i=1}^{n} \lambda_i \tag{8}$$

If the result produced by flow distribution is more in line with the actual transfer volume undertaken by the transfer station, it indicates that the flow distribution is working well.

4. Empirical Studies

Visual Studio 2019 software (C#) was used to design the search path algorithm and Cplex solver (C# programming language) was used to solve the flow distribution model. It is a linear programming model that is efficient for use in a dynamic time–space service network of any size. Concretely, the traffic assignment of cargo flows is a combinatorial optimization problem. Given that the problem includes trains and demand, its scale is related to the quantity of demand (denoted by d), the number of trains (denoted by t), and the maximum value of k. The problem has in general (d^k) variables and ($d + t + d^k$) constraints, and the global optimal solution was obtained within 180 min in this study (path search took 165 min and model solving took 15 min).

4.1. Related Parameter Values

The model and algorithm were verified with the actual operation data of RLPT and the train schedule was provided by CRE in March 2018. There are 12,471 daily OD demands, 415 RLPT handling stations, and 130 transfer stations, while 1880 passenger trains are equipped with luggage wagons. Based on train schedules and station information, a dynamic time–space service network of RLPT with 44,122 time–space nodes and 399,548 time–space arcs was constructed.

4.1.1. Parameter Values in Path Search Algorithm

The actual operation data of CRE in 2018 were used to set various parameters in the algorithm. Assuming that loading and unloading conditions at each station are the same, minimum loading and unloading operation time is 2 min, minimum transit operation time is 5 h, and loading and unloading capacity and transit capacity of goods are both 300 kg/min. One luggage vehicle is arranged in each passenger train group. The carrying capacity of the vehicle is 12 t which considers that small goods will be tossed around lightly. Path search is carried out based on train running time as weight, in order to limit the search breadth and depth of the algorithm; it is necessary to find up to 10 feasible paths for each demand, and each path has a maximum of two transfers.

4.1.2. Freight Rates and Costs in the Model

1. Transport price r_d for every OD

According to the actual operation data of CRE in 2018, the start station code, end station code, batch, number, weight, unit transport price, and time limit of different demands are shown in Table 7 (data on partial transportation demands).

Table 7. Start station code, end station code, batch, number, weight, time limit, and unit transport price (r_d) of different demands.

Start Station Code	End Station Code	Batch	Number	Weight (kg)	Unit Transport Price (kg/yuan)	Time Limit (day)
0902	0102	5	6	21	2.19	2
0904	1201	1	3	21	5.20	1
1203	3226	3	3	21	2.81	3
1001	3341	2	1	21	2.63	2
4719	3348	4	1	21	0.98	2
0901	9887	25	772	10,480	3.69	2
1201	9887	28	1588	18,699	1.57	2

2. Transport cost ω_{d^k} and loading or unloading operation cost τ of every path d^k

According to the Freight Rates Management Department of the China Railway General Corporation, the loading or unloading operation cost τ (yuan/kg) is 2, the transport cost ω_{d^k} of the path includes a locomotive traction fee ϕ_{d^k}, transfer operation fee ψ_{d^k}, and transportation time cost Ω_{d^k}, as follows:

- Locomotive traction fee ϕ_{d^k}

This is the cost incurred by the locomotive acting as the carrier of luggage for the traction train. The cost of locomotive traction for one kilometer per kilogram of luggage is called the unit locomotive traction fee, which is yuan/(kg*km). We define f_a as the unit locomotive traction fee when the locomotive acts as arc a, and if l_a is the distance of arc a, then the locomotive traction fee of path d^k can be expressed as

$$\phi_{d^k} = \sum_{a \in d^k} f_a \cdot l_a \tag{9}$$

- Transfer operation fee ψ_{d^k}

This is the cost incurred by the transfer operation. The transfer operation fee of demand is defined as the cost incurred by one transfer operation per kilogram of goods, in yuan/kg. The transit operation fee of path d^k is related to the number of transit operations and the unit transit operation fee of goods. We define μ and θ_{d^k} as the unit transit cost of goods and the number of transit times of route b, respectively. Then the transfer operation fee of path d^k can be expressed as

$$\psi_{d^k} = \mu \cdot \theta_{d^k} \tag{10}$$

- Transportation time cost Ω_{d^k}

Assuming that the transportation time of path d^k is T_{d^k}, we define V as the time cost calculation coefficient, in yuan/(min*kg). The transportation time cost Ω_{d^k} of path d^k is

$$\Omega_{d^k} = V \cdot T_{d^k} \tag{11}$$

Then the formula for calculating the cost of path d^k is as follows:

$$\omega_{d^k} = \phi_{d^k} + \psi_{d^k} + \Omega_{d^k} = \sum_{a \in d^k} f_a \cdot l_a + \mu \cdot \theta_{d^k} + V \cdot T_{d^k} \tag{12}$$

According to the actual operation data of CRE in 2018, the average locomotive traction fee f_a, the average unit transit cost μ, and the time cost calculation coefficient V were determined to be 0.05, 0.5, and 0.004, respectively.

3. Penalty charges ρ for unmet demands

Customers hope their goods will arrive at the station within the specified time range (time limit: T_{arrive}/min). When the transportation time (T_s/min) exceeds the expected arrival time, it can be considered that this OD demand has not been met, and the railway department must reduce the transportation cost to some extent. We define ξ_d and ρ as penalty coefficient of unit goods exceeding expected arrival time and penalty cost per unit goods (yuan/ton), respectively; then the required time penalty cost can be expressed as

$$\rho = \begin{cases} 0 & (T_s - T_{arrive}) \geq 0 \\ \xi_d |T_s - T_{arrive}| & (T_s - T_{arrive}) < 0 \end{cases} \tag{13}$$

Based on research of the penalty coefficient of RLPT by Zheng (2012), the average penalty coefficient ξ_d is determined to be 1.2.

4.2. Results and Discussion

Under the dynamic time–space service network, the total number of demand paths that can be solved by the A* algorithm is 117,227. The RLPTS of partial demands, transfer volume of transfer stations and train capacity utilization ratio are shown in Tables 8–10, respectively. (Tables 8–10 in the Supplementary Materials are the complete data calculated.)

Table 8. The RLPTS of partial demands.

Demand ID	Start Station Name	End Station Name	RLPTS
1	Changsha	Qiqihaer	(Changsha, 00T124A7,ShenyangBei)(ShenyangBei,0K1082A4,Qiqihaer *)
1	Changsha	Qiqihaer	(Changsha,00T124A8,ShenyangBei)(ShenyangBei,0K1082A4,Qiqihaer *)
1	Changsha	Qiqihaer	(Changsha,00T124A7,ShenyangBei)(ShenyangBei,0K1082A5,Qiqihaer *)
1	Changsha	Qiqihaer	(Changsha,00T124A8,Zhangchun *)(Zhangchun,0K1082A5,Qiqihaer *)
1	Changsha	Qiqihaer	(Changsha,000T14A5,ShenyangBei *)(ShenyangBei,0K1082A4,Qiqihaer *)
1	Changsha	Qiqihaer	(Changsha,00T254A0,Tianjin *)(Tianjin,0K1082A4,Qiqihaer *)
1	Changsha	Qiqihaer	(Changsha,000T14A5,ShenyangBei *)(ShenyangBei,0K1082A5,Qiqihaer *)
1	Changsha	Qiqihaer	(Changsha,00T254A0,Tianjin *)(Tianjin,0K1082A5,Qiqihaer *)
1	Changsha	Qiqihaer	(Changsha,000Z14A0,ShenyangBei *)(ShenyangBei,0K1082A4,Qiqihaer *)
1	Changsha	Qiqihaer	(Changsha,000Z14A0,ShenyangBei *)(ShenyangBei,0K1082A5,Qiqihaer *)
2	Botou	Qiqihaer	(Botou,0K1450A2,ShenyangBei)(ShenyangBei,00K546A3,Qiqihaer *)
2	Botou	Qiqihaer	(Botou,0K1450A1,Tianjin)(Tianjin,00K546A3,Qiqihaer *)
2	Botou	Qiqihaer	(Botou,00K956A2,Tianjin)(Tianjin,00K546A3,Qiqihaer *)
2	Botou	Qiqihaer	(Botou,001450A0,Tianjin)(Tianjin,00K546A3,Qiqihaer *)
2	Botou	Qiqihaer	(Botou,001450A0, Zhangchun)(Zhangchun,0K1082A4,Qiqihaer *)
2	Botou	Qiqihaer	(Botou,001450A0, Zhangchun)(Zhangchun,0K1082A5,Qiqihaer *)
2	Botou	Qiqihaer	(Botou,00K956A3,Tianjin)(Tianjin,0K1082A4,Qiqihaer *)
2	Botou	Qiqihaer	(Botou,0K1450A1,Tianjin)(Tianjin,0K1082A4,Qiqihaer *)
2	Botou	Qiqihaer	(Botou,00K956A2,Tianjin)(Tianjin,0K1082A5,Qiqihaer *)
2	Botou	Qiqihaer	(Botou,00K956A3,Tianjin)(Tianjin,0K1082A5,Qiqihaer *)

Notes: * represent that the station is departure station or end station of the train.

Table 9. Transfer volume of transfer stations.

Station Name	Transit Volume (kg)
Haerbinxi	860
Qiqihaer	3097
Zhangchun	28,214
Shenyangbei	20,662
Shenyang	14,015
Jilin	3424
Jinzhou	31,063
Beijingxi	1270
Beijing	6412
Tianjin	47,654
Shijiazhuang	23,874

Table 10. Train capacity utilization ratio.

Train Code	Utilization Rate (%)
0000K5A0	0.11
0000T1A0	0.01
0000T2A0	0.04
0000T7A0	0.03
0000T8A0	0.12
0000T9A2	0.05
0000Z1A0	0.04
0000Z2A0	0.27
0000Z3A0	0.66
0000Z3A1	0.53

The numbers of direct paths (DPs), one transit paths (OTPs), and two transit paths (TTPs) are shown in Figure 4.
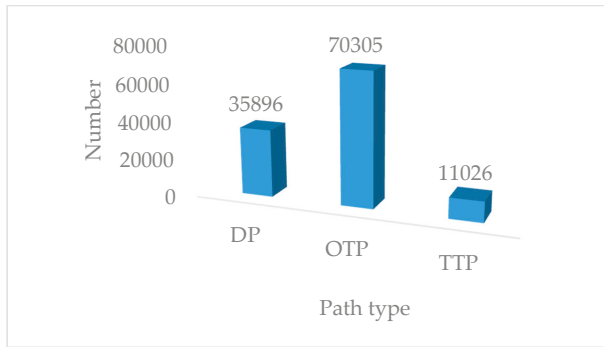
Figure 4. Numbers of different types of paths. DP, direct path; OTP, one transit path; TTP, two transit path.

The ATT calculated by the model is 0.608; the closer ATT is to 0, the more the goods tend to be transported by direct mode, indicating that the result of flow distribution is better. Compared with the values of 1.029 and 2 of Zu (2009) and Zheng (2012), it is greatly improved. The proportions of traffic volume through DP, OTP, and TTP are shown in Figure 5. It indicates that most of the demands can be completed through the generated DP and OTP, which realizes well the basic principles of RLPT organization with less transit as far as possible, and the validity of the model is proved.
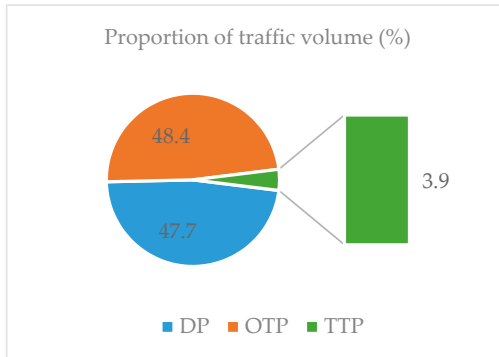
Figure 5. Proportion of traffic volume through different types of paths.

The results show that 97.6% of the transportation demand is completed, which can basically meet the current RLPT demand. Unshipped demand is concentrated in Xuzhou, Guiyang, Tianjin, Lanzhou, Beijing West, and other stations, mainly because the demand for transportation or transition at these stations is high, and the capacity of trains passing through the stations is insufficient, which is basically in line with the actual situation.

The transfer capacity of some transfer stations is shown in Figure 6. Zhengzhou, Xuzhou, Xi 'an, Wuchang, and other stations have undertaken a large number of transfer operations, which is due to an excessive number of transit trains passing through these stations.
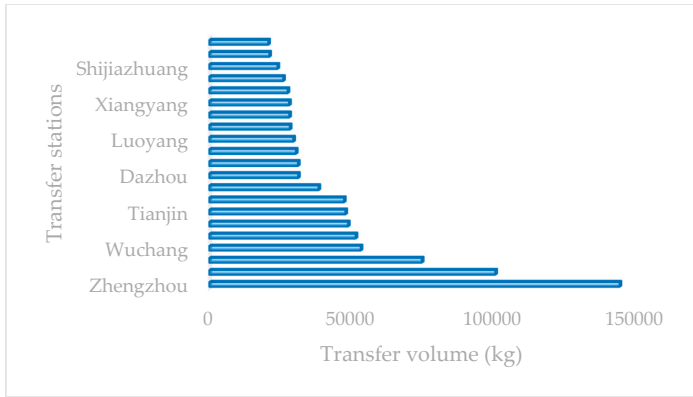
Figure 6. Transfer capacity of some transfer stations.

A total of 1880 trains is involved in RLPT, and the numbers of trains with different TCURs is shown in Figure 7. Overall, TCUR is still considered to be at a low level. It shows that the railway department has provided sufficient transport capacity for RLPT to meet the current market demand.
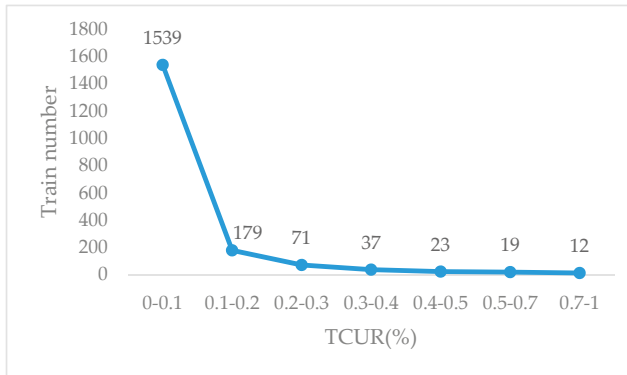
Figure 7. Numbers of trains with different train capacity utilization ratios (TCURs).

Take Harbin West–Shanghai, with a demand volume of 3409 kg, as an example to verify and illustrate the two-stage RLPTS formulation method proposed in this paper. Referring to the actual operation data of CR-SF, the average delivery time for S.F. Express in the same city is 2 h. Considering that the delivery time of goods to consignees should not be too late, it is stipulated that goods arriving after 21:00 will be postponed to the next day, and the delivery time will start at 08:00 every day. The flow distribution results are shown in Table 11. As can be seen, the timeliness of path 1 is the highest; in the case of meeting capacity, the flow distribution model considering time cost will give flow distribution priority to path 1 with higher timeliness, which can avoid flow allocation issues on the unfeasible path and verifies the validity of the model.

Table 11. Harbin West–Shanghai traffic volume distribution results.

Path	Sent Time	Train Code	Transfer Station	Arrival Time	Customer Receipt Time	Door-to-Door Timeliness	Volume (kg)
1	00:51	Z174	—	00:49 (2nd day)	14:49 (2nd day)	27 h, 58 min	3409
2	00:51	Z174 K292	Suzhou	05:34 (3rd day)	10:00 (3rd day)	47 h, 6 min	0
3	00:51	Z174 K378	Suzhou	05:24 (3rd day)	10:00 (3rd day)	47 h, 6 min	0

The timeliness comparison of paths calculated by the model and algorithm and related products of S.F. Express are shown in Figure 8. It can be seen that the transportation timeliness of path 1 undertaking flow is better than that of S.F. Express, which verifies the accuracy of the model and algorithm.
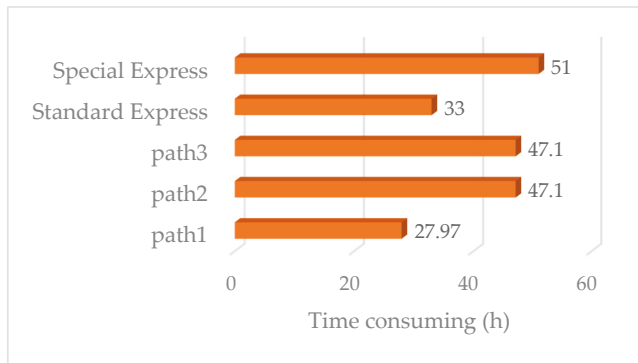
Figure 8. Timeliness comparison of paths calculated by model and algorithm and related products of S.F. Express.

4.3. Result Comparison

This paper further verifies the algorithm's superiority and takes the RLPTS of "Beijing–Guangzhou" as an example to compare the RLPTS generated here with the RLPTS currently used by CRE. The contrast of the two plans is shown in Table 12.

Table 12. Contrast of two RLPTS.

RLPTS in This Paper				RLPTS Currently Used			
Train Number	Transfer Station	Cost (yuan)	Time (min)	Train Number	Transfer Station	Cost (yuan)	Time (min)
Z12	–	3281.06	1313	T15	–	3210.06	1326
T12	–	2659.87	1320	T29	–	2541.27	1348
2251, K93	Chengde	2226.74	1724	T1, K93	Changsha	2353.09	1885
K48, Z12	Tianjin	977.46	1933	K17, T25	Zhengzhou	1401.73	2013

As seen by the contrast in Table 12, the RLPTS generated in this paper gives two through paths and two paths with one transfer. The transfer frequency of this plan equals that of the RLPTS currently used, but with less time consumption and lower general cost. Therefore, the RLPTS in this paper is feasible, and better than the RLPTS currently used from the perspective of time and cost.

5. Conclusions

In this paper, we analyzed the characteristics of RLPT demand and defined the guiding ideology of RLPTS formulation with timeliness as the core. Based on its characteristics, we gave a formulation idea of a two-stage method of RLPTS. That is, we decomposed the RLPTS formulation problem into

subproblems, one of which was the construction of a dynamic time–space service network based on passenger train schedules and demand information. Then, based on the time–space network, an improved A* algorithm was used to search feasible paths of RLPT. The other subproblem involved building a flow distribution model by considering the constraints of path capacity, capacity of luggage vehicles, and transport timeliness. The main innovation points of the algorithm and model proposed in this paper were as follows: (1) based on passenger schedules and demand information, we constructed a dynamic time–space service network of RLPT; (2) the initial constructed time–space network was processed into a closed time–space network at both ends, and the A* algorithm adapted to the network was adopted to generate a feasible path set of all transportation demands; and (3) considering the relevant important constraints, a flow distribution model was constructed. According to the solution results of the model, ATT, TCUR, and the transfer volume of transfer station were calculated. In the end, the RLPTS for all transportation demands was obtained, and the current resource utilization situation and development bottleneck of RLPT were analyzed.

The numerical studies demonstrated the following: (1) the ATT of feasible paths calculated by our proposed algorithm was close to 0, which is in line with the basic principle of minimizing transit for RLPT, that is, demand tends to be transported by direct paths; and (2) the RLPTS solved by the model can basically meet the current demand. In addition, it can be seen from the calculated TCUR and transit volume of transfer stations that the current RLPT capacity is larger than current demand for transportation, and some transfer stations have large cargo flow pressure, which can be improved through construction of related infrastructure.

Compared with the problems that exist in the current RLPTS formulation method, we demonstrated ways to resolve the issues with a two-stage method, which can reduce the difficulty of solving the problem and improve the efficiency of the scheme formulation. At the same time, the two-stage method can adapt to any dynamic changes in demand, ensure the timeliness of transportation, avoid the allocation of flow on unfeasible paths, and also consider the formulation of schemes from the perspective of global optimization, which is suitable for solving large-scale time–space network problems. Last but not least, the numerical studies demonstrate that this method can accomplish the entire road with the help of RLPTS within a short period of time and verifies the feasibility and effectiveness of the model and algorithm.

Although the model and algorithm proposed in this paper are highly efficient under certain assumptions, they do not consider the impact of the volume of goods, which to some extent leads to the limitation of problem solving. Future research will consider the volume and weight of cargo comprehensively and optimize the model and algorithm from the perspective of practical application.

Abbreviations

All abbreviations are listed as follows:

CRE	China Railway Express
RLPTS	railway luggage and package transport scheme
RLPT	railway luggage and package transportation
TRA	train running arc
DA	delay arc
TA	transit arc
VSN	virtual start node
VEN	virtual end node
VSA	virtual start arc
VEA	virtual end arc
ATT	average transit time
TCUR	train capacity utilization ratio

References

1. Armstrong & Associates, Inc. *Global and Regional Infrastructure, Logistics Costs, and Third-Party Logistics Market Trends and Analysis*; Armstrong & Associates, Inc.: Milwaukee, WI, USA, 2016.
2. Cao, L.H. Research on Package Pathway Selection Problem with Capacity Constrains in Time-Varying Network. Ph.D. Thesis, Beijing Jiaotong University, Beijing, China, 2007.
3. Li, X.-J. Research on Railway Package Transport Organization and Optimization. Ph.D. Thesis, Beijing Jiaotong University, Beijing, China, 2006.
4. Shen, R. Research on Service Network Design Theory and Method of Railway Package Transport. Ph.D. Thesis, Beijing Jiaotong University, Beijing, China, 2006.
5. He, Z.H. Thought on organization method of passenger package transportation of passenger dedicated lines. *Railw. Transp. Econ.* **2006**, *28*, 65–66.
6. Huang, Z. Research on the transport system of dedicated passenger transport lines. *Railw. Purch. Logist. J.* **2007**, *2*, 21–22.
7. Xu, C.C. Research on the application of railway luggage and package train. *J. Beijing Jiaotong Univ.* **2008**, *5*, 104–106.
8. Zu, Y.; Li, Y.Q. Research on the development of railway express freight transport. *China Storage Transp.* **2019**, *7*, 91–93.
9. Wang, G.D. Research on organization method and optimization of railway luggage and package transportation. *Technol. Enterp.* **2012**, *16*, 88.
10. Feng, S.R. Marketing strategy analysis of railway luggage and package transportation market. *Railw. Econ. Res.* **2015**, *5*, 39–41.
11. Chen, J.L. Reflections on the development of railway express service in China. *China Transp. Rev.* **2006**, *2*, 71–74.
12. Chen, J.L. Innovation of railway part load freight service system to meet market demand. *Railw. Freight Transp.* **2006**, *7*, 1–3.
13. Ji, C.X.; Liu, J. Research on Marketing Strategy of Railway Luggage and package transportation. *J. Beijing Jiaotong Univ.* **2000**, *24*, 100–105.
14. Li, H. A preliminary study on the development of railway express transportation market. *Railw. Transp. Econ.* **2006**, *28*, 46–47.
15. Yi, C.Z.; Zhong, Y. Problems in railway baggage transportation and promotion strageies. *J. Beijing Jiaotong Univ.* **2001**, *25*, 98–100.
16. Zhang, G.P. Marketing strategy of railway luggage and package express. *Transp. Econ.* **2005**, *27*, 66–68.
17. Huang, P.; Zhang, Z.Y. Research on model and algorithms of transportation network traffic allocation problem. *Chin. J. Manag. Sci.* **1999**, *7*, 48–54.
18. Yan, H.X.; Liang, D.; Zhang, T.W. Optimal model of railway network distribution. *J. Xinan Jiaotong Univ.* **2007**, *42*, 758–762.
19. Liu, C.; Lin, B.L.; Wang, J.X.; Liu, S.; Wu, J.; Li, J. Flow assignment model for quantitative analysis of diverting bulk freight from road to railway. *PLoS ONE* **2017**, *12*, e0182179. [CrossRef] [PubMed]

20. Wang, Y.; Liu, J. Study on the method of optimizing the schemes of railway luggage and package express special train. *J. Transp. Syst. Eng. Inf. Technol.* **2007**, *7*, 125–129.
21. Lin, B.L.; Wang, Z.M.; Ji, L.J.; Tian, Y.M.; Zhou, G.Q. Optimizing the freight train connection service network of a large-scale rail system. *Transp. Res. B Meth.* **2012**, *46*, 649–667. [CrossRef]
22. Zhu, E.; Cranic, T.G.; Gendreau, M. Scheduled Service Network Design for Freight Rail Transportation. *Oper. Res.* **2014**, *62*, 383–400. [CrossRef]
23. Newton, H.N.; Barnhart, C.; Vance, P.H. Constructing railroad blocking plans to minimize handling costs. *Transport. Sci.* **1998**, *32*, 330–345. [CrossRef]
24. Barnhart, C.; Jin, H.; Vance, P. Railroad blocking: A network design application. *Oper. Res.* **2000**, *48*, 603–614. [CrossRef]
25. Bai, R.; Wallace, S.W.; Li, J.; Chong, A.Y.L. Stochastic service network design with rerouting. *Transp. Res. B Meth.* **2014**, *60*, 50–65. [CrossRef]
26. Dong, X.Y.; Liu, J.; Ji, C.X. Design and research on network model of express freight transport based on multiple transport modes. *Logist. Technol.* **2006**, *10*, 36–39.
27. Ji, S.F.; Luo, R.J. A hybrid estimation of distribution algorithm for multi-objective multi-sourcing intermodal transportation network design problem considering carbon emissions. *Sustainability* **2017**, *9*, 1133.
28. Di, X.; Ma, R.; Liu, H.X.; Ban, X.G. A link-node reformulation of ridesharing user equilibrium with network design. *Transp. Res. B Meth.* **2018**, *112*, 230–255. [CrossRef]
29. Zu, Y.; Tian, N.; Yang, D.Y. Route algorithms for railway luggage and package transportation. *China Railw. Sci.* **2008**, *29*, 111–115.
30. Zu, Y.; Tian, N.; Yang, D.Y. Study on the programming model of railway luggage transportation. *J. China Railw. Soc.* **2009**, *31*, 20–24.
31. Chen, J.L. Study on compiling method of railway packaging and transportation schemes. *China Railw. Sci.* **2012**, *1*, 108–112.
32. Liu, J.T.; Zhou, X.S. Capacitated transit service network design with boundedly rational agents. *Transp. Res. B Meth.* **2016**, *93*, 225–250. [CrossRef]
33. Liu, Y.; Zu, X.N.; Yan, B.C. Optimization of high-speed railway luggage transportation scheme based on existing operating diagram. *J. Wuhan Univ. Technol. Transp. Sci. Eng.* **2016**, *40*, 1038–1042.
34. Liu, X.W. Study on Time Reliability of Railway Baggage Train. Master's Thesis, Xinan Jiaotong University, Chengdu, China, 2016.
35. Yang, J.H.; Liu, L.Z.; Li, X.J. Study on optimizing the fast transport of scattered goods by railway luggage trains. *J. Railw. Sci. Eng.* **2016**, *13*, 1426–1432.
36. Lin, B.L. A study of car-to-train assignment problem for rail express cargos on scheduled and unscheduled train service network. *arXiv* **2018**, arXiv:1803.05760v1. [CrossRef] [PubMed]
37. Lin, B.L.; Liu, C.; Wang, J.X.; Liu, S.Q.; Wu, J.P.; Li, J. Modeling the railway network design problem: A novel approach to considering carbon emissions reduction. *Transp. Res. Part D Transp. Environ.* **2017**, *56*, 95–109. [CrossRef]
38. European Commission. *Roadmap to a Single European Transport Area—Towards a Competitive and Resource Efficient Transport System*; White Paper; European Commission: Brussels, Belgium, 2011; pp. 1–31.
39. Liu, K. Research on the Planning and Design of Railway Express Service Network. Ph.D. Thesis, Lanzhou Jiaotong University, Lanzhou, China, 2014.
40. Deng, S.W. Research on High-Speed Rail Express Service Network Design. Ph.D. Thesis, Xinan Jiaotong University, Chengdu, China, 2016.
41. Oh, S.C. A multi-commodity, multi-modal network flow model for logistics management. *Transp. Res. Part A* **1996**, *1*, 64.
42. Haghani, A.; Oh, S.C. Formulation and solution of a multi-commodity, multi-modal network flow model for disaster relief operations. *Transp. Res. Part A Policy Pract.* **1996**, *30*, 231–250. [CrossRef]
43. Kuby, M.J.; Gray, R.G. The hub network design problem with stopovers and feeders: The case of Federal Express. *Transp. Res. Part A Policy Pract.* **1993**, *27*, 1–12. [CrossRef]
44. Barnhart, C.; Schneur, R.R. Air network design for express shipment service. *Oper. Res.* **1996**, *44*, 852–863. [CrossRef]
45. Kim, D.; Barnhart, C. Multimodal express shipment service design: Models and algorithms. *Comput. Ind. Eng.* **1997**, *33*, 685–688. [CrossRef]

46. Crainic, T.G. Service network design in freight transportation. *Eur. J. Oper. Res.* **2000**, *122*, 272–288. [CrossRef]

47. Le, B.A.; Crainic, T.G. A cooperative parallel meta-heuristic for the vehicle routing problem with time windows. *Comput. Oper. Res.* **2005**, *32*, 1685–1708.

48. Zäpfel, G.; Wasner, M. Operational Planning and Optimization of Hub-and Spoke Transportation Networks for Area Wide Groupage Services. *Models Methods Decis. Support Manag.* **2001**, *130*, 263–284.

49. Farvolden, J.M.; Powell, W.B. Subgradient methods for the service network design problem. *Transp. Sci.* **1994**, *28*, 256–272. [CrossRef]

50. Brander, A.W.; Sinclair, M.C. A comparative study of k-shortest path algorithms. *Perform. Eng. Comput. Telecommun. Syst.* **1996**, *6*, 370–379.

51. Hershberger, J.; Maxel, M.; Suri, S. Finding the k shortest simple paths: A new algorithm and its implementation. *ACM Trans. Algorithms (TALG)* **2007**, *3*, 45. [CrossRef]

52. Plotkin, D. Carrying freight on high-speed rail lines. *J. Transp. Eng.* **1997**, *123*, 199–201. [CrossRef]

53. Allman, W.P. Application series II an optimization approach to freight car allocation under time-mileage perdiem rental rates. *Manag. Sci.* **1972**, *18*, 567–574. [CrossRef]

54. Spieckermann, S.; Voß, S. A case study in empty railcar distribution. *Eur. J. Oper. Res.* **1995**, *87*, 586–598. [CrossRef]

55. Holmberg, K.; Joborn, M.; Lundgren, J.T. Improved empty freight car distribution. *Transp. Sci.* **1998**, *32*, 163–173. [CrossRef]

Rainfall Runoff Analysis and Sustainable Soil Bed Optimization Engineering Process: Application of an Advanced Decision-Making Technique

**Muhammad Hamza Hanif [1], Muhammad Adnan [1], Syyed Adnan Raheel Shah [1,*],
Nasir Mahmood Khan [2], Mehwish Nadeem [1], Jahanzeb Javed [1], Muhammad Waseem Akbar [1],
Ali Farooq [1] and Muhammad Waseem [3]**

[1]   Department of Civil Engineering, Pakistan Institute of Engineering & Technology, Multan 60000, Pakistan;
      engr.hamzahanif@gmail.com (M.H.H.); muhammadadnan@piet.edu.pk (M.A.);
      mehwishnadeem@piet.edu.pk (M.N.); engr.jahanzeb7665@gmail.com (J.J.);
      waseemakber84@gmail.com (M.W.A.); ali.farooq558@gmail.com (A.F.)
[2]   Pakistan Engineering Council, Ataturk Avenue (East), G-5/2, Islamabad 44000, Pakistan; kmnasir@pec.org.pk
[3]   Department of Environmental Chemistry, Bayreuth Centre for Ecology and Environmental Research,
      University of Bayreuth, 95440 Bayreuth, Germany; muhammad.waseem@uni-bayreuth.de
*   Correspondence: syyed.adnanraheelshah@uhasselt.be or Adnanshah@piet.edu.pk; Tel.: +92-300-791-4248

Abstract: Sustainable engineering practices always provide an opportunity for engineers to produce long-term solutions. In the fields of construction and irrigation, soil bed formation symmetry is very important, especially in the case of its behavior with reference to water runoff, whether natural or artificial. In this study, different soil bed formations were tested with the help of advanced hydrology apparatus under severe rainfall conditions. A major focus was to observe the water retention and volume discharge with reference to soil combinations and slope level change. Furthermore, an advanced decision-making technique incorporating artificial neural networks (ANNs) was used to predict and explore the interrelationship behavior of different parameters. It was observed that ST-1 (100% clay) performed well as it tried to retain a large quantity of water (7.28 L/min), making it suitable for irrigation, while ST-2 (100% sand) performed better for structures, as sand tries to quickly drain water, thus retaining less water (0.16 L/min). Change of slope was also another factor; at a 3% slope level along with 100% clay, water resistance was higher as compared to sand. Soil type-3 (ST-3) helped in the retention of water even at a 3% soil bed slope. This study will help engineers and designers in the optimization of soil bed formation for construction and irrigation purposes.

Keywords: Sustainability; Rainfall; Runoff; Soil; Advance Hydrology Apparatus; Symmetry

---

1. Introduction

A rainfall hydrological system is a significant apparatus used for the study of soil erosion, surface runoff, sediment transport, and infiltration, and it also permits generating the rainfall runoff process with replication under precise circumstances [1]. This hydrological apparatus simulates the rainfall generation at recognized intensity and soil depth in a precise way. During the development of structures, soil bed symmetry is very important, as behaviour changes with the abrupt change in formation of soil layers. Similarly, in the field of irrigation, soil bed performs with the transport of water, that effects the supply of proper water quantity to certain crops. Symmetry in soil combination helps in proper supply of water without wastage or absorption. In developing countries, where agriculture dominates the economy, an additional burden is exerted on land and water resources with the increase in population, leading to water utilization problems. Thus, under such multifaceted water resource conditions, these

kinds of field experiments are very beneficial. Using a rainfall simulator to determine rainfall runoff backup, the main goal is to match the runoff produced using the rainfall apparatus with natural storms [2]. Around the world, researchers focused on points regarding comparative results of surface fraction and subsurface runoff. There are two difficulties when linking runoff facilities from natural and virtual rainstorms; the first is scaling the results up from a minor simulator to a watershed/basin, and the second is regenerating the kinetic energy of a specific storm with the hydrologic apparatus. Duplicating the natural intensity of rainfall and rainfall duration with a simulator represents the finest method to regenerate the kinetic energy of natural storms. Thus, for this purpose, there is a need for previous hydrological data to select the necessary parameters of rainfall duration and intensity. Our main focus here is to discuss rainfall runoff with reference to soil bed variation, which plays an essential role in daily life and engineering design parameters. Different kinds of models, i.e., black box, physical-based, and ANNs (artificial neural networks), were used to model difficult hydrological operations, including rainfall runoff [3,4] and the precipitation–runoff relationship [5]. However, due to difficulties and spatiotemporal variation, some of the models can accurately determine these operations. In the last few years, a very popular model used to solve these complex nonlinear operations was the artificial neural networks (ANN). ANN models have the ability to explore different relationships such as the rainfall runoff process [2], precipitation totals, average runoff and temperature relationships [5], river flow and rainfall [6], humidity, wind, vorticity, air temperature, and precipitable water [7], streamflow forecasting [8], discharge and rainfall [9], catchment area and precipitation [10], peak discharge and rainfall pattern [11], runoff and rainfall [12], precipitation, air temperature, snowmelt equivalent, stream discharge, soil characteristics, and groundwater characteristics [13], and flow, dry and wet season rainfall, and change of basin [14]. ANNs have the ability to develop the relationship between inputs and outputs without knowing a priori knowledge under study. In hydrology, the major research challenge is to produce models which have the ability to simulate catchments; thus, these models are used for future forecasting of river discharge, which is compulsory for secure hydraulic and hydrological engineering design and water management.

The utilization of ANNs provided the addition of new applications to model these systems. They were implemented as a prosperous method to solve different problems related to water resource engineering. Climate change, the evapotranspiration process, river flow forecasting, reservoir inflow modeling, groundwater quality prediction, and simulation of rainfall runoff events are some applications involving water resources where ANNs were utilized [14], including pattern-learning, daily, weekly, and monthly sediment yield [15], forecasting daily stream flows [16], and the rainfall and water level of rivers [17]. Complex watershed rainfall processes which are non-linear and dynamic in nature [6,8] and unit hydrograph derivations can also be solved using ANN models. Flood forecasting for two floods disposed to catchments was studied using hourly hydrometric statistics in England [18]. For daily flow modeling during monsoons in Pakistan and different countries, daily rainfall data were used as input in ANNs [9]. Although there are other techniques similar to ANNs, such as statistics, artificial intelligence, machine learning, data mining, etc. [10], ANN models were applied for rainfall forecasting [7] and provided better results as compared to multiple linear regression modeling (MLR) [12]. Furthermore, neuro-fuzzy and regression models were also used, and their comparison for the forecast of outflow of an on-farm reservoir was studied [19]. Artificial neural network (ANN) and fuzzy logic (FL) models were applied for predicting event-based rainfall runoff [20]. The finite element method (FEM) and an artificial neural network (ANN) model were developed to simulate water flow through dams [21]. The ANN technique was applied to model watershed runoff in three basins with different climatic and physiographic characteristics [22]. During comparative analysis, ANNs were found to be superior for water-related research. For river watersheds, monthly streamflow was also forecasted using ANNs [22]. In Maryland, an ANN model was developed to estimate daily runoff for daily snowmelt, temperature, and precipitation for a watershed [13]. One of the main research aims is to develop a model showing the accuracy of the results. Such models can measure the river discharge variation with time, which is needed for hydrologic and hydraulic engineering design and water resource management. The main

focus of this study was to perform laboratory trials for the development of rainfall runoff data with the advanced hydrologic system. Then, for the confirmation of predicted data, modeling was done for the evaluation of observed runoff data using an ANN.

In this study, the change in soil bed symmetry with respect to changes in slope is to be tested under severe runoff conditions, to analyze the behaviour of different soil combinations and their symmetry under heavy rainfall. Furthermore, an ANN model was used following training and testing of the networks using data collected with different characteristics of soil, slope, and rainfall intensity. The predictive capability of the network performance and the calibration of data were examined using various training and validation datasets. The focus of the study was the selection and performance of soil beds under heavy rainfall for construction and irrigation purposes.

2. Materials and Methods

2.1. Advanced Hydrology Apparatus

Runoff analysis was performed on the advanced hydrology apparatus shown in Figure 1. This apparatus is very useful for hydraulic studies, such as the abstraction of wells, rainfall runoff, and the development of river characteristics. This apparatus gives realistic approachable results in the laboratory with no special requirements. This system is well designed for studying the hydrological cycle in terms of rainfall with respect to geography, as well as the runoff process for wells.
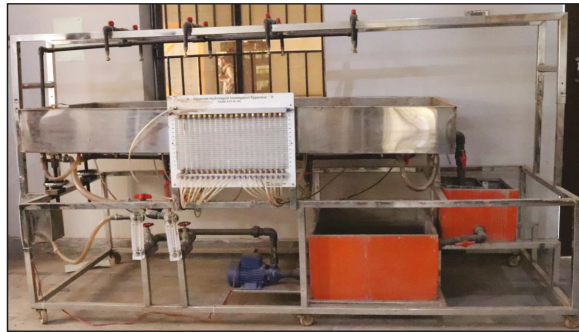
Figure 1. Rainfall simulator—advanced hydrology apparatus.

2.2. Flume

A flat veneer of a steady rectangular sampler was used with a width of 1 m and a length of 2 m. It also contained an adjustable slope ranging from 0% to 5%. The flume was filled with different soils (sand, clay, etc.) with different ratios as shown in Figure 2. The runoff calculation device was attached along with a timer device to perform time-variant analysis.

2.3. Rainfall Intensity Pattern

Rainfall was tested with different intensities on different slopes. Heavy rainfall profiles were used to test the soil behavior under the worst/severe conditions of rainfall, selecting soil combinations for the construction of structures like buildings and barrages. The patterns are given below in Table 1.

Table 1. Rainfall intensity patterns.

Slopes	Rainfall Intensities (mm/min)
0%	12
1%	12.5
2%	13
3%	13.5
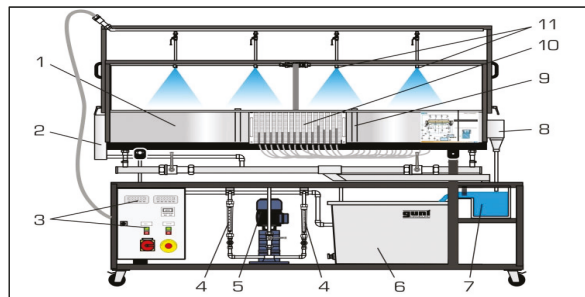
Figure 2. Schematic of advanced hydrology apparatus [23]: 1—experiment tank; 2—chamber; 3—display and control elements; 4—flow meter (supply); 5—pump; 6—storage tank; 7—measuring tank (drain); 8—chamber; 9—well; 10—tube manometers; 11—nozzles of the precipitation device.

2.4. Slope Variation

The tests were performed on different slopes of 0%, 1%, 2%, and 3% for observing the varied behavior of rainfall on the soils. Slopes were used as shown in Table 1, as it is rare to encounter level ground in real situations. Sometimes, the ground has to be leveled before construction, and it is not possible to change the slope.

2.5. Soil Properties and Bed Formation Variation

In this process, different soils were used with various contents as shown in Table 2. Two mediums are usually used or found naturally in the ground, i.e., clay and sand, whereby sand acts as a stabilizer for natural weak clay/soils [24,25]. Sometimes a mix of these can be used for the construction of structures. Combinations of soil types along with the properties selected for analysis are shown in Table 2. Soil properties included maximum dry density (MDD), optimum moisture content (OMC), soil pattern based on the American Association of State Highway and Transportation Officials (AASHTO), soil category based on the Unified Soil Classification System (USCS), and Atterberg's limits, including plastic limit (PL), liquid limit (LL), and plasticity Index (PI).

Table 2. Soil properties and bed profile pattern.

Soil Types	Soil Combination	MDD	OMC	Soil	Category	LL	PL	PI
		(pcf)	(%)	AASHTO	USCS			
ST1	Clay (100%)	122.2	12.10	A-7-6	CL	30	18.24	11.76
ST2	Sand (100%)	108.3	14.35	A-3	SP	17	0	0
ST3	Clay/sand (50%/50%)	133.97	9.20	A-4	ML	22	0	0
ST4	Clay/sand (70%/30%)	134.41	7.44	A-4	CL	23.85	15.38	8.47
ST5	Clay/sand (80%/20%)	134.39	12.01	A-4	CL	24	16.23	7.77

Note: (errors and omissions excepted), Abbreviations: maximum dry density (MDD), optimum moisture content (OMC), (American Association of State Highway and Transportation Officials (AASHTO) These all are categories: A-7-6, A-3, A-4, (Unified Soil Classification System (USCS) category: CL-Clay of Low plasticity, SP-Poorly graded Sand, ML-Micaceous/Silt of Low plasticity), plastic limit (PL), liquid limit (LL), and plasticity index (PI).

2.6. Flood Timing Pattern

Flooding happens in floodplains where rainfall over occurs over a few days or more, or where severe rainfall occurs for a short time period of time, in addition to other factors such as river overflow. Here, flood prediction and modeling referred to the progression of rainfall using a flood hydrograph and the translation of that hydrograph into a hydrologic system. The relationship between rainfall and runoff is a suitable approach for flood forecasting. For the flood forecasting, we obtained the

hydrographic results shown in Figure 3 for our data with different soil variations and slope changes (0%, 1%, 2%, and 3%).

(a)

(b)

(c)

(d)

(e)
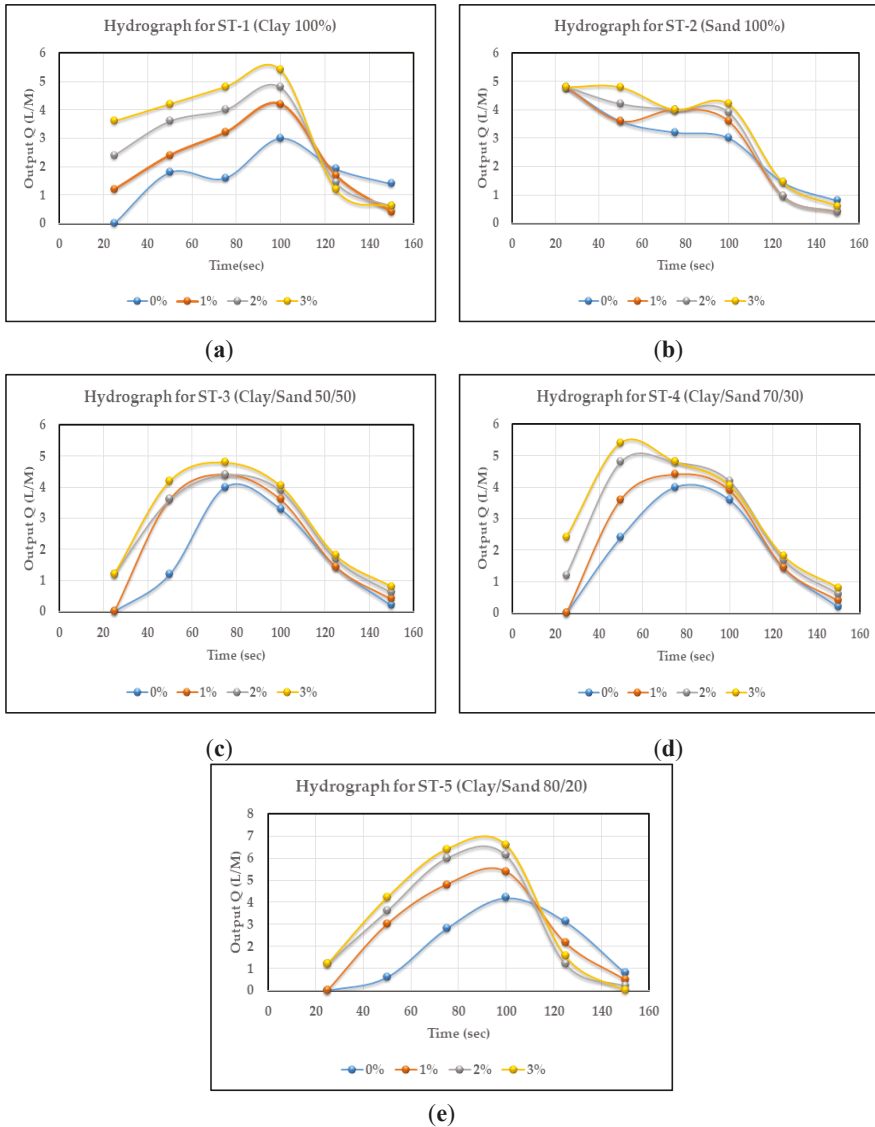
Figure 3. Hydrographs of flooding behavior for (**a**) ST-1, (**b**) ST-2, (**c**) ST-3, (**d**) ST-4, and (**e**) ST-5 with various slopes.

2.7. Artificial Neural Network (ANN)

In the research field, ANN is a statistical artificial intelligence technique used to correlate numerous inputs and precise outputs for forecasting; this technique is appropriate for the analysis of runoff. An ANN comprises the input layer, the hidden layer, and the output layer, as displayed in Figure 4. For complex pattern problems, the number of hidden layers can be increased or decreased. Basically,

ANNs are developed based on a minimum set of actual input and output statistics, resulting in a set of coefficients (signified as weights w_k and w_{kj}) [2]. This process initially examines the inputs and outputs for the best nonlinear connection. ANNs contain input (x_j) linear functions worked upon by a transfer function (a linear regression), represented in Equation (1), whereby each input contributes to the hidden unit. Using Equations (1) and (2), we can mathematically describe the system [5,7,11,20].

$$u_{k=} \varnothing \left[\sum_{j=1}^{m} w_{kj} x_j + b_{kj} \right], \tag{1}$$

$$y_i = \varnothing \left[\sum_{k=1}^{i} w_k u_k + b_k \right], \tag{2}$$

where $x_1, x_2, \ldots, x_m$ denote the input values, $\varnothing$ is a hyperbolic tangent type transfer function, $w_{k1}, w_{k2}, \ldots, w_{km}$ and $w_1, w_2, \ldots, w_k$ are the coefficients of the network, hidden nodes are denoted by $u_1, u_2, \ldots, u_k$, b_{kj} and b_k are constants, similar to linear regression constants, and y_i is the network output signal. The final output of the system is determined based on the linear function within the hidden nodes as a function of the constant shown in Equation (2) [2,14]. The data utilized for the development of the ANN model are described in Table 3. The formation of the ANN is shown in Figure 4, developed using various input variables (soil type, slope, rainfall intensity, and output discharge) and outputs (water retention and volume observed).

Table 3. Data description of parameters.

Parameters	Description	Mean	SD	Minimum	Median	Maximum
Water retention	Water retained by soil	2.756	2.41	0.04	2.15	7.28
Volume Observed	Volume of water recovered in tank (L)	20.6	3.067	15	20.25	26.25
Soil types	Soil combination 1—(100% clay), 2—(100% sand), 3—(50% clay and 50% sand), 4—(70% clay and 30% sand), 5—(80% clay and 20% sand)	-	-	1	-	5
Rainfall intensity	Rainfall intensity (mm/min)	12.75	0.574	12	12.75	13.5
Bed slope (%)	Level of soil bed change	1.5	1.147	0	1.5	3
Output discharge	Volume of water output (L/min)	15.744	3.295	9.72	16.84	19.96
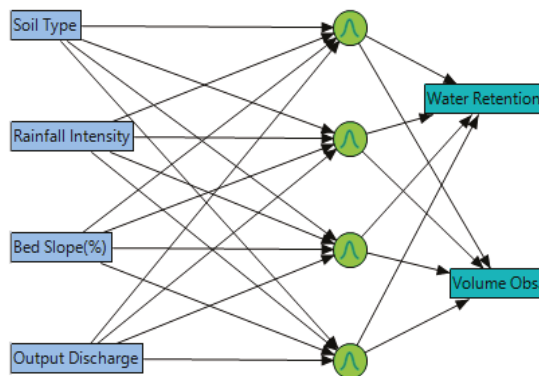
Figure 4. Artificial neural network: schematic illustration with a single hidden layer.

During the calculation of outputs (water retention and volume observed), the weights of each node were calculated using the complex mechanism of the ANN, the parametric estimates of which are given in Table 4.

Table 4. Parametric estimates for runoff analysis with respect to soil formation.

Input Parameters	Code	H1_1	H1_2	H1_3	H1_4
Soil types	1	0.000407	−0.8086	0.027309	0.22151
Soil types	2	−0.42179	−0.83072	0.512097	−0.76482
Soil types	3	−0.00634	−0.56721	0.219779	−0.06265
Soil types	4	0.014552	−0.96278	−0.24516	0.00394
Rainfall intensity	-	0.030138	−0.1482	0.973398	0.3635
Bed slope (%)	0	−0.06142	−0.05476	−0.77032	−0.24006
Bed slope (%)	1	−0.24751	0.629756	0.572158	−0.34591
Bed slope (%)	2	−0.10904	−0.14146	0.701974	0.149358
Output discharge	-	−0.47532	−0.04316	0.207968	−0.05518
Intercept	-	0.767819	1.601076	−12.8997	−4.8644
Output Parameters	**Intercept**	**H1_1**	**H1_2**	**H1_3**	**H1_4**
Water retention	3.289303	−5.53419	3.365286	−1.03429	2.874236
Volume observed	20.98531	0.724728	−7.21353	5.411468	−1.7103

3. Results and Discussion

3.1. Application of Artificial Neural Network (ANN)

The ANN model for the water retention of the soils and the runoff discharge with reference to changes in soil and bed slope evaluation was developed using JMP Pro. environment, version 13. We collected 20 data points for runoff discharge using the advanced hydrology apparatus for heavy rainfall intensity at various slopes and soil types. These data were considered for model development using various input variables (soil type, slope, rainfall intensity, and output discharge), and the outputs were water retention and volume observed. The database used for ANN model development is specified in Table 4. For the progress of the ANN model, the observed data were used as follows: 80% for training and 20% for validation. The behavior of the model during training, testing, and validating is represented in Figure 3, which shows its ability to predict the required output. With regard to the correlation coefficient value (*R*), a value close to 1 was achieved, showing that the model should perform well. The training process of the ANN required minimum overall error for the two outputs of the testing dataset. The validation sets were also used to confirm that the model performed suitably in terms of predicting runoff.

3.2. Model Parameters

The ANN model was developed, and the results were analyzed according to the available variables so as to test its prediction power and accuracy. The JMP Pro tool was used to analyze the developed model. The two parameters under focus were the root-mean-squared error (RMSE), which is the difference between the actual and the predicted value, and the difference in the coefficient of determination (R^2) [26,27], as given below in Equations (3) and (4), respectively.

$$RMSE = \sqrt{\left(\frac{1}{N}\sum_{n=1}^{N}(actual - predicted)^2\right)}, \tag{3}$$

$$R^2 = 1 - \frac{SSE}{SS_y}, \tag{4}$$

where SSE is the sum of squared errors of prediction, and SS_y is the total variation. Usually, the performance of a model is compared using the coefficient of determination (R^2), where a better fit is represented by a value closer to 1, and a poor fit has a value which approaches 0 [26,27]. ANNs use a back-propagation neural system which involves a complete learning rate and momentum, including a set of nodes, hidden layers, and an order of hidden layers [26], as well as a practical estimation of parameters such as the learning rate [26]. K-fold cross-validation (considering 80% for training and 20% for validation) was utilized to predict and validate the prediction model. The performance coefficient, root-mean-square error (RMSE), and the coefficient of determination (R^2) were utilized to identify the predictive power of the developed model [26]. Table 5 shows the estimated parameters and the prediction of the water retention and volume observed. Data were divided according to five segments using the K-fold mechanism; thus, 16 samples were used for training and four samples were used for validation. An R^2 value closer to 1 denotes the highest level of prediction accuracy of the developed model, as seen for water retention (0.99 for training and 0.98 for validation) and volume observed (0.97 for training and 0.99 for validation). The RMSE should be as low a value as possible, as seen for water retention (0.08 for training and 0.26 for validation) and volume observed (0.53 for training and 0.10 for validation).

Table 5. Model parameter estimates for training and validation data. RMSE—root-mean-square error.

Measures	Training	Validation
Water Retention		
R^2	0.9988175	0.9857542
RMSE	0.0817272	0.2636254
Number of samples	16	4
Volume Observed		
R^2	0.9710259	0.9961819
RMSE	0.5321165	0.1010018
Number of samples	16	4

3.3. Prediction Profiler

After producing the prediction pattern for the ANN model, the prediction profile produced during the analysis was used to study the impact of output discharge, slope, soil type, and rainfall intensity. Figure 5 shows the impact of these variables on the water retention and volume observed.
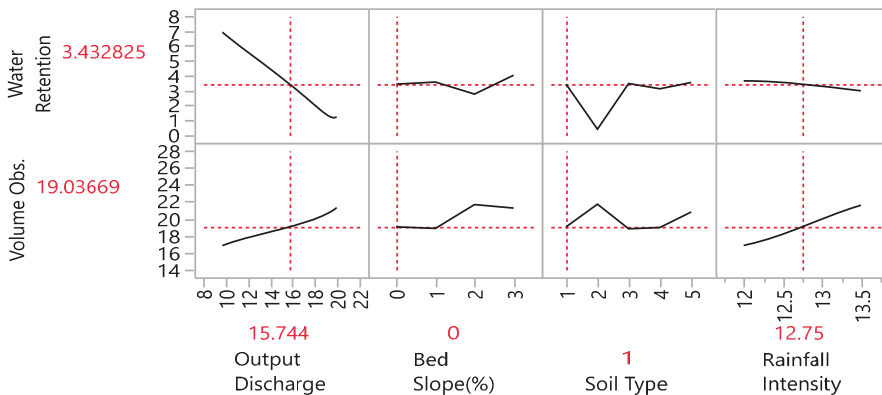
Figure 5. Prediction profile graph for water retention and volume observed.

The variables describing volume observed and water retention are denoted as Y_1 and Y_2, whereas variables X_1, X_2, X_3, and X_4 represent output discharge, bed slope, soil type, and rainfall intensity. Through the comparison of X and Y variables, we determined that output discharge increases with increasing observed volume and decreasing water retention. When the bed slope increases, observed volume also increases due to less water retained, and water starts flowing faster as compared to a parallel surface. Observed volume also increases with an increase in rainfall intensity when bed changes parallel to the slope, while water retention decreases.

3.4. Interaction Profiles

While the prediction profile allows determining the individual performance of variables, the interaction profile provides an overview to analyze the performance of certain variable with reference to other factors. In Figures 6 and 7, the performances of the minimum and maximum ranges of variables with reference to target variables were studied. Soil type contributes to a change in water retention pattern, especially after the addition of clay, reaching a certain optimum level. Clay fully retains water while sand tries to drain it as fast as possible.
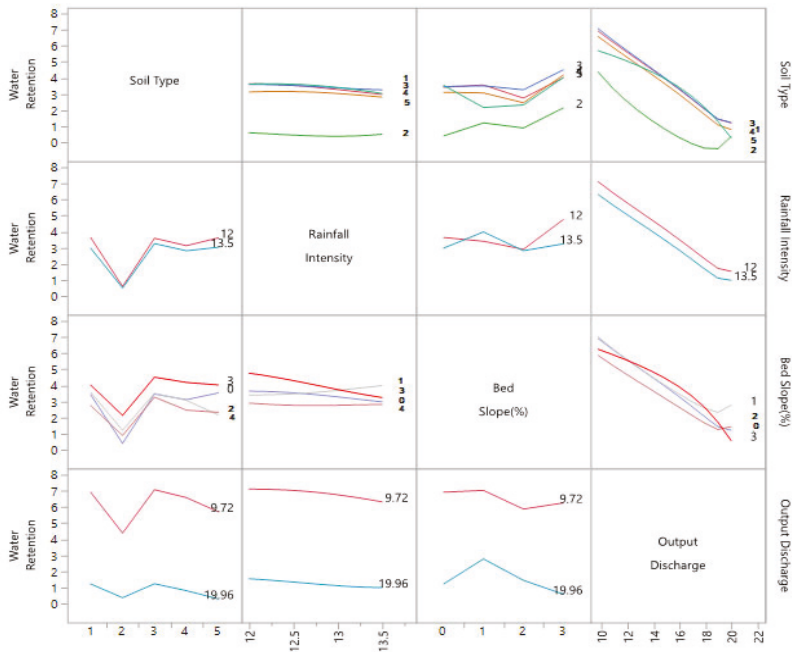
Figure 6. Interaction profile of variables with respect to water retention.

For soil 1, minimum and maximum discharge with respect to water retention firstly decreased, then increased, then slightly decreased again. For soil 2, there was a continuous decrease. For soil 3, there was an initial increase, followed by a decrease; however, the minimum output discharge increased slightly once more. Upon increasing the bed slope, water retention continuously decreased, except for soil 1, where water retention firstly decreased, then increased, and then slightly decreased again. Water retention was maximum on parallel surfaces for every soil with an increase in rainfall intensity; however, when the slope increased, the water retention decreased with increased rainfall intensity. For soil 1, water retention continuously decreased slightly. For soil 2, it fluctuated slightly, and, for soil 3, water retention decreased continuously. For soil 1, the minimum and maximum discharge with respect to volume observed firstly increased, then decreased, and then slightly increased again.

For soil 2, it continuously increased slightly. For soil 3, the maximum discharge firstly decreased and then increased, but the minimum output discharge started increasing followed by a slight decrease. Upon increasing the bed slope, the volume observed continuously increased. Volume observed was minimum on parallel surfaces due to water retention for every soil with an increase in rainfall intensity; however, when the slope increased, then the water retention decreased, and the volume observed increased with an increase in rainfall intensity. For soils 1 and 3, the volume observed continuously increased slightly, while, for soil 2, it fluctuated slightly.
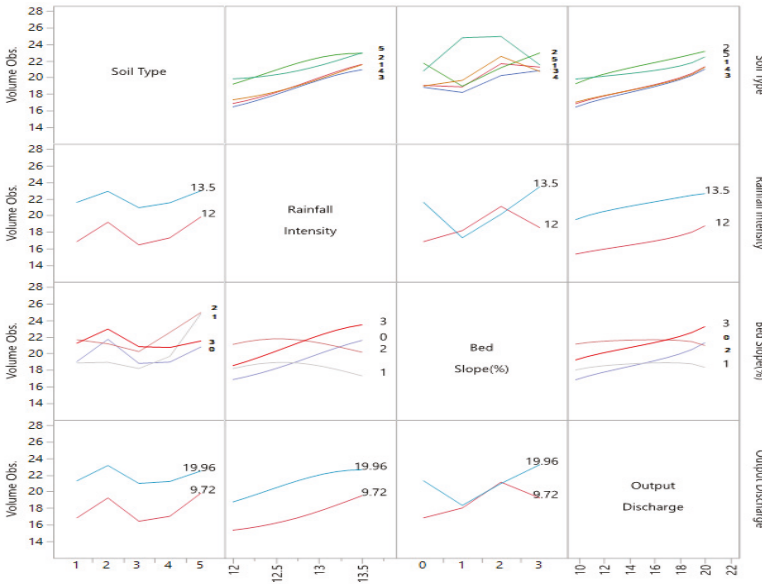
Figure 7. Interaction profile of variables with respect to water volume observed.

3.5. Variable Importance

Here, we identified the important variables affecting the volume observed and water retention with respect to output discharge, bed slope, soil type, and rainfall intensity, as shown in Table 6. Through the comparison of X and Y variables, we found that soil type and bed slope were very important factors in terms of output discharge.

Table 6. Variable importance profile of water retention and volume observed.

Parameter	Main Effect	Total Effect	Profile
Water Retention			
Output discharge	0.251	0.566	
Soil type	0.302	0.302	
Bed slope (%)	0.302	0.302	
Rainfall intensity	0.145	0.145	
Volume Observed			
Bed slope (%)	0.305	0.522	
Output discharge	0.192	0.339	
Soil type	0.305	0.305	
Rainfall intensity	0.197	0.197	

Table 6. *Cont.*

Parameter	Main Effect	Total Effect	Profile
Overall			
Output discharge	0.221	0.452	
Bed slope (%)	0.304	0.412	
Soil type	0.304	0.304	
Rainfall intensity	0.171	0.171	

4. Conclusions

This study focused on the optimization of soil bed formation symmetry with reference to stormy runoff analysis. It involved changes in soil combination and slope level under heavy runoff conditions. During the performance of laboratory experiments, testing was performed to analyze rainfall runoff behavior for different soils, due to their different properties. Experimental conditions considered various rainfall intensities to examine the soil behavior. Changes in soil combinations (ST 1 (100% clay), ST 2 (100% sand), ST 3 (50% clay and 50% sand), ST 4 (70% clay and 30% sand), and ST 5 (80% clay and 20% sand) were analyzed according to changes in slope (0%, 1%, 2%, and 3%) in terms of water retention and volume observed. We conclude that a leveled soil bed absorbs more water compared to a sloped soil bed. During construction, soil serves the purpose of a foundation, behaving differently with respect to varying water conditions. Soil with less water retention is preferred and, in that case, 100% sand or an 80%/20% combination of sand and clay are suitable for this purpose. In irrigation systems, soil and water have a very strong relationship; thus, based on our experimental results, we determined the optimal soil bed properties needed to resist atmospheric conditions. We observed that clay is better for water retention. It was observed that ST-2 (100% sand) performed well in terms of water retention (0.16 L/min) making it suitable for structures, while ST-1 (100% clay) performed well for irrigation purposes, as clay retains a large quantity of water (7.28 L/min). Sand contributes to stabilizing the soil before construction; thus, combinations of sand and clay were also tested with changing percentages. At a slope level of 3% along with 100% clay and sand, water behavior was almost similar. However, the combination of soil type 3 (ST-3) helped with the retention of water. For the prediction of outputs and relationship analysis, the ANN technique is superior to other techniques. The results using ANN explained the clear relationship between various input variables (soil type, slope, rainfall intensity, and output discharge) with outputs of water retention and volume observed. Therefore, we conclude that soil combination type and slope level should be monitored when undertaking construction.

Author Contributions: Conceptualization, S.A.R.S., and M.A.; methodology, M.H.H., S.A.R.S., and M.A.; software, M.H.H. and S.A.R.S.; validation, N.M.K. and M.N.; formal analysis, M.H.H., J.J., and M.W.A.; investigation, M.H.H., J.J., M.W.A., and A.F.; resources, M.H.H., J.J., M.W.A., and A.F.; data curation, M.H.H., S.A.R.S., and M.A.; writing—original draft preparation, M.H.H., S.A.R.S., and M.A.; writing—review and editing, N.M.K., M.W. and M.N.; visualization, S.A.R.S.; supervision, M.A., M.N., and N.M.K.; project administration, S.A.R.S.

Conflicts of Interest: The authors declare no conflict of interest.

References

1. Chouksey, A.; Lambey, V.; Nikam, B.; Aggarwal, S.; Dutta, S. Hydrological modelling using a rainfall simulator over an experimental hillslope plot. *Hydrology* **2017**, *4*, 17. [CrossRef]
2. Chakravarti, A.; Joshi, N.; Panjiar, H. Rainfall Runoff Analysis Using the Artificial Neural Network. *Indian J. Sci. Technol.* **2015**, *8*, 1–7. [CrossRef]
3. ASCE Task Committee on Application of Artificial Neural Networks in Hydrology. Artificial neural networks in hydrology. I: Preliminary concepts. *J. Hydrol. Eng.* **2000**, *5*, 115–123. [CrossRef]
4. ASCE Task Committee on Application of Artificial Neural Networks in Hydrology. Artificial neural networks in hydrology. II: Preliminary concepts. *J. Hydrol. Eng.* **2000**, *5*, 124–137. [CrossRef]

5. Kalteh, A.M. Rainfall-runoff modelling using artificial neural networks (ANNs): Modelling and understanding. *Casp. J. Environ. Sci.* **2008**, *6*, 53–58.
6. Dawson, C.W.; Wilby, R. An artificial neural network approach to rainfall-runoff modelling. *Hydrol. Sci. J.* **1998**, *43*, 47–66. [CrossRef]
7. Ramirez, M.C.V.; de Campos Velho, H.F.; Ferreira, N.J. Artificial neural network technique for rainfall forecasting applied to the Sao Paulo region. *J. Hydrol.* **2005**, *301*, 146–162. [CrossRef]
8. Chiang, Y.-M.; Chang, L.-C.; Chang, F.-J. Comparison of static-feedforward and dynamic-feedback neural networks for rainfall–runoff modeling. *J. Hydrol.* **2004**, *290*, 297–311. [CrossRef]
9. De Vos, N.; Rientjes, T. Constraints of artificial neural networks for rainfall-runoff modelling: Trade-offs in hydrological state representation and model evaluation. *Hydrol. Earth Syst. Sci. Discuss.* **2005**, *2*, 365–415. [CrossRef]
10. Rajurkar, M.; Kothyari, U.; Chaube, U. Modeling of the daily rainfall-runoff relationship with artificial neural network. *J. Hydrol.* **2004**, *285*, 96–113. [CrossRef]
11. Smith, J.; Eli, R.N. Neural-network models of rainfall-runoff process. *J. Water Resour. Plan. Manag.* **1995**, *121*, 499–508. [CrossRef]
12. Riad, S.; Mania, J.; Bouchaou, L.; Najjar, Y. Rainfall-runoff model usingan artificial neural network approach. *Math. Comput. Model.* **2004**, *40*, 839–846. [CrossRef]
13. Tokar, A.S.; Johnson, P.A. Rainfall-runoff modeling using artificial neural networks. *J. Hydrol. Eng.* **1999**, *4*, 232–239. [CrossRef]
14. Chen, S.; Wang, Y.; Tsou, I. Using artificial neural network approach for modelling rainfall–runoff due to typhoon. *J. Earth Syst. Sci.* **2013**, *122*, 399–405. [CrossRef]
15. Agarwal, A.; Singh, R.D.; Mishra, S.K.; Bhunya, P.K. ANN-based sediment yield models for Vamsadhara river basin (India). *Water Sa* **2005**, *31*, 85–100. [CrossRef]
16. Birikundavyi, S.; Labib, R.; Trung, H.T.; Rousselle, J. Performance of neural networks in daily streamflow forecasting. *J. Hydrol. Eng.* **2002**, *7*, 392–398. [CrossRef]
17. Campolo, M.; Andreussi, P.; Soldati, A. River flood forecasting with a neural network model. *Water Resour. Res.* **1999**, *35*, 1191–1197. [CrossRef]
18. Dawson, C.; Wilby, R. Hydrological modelling using artificial neural networks. *Prog. Phys. Geogr.* **2001**, *25*, 80–108. [CrossRef]
19. Sonawane, A.; Hasan, M.; Rajwade, Y.; Desai, S.; Rajurkar, G.; Shinde, V.; Singh, M. Comparison of Neuro-Fuzzy and Regression Models for Prediction of Outflow of on-farm Reservoir. *Int. J. Agric. Environ. Biotechnol.* **2013**, *6*, 311.
20. Tayfur, G.; Singh, V.P. ANN and fuzzy logic models for simulating event-based rainfall-runoff. *J. Hydraul. Eng.* **2006**, *132*, 1321–1330. [CrossRef]
21. Tayfur, G.; Swiatek, D.; Wita, A.; Singh, V.P. Case study: Finite element method and artificial neural network models for flow through Jeziorsko earthfill dam in Poland. *J. Hydraul. Eng.* **2005**, *131*, 431–440. [CrossRef]
22. Tokar, A.S.; Markus, M. Precipitation-runoff modeling using artificial neural networks and conceptual models. *J. Hydrol. Eng.* **2000**, *5*, 156–161. [CrossRef]
23. AHA. Advance Hydrology Apparatus. Advanced Hydrological Investigations. 2019. Available online: https://www.gunt.de (accessed on 13 January 2019).
24. Kollaros, G.; Athanasopoulou, A. Sand as a Soil Stabilizer. *Bull. Geol. Soc. Greece* **2016**, *50*, 770–777. [CrossRef]
25. Matter, S. What Type of Soil is Good for a Foundation for Buildings or Houses? 2015. Available online: https://soilsmatter.wordpress.com/2015/05/01/what-type-of-soil-is-good-for-a-foundation-for-buildings-or-houses/ (accessed on 18 July 2019).
26. Siddique, R.; Aggarwal, P.; Aggarwal, Y. Prediction of compressive strength of self-compacting concrete containing bottom ash using artificial neural networks. *Adv. Eng. Softw.* **2011**, *42*, 780–786. [CrossRef]
27. Mansoor, J.; Shah, S.; Khan, M.; Sadiq, A.; Anwar, M.; Siddiq, M.; Ahmad, H. Analysis of Mechanical Properties of Self Compacted Concrete by Partial Replacement of Cement with Industrial Wastes under Elevated Temperature. *Appl. Sci.* **2018**, *8*, 364. [CrossRef]

Article

Study on Stiffness-Oriented Cable Tension Distribution for a Symmetrical Cable-Driven Mechanism

Kaisheng Yang [1,2,3], Guilin Yang [1,*], Si-Lu Chen [1], Yi Wang [1,2], Chi Zhang [1], Zaojun Fang [1], Tianjiang Zheng [1] and Chongchong Wang [1]

[1] Zhejiang Key Lab of Robotics and Intelligent Manufacturing Equipment Technology, Ningbo Institute of Material Technology and Engineering, Chinese Academy of Sciences (CAS), Ningbo 315201, China; yangkaisheng@nimte.ac.cn (K.Y.); chensilu@nimte.ac.cn (S.-L.C.); wangyi216@nimte.ac.cn (Y.W.); zhangchi@nimte.ac.cn (C.Z.); fangzaojun@nimte.ac.cn (Z.F.); zhengtianjiang@nimte.ac.cn (T.Z.); wangchongchong@nimte.ac.cn (C.W.)

[2] College of Materials Science and Opto-Electronic Technology, University of Chinese Academy of Sciences (UCAS), Beijing 100049, China

[3] Zhejiang Marine Development Research Institute, Zhoushan 316021, China

* Correspondence: glyang@nimte.ac.cn

Abstract: In this paper, we focus on the issues pertaining to stiffness-oriented cable tension distribution for a symmetrical 6-cable-driven spherical joint module (6-CSJM), which can be employed to construct modular cable-driven manipulators. Due to the redundant actuation of the 6-CSJM, three cables are employed for position regulation by adjusting the cable lengths, and the remaining three cables are utilized for stiffness regulation by adjusting the cable tensions, i.e., the position and stiffness can be regulated simultaneously. To increase the range of stiffness regulation, a variable stiffness device (VSD) is designed, which is serially connected to the driving cable. Since the stiffness model of the 6-CSJM with VSDs is very complicated, it is difficult to directly solve the cable tensions from the desired stiffness. The stiffness-oriented cable tension distribution issue is formulated as a nonlinear constrained optimization problem, and the Complex method is employed to obtain optimal tension distributions. Furthermore, to significantly improve the computation efficiency, a decision variable elimination technique is proposed to deal with the equality constraints, which reduces decision variables from 6 to 3. A comprehensive simulation study is conducted to verify the effectiveness of the proposed method, showing that the 6-CSJM can accurately achieve the desired stiffness through cable tension optimization.

Keywords: cable-driven manipulator; redundant actuation; variable stiffness; tension distribution; optimization

---

1. Introduction

Cable-driven manipulators (CDMs) are a special class of mechanisms in which cables are employed as the driving elements. Compared to the conventional rigid robotic manipulators, CDMs have advantages of large workspace, low moving mass, high payload-to-weight ratio, and variable stiffness. As such, they have been applied in inspection and repair [1–3], human-robot interaction [4–6], moving and lifting payloads [7–9] and wearable robots [10–14]. Since cables have unilateral driving properties, i.e., can pull but cannot push, the number of driving cables in a CDM is greater than the number of its Degree-of-Freedom

(DOF), yielding redundant actuation. Thus, there exist an infinite number of cable tension distribution settings for any given pose of a CDM. As the stiffness of a CDM can be regulated by adjusting the cable tensions [15], a redundantly actuated CDM has the merit of variable stiffness for safe human-robot interactions. Therefore, a CDM is a promising candidate of collaborative robots to perform various manipulation tasks in human environment [16,17].

In the last decades, the design [18,19], kinematics [20], workspace [21,22], motion control [23] and stiffness [24–26] of CDMs have been studied by many researchers. For the issue of cable tension distribution, some researchers studied the cable tension distribution of a CDM to minimize a p-norm (such as 1-norm, or 2-norm) of the tensions, aiming to reduce the energy consumption [27–32]. In [33], an analytical method is proposed to minimize magnitude sum of cable tensions for a completely restrained 6-DOF CDM, in order to obtain the optimal tension distribution for lowest energy consumption. However, such a method is not applicable for CDMs with more than one redundant cable. In [34], a cable tension distribution method is proposed to control the cable-driven platform on a given trajectory, which is formulated as a constrained optimization problem to minimize the 2-norm of the cable tensions. Two algorithms based on interval analysis and gradient-based optimizer are investigated to compute the optimal cable tension solutions. However, these norm-based optimization methods would generally suggest the results being close to the lower tension limits. This potentially resulted in low robot stiffness and left the cable tend to be slack. To solve this issue, in [35], a non-iterative method is proposed to find out the safe tension distributions being away from the tension limits. However, this method is computational intensive when the number of cables increases. In [36], the issue of stiffness-oriented cable tension distribution is studied and a gradient projection based method is developed to regulate the stiffness of a CDM by adjusting cable tensions. However, this method employs the determinant of the stiffness matrix as the cost function, rather than all entries of the stiffness matrix. It is difficult to achieve the desired stiffness accurately. In summary, the issue of the cable tension distribution for accurately achieving a desired feasible stiffness of a CDM has not been addressed well.

In this paper, we focus on the issue of stiffness-oriented cable tension distribution for a symmetrical *6-cable-driven spherical joint module* (6-CSJM), which can be employed as a fundamental block for building modular CDMs. For such a 6-CSJM, due to its redundant actuation, three cables are enough for position control, and the remaining three cables can be utilized for stiffness regulation. To increase the range of stiffness regulation, a *variable stiffness device* (VSD) is designed to connect to the driving cable serially. Compared to other design [18], this VSD is fixed on the platform, rather than directly attached to the midway of the hanging cables. Such VSD arrangement reduces the VSD's disturbance to the cable tensions effectively. Consequently, the position and stiffness of a 6-CSJM can be regulated simultaneously, such that its position can be controlled by adjusting the three cable lengths, while its stiffness can be controlled by adjusting the remaining three cable tensions. The stiffness model of the 6-CSJM indicates that its stiffness is related to both the geometry change of the 6-CSJM and stiffness of the driving cable with a VSD [37]. Due to the complexity of the stiffness model, it is difficult to obtain the cable tension distribution from a desired stiffness directly. Hence, we formulate the issue of stiffness-oriented cable tension distribution as a nonlinear constrained optimization problem. The cost function is constructed based on all entries of the stiffness matrix of the 6-CSJM, rather than its determinant. Furthermore, we set safe tension zone for the cable and the VSD to avoid the cable being slack and the tension exceeding the torque limit of the driving motor. A variable elimination technique is proposed to deal with the three equality constraints in the optimization model and the decision variables are significantly reduced from 6 to 3. Since the stiffness model of the 6-CSJM with nonlinear VSDs is complicated, the widely used gradient-based optimization algorithm is not appropriate. Instead, the Complex method is employed, since it merely require cost function values in the optimization process [38]. The effectiveness of the proposed method is validated by a comprehensive simulation. In summary, the major merit of the proposed stiffness-oriented cable

tension distribution method is that it provides an effective way to achieve accurate stiffness regulation and position control simultaneously.

2. Design of the 6-CSJM with VSDs

The cable-driven spherical joint module (CSJM) consists of a moving-platform, a base and a passive spherical joint. The moving-platform is driven by cables. Since the cables can pull but cannot push, for the 3-DOF CSJM, the number of driving cables, n, should satisfy $n \geq 4$ [39]. To have a symmetrical design, six cables are employed in this CSJM. As shown in Figure 1, there are six small holes on both of the moving-platform and the base for cables passing through, denoted by A_i ($i = 1, 2, \cdots, 6$) and B_j ($j = 1, 2, \cdots, 6$), respectively. Geometrically, $A_2A_3 = A_4A_5 = A_6A_1 = l_A$, $B_1B_2 = B_3B_4 = B_5B_6 = l_B$, $A_1A_2 = A_3A_4 = A_5A_6 = e_A$ and $B_2B_3 = B_4B_5 = B_6B_1 = e_B$. O, O_A and O_B are the centers of the passive spherical joint, moving-platform and base plate, respectively, in which $OO_A = h_A$ and $OO_B = h_B$. In order to describe the motion, we set the base frame $\{B\}$ being attached to the base, and the moving frame $\{A\}$ being attached to the moving-platform. When the 6-CSJM is at home pose, the moving-platform is parallel to the base and the two frames coincide with each other.
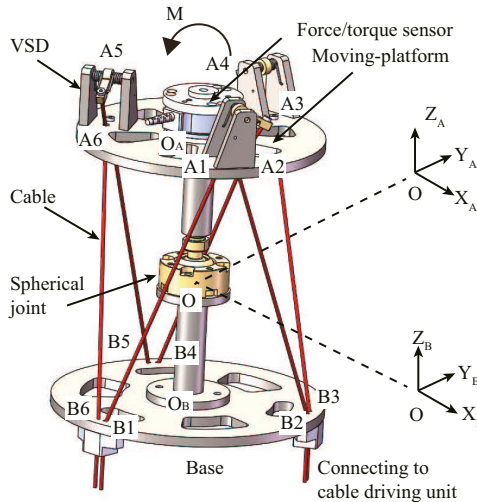
Figure 1. CAD model of the 6-CSJM.

Due to the redundant actuation of the 6-CSJM, three cables are enough for position regulation and the other three cables can be employed for stiffness regulation. Thus, the position and stiffness can be regulated simultaneously. Considering the symmetry of the 6-CSJM, six driving cables are divided into two groups. Cable 1, 3 and 5 are grouped for position regulation, which can be realized by adjusting the cable lengths. Meanwhile, Cable 2, 4 and 6 are grouped for stiffness regulation, which can be realized by adjusting the cable tensions. In order to increase the range of stiffness regulation, a novel VSD is designed and it is connected to the cable in series. The CAD model and kinematic diagram of the VSD are shown in Figure 2. This VSD is basically a 1-DOF cable-driven mechanism, in which a set of torsional springs with constant stiffness are employed to connect the rotating rigid link to the shaft of the revolute joint. Compared to the other designs [18], our VSDs are fixed on the platform, rather than directly attached to

the midway of the hanging cables. Such design effectively reduces the perturbation to the cable tensions from the gravity of the VSDs.
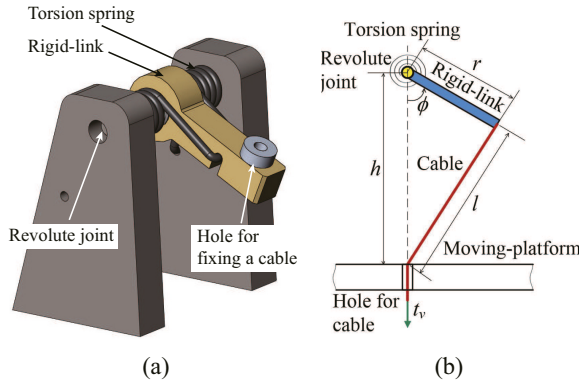
Figure 2. Design of the VSD. (**a**) CAD model of the VSD; (**b**) Diagram of the VSD.

In this 6-CSJM, three VSDs (VSD 2, 4 and 6) are installed on the top of the moving-platform. Cable 2, 4 and 6 are fixed to VSD 2, 4 and 6, go through the holes A_2, A_4 and A_6 on the moving-platform, and then go through the holes B_2, B_4 and B_6 on the base, finally be connected to the cable-driven motors, respectively. Cable 1, 3 and 5 are fixed in the holes A_1, A_3 and A_5 on the moving-platform, go through the holes B_1, B_3 and B_5 on the base, finally be connected to the cable-driven motors, respectively. In order to measure the external load applied on the moving-platform, a force/torque sensor is installed on the moving-platform.

3. Stiffness Model of the VSD

As shown in Figure 2b, the cable length l in the VSD satisfies

$$l = \sqrt{h^2 + r^2 - 2hr\cos\phi}, \tag{1}$$

where h is the height of the revolute joint, r is the length of the rigid-link and ϕ is the angle of the rigid-link. The cable tension t_v applied on the VSD satisfies the equilibrium equation of the VSD, hence it can be represented as

$$t_v = \frac{lk_s(\phi_0 - \phi)}{hr\sin\phi}, \tag{2}$$

where k_s is the stiffness of the torsional spring and ϕ_0 is the initial value of angle ϕ. In this design, $k_s = 1.20$ Nm/rad, $r = 0.018$ m, $h = 0.03$ m, and $\phi_0 = 0.53$ rad. According to (1) and (2), the cable length l and the cable tension t_v are both dependent on the angle ϕ. Denote $l = l(\phi)$ and $t_v = t_v(\phi)$, then the stiffness of the VSD, k_v, can be represented as

$$k_v = \frac{\mathrm{d}t_v}{\mathrm{d}l} = \frac{\mathrm{d}t_v}{\mathrm{d}\phi} \bigg/ \frac{\mathrm{d}l}{\mathrm{d}\phi}. \tag{3}$$

It shows that the stiffness k_v is also dependent on the angle ϕ. The expression of the k_v and t_v are both complicated in terms of ϕ. It is difficult to obtain the explicit solution of ϕ from t_v. Hence, it is a tough job to obtain exact explicit formulation of k_v in terms of t_v. In order to simplify the calculation,

we approximate the expression of k_v in terms of t_v by a polynomial (4), with 95% confidence bounds and *R-square* = 0.996, i.e.,

$$k_v = 8.005t_v^2 - 239.4t_v + 5415. \tag{4}$$

The curve of k_v with respect to t_v is shown in Figure 3, indicating that the stiffness is nonlinear and it increases when the cable tension increases. On the other hand, the displacement of the cable in the VSD, $\Delta l = l_0 - l$, can be expressed in terms of t_v approximately as following

$$\Delta l = -1.687 \times 10^{-6} t_v^2 + 2.729 \times 10^{-4} t_v. \tag{5}$$
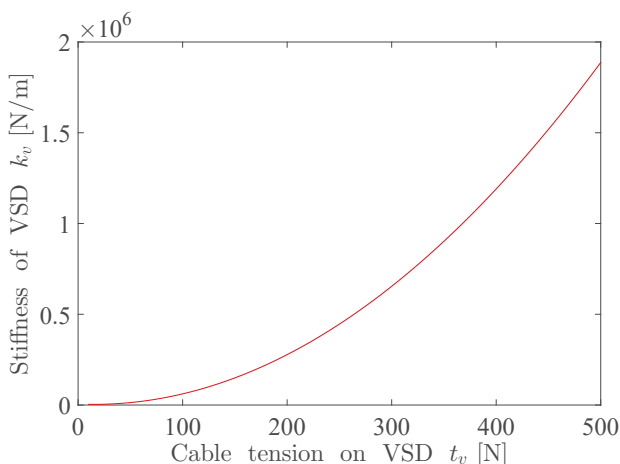
Figure 3. Curve of the stiffness of the VSD in terms of the cable tension applied on the VSD.

Considering the torque limit of cable driving motor and the tensile strength of the cable, and to avoid the cable being slack, the cable tensions should be limited. Here, we set 10 N$\leq t_v \leq$ 100 N for the cable tension t_v applied on the VSD, terming it as the safe tension zone of the VSD. Similarly, we also set 10 N$\leq t_c \leq$ 100 N as the safe tension zone for the driving cables without connecting to a VSD.

4. Stiffness Model of the 6-CSJM

4.1. Kinematic Analysis of the 6-CSJM

In the 6-CSJM, the moving-platform realizes 3-DOF rotational motions about the spherical joint. The pose of the moving-platform, described by the pose of the moving frame {A} with respect to the base frame {B}, is a rotational matrix $\boldsymbol{R} \in SO(3)$. Thus, the motion of the moving-platform is a curve on $SO(3)$, denoted as $\boldsymbol{R}(t)$. It satisfies

$$\boldsymbol{R}(t) = e^{\hat{\sigma}_1 \zeta_1(t) + \hat{\sigma}_2 \zeta_2(t) + \hat{\sigma}_3 \zeta_3(t)}, \tag{6}$$

where $\hat{\sigma}_1$, $\hat{\sigma}_2$ and $\hat{\sigma}_3$ are the basis of Lie algebra $so(3)$, and $\boldsymbol{\zeta}(t) = (\zeta_1(t), \zeta_2(t), \zeta_3(t))^T$ is the canonical coordinate of $\boldsymbol{R}(t)$ with respect to the basis. Here, we choose $\sigma_1 = (1,0,0)^T$, $\sigma_2 = (0,1,0)^T$ and

$\sigma_3 = (0,0,1)^T$, then $\hat{\sigma}_1$, $\hat{\sigma}_2$ and $\hat{\sigma}_3$ represent instantaneous rotations of the moving-platform about the axes X_B, Y_B and Z_B, respectively, where the operation $\hat{(\cdot)}$ is defined as

$$\lambda = \begin{pmatrix} \lambda_1 \\ \lambda_2 \\ \lambda_3 \end{pmatrix} \rightarrow \hat{\lambda} = \begin{pmatrix} 0 & -\lambda_3 & \lambda_2 \\ \lambda_3 & 0 & -\lambda_1 \\ -\lambda_2 & \lambda_1 & 0 \end{pmatrix}. \tag{7}$$

Since $\boldsymbol{\zeta}(t) = (\zeta_1(t), \zeta_2(t), \zeta_3(t))^T$ is a vector of the rotational angles, describing the motion of the moving frame {A} with respect the base frame {B}, the velocity of the moving-platform satisfies

$$\boldsymbol{\omega} = \dot{\boldsymbol{\zeta}}(t) = \frac{d\boldsymbol{\zeta}(t)}{dt}. \tag{8}$$

As shown in Figure 1, denote $\boldsymbol{a}_i = \overrightarrow{OA_i}$ and $\boldsymbol{b}_i = \overrightarrow{OB_i}$ as the position vectors of A_i and B_i in frame {B}, respectively, the vector of the ith $(i = 1, 2, \cdots, 6)$ cable from A_i to B_i, denoted as $\boldsymbol{c}_i \in \mathbb{R}^3$, satisfies

$$\boldsymbol{c}_i = \overrightarrow{A_i B_i} = \overrightarrow{OB_i} - \overrightarrow{OA_i} = \boldsymbol{b}_i - \boldsymbol{a}_i, \tag{9}$$

Here, $\boldsymbol{a}_i$ can be expressed as $\boldsymbol{a}_i = R\boldsymbol{a}_i^A$, where $\boldsymbol{a}_i^A$ is the position vector of point A_i in frame {A}. Define $c_i = |\boldsymbol{c}_i|$ and $\boldsymbol{u}_i = \boldsymbol{c}_i/c_i$, then $\boldsymbol{c}_i = c_i \boldsymbol{u}_i$. By differentiating (9) with respect to time, we have

$$\dot{\boldsymbol{c}}_i = \dot{c}_i \boldsymbol{u}_i + c_i \boldsymbol{\omega}_i \times \boldsymbol{u}_i = -\boldsymbol{\omega} \times \boldsymbol{a}_i, \tag{10}$$

where $\boldsymbol{\omega}_i$ is the angular velocity of the ith cable in frame {B}. Dot-multiplying both sides of (10) by $\boldsymbol{u}_i$, we obtain

$$\dot{c}_i = -(\boldsymbol{a}_i \times \boldsymbol{u}_i) \cdot \boldsymbol{\omega} = -(\boldsymbol{a}_i \times \boldsymbol{u}_i)^T \boldsymbol{\omega}, \tag{11}$$

or the equivalent matrix form as

$$\dot{\boldsymbol{C}} = -\boldsymbol{J}\boldsymbol{\omega} = -\boldsymbol{J}\dot{\boldsymbol{\zeta}}, \tag{12}$$

where $\boldsymbol{C} = (c_1, c_2, \cdots, c_6)^T \in \mathbb{R}^6$ and $\boldsymbol{J} = (\boldsymbol{a}_1 \times \boldsymbol{u}_1, \boldsymbol{a}_2 \times \boldsymbol{u}_2, \cdots, \boldsymbol{a}_6 \times \boldsymbol{u}_6)^T$. Equation (12) represents the velocity of the cable elongation in terms of the change rate of the coordinate.

4.2. The Stiffness Model of the 6-CSJM

In this paper, the stiffness of the ith driving cable k_{ci} $(i = 1, 2, \cdots, 6)$ satisfies $k_{c1} = k_{c2} = k_{c3} = k_{c4} = k_{c5} = k_{c6} = k_c$, where the stiffness of the cable $k_c = 8.0 \times 10^4$ N/m. When a driving cable is connected to a VSD, the overall stiffness of the cable with the VSD, denoted as k_{cv}, satisfies

$$\frac{1}{k_{cv}} = \frac{1}{k_c} + \frac{1}{k_v}, \tag{13}$$

where k_v is the stiffness of the VSD.

Denote $\boldsymbol{M}$ as the total load applied to the moving-platform, $\boldsymbol{T}_i$ $(i = 1, 2, \cdots, 6)$ as the tension vector of the ith cable, and $\boldsymbol{T} = (t_1, t_2, \cdots, t_6)^T$, where $t_i = |\boldsymbol{T}_i|$, the static equilibrium equation of the moving-platform is given below

$$\boldsymbol{M} \cdot d\boldsymbol{\zeta} + \boldsymbol{T} \cdot d\boldsymbol{C} = 0. \tag{14}$$

Substituting (12), i.e., $d\boldsymbol{C} = -\boldsymbol{J}d\boldsymbol{\zeta}$, into (14), we have

$$\boldsymbol{M} = \boldsymbol{J}^T \boldsymbol{T} = \boldsymbol{S}\boldsymbol{T}, \tag{15}$$

where $S = J^T$ is called *structure matrix*. The differential form of (15) is given below

$$dM = dST + SdT. \tag{16}$$

According to the analysis above, we have

$$dM = K_m d\zeta, \tag{17}$$

$$dST = Zd\zeta, \tag{18}$$

$$dT = K_{\text{diag}}dC = K_{\text{diag}}Jd\zeta. \tag{19}$$

Here, $K_m \in \mathbb{R}^{3\times3}$ is the stiffness matrix of 6-CSJM to be determined, $K_{\text{diag}} = \text{diag}\{k_1, k_2, \cdots, k_6\} \in \mathbb{R}^{6\times6}$ is a diagonal matrix whose element k_i represents the stiffness of the ith $(i = 1, 2, \cdots, 6)$ cable, and Z is defined by

$$Z = (\frac{\partial S}{\partial \zeta_1}T, \frac{\partial S}{\partial \zeta_2}T, \frac{\partial S}{\partial \zeta_3}T) \in \mathbb{R}^{3\times3}. \tag{20}$$

The diagonal element of K_{diag} satisfies $k_i = k_{cvi}$ if there is a VSD connected to the cable, or $k_i = k_{ci}$ if there is no VSD connected to the cable.

Substituting (17), (18) and (19) into (16), the stiffness model of the the 6-CSJM is expressed as

$$K_m = SK_{\text{diag}}S^T + Z = K_c + K_g. \tag{21}$$

The first part K_c yields

$$K_c = SK_{\text{diag}}S^T \in \mathbb{R}^{3\times3}, \tag{22}$$

which represents the stiffness caused by the elongation of the cable (with the VSD) and it is a symmetric matrix. The second part K_g yields

$$K_g = Z \in \mathbb{R}^{3\times3}, \tag{23}$$

which represents the stiffness caused by the change of the geometry of the 6-CSJM.

5. Stiffness-Oriented Cable Tension Distribution Method

As stated in the prior section, Cable 1, 3 and 5 are employed for position control, while Cable 2, 4 and 6 are employed for stiffness regulation. According to (9), the desired feasible pose $R_{\text{des}} \in \mathbb{R}^{3\times3}$ can be easily realized by adjusting the lengths of Cable 1, 3 and 5. For stiffness regulation, we should adjust the tensions of Cable 2, 4 and 6 to achieve the desired feasible stiffness. However, due to the complexity of the stiffness model (21), it is difficult to solve the cable tension distribution from the desired feasible stiffness directly. Instead, we formulate the stiffness-oriented cable tension distribution issue as an optimization problem.

5.1. Formulation of the Optimization Model

Denote $K_{\text{des}} = \{k_{\text{des}(ij)}\} \in \mathbb{R}^{3\times3}$ $(i, j = 1, 2, 3)$ as the desired stiffness matrix of the 6-CSJM at a given pose R_{des}, and $K_{\text{act}} = \{k_{\text{act}(ij)}\} \in \mathbb{R}^{3\times3}$ $(i, j = 1, 2, 3)$ as the actual stiffness matrix, a desired stiffness matrix is computed with the given cable tensions according to the stiffness model (21) and an actual stiffness matrix is computed with the actual cable tensions or measured by the equipments. For this issue, we require the actual stiffness matrix to achieve the desired stiffness matrix, hence a scalar, d_K, is defined to evaluate the distance of the two stiffness matrices.

$$d_K = \sqrt{\frac{1}{9}\sum_{i=1}^{3}\sum_{j=1}^{3}(k_{\text{des}(ij)} - k_{\text{act}(ij)})^2},\tag{24}$$

where all entries of the stiffness matrix are employed, rather than its determinant. Eventually, we define a cost function $f(T) = d_K(T)$, and formulate an optimization model for the stiffness-oriented cable tension distribution issue

$$\text{Minimize: } f(T),\tag{25a}$$
$$\text{Subject to: } ST - M = 0,\tag{25b}$$
$$\underline{t_v} \le t_{vi} \le \bar{t}_v \ (i=1,2,3),\tag{25c}$$
$$\underline{t_c} \le t_{cj} \le \bar{t}_c \ (j=1,2,3),\tag{25d}$$

where $[\underline{t_v}, \bar{t}_v]$ is the safe tension zone of VSDs, and $[\underline{t_c}, \bar{t}_c]$ is the safe tension zone of cables.

5.2. Elimination of Equality Constraint

The nonlinear optimization model (25) has both equality and inequality constraints. Here, a variable elimination technique is proposed to deal with the equality constraints and the decision variables are significantly reduced from 6 to 3. Denote $T_p = (t_1, t_3, t_5)^T \in \mathbb{R}^3$, $T_s = (t_2, t_4, t_6)^T \in \mathbb{R}^3$, $S_p = (s_1, s_3, s_5) \in \mathbb{R}^{3\times3}$, and $S_s = (s_2, s_4, s_6) \in \mathbb{R}^{3\times3}$, where t_i ($i = 1, 2, \cdots, 6$) is the tension of the ith cable, and s_i ($i = 1, 2, \cdots, 6$) is the ith column vector of the matrix S. Then we can write (25b) as

$$S_p T_p = M - S_s T_s.\tag{26}$$

The cable tension vector T_p for position control can be represented by

$$T_p = S_p^{-1}(M - S_s T_s).\tag{27}$$

Equation (27) implies that T_p is dependent on T_s. Denote $T = q(T_s)$ and $g(T_s) = f(q(T_s))$, then the model (25) can be written as

$$\text{Minimize: } g(T_s),\tag{28a}$$
$$\text{Subject to: } \underline{t_v} < t_i < \bar{t}_v \ (i=2,4,6),\tag{28b}$$
$$\underline{t_c} < t_j < \bar{t}_c \ (j=1,3,5).\tag{28c}$$

Remarkably, (28) only contains inequality constraints. In prior works, such optimization model are usually solved by gradient-based methods. However, the derivative of the cost function of this model is complicated and difficult to obtained. Thus, the Complex method is employed as the optimization algorithm to solve this model, since it merely require cost function values.

5.3. Optimization Procedures via Complex Method

When applying the Complex method, there are three decision variables from $T_s = (t_2, t_4, t_6)^T$ and six inequality constraints from (28b) and (28c). The procedures are described as following:

(i) *Formation of the initial Complex:* An initial Complex with six vertices $T_s^{(1)}, T_s^{(2)}, \cdots, T_s^{(6)}$ is setup in the feasible region randomly.

(ii) *Generation of a new complex:* The values of the cost function at the vertices are computed. The worst point $T_s^{(W)}$, where the cost function obtains the largest value, will be replaced by the mapping point $T_s^{(M)}$. In this way, a new Complex is generated. Here, the mapping point $T_s^{(M)}$ is computed by

$$T_s^{(M)} = T_s^{(C)} + \alpha(T_s^{(C)} - T_s^{(W)}), \tag{29}$$

where $T_s^{(C)}$ is the center of the other 5 points except the worst point $T_s^{(W)}$, and α is the *reflection factor*. The initial value of $\alpha = 1.3$. If $T_s^{(M)}$ is not in the feasible region, it should be computed again with $\alpha \leftarrow \frac{\alpha}{2}$, while its minimum value $\alpha_{min} = 10^{-5}$.

(iii) *Condition of loop stopping:* If the *error tolerance*, $\epsilon \leq \epsilon_{min} = 10^{-7}$, the iterative procedure will terminate, and we go to (iv). Otherwise, we go back to (i). Here, ϵ is defined as

$$\epsilon = \sqrt{\frac{1}{6} \sum_{j=1}^{6} [g(T_s^{(j)}) - g(T_s^{(B)})]^2}. \tag{30}$$

In (30), $g(T_s^{(j)})$ $(j = 1, 2, \cdots, 6)$ is the value of the cost function at the vertex of the current Complex. $T_s^{(B)}$ is the best point, such that its cost function has the minimum value.

(iv) *Finalization of optimal solution:* The best point $T_s^{(B)}$ is selected as the optimal solution T_{opt}. From here, the optimal cable tension distribution is obtained for the desired feasible stiffness.

(v) *Validation of stiffness model:* The actual stiffness K_{act} is computed by substituting the optimal cable tensions T_{opt} into the stiffness model (21). The error η is defined to evaluate the difference between K_{des} and K_{act},

$$\eta = \frac{||K_{des} - K_{act}||_F}{||K_{des}||_F}, \tag{31}$$

where $|| \cdot ||_F$ represents the *Frobenius norm* of the matrix.

6. Simulation

In order to validate the proposed method, a comprehensive simulation is carried out. The dimension parameters of the 6-CSJM for simulation are given by $l_A = 0.100$ m, $l_B = 0.130$ m, $e_A = 0.005$ m, $e_B = 0.005$ m, $h_A = 0.080$ m, and $h_B = 0.080$ m.

6.1. Simulation Cases

Firstly, we consider two cases of the 6-CSJM with different poses and loads, i.e., Case 1 with desired pose R_{des1} and load M_1, Case 2 with desired pose R_{des2} and load M_2. The desired poses R_{des1} and R_{des2} are given by $\zeta_1 = (0.05, 0.07, 0.03)^T$ and $\zeta_2 = (0.09, 0.14, 0.12)^T$, respectively. The load M_i represents the external moment at pose R_{desi} $(i = 1, 2)$, which are given by $M_1 = (-0.98, 0.48, -0.11)^T$ Nm and $M_2 = (-1.13, -1.59, -0.33)^T$ Nm, respectively.

Since the stiffness of the 6-CSJM is a 3×3 matrix, we employ the determinants of the stiffness matrices to evaluate the ranges of the stiffness. The result is shown in Figure 4, suggesting the ranges of the stiffness of the 6-CSJM are adequate for regulation.
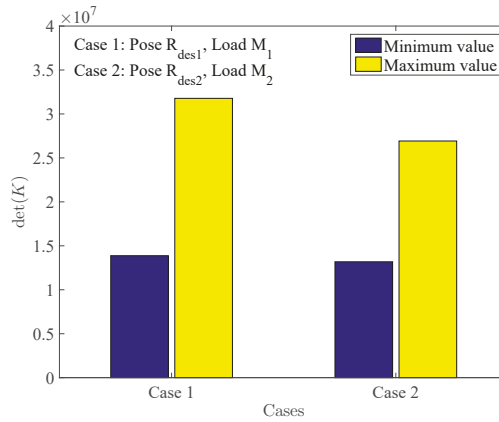
Figure 4. Determinant of the stiffness matrices of the 6-CSJM for the two cases.

Followed by this, we choose two desired feasible stiffness matrices for each of the above two cases and generate four sub-cases, as shown in Table 1, so that we can evaluate the effectiveness of our method for the 6-CSJM at different poses, with different loads and desired stiffness.

Taking Case 1-a as an example, for the position regulation, the desired pose R_{des1} can be realized by adjusting the lengths of Cable 1, 3 and 5, where the lengths of Cable 1, 3 and 5 can be computed according to (9), i.e., $c_1 = 0.17$ m, $c_3 = 0.17$ m and $c_5 = 0.18$ m. For the stiffness regulation, firstly, the structure matrix S for pose R_{des1} is obtained by the definition $S = J^T$

$$S = \begin{pmatrix} 0.05 & 0 & -0.04 & -0.04 & 0 & 0.05 \\ 0.03 & 0.06 & 0.03 & -0.03 & -0.05 & -0.02 \\ -0.02 & 0.02 & -0.02 & 0.02 & -0.02 & 0.02 \end{pmatrix}.$$

Subsequently, according to the proposed method in the prior Section, we obtain the optimal cable tensions $T_{opt} = (42.6, 10.9, 51.4, 57.7, 20.1, 62.2)^T$ N. In the simulation, the corresponding actual stiffness K_{act} is computed by the optimal cable tensions according to the stiffness model (21) and its error with the desired stiffness are listed in Table 1. The simulation of the other cases are conducted in the similar way as Case 1-a. The values of optimal cable tensions for the four sub-cases are shown in Figure 5, which illustrates that they are all in the safe tension zone. The actual stiffness and errors of the four sub-cases are all listed in Table 1.

Table 1. Simulation in four sub-cases with different poses, loads and stiffness.

Case	Pose	Load M	Desired Stiffness K_{des}			Actual Stiffness K_{act}			Error η
Case 1-a	R_{des1}	M_1	385.7	−3.6	−23.2	385.7	−3.6	−23.2	0.001%
			−3.4	354.0	−26.1	−3.4	354.0	−26.1	
			−22.8	−25.5	133.4	−22.7	−25.5	133.4	
Case 1-b	R_{des1}	M_1	434.2	−0.6	−24.1	434.2	−0.6	−24.1	0.001%
			−0.5	416.4	−17.4	−0.5	416.4	−17.4	
			−23.6	−16.8	156.5	−23.6	−16.8	156.4	
Case 2-a	R_{des2}	M_2	411.5	−12.8	−34.0	411.5	−12.8	−34.0	0.001%
			−12.4	344.2	−52.6	−12.4	344.2	−52.6	
			−32.5	−51.9	147.3	−32.5	−51.9	147.3	
Case 2-b	R_{des2}	M_2	347.7	12.4	−54.2	347.7	12.4	−54.2	0.001%
			12.8	353.4	−46.3	12.8	353.4	−46.3	
			−52.6	−45.5	144.6	−52.6	−45.5	144.6	
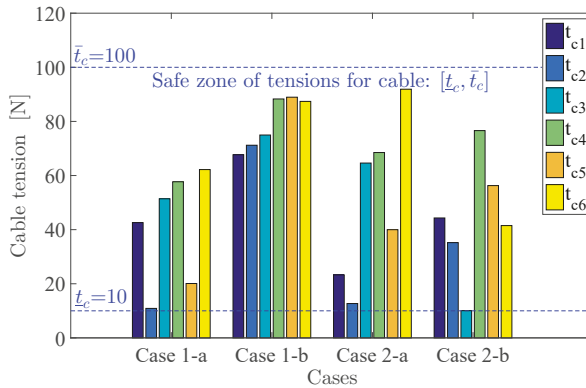
Figure 5. Optimal cable tensions for the four sub-cases, with the safe tension zones of cables $[\underline{t}_c, \bar{t}_c]$.

6.2. Discussion

The stiffness model (21) is too complicated to solve the cable tension distribution from the desired feasible stiffness directly. Hence we formulate the stiffness-oriented cable tension distribution issue as a constrained optimization problem. Most of the previous research works employ the determinant of the stiffness matrix as the cost function, so that the desired stiffness cannot be achieved accurately. In this paper, we employ all entries of the stiffness matrix to construct the cost function, which is more effective and accurate for stiffness regulation. Besides, we reduce the number of the decision variables from 6 to 3, by eliminating the equality constraints of the optimization model. To solve the nonlinear optimization model, we employ the Complex method to obtain the optimal cable tensions for the desired stiffness. In the simulation, the optimal cable tensions are obtained by using the proposed method, under four sub-cases with different poses, loads and desired stiffness matrices. The result shows that the cable tensions are all in the safe tension zones $[\underline{t}_c, \bar{t}_c]$ (Figure 5), and each entry of the actual stiffness matrix K_{act} is very close to that of desired stiffness matrix K_{des} (Table 1). Hence, the presented method is effective to solve the issue of stiffness-oriented cable tension distribution for the 6-CSJM.

7. Conclusions

In this paper, we focus on the issue of stiffness-oriented cable tension distribution for a symmetrical 6-CSJM, which is designed as a fundamental building block for building modular CDMs. For the 6-CSJM, three cables are enough to regulate position by adjusting the cable lengths, and the remaining three cables can be employed to regulate stiffness by adjusting the cable tensions. That means the position and stiffness can be regulated simultaneously. However, it is difficult to solve the cable tensions from the desired stiffness directly. Instead, we formulate this issue as a nonlinear optimization model with equality and inequality constraints. In order to obtain accurate solution for the issue, all the entries of the stiffness matrix is employed to construct the cost function of the optimization model, rather than its determinant. Furthermore, as it is troublesome to handle equality constraints in an non-linear optimization problem, a variable elimination technique is proposed to deal with the three equality constraints in the optimization model and the decision variables are significantly reduced from 6 to 3. The Complex method is imployed to search for the optimal cable tension distribution for a desired stiffness matrix. A comprehensive simulation is conducted to verify the effectiveness of the proposed method, with different poses, loads and desired stiffness. Simulation results illustrate that the proposed method is effective for the 6-CSJM to achieve desired stiffness closely with optimized cable tensions. Besides, the proposed stiffness-oriented tension distribution method can be implemented to not only a 6-CSJM but also a modular CDM to achieve compliant motions in a human-involved environment. In our future work, we would fabricate a prototype of the 6-CSJM as well a modular CDM, and develop an experimental testbed to implement and verify the proposed tension distribution method.

Author Contributions: K.Y. and G.Y. developed the main idea of this paper; S.-L.C. and C.Z. provided technical support in implementing the idea; Y.W. designs part of the CAD model; Z.F., T.Z. and C.W. helped to review and improve the paper.

Conflicts of Interest: The authors declare no conflict of interest.

References

1. Dong, X.; Axinte, D.; Palmer, D.; Cobos, S.; Raffles, M.; Rabani, A.; Kell, J. Development of a slender continuum robotic system for on-wing inspection/repair of gas turbine engines. *Robot. Comput. Integr. Manuf.* **2017**, *44*, 218–229. [CrossRef]
2. Wang, M.; Palmer, D.; Dong, X.; Alatorre, D.; Axinte, D.; Norton, A. Design and Development of a Slender Dual-Structure Continuum Robot for In-Situ Aeroengine Repair. In Proceedings of the IEEE/RSJ International Conference on Intelligent Robots and Systems (IROS), Madrid, Spain, 1–5 October 2018; pp. 5648–5653.
3. Axinte, D.; Dong, X.; Palmer, D.; Rushworth, A.; Guzman, S.C.; Olarra, A.; Arizaga, I.; Gomez-Acedo, E.; Txoperena, K.; Pfeiffer, K.; et al. MiRoR-Miniaturized Robotic Systems for HolisticIn-SituRepair and Maintenance Works in Restrained and Hazardous Environments. *IEEE/ASME Trans. Mechatron.* **2018**, *23*, 978–981. [CrossRef]
4. Wang, H.; Wang, C.; Chen, W.; Liang, X.; Liu, Y. Three-dimensional dynamics for cable-driven soft manipulator. *IEEE/ASME Trans. Mechatron.* **2017**, *22*, 18–28. [CrossRef]
5. Xu, F.; Wang, H.; Au, K.W.S.; Chen, W.; Miao, Y. Underwater dynamic modeling for a cable-driven soft robot arm. *IEEE/ASME Trans. Mechatron.* **2018**, *23*, 2726–2738. [CrossRef]
6. Cui, Z.; Tang, X.; Hou, S.; Sun, H. Research on controllable stiffness of redundant cable-driven parallel robots. *IEEE/ASME Trans. Mechatron.* **2018**, *23*, 2390–2401. [CrossRef]

7. Campeau-Lecours, A.; Foucault, S.; Laliberte, T.; Mayer-St-Onge, B.; Gosselin, C. A cable-suspended intelligent crane assist device for the intuitive manipulation of large payloads. *IEEE/ASME Trans. Mechatron.* **2016**, *21*, 2073–2084. [CrossRef]

8. Dion-Gauvin, P.; Gosselin, C. Dynamic point-to-point trajectory planning of a three-DOF cable-suspended mechanism using the hypocycloid curve. *IEEE/ASME Trans. Mechatron.* **2018**, *23*, 1964–1972. [CrossRef]

9. Wang, H.; Kinugawa, J.; Kosuge, K. Exact kinematic modeling and identification of reconfigurable cable-driven robots with dual-pulley cable guiding mechanisms. *IEEE/ASME Trans. Mechatron.* **2019**, *24*, 774–784. [CrossRef]

10. Kuan, J.; Pasch, K.A.; Herr, H.M. A high-performance cable-drive module for the development of wearable devices. *IEEE/ASME Trans. Mechatron.* **2018**, *23*, 1238–1248. [CrossRef]

11. Thompson, N.; Sinha, A.; Krishnan, G. Characterizing Architectures of Soft Pneumatic Actuators for a Cable-Driven Shoulder Exoskeleton. In Proceedings of the IEEE International Conference on Robotics and Automation (ICRA), Montreal, QC, Canada, 20–24 May 2019; pp. 570–576.

12. Choi, H.; Kang, B.B.; Jung, B.; Cho, K. Exo Wrist: A Soft Tendon Driven Wrist Wearable Robot with Active Anchor for Dart Throwing Motion in Hemiplegic Patients. *IEEE Robot. Autom. Lett.* **2019**. [CrossRef]

13. Hidayah, R.; Chamarthy, S.; Shah, A.; Fitzgerald-Maguire, M.; Agrawal, S.K. Walking With Augmented Reality: A Preliminary Assessment of Visual Feedback with a Cable-Driven Active Leg Exoskeleton (C-ALEX). *IEEE Robot. Autom. Lett.* **2019**, *4*, 3948–3954. [CrossRef]

14. Chen, Q.; Zi, B.; Sun, Z.; Li, Y.; Xu, Q. Design and Development of a New Cable-Driven Parallel Robot for Waist Rehabilitation. *IEEE/ASME Trans. Mechatron.* **2019**, *24*, 1497–1507. [CrossRef]

15. Borgstrom, P.H.; Jordan, B.L.; Sukhatme, G.S.; Batalin, M.A.; Kaiser, W.J. Rapid Computation of Optimally Safe Tension Distributions for Parallel Cable-Driven Robots. *IEEE Trans. Robot.* **2009**, *25*, 1271–1281. [CrossRef]

16. Nakamura, T.; Tanaka, D.; Maeda, H. Joint Stiffness and Position Control of an Artificial Muscle Manipulator for Instantaneous Loads Using a Mechanical Equilibrium Model. *Adv. Robot.* **2011**, *25*, 387–406. [CrossRef]

17. Kajikawa, S.; Ito, T.; Hase, H. Stiffness control of variable stiffness joint using electromyography signals. In Proceedings of the IEEE International Conference on Robotics and Automation (ICRA), Karlsruhe, Germany, 6 May 2013; pp. 4928–4933.

18. Lim, W.B.; Yeo, S.H.; Yang, G.; Chen, I.M. Design and analysis of a cable-driven manipulator with variable stiffness. In Proceedings of the IEEE International Conference on Robotics and Automation (ICRA), Karlsruhe, Germany, 6 May 2013; pp. 4519–4524.

19. Cui, X.; Chen, W.; Jin, X.; Agrawal, S.K. Design of a 7-DOF cable-driven arm exoskeleton (CAREX-7) and a controller for dexterous motion training or assistance. *IEEE/ASME Trans. Mechatron.* **2017**, *22*, 161–172. [CrossRef]

20. Lim, W.B.; Yeo, S.H.; Yang, G.; Mustafa, S.K. Kinematic analysis and design optimization of a cable-driven universal joint module. In Proceedings of the IEEE/ASME International Conference on Advanced Intelligent Mechatronics, Sinagopore, 14–17 July 2009; pp. 1933–1938.

21. Mustafa, S.K.; Song, H.Y.; Cong, B.P.; Yang, G.; Wei, L. A biologically-inspired anthropocentric shoulder joint rehabilitator: workspace analysis and optimization. In Proceedings of the IEEE International Conference on Mechatronics and Automation, Niagara Falls, ON, Canada, 29 July–1 August 2005; pp. 1045–1050.

22. Abbasnejad, G.; Eden, J.; Lau, D. Generalized Ray-Based Lattice Generation and Graph Representation of Wrench-Closure Workspace for Arbitrary Cable-Driven Robots. *IEEE Trans. Robot.* **2019**, *35*, 147–161. [CrossRef]

23. Porto, R.A.; Nageotte, F.; Zanne, P.; Mathelin, M.D. Position control of medical cable-driven flexible instruments by combining machine learning and kinematic analysis. In Proceedings of the International Conference on Robotics and Automation (ICRA), Montreal, QC, Canada, 20–24 May 2019; pp. 7913–7919.

24. Behzadipour, S.; Khajepour, A. Stiffness of cable-based parallel manipulators with application to stability analysis. *J. Mech. Des.* **2006**, *128*, 303–310. [CrossRef]

25. Azadi, M.; Behzadipour, S.; Faulkner, G. Antagonistic variable stiffness elements. *Mech. Mach. Theory* **2009**, *44*, 1746–1758. [CrossRef]

26. Cui, Z.; Tang, X.; Hou, S.; Sun, H.; Wang, D. Calculation and Analysis of Constant Stiffness Space for Redundant Cable-Driven Parallel Robots. *IEEE Access* **2019**, *7*, 75407–75419. [CrossRef]

27. Gosselin, C. On the Determination of the Force Distribution in Overconstrained Cable-driven Parallel Mechanisms. *Meccanica* **2011**, *46*, 3–15. [CrossRef]

28. Cong, B.P.; Song, H.Y.; Yang, G.; Chen, I.M. Workspace analysis of fully restrained cable-driven manipulators. *Robot. Auton. Syst.* **2009**, *57*, 901–912.

29. Oh, S.R.; Agrawal, S.K. Cable Suspended Planar Robots with Redundant Cables: Controllers with Positive Tensions. *IEEE Trans. Robot.* **2005**, *21*, 457–465.

30. You, X.; Bing, L.; Chen, W.; Yu, S. Tension distribution algorithm of a 7-DOF cable-driven robotic arm based on dynamic minimum pre-tightening force. In Proceedings of the IEEE International Conference on Robotics and Biomimetics (ROBIO), Phucket, Thailand, 7–11 December 2011; pp. 715–720.

31. Cote, A.F.; Cardou, P.; Gosselin, C. A tension distribution algorithm for cable-driven parallel robots operating beyond their wrench-feasible workspace. In Proceedings of the International Conference on Control, Automation and Systems, Jeju, Korea, 18–21 October 2017; pp. 68–73.

32. Hassan, M.; Khajepour, A. Optimization of Actuator Forces in Cable-Based Parallel Manipulators Using Convex Analysis. *IEEE Trans. Robot.* **2008**, *24*, 736–740. [CrossRef]

33. Fang, S.; Franitza, D.; Torlo, M.; Bekes, F.; Hiller, M. Motion Control of a Tendon-BasedParallel Manipulator Using Optimal Tension Distribution. *IEEE/ASME Trans. Mechatron.* **2004**, *9*, 561–568. [CrossRef]

34. Bruckmann, T.; Pott, A.; Hiller, M. Calculating force distributions for redundantly actuated tendon-based Stewart platforms. In *Advances in Robot Kinematics*; Springer: Berlin, Germany, 2006; pp. 403–412.

35. Mikelsons, L.; Bruckmann, T.; Hiller, M.; Schramm, D. A real-time capable force calculation algorithm for redundant tendon-based parallel manipulators. In Proceedings of the IEEE International Conference on Robotics and Automation, Pasadena, CA, USA, 19–23 May 2008; pp. 3869–3874.

36. Lim, W.B.; Song, H.Y.; Yang, G. Optimization of Tension Distribution for Cable-Driven Manipulators Using Tension-Level Index. *IEEE/ASME Trans. Mechatron.* **2014**, *19*, 676–683. [CrossRef]

37. Yang, K.; Yang, G.; Wang, J.; Zheng, T.; Wei, Y. Design analysis of a 3-DOF cable-driven variable-stiffness joint module. In Proceedings of the IEEE International Conference on Robotics and Biomimetics (ROBIO), Qingdao, China, 3–7 December 2016; pp. 529–534.

38. Box, M.J. A New Method of Constrained Optimization and a Comparison With Other Methods. *Comput. J.* **1965**, *8*, 42–52. [CrossRef]

39. Yang, G.; Lin, W.; Kurbanhusen, M.S.; Bang, P.C.; Yeo, S.H. Kinematic design of a 7-DOF cable-driven humanoid arm: A solution-in-nature approach. In Proceedings of the EEE/ASME International Conference on Advanced Intelligent Mechatronics (AIM), Monterey, CA, USA, 24–28 July 2005; pp. 444–449.

Routing for Hazardous Materials Transportation in Urban Areas

Lukai Zhang [1], Xuesong Feng [1,*], Yan Yang [2] and Chuanchen Ding [1]

[1]   School of Traffic and Transportation, Beijing Jiaotong University, No.3 Shangyuancun, Haidian District, Beijing 100044, China

[2]   Guangxi Traffic Technician College, No.9 Yongwu Road, Nanning 530001, China

*   Correspondence: xsfeng@bjtu.edu.cn; Tel.: +86-1860-024-6488

Abstract: Hazardous materials (HAZMAT) are important for daily production in cities, which usually have a high population. To avoid the threat to public safety and security, the routes for HAZMAT transportation should be planned legitimately by mitigating the maximum risk to population centers. For the objective of min-max local risk in urban areas, this study has newly proposed an optimization model where the service of a link for HAZMAT transportation was taken as the key decision variable. Correspondingly, the symmetric problem of min-max optimization takes significant meanings. Moreover, in consideration of the work load of solving the model under a lot of decision variables, a heuristic algorithm was developed to obtain an optimal solution. Thereafter, a case study was made to test the proposed model and algorithm, and the results were compared with those generated by deterministic solving approaches. In addition, this research is able to be an effective reference for authorities on the management of HAZMAT transportation in urban areas.

1. Introduction

Hazardous materials (HAZMAT) are important for the daily production of cities, while the undesirable harmfulness they represent cannot be neglected. Many incidents of HAZMAT contamination have occurred during the processes of transportation, leading to serious consequences to the society. According to the statistics of the US Department of Transportation [1], there were 140,742 HAZMAT transportation incidents on roads in the decade 2004–2013. Hence, it is rather essential to mitigate risk in the process of HAZMAT transportation, especially for urban areas with many population centers. These centers include schools, hospitals, resident communities, and so on. For a HAZMAT transportation route, the risk to population centers along the way should be reduced as much as possible. Hence, it is necessary to solve the routing problem using accurate mathematical methods in which optimization approaches take the majority of research field.

In fact, there have been quite a few studies on routing for HAZMAT transportation by different modes. For the design of HAZMAT transportation networks, Kara and Verter proposed a linear integer bi-level programming model that could be transformed to a single mixed integer form by Kuhn-Tucker constraints [2]. For the mitigation of global risk, Erkut and Alp proposed a spanning tree to cover the large gathering area [3]. In a bi-level programming model solved by a heuristic algorithm, two optimization objectives were risk and transit cost [4]. Moreover, a path-based approach for HAZMAT transport network design was proposed by Verter and Kara [5]. Bianco et al. studied a bi-level programming model, in which the upper level was to minimize the maximum risk among certain links and the lower level was minimizing the total risk [6]. Xie et al. proposed the multi-modal HAZMAT routing problem based on an integrated model consisting of practical constraints [7].

Furthermore, a game-theoretic approach for regulating HAZMAT transportation was developed [8]. Fan et al. made an urban HAZMAT transportation model with road closure consideration to deal with traffic restrictions [9]. Bronfman et al. developed the max-min HAZMAT routing problem to ensure security along transport routes [10].

In addition, there has been some research on transportation network optimization by economic measures, such as studies on social welfare and toll policies [11–13]. To facilitate capacity planning, assessment, and querying activities in multi-modal HAZMAT transportation systems, Bevrani et al. developed a comprehensive linear programming model that includes congestion functions, analytical, structural and parametric changes [14]. Similarly, an improved multi-commodity network flow (MCNF) model was introduced to holistically assess a multi modal transportation system and to identify the optimal flows achievable [15]. Taking uncertainty scenarios into consideration, a reliable multi-modal multi-commodity model was made by Mohammadi et al. [16]. Taslimi et al. designed a comprehensive modelling framework for HAZMAT transport network design, HAZMAT response team location and equity of risk [1]. Moreover, Hosseini and Verma proposed a Value-at-Risk approach to routing rail HAZMAT shipments [17]. Fontaine and Minner introduced the method of Benders decomposition to solve complicated HAZMAT transport network design problems [18]. To address the impact of time windows and fuzzy demands on route selection, Fazayeli et al. presented a two-part genetic algorithm to obtain the optimal scheme [19]. Ghaderi and Burdett developed an integrated location and routing approach for transporting hazardous materials in a bi-modal transportation network with stochastic restrictions on reliability [20]. Jabbarzadeh et al. introduced an optimization approach to planning rail HAZMAT shipments in the presence of random disruptions [21]. To deal with traffic restriction constraints in HAZMAT transportation networks, Hu et al. made a multi-objective location-routing model for hazardous materials logistics [22].

These studies involve various kinds of optimization objectives and decision measures. However, there has not been a study that specializes in the problem of total risk under the condition of maximum local risk in urban areas. Furthermore, the most closely related work with routing for HAZMAT transportation in cities was performed by Bronfman et al., who focused on a single transportation route for HAZMAT and the maximum distance for security [10]. In light of the demonstrated advantage of the minimum local consequence model over previous catastrophic avoidance techniques, here we make the first attempt to develop a method for minimizing the maximum local risk framework for urban road HAZMAT shipments. It is important that the proposed framework is distinct from that in Bronfman et al. in the following ways: 1) characteristics of risk criteria—for example, affected population due to HAZMAT release in transportation incidents; 2) compared with single route planning, the application of multiple shipments with various origin-destination pairs is a more realistic scenario; and 3) for an optimal heuristic algorithm used for large real instances, it is necessary to incorporate iterative characteristics in computation. Thereafter, this paper will propose an optimization method where all transportation routes of HAZMAT were considered and the maximum local risk to population centers was mitigated. Hence, it is necessary to make comprehensive analysis for the symmetric problem of min-max optimization. The remaining parts of this paper are organized as follows. In Section 2, a linear integer optimization model is established. Moreover, the corresponding heuristic algorithm for the proposed model is made in Section 3. Furthermore, Section 4 describes a case study. Finally, Section 5 provides the conclusions of this study and discusses future research issues.

2. An Optimization Model

In the routing for HAZMAT transportation, all routes should be planned by the authority that focuses on the risk in urban areas. For such a practical problem, comprehensive factors are involved under the constraints of application. Hence, some necessary hypotheses should be presented before the description of the optimization model.

2.1. Problem Hypotheses

In this section, the relevant factors and conditions were assumed to facilitate modelling analysis and quantitative research. In practical applications such as decision support, this method can be further extended by combining specific limited factors to ensure the accuracy and universality of basic theories.

Hypothesis 1: *Time dimension of the problem. This optimization problem is assumed to be static, and the time-dependent conditions are simplified. For a purpose of reasonable abstract definition, the values of dynamic parameters are assumed to be averaged, for example, affected population due to HAZMAT shipments. If necessary, the basic conditions are able to be expanded for more complicated planning of HAZMAT transportation.*

Hypothesis 2: *Connectivity of the transportation network. In this study, the basic road network is a completely connected graph. For any shipment of HAZMAT, there is at least one path from the origin to the destination (OD pair).*

Hypothesis 3: *Impact of the geographic shape. All population centers are assumed to be points in the calculation while the corresponding sizes are ignored. Moreover, the distance from a population center to a transport link is assumed as the Euclidean distance between the center point and the closest point on the link.*

Hypothesis 4: *Impact of incident possibility. It is assumed that all vehicles are in stable condition and the probabilities of incident are unknown in the transportation network. Hence, the risk caused by HAZMAT only consists of threatened consequences to population centers.*

Hypothesis 5: *Traffic conditions in the network. From a perspective of macro modelling, this study focuses on the optimization effect of the relevant network characteristics. For the incident risk, the traffic conditions are assumed to be optimistic. Furthermore, the probability of incident is not incorporated in the risk assessment of this study. Moreover, the traffic conditions can be analyzed further in future studies with perspectives of micro modelling.*

2.2. Model Establishment

$$\min Z = \sum_{s \in S} R^s. \tag{1}$$

where,

S: Set of HAZMAT shipments, indexed by s, and the number of shipments is λ.
R^s: Auxiliary decision variable, maximum local risk caused by the closest link of shipment s to population centers, unit: persons per kilometer.

$$\sum_{(i,j) \in A} n^s \rho^c (1/d_{cs}^{ij}) v_{cs}^{ij} \leq R^s \quad \forall c \in N^c, s \in S. \tag{2}$$

where,

n^s: Transportation demand of shipment s, measured by the number of standardized vehicles;
i, j: Nodes of road transportation network in the urban area, and the number of nodes is ε;
A: Set of links of road transportation network in the urban area, $(i, j) \in A$, and the number of links is φ;
N^c: Set of population centers, indexed by c;
ρ^c: Population quantity of center c, unit: persons, and the number of centers is μ;

d_{cs}^{ij}: Euclidean distance between center c and its closest point on link (i, j) of shipment s, illustrated in Figure 1, unit: kilometers;

v_{cs}^{ij}: Decision variable, which is equal to 1 if link (i, j) used for HAZMAT shipment s is the closest link to c, 0 otherwise.
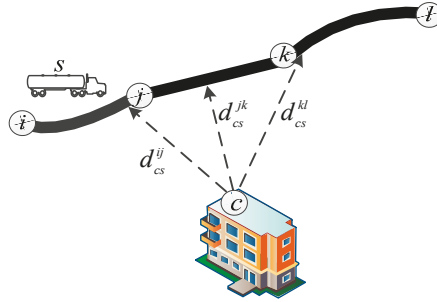
Figure 1. Illustration for the closest distance between a population center and a link.

$$v_{cs}^{ij} \leq x_s^{ij} \quad \forall \, (i, j) \in A, \, c \in N^c, \, s \in S. \tag{3}$$

where,

x_s^{ij}: Decision variable, which is equal to 1 if link (i, j) is used for HAZMAT shipment s, 0 otherwise.

$$\sum_{(i,j)\in A} v_{cs}^{ij} \leq 1 \quad \forall \, c \in N^c, \, s \in S. \tag{4}$$

where,

v_{cs}^{ij}: This notation has been explained in Formula (2).

$$x_s^{ij} - \sum_{(m,n)\in A \mid d_{cs}^{mn} \leq d_{cs}^{ij}} v_{cs}^{mn} \leq v_{cs}^{ij} \quad \forall \, (i, j) \in A, \, c \in N^c, \, s \in S. \tag{5}$$

where,

v_{cs}^{mn}: Referring to the definition of v_{cs}^{ij};

d_{cs}^{mn}: Referring to the definition of d_{cs}^{ij}.

Formula (6) offers the constraint of transit flow conservation for a link, which divides the nodes into three types. Furthermore, Formula (7) delimits the auxiliary decision variable, and the maximum local risk caused by the closest link of a shipment to a population center is nonnegative. Finally, it is necessary to describe the binary constraints of decision variables in Formula (8) and Formula (9).

$$\sum_{(i,j)\in A} x_s^{ij} - \sum_{(j,i)\in A} x_s^{ji} = \begin{cases} 1 & \text{if } i = o(s) \\ -1 & \text{if } i = d(s) \\ 0 & \text{otherwise} \end{cases} \quad \forall \, i \in N, \, s \in S. \tag{6}$$

where,

$o(s)$: Origin of HAZMAT shipment s;

$d(s)$: Destination of HAZMAT shipment s.

$$R^s \geq 0. \tag{7}$$

where,

R^s: Nonnegative constraint for auxiliary decision.

$$x_s^{ij} \in \{0, 1\} \quad \forall\ (i, j) \in A,\ s \in S. \tag{8}$$

where,

x_s^{ij}:   Constrained to be binary.

$$v_{cs}^{ij} \in \{0, 1\} \quad \forall\ (i, j) \in A,\ c \in N^c,\ s \in S. \tag{9}$$

where,

v_{cs}^{ij}:   Constrained to be binary.

3. Algorithm Design

Although there are continuous variables (i.e., R^s for all shipments) in the proposed model, they only play the role of auxiliary decision variables. This problem is a linear integer program which can be solved by common techniques theoretically, and it does not belong to the NP-hard class. However, the complexity of the problem not only depends on the types of variables, but also lies with the numbers of variables and constraints. From the formulations in Section 2, it is able to be found that there are $\lambda + \lambda \varphi \mu + \lambda \varphi$ decision variables and $2\lambda \mu + 2\lambda \varphi \mu + \lambda \varepsilon + \lambda$ constraints. Thereafter, the work load of computation is rather heavy, even for small instances in simple urban areas. Moreover, the complexity of calculation leads to the limited application in practical operation, although the linear model with integer variables could be theoretically solved by commercial software such as CPLEX [1]. Hence, there is a need to explore more effective solving approaches, and feasible heuristic algorithms are also able to be considered in depth [10]. In addition, this study has developed a heuristic calculation under principles of minimizing the maximum local risk for all HAZMAT shipments in the urban area.

The main concept behind this heuristic algorithm is that a risk radius can be used to control the searching step for an optimal HAZMAT shipment route. Moreover, the structure of the road network is reconstructed in iterations where the undesirable links are eliminated one after one. Finally, an optimal HAZMAT shipment route would be determined in the unchanged network. The item $\omega_{cs}^{ij} = n^s \rho^c (1/d_{cs}^{ij})$ is denoted as the equivalent local risk under the inverse impact of distance. For a certain type of HAZMAT transported in urban areas, when there is a disruption in the shipment s, much of the consequence would be within the zone with a certain radius γ^s illustrated in Figure 2. Thus, the valid local risk is represented as $\omega_{cs}^{ij} = n^s \rho^c (1/d_{cs}^{ij}) \big| d_{cs}^{ij} \leq \gamma^s$. Furthermore, the maximum local risk along the route of a shipment is $\omega_s^{ij} = \max_{c \in N^c} \omega_{cs}^{ij} \big| d_{cs}^{ij} \leq \gamma^s$.
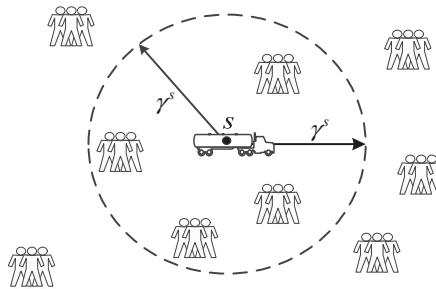
Figure 2. Illustration for consequence scope within a radius.

In addition, the solution of routing for HAZMAT shipments is to search for feasible route schemes when the objective and constraints are taken into consideration. Thereafter, for a HAZMAT shipment s, F_s^t is denoted as the t_{th} candidate route in the transportation network. Thus, the maximum local risk to population centers along route F_s^t is $\omega^{F_s^t} = \min\limits_{(i,j) \in F_s^t} \omega_s^{ij}$, and the calculation is in accordance with the optimization objective of minimizing the maximum local risk for all shipments. The flow chart of the heuristic algorithm is illustrated in Figure 3, and the corresponding detailed steps are as follows.
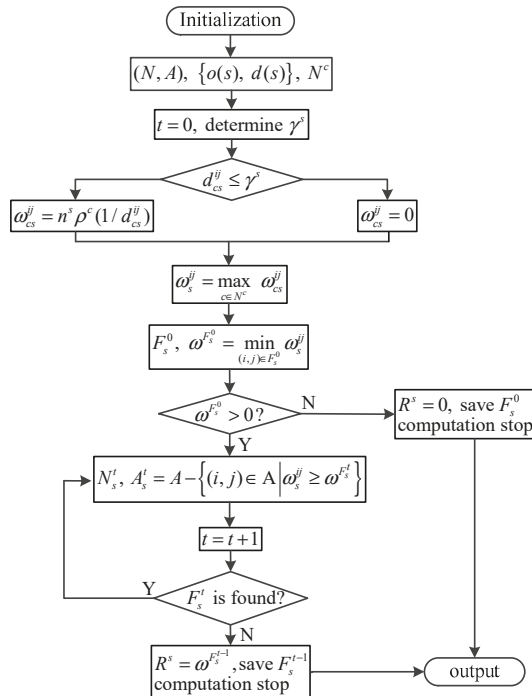
Figure 3. Flow chart of the heuristic algorithm.

Step 1: Initialization. List the structure of the transportation network (N, A) including nodes and links, OD pairs for HAZMAT shipments and population centers in the area.

  Step 1-1: Set the counter $t = 0$, and determine the risk radius γ^s according to the type of HAZMAT for all shipments.

  Step 1-2: $\forall\, s \in S,\ c \in N^c,\ (i,j) \in A \big| d_{cs}^{ij} \leq \gamma^s$, compute the local risk along the route of shipment s as ω_{cs}^{ij}. While $\forall\, s \in S,\ c \in N^c,\ (i,j) \in A \big| d_{cs}^{ij} > \gamma^s$, set $\omega_{cs}^{ij} = 0$.

  Step 1-3: For all $s \in S,\ (i,j) \in A$ in the HAZMAT transportation network, compute the maximum local risk along the route of shipment s as ω_s^{ij}.

Step 2: Initial Route. For all $s \in S$, the Dijkstra algorithm is used to search for a shortest route between $o(s)$ and $d(s)$ [23], and the route is denoted as F_s^0 for shipment s. Thereafter, the maximum local risk to population centers along route F_s^0 is calculated as $\omega^{F_s^0}$.

  Step 2-1: If $\omega^{F_s^0} = 0$, F_s^0 is an optimal solution route for shipment s, and $R^s = 0$. The computation for shipment s stops, turn to next shipment until all shipments are checked.

Step 2-2: If $\omega^{F_s^0} > 0$, there is possible to search for a better route. For the corresponding $s \in S$ turn to Step 3 for computation.

Step 3: Route update. The initial route is improved by the following sub-steps.

Step 3-1: $\forall s \in S$, the set of links is obtained as $A_s^t = A - \left\{ (i, j) \in A \middle| \omega_s^{ij} \geq \omega^{F_s^t} \right\}$. When $t = 0$, $A_s^{t-1} = A$. Denote N_s^t as the set of relevant nodes, and the candidate graph in t_{th} iteration for shipment s is $\left(N_s^t, A_s^t \right)$. Thereafter, the counter $t = t + 1$.

Step 3-2: $\forall s \in S$, search for a feasible route F_s^t over $\left(N_s^t, A_s^t \right)$ between $o(s)$ and $d(s)$.

Step 3-2-1: If no feasible route F_s^t is found, the candidate graph in t_{th} iteration for shipment s is disconnected, F_s^{t-1} is an optimal solution route for shipment s, and $R^s = \omega^{F_s^{t-1}}$. The computation for shipment s stops, turn to next shipment until all shipments are checked.

Step 3-2-2: If a feasible route F_s^t is found, turn to Step 3-1.

Step 4: Scheme check. In the completely connected transportation network, any shipment is able to be assigned an optimal route, and all optimal routes are the final output.

It is worth pointing out that the calculation process in the algorithm is convergent, as all steps would be finished in finite iterations. As a convergence principle, the maximum local risk to population centers along a route should be under the condition $\omega_s^{ij} \geq \omega^{F_s^t}$. Hence, no matter how complicated the transportation network is, the optimal route is feasible when the network is completely connected. In addition, the application of the shortest route ensures the uniqueness of a solution, avoiding "multi-route" generation in the iterations [24].

4. Case Study

To test the effectiveness of the proposed model and algorithm, the local area of a city in North China was taken as the research subject. In the studied area, there were 337 nodes (numbered from N1 to N337) and 614 directed links (numbered from L1 to L614) to make up the transportation network. Moreover, 16 population centers (including universities, large residence communities and railway stations, numbered from C1 to C16) are regulated to be protected from undesired risk due to HAZMAT transportation, and the relevant population values are shown in Table 1. Furthermore, there were 12 shipments (numbered from S1 to S12) with different transportation demand and OD pairs listed in Table 2. The original assignment of computational data was taken as a reference for further calculation and analysis.

The experimental results were organized into two parts. The first part shows analysis of a brief comparison between the deterministic solving method by commercial software and the proposed heuristic algorithm. The second part shows detailed sensitivity analysis with respect to the value of risk radius due to HAZMAT transportation. In addition, the proposed model is optimally solved by CPLEX 12.8 solver, and the heuristic algorithm is coded and implemented in MATLAB R2018b. All solving processes were based on a PC with 4 GB of RAM. Thereafter, the main features of the proposed model and algorithm were as follows.

Table 1. Population centers in the case network.

Center	C1	C2	C3	C4	C5	C6	C7	C8
Population	4270	4910	5180	7100	6850	5190	6230	10020
Center	**C9**	**C10**	**C11**	**C12**	**C13**	**C14**	**C15**	**C16**
Population	9470	5960	8030	12030	7310	7210	5540	14640

Table 2. Shipments in the case network.

Shipment	S1	S2	S3	S4	S5	S6
OD pair	N1-N226	N2-N305	N3-N271	N4-N225	N5-N193	N6-N236
Demand	10	15	20	25	10	15
Shipment	S7	S8	S9	S10	S11	S12
OD pair	N7-N164	N8-N322	N9-N150	N10-N297	N11-N148	N12-N249
Demand	20	25	10	15	20	25

Figure 4 shows the convergence of a computation process by the heuristic algorithm where the risk radius was set as 1.0 km. As an illustration of the changing line, the objective remains unchanged after certain descending iterations, indicating that the computation was convergent. Furthermore, for the problem of searching for feasible routes in a connected graph, the number of links to be eliminated was finite, and the links had to be eliminated at each step [10]. The computation converged on the optimum solution, because it either finds a route with $R^s = 0$, or there is no best feasible solution than the last route found right before the problem becomes unsolvable. Moreover, the computation was polynomial, as at every iteration the Dijkstra algorithm for the shortest route was used, which is polynomial. Hence, the maximum number of iterations is the number of links, that is, 337 in the case network.
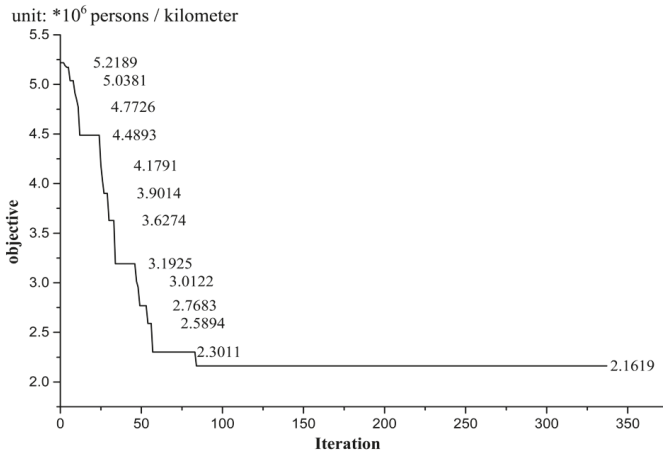
Figure 4. The convergence of a computation process by the heuristic algorithm.

Illustrated in Table 3, three indices were calculated for the comparison between deterministic solving and the heuristic algorithm. To highlight the different impacts on computation workload, three groups of shipments were taken into consideration. For the comparison of optimal objective, the results by deterministic solving were better than the ones generated by the proposed heuristic algorithm. However, the gap of calculated results tended to be smaller when the shipments are increased. For the maximum risk of a route, the difference between deterministic solving and the heuristic algorithm was not obvious. For the maximum risk with shipments S1–S12, there was no gap between the two solving methods. Furthermore, it was clear that the heuristic algorithm takes less run time for computation. In addition, the more the shipments were, the long run time was. On the whole, the deterministic solving by CPLEX 12.8 achieved better solutions than the proposed heuristic algorithm, but the gap was reduced when the shipping demand increased. Meanwhile, the proposed heuristic algorithm has an advantage on run time compared to the deterministic solving, and the difference was rather obvious when there are more shipments.

Table 3. Comparison between deterministic solving and the heuristic algorithm. (Risk radius = 1.0 km).

Index	Shipment Set	Deterministic Solving by CPLEX 12.8	The Proposed Heuristic Algorithm	Gap
Optimal objective (persons/km)	S1–S4	0.6335×10^6	0.7156×10^6	12.97%
	S1–S8	1.3371×10^6	1.5075×10^6	12.74%
	S1–S12	$1,9268 \times 10^6$	2.1619×10^6	12.20%
Max R^s (persons/km)	S1–S4	2.5083×10^5	2.6241×10^5	4.62%
	S1–S8	2.5083×10^5	2.6241×10^5	4.62%
	S1–S12	2.7358×10^5	2.7358×10^5	0.00%
Run time (s)	S1–S4	1.8729×10^4	0.8461×10^4	121.36%
	S1–S8	3.6114×10^4	1.3715×10^4	163.32%
	S1–S12	5.3782×10^4	1.9295×10^4	178.73%

As shown in Table 4, the risk radius γ^s takes significant impact on the calculated results by the proposed heuristic algorithm. From the general trend, both the optimal objective and the maximum local risk decreased with the increasing risk radius. The results indicate that when the value of risk radius was very large, more population centers were likely to be influenced by the risk due to HAZMAT transportation, thus the relevant routes of shipments should be planned away from the population centers as far as possible. Thereafter, the corresponding results would be better than the ones with smaller risk radiuses. However, when the risk radius was $\gamma^s > 2.5$, the results remained unchanged, as there was no feasibility for planning more optimal routes. In addition, the following analysis will focus on the impact of risk radius on computation efficiency.

The illustration in Figure 5 shows the impact of risk radius on computation efficiency, including run time and critical iteration in the computing process. It can be inferred that the computation efficiency decreased with the increasing risk radius, as the difficulty of searching for optimal routes was raised. Moreover, the risk radius for calculation should be determined in accordance with practical demands. Furthermore, it is worth pointing out that computational experiments with parallel values of risk radius are able to be taken into consideration.

Table 4. Impact of risk radius on optimal indices (Shipment set S1–S12).

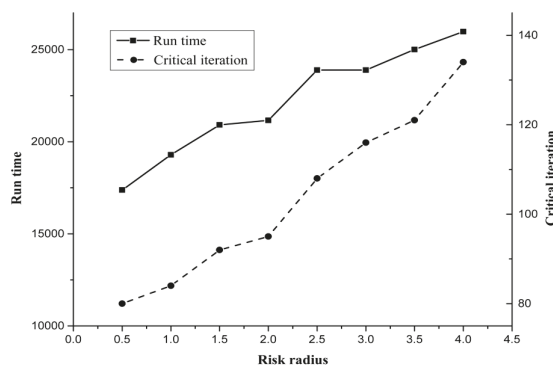| Risk Radius (km)	Optimal Objective (persons/km)	Max R^s (persons/km)
0.5	2.2348×10^6	3.0155×10^5
1.0	2.1619×10^6	2.7358×10^5
1.5	2.0862×10^6	2.5183×10^5
2.0	2.0047×10^6	2.4924×10^5
2.5	1.9490×10^6	2.4418×10^5
3.0	1.9205×10^6	2.3561×10^5
3.5	1.9205×10^6	2.3561×10^5
4.0	1.9205×10^6	2.3561×10^5

Figure 5. Impact of risk radius on computation efficiency (Shipment set S1–S12).

5. Conclusions

For the problem of routing for HAZMAT shipments in urban areas, this study develops an optimization model with a heuristic algorithm. To ensure the safety and security of population centers, the maximum risk due to HAZMAT transportation should be mitigated as much as possible. Thus, the objective of min-max local risk is proposed, and the service of a link for HAZMAT transportation is taken as the key decision variable. Moreover, in consideration of the work load of solving the model under a lot of decision variables, a heuristic algorithm was designed to obtain an optimal solution. Thereafter, a case study was made to testify the proposed model and algorithm, and the results were compared with the ones by deterministic solving approaches. This paper makes a three-fold contribution: 1) this is the first work that incorporates the characteristics of maximum local risk to population centers, and then outlines a min-max optimization model to mitigate risk from road HAZMAT shipments in urban areas; 2) this is the only effort that proposes multiple shipments with multiple routes to plan urban HAZMAT transportation using the optimal configuration of avoiding local consequence; and 3) this is the only work that demonstrates that the proposed methodology not only facilitates single population-averse routing of urban HAZMAT shipments, but can also deal with more kinds of risk based on the criteria preference (or tolerance) of the decision makers. In addition, this research is able to be effective reference for authorities on the management of HAZMAT transportation in urban areas.

In this research, more kinds of deterministic solving approaches are able to be considered. Furthermore, the proposed modelling method has not achieved the impact of some factors, such as vehicle type and geographic shape of population centers. This situation should be improved in future studies. Moreover, applying the emergency response is worthy of exploration, including relevant location and service assignment. In addition, incident probabilities could be analyzed in depth, in order to describe the problem comprehensively.

Author Contributions: Data curation, X.F.; Formal analysis, C.D.; Methodology, L.Z.; Resources, X.F.; Writing—original draft, L.Z.; Writing—review & editing, Y.Y.

References

1. Taslimi, M.; Batta, R.; Kwon, C. A comprehensive modeling framework for hazmat network design, hazmat response team location, and equity of risk. *Comput. Oper. Res.* **2017**, *79*, 119–130. [CrossRef]
2. Kara, B.Y.; Verter, V. Designing a road network for hazardous materials transportation. *Transp. Sci.* **2004**, *38*, 188–196. [CrossRef]
3. Erkut, E.; Alp, O. Designing a road network for hazardous materials shipments. *Comput. Oper. Res.* **2007**, *34*, 1389–1405. [CrossRef]
4. Erkut, E.; Gzara, F. Solving the HAZMAT transportation network design problem. *Comput. Oper. Res.* **2008**, *35*, 2234–2247. [CrossRef]
5. Verter, V.; Kara, B.Y. A path-based approach for hazmat transport network design. *Manag. Sci.* **2008**, *54*, 29–40. [CrossRef]
6. Bianco, L.; Caramia, M.; Giordani, S. A bi-level flow model for HAZMAT transportation network design. *Transp. Res. Part C Emerg. Technol.* **2009**, *17*, 175–196. [CrossRef]
7. Xie, Y.; Lu, W.; Wang, W.; Quadrifoglio, L. A multimodal location and routing model for hazardous materials transportation. *J. Hazard. Mater.* **2012**, *227*, 135–141. [CrossRef]
8. Bianco, L.; Caramia, M.; Giordani, S.; Piccialli, V. A game-theoretic approach for regulating hazmat transportation. *Transp. Sci.* **2016**, *50*, 424–438. [CrossRef]
9. Fan, T.; Chiang, W.C.; Russell, R. Modeling urban hazmat transportation with road closure consideration. *Transp. Res. Part D Transp. Environ.* **2015**, *35*, 104–115. [CrossRef]

10. Bronfman, A.; Marianov, V.; Paredes-Belmar, G.; Lüer-Villagra, A. The maximin HAZMAT routing problem. *Eur. J. Oper. Res.* **2015**, *241*, 15–27. [CrossRef]

11. Brotcorne, L.; Labbe, M.; Marcotte, P.; Savard, G. Joint design and pricing on a network. *Oper. Res.* **2008**, *56*, 1104–1115. [CrossRef]

12. Marcotte, P.; Mercier, A.; Savard, G.; Verter, V. Toll Policies for Mitigating Hazardous Materials Transport Risk. *Transp. Sci.* **2009**, *43*, 228–243. [CrossRef]

13. Li, T.; Sun, H.; Wu, J.; Ge, Y. Optimal toll of new highway in the equilibrium framework of heterogeneous households' residential location choice. *Transp. Res. Part A Policy Pract.* **2017**, *105*, 123–137. [CrossRef]

14. Bevrani, B.; Burdett, R.L.; Bhaskar, A.; Yarlagadda, P.K.D.V. A capacity assessment approach for multi-modal transportation systems. *Eur. J. Oper. Res.* **2017**, *263*, 864–878. [CrossRef]

15. Bevrani, B.; Burdett, R.L.; Bhaskar, A.; Yarlagadda, P.K.D.V. A multi commodity flow model incorporating flow reduction functions. *Flex. Serv. Manuf. J.* **2019**, in press. [CrossRef]

16. Mohammadi, M.; Jula, P.; Tavakkoli-Moghaddam, R. Design of a reliable multi-modal multi-commodity model for hazardous materials transportation under uncertainty. *Eur. J. Oper. Res.* **2017**, *257*, 792–809. [CrossRef]

17. Hosseini, S.D.; Verma, M. A Value-at-Risk (VAR) approach to routing rail hazmat shipments. *Transp. Res. Part D Transp. Environ.* **2017**, *54*, 191–211. [CrossRef]

18. Fontaine, P.; Minner, S. Benders decomposition for the Hazmat Transport Network Design Problem. *Eur. J. Oper. Res.* **2018**, *267*, 996–1002. [CrossRef]

19. Fazayeli, S.; Eydi, A.; Kamalabadi, I.N. Location-routing problem in multimodal transportation network with time windows and fuzzy demands: Presenting a two-part genetic algorithm. *Comput. Ind. Eng.* **2018**, *119*, 233–246. [CrossRef]

20. Ghaderi, A.; Burdett, R.L. An integrated location and routing approach for transporting hazardous materials in a bi-modal transportation network. *Transp. Res. Part E Logist. Transp. Rev.* **2019**, *127*, 49–65. [CrossRef]

21. Jabbarzadeh, A.; Azad, N.; Verma, M. An optimization approach to planning rail hazmat shipments in the presence of random disruptions. *Omega* **2019**. [CrossRef]

22. Hu, H.; Li, X.; Zhang, Y.; Shang, C.; Zhang, S. Multi-objective location-routing model for hazardous material logistics with traffic restriction constraint in inter-city roads. *Comput. Ind. Eng.* **2019**, *128*, 861–876. [CrossRef]

23. Zhang, W.; Jiang, C. Optimization studies on an improved Dijkstra algorithm. In Proceedings of the 3rd International Conference on Information Technology and Science Management (ICITST 2011), Abu Dabi, UAE, 11–14 December 2011; pp. 2918–2921.

24. Feng, X.; Zhu, X.; Qian, X.; Jie, Y.; Ma, F.; Niu, X. A new transit network design study in consideration of transfer time composition. *Transp. Res. Part D Transp. Environ.* **2019**, *66*, 85–94. [CrossRef]

High-Precision Authentication Scheme Based on Matrix Encoding for AMBTC-Compressed Images

Guo-Dong Su [1,2,3], Chin-Chen Chang [2] and Chia-Chen Lin [4,*]

1   The School of Electronic and Information Engineering, Fuqing Branch of Fujian Normal University,
    Fuzhou 350300, China
2   Department of Information Engineering and Computer Science, Feng Chia University,
    Taichung 40724, Taiwan
3   Engineering Research Center for ICH Digitalization and Multi-Source Information Fusion, Fujian University,
    Fuzhou 350300, China
4   Department of Computer Science and Information Management, Providence University,
    Taichung 433, Taiwan
*   Correspondence: mhlin3@pu.edu.tw

Abstract: In this paper, a high-precision image authentication scheme for absolute moment block truncation coding (AMBTC)-compressed images is presented. For each block, two sub-bitmaps are conducted using the symmetrical separation, and the six-bit authentication code is symmetrically assigned to two sub-codes, which is virtually embedded into sub-bitmaps using the matrix encoding later. To overcome distortion caused by modifications to the bitmap, the corresponding to-be-flipped bit-location information is recorded instead of flipping these bits of the bitmap directly. Then, the bit-location information is inserted into quantization levels based on adjusted quantization level matching. In contrast to previous studies, the proposed scheme offers a significantly improved tampering detection ability, especially in the first hierarchical tampering detection without remediation measures, with an average tampering detection rate of up to 98.55%. Experimental results show that our approach provides a more stable and reliable tampering detection performance and sustains an acceptable visual quality.

Keywords: image authentication; AMBTC; matrix encoding; adjusted quantization levels matching

1. Introduction

Recently, as engineering technology has rapidly developed, the performance of computers has become increasingly stronger in terms of computing ability, storage capacity, etc. At the same time, the higher transmission capacity offered by wired/wireless networks allows users to share data anywhere, anytime. Obviously, digital images can be conveniently and transparently transmitted via the Internet; however, the Internet cannot always promise reliable and secure transmission, since it is openly accessible. In other words, it is easy for an intruder to intercept data transmitted over the Internet and then corrupt them, intentionally or non-intentionally. For example, attackers can insert vulgar words into a digital image in an imperceptible manner. Such malicious behavior presents a huge challenge to the security, usability, and integrity of personal information. Therefore, it is urgent to protect the integrity and verifiability of the digital image. Under this scenario, it is expected that a technique is provided to solve this problem.

Researchers have conducted a series of scientific studies on image authentication. Roughly, authentication methods can be classified into two categories: Digital signature-based methods [1–4] and digital watermark-based methods [5–31]. Generally, the digital signature-based method performs the encryption of the hashed results of the features of the image using a private key to form a

unique signature, which will be used later for authentication. The process of authentication can be implemented by comparing the hashing result of the image under question and the original hashed version, which can be decrypted from the signature using an associated public key. By this way, the digital signature-based method performs well on image authentication because it is extremely sensitive to any kind of modification to the image, even if only one bit has been modified. Sometimes, the digital image may be allowed a little distortion in some applications, as long as the tamper regions can be localized precisely. Unfortunately, the digital signature-based method is not workable under this scenario.

The digital watermark-based method imperceptibly embeds relevant or irrelevant information called the authentication code (AC) into a digital image. The digital watermark-based method includes three categories: Fragile, semi-fragile, and robust watermarking. Of these, fragile watermarking embeds the authentication code into the cover image and makes it very sensitive to the modification of the image so that it can be used to verify its authenticity. In the authentication phase, receiver(s) can judge whether the image has been tampered with by comparing the extracted and recalculated authentication code. If they are the same, the received image has not been tampered with, and vice versa.

In recent decades, several forms of fragile watermarking-based image authentication have been proposed. An early fragile watermarking-based method was proposed by [5], where the authentication code is generated from the parity check of the pixel value and embedded into the least significant bit (LSB) of the original image. A possibility of false judgement exists since the tampered 1 LSB could be the same as the computed parity check value of the tampered 7 most significant bits (MSBs). Other fragile watermarking methods based on cryptographic theory were presented by [6–8]. Here, authentication codes are derived from a hashing function with various inputs, such as the image content, image index, block index, and pseudo-random number. These methods offer acceptable tampering detection performance. However, some of them could not withstand a vector quantization attack [9] or the tampering coincidence problem [10]. To overcome those problems, other fragile watermarking strategy-based block mappings were proposed by [11–16]. In these schemes, the original image is divided into non-overlapping blocks and the authentication code is generated by employing different kinds of technologies for each block, including the discrete cosine transform (DCT)-based method [11,12], the singular value decomposition (SVD)-based method [13,14], and the coding-based method [15,16]. Then, the authentication code of block is scrambled, mapped to the other block, and then inserted into it. The block mapping is one-to-one. Verification is conducted by comparing the extracted and recalculated authentication code. These schemes [11–15] also adopt a multi-hierarchical tampering detection strategy to improve the tampering detection rate; for example, a first hierarchical tampering detection strategy is used to initially identify the tampered area and a second hierarchical tampering detection strategy serves as a remediation measure. As a consequence, these approaches have high precision in tampering detection. Hence, their schemes make it more probable that the tampering region can be restored with respect to satisfactory recovered image quality.

Image authentication technology is also widely used in the compression domain. The aim of image compression algorithms, such as joint photographic experts group (JPEG) [17,18], vector quantization (VQ) encoding [19,32], and absolute moment block truncation coding (AMBTC) [33], is to reduce the size of an image to alleviate the burden of data communication. Of these, AMBTC is a variation of block truncation coding (BTC) [34]. Considering the BTC family is simple and less computationally complex while AMBTC offers better image quality than BTC, many scholars have proposed image authentication schemes for either BTC- or AMBTC-compressed images in the last decade. In 2004, Tu and Hsu [20] proposed a copyright protection scheme for digital images based on BTC. The authentication code, called the ownership share, is constructed by combining the determined authentication code with the binary image generated from the permuted host image using BTC. It is stored by a trusted third party for future authentication. On average, this scheme can extract the authentication code at around 92.13%. In 2009, Jiang et al. [21] proposed a fragile watermarking method that inserts the authentication

code into the host image according to the parity of the reconstruction levels of the BTC quantizer. In 2011, Yang and Lu [22] proposed an image authentication method using BTC. Their authentication code is embedded into the block according to the odevity of the number of '1's in the bitmap. If the authentication code bit is '1', the number of '1's in the bitmap is made odd by changing, at most, the three-pixel value of the block. If the authentication code bit is '0', the number of '0's in the bitmap is modified following a similar rule. In the tampering detection phase, the authentication code can be extracted according to the odevity of the number of '1's in each block. In 2013, Hu et al. [23] proposed a fragile watermarking method based on AMBTC. In their approach, the authentication code is derived using a pseudo-random generator. For each block, the corresponding bitmap is further divided into k sub-bitmaps with the same size. Then, based on the idea of bit-flipping in [35], each sub-bitmap is used to carry a one-bit authentication code by adjusting the parity of the number of '1's to make it equal to that of the one-bit authentication code. Moreover, to achieve the better image quality, the most suitable flipping bit was determined using the least distortion criterion [24]. Besides, two quantization levels are recomputed to further improve the quality of the compressed image block. The renewed AMBTC compression codes are further compressed using the linear prediction technique and the Huffman coding technique to cut down the storage cost of the AMBTC compression codes. Among these methods [22,23], weaknesses have been noted, in that changing the bitmap may further distort reconstructed image quality.

To solve this problem, Hu et al. [25] in 2013 proposed another image authentication scheme for BTC-compressed images. For each image block, the AC was thus embedded into quantization levels by adjusting the k-bit parity value of their difference to be the same as the k-bit AC. In 2014, Nguyen et al. [26] discovered the mean square error provided by scheme [25] was increased because of adjustment of the quantization levels. Thus, a reference table was designed to carry the AC to achieve a better image quality. The *PSNR* provided by their scheme is around 32.43 dB. In the same year, Lin et al. [27] adopted the odevity of the bitmap of AMBTC compression codes to derive the authentication code and then inserted the authentication code into the quantization levels. To enhance the security of the authentication code, the embedding position of the authentication code would be selected with the aid of a pseudo-random sequence. For tampering detection, a two-hierarchy tampering detection strategy is employed to increase performance. In the end, 15 of 16 tampered blocks can be successfully detected when each block carries a four-bit authentication code. Compared to Hu et al. [23], the method proposed by Lin et al. [27] has better visual quality and good detection accuracy. In 2016, Li et al. [28] proposed a novel image authentication scheme to verify the integrity of the AMBTC-compressed image. For each block, the authentication code is inserted into the quantization levels according to the determined reference matrix. The length of the to-be-inserted authentication code can be flexibly decided as the user requires. In this way, their true detection ratio is close to 93.75%, while the authentication code is designed as four bits. For these schemes [25–28], there is room for improvement in detecting the compression codes' attack and collage attack.

To achieve this goal, in 2017, Lin et al. [29] proposed a hybrid image authentication method to protect the integrity of the AMBTC-compressed image. To begin with, they considered the bitmap of the smooth area rather than the complex area as more suitable for parity-check coding [36]. Hence, their scheme first classified the image's blocks into two groups: Smooth and complex. For the smooth group, they forced the parity of the sub-bitmap to match that of the to-be-embedded authentication bit using the bit-flipping technique. For the complex block, on the other hand, the authentication code is embedded into the quantization levels according to a reference table. The different traversal sequence, decided by the number of '1's in a bitmap, is chosen as the hiding sequence to carry the authentication code. In the tampering detection phase, a hybrid strategy is used to ensure superior localization accuracy along with better visual image quality. Experimental results confirm Lin et al.'s scheme outperforms previous schemes on the image quality of watermarked images and tamper detection. However, it is a little regrettable that the scheme [29] did not completely solve the compression codes' attack. Hence, in 2018, Hong et al. [30] proposed an efficient image authentication method for

AMBTC-compressed images using adaptive pixel pair matching. In their scheme, image blocks are classified into edge and non-edge blocks using a predetermined threshold. For each block, the bitmap and location information are inputted into a hashing function to generate the authentication code. The length of the authentication code ranges from one to four bits and can be flexibly determined, according to the type of image block. Then, the authentication code is embedded into the quantization levels using an adaptive reference table. Their scheme significantly reduces image distortion caused by embedding the authentication code and provides a lower false detection rate, averaging at 0.17%. However, their embedding strategy could break the natural relationship between high and low quantization levels; thus, it can only confirm the authenticity of AMBTC compression codes rather than being effective for AMBTC-compressed images. Additionally, their embedding strategy does not always guarantee the minimum distortion for an embedded edge block because a predetermined distance between two quantization levels must be maintained after authentication code embedding.

The same year, Hong et al. [31] proposed two image authentication schemes, i.e., LSBP and MSBP, for tampering detection for AMBTC compression codes. For each block, their schemes can embed an $(a + b)$-bit authentication code generated from the bitmap and quantization levels' MSBs. LSBP is a strategy that embeds the a-bit authentication code into a high quantization level and the b-bit authentication code into a low quantization level using LSBs replacement. Due to the rough embedding strategy, MSBP is suggested to minimize distortion using an MSBs perturbation technique. Their schemes have the ability to achieve a tampering detection rate of more than 93.75%. However, in a few cases, their scheme fails to authenticate the watermarked image due to having broken the natural correlation between quantization levels.

Table 1 gives summaries of those authentication schemes [23,25–31]. In short, some of them [26, 28–30] need to store a reference matrix during the AC embedding and authentication phase, and some schemes [23,25–29] have a limitation against the compression codes' attack or collage attack. Also, most existing methods [23,26–30] have the weakness that the upper bound of their first hierarchical tampering detection accuracy is around 93.75%. Hence, most of them employ a second hierarchical tampering detection strategy, such as neighborhood elimination, to improve the tampering detection rate. To overcome those problems, this paper proposes a novel image authentication scheme that protects the integrity of both AMBTC compression codes and AMBTC-compressed images. The proposed scheme does not need a reference matrix during AC embedding and extraction and can resist both the compression codes' attack and collage attack. Our approach achieves a higher tampering detection rate in the first hierarchical tampering detection round without a remediation mechanism and sustains acceptable visual quality.

Table 1. Comparisons of the proposed scheme and other schemes [23,25–31].

Methods	Tampering Detection Result for First Stage (%)	Requirement of Reference Matrix	Main Limitation
Scheme in [23]	93.75	No	
Scheme in [25]	96.87	No	Compression codes' attack, Collage attack
Scheme in [26]	93.75	Yes	
Scheme in [27]	93.75	No	
Scheme in [28]	93.75	Yes	
Scheme in [29]	93.75	Yes	Compression codes' attack
Scheme in [30]	93.75	Yes	More computation
Scheme in [31]	98.50/99.61	No	Collage attack
Proposed scheme	99.85	No	-

The rest of this paper is organized as follows: We briefly review related works in Section 2, including AMBTC compression technology and matrix encoding; in Section 3, we describe the proposed scheme in detail; in Section 4, we perform a series of experiments to show the performance of our approach; finally, we provide conclusions in Section 5.

2. Related Works

In this section, we first introduce the AMBTC compression technique for an image in Section 2.1 and then look at the matrix encoding for data hiding in Section 2.2.

2.1. AMBTC Compression

In some cases, to increase the speed of transmission, users have to reduce the size of the digital image in advance with compression techniques, whether lossy or lossless. AMBTC is a widely used compression technology due to its simple computation [33]. Meanwhile, AMBTC is a variation of BTC [34] with better reconstructed image quality. Assume there is a to-be-compressed image, *I*, of $X \times Y$ pixels. The image, *I*, is thus divided into $x \cdot y$ non-overlapping blocks, with the size of each block being $w \times w$ pixels. In general, *w* is set to 4 in both BTC and AMBTC. Assume $p_{(1, 1)}, p_{(1, 2)}, \cdots, p_{(1, w)};$ $p_{(2, 1)}, p_{(2, 2)}, \cdots, p_{(2, w)}; \cdots; p_{(w, 1)}, p_{(w, 2)}, \cdots, p_{(w, w)}$ are the pixel values of each block. The detailed process of AMBTC compression is described as follows. First, the average, μ, of those pixels' values in a block is calculated by:

$$\mu = \frac{1}{w \cdot w} \sum_{r=1}^{w} \sum_{c=1}^{w} p_{(r,c)}, \tag{1}$$

where $p_{(r, c)}$ is the pixel value of a block in the to-be-compressed image, *I*.

According to the average value, μ, the pixels in a block can be partitioned into two subgroups according to the following rules:

$$\begin{cases} p_{(r,c)} \in G_{S0}, \text{ if } p_{(r,c)} < \mu, \\ p_{(r,c)} \in G_{S1}, \text{ if } p_{(r,c)} \geq \mu, \end{cases} \tag{2}$$

where $1 \leq r, c \leq w$, G_{S0} is a subgroup that contains all pixels whose values are lower than the average value, μ, and G_{S1} is a subgroup that contains the pixels not included in G_{S0}.

Later, the average value for each subgroup is calculated as follows:

$$l = \frac{1}{k_0} \sum_{p_{(r,c)} \in G_{S0}} p_{(r,c)}, \tag{3}$$

$$h = \frac{1}{k_1} \sum_{p_{(r,c)} \in G_{S1}} p_{(r,c)}, \tag{4}$$

where k_0, k_1 are the numbers of pixels in the subgroups, G_{S0}, G_{S1}, respectively, and $k_0 + k_1 = k$, $k = w \cdot w$. Here, *h* is the high quantization level and *l* is the low quantization level. A bitmap (*bm*) for the current block is generated based on the following rules: (1) If the pixel belongs to the subgroup, G_{S0}, its corresponding position in the bitmap is marked '0'; (2) if the pixel belongs to the subgroup, G_{S1}, its corresponding position in the bitmap is marked '1'. The generation rule for the bitmap is described as follows:

$$bm_{(r,c)} = \begin{cases} 0, p_{(r,c)} \in G_{S0} \\ 1, p_{(r,c)} \in G_{S1} \end{cases}, \text{ for } 1 \leq r, c \leq w. \tag{5}$$

In this way, the AMTBC compression code for one block is derived in the form of a trio (*h*, *l*, *bm*). On the receiving side, the decoding process is quite simple. A reconstructed block can be derived based on the following rules:

$$p'_{(r,c)} = \begin{cases} l, \text{ if } bm_{(r,c)} = 0 \\ h, \text{ if } bm_{(r,c)} = 1 \end{cases}, \text{ for } 1 \leq r, c \leq w, \tag{6}$$

where $p'_{(r,c)}$ is the pixel value of the reconstructed image. Once all blocks have been processed by Equation (6), the reconstructed image is obtained.

2.2. The Matrix Encoding

The (7, 4) Hamming code [37,38] was invented in 1950 by Richard Hamming as a linear error-correction code. The basic idea of the (7, 4) Hamming code is that some attached information, i.e., three parity check bits, are added to the original four-bit data. As a result, the recipient can detect and correct a single-bit error with the help of the parity check matrix, H, as shown in Equation (7). The result of the equation $(H \times RCW^T)^T$ indicates where the error bit occurs, with RCW representing the received codeword. Assume a codeword that meets the verification rules is $CW = (1101001)$, and the received codeword is $RCW = (1100001)$, and the syndrome vector, $z^T = (100)^T$, is equal to the fourth column of the parity check matrix, H. This means that a single-bit error is detected and the error bit in this RCW is in the fourth position.

$$
\begin{aligned}
z &= (H \times RCW^T)^T \\
&= \left(\begin{bmatrix} 0 & 0 & 0 & 1 & 1 & 1 & 1 \\ 0 & 1 & 1 & 0 & 0 & 1 & 1 \\ 1 & 0 & 1 & 0 & 1 & 0 & 1 \end{bmatrix} \times \begin{bmatrix} 1 \\ 1 \\ 0 \\ 0 \\ 0 \\ 0 \\ 1 \end{bmatrix} \right)^T \\
&= (100).
\end{aligned}
\tag{7}
$$

Based on the (7, 4) Hamming code, Ron Crandall proposed an efficient embedding method known as matrix encoding [39]. In matrix encoding, for a (1, n, k) code, the n modifiable bit-places are used to carry the k-bit secret message by flipping at most one modifiable place, where $n = 2^k - 1$. In this paper, we pay more attention to the (1, 7, 3) code.

First, a coset of the (7, 4) Hamming code with a parity check matrix, H, is constructed, as shown in Table 2. To show the embedding process intuitively, an example is given as follows.

Table 2. The cosets of the (7, 4) Hamming code with the parity check matrix, H.

ID	0	1	2	3	4	5	6	7
Syndrome	000	001	010	011	100	101	110	111
Coset leader	0000000	1000000	0100000	0010000	0001000	0000100	0000010	0000001

Let us assume the to-be-embedded message is $S = (s_1, s_2, s_3)$ and the cover vector is $CV = (c_1, c_2, c_3, c_4, c_5, c_6, c_7)$. The details of the embedding process are as follows.

Step 1: Compute $M = (H \times CV^T)^T$ to derive vector M.

Step 2: Calculate the syndrome vector, $z = M \oplus S$.

Step 3: Search for the same syndrome value as z in Table 2, then the gth column can be located, where $0 \le g \le 7$. The corresponding identifier (ID) is also g, which is the to-be-flipped bit-location later in this paper. At the same time, the corresponding coset leader vector is mapped as e_g.

Step 4: Change the gth bit of the cover vector CV by $CV' = CV \oplus e_g$. Note that if the syndrome value, $z = (000)$ or $g = 0$, then there is nothing to be changed; that is, $CV' = CV$.

Finally, the embedding process ends and CV' carries the three-bit secret message. The decoding process is simple, using $S' = (H \times (CV')^T)^T$, where S' is the extracted message and is the same as the secret message S, as long as no error occurred.

For example, assume $S = (101)$ and $CV = (1101001)$. The computed M is (000) and the syndrome z is (101). By searching Table 2, the fifth column is located, ID = 5 is found, and its corresponding

coset leader, e_5 = (0000100), is determined. Finally, the embedding process is carried out and the cover vector, *CV*, is changed to *CV'* = (1101101). For the recipient, the secret, *S'*, can be extracted by $S' = \left(H \times (CV')^T\right)^T = (101)$. That is to say, the seven-bit cover vector can carry the three-bit message by changing at most one bit.

3. Proposed Scheme

To increase the tampering localization accuracy after the first hierarchical tampering detection, the bitmap carries more authentication code for each block using the matrix encoding scheme. Meanwhile, to overcome the distortion caused by changing the bitmap, the corresponding to-be-flipped bit-location information, *G*, is recorded instead of flipping this bit of the bitmap directly. Then, this bit-location information is embedded into the quantization levels based on adjusted quantization level matching. Finally, a flowchart of the authentication code generation and embedding is shown in Figure 1. Besides, to better present the proposed scheme, the main symbols used in this paper and their definitions are listed in Table 3.
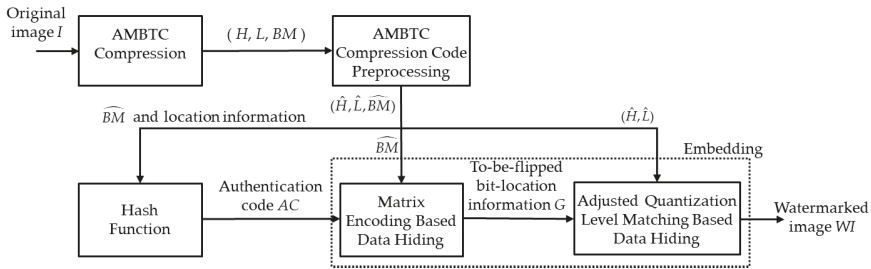

Figure 1. Flowchart of the authentication code generation and embedding.

Table 3. Main symbols used in this paper and their definitions.

Symbols	Definitions	Symbols	Definitions
I	Original image	*WI*	Watermarked image
H	Parity check matrix	*TM*	Tampered map
h	High quantization level for a block in *I*	H	A set of *h*
l	Low quantization level for a block in *I*	L	A set of *l*
bm	Bitmap for a block in *I*	*BM*	A set of *bm*
$\hat{h}$	Preprocessed high quantization level	$\hat{H}$	A set of $\hat{h}$
$\hat{l}$	Preprocessed low quantization level	$\hat{L}$	A set of $\hat{l}$
$\widehat{bm}$	Preprocessed bitmap	$\widehat{BM}$	A set of $\widehat{bm}$
h'	High quantization level for a block in *WI*	*H'*	A set of *h'*
l'	Low quantization level for a block in *WI*	*L'*	A set of *l'*
bm'	Bitmap for a block in *WI*	*BM'*	A set of *bm'*
g_1, g_2	Bit-location information of a block	*ac*	Authentication code for a block

3.1. AMBTC Compression and Preprocessing Phase

In this paper, the original image, *I*, is divided into non-overlapping blocks, and then the AMBTC compression technique as mentioned in Section 2.1 is performed for image block compression. As a result, AMBTC compression codes are derived and denoted as (*H*, *L*, *BM*), where *H*, *L*, and *BM* represent the sets of high quantization level, low quantization level, and bitmap, respectively. For convenience, let us assume (*h*, *l*, *bm*) is a triple of AMBTC compression codes for one block. The preprocessing of the AMBTC compression code for a block is done as follows:

$$\begin{cases} \hat{l} = l, \ \hat{h} = h + 1, \ \widehat{bm} = bm \ \& \ bm_{(u,v)} = 0, & \text{if } l = h = 0, \\ \hat{l} = l - 1, \ \hat{h} = h, \ \widehat{bm} = bm \ \& \ bm_{(u,v)} = 0, & \text{if } 0 < l = h \leq 255, \\ \hat{l} = l, \quad \hat{h} = h, \ \widehat{bm} = bm, & \text{if } l \neq h, \end{cases} \tag{8}$$

where u and v are constants, and $\hat{h}$, $\hat{l}$, and $\widehat{bm}$ are the high quantization level, low quantization level, and bitmap of a preprocessed AMBTC compression code, respectively. After all blocks have been preprocessed in the same way, the preprocessed AMBTC compression codes $(\hat{H}, \hat{L}, \hat{BM})$ were obtained. Note that the $bm_{(u,v)}$ should not be used in the embedding procedure. In our experiments, (u, v) is set to (3, 1), based on experimental results.

We preprocess to check whether the h is equal to l. If it is, the bits in the bm are all equal to '1' and the preprocessing should thus be conducted; otherwise, nothing should be done. Preprocessing ensures the recipient can obtain the same AMBTC compression codes from the reconstructed image, as long as no malicious attack occurs. Two examples of preprocessing are the red dotted squares shown in Figure 2. In Figure 2a, since h is not equal to l, the AMBTC compression code remains the same $(\hat{h}, \hat{l}, \widehat{bm}) = (h, l, bm)$. Meanwhile, in Figure 2b, since h is equal to l, the AMBTC compression code is preprocessed as $(\hat{h}, \hat{l}, \widehat{bm}) = (h, l - 1, bm \ \& \ bm_{(3,1)} = 0)$.
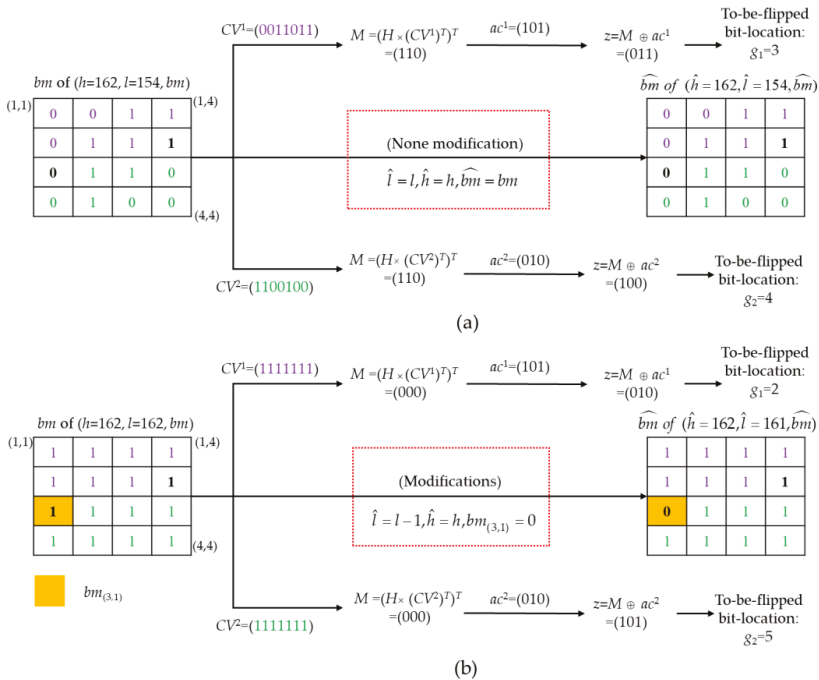
Figure 2. Examples of preprocessing and generation of the to-be-flipped bit-location information when (**a**) $h \neq l$; (**b**) $h = l \ \& \ l \neq 0$.

3.2. Authentication Code Generation Phase

After the processed AMBTC compression code is generated, for each block, our approach generates a six-bit authentication code by feeding the block's $\widehat{bm}$ and location information into a hash function. This six-bit authentication code is further separated into two three-bit sub-codes, which are embedded into the bitmap using matrix encoding. Let us assume that the binary form of a six-bit

authentication code is $ac = (ac_1, ac_2, ac_3, ac_4, ac_5, ac_6)$; the first three-bit sub-code is then defined as $ac^1 = \left(ac_1^1, ac_2^1, ac_3^1\right) = (ac_1, ac_2, ac_3)$ and the second three-bit sub-code as $ac^2 = \left(ac_1^2, ac_2^2, ac_3^2\right) = (ac_4, ac_5, ac_6)$.

3.3. Embedding Phase

The flowchart of the authentication code embedding phase is shown in Figure 1. First, the authentication code is embedded into the bitmap. In fact, we only record the to-be-flipped bit-location information. No modification has been done in *bm*, as will be described in Section 3.3.1. Second, the to-be-flipped bit-location information is inserted into the two quantization levels, as will be described in Section 3.3.2.

3.3.1. The Matrix Encoding Based Data Hiding

After authentication code generation and AMBTC compression codes' preprocessing, the authentication code will be embedded into the bitmap for each block. The algorithm of the embedding process is described as follows.

Input: Original image, *I*.

Output: To-be-flipped bit-location information, *G*.

Step 1. Divide the original image, *I*, into non-overlapping blocks by a size of 4×4 pixels.

Step 2. Generate the AMBTC compression codes (*H*, *L*, *BM*) for the image, *I*, as explained in Section 2.1. For each block, assume its preprocessed AMBTC compression code is $(\hat{h}, \hat{l}, \hat{bm})$.

Step 3. Generate the authentication code, *AC*, as explained in Section 3.2. For each block, assume the first three-bit sub-code is $ac^1 = \left(ac_1^1, ac_2^1, ac_3^1\right)$ and the second three-bit sub-code is $ac^2 = \left(ac_1^2, ac_2^2, ac_3^2\right)$.

Step 4. Extract the first seven bits of *bm* as the first cover vector, $CV^1 = \left(cv_1^1, cv_2^1, cv_3^1, cv_4^1, cv_5^1, cv_6^1, cv_7^1\right)$ $= (bm_{(1,1)}, bm_{(1,2)}, bm_{(1,3)}, bm_{(1,4)}, bm_{(2,1)}, bm_{(2,2)}, bm_{(2,3)})$. Extract the last seven bits of *bm* as the second cover vector, $CV^2 = \left(cv_1^2, cv_2^2, cv_3^2, cv_4^2, cv_5^2, cv_6^2, cv_7^2\right) = (bm_{(3,2)}, bm_{(3,3)}, bm_{(3,4)}, bm_{(4,1)}, bm_{(4,2)}, bm_{(4,3)}, bm_{(4,4)})$.

Step 5. Perform matrix encoding, as explained in Section 2.2, to embed the first three-bit sub-code, ac^1, into the first cover vector, CV^1, then derive the to-be-flipped bit-location, g_1. The second three-bit sub-code, ac^2, is embedded into the second cover vector, CV^2, and then used to derive the to-be-flipped bit-location, g_2. Note that we only record the to-be-flipped bit-location information but nothing is modified for the *bm*. Hence, for each block, two-tuple location information (g_1, g_2) can be derived.

Step 6. Perform Steps 2 to 5 until all blocks have been processed.

Step 7. Output all location information (g_1, g_2) for each block to the to-be-flipped bit-location information, *G*.

Step 8. End.

After matrix encoding is completed, the to-be-flipped bit-location information, *G*, is obtained. We provide two examples to demonstrate the generation of the to-be-flipped bit-location information, as shown in Figure 2. In Figure 2a, the first seven bits of *bm* are recombined as the first cover vector, CV^1, shown in purple. The last seven green bits comprise the second cover vector, CV^2. Later, matrix encoding is conducted, as described in Section 2.2, and then the two-tuple location information ($g_1 = 3, g_2 = 4$) will be derived and used as the to-be-hidden message in the next section. In this case, the AMBTC compression code is not changed. Similarly, Figure 2b presents a special case, i.e., *h* is equal to *l* and all bits in *bm* are 1. Thus, the preprocessing of the AMBTC compression code should be done, as described in Section 3.1; i.e., *l* is decreased by 1 and the $bm_{(3,1)}$ is set to 0. In this case, *l* and *bm* are slightly modified. Also, two-tuple location information ($g_1 = 2, g_2 = 5$) will be derived and used as the to-be-hidden message in the following phase. The yellow grid represents the chosen $bm_{(3,1)}$, as described in Section 3.1.

3.3.2. Adjusted Quantization Levels Matching Based Data Hiding

After the matrix encoding procedure, the two-tuple to-be-flipped bit-location information, G, is individually inserted into two quantization levels. The algorithm of the adjusted quantization level matching-based data hiding is described as follows.

Input: Preprocessed AMBTC compression codes $(\hat{H}, \hat{L}, \hat{BM})$, to-be-flipped bit-location information, G.
Output: Watermarked image, *WI*.

Step 1. Get a triple $(\hat{h}, \hat{l}, \hat{bm})$ for one block from preprocessed AMBTC compression codes $(\hat{H}, \hat{L}, \hat{BM})$.
Step 2. Get the corresponding to-be-flipped bit-location information (g_1, g_2) for this block from G.
Step 3. Calculate the factors for $\hat{h}$ and $\hat{l}$ for the current block by:

$$
\begin{cases}
f_h = \left\lfloor \frac{\hat{h}}{2^3} \right\rfloor, \\
f_l = \left\lfloor \frac{\hat{l}}{2^3} \right\rfloor,
\end{cases}
\tag{9}
$$

where f_h and f_l represent the factors of $\hat{h}$ and $\hat{l}$, respectively.
Step 4. Calculate the remaining values for $\hat{h}$ and $\hat{l}$ for the current block by:

$$
\begin{cases}
rv_h = \hat{h} \bmod 2^3, \\
rv_l = \hat{l} \bmod 2^3,
\end{cases}
\tag{10}
$$

where rv_h and rv_l represent the remainder values of $\hat{h}$ and $\hat{l}$, respectively.
Step 5. Perform adjusted quantization level matching-based data hiding. If the remainder, rv_h, is equal to g_1, the matching work of $\hat{h}$ is done; otherwise, the candidates at the quantization level, $\hat{h}$, should be adjusted by:

$$
\begin{cases}
h_1 = f_h \cdot 2^3 + g_1, \\
h_2 = \begin{cases}
h_1 + 2^3, & \text{if } h_1 < \hat{h}, \\
h_1 - 2^3, & \text{if } h_1 > \hat{h}, \\
h_1, & \text{if } h_1 = \hat{h},
\end{cases}
\end{cases}
\tag{11}
$$

where h_1 and h_2 are the candidates at the quantization level, $\hat{h}$. Here, if h_2 is lower than zero or higher than 255, h_2 must be set to h_1. Similarly, if the remainder, rv_l, is equal to g_2, the matching work of $\hat{l}$ is done; otherwise, the candidates at the quantization level, $\hat{l}$, should be adjusted by:

$$
\begin{cases}
l_1 = f_l \cdot 2^3 + g_2, \\
l_2 = \begin{cases}
l_1 + 2^3, & \text{if } l_1 < \hat{l}, \\
l_1 - 2^3, & \text{if } l_1 > \hat{l}, \\
l_1, & \text{if } l_1 = \hat{l},
\end{cases}
\end{cases}
\tag{12}
$$

where l_1 and l_2 are the candidates at quantization level $\hat{l}$. l_2 must be set to l_1 if l_2 is lower than zero or higher than 255.
Step 6. Let $h_{cf} = h_a$ and $l_{cf} = l_b$ be the final, selected solution under the constraint of the least distortion, $dist_{(a,b)}$, which can be calculated by:

$$
dist_{(a,b)} = \sum_{r=1}^{4} \sum_{c=1}^{4} \begin{cases}
(p_{(r,c)} - h_a)^2 & \text{if } bm_{(r,c)} = 1, \\
(p_{(r,c)} - l_b)^2 & \text{if } bm_{(r,c)} = 0,
\end{cases}
\tag{13}
$$

where $a, b \in [1, 2]$, $h_a \in [h_1, h_2]$, $l_b \in [l_1, l_2]$. Besides, in a few cases, this situation may happen, that is, h_{cf} will be equal to l_{cf}, then h_{cf} or l_{cf} will be forced to be justified once again by the following rule:

$$
\begin{cases}
l_{cf} = l_{cf} - 2^3, & \text{if } l_{cf} > 247, \\
h_{cf} = h_{cf} + 2^3, & \text{otherwise.}
\end{cases}
\tag{14}
$$

Step 7. Perform Steps 1 to 6 until all blocks have been processed.

Step 8. Output the watermarked AMBTC compression code for each block, and the watermarked image, *WI*, is achieved.

Step 9. End.

An example is given to show the detailed processing of the adjusted quantization level matching-based data hiding in Figure 3. Here, for convenience, we assume $dist_{(1,1)}$ is the least distortion after calculation using Equation (13) in this example.
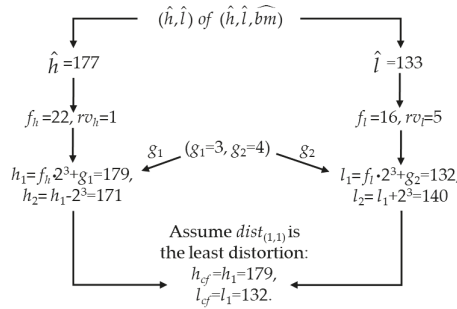

Figure 3. Example of adjusted quantization levels matching based data hiding.

3.4. Tampering Detection Phase

Once the recipient receives the watermarked image, *WI*, or the watermarked AMBTC compression codes, the precise tampering detection can be done in respect to whether the tampering occurred or not. Figure 4 depicts the flowchart of tampering detection. First, the bit-location information is extracted from the AMBTC compression codes. Then, the authentication code is calculated and reconstructed. Finally, the extracted and recalculated authentication code are compared to determine whether each block has been tampered with.
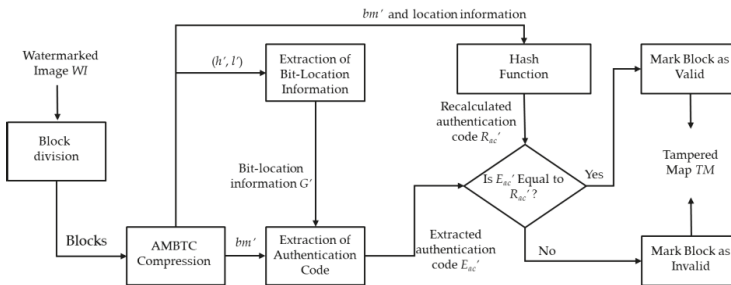
Figure 4. Flowchart of tampering detection.

3.4.1. Extraction of Bit-Location Information

The algorithm for bit-location information extraction is described as follows.

Input: Watermarked image, *WI*.

Output: Bit-location information, G'.

Step 1. Divide the watermarked image, *WI*, into non-overlapping blocks by a size of 4×4 pixels.

Step 2. Perform the AMBTC compression technique for one block to derive the corresponding AMBTC compression code (h', l', bm').

Step 3. Extract the bit-location information (g_1', g_2') for this block by the following equation:

$$\begin{cases} g_1' = h' \mathrm{mod} 2^3, \\ g_2' = l' \mathrm{mod} 2^3, \end{cases} \tag{15}$$

Step 4. Perform Steps 2 and 3 until all blocks have been processed.

Step 5. Output all location information (g_1', g_2') for each block to provide the bit-location information, G'.

Step 6. End.

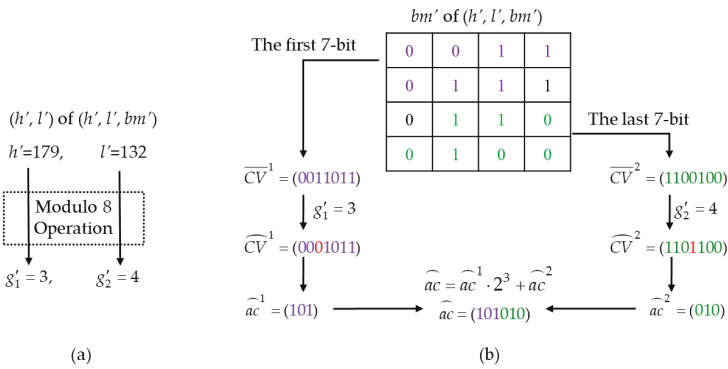An example of bit-location information extraction is given in Figure 5a.

Figure 5. Examples: (**a**) example of extracting bit-location information, (**b**) example of extracting authentication code.

3.4.2. Extraction of the Authentication Code

The algorithm of authentication code extraction is described as follows.

Input: AMBTC compression codes (H', L', BM'), bit-location information, G'.

Output: Extracted authentication code, EAC.

Step 1. Get a triple (h', l', bm') for one block from AMBTC compression codes (H', L', BM').

Step 2. Get a tuple bit-location information (g_1', g_2') for the corresponding block from G'.

Step 3. Recombine the first seven bits of bm' as the first cover vector, $\overline{CV}^1 = \left(cv_1^1, cv_2^1, cv_3^1, cv_4^1, cv_5^1, cv_6^1, cv_7^1\right)$. Recombine the last seven bits of bm' as the second cover vector, $\overline{CV}^2 = \left(cv_1^2, cv_2^2, cv_3^2, cv_4^2, cv_5^2, cv_6^2, cv_7^2\right)$.

Step 4. Flip the g_1'th bit for the first cover vector, $\overline{CV}^1$, and denoted as $\widehat{CV}^1$, then flip the g_2'th bit for the first cover vector, $\overline{CV}^2$, and denoted as $\widehat{CV}^2$. Note that if g_1' or g_2' is equal to zero, the corresponding flipping operation is skipped. In Figure 5b, the red digit represents the flipped bit-location.

Step 5. Extract the authentication code. Two three-bit sub-codes $(\widehat{ac}^1, \widehat{ac}^2)$ can be computed by:

$$\begin{cases} \widehat{ac}^1 = \left(H \times \left(\widehat{CV}^1\right)^T\right)^T, \\ \widehat{ac}^2 = \left(H \times \left(\widehat{CV}^2\right)^T\right)^T. \end{cases} \tag{16}$$

Then, the six-bit authentication code, $\widehat{ac}$, can be derived by:

$$\widehat{ac} = \widehat{ac}^1 \cdot 2^3 + \widehat{ac}^2. \tag{17}$$

Step 6. Perform Steps 1 to 5 until all blocks have been processed.

Step 7. Output the authentication code, $\widehat{ac}$, for each block to provide the extracted authentication code, *EAC*.

Step 8. End.

Figure 5b shows an example of authentication code extraction.

3.4.3. Tampering Detection

The algorithm of the tampering detection is described as follows.
Input: Extracted authentication code, *EAC*.
Output: Tampered map, *TM*.

Step 1. Generate the authentication code, as mentioned in Section 3.2, and denote it as *RAC*.

Step 2. Get an authentication code for one block from *RAC* and denote it as R_{ac}'.

Step 3. Get an authentication code for the corresponding block from *EAC* and denote it as E_{ac}'.

Step 4. Mark the tampered map, *TM*, according to the comparison results of R_{ac}' and E_{ac}'. If they are equal, the corresponding position of *TM* is marked as '0', which means the current block is valid; otherwise, it is marked as '1', which indicates the current block is invalid.

Step 5. Perform Steps 2 to 4 until all blocks have been processed.

Step 6. Output the tampered map, *TM*.

Step 7. End.

Without loss of generality, a second hierarchical tampering detection algorithm [29,30] is also provided in our experiments. This improves the tampering detection rate, even if excellent detection performance is already offered by the first hierarchical tampering detection algorithm.

4. Experimental Results

In this section, a series of experiments and analyses are performed to demonstrate the performance of the proposed method. All experiments were implemented in Matlab R2017a on a PC with Intel® Core (TM) i7-3770 CPU @3.4 GHz, 8 GB RAM (Intel Corporation, Santa Clara, CA, USA). Nine classic grayscale images with the size of 512×512 served as test images, as shown in Figure 6. Several attacks were employed to test the performance of our proposed scheme on tampering detection, including cropping attack, constant average attack, collage attack, and AMBTC compression codes' attack. All test images were compressed using the AMBTC compression technique with the size of 4×4 pixels.
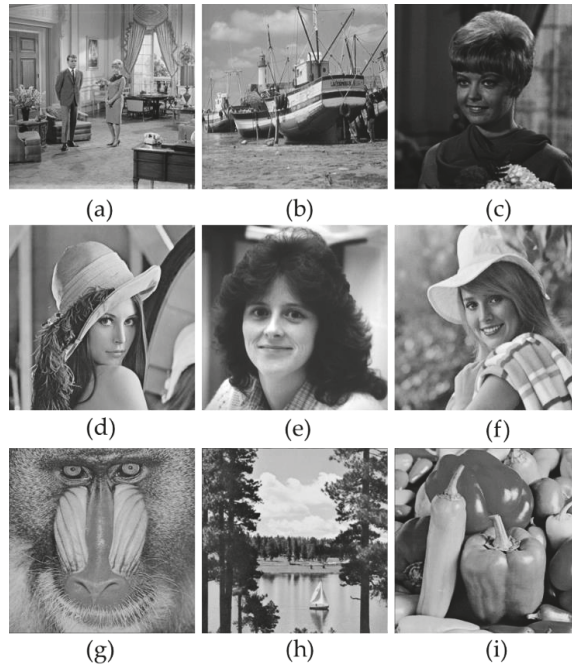
Figure 6. Nine 512×512 grayscale images. (**a**) Couple; (**b**) boat; (**c**) Zelda; (**d**) Lena; (**e**) woman; (**f**) Elaine; (**g**) baboon; (**h**) lake; (**i**) peppers.

4.1. Statistical Metrics

The following statistical metrics were utilized to demonstrate the superior performance of our approach.

(a) Peak signal-to-noise ratio (*PSNR*) [14]: Measures the difference between the watermarked image and the original image:

$$PSNR = 10 \cdot \log_{10} \left(\frac{255^2}{\frac{1}{X \cdot Y} \cdot \sum\limits_{i=1}^{X} \sum\limits_{j=1}^{Y} \left(p_{wi}(i,j) - p_{oi}(i,j) \right)^2} \right), \tag{18}$$

where $X \times Y$ is the size of an image; $p_{wi}(i,j)$ represents the pixel value of the watermarked image, and $p_{oi}(i,j)$ represents the pixel value of the original image.

(b) Tampering detection rate (*TDR*) [14]: Measures the percentage of tampered pixels detected in a tampered area:

$$TDR = \frac{\text{No. of detected tampered pixels}}{\text{All pixels in tampered region}}. \tag{19}$$

(c) False positive rate (*FPR*) [14]: Measures the percentage of non-tampered pixels misjudged as tampered, among all tampered pixels:

$$FPR = \frac{\text{No. of false misjudged pixels}}{\text{All tampered pixels}}. \tag{20}$$

(d) False negative rate (*FNR*) [14]: Measures the percentage of tampered pixels misjudged as non-tampered, among all non-tampered pixels:

$$FNR = \frac{\text{No. of false misjudged pixels}}{\text{All non} - \text{tampered pixels}}. \tag{21}$$

4.2. Tampering Detection Analyses

In our experiments, we performed more than 14 kinds of attacks to show the stable and reliable localization ability and superior performance of the first hierarchical tampering detection algorithm. The details are as follows.

4.2.1. Cropping Attack

We used three grayscale images, Lena, Elaine, and woman, to simulate the cropping attack. Their watermarked images are shown in Figure 7a–c, with *PSNRs* of 31.99, 32.41, and 35.03 dB, respectively. The tampered Lena image is shown in Figure 7d, with some inside blocks cropped with a rectangle. The corresponding tampering detection result using the first hierarchical tampering detection method is shown in Figure 7g, with a *TDR* of 98.75%. The tampered Elaine image is attacked by outside cropping within the larger area, as shown in Figure 7e. The corresponding tampering detection result delivered by the first hierarchical tampering detection algorithm is shown in Figure 7h, with a *TDR* of 98.60%. Finally, we employed an inside cropping attack with an irregular shape to replace some blocks of the watermarked woman image, as shown in Figure 7f. Certainly, the proposed scheme achieves a high tampering detection rate, with a *TDR* of 98.99%. Thus, our approach achieves superior detection and localization to both the inside cropping attack and the outside cropping attack.
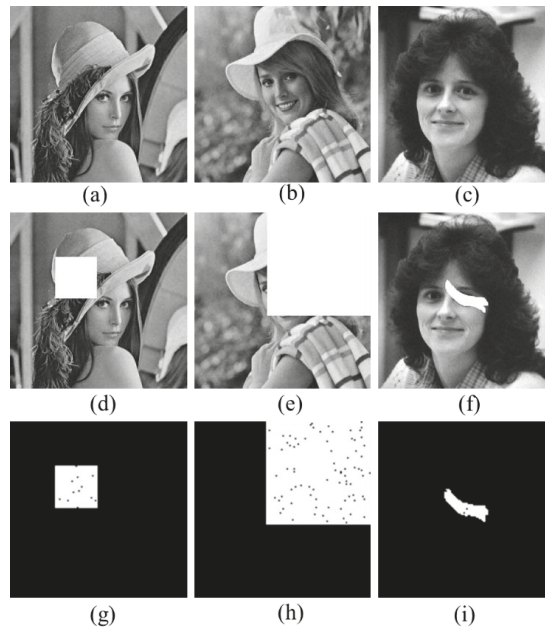

Figure 7. Cropping attack: watermarked images for (**a**) Lena (*PSNR* = 31.99 dB); (**b**) Elaine (*PSNR* = 32.41 dB); (**c**) woman (*PSNR* = 35.03 dB). Tampered images for (**d**) Lena, (**e**) Elaine, (**f**) woman. Tampering detection results after first hierarchy for (**g**) *TDR* = 98.75%; (**h**) *TDR* = 98.60%; (**i**) *TDR* = 98.99%.

Furthermore, the tampering detection performance for the cropping attack is demonstrated in Table 4. As we can see, after the first hierarchical tampering detection algorithm, the number of tampered blocks for the tampered Lena, Elaine, and woman images are 949, 5620, and 293, respectively. Our approach achieves a high *TDR*, with an average of 98.78%, and a low *FPR* and *FNR*, with averages of 0 and 0.3356, respectively. Additionally, a second hierarchical tampering detection strategy was used in this paper, and the corresponding detection performance is shown in Table 4. Here, the *TDR* is close to 100% and the *FNR* and *FPR* are close or equal to 0.

Table 4. Tampering detection performance of the cropping attack.

Original Images	Number of Tampered Blocks (4 × 4)			The First Hierarchical Tampering Detection Results (%)			The Second Hierarchical Tampering Detection Results (%)		
	Total	First Hierarchy	Second Hierarchy	*TDR*	*FPR*	*FNR*	*TDR*	*FPR*	*FNR*
Lena	961	949	961	98.75	0	0.0777	100	0	0
Elaine	5700	5620	5698	98.60	0	0.7432	99.96	0	0.0187
Woman	296	293	296	98.99	0	0.0186	100	0	0
Average				98.78	0	0.3356	99.99	0	0.0063

4.2.2. Constant Average Attack

Two watermarked images using our proposed scheme, Zelda and baboon, are shown in Figure 8a,d, with *PSNRs* of 35.07 and 27.78 dB, respectively. The constant average attack is an attack that replaces all pixels of one block with the average value of the current block. Figure 8b shows the tampered Zelda image. Within a 2 × 2 block, all pixels are modified by the mean value. As we can see, it is difficult to identify the change visually. The corresponding tampering detection result using the first hierarchical tampering detection method is shown in Figure 8c, with a *TDR* of 96.42%. Figure 8e shows the tampered baboon image under the constant average attack. Within a 4 × 4 block, all pixels are replaced by the mean value. The corresponding tampering detection result from the first hierarchical tampering detection algorithm is shown in Figure 8f, with a *TDR* of 99.02%.
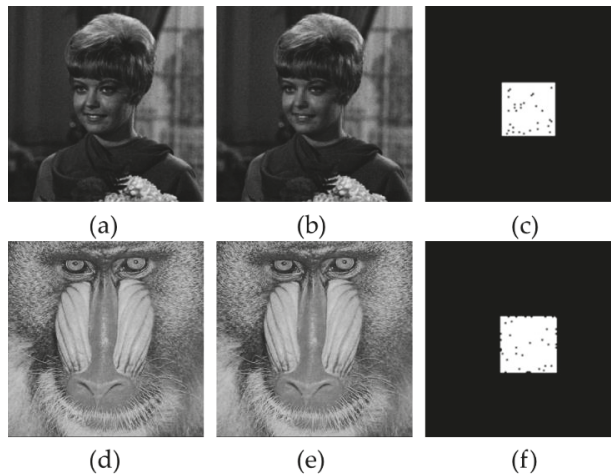

Figure 8. Constant average attack: watermarked images for (**a**) Zelda (*PSNR* = 35.07 dB); (**d**) baboon (*PSNR* = 27.78 dB). Tampered images for (**b**) Zelda (2 × 2); (**e**) baboon (4 × 4). Tampering detection results after the first hierarchy for (**c**) *TDR* = 96.42%; (**f**) *TDR* = 99.02%.

Meanwhile, Table 5 shows the tampering detection performance of the constant average attack. As we can see, after the first round of hierarchical tampering detection, the *TDR* of the four experiments is higher than 96.42% and there is low *FNR* and *FPR*. The second hierarchical tampering detection strategy was also employed, and the corresponding detection performance is rather good. For both, the *TDR* is close to 100% and the *FPR* and *FNR* are close to 0.

Table 5. Tampering detection performance of the constant average attack.

Size of Blocks	Original Images	Number of Tampered Blocks			The First Hierarchical Tampering Detection Results (%)			The Second Hierarchical Tampering Detection Results (%)		
		Total	First Hierarchy	Second Hierarchy	TDR	FPR	FNR	TDR	FPR	FNR
4 × 4	Zelda	1225	1196	1225	97.63	0	0.1909	100	0	0
	Baboon	1225	1213	1225	99.02	0	0.0791	100	0	0
2 × 2	Zelda	1369	1320	1367	96.42	0	0.3253	99.85	0	0.0133
	Baboon	1369	1333	1368	97.37	0	0.2392	99.93	0	0.0067
	Average				97.61	0	0.2086	99.95	0	0.0050

4.2.3. Collage Attack

In this section, an image is tampered with by copying image blocks from other watermarked images and pasting them into arbitrary positions in the watermarked image; this is called a collage attack. In Figure 9, we can see the watermarked images of lake, peppers, boat, and couple, with *PSNRs* of 29.88, 32.15, 30.89, and 30.38 dB, respectively. The first example of collage attack, shown in Figure 9c, is generated by copying the vegetables from Figure 9b into Figure 9a while preserving their relative spatial locations. After the first hierarchical tampering detection, the corresponding tampering detection result is shown in Figure 9d, with a *TDR* of 98.45%. Similarly, we copied some blocks from the watermarked couple image, shown in Figure 9f, into the watermarked boat image, shown in Figure 9e on the bottom left. The tampered boat image is presented in Figure 9g. Verification was performed using our tampering detection approach, with a *TDR* of 98.59%, as shown in Figure 9h.

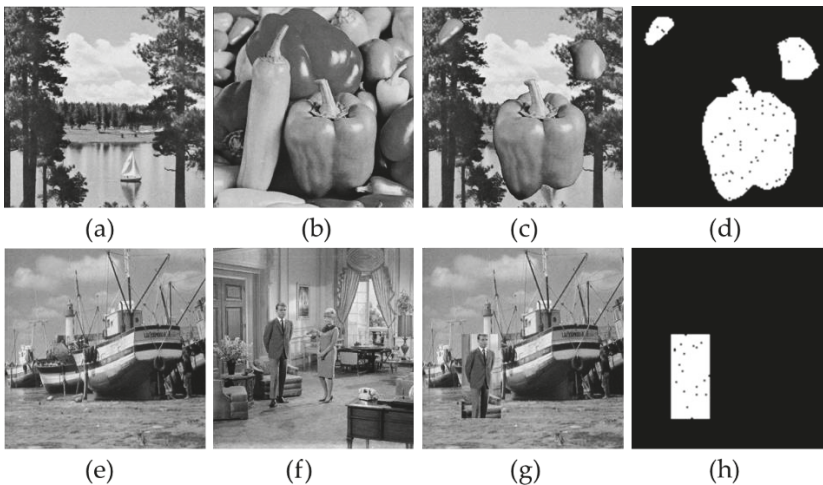| (a) | (b) | (c) | (d) |
| (e) | (f) | (g) | (h) |

Figure 9. Collage attack: watermarked images for (**a**) lake (*PSNR* = 29.88 dB); (**b**) pepper (*PSNR* = 32.15 dB); (**e**) boat (*PSNR* = 30.89 dB); (**f**) couple (*PSNR* = 30.38 dB). Tampered images for (**c**) lake; (**g**) boat. Tampering detection results after the first hierarchy for (**d**) *TDR* = 98.45%; (**h**) *TDR* = 98.59%.

Table 6 lists the detailed tampering detection performance of the proposed scheme. The tampering detection rate reaches 98%, with an *FPR* of 0 and a lower *FNR*. Furthermore, a two-hierarchy tampering detection strategy was also employed on this kind of attack, resulting in superior tampering detection, as shown in the last three columns of Table 6.

Table 6. Tampering detection performance of the collage attack.

Original Mages	Number of Tampered Blocks (4 × 4)			The First Hierarchical Tampering Detection Results (%)			The Second Hierarchical Tampering Detection Results (%)		
	Total	First Hierarchy	Second Hierarchy	*TDR*	*FPR*	*FNR*	*TDR*	*FPR*	*FNR*
Lake	4126	4062	4121	98.45	0	0.5194	99.88	0.0485	0.0408
Boat	1350	1331	1350	98.59	0	0.1262	100	0	0
Average				98.52	0	0.3228	99.94	0.0243	0.0204

4.2.4. AMBTC Compression Codes' Attacks

In this section, kinds of experiments are performed to test the tampering detection performance of the AMBTC compression codes' attack. We applied these attacks to the original 512 × 512 Lena image.

(a) Attack the quantization levels

We first tampered with either the high quantization level or the low quantization level of the 120 × 120 AMBTC compression codes, illustrated in Figure 10a. The modification is so natural that it is impossible to identify visually. Figure 10e shows the detection result obtained after the first hierarchical tampering detection, with a *TDR* of 100%. The corresponding experimental results appear in Table 7.
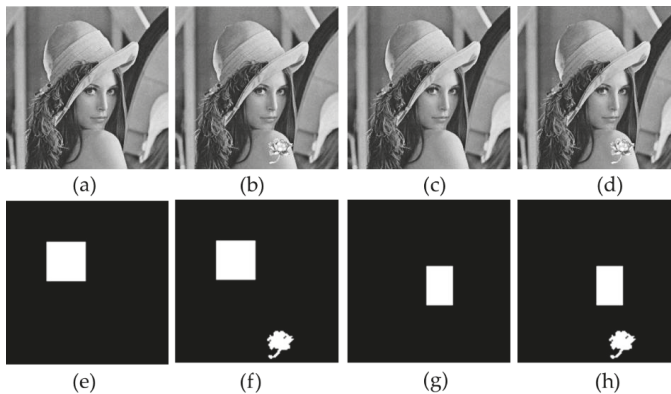

Figure 10. AMBTC compression codes' attacks: Tampered Lena images by kinds of attacks: (**a**) *H* or *L*; (**b**) (*H* or *L*) and flower; (**c**) *BM*; (**d**) *BM* and flower. Tampering detection results after the first hierarchy for kinds of attacks: (**e**) *TDR* = 100%; (**f**) *TDR* = 99.42%; (**g**) *TDR* = 100%; (**h**) *TDR* = 99.22%.

(b) Attack the quantization levels with a flower

Secondly, based on the experiment of attacking the quantization levels, at the same time, we tried to copy and paste a flower onto Lena's shoulder, as shown in Figure 10b. It is not easy to detect the attack under this scenario. The corresponding tampering detection result using the first hierarchical tampering detection method is shown in Figure 10f, with a *TDR* of 99.42%. Other statistical parameters are listed in the fourth row of Table 7.

Table 7. Tampering detection performance of the AMBTC compression codes' attack.

Original image	Kinds of Attacks	Number of Tampered Blocks (4 × 4)			The First Hierarchical Tampering Detection Results (%)			The Second Hierarchical Tampering Detection Results (%)		
		Total	First Hierarchy	Second Hierarchy	TDR	FPR	FNR	TDR	FPR	FNR
Lena	(*H* or *L*)	961	961	961	100	0	0	100	0	0
	(*H* or *L*) and flower	1211	1204	1208	99.42	0	0.0461	99.75	0.0827	0.0198
	BM	651	651	651	100	0	0	100	0	0
	BM and flower	901	894	898	99.22	0	0.0452	99.67	0.1112	0.0194
Average					99.66	0	0.0228	99.86	0.0485	0.0098

(c) Attack the bitmap

We also simply tampered with the bitmap of the 120 × 80 AMBTC compression codes, shown in Figure 10c. Again, it is hard to notice any change to the Lena image. The tampered area is around Lena's face, and Figure 10g shows the tampering detection result after the first hierarchical tampering detection, with a *TDR* of 100%. Some experimental results are listed in the fifth row of Table 7.

(d) Attack the bitmap and copy/paste a flower

We now tampered with the Lena image by modifying the bitmap and adding a flower near her shoulder, as illustrated in Figure 10d. The tampering detection result delivered by our approach is shown in Figure 10h, with a *TDR* of 99.22%. In Table 7, the sixth row shows the detailed detection results, with lower *FPR* and *FNR*.

In summary, we implemented multiple experiments to test the performance of our proposed tampering detection scheme, including the cropping attack, constant average attack, collage attack, and AMBTC compression codes' attacks. After the first hierarchical tampering detection, our proposed scheme can offer a high *TDR* along with low *FPR* and *FNR* for all kinds of attacks.

4.3. Performance Comparisons

Table 8 compares the *PSNRs* of the reconstructed images by using the original AMBTC compression codes and watermarked AMBTC compression codes generated through our proposed scheme. The watermarked images have a few more distortions than the image reconstructed using the original AMBTC compression codes. The average *PSNR* of the watermarked image using our approach is around 31.66 dB; in other words, we sustained acceptable visual quality while achieving highly accurate tampering detection.

Table 8. *PSNRs* of the reconstructed image by the different schemes with block size 4 × 4.

Original Images	PSNRs (dB)	
	AMBTC	Proposed Scheme
Couple	31.27	30.38
Boat	31.87	30.89
Zelda	37.99	35.07
Lena	33.23	31.99
Woman	37.98	35.03
Elaine	33.91	32.41
Baboon	28.30	27.78
Lake	29.88	29.21
Peppers	33.43	32.15
Average	33.10	31.66

Table 9 compares the tampering detection performance among three existing schemes and our proposed scheme. The upper bounds of the number of authentication bits in Lin et al.'s scheme [29], Hong et al.'s scheme [30], and the proposed scheme are four, four, and six, respectively. Thus, the proposed scheme obtains higher tampering detection accuracy than the other two with the assistance of one six-bit authentication code per block. The experimental results provide the expected effect; that is, the average *TDR* of our proposed scheme is about 98.55% in the first hierarchical tampering detection procedure, which is about 4.8% higher than those of Lin et al.'s scheme [29] and Hong et al.'s scheme [30]. In other words, our approach can offer a more stable and reliable tampering detection performance. In Lin et al.'s scheme [29] and Hong et al.'s scheme [30], the stego-images' quality with the four-bit authentication code has average *PSNRs* of 33.07 and 32.33 dB, respectively. Also, we can observe that Hong et al.'s scheme [31] proposes two embedding strategies that can embed an eight-bit authentication code into each block, resulting in a *TDR* of 99.61% and average *PSNRs* of 28.92 and 29.84 dB. Meanwhile, with the same size of the authentication code, i.e., six bits, our proposed scheme and the Hong et al. scheme [31] have the same effect with respect to the *TDR*. The average *PSNR* of our approach is 0.39 dB higher than that of the LSBP scheme and 0.05 dB lower than that of the MSBP scheme. Hong et al.'s scheme tries at least six possible combinations to find the minimal distortion during authentication code embedding with MSBP. Therefore, it can be concluded they maintain image quality at the cost of execution efficiency. Also, a large proportion of image authentication methods employ multi-hierarchical tampering detection strategies as a remedial measure to improve their *TDR*. In Table 9, we report the detection performance offered by Lin et al.'s scheme [29], Hong et al.'s scheme [30,31], and the proposed scheme. The four schemes had very similar tampering detection rates after the second hierarchical remediation measure. However, our proposed scheme outperforms the others when considering tampering detection performance and the image quality of the watermarked images from the first hierarchical tampering detection.

Table 9. Tampering detection performance of different schemes.

Methods	Number of Authentication Bits	Hierarchy of Detection Strategies	*TDR* of First Hierarchy (%)	*TDR* of Multi-Hierarchy (%)	Average *PSNRs* (dB)
Lin et al. [29]	4	2	93.75	98.19	33.07
Hong et al. [30]	4	2	93.75	99.83	32.33
Hong et al. [31] (LSBP)/(MSBP)	6	2	98.50	99.66	31.27/31.73
	8		99.61		28.92/29.84
Proposed scheme	6	2	98.55	99.85	31.66

Table 10 summarizes comparisons between the proposed scheme and other work [29–31]. It can be observed that Lin et al.'s scheme generates an authentication code by using a pseudo-random generator, while Hong et al.'s scheme [30] and the proposed scheme do so by hashing the bitmap and location information, and Hong et al.'s scheme [31] generates the authentication by hashing the bitmap and quantization levels' MSBs. Lin et al.'s scheme [29] can resist the cropping attack, constant attack, and collage attack, but is weak against tampering with the bitmap of the complex blocks because it only embeds the authentication code into the quantization levels. The two schemes proposed by Hong et al. [30,31] are sensitive to AMBTC compression codes' attacks since they embed the authentication code generated to refer to the bitmap into the quantization levels. However, in some cases, the natural relationship between two quantization levels is broken for some blocks, making it only possible to verify the authenticity of the AMBTC compression codes and not that of the AMBTC-compressed image. Hence, in their schemes, it seems likely that only professional technicians will be able to implement the cropping attack, constant average attack, or collage attack.

Also, Hong et al.'s scheme [31] is poor against the collage attack. In our approach, we embed the authentication code in the bitmap in a virtual manner and insert the bit-location information into the quantization levels later. This strategy maintains effective interlocking among the authentication code, the quantization levels, and the bitmap. If any slight modifications are encountered in the quantization levels or bitmap, the correlation between them will be broken. Thus, the proposed scheme can not only resist AMBTC compression codes' attacks but also detect the cropping attack, constant average attack, and collage attack. Undoubtedly, the experimental results show that our approach provides more stable and reliable tampering detection performance by simply conducting first hierarchical tampering detection and also sustains acceptable visual quality.

Table 10. Comparisons with various schemes.

Compared Lists	Lin et al.'s Scheme [29]	Hong et al.'s Scheme [30]	Hong et al.'s Scheme [31]	Proposed Scheme
Components to embed *AC*	Quantization levels or bitmap	Quantization levels	Quantization levels	Quantization levels and bitmap
Generation of *AC*	Pseudo-random generator	Hash function	Hash function	Hash function
Detection of the special modification of bitmap	No	Yes	Yes	Yes
Detection of the special modification of quantization levels	No	Yes	Yes	Yes
Detection of the cropping attack	Yes	Yes	Yes	Yes
Detection of the constant average attack	Yes	Yes	Yes	Yes
Detection of the collage attack	Yes	Yes	No	Yes
Authentication for AMBTC compression codes	Yes	Yes	Yes	Yes
Authentication for AMBTC compressed image	Yes	No	No	Yes

Table 11 summarizes comparisons among the proposed scheme and the authentication methods for compressed images using other compression techniques. Herein, the smaller the detectable block size is, the precision the detecting unit is, and the larger the size of AC is, the more tampering detection accuracy it has. We can observe that the JPEG-based authentication schemes [17,18] embed the AC in the frequency domain. Although their schemes provide a better visual quality of the watermarked image, they have a weakness in their tampering detection accuracy because the size of the AC they embedded is one bit and three bits, respectively. It is also apparent that the schemes [18,19] provide a detectable block size of 8 × 8 pixels, which means that a lower precision of the detecting unit they are in. Besides, we also can find that our approach and scheme [19] work on the spatial domain. Our approach provides a better performance in tampering detection and image quality than that of the VQ-based scheme [19]. Moreover, the tamper detection performance of our proposed scheme is significantly better than the existing three schemes. Besides, we also can find that our approach and scheme [19] work on the spatial domain. Our approach provides a better performance in tampering detection and image quality than that of the VQ-based scheme [19].

Table 11. Comparisons with other schemes based on different compression techniques.

Methods	Compression Methodology	Domain	Detectable Block Size	Length of AC for a Block	*PSNR* (dB)
Scheme in [17]	JPEG	Frequency	4×4	1	[40.33, 44.12]
Scheme in [18]	JPEG	Frequency	8×8	3	44.63
Scheme in [19]	VQ	Space	$4 \times 4, 8 \times 8$	[1, 3]	$\approx$[29.00, 31.50]
Proposed scheme	AMBTC	Space	4×4	[1, 6]	[31.66, 33.10]

5. Conclusions

This paper proposed a novel precise image authentication scheme to protect the integrity of AMBTC-compressed images. The authentication code is generated by hashing the processed bitmap and block's location information. For each block, a six-bit authentication code is virtually inserted into the bitmap using matrix encoding. Instead of changing the bitmap, we only recorded the to-be-flipped bit-location information without modifying the bitmap in each block. This bit-location information is embedded into two quantization levels based on adjusted quantization levels matching. Experiments were performed to evaluate the performance of our approach. The results showed that our approach provides more stable and reliable tampering detection performance than previous work and sustains acceptable visual quality. In the future, we will try to use the bitmap adequately to provide strong tampering detection performance while improving image quality. Moreover, we will also pay more attention to the authentication schemes for compression codes.

Author Contributions: C.-C.C. conceived and designed the experiments; G.-D.S. performed the experiments and wrote the paper; and C.-C.L. analyzed the data.

Conflicts of Interest: The authors declare no conflict of interest.

References

1. Schneider, M.; Chang, S.F. A robust content based digital signature for image authentication. In Proceedings of the 3rd IEEE International Conference on Image Processing, Lausanne, Switzerland, 19 September 1996; pp. 227–230.
2. Tabatabaei, S.A.H.; Ur-Rehman, O.; Zivic, N.; Ruland, C. Secure and robust two-phase image authentication. *IEEE Trans. Multimed.* **2015**, *17*, 945–956. [CrossRef]
3. Yan, C.P.; Pun, C.M. Multi-scale difference map fusion for tamper localization using binary ranking hashing. *IEEE Trans. Inf. Forensics Secur.* **2017**, *12*, 2144–2158. [CrossRef]
4. Chen, Z.; Li, L.; Peng, H.; Liu, Y.; Yang, Y. A novel digital watermarking based on general non-negative matrix factorization. *IEEE Trans. Multimed.* **2018**, *20*, 1973–1986. [CrossRef]
5. Walton, S. Image authentication for a slippery new age. *Dr. Dobb's J.* **1995**, *20*, 18–26.
6. Wong, P.W.; Memon, N. Secret and public key image watermarking schemes for image authentication and ownership verification. *IEEE Trans. Image Process.* **2001**, *10*, 1593–1601. [CrossRef] [PubMed]
7. Haouzia, A.; Noumeir, R. Methods for image authentication: A survey. *Multimed. Tools Appl.* **2008**, *39*, 1–46. [CrossRef]
8. Ozyurt, F.; Tuncer, T.; Avci, E. A novel probabilistic image authentication method based on universal hash function for RGB images. In Proceedings of the 2018 International Conference on Computing Sciences and Engineering (ICCSE), Kuwait City, Kuwait, 11–13 March 2018; pp. 1–6.
9. Holliman, M.; Memon, N. Counterfeiting attacks on oblivious block-wise independent invisible watermarking schemes. *IEEE Trans. Image Process.* **2000**, *9*, 432–441. [CrossRef] [PubMed]
10. Zhang, X.; Wang, S.; Qian, Z.; Feng, G. Reference sharing mechanism for watermark self-embedding. *IEEE Trans. Image Process.* **2011**, *20*, 485–495. [CrossRef] [PubMed]

11. Zhang, X.; Xiao, Y.; Zhao, Z. Self-embedding fragile watermarking based on DCT and fast fractal coding. *Multimed. Tools Appl.* **2015**, *74*, 5767–5786. [CrossRef]

12. Chang, C.C.; Lu, T.C.; Zhu, Z.H.; Tian, H. An effective authentication scheme using DCT for mobile devices. *Symmetry* **2018**, *10*, 13. [CrossRef]

13. Dadkhah, S.; Manaf, A.A.; Hori, Y.; Hsssanien, A.E.; Sadeghi, S. An effective SVD-based image tampering detection and self-recovery using active watermarking. *Signal Process. Image Commun.* **2014**, *29*, 1197–1210. [CrossRef]

14. Shehab, A.; Elhoseny, M.; Muhammad, K.; Sangaiah, A.K.; Yang, P.; Huang, H.; Hou, G. Secure and robust fragile watermarking scheme for medical images. *IEEE Access* **2018**, *6*, 10269–10278. [CrossRef]

15. Qin, C.; Ji, P.; Wang, J.; Chang, C.C. Fragile image watermarking scheme based on VQ index sharing and self-embedding. *Multimed. Tools Appl.* **2017**, *76*, 2267–2287. [CrossRef]

16. Fan, M.; Wang, H. An enhanced fragile watermarking scheme to digital image protection and self-recovery. *Signal Process. Image Commun.* **2018**, *66*, 19–29. [CrossRef]

17. Qi, X.; Xin, X. A singular-value-based semi-fragile watermarking scheme for image content authentication with tamper localization. *J. Vis. Commun. Image Represent.* **2015**, *30*, 312–327. [CrossRef]

18. Preda, R.O.; Vizireanu, D.N. Watermarking-based image authentication robust to JPEG compression. *Electron. Lett.* **2015**, *51*, 1873–1875. [CrossRef]

19. Chuang, J.C.; Hu, Y.C. An adaptive image authentication scheme for vector quantization compressed image. *J. Vis. Commun. Image Represent.* **2011**, *22*, 440–449. [CrossRef]

20. Tu, S.F.; Hsu, C.S. A BTC-based watermarking scheme for digital images. *Int. J. Inf. Secur.* **2004**, *15*, 216–228. [CrossRef]

21. Jiang, M.F.; Zhu, N.B. Image fragile watermarking algorithm based on BTC domain. *Sci. Technol. Eng.* **2009**, *9*, 717–720.

22. Yang, C.N.; Lu, Z.M. A Blind image watermarking scheme utilizing BTC bitplanes. *Int. J. Digi. Crime Forensics* **2011**, *3*, 42–53. [CrossRef]

23. Hu, Y.C.; Lo, C.C.; Chen, W.L. Joint image coding and image authentication based on absolute moment block truncation coding. *J. Electron. Imaging* **2013**, *22*, 013012. [CrossRef]

24. Yang, H.; Kot, A.C. Pattern-based data hiding for binary image authentication by connectivity-preserving. *IEEE Trans. Multimed.* **2007**, *9*, 475–486. [CrossRef]

25. Hu, Y.C.; Lo, C.C.; Wu, C.M.; Chen, W.L.; Wen, C.H. Probability-based tamper detection scheme for BTC-compressed images based on quantization levels modification. *Int. J. Secur. Its Appl.* **2013**, *7*, 11–32.

26. Nguyen, T.S.; Chang, C.C.; Chung, T.F.A. Tamper-detection scheme for BTC-compressed images with high-quality images. *KSII Trans. Internet Inf. Syst.* **2014**, *8*, 2005–2021.

27. Lin, C.C.; Huang, Y.; Tai, W.L. A high-quality image authentication scheme for AMBTC-compressed images. *KSII Trans. Internet Inf. Syst.* **2014**, *8*, 4588–4603.

28. Li, W.; Lin, C.C.; Pan, J.S. Novel image authentication scheme with fine image quality for BTC-based compressed images. *Multimed. Tools Appl.* **2016**, *75*, 4771–4793. [CrossRef]

29. Lin, C.C.; Huang, Y.; Tai, W.L. A novel hybrid image authentication scheme based on absolute moment block truncation coding. *Multimed. Tools Appl.* **2017**, *76*, 463–488. [CrossRef]

30. Hong, W.; Chen, M.; Chen, T.S.; Huang, C.C. An efficient authentication method for AMBTC compressed images using adaptive pixel pair matching. *Multimed. Tools Appl.* **2018**, *77*, 4677–4695. [CrossRef]

31. Hong, W.; Zhou, X.; Lou, D.C.; Huang, X.; Peng, C. Detectability improved tamper detection scheme for absolute moment block truncation coding compressed images. *Symmetry* **2018**, *10*, 318. [CrossRef]

32. Nasrabadi, N.M.; King, R.A. Image coding using vector quantization: A review. *IEEE Trans. Commun.* **1988**, *36*, 957–971. [CrossRef]

33. Lema, M.; Mitchell, R. Absolute moment block truncation coding and its application to color images. *IEEE Trans. Commun.* **1984**, *32*, 1148. [CrossRef]

34. Delp, E.J.; Mitchell, O.R. Image compression using block truncation coding. *IEEE Trans. Commun.* **1979**, *27*, 1335. [CrossRef]

35. Zhang, X. Reversible data hiding in encrypted image. *IEEE Signal Process. Lett.* **2011**, *18*, 255–258. [CrossRef]

36. Nguyen, D.V.; Vasic, B. Two-bit bit flipping algorithms for LDPC codes and collective error correction. *IEEE Trans. Commun.* **2014**, *62*, 1153–1163. [CrossRef]

37. Hamming, R.W. Error Detecting and Error Correcting Codes. *Bell Syst. Tech. J.* **1950**, *29*, 147–160. [CrossRef]

38. Chen, K.; Chang, C.C. Real-time error-free reversible data hiding in encrypted images using (7, 4) hamming code and most significant bit prediction. *Symmetry* **2019**, *11*, 51. [CrossRef]

39. Liu, S.; Fu, Z.; Yu, B. Rich QR codes with three-layer information using hamming code. *IEEE Access* **2019**, *7*, 78640–78651. [CrossRef]